

Vibrational spectroscopy of phytochromes and phytochrome-related photoreceptors

vorgelegt von
Diplom-Chemiker
Francisco Javier Velázquez Escobar
aus D.F., Mexiko

von der Fakultät II – Mathematik und Naturwissenschaften
der Technischen Universität Berlin
zur Erlangung des akademischen Grades
Doktor der Naturwissenschaften
– Dr. rer. nat. –
genehmigte Dissertation

Promotionsausschuss:

Vorsitzender: Prof. Dr. Roderich Süßmuth
Berichter: Prof. Dr. Peter Hildebrandt
Berichter: Prof. Dr. Wolfgang Gärtner

Tag der wissenschaftlichen Aussprache: 18. März 2015

Berlin 2015

Al Ingeniero Tarahumara

En el sueño del hombre que soñaba, el soñado se despertó.

Jorge Luis Borges, Las Ruinas Circulares, Ficciones [20]

Publications

Parts of this work have been published in the following articles:

1. F. Velazquez Escobar, D. von Stetten, M. Günther, A. Keidel, N. Michael, T. Lamparter, L.-O. Essen, J. Hughes, W. Gärtner, M.-A. Mroginiski and P. Hildebrandt, *Conformational heterogeneity of the Pfr chromophore in plant and cyanobacterial phytochromes*, *Frontiers in Molecular Biosciences*, submitted (2015).
2. F. Velazquez Escobar, P. Piwowski, J. Salewski, N. Michael, M. Fernandez Lopez, A. Rupp, B. Qureshi, P. Scheerer, F. Bartl, N. Frankenberg-Dinkel, F. Siebert, M.-A. Mroginiski and P. Hildebrandt, *A protonation- coupled feedback mechanism controls the signaling process in bathy phytochromes*, *Nature Chemistry*, in press (2015).
3. F. Velazquez Escobar, T. Hildebrandt, T. Utesch, F.-J. Schmitt, I. Seuffert, N. Michael, C. Schulz, M.-A. Mroginiski, T. Friedrich and P. Hildebrandt, *Structural parameters controlling the fluorescence properties of phytochromes*, *Biochemistry*, **53**, 20–29 (2014).
4. F. Velazquez Escobar, T. Utesch, R. Narikawa, M. Ikeuchi, M.-A. Mroginiski, W. Gärtner and P. Hildebrandt, *Photoconversion mechanism of the second GAF domain of cyanobacteriochrome AnPixJ and the cofactor structure of its green-absorbing state*, *Biochemistry*, **52**, 4871–4880 (2013).
5. B. Zienicke, I. Molina, R. Glenz, P. Singer, D. Ehmer, F. Velazquez Escobar, P. Hildebrandt, R. Diller and T. Lamparter, *Unusual pectral properties of bacterio-phytochrome Agp2 result from a deprotonation of the chromophore in the red-absorbing form Pr*, *Journal of Biological Chemistry*, **288**, 31738–31751 (2013).
6. J. Salewski, F. Velazquez Escobar, S. Kaminski, D. von Stetten, A. Keidel, Y. Rippers, N. Michael, P. Scheerer, P. Piwowski, F. Bartl, N. Frankenberg-Dinkel, S. Ringsdorf, W. Gärtner, T. Lamparter, M.-A. Mroginiski and P. Hildebrandt, *Structure of the biliverdin cofactor in the Pfr dtate of bathy and prototypical phytochromes*, *Journal of Biological Chemistry*, **288**, 16800–16814 (2013).
7. M.-A. Mroginiski, D. von Stetten, S. Kaminski, F. Velazquez Escobar, N. Michael, G. Daminelli-Widany and P. Hildebrandt, *Elucidating photoinduced structural changes in phytochromes by the combined application of resonance Raman spectroscopy and theoretical methods*, *Journal of Molecular Structure*, **993**, 15–25 (2011).

Talks:

1. “*Espectroscopía vibracional de fitocromos bacterianos*”, invited seminar in the *Fernando Goldbaum Group*, Instituto Fundación Leloir, September 18th, 2014, Buenos Aires (Argentina)
2. “*Modulation of the signal transduction activity in bathy phytochromes via photo-induced and thermal cofactor isomerisation*”, invited lecture, *16th International Congress of Photobiology*, Universidad Nacional de Córdoba, September 7–12, 2014, Córdoba (Argentina)
3. “*Análisis del cromóforo del fitocromo en el estado Pfr*”, invited lecture, *Segunda Reunión de Fotobiólogos Moleculares Argentinos GRAFOB II*, Universidad Nacional de Córdoba, October 22–25, 2013, Córdoba (Argentina)
4. “*Elucidating the chromophore structure and protonation dynamics of bathy phytochromes*”, invited lecture, *International Conference On Tetrapyrrole Photoreceptors Of Photosynthetic Organisms 2013*, Huazhong Agricultural University, September 11–15, 2013, Wuhan (China)
5. “*Elucidating the chromophore structure and protonation dynamics of bathy phytochromes*”, invited lecture, *International Conference On Tetrapyrrole Photoreceptors Of Photosynthetic Organisms 2011*, Harnack Haus, July 24–28, 2011, Berlin (Germany)

Poster contributions:

1. “*Cofactor structural changes and protonation dynamics in bathy phytochromes*”, Annual Meeting of the German Biophysical Society, September 23–26, 2012, Göttingen (Germany)
2. “*Resonance Raman Spectroscopy of bacterial and cyanobacterial phytochromes: insights into the chromophore structure*”, International Conference on Tetrapyrrole Photoreceptors of Photosynthetic Organisms 2011, July 24–28, 2011, Berlin (Germany)
3. “*Cyanobacteriochrome AnPixJ: a novel red light induced photoprocess*”, International Conference on Tetrapyrrole Photoreceptors of Photosynthetic Organisms 2011, July 24–28, 2011, Berlin (Germany)

Zusammenfassung

Im dieser Arbeit wurde ein integrierter schwingungsspektroskopischer Ansatz zur Untersuchung der Mechanismen der Licht-induzierten Prozesse in Phytochromen angewandt. Diese Photorezeptor-Proteine binden ein offenkettiges Tetrapyrrol als Cofaktor. Hauptsächlich als kanonische (Pflanzen), prototypische (Bakterien, Pilze), Bathy-Phytochrome (Bakterien) und Cyanobakteriochrome (Cyanobakterien) klassifiziert, regulieren Phytochrome diverse biologische Prozesse (z. B. Blühverhalten, Phototaxis und Pigment-Synthese).

In drei verschiedenen prototypischen Bakteriophytochromen (Agp1, CphB und Rph2) wurden die Chromophor-Strukturänderungen im Laufe des Übergangs vom dunkel-adaptierten (Pr) zum Licht-induzierten Zustand (Pfr) mittels (pre-)Resonanz-Raman (RR) Spektroskopie charakterisiert, die die selektive Chromophor-Banden-Verstärkung gegenüber der Proteinmatrix ermöglicht. Dabei wurde ein allgemeines Temperatur-abhängiges Reaktionsmuster für Pr-zu-Pfr Übergang identifiziert. Die Reaktionsfolge umfasst die Z/E- Isomerisierung (Lumi-R), den Kooplanaritätsverlust (Meta-Ra) und die transiente Deprotonierung des Chromophors (Meta-Rc). Eine spezifische Protein-Faltungsänderung führt endgültig zum Pfr-Zustand. Die Protein- β -Faltblatt-Helikalisierung wurde mittels Infrarot (IR) Spektroskopie bestimmt und ist in Übereinstimmung mit publizierten kristallografischen Daten.

Die RR Pfr Spektrenanalyse erlaubte die Zuordnung von Chromophor-Konformationsheterogenitäten (ZZE) bei prototypischen Phytochromen jenseits der kristallographischen Auflösung. Die Flexibilität an der AB und CD Methinbrücken des Chromophors ist mutmaßlich mit der Deaktivierung des Pfr-Zustands gekoppelt. Im Gegensatz dazu nimmt der Cofaktor eine homogene Struktur im dunkel-adaptierten Pfr-Zustand der Bathy-Phytochrome (Agp2, Pap1) ein. Offensichtlich zwingt die starke Wasserstoffbrückenbindung zwischen der Asp194 Seitenkette und dem Ring D den Cofaktor in eine definierte Geometrie. Dies wurde durch QM/MM-Rechnungen vorausgesagt und experimentell auf Grund des äußerst langsamen Pyrrol-Stickstoff Protonen-Austausches am ring D des Chromophors bestätigt.

Bei den Bathy-Phytochromen sind die Deprotonierung einer Propionsäurenkette des Chromophors und die Strukturänderung der PHY-Domäne (α -Helix-zu- β -Faltblatt) zur Bildung des Licht-aktivierten Pr-Zustandes notwendig. Die (De)aktivierung des Signalmoduls erfolgt über den thermischen Zerfall des Pr-Zustands. Dieser basiert auf der Keto-Enol-Tautomerie am Ring D, welche durch das Säure-Base Gleichgewicht an

der benachbarten HisH278 moduliert wird. Dieser Keto-Enol-gesteuertes Mechanismus bildet wahrscheinlich ganz den entscheidenden Schritt für den thermischen Zerfall Licht-aktivierte Zustände auch bei prototypischen Phytochromen (Pfr-zu-Pr) sowie bei Cyanobakteriochromen dar.

Die Chromophor-Heterogenität im Pr-Zustand von Cph1 Phytochrom wird durch den Protonierungszustand am konservierten His260 gesteuert. Dies wurde an Hand von RR Spektroskopie an Cph1-Varianten, inklusive Chromophor-Isotopomeren und His260-Substitution ermittelt. Weiterhin spielt diese Aminosäure eine wesentliche Rolle während der Chromophor-Reprotonierung im Pfr-Zustand.

Gemäß den RR Spektren, nimmt der Chromophor im dunkel-adaptierten Pr-Zustand des rot/grün-Cyanobakteriochroms ApxJ dieselbe ZZZ-Konformation wie in kanonischen Phytochromen. Die Licht-induzierte Form zeigt eine ähnliche protonierte ZZE-Geometrie wie im Pfr-Zustand. Allerdings ändert die Hydratisierung der Bindungstasche die elektronische Chromophor-Struktur, welches zu einer Blauverschiebung des ersten angeregten Zustandes und der Methin-Streckschwingungsmoden (Pg-Zustand) führt. Wasserzutritt wird durch Trp90 vermittelt, wie von Molekulardynamik-Simulationen vorhergesagt wurde.

Die strukturelle Flexibilität am Ring A und D sowie die Wasserstoffbrückenbindung der terminalen C=O Gruppen steuern in der Rph2-Chromophorbindungsdomänen das Verhältnis zwischen photochemischer Konversion und Fluoreszenz. Veränderungen dieser Parameter mittels spezifischer und zufälliger Mutagenese kann an Hand der Markerbanden im RR Spektrum detektiert werden, was das Design Infrarot-fluoreszierender Phytochrom-Varianten für künftige *in-vivo* Fluoreszenz-Mikroskopie-Anwendungen leiten kann.

Abstract

In the present work an integral vibrational spectroscopic approach was applied to investigate the mechanisms of the photoinduced processes in phytochromes. These photoreceptor proteins bind an open-chain tetrapyrrole as a cofactor. Mainly classified in canonical (plants), prototypical (bacteria, fungi), bathy phytochromes (bacteria) and cyanobacteriochromes (cyanobacteria), they regulate diverse biological processes (e.g. flowering, phototaxis and pigment expression).

The chromophore structural changes during the transition from the dark adapted (Pr) to the light-induced state (Pfr) in three different prototypical bacterio-phytochromes (Agp1, CphB and Rph2) were characterized employing (pre-)Resonance Raman (RR) spectroscopy, thus selectively probing chromophore bands over the protein matrix. A common unidirectional temperature-dependent Pr-to-Pfr reaction pathway was identified. This reaction sequence involves the chromophore *Z/E*-isomerization (Lumi-R), the loss of bilin coplanarity (Meta-Ra) and a transient deprotonation, (Meta-Rc), followed by protein refolding which eventually leads to Pfr state formation. The last step involves a β -sheet-to- α -helix transition, as determined by infrared (IR) spectroscopy in line with published crystallographic data.

Band analysis of the RR spectra of Pfr in prototypical phytochromes allowed the identification of conformational heterogeneities of the chromophore (ZZE) –which are beyond the resolution of protein crystallography. The bilin flexibility at the AB and CD methine bridge is presumably associated with the thermal Pfr-deactivation pathway. In contrast, the chromophore in the dark-adapted Pfr state of bathy phytochromes (Agp2, Pap1) adopts a homogeneous structure, most likely due to the strong hydrogen bonding with the side chain of an adjacent Asp194 residue forces the bilin cofactor into a defined geometry. Hydrogen bond interaction and accurate geometry were predicted by QM/MM calculations and experimentally validated by the extremely slow pyrrole-nitrogen proton exchange at the bilin ring D.

Formation of the light-activated Pr-state in bathy phytochromes involves the deprotonation of the bilin propionic side chain and α -helix-to- β -sheet refolding in the PHY-tongue. Output module (de)activation via the thermal decay of the Pr state is based on a keto-enol tautomerism at the terminal ring D, modulated by an acid-based equilibrium of the nearby His278. This keto-enol controlled mechanism is likely to represent a general decay mechanism of the light-activated states also in prototypical phytochromes (Pfr-to-Pr) and cyanobacteriochromes.

Within the Pr state of Cph1 phytochrome, the chromophore heterogeneity is controlled by the protonation state of the conserved His260, as determined by RR spectroscopy of Cph1 variants including chromophore isotopomers and His260 substitution. This residue plays a crucial role during the chromophore reprotonation in the Pfr state.

According to the RR spectra, the dark adapted Pr state of red/green ApxJ cyanobacteriochrome adopts the same ZZZ-chromophore-conformation as in canonical phytochromes. The light-activated form also displays a similar protonated ZZE-geometry as Pfr; however the electronic structure is altered by an increased hydration of the chromophore pocket, leading to a blue shift of the first electronic transition and of the methine bridge stretching modes (Pg state). Water influx is mediated by Trp90 as predicted by molecular dynamics simulations.

The structural flexibility at the rings A and D as well as hydrogen bonding of the terminal C=O groups control the interplay between photochemical conversion and fluorescence in the Rph2 chromophore binding domain. Alteration of these parameters via site-directed and random mutagenesis is reflected by marker bands in the RR spectrum. Thus, RR spectroscopy may guide the design of infrared fluorescent phytochrome variants for future applications for *in-vivo* fluorescence microscopy.

Contents

Publications	7
Zusammenfassung	9
Abstract	11
Contents	13
Abbreviations	17
1. Introduction	19
2. The phytochrome family	23
2.1. General phytochrome structural properties	24
2.2. Canonical and prototypical phytochromes	30
2.3. Bathy phytochromes	34
2.4. Cyanobacteriochromes	36
3. Materials and Methods	39
3.1. Phytochrome samples	39
3.2. Sample preparation and handling	44
3.3. Absorption Measurements	45
3.4. Theory of vibrational spectroscopy	46
3.4.1. Quantum mechanical treatment of the Raman effect	47
3.4.2. FT-Resonance Raman Spectroscopy	50
3.4.3. FT-Raman Spectrometer Setup	53
3.5. FT-Resonance Raman measuring protocol	54
3.6. Soret-Resonance Raman (sRR) setup and measuring protocol	59
3.7. RR spectra subtraction and fitting procedure	61
3.7.1. Subtraction procedure	61
3.7.2. Component Analysis	63
3.8. FT-IR setup and measuring protocol	64
3.9. Interpretation of phytochrome vibrational spectra	67
3.9.1. Figure notation	68
3.9.2. RR spectral regions	69
3.9.3. RR active chromophore marker bands	71
3.9.4. IR active chromophore bands	72

4. Results: pH dependence of the Cph1 parent states	75
4.1. Analysis of the Pr and Pfr state pH titration	75
4.2. Structural analysis of the Pr-I and Pr-II conformers	81
4.3. Structural analysis of the protonated Pfr state and deprotonated species	87
4.4. pH-dependence of the H260Q mutant	87
4.5. Discussion	90
5. Results: Pr-to-Pfr chromophore changes in prototypical phytochromes	97
5.1. Role of the PHY domain during the Pr-to-Pfr conversion	97
5.2. Assignment of the BC C=C stretching mode in the Pr and Pfr state . .	97
5.3. Temperature-dependent Pr-to-Pfr evolution in Agp1 phytochrome	101
5.3.1. Identification of possible pure intermediate spectra	102
5.3.2. Global analysis Pr-to-Pfr	103
5.3.3. Analysis of the pure component spectra	105
5.4. Pr-to-Pfr conversion in Rph2 phytochrome and PHY domain role . . .	111
5.4.1. Pr-to-Pfr transition and chromophore structure in the Pfr state	111
5.4.2. C=O mode assignment/ amide I in Rph2 and CphB	113
5.4.3. Pr-to-Pfr intermediates of the Rph2 photosensory domain . . .	117
5.4.4. PHY-domain deletion alters intermediate formation	119
5.5. RR Characterization of the CphB Phytochrome	121
5.5.1. Pr-to-Pfr Intermediates	121
5.5.2. Role of the ionic strength towards the Pr-to-Pfr pathway	124
5.5.3. Pr-to-Pfr: ionic strength in Agp1 and Cph1 phytochromes	126
5.5.4. Pfr-to-Pr reverse pathway	128
5.6. Discussion	132
5.6.1. Pr-to-Pfr intermediates in prototypical phytochromes	132
5.6.2. Pr-to-Pfr: chromophore structural changes	133
5.6.3. Role of the PHY-domain during the Pr-to-Pfr transition	135
6. Results: Chromophore structure elucidation in bathy phytochromes	139
6.1. BV in Pfr state bathy and prot. phytochromes	139
6.2. Pr-to-Pfr thermal keto-enol tautomerism	157
7. Results: Pr fluorescence tuning parameters in Rph2 phytochrome	205
7.1. RR investigation of Rph2-phyt. based IRFP-prot.	205
8. Results: Cyanobacteriochromes	233
8.1. Photoconversion mechanism in AnPixJ GAF-only CBRC	233
9. Summary	259
A. Additional setup diagrams and performance measurements	265
B. Supplementary spectra: pH dependence in Cph1 phytochrome	273

C. Supplementary spectra: prototypical phytochromes Pr-to-Pfr reaction	283
D. Supplementary spectra: Pfr and Pr state in bathy phytochromes	295
E. Supplementary data and frequency tables	317
List of Figures	337
List of Tables	341
Bibliography	343

Abbreviations

ABS	absorbance
ALA	α -aminolevulinic acid
ATP	adenosine triphosphate
ATR	Attenuated total reflection
BNC	Bayonet Neill-Concelman
CaF ₂	Calcium fluoride
CBCR	cyanobacteriochrome
cw	continuous wave
DMSO	Dimethyl sulfoxide
EDTA	Ethylenediaminetetraacetic acid
FWHM	full width at half maximum
HeNe	Helium-Neon
HKRD	histidine kinase related domain
LED	Light emitting diode
LHC	Light Harvesting Complex
lwd	long working distance
n. a.	natural abundance
PCB	phycocyanobilin
PSM	photosensory module
PVB	phycoviolobiline
RT	room temperature
SAR	Specific Absorbance Ratio
SC	single channel
SCS	scattering cross section
SEC	Size Exclusion Chromatography
sRR	soret Resonance Raman
TRIS-Cl	tris(hydroxymethyl)aminomethane hydrochloride
TTL	transistor-transistor logic

1. Introduction

Sunlight plays a crucial role for bacteria and eukaryotic organisms, either as energy or information source. In this respect, the distinct spectral ranges are processed for a variety of functions. Moreover, environmental modifications of the light conditions have a strong impact in their development. Hence, it is pertinent to sense, react and eventually adapt to those changes.

On the cellular level, these processes are controlled by a variety of biological photoreceptors. These molecules are composed of a protein matrix and a reaction center, either a metal complex or an organic cofactor. Among these photoreceptors, phytochromes belong to the class of bilin or open-chain tetrapyrrole proteins [27, 50]. Ubiquitous in plants [34, 173], phytochromes are also found in cyanobacteria [87], bacteria [43] and fungi [18, 25, 62, 95, 121]. In plants, phytochromes are involved, *inter alia*, in germination, flowering, shade avoidance and etiolation [27, 108, 121, 142, 160]. In bacteria and cyanobacteria phytochromes regulate phototaxis [148], but also the composition of the light harvesting complex [67, 70]. Finally, phytochrome is involved in the sexual development of fungi [18]. Up to date, over 150 different phytochromes and phytochrome-related proteins have been characterized [149, 155].

The central dogma of the phytochrome family defined the principal reaction as the photoconversion between a dark adapted red absorbing form (Pr state, *e.g.* $\lambda_{max}(\text{Pr}) = 660 \text{ nm}$) and a physiologically active or signaling far red absorbing form (Pfr state, *e.g.* $\lambda_{max}(\text{Pfr}) = 730 \text{ nm}$) [117]. This definition became obsolete with the discovery of further phytochrome-related protein subfamilies: the bathy phytochromes [94] and the cyanobacteriochromes [89, 153]. Unlike any other photoreceptor family, phytochromes cover a wide spectral range from the near-UV to the near IR [151, 152].

Despite the large differences regarding the distinct absorption properties, protein sequence and biological function; the most important features are conserved among all phytochrome proteins. First, all phytochromes contain an open-chain tetrapyrrole as chromophore. Second, phytochromes can exist in two distinct reversibly photoswitchable forms: a dark adapted and a light induced-state, which display distinct absorption properties. Third, the primary photochemical event, involves a double bond isomerization at a methine bridge. Finally, the protein environment of the chromophore pocket possesses largely conserved motifs. The phytochrome protein structure can be divided in an input (sensory domain) and a catalytic or output module (*e.g.* kinase or related activity) [27].

Details on the protein structure and the chromophore geometry are available for the dark adapted or thermally stable states (generally Pr state). While the phytochrome binding domain [12, 210, 216] as well as the photosensory domain [7, 33, 49, 214] have been extensively studied by X-ray crystallography, the complete phytochrome protein structure, including the output module has not yet been determined [13]. These structural data [190, 215], however, do not reveal information about the photo-induced reaction mechanism including the involvement of proton translocations. Here, spectroscopic techniques, such as (transient) absorption [23], NMR [157], and vibrational spectroscopies are required [53, 79, 171, 217]. These methods have substantially expanded the knowledge about the underlying molecular events and their dynamics.

Among them, vibrational spectroscopic methods are very instructive and reveal detailed structural information both on the chromophore and the protein. Resonance Raman (RR) spectroscopy is suitable for selectively probing the vibrational modes of the chromophore [53, 119, 129]. Complementary cofactor information as well as protein-structural changes can be elucidated by difference infrared (IR) spectroscopy [57, 171]. In combination with theoretical methods [130, 159] and backed by 3D structural data from crystallography [49, 214], vibrational spectroscopy integrates the elucidation of structural details and dynamic processes towards a comprehensive structure-function understanding of phytochrome proteins [206–208].

Building upon these recent developments, the present thesis was dedicated to contribute to a deeper understanding on the mechanism of the photoinduced processes of phytochromes, using an integral vibrational spectroscopic approach. Special emphasis is laid on several key topics that are essential for elucidating the molecular basis of the photoreceptor function. First, the parent states of several phytochromes were studied taking advantage of the fact that specifically resonance Raman spectroscopy is sensitive to structural details of the chromophore and its immediate environment that are beyond the resolution of protein crystallography. These are, for instance, conformational heterogeneities and proton-dependent equilibria which both may have a strong impact of the thermal and photochemical reactivity of the chromophore (chaps. 4 and 6). These investigations also aim at identifying those structural parameters that govern the photophysical properties of the chromophore, such as the relationship between photochemical conversion and fluorescence and the control of the excitation energies (chaps. 8 and 7). Second, the photoinduced conversions between the parent states were investigated for various phytochromes to identify common mechanistic patterns. These studies also include the analysis of the thermal decay mechanism of the light-induced state and its relationship with the (de)activation of the output module (chaps. 5 and 6).

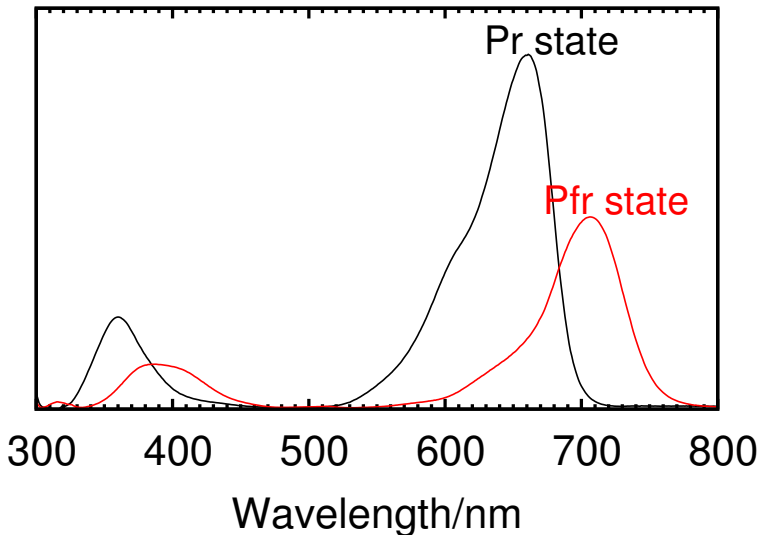


Figure 1.1: Absorption spectrum of prototypical phytochrome Cph1 (Cph1Δ2 deletion mutant) in the dark adapted Pr and in the light-induced Pfr state (red).

2. The phytochrome family

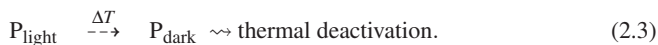
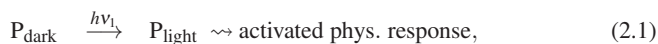
The phytochrome family comprehends nowadays a wide manifold related biliproteins [149]. Originally found in plants [21, 34], the number of characterized phytochrome-related proteins has substantially increased, leading to an expanded structural and spectroscopic variety [43, 87, 89].

Hence, the general phytochrome concept was redefined considering the following shared properties. First, all photoreceptor proteins –within the extended phytochrome family– bind an open chain tetrapyrrole as cofactor and photo-switchable sensor. Second, upon light absorption, photo-conversion between a dark adapted and a light-induced state takes place. In this respect, phytochrome proteins are clustered according to their structural and spectroscopic properties. Further categorization based on the functional diversity is not considered since such classification exceeds the current spectroscopic approach. In this work, phytochromes are catalogued according to the following sub-families:

- **Canonical phytochromes** This is the core group within the phytochrome family, comprising only the distinct plant phytochromes [24, 27].
- **Prototypical phytochromes** All other proteins with spectroscopic similarity to plant phytochromes [87, 112, 143], including photoconversion between the dark adapted Pr to the far red absorbing Pfr form.
- **Non-canonical phytochromes** Further related proteins with structural similarities to the canonical and prototypical phytochromes (*e.g.* protein sequence) but diverse spectroscopic properties are gathered in this subgroup. These phytochromes are typically found in non-photosynthetic [15] and photosynthetic bacteria [67] and fungi [18]. The most prominent non-canonical subfamily refers to the bathy phytochromes [94, 193]. Unlike prototypical phytochromes, the Pfr form is the dark adapted parent state [214].
- **Cyanobacteriochromes** This recently discovered phytochrome subfamily [220], refers to chromoproteins with highly diverse photochemical properties. In general, the most common phenotype is addressed to the light-dependent acclimation in cyanobacteriochromes [149]. Like prototypical phytochromes in cyanobacteria, the cyanobacteriochromes (CBCRs) attach the same tetrapyrrole as chromophore precursor [150] (*vide infra*). However, subsequent chemical modifications of the bilin moiety or its immediate environment constitute a wide

range of bimodal protein sensors with diverse electronic properties covering the complete UV/visible spectral range (300–700 nm) [89].

Phytochrome central dogma All phytochrome and related proteins are generally synthesized in the dark adapted form (red light-absorbing Pr form in canonical and prototypical phytochromes). Subsequent light absorption of the suitable wavelength $h\nu_1$ triggers the photochemical interconversion to the active form which is either batho- or ipsochromically shifted (far red-light absorbing Pfr form). Subsequently the reverse conversion from the active to the dark adapted phytochrome form is either promoted by the appropriate light absorption $h\nu_2$ or through a thermal reaction, thus cancelling or deactivating the signaling response of the light induced form.



In plant phytochromes the Pfr state is the active or signaling form. Supporting evidence of the canonical central dogma has been gathered for years [27, 37, 64, 168]. Signaling activity for related proteins is still matter of extensive research and due to its complexity it cannot be addressed in a general way. Yet, the strong dependence of the light-activated phytochrome form and its signaling function certainly applies for every phytochrome. A general description of the signal transduction pathways in plant phytochromes is given below (see section 2.2).

2.1. General phytochrome structural properties

Phytochrome nomenclature Based on the diversity of the phytochrome family and due to the increased number of recently characterized related photoreceptor proteins, a universal and consistent nomenclature for proteins within the extended phytochrome family is still lacking. In the past years, an nomenclature was developed by unifying a phylogenetic and a biochemical characterization of the phytochrome super family [27]. For the sake of simplicity, yet most importantly to provide continuity to the work of previous vibrational spectroscopy investigations [73, 102, 118, 183, 184, 189, 205], the four-letter-code for the phytochrome nomenclature was consecutively implemented. For example, the notation Pap1 refers to *Pseudomonas aeruginosa* phytochrome 1 [188]. In the literature this phytochrome is found under the designation PaBphP. In

this respect, the last letter-code provides a specific notation if more phytochrome proteins are found in the same organism. In case of the cyanobacteriochromes, the existing nomenclature was modified to fulfill the four-letter-code consensus. In some specific cases, for example, AnPixJ was shortened to ApxJ and TepixJ to TpxJ. Hence, and unless specified differently, this type of protein nomenclature was generally applied along the current work.

In addition, a complementary notation allowed the correct identification of mutants. For example, the deletion mutant of the cyanobacterium phytochrome 1 –lacking the signaling module, was denoted Cph1 Δ 2. Furthermore, for the proper denomination of full-length or wildtype species the suffix ‘-WT’ complemented the four-letter code. For example in case of the wildtype protein of Pap1, it is referred to Pap1-WT. Specific suffix notations and exceptions are extensively described in section 3.1.

Protein domains Plant, cyanobacterial, bacterial and further related proteins consist of a *N*-terminal photosensory [121] and a *C*-terminal regulatory or catalytic module [219]. Some examples of the protein domain arrangement are displayed in fig. 2.1. The final signal transmission occurs at the *C*-terminal regulatory module. Here the phytochrome catalytic activity is given by a histidine-kinase or related domain (HK or HKRD) [15, 70, 84, 94, 110, 193, 218]. This domain exhibits an ATP dependent phosphate transferase activity. As already mentioned, the signaling mechanism in plant phytochromes significantly differs from other organisms.

In general, the *N*-terminal photosensory module is composed of three domains: PAS (PER/ARNT/SIM), GAF (derived from “cGMP-specific phosphodiesterase”, “cyanobacterial Adenylate-cyclase” and “formate hydrogen lyase transcription activator, FhlA”) and PHY domain (Phytochrome domain). In the literature, the PAS domain is also denoted as PLD (PAS-like domain). The PER/ARNT/SIM nomenclature refers to “period clock protein” (PER), “aromatic hydrocarbon receptor nuclear translocator” (ARNT) and “single minded protein” (SIM). It has been shown that PAS and GAF domains possess related protein folding [82].

The full sequence of canonical phytochromes is generally defined as PAS-GAF-PHY-HKRD construct. Thus, for chromophore attachment only the chromophore binding domain (CBD) is required. This comprehends solely the lyase-active PAS-GAF module. In plant phytochromes, the photosensory module includes an additional *N*-terminal domain (see fig. 2.1), characterized by its serine-threonine-rich sequence (S/T or P1 domain) [9, 121]. Bacterial and cyanobacterial proteins lack *C*-terminal regulatory PAS-domains. This protein constructs play a crucial role in plant phytochrome homodimerization [9]. Nevertheless, there seem to be some exceptions in the bacterial phytochrome subfamily. For example, the full structure of the Rph1 phytochrome (*Rhodospseudomonas palustris* phytochrome 1, also known as RpBphP1) presents no

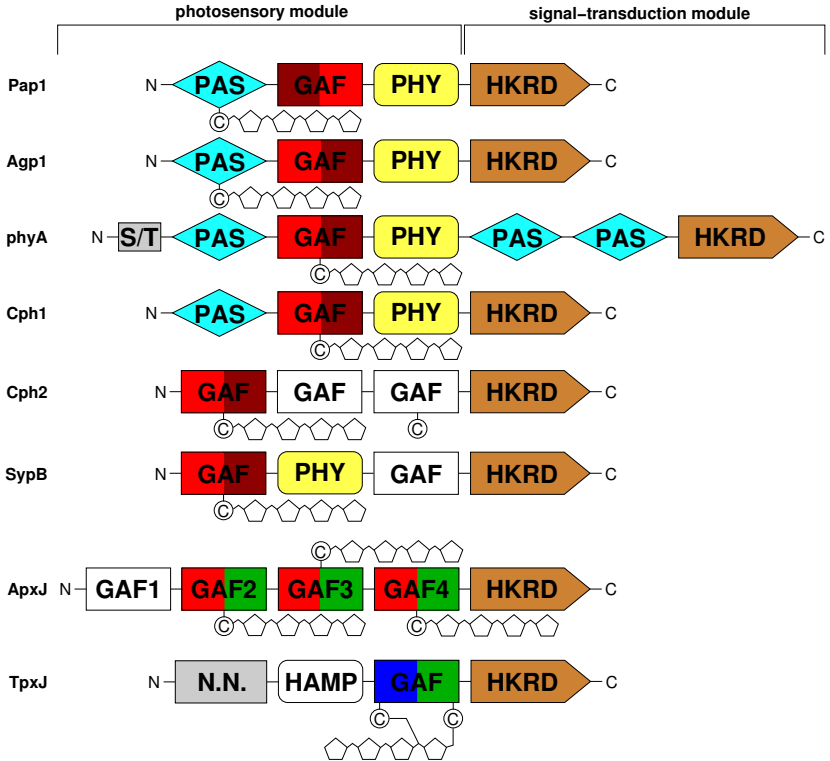


Figure 2.1: Protein structure arrangements in different phytochrome variants. The plant phytochrome phyA represents the most relevant species and is therefore considered as reference for further comparisons. The different domains PAS, GAF, PHY, HKRD and others are shown according to the N- to C-terminal phytochrome sequence. Almost all phytochrome variants hold only a single chromophore binding site at a conserved cysteine residue (either at the PAS or GAF domain). Cyanobacteriochrome proteins might either bind the chromophore over a second cysteine (TpxJ) [150] or bind more than one chromophore per single protein (multi-GAF-domain cyanobacteriochromes, e.g. ApxJ) [89]. In addition to that, cyanobacteriochromes differ from canonical phytochromes at the C-PAS domain region [149]. The different absorption properties for each protein are indicated by the coloring in the GAF-domain box. Adapted from ref. [27, 89, 184].

histidine-kinase activity in the regulatory module [13]. On the other hand, light signaling occurs over a PAS/PAC-HOS (two Helix Output Sensor). Apparently, the existence of a PAS-sequence in Rph1 might be considered as part of the missing link from the *N*-terminal photosensory domain between plant and bacterial phytochromes.

Chromophore attachment in plant and cyanobacterial phytochromes occurs at a conserved cysteine in GAF domain (phyA and Cph1 in fig. 2.1). In contrast to that, the covalent bilin assembly in bacterial phytochromes (Agp1 and Pap1) takes place at the PAS domain [112, 193]. In cyanobacteriochromes the chromophore attachment also happens in the GAF domain. Furthermore, the spectral properties of certain cyanobacteriochromes, like in TpxJ from *Thermosynechococcus elongatus* (blue \rightleftharpoons green photoconversion) are additionally tuned by a second bilin attachment site within the GAF-sequence [154, 203]. Bipodal chromophore attachment as well as specific bilin-protein interaction lead to a wide-range of spectral properties solely observed in the cyanobacteriochrome family [81, 89, 91, 134, 220].

Despite the wide diversity in the cyanobacteriochrome family, several examples of red/far-red proteins have been found. Some of them show interesting structural deviations from the protein-domain arrangement in canonical phytochromes. Intramolecular light signaling in canonical phytochromes is modulated by the PHY-domain [148]. In contrast, light signaling in the cyanobacterium phytochrome 2 (Cph2) occurs over a multi-GAF domain arrangement [7, 121]. In addition, Cph2 also lacks the *N*-terminal PAS-domain. In agreement with that, the *Synechococcus* phytochrome B (SypB) also lacks these canonical protein domains. Yet, in contrast to Cph2, the wildtype SypB sequence contains the PHY-motif. Here, and alike canonical phytochromes, deletion of the characteristic phytochrome domain still leads to a photo-active protein. Thus the far-red-absorbing photoproduct lacks the conserved spectroscopic characteristics of a canonical Pfr form [39, 179, 204]. Interestingly, the regulatory function in the native form of Cph2 and SypB is addressed to HKRD domain (see fig. 2.1).

Even with the structural and functional differences among all phytochromes, the GAF motif is highly conserved and it therefore plays a crucial role in the chromophore assembly.

Chromophore Like α -phycoyanine and allophycocyanin, phytochrome apoproteins bind an openchain tetrapyrrole molecule with a highly conjugated π -system [174]. Plant phytochrome assembly phytochromobilin (P Φ B) as native chromophore [177], whereas phycoyanine and cyanobacterial phytochromes assemble phycoyanobilin as a cofactor [87]. In contrast to cyanobacteria and other photosynthetic organisms [11], fungi and non-photosynthetic bacteria lack the ferredoxin-dependent phytylkinase pathways (*vide infra*). Both are necessary for biliverdin to P Φ B [58, 105] or PCB reduction [59]. However, several phytochrome-related genes in bacteria have

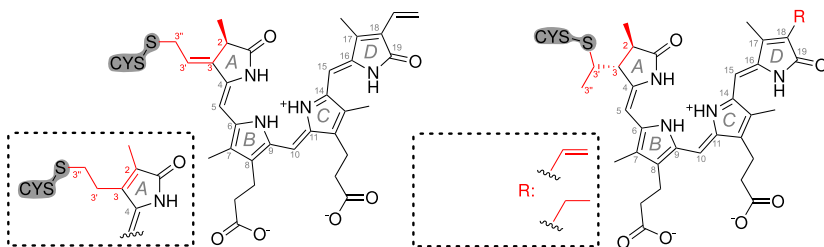


Figure 2.2: Structural formula of all chromophore precursors: BV, PΦB and PCB. All bilin molecules are displayed in the ZZZssa geometry. Differences in the side chain groups (rings A and D) are indicated in red. Ring nomenclature is given in gray.

been classified. In these organisms, biliverdin IX α was identified as native chromophore for bacterial phytochromes [15].

All three different chromophore precursors display a similar structure, especially concerning rings B and C and the herein attached propionic side chains. Here the main difference is found in the double bond character of rings A and D. In addition, ring A in PΦB and PCB chromophore already contains a chiral center (methyl group at the C₂-position), thus the given stereo-information might be involved in the specificity of the chromophore photo-isomerization [154].

The diverse tetrapyrrole molecules are degradation products of the oxidative haem metabolism. Here, BV is the first product, synthesized by enzymatic haem cleavage at the α -position. The reaction takes place at a ferredoxin-dependent haem oxygenase (HO or HOx) [58, 194]. In cyanobacteria BV is subsequently converted to PCB by the ferredoxin dependent bilin reductase of the PcyA family. The reduction pathway follows a four-electron mechanism [59]. Higher plants transform BV to PΦB over a two-electron reduction pathway. Here, the enzymatic reaction involves a bilin-reductase-phytochromobilin-synthetase (HY2) [105].

Pyrrole ring nomenclature is indicated in fig. 2.2. The denomination follows in alphabetic order starting with ring A where the chromophore-protein attachment takes place. Subsequent rings are denoted B, C and D. In this respect the notation AB, BC and CD refer to the methine bridge located between the corresponding two adjacent pyrrole rings. The chromophore geometry is given in respect to the double bond configuration (*Z/E* or *ger. entgegen/zusammen*) and the single bond conformation (*a/s* or *anti/syn*) of each of the three methine bridges. As a result of this notation, the chromophore geometry can be then adequately described for each state or intermediate along the phytochrome photocycle, *e.g.* in the Pr state normally the chromophore is

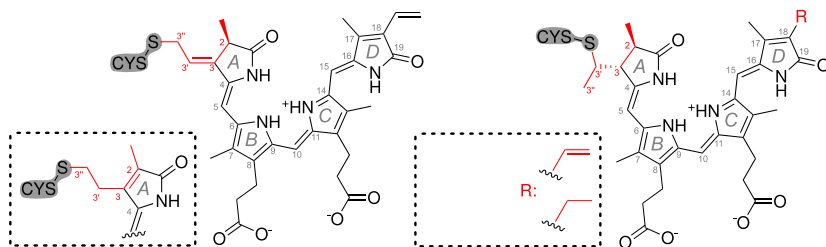


Figure 2.3: Different types of chromophore attachment to the phytochrome-apoprotein. Left panel: two distinct thioether linkages. In both cases, attachment occurs via a conserved cysteine residue at the PAS domain. BV attachment at $C_{3'}$ -atom in prototypical phytochromes leads to an exocyclic double bond rearrangement. Bathy phytochromes bind BV over endocyclic retention of the ring double bond (left side inset). Here the conjugated character in ring A prevails. In contrast, plant (PΦB) and cyanobacterial phytochromes (PCB) bind the chromophore at the $C_{3'}$ -atom.

found in the ZZZ_{ssa} geometry, whereas in the Pfr state the cofactor adopts a ZZE_{ssa} structure.

After chromophore assembly, the ring A is chemically altered. These structural modifications differ depending on the organism and chromophore type (see fig. 2.3). In general, the bilin-attachment follows a nucleophilic addition reaction pathway. In case of PCB and PΦB-binding phytochromes, the cysteine-thiol-residue ($R-S^-$) binds the chromophore at the C_3 -atom. In contrast to that, BV-binding phytochromes differ in the binding mechanism. In both cases the chromophore attachment occurs at the $C_{3'}$ -atom. In addition, a double bond rearrangement occurs in prototypical BV-phytochromes leading to a saturated ring A with a sp^3 -(R)- C_2 -atom (carrying a methyl residue) and exocyclic double bond at C_3 and $C_{3'}$. Chromophore assembly in bathy phytochromes occurs also at the $C_{3'}$ -atom of the BV cofactor, but the double bond in ring A is conserved.

The elucidation of the proper chromophore attachment in PCB and BV-binding phytochromes has been strongly supported by the availability of crystal structures [49, 210, 214, 216]. Yet X-ray radiation damage, certainly compromises the electron-density interpretation [209], since the thioether linkage is easily degraded after radiation exposure [36]. A combined experimental and theoretical Raman spectroscopic approach [159], has strongly contributed not only to the assignment of the gross chromophore structure, but also provided conclusive information concerning the chromophore-protein assembly.

2.2. Canonical and prototypical phytochromes

In all canonical and prototypical phytochromes, the chromophore adopts a ZZZssa in the Pr and the ZZEssa geometry in the Pfr state. Furthermore, the cofactor is fully protonated in both parent states. The model of the plant phytochrome photocycle seems to satisfactorily describe the light-induced events in prototypical species. In this respect, a transient proton translocation and a specific protein-folding step play generally a crucial role in the intramolecular signaling between the sensory and signal-transduction module [33, 190].

Pr chromophore structure The availability of X-ray Pr structures in bacterial [12, 161, 209, 210, 216], cyanobacterial [7, 49, 115] and plant phytochromes [32] provided a reliable picture of the cofactor-protein interaction, as well as the general understanding of the protein folding situation. The binding pocket in all Pr structures seems to be largely conserved. Smaller differences refer to the distinct chromophore attachment, ring A hybridization, tilt-angle of ring D and vinyl (ethyl) side chain and ring B and C propionic side chain orientation. Detailed description of the crystallographic works can be found in the given references. An insight picture of the chromophore binding pocket is shown in fig. 2.4. Important features are the pyrrole water, the conserved residues in the binding pocket and the PHY-domain tongue motif, which seals the binding domain and has also a relevant function in the signaling pathway.

Unavailability of the Pfr structure The intrinsic lability of the signaling Pfr state in canonical (prototypical) phytochromes aggravates crystallization. A recent crystallographic study on the Pr-to-Pfr folding transition in *Deinococcus radiodurans* phytochrome (Dph1) contributed to the understanding of the primary signaling events, thus uncovering the relevance of the tongue motif in the PHY domain (*vide infra*) [33, 190]. The Pfr formation is intimately linked to the β -sheet-to- α -helix transition of the tongue motif. However the chromophore structure could not be resolved. Thus, the Pfr structure of the bathy phytochrome from *Pseudomonas aeruginosa* (Pap1) provides the most detailed structural picture of the protein and chromophore moiety in that state [214]. The bathy Pfr state is thermally stable, whereas prototypical phytochromes manifest a Pfr-thermal lability, due to the dark reversion to the initial Pr state (*vide infra*). Thus, a fundamental difference in the chromophore-protein interaction between the prototypical and the bathy Pfr state cannot be ignored. In this respect the structural information provided by spectroscopic methods plays a crucial role in the elucidation of the canonical Pfr bilin structure and the cofactor-protein interaction. A putative AB methine bridge E-isomer [197] was initially postulated for the far red absorbing state in the shortened GAF-only SypB cyanobacteriochrome. However this protein-fragment lacks

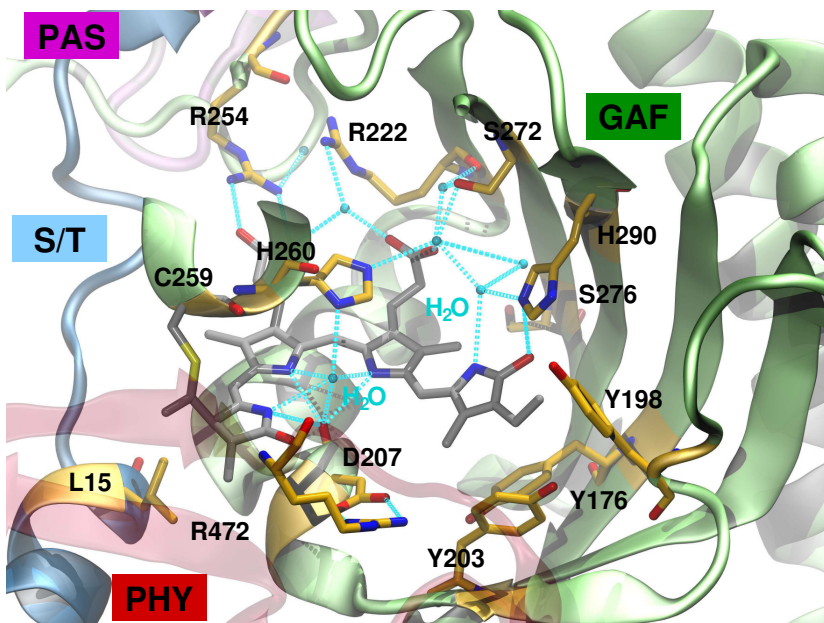


Figure 2.4: Detailed view of the chromophore pocket in the Cph1 Δ 2 Pr crystal structure (2VEA) [49]. The ZZZssa PCB chromophore structure and the binding site C259 are displayed in gray. Conserved residues are shown in yellow. Crystal water molecules are displayed in cyan. In addition, the BV-binding site of bacterial phytochrome is displayed; however, this residue is naturally mutated to a lysine (K15) in Cph1 Δ 2. Also shown is the protein structure including the C-terminal S/T (blue), PAS (purple), GAF (green) and PHY domains (tongue motif shown in transparent red). The figure was generated using VMD 1.86 and rendered using the TACHYON package (also in fig. 2.6 and 2. 7) [88].

the PHY-domain, which stabilizes the correct Pfr formation. Secondly, the AB-double bond isomerization is highly unfavourable and very unlikely to occur [179].

In canonical phytochromes, the high flexibility of the chromophore induces a certain degree of structural heterogeneity for both parent states [98, 100, 136, 159, 185].

Phytochrome photocycle All canonical and prototypical phytochromes convert from the dark adapted Pr form to the signaling Pfr state [27]. In case of plant phytochromes, this involves also migration from the cytosol to the cell nucleus as a further step in the signaling cascade [9, 177]. The photocycle comprehends two photo-induced pathways: the Pr-to-Pfr and back reaction (Pfr-to-Pr). The first step in both directions is a chromophore photo-isomerization at CD Z/E (E/Z) methine bridge C₁₅=C₁₆ double

bond (see fig. 2.3). In the Pr-to-Pfr transition, intermediate states formation is associated with protein folding events as well as transient chromophore-proton translocation that precedes the formation of the Pfr state. The back reaction occurs over a different pathway and intermediate states.

The phytochrome photocycle and the corresponding parent and intermediate states are described according to the phyA photocycle nomenclature [26, 28, 46, 47, 199]. Photoisomerization from the initial Pr state to Lumi-R takes place via a short-living excited state (excited state decay in 100-500 fs) within 20-100 ps (fig. 2.5) [100]. Lumi-R is associated with a very low quantum-yield, since the steric constraints at the conical intersection of the Pr*/Lumi-R* potential surfaces favors the Pr back formation [42]. The Z/E-isomerization leads to a highly tensed chromophore structure [5, 6]. As expected, larger protein rearrangements are not observed [57]. According to cryogenic experiments this intermediate species is observed in a wide range between $-190\text{ }^{\circ}\text{C}$ and $-100\text{ }^{\circ}\text{C}$ [40, 46, 102].

The Lumi-R intermediate subsequently decays thermally to the Meta-Ra species. The chromophore is found in a more relaxed ZZE-geometry and the pocket partially adapts to the photo-induced changes of the chromophore. Hence, protein residues reorient preparing the protein moiety to even larger structural changes. The Meta-Ra has a longer decay time (ns to μs). In terms of cryogenic trapping, this corresponds to a temperature range from $-100\text{ }^{\circ}\text{C}$ to $-60\text{ }^{\circ}\text{C}$. Prior to the Pfr state formation, the chromophore is transiently deprotonated in the Meta-Rc state. Thus, losing its cationic nature at rings B and C and adopting a more distorted geometry. The protein moiety experiences long-range folding events. The Meta-Rc lifetime is in the longer μs and lower ms range. Thermally the Pr-to-Pfr conversion is blocked in the Meta-Rc intermediate between -40 and $-20\text{ }^{\circ}\text{C}$.

In a similar way as in the Pr-to-Pfr reaction, the E/Z-photoisomerisation in the Pfr-to-Pr pathway leads to the formation of the Lumi-F intermediate [38], subsequent decay to the Meta-F also involves major residue reorientation as in the Meta-Ra intermediate. Unlike the forward reaction, a transient deprotonation of the chromophore at the Meta-F(a) level, has not yet been observed. Characterization of the reverse photoreaction is technically challenging, therefore it is considerably less explored than the forward pathway. The Pfr-to-Pr pathway has been studied using different spectroscopic techniques. In addition to the characterization of the absorption properties [98], vibrational spectroscopy [6, 55, 119] and NMR [156] have achieved considerable progress towards understanding the structural changes along the reverse pathway.

Photocycle kinetics Similar to the photocycle in plant phytochromes [5, 66, 107], also in bacterial phytochromes the quantum yield for the Pr \rightarrow Pfr conversion (0.078 for Agp1) is considerably higher than for the backreaction Pfr \rightarrow Pr (0.004) [112, 164]. In

contrast to that, the quantum yield for cyanobacterial Cph1 is equal (0.16) in both directions [195]. Temperature plays a crucial role for the photoinduced Lumi-R (Lumi-F) formation and the subsequent in Pr→Pfr conversion (Pfr→Pr). From cryogenic trapping experiments, it is known that the forward photoinduced reaction in plant phytochrome is hindered at $-140\text{ }^{\circ}\text{C}$. In other prototypical phytochromes, the conversion only occurs at temperatures above $-100\text{ }^{\circ}\text{C}$ and trapping of the first red intermediate has not been achieved [56, 102, 145, 205]. Different phytochrome proteins (Agp1 [23], Cph1 [78, 195, 198], CphA [92], Rph3 [201] and phyA [17, 131]) display comparable number of relaxation steps and decay constants after excitation of the Pr state. For the wild type Agp1 phytochrome the decay steps defined as Lumi-R→Meta-Ra, Meta-Ra→Meta-Rc, Meta-Rc→Pfr occurred with time constants of 230 μs , 3.1 ms and 260 ms, respectively [23]. In plant and Cph1 phytochrome a similar relaxation profile during the Pr-to-Pfr conversion was observed [145, 146, 195]. As derived from kinetic isotope effect for all three relaxation steps, proton transfer takes place during the Pfr formation [23].

Kinetics of the thermal reversion In addition to the light-induced isomerization from the signaling state (Pfr state in canonical and prototypical phytochromes and Pr state in bathy phytochromes) to the dark adapted form, a thermal deactivation pathway (see fig. 2.5) involves CD methine bridge isomerization via enolization of the lactam group at ring D (keto-enol or lactam-lactim transition). This pathway has been postulated [155], however only recently a spectroscopic proof was obtained (see section 6.2 or ref. [207]). The thermal reaction occurs on a considerably larger time scale than the photoinduced process. For the thermal Pr-to-Pfr decay in bathy phytochromes, time constants may vary from minutes to several hours.

Phytochrome signaling After light sensing via the chromophore, intramolecular signaling occurs probably via a proton-coupled protein refolding mechanism, thus activating the C-terminal catalytic module. The phytochrome signaling mechanism in plants opposes the mechanism in cyanobacteria. Bilin attachment to plant phytochrome inhibits N-terminal Ser/Thr-kinase signaling and red light activates C-terminal histidine-kinase signaling. Whereas cyanobacterial signaling is first activated by bilin attachment and interrupted after red light sensing. Signal transduction in bacterial phytochromes is primitive and comparable to the pathway in cyanobacteria. In all organisms, C-terminal autophosphorylation is dependent on the homo-dimerization of phytochrome molecules. Bacterial phytochromes lacking catalytic activity interact with kinase-related response regulator(s), thus activating the phosphorylation mechanism. Output signals are transferred then from the regulator partner or target cluster. Plant phytochrome signaling is more sophisticated, involving a still unknown number

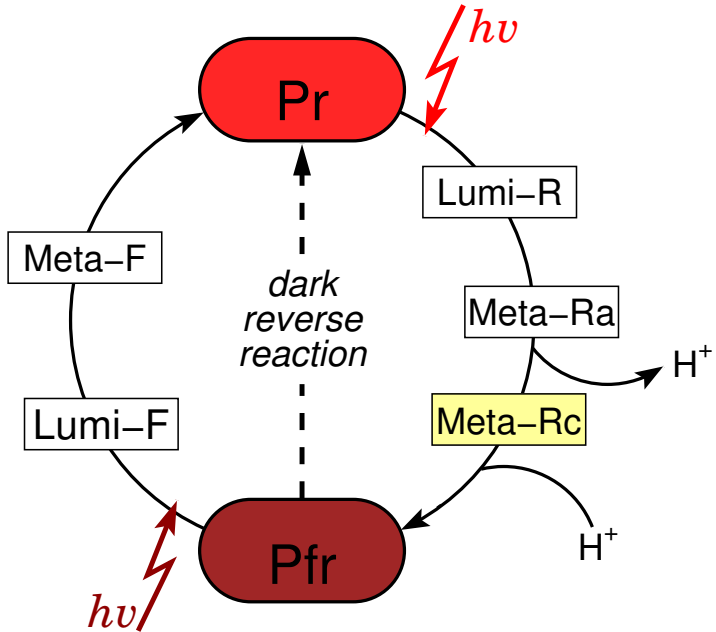


Figure 2.5: Photocycle of canonical and prototypical phytochromes. After absorption of red light (far red light), the Pr state (Pfr state) undergoes a photoconversion to the Pfr state (Pr state). Alternatively, the Pfr-to-Pr reaction occurs over a thermal pathway (dark conversion, dotted line) [60, 155].

of complex steps of downstream signaling components as well as nuclear translocation events [27].

2.3. Bathy phytochromes

Pfr state and photocycle Unlike canonical phytochromes, the dark adapted state of bathy phytochromes is the Pfr state [94]. A detailed structural characterization of the bilin geometry (see ref. [214]) was provided for the Pfr state in *Pseudomonas phytochrome* (Pap1) bathy phytochrome, as well as for the early photoinduced intermediates [215]. The chromophore structure in the Pfr state of Pap1 is found to be almost identical as in *Agrobacterium tumefaciens* phytochrome 2 (Agp2, see fig. 2.6) [159]. Despite the distinct chromophore geometry, the Pap1 Pfr structure showed interesting differences to the canonical Pr structure. First, a strong hydrogen bonding of the chromophore's ring D to the aspartate of the conserved DIP motif was found. Second, instead of a

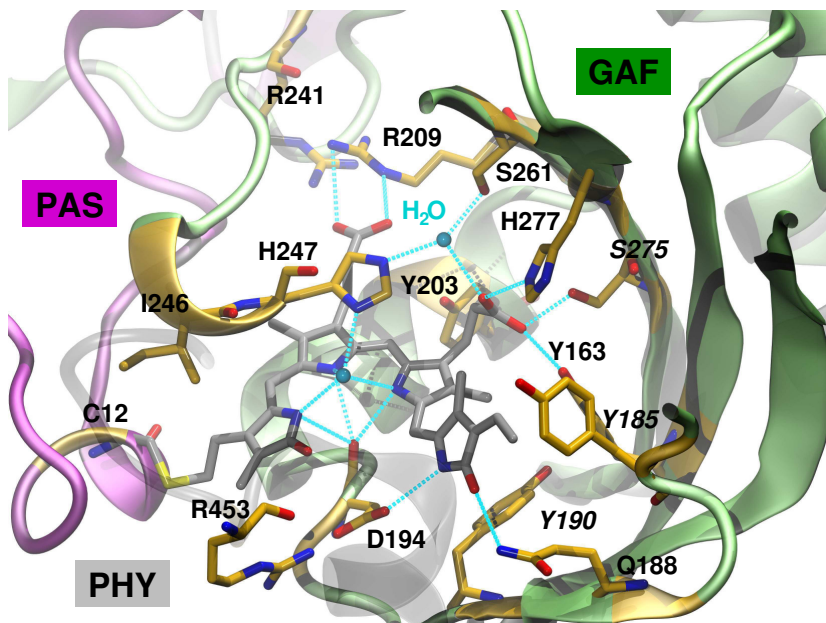


Figure 2.6: Chromophore pocket of Pap1 bathy phytochrome (3C2W). Most interesting features are the DIP-aspartate interaction with ring D. Color code of the structure representation followed that of fig. 2.4; in addition, the distinct folding of the tongue (PHY domain) is highlighted in transparent gray. Residues Q188 and Y203 were solely observed in Pap1 but not in Cph1 Δ 2. The binding pocket of Agp2 displays a strong homology to Pap1; however the natural mutations Y185F, Y90F and S275A provide a more hydrophobic environment for the D ring than in Agp2.

β -sheet, the PHY-tongue exhibits an α -helix. Furthermore the elucidation of the intermediate Lumi-F structures in Pap1 allowed for the understanding of the chromophore moiety and propionic side chains, as well as reorientation of key residues in the binding pocket. The main event of the Pfr-to-Lumi-F transition is the E/Z isomerization and the breakage of the ring D and DIP-aspartate bonding. However, the low-resolution difference structures of the intermediates are associated with considerable uncertainties. The Pfr-to-Pr reaction is related to the prototypical pathway since in the Lumi-F, Meta-F and Pr transitions presumably occur without proton-translocation. The photo-induced reverse pathway has been studied [221]. However, a detailed structural elucidation is still not available.

A recent structure of the bathy phytochrome *Rhodospseudomonas palustris* phytochrome 1 (Rph1), containing a fraction of the signaling domain, was determined, how-

ever the low resolution of relevant structural motifs impedes a reliable comparison with any phytochrome structure [13].

2.4. Cyanobacteriochromes

While steadily new cyanobacteriochromes (CBCRs) are discovered and identified [45, 149], structural details and photochemical properties of these proteins yet remain unresolved. Most prominent proteins are red/far red, red/green and blue/green CBCRs (see fig. 2.1). Within the red/green and blue/green proteins, the nature of the parent state can vary. For example, the dark adapted state of SyCikA is the Pg state containing a ZZZssa chromophore [134]. The dark adapted state in AnPixJ is the Pr state [132]. However, the chromophore adopts also a ZZZssa geometry [133]. Thus, two largely similar chromophore structures are associated with different spectroscopic properties. Here, the chromophore pocket plays a crucial role tuning the π -electron system of the chromophore, either via electrostatic interactions or like in the blue/green CBCRs through additional transient covalent chromophore-protein bonds ([89, 153, 203]). In this case, different blue/green and green/blue proteins have been identified. Most prominent is the TePixJ (TpxJ), with a dark adapted Pb-state and a light induced but thermo-stable Pg state [91].

Pr state structure The structure of the GAF-only cyanobacteriochromes in the Pr state exhibits the PCB-chromophore in both, the solution NMR structure of SypB [39, 202] and the X-ray structure of AnPixJ-g2 (ApxJ) [133] in a similar ZZZssa geometry as in prototypical phytochromes and in Cph2 phytochrome [7]. However, the SypB Pr structure is highly distorted. Most relevant features of the ApxJ structure are the shorter GAF domain, lacking the loop region of the eight-knot motif, which is involved in canonical PAS-GAF domain interaction and other small structural differences [133]. Furthermore, specific details in the pocket are of relevance for the distinct bilin-protein interaction. Unlike canonical phytochromes, an aspartate (D291) interacts via its carboxylate side chain with the A, B and C pyrrole rings. This residue belongs to a cyanobacteriochrome-specific DXCF-motif, equivalent to the prototypical DIP sequence [150]. In addition to that, a tryptophan and structurally relevant-tyrosine residues are embedded in the chromophore pocket, controlling the hypsochromic shift of the ZZE-conformer.

Pg structure The GAF-only structure in the green absorbing state showed a ZZEssa phycoviolobin chromophore (AB methylene bridge) with a Pfr-like ring D-aspartate interaction. However the Pg-pocket differs considerably (see fig. 2.7). The second cysteine involved in the Pb-state formation, is found within the DXCF-motif.

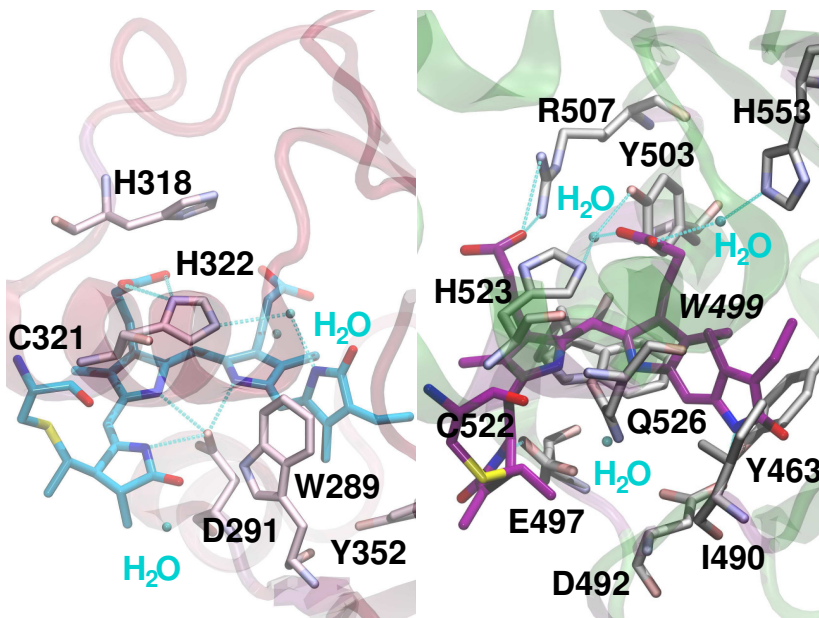


Figure 2.7: Chromophore pocket of AnPixJ-g2 (ApxJ, 3W2Z, left) and TePixJ-g (TpxJ, 3VV4, right). Relevant or conserved residues are indicated. Color code of the representation is specified in fig. 2.4.

Photocycle principle While the photocycle of the red/green CBCRs has been extensively characterized [63, 96, 97, 208], less structural details of the blue/green protein photocycle are known [76]. However, recent investigations were dedicated to structural elucidation along the photocycle. In accordance with canonical phytochromes, the main event involves a Z/E isomerization at CD methine bridge leading to the Lumi-intermediate. Subsequent relaxation processes involve protein reorientation and transient chromophore deprotonation. In the case of the blue-shifted CBCRs a second cysteine might transiently bind the chromophore either at the BC or at AB methine bridge [90]. This novel step is CBCRs-specific. While proton-translocation plays a crucial role within the red/green photocycle, it is unclear if such a reaction is found in other cyanobacteriochromes.

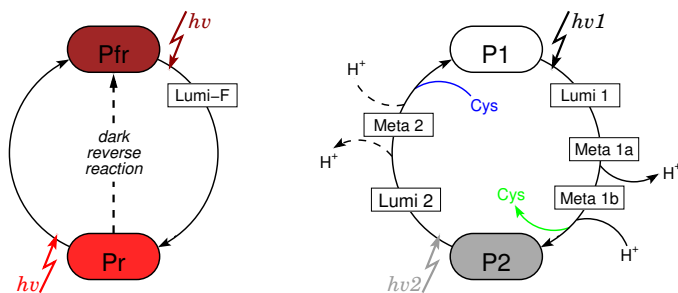


Figure 2.8: Photocycle model of two non-canonical phytochromes. The forward reaction in bathy phytochromes comprehends Pfr-to-Pr conversion (left). Reverse reaction occurs either photochemically or over an alternate thermal pathway. Structural details are available for the first Pfr-to-Pr intermediate (Lumi-F) [98]. In cyanobacteriochromes (right), the forward reaction includes the following steps: dark adapted state P1→Lumi-1 (*Z/E* or *E/Z* isomerization)→Meta-1a→Meta-1b (deprotonation) and finally P2 formation. Reverse P1-to-P2 state reaction is comparable, albeit not identical. For example, it is not clear if transient deprotonation is involved (dotted line). In case of blue/green cyanobacteriochromes, attachment (release) of a second cysteine is also involved in the forward (reverse) reaction [61].

3. Materials and Methods

3.1. Phytochrome samples

Samples were kindly provided by our numerous collaborators as well as by our skillful technician. A summary of the investigated phytochrome species and its different variants is given below.

Protein	Organism	Cofactor	Domains
Agp1	<i>Agrobacterium tumefaciens</i>	BV	PAS-GAF-PHY-HK (WT)
		BV	PAS-GAF-PHY (M15)
Agp2	<i>Agrobacterium tumefaciens</i>	BV	PAS-GAF-PHY-HK (WT)
		BV	PAS-GAF-PHY (M2)
ApxJ	<i>Anabaena</i> PCC 7120	PCB	GAF2 (GAF)
Cph1	<i>Synechocystis</i>	PCB	PAS-GAF-PHY ($\Delta 2$)
CphB	<i>Calothrix / Tolypothrix</i>	BV	PAS-GAF-PHY-HK (WT)
Pap1	<i>Pseudomonas aeruginosa</i>	BV	PAS-GAF-PHY-HK (WT)
Rph2	<i>Rhodopseudomonas palustris</i>	BV	PAS-GAF (PG)
			PAS-GAF-PHY (PGP)
SypB	<i>Synechococcus</i>	PCB	C-trunc.-GAF-PHY
TpxJ	<i>Thermosynechococcus elongatus</i>	PVB	GAF
Xcp1	<i>Xanthomonas campestris</i>	BV	PAS-GAF-PHY-PAC (WT)

Table 3.1: List of investigated phytochrome proteins. Samples with different domain or sequence length are also included in this table. Specific nomenclature is given in brackets. All proteins are noted following previous nomenclature definition [184, 205].

Agp1 All different species of *Agrobacterium tumefaciens* phytochrome 1 samples were prepared by Norbert Michael, member of our research group. Heterologous protein over-expression was performed using an *E. coli* host system [109, 111, 137]. In the protein sequence a C-terminal His-tag hexacodon was included which facilitates protein purification via Ni-NTA affinity chromatography. Further purification and expression details are given elsewhere [111]. Chromophore (BV) assembly was performed *in-vitro*. The covalent bilin binding occurs over cysteine C20 (PAS domain) forming the classical exocyclic double bond flipping of the chromophore's ring A [112].

- **Agp1-WT** is the full length Agp1 protein and contains both the sensory module (PAS-GAF-PHY), as well as the signal transduction or catalytic domain (HK). The Agp1 variant (754 amino acids, 84 kDa) dimerizes like other prototypical phytochromes.
- **Agp1-M15** is a deletion mutant which only includes the N-terminal PAS-GAF-PHY construct (504 amino acids, 56.00 kDa), also known as photosensory module. Like the wild type, this deletion mutant also forms dimers in solution [138].
- **Agp1-FMR** phytochrome is basically an M15N9-Variant, in which the first 9 N-terminal residues are deleted. It contains 3 point surface mutations (F289A, M295A and R296S) which hinder dimerization [138] and reduce surface entropy, thus making it suitable for crystallization [161, 162]. The spectroscopic features are nevertheless equal to the M15 species.

Additionally, a Agp1-FMR adduct with isotopic labelled $^{13}\text{C}_{10}$ -BV chromophore was assembled. The ^{13}C -bilin was synthesized [116] in the group of Wolfgang Gärtner (MPI CEC Mülheim).

Agp2 Samples of the bathy phytochrome Agp2 were provided by Norbert Michael (TU Berlin) and Isabel Molina (Lamparter Lab, KIT). The latter ones were solely used for pH titration of the Pr state [221] (see also fig. D.15). In general, protein expression and purification are in line with the standard Agp1 protocol [139, 161]. Like Agp1 and other bacterial phytochromes, Agp2-phytochrome binds also BV as a native chromophore. The covalent bilin attachment occurs at the C20 residue (PAS domain). Thus, unlike prototypical phytochromes, the chromophore attachment occurs at the C3"-position (see fig. 2.3) leading to an endocyclic double bond (further details are given in section 2.2).

- **Agp2-M1** or wildtype Agp2 (WT) is the full-length species (856 amino acids, 94.77 kDa), containing the N-terminal PAS-GAF-PHY domains as well as the kinase module (HK).
- **Agp2-M2** is the fully photo-active sensory module of Agp2 (PAS-GAF-PHY, 507 amino acids, 56.84 kDa), lacking the transmitter or kinase module.

Furthermore, a fully ^{13}C isotopically labelled Agp2 apoprotein was expressed. For this purpose, cell growth was induced by adding $^{13}\text{C}_6$ -glucose (99%, Cambridge Isotope Laboratories) instead of the natural abundant (n. a.) compound. The ^{13}C -labelled holoprotein contained a non-labelled BV chromophore.

ApjJ Cyanobacteriochrome AnPixJ constitutes a multi GAF phytochrome related photoreceptor. Within this work only the GAF2-only red/green absorbing phytochrome [132, 133] was investigated (22.75 kDa, 198 amino acids, PDB: 3W2Z). ApjJ-GAF2 binds PCB covalently at the C122 position (C321 in the full length protein). The GAF2-only cyanobacteriochrome was kindly provided by Rei Narikawa (University of Tokyo) and prepared in the laboratories of Wolfgang Gärtner (MPI Mülheim CEC) [208].

Cph1 Samples of Cph1 were expressed, and purified by Jo Maillet or Christina Lange in the group of Jon Hughes (University of Gießen). The Cph1 Δ 2 variant is a C-terminal deletion mutant lacking the histidine kinase domain (514 amino acids, 59.00 kDa, PDB: 2VEA) [49]. This recombinant prototypical phytochrome found in *Synechocystis* sp. PCC6803 [93] binds PCB as native chromophore at the C259 position (GAF domain). Photochemical and spectral properties of the wildtype and the Δ 2-mutant are comparable [86, 87]. In general, the *in-vivo* and *in-vitro* assembled Cph1 Δ holoprotein displayed equivalent spectroscopic properties in the Pr state [205].

- **Cph1 Δ 2-H60Q mutant** was used to probe the direct chromophore-interaction role of the highly conserved histidine 260 [74]. Via site-directed mutagenesis this residue was replaced by an glutamine, thus changing the pK_A in the chromophore pocket.

For specific vibrational assignment experiments, a $^{13}\text{C}_5$ -PCB labelled chromophore was assembled to the Cph1 Δ 2-variant (courtesy of Wolfgang Gärtner's Group, MPI CEC Mülheim).

CphB In the cyanobacterium *Calothrix* PCC 7601, two phytochrome proteins were identified CphA and CphB [85]. While CphA shows reasonable homology to Cph1, CphB (764 amino acids, 87 kDa) has the unique property of assembling BV as native chromophore at the C24 position (PAS domain) [143]. Wildtype CphB also shows a prototypical domain structure (PAS-GAF-PHY-HK). Like Agp1, CphB was also assembled with isotopic labelled $^{13}\text{C}_{10}$ -BV chromophore. Both CphB containing the n. a. and the isotopically labelled chromophore were kindly provided by Wolfgang Gärtner.

Pap1 The second bathy phytochrome investigated in this work was the full-length holoprotein of *Pseudomonas aeruginosa* [188] (728 amino acids, 80.1 kDa), also known as PaBphP [10, 35, 211]. The native chromophore, BV, is covalently attached via the C12 residue (PAS domain). Pap1 shows equivalent spectral properties as its Agp2 analogue. Apoprotein expression was performed heterologously. The purification process is described elsewhere [193]. Holoprotein assembly was performed *in-vitro* by addition of the native BV chromophore or via apoprotein incubation with the BphO(PigA)-BV complex [211].

- **BV IX δ (BV δ)** Despite the lower BV δ affinity (non-native chromophore), the formation of a photoactive holoprotein was clearly achieved [211]. Spectral properties are similar to native Pap1 containing the chromophore (BV or BVIX α). Further purification steps were performed following the standard protocol. The chromophore nomenclature (α or δ) refers to the methine-bridge position where the heme ring is cleaved [59] and subsequent pyrrole oxidative addition occurs (see fig. D.11). In case of *Pseudomonas aeruginosa* selective δ -opening is achieved by an unusual heme orientation in the (heme) oxygenase reaction center [35].

Rph2 This phytochrome, also known as RpBphP2, was found in *Rhodospseudomonas palustris*, along with two other phytochromes P1 and P3 (Rph1 and Rph3) [67]. Recent investigations demonstrated the existence of further *R. palustris* phytochromes (Rph4 to Rph6) [68, 69]. This photoreceptor regulates the light harvesting complex (LHC) expression of the photosynthetic organism [70]. Like other prototypical phytochromes, Rph2 binds BV as a native chromophore, adopting the expected exocyclic double bond rearrangement at ring A. The binding site of Rph2 is located at the C15 position (PAS domain). Recombinant Rph2 phytochrome variants were heterologously expressed in *E. coli*. Within the expression vector a Haem-oxygenase encoding gene was inserted [13, 70], therefore the BV assembly could be easily achieved *in-vivo*. Unlike other bacterial phytochromes, the coexpression of BV in *E. coli* led to extremely good SAR-values ($A_{Pr,max}/A_{280}$) of 1.7 to 2.4. All Rph2 samples were expressed and purified by Thomas Hildebrandt or Nesliah Tavraz in the group of Thomas Friedrich (TU Berlin). The following Rph2 variants were investigated:

- **Rph2-PGP:** contains only the photosensory module (501 amino acids, 55 kDa), consistent with other PAS-GAF-PHY variants of several canonical phytochromes, all spectroscopic properties are equal to those of the full-length protein [206].
- **Rph2-PG** is the deletion mutant (316 amino acids, 37 kDa) containing only the chromophore binding domain (CBD). Both domains (PAS and GAF) are

sufficient for chromophore assembly. Compared to the PGP variant, the Pr state shows largely the same absorption properties, yet Pfr-formation is considerably altered due to the lack of the PHY domain.

- **Rph2-iRFP** is an optimized infrared fluorescent mutant (iRFP-mutant). In this variant a set of 13 single-point mutations (S13L, A92T, V104I, V114I, E161K, Y193K, F198Y, D202T, I203V, Y258F, A283V, K288T and N290Y) was generated and optimized via random mutagenesis screening [52]. This Rph2 variant is completely photo-inactive. Despite a 10 nm blue shift of the Pr absorption maximum, spectroscopic properties are comparable to the Pr state in the PGP and PG variants [52].

SypB Within the genome of the thermophilic cyanobacterium *Synechococcus OS-B'* the SypB-Cph1 sequence (SypB) was identified [4, 14]. The protein structure of this cyanobacteriochrome lacks the PAS domain. In recent years similar systems have been characterized, i.e. SypA (cyanobacterial phytochrome found in *Synechococcus OS-A* and Cph2 from *Synechocystis*) [213]. Within the cyanobacteriochromes, this phytochrome-related species show general spectroscopic similarities to its canonical analogues. SypB was heterologously expressed in *E. coli*. Heme oxygenase and biliverdin reductase (BVR) were coexpressed with the SypB apoprotein, to allow the controlled *in-vivo* assembly of the native PCB chromophore [65]. The SypB apophytochrome binds the chromophore covalently at position C138. Within this work only a C-terminal truncated GAF-PHY protein [184, 204], containing a Y142F mutation was investigated. Unlike to the native species, the Pfr formation in the mutant is only possible at temperatures above 40 °C (data not shown). SypB-samples were kindly provided by Andrew Ulijasz (Richard D. Viestra group, University of Wisconsin-Madison).

TpxJ The cyanobacteriochrome sample from *Thermosynechococcus elongatus* were provided also by Andrew Ulijasz. TpxJ belongs to the same phytochrome-related family as ApxJ and SypB [89, 91, 153]. The investigated TpxJ variant was expressed as a GAF-only protein (165 aa, 19.0 kDa). PCB is assembled as native chromophore and is subsequently reduced to PVB [48, 90]. The first binding site is located at C522 (C259 in Cph1), whereas the second cysteine is found at position C494 [203]. Heterologous protein expression was performed under the same protocol as SypB. Chromophore assembly was also achieved prior protein-cell extraction. Within this work the native GAF-only domain was investigated, along with a C494A mutant. Furthermore a specifically ¹³C-labelled chromophore was synthesized via addition of 5-¹³C- α -aminolevulinic acid (ALA) to the minimal expression medium [147]. Hereby a 4,5,9,10,11,15,19-¹³C labelled PCB chromophore was obtained and subsequently *in-vivo* assembled and modified to the native PVB cofactor.

Xcp1 The bacterial phytochrome from *Xanthomonas campestris* was provided by Hernán Bonomi (Fernando Goldbaum group, Instituto Leloir Fundación, Buenos Aires) (640 aa, 71.2 kDa). The Xcp1 phytochrome belongs to the bathy phytochrome family. The dark adapted Pfr state shows strongly similar absorption properties as Pap1 and Agp2 phytochromes (see fig. D.20). While the photo-sensory domain of Xcp1 is generally reminiscent to the two bathy phytochromes, the catalytic domain lacks the autophosphorylation activity. In this respect, strong similarities were found to the PAS signaling domain of Rph1 [12]. Here, signaling probably occurs via direct interaction with the receptor proteins without any autophosphorylation process involved. Preliminary X-ray data of the full-length protein are already available [101].

3.2. Sample preparation and handling

Phytochrome sample preparation as well as all the subsequent steps prior and during spectroscopic measurements were performed generally under save green light (LED $\lambda_{\max} = 515\text{-}530$, $\Delta\lambda = 20$ nm). In case of the cyanobacteriochromes TpxJ and ApxJ (only during the investigation of the green absorbing state and the subsequently formed G-intermediates) sample handling was performed under red light (LED $\lambda_{\max} = 660$, $\Delta\lambda = 20$ nm).

Buffers Generally, phytochrome samples were prepared in a TS50 buffer (H_2O , 50 mM TRIS-Cl, 300 mM NaCl, 5 mM EDTA, pH = 7.8). For pH series a stronger buffer capacity was needed, therefore the TRIS-Cl concentration was increased to 100 mM (TS100 buffer). The investigated pH range was restricted to values within pH = 6.0 and pH = 10.0. For each investigated pH-value a specific buffer solution was prepared. Adjustment of the pH value was achieved either with 2 M HCl or with 2 M NaOH solution (D_2O buffer, 2 M DCl or 2 M NaOD). Determination of the pH value was performed with pH-ISE-meter (Denver Instruments, Model 225), equipped with the suitable pH-electrode. Prior to pH-measurements, the electrode was calibrated with 4.01, 7.00 and 10.01 pH-standard solutions (Merck). H_2O solutions were prepared with purest Millipore water. For the isotopic H/D-exchange of the pyrrole nitrogen protons (N-H groups) and protein exchangeable protons, buffer solutions (either TS50 or TS100) were prepared using 99.95% D_2O (Deutero GmbH) instead. Standard H/D exchange was achieved using a TS50 solution with a pD-value of 7.8 (pH = 7.4) [106].

Concentration Protein samples were dialyzed and concentrated using Millipore Microcon (YMC 30000 or 10000) filters. Sample concentration was increased via centrifugation (Eppendorf centrifuge 5424 R) at 20000g (14500 rpm). Each centrifugation

step took between 10 and 30 minutes –depending on the sample viscosity. Generally, the final sample concentration was approx. 500 μM or 33 mg/ml. Initial and final protein concentration was determined via UV/VIS measurements by analyzing the protein absorption OD_{280} , as well as the SAR-value (*vide infra*). Starting from a 500 μl diluted protein solution, the final volume was approx. 20 μl . In contrast to previous works [184, 205], the reduction of the final protein concentration was the key for the detection of the low temperature intermediates (see section 5.3).

Buffer exchange Either for H/D exchange or for a pH-series, the concentrated protein solution had to be dialyzed to the desired pH value. The sample was then diluted with the required buffer solution again up to 500 μl . Subsequently the concentration was increased after a centrifuge cycle. For the pH series, the buffer exchange was performed stepwise, thus changing the pH-value in $\Delta\text{pH} = \pm 0.5$ at each centrifugation step. After reaching the desired pH-value, the sample was then washed three times with the corresponding buffer solution. With this gradual buffer exchange procedure, denaturation process could be ruled out. Furthermore the reversibility of the method was inspected by bringing the sample back to the original pH value. The vibrational spectra before and after the variation of the pH value or buffer exchange were identical (see chapter 4). In case of the H/D exchange of the protonable groups in the protein and especially of the chromophore pyrrole nitrogens, the following procedure was employed. The concentrated protein sample was dialyzed with an 10:1 excess of D_2O -buffer. The dialysis and centrifugation steps were repeated at least four times. After the final D_2O -dilution, the protein solution was concentrated again up to 500 μM . In general, H/D-exchange of all four protonable N-H groups in the chromophore was achieved. The only exception were the bathy phytochromes in the dark adapted Pfr state. Detailed description of the isotopic labelling of the chromophore in Agp2, Pap1 and Xcp1 is given in section 6.

3.3. Absorption Measurements

All absorption measurements were performed at room temperature using a Cary 50 Bio-Spectrometer operated with Agilent-Cary Software. Protein solutions were measured in a UV quartz cuvette with a total volume of 500 μl (Blaubrand QS 1.000). Concentrated samples were diluted to an $\text{OD} < 2$, corresponding to a protein concentration of 2 to 3 μM .

UV/VIS protocol Absorption spectra were recorded between 200 and 900 nm (1 nm resolution). First, standard baseline correction was performed by measuring the pure buffer solution as blank and the zero-transmission (blocked beam path). Generally,

the UV/VIS measurements served as reference for testing the light exposure conditions in preparation to the RR (IR) measurements (*vide infra*). Furthermore, UV/VIS experiments gave also a first hint about the parent state (*e.g.* Pr-to-Pfr) photoconversion efficiency. In addition, thermal decay as well as stability of the room temperature species after light exposure were also tested by analyzing the changes in the recorded absorption spectrum. Moreover, UV/VIS measurements allowed probing the quality of the holoprotein sample by the evaluation of the SAR-value of the corresponding sample. This experimental reference is defined as the ratio of the chromophore absorption maximum in the pure dark adapted state (Q-band) and the protein absorption at 280 nm.

Kinetic measurements were performed by monitoring the intensity evolution at a defined wavelength as a function of time. For example, the thermal decay of the labile Pr-state to the dark adapted Pfr-state in bathy phytochromes was detected at the maximum Pfr-absorption (751–757 nm) with a time resolution of 125 ms or lower. Prior to the measurement, the sample absorption was normalized to zero. After a thermal equilibration period of 10–20 s, far red irradiation (780–785 nm) of the sample followed in a time window of 20 s. Extension of the irradiation period did not improve the photochemical equilibrium. To avoid overlapping of the absorption signal with the irradiation light, kinetic detection was interrupted during the exposure time. After irradiation, the signal decayed to the lowest value (negative), whereas during the subsequent recovery period the signal increased and eventually converged to zero (Pfr state recovery). The thermal decay (or recovery) was followed until the detected light reached values around the normalized zero-absorption. Kinetic data were analyzed using OCTAVE or the ORIGIN7 software package or higher (OriginLab, Northampton, MA). Each decay curve could be successfully simulated using an exponential decay function of the second order (see figures in appendix D).

3.4. Theory of vibrational spectroscopy

Molecular vibrations can be excited in two different ways, by absorption of a photon with the suitable energy or via inelastic scattering of the incident light [77]. A non-linear (linear) molecule with an N number of atoms has $3N$ degrees of freedom. Apart from translational motion and rotation, $3N - 6$ ($3N - 5$) degrees of freedom correspond to the number of normal vibrations in a molecule. A single normal mode is defined as the motion in which all atoms in a molecule oscillate with the same frequency, but with different amplitude [212].

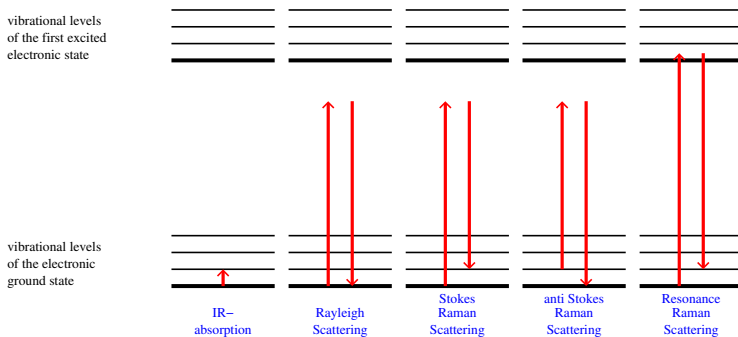


Figure 3.1: Energy-level-diagram: vibrational absorption and scattering processes. Adapted for this current work from ref. [72].

3.4.1. Quantum mechanical treatment of the Raman effect

Raman Scattering In IR absorption spectroscopy a single-photon transition due to interaction with polychromatic radiation is observed (see fig. 3.1). This process requires a transition of the molecular dipolmoment μ with respect to the normal coordinates Q_k ,

$$I_{\text{IR}} \propto \left(\frac{\partial \mu}{\partial Q_k} \right)^2. \quad (3.1)$$

On the other hand, the Raman effect is based on a scattering process [113, 144, 163]. The different light scattering processes are presented in fig. 3.1. During the interaction between electromagnetic radiation and molecules most of the photons are scattered in an elastic manner, such that during this event no energy exchange has taken place. This process is known as Rayleigh scattering. A small fraction of the incident light quanta exchanges energy with the interacting molecules, originating a vibronic transition. In this case, the scattered photon has lower (Stokes) or higher (anti-Stokes) energy than the incident light. The hereby induced energy difference has the absolute value of $h\Delta\nu$, whereas $\Delta\nu$ is given in wavenumbers (cm^{-1}) and represents the experimentally measured Raman-Shift. Within this work the quantum mechanical description of the Raman effect is restricted to the Stokes Raman scattering process [41, 172, 184].

A molecular electric dipole moment μ_{ind} is induced through the interaction with the electric field \mathbf{E} of the incident electromagnetic wave,

$$\mu_{\text{ind}} = \alpha \mathbf{E}. \quad (3.2)$$

The intensity of the scattered radiation is then proportional to the square of the induced dipole moment and therefore

$$I_{\text{scattered}} \propto (\mu_{\text{ind}})^2 = (\alpha \mathbf{E})^2, \quad (3.3)$$

whereas α represents the molecular polarizability tensor in all three dimensions,

$$\alpha = \begin{pmatrix} \alpha_{xx} & \alpha_{xy} & \alpha_{xz} \\ \alpha_{yx} & \alpha_{yy} & \alpha_{yz} \\ \alpha_{zx} & \alpha_{zy} & \alpha_{zz} \end{pmatrix}. \quad (3.4)$$

This can be extended as Taylor series with respect to the normal coordinates Q_k .

$$\alpha = \alpha_0 + \sum_{k=1}^{3N-6} \left(\frac{\partial \alpha}{\partial Q_k} \right)_0 Q_k + \dots, \quad (3.5)$$

the term α_0 represents the predominant contribution of the Rayleigh scattering. Due to the first order terms, a considerable Raman intensity I_{Raman} for a specific vibrational mode is then observed when the polarizability α along the normal coordinate experience a variation, thus

$$I_{\text{Raman}} \propto \left(\left(\frac{\partial \alpha}{\partial Q_k} \right)_0 Q_k \right)^2. \quad (3.6)$$

Within the transition from the initial $|i\rangle$ to a final vibrational state $|f\rangle$, the transition dipolmoment $[\alpha]_{\text{fi}}$ is defined as

$$[\alpha]_{\text{fi}} = \langle i | \alpha | f \rangle. \quad (3.7)$$

The Raman intensity is then derived from

$$\left\langle i \left| \left(\frac{\partial \alpha}{\partial Q_k} \right)_0 Q_k \right| f \right\rangle \propto \left(\frac{\partial \alpha}{\partial Q_k} \right)_0 \delta_{i \pm 1, f}, \quad (3.8)$$

with $\delta_{i, f}$ as the notation for the Kronecker-Delta (videlicet only 1 if $i = f \pm 1$).

The matrix elements from the polarizability transition $[\alpha_{\rho, \sigma}]_{\text{fi}}$ ($\rho, \sigma = x, y, z$) are derived from the Kramers-Heisenberg-Dirac equation based on second order perturbation theory [41, 141],

$$[\alpha_{\rho, \sigma}]_{\text{fi}} = \frac{2\pi}{h} \sum_r \left(\frac{\langle f | \mu_\rho | r \rangle \langle r | \mu_\sigma | i \rangle}{(\nu_r - \nu_i) - \nu_0 + i\Gamma_r} + \frac{\langle f | \mu_\sigma | r \rangle \langle r | \mu_\rho | i \rangle}{(\nu_r - \nu_i) + \nu_0 + i\Gamma_r} \right). \quad (3.9)$$

Here μ_ρ (with: $\rho = x, y, z$) stands for the component of the dipole moment operator in the ρ -directon and ν_0 is defined as the exciting source frequency. Summation occurs

over the vibrational states $|v_r\rangle$ from all intermediate states $|r\rangle$. The damping factor Γ_r is a function of the life time of the state $|r\rangle$.

Resonance enhancement In the Resonance Raman effect, the excitation frequency ν_0 lies close to an electronic transition ($\nu_r - \nu_i$). Here the summation over all other electronic transitions and the second sum term on the right side of equation 3.9 can be neglected.

The vibronic wave functions $|i\rangle$, $|r\rangle$ and $|f\rangle$ of the vibronic states $|v_i\rangle$, $|v_r\rangle$ and $|v_f\rangle$ with the eigenfrequencies ν_i , ν_r and ν_f can be dissected. On the basis of the Born-Oppenheimer approximation, it is possible to separate the electron wave functions (with $|g\rangle$ referring to the ground state and $|e\rangle$ to the excited state):

$$|i\rangle = |g\rangle|v_i\rangle, \quad (3.10)$$

$$|r\rangle = |e\rangle|v_r\rangle, \quad (3.11)$$

$$|f\rangle = |g\rangle|v_f\rangle. \quad (3.12)$$

Accordingly, the transition dipole moment from equation 3.9 can be represented as

$$\langle f|\mu_\rho|r\rangle = \langle v_f|\langle g|\mu_\rho|e\rangle|v_r\rangle = \langle v_f|M_\rho|v_r\rangle, \quad (3.13)$$

$$\langle r|\mu_\sigma|i\rangle = \langle v_r|\langle e|\mu_\sigma|g\rangle|v_i\rangle = \langle v_r|M_\sigma|v_i\rangle, \quad (3.14)$$

with the pure electronic transition dipole moments

$$M_\rho = \langle g|\mu_\rho|e\rangle, \quad (3.15)$$

$$M_\sigma = \langle e|\mu_\sigma|g\rangle. \quad (3.16)$$

If the transition dipole moments are developed in a Taylor series (Herzberg-Teller equation),

$$M(\mathbf{Q}) = M_0 + \sum_{k=1}^{3N-6} \left(\frac{\partial M}{\partial Q_k} \right)_0 Q_k + \dots, \quad (3.17)$$

with the subsequent insertion of equations 3.13, 3.16 und 3.17 into equation 3.9, the following equation is obtained

$$[\alpha_{\rho,\sigma}]_{fi} = A + B + \dots \quad (3.18)$$

with the so-called Albrecht-A- and B-terms defined as [2, 3, 172, 192],

$$A = M_{0\rho}M_{0\sigma} \sum_{v_e} \frac{\langle v_f|v_r\rangle\langle v_r|v_i\rangle}{(\nu_r - \nu_i) - \nu_0 + i\Gamma_r}, \quad (3.19)$$

$$\begin{aligned}
B &= M_{0\rho} \left(\frac{\partial M_\sigma}{\partial Q_k} \right)_0 \sum_{v_e} \frac{\langle v_f | v_r \rangle \langle v_r | Q_k | v_i \rangle}{(v_r - v_i) - \nu_0 + i\Gamma_r} \\
&+ \left(\frac{\partial M_\rho}{\partial Q_k} \right)_0 M_{0\sigma} \sum_{v_e} \frac{\langle v_f | Q_k | v_r \rangle \langle v_r | v_i \rangle}{(v_r - v_i) - \nu_0 + i\Gamma_r}, \quad (3.20)
\end{aligned}$$

whereas the summation over the vibrational states occurs only for the resonant electronic state. Based on the symmetry properties of the electronic transitions and the normal modes, selection rules for the *A*- and *B*- term scattering can be obtained. This is only true for symmetric molecules. However, the phytochrome cofactor lacks any essential symmetry, therefore symmetry selection rules cannot be applied to this system. Instead, the individual terms of eqn. 3.19 and eqn. 3.20 have to be considered. If the resonance transition and overlap integrals $\langle v_f | v_r \rangle$ and $\langle v_r | v_i \rangle$ (Frank-Condon factors) are different from zero, the contribution of the *A*-term increases. This is the case for vibrational modes, which experience coordinate alterations during the electronic transition. If $\langle v_f | Q_k | v_r \rangle$ and $\langle v_r | Q_k | v_i \rangle$ are unequal to zero, resonance enhancement over the *B*-term occurs. Such a scenario is observed if the resonant state couples to an other electronic state via a vibrational mode Q_k . Within this work, the selected resonance conditions lead to an enhancement of the Raman intensity based on both terms [118].

Investigation of tetrapyrroles under pre-resonance conditions with the first excited state shows comparable relative band intensities to measurements under rigorous resonance [5, 53, 184]. Interestingly, the calculated non-resonant band intensities are in good agreement with the experimental results obtained with an 1064 nm excitation [124]. Recent investigations on the Cph2 phytochrome performed under 785 nm excitation showed no considerable discrepancies with the previously described methods [7].

Furthermore, measurements under Soret resonance conditions (second excited state) showed that the overall spectral features are conserved [51, 83, 184] and in general agreement with the calculated Raman intensities. Nevertheless, some interesting differences were observed [184].

3.4.2. FT-Resonance Raman Spectroscopy

Fourier Transform Spectroscopy In each spectroscopic method to obtain a spectrum, the electromagnetic radiation is decomposed. The detected radiation can be understood as a superposition of a vast number of even waves with different frequencies. Spectral decomposition can be achieved over different techniques.

The most common technique in the field of Raman spectroscopy are the dispersive spectrometers. In this case, light dissection occurs via grating (*e.g.* monochromator,

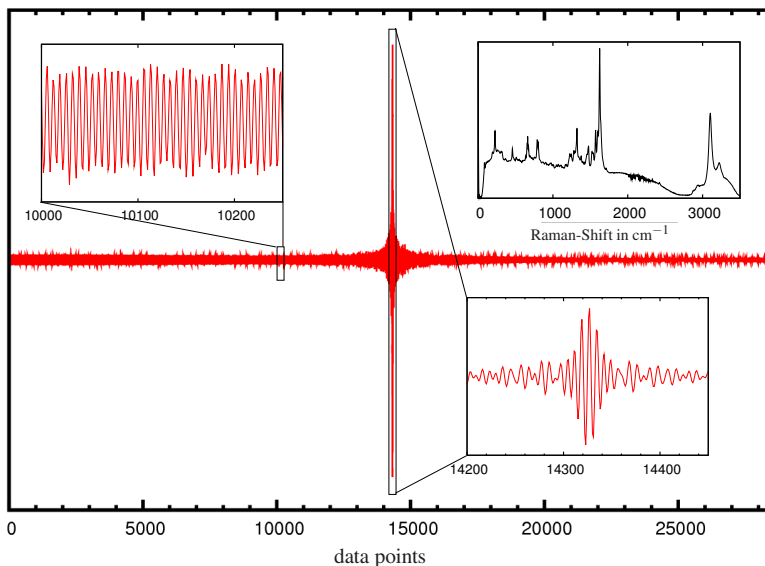


Figure 3.2: FT-RR-Spectroscopy: In this figure the main range of a recorded interferogram from the Pr state of the Agp1 phytochrome can be observed. At the top right side, the whole range FT-spectrum is plotted ($0\text{--}3500\text{ cm}^{-1}$). Relevant chromophore bands are solely observed within the range of $400\text{ to }1800\text{ cm}^{-1}$. Between $3000\text{ and }3500\text{ cm}^{-1}$, O-H stretching modes of the H_2O molecules are observed. In addition, two different regions of the interferogram are displayed. At the bottom (right) the interferogram center and maximum. At the left top side of the figure a random datapoint region, far from the maximum is displayed. This figure was kindly provided by Dr. David von Stetten [184].

spectrograph). The radiation components are spatially decomposed. Hence the spectrum is recorded and obtained directly. Unlike the dispersive Raman method, in FT-IR and FT-Raman spectrometers the electromagnetic radiation is detected as an interferogram which is digitally converted from the real into the frequency space (k -space) via the Fourier transformation (see fig. 3.2).

Light or amplitude intensity $I(x)$ is detected as a function of the position of the movable mirror Δx . The detected signal can be enhanced or weakened due to constructive or destructive interference of the different frequencies ν . The interference depends on the mirror position difference $2\Delta x$. The recorded interferogram $I(x)$ and its cor-

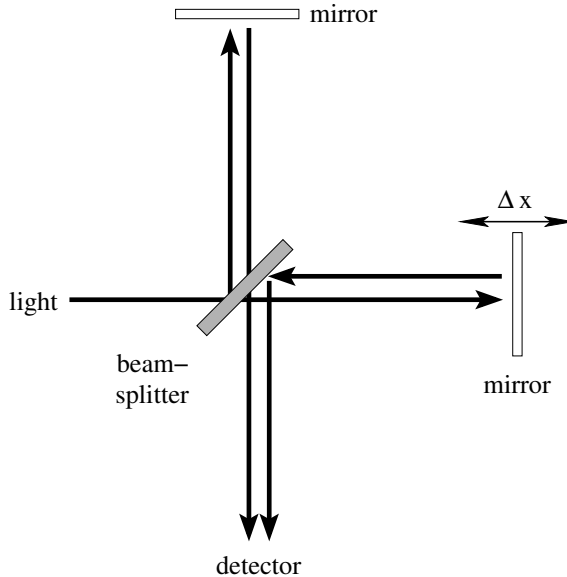


Figure 3.3: Michelson Interferometer: schematic representation from the optical path (from ref. [184]).

responding spectral deconvolution $B(\nu)$ can be converted into each other via Fourier transformation:

$$I(x) = \int_{-\infty}^{+\infty} B(\nu) \cos(2\pi\nu x) d\nu, \quad (3.21)$$

$$B(\nu) = \int_{-\infty}^{+\infty} I(x) \cos(2\pi\nu x) dx. \quad (3.22)$$

The integral in eqn. 3.22 considers an endless motion of the moveable mirror and therefore infinite Δx data points. In the present spectrometer setup the mirror distance is restricted only to some centimeters. To avoid artifacts due to the mirror motion restrictions within the interferometer, the interferogram is multiplied with an apodization function prior to the Fourier transformation. The bandshape in the spectrum $B(\nu)$ depends directly on the apodization function. Within this work, all RR spectra were

transformed using a triangular apodization function. In case of the IR spectra the standard Blackman-Harris function was applied.

The advantages of the FT spectroscopy are:

- **Multiplex (Fledgett):** In spectroscopy the detected signal can be separated in two components, the optical signal and the background noise. Within the FT method the contribution of the latter one is distributed over the whole spectral range. In contrast to that, the overall noise contributes to each data point using an dispersive spectrometer. The signal-to-noise ratio increases linearly with \sqrt{N} , whereas N represents the number of resolutions elements. For example, within a spectral range of 2000 cm^{-1} with a resolution of 4 cm^{-1} the N value is 500. Hence, signal to noise ratio is then 22 [172]. The measuring time is dramatically reduced if one considers the fact that in the FT method the whole spectral range is simultaneously recorded.
- **Jaquinot-advantage:** For a good spectral resolution with dispersive devices a slit is mandatory. However, the number of detected photons is then considerably reduced. In case of FT spectroscopy, a collimator aperture is used instead of a slit to focus the incident light into the interferometer. The selected aperture diameter can be extended in a way that the light losses are considerably reduced. This is only possible in the FT spectroscopy, since the overall intensity of all frequencies is simultaneously detected.
- **Connes-advantage:** The mirror position and thereby the accuracy of each data point is permanently monitored over the interferogram of the HeNe laser. This allows a highly precise definition of the absolute wavenumbers. Additional calibration procedure is then not necessary.

3.4.3. FT-Raman Spectrometer Setup

FT spectrometer All RR spectra were recorded in a FT-Raman spectrometer RFS 100/S (Bruker GmbH) [29]. Excitation was performed with an cw diode-pumped Nd:YAG laser (DPY 301 II0.50 EM, Coherent). The maximal laser power was 1.2 W (original specification 1.5 W) at 1064 nm with a line width of $<1\text{ cm}^{-1}$. Light collection occurred in backscattering geometry (180° angle orientation of incident and scattered light). Elastic scattered Rayleigh light was mainly eliminated with a notch filter prior entering the interferometer. Remaining inelastically scattered light was detected with a liquid nitrogen cooled germanium element. Digitalized data was further processed in a PC equipped with the suitable software package (*vide infra*).

Rock-solid-Interferometer Instead of a Michelson interferometer, the RFS 100/S spectrometer is equipped with a Rocksolid™ variant. This system allows a precise

adjustment in the increase and decrease of the optical pathway via rocking over the rotation axis to the interconnected corner cube mirrors. This setup is barely sensitive against angle tilting of the moving mirror. Furthermore the spectrometer is almost permanently aligned and is not affected by external thermal effects. One disadvantage of the Rock-solid setup is the introduction of additional reflections within the optical pathway. Like in the Michelson interferometer, the position of the moveable mirror is also determined as a multiple of the helium neon laser frequency [29].

Confocal Raman measurements For single crystal measurements the RAMANSCOPE IIITM-setup was used [31]. The Bruker system is based on an OLYMPUS confocal microscope, which is coupled with the RFS 100/S spectrometer via a double optical fiber system. The first one conducts the exciting laser into the microscope ($\varnothing = 50 \mu\text{m}$) and the second one collects the back scattered light into the spectrometer. Prior to entering the second optic fiber, the Rayleigh line is blocked via a cutoff filter (see fig. A.2). The advantages of the FT spectroscopy are partially lost in the Ramanscope, due to the introduction of the confocal pathway (Jaquinot advantage, *vide supra*). Nevertheless, due to the strongly focused incident light and the accurate positioning of the laser spot, measuring of single phytochrome crystals could be easily achieved. Unlike previous experiments [185] buffer contribution could be overcome (see section D), due to the strong focusing on the crystal area. Further setup and performance details can be found in the appendix A [31].

Data analysis Data analysis was performed using the OPUS 5.5 software or higher. Prior to the Fourier transformation the software-package performed several operations which were mandatory (*e.g.* discrimination of bad interferogram scans). The recorded interferogram was multiplied with a trigonal apodization function and with a zero filling factor of two. If necessary, background signal and background scattering in the recorded spectra were corrected manually with a polynomial function. White light correction was not necessary. Further spectra evaluation is described in section 3.7.

3.5. FT-Resonance Raman measuring protocol

The experimental FT-RR protocol and setup were adapted from previous works [73, 102, 118, 184, 205]. Specific details of non-standard experiments are indicated in the results section. Recorded spectra were calibrated with a toluene standard. Systematic frequency shift of the overall spectrum ($<3 \text{ cm}^{-1}$) compared to previous investigations was observed [102, 184].

Cryostat All RR measurements, including also sRR measurements (*vide infra*) were performed using a Resultec/Linkam cryostat. Temperature control is achieved via active liquid nitrogen cooling and compensated with a heating wire, thus allowing rapid temperature stabilization as well as fast cooling and heating. Due to the very thin quartz window, which isolates the sample from the surrounding, significant absorption or reflection of the incident as well as the scatter light can be discarded. The sample was placed in an aluminum holder (maximal sample volume of 7 μ l). After that it was brought to measuring temperature. Generally, standard measurements were performed at -140 °C. In case of the bathy phytochromes, measurements were performed at -190 °C, thus allowing a better comparison between FT-RR and sRR measurements (data not shown). In addition, this measuring temperature, also allowed a more accurate determination of the initial Pfr-photoproduct in bathy phytochromes and its corresponding temperature profile (data not shown). It has been assumed that room temperature spectra show negligible differences with the corresponding spectra recorded at low temperatures [183, 184, 205, 206]. Current investigations on the Pfr state in prototypical bacterial phytochromes showed that this assumption has a clear exception [159].

Light exposure Depending on the investigated phytochrome system and its absorption properties, different light conditions were selected. A detailed description for the room temperature sample irradiation procedures follows:

- **BV binding phytochromes:** the Pr-to-Pfr conversion was induced by red light exposure over 2 minutes (LED 660 nm). For the light induced back reaction, the sample in the Pfr state was irradiated only for 10 seconds with a 785 nm laser LED or with an 780 nm LED array.
- **PCB binding phytochromes:** here the same protocol was used as in the BV-phytochromes. Only for the Pfr-to-Pr conversion a 730 nm cut-off filter and white light source (alternatively a 750 nm laser diode array) were used.
- **Ap_xJ:** the Pg-formation was achieved with the conventional red light exposure (*vide supra*). Light induced conversion to the Pr-state was achieved by irradiation over two minutes at RT with green light (LED 530 nm).
- **Tp_xJ:** here, conversion between the Pb and Pg state was achieved by light exposure (2 min.) of blue light (Pb-to-Pg, 430 nm inference filter) or green light (Pg-to-Pg, 530 nm LED).

Accumulation of the intermediate species was achieved by light exposure at the corresponding irradiation temperature with the suitable light source (measurements of intermediate spectra see below). According with the applied steady-state conditions,

irradiation time was then incremented to 10 minutes reaching the photostationary equilibrium at every irradiation temperature.

FT-RR measuring protocol For each measurement about 5 to 7 μl of the protein solution were necessary. The selected low probing temperatures (-140 or -190 $^{\circ}\text{C}$) prevent any undesired thermal conversion during RR spectra accumulation.

The 1064 nm laser power was set to 780 mW. Laser power was measured with a COHERENT powermeter (FieldMax-II with PM100-19C sensor). To monitor possible laser induced damages, samples were measured several times and over long time periods. Despite the strong laser power, no changes in the sample spectra could be detected, even after a series of spectra. The spectral resolution of the spectrometer was set to 4 cm^{-1} . Selection of a higher resolution (2 cm^{-1}), increased only the accumulation time, without a considerable increase of the spectral quality. For a single spectrum, generally 2000 interferometer scans were averaged prior the Fourier transformation. Each scan was recorded in about 2 seconds. In total, recording of a single spectrum took 1-2 hours.

Using RR spectroscopy differences between two distinct states can be addressed more accurately than with other methods like absorption spectroscopy. Most of the Raman bands can be used as a fingerprint for the chromophore structure in a specific state. The recorded RR spectrum contains mainly contributions of the chromophore vibrations, whereas protein bands exhibit only minor contributions to the overall spectrum. The most characteristic protein bands are the amide-I, CH_2 -methylene and phenylalanine (phenyl ring vibration) modes.

The first electronic transition in open chain tetrapyrroles is observed in the range of 660–750 nm. In this respect, the 1064 nm excitation laser is capable of enhancing vibrational modes in this molecule. In contrast to rigorous and Soret enhancement, this method provides the advantage of overcoming fluorescence and most importantly it does not induce any undesired photochemical processes (data not shown).

An example of irradiation and measuring protocol is given for the cryogenic trapping of the Pr-to-Pfr intermediate species of Agp1 (see fig. 3.4). For the investigation of the complementary reaction pathway in bathy phytochromes, similar conditions were applied, using the far red light source for the cryogenic accumulation of possible Pfr-to-Pr intermediates.

Experimental challenges of the FT measurements Here is a list of the experimental difficulties that had to be overcome during FT-RR experiments:

- **Sample concentration:** we tried to reduce the sample concentration from 3 mM (20% protein weight), which was commonly used in previous works, to a lower value. This would give us the advantage to avoid protein aggregation of

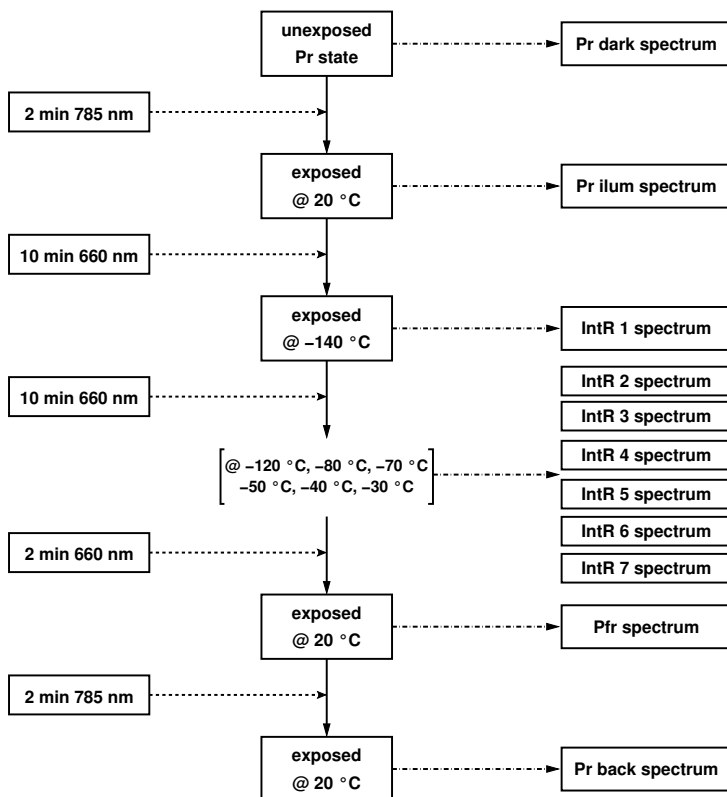


Figure 3.4: Schematic representation of each step during the cryogenic trapping of intermediate species along the Pr-to-Pfr conversion of Agp1-FMR. Left: exposure time and irradiation wavelength. In the central column the irradiation temperatures are shown. Right: the nomenclature for each recorded spectrum is given in the boxes. Spectra of low temperature irradiation conditions are shorted as “IntR”. For example the IntR1 and IntR2 spectra refer to the irradiation temperatures of -140 °C and -120 °C respectively.

more delicate phytochrome samples. Yet the most important reason was to allow a better detection of photo-induced intermediates. The use of a defined protein concentration also permits a quantitative analysis of the phytochrome RR spectra. This was important for pH titration or intermediate species identification. The reduction of the protein concentration was then compensated with longer measuring periods.

- **Photochemical quantum yield:** In most cases the quantum yield of the phytochromes is below $< 20\%$. Overlapping of the Q-band of both parent states leads to a photo stationary equilibrium. Therefore, the spectra of a pure state have to be generated via spectral subtraction. Two complex examples are presented in section 4.1 (Cph1) and section 5.3 (Agp1). In general, pure Pfr or Pr spectra could be easily generated. In contrast to canonical phytochromes, pure parent state extraction was easier in cyanobacteriochromes. Specially in ApxJ, where the Q-band maximum of both parent states is separated for more than 100 nm. Hence, complete population of one or the other state can be easily photochemically induced.
- **Photo-induced back-reaction:** The photochemical process of thermally unstable parent states (*e.g.* in case of the canonical phytochromes the Pfr state) occurs already at the detection temperatures (-190 and -140 °C). During the spectra analysis a putative overlap of the parent state species with the contribution of the intermediate states had to be taken into consideration. However in general, intermediate contribution was relatively low at measuring temperatures.
- **Buffer:** The Raman intensity of the O-H (O-D) stretching vibration of H₂O and D₂O is very strong. The frequency of this modes is observed at considerably higher values ($2500-3300\text{ cm}^{-1}$), far beyond from the region where chromophore bands are expected. Generally, the components of TRIS buffer show negligible contribution to the overall Raman spectrum. Only strong Raman scatterers like DMSO or glycerol might show overlapping peaks with chromophore bands. In those cases the buffer contribution had to be subtracted from the overall spectrum.
- **Free chromophore:** in case of the *in vitro* assembled phytochromes, residual free chromophore molecules cannot always be fully separated from the holoproteins, even after SEC purification. The spectral contribution might obscure band assignment of the correctly assembled chromophore.
- **Fluorescence:** this can be overcome by the appropriate baseline subtraction. The origin of this fluorescence is generally associated with the presence of free chromophore. While this represents a minor challenge for the FT measurements, it is one of the major obstacles while measuring in full resonance (*vide infra*).
- **Low SAR values:** excess of apoprotein can be estimated via the SAR-value (see section 3.3). In principle, the spectral contribution of the apoprotein is low and can be corrected via subtraction of the pure apoprotein component spectrum. In some specific cases where the SAR value is considerably low, the intensity of apoprotein component spectrum might increase and become comparable to that of the chromophore peaks. Here, an unambiguous structural elucidation of the chromophore can be compromised.

- **Sample holder:** No detectable signal of the aluminum sample holder as well as the quartz window were observed.
- **Room light:** the construction of the spectrometer shields it from the incident room light. Only the sample chamber and cryostat holder are potentially light exposed. For that and also for sample protection, all measurements were performed in the dark or at reduced light conditions (save green or red light).

Determination of the minimal detectable concentration Systematic investigation and determination of the minimal detectable phytochrome concentration with the FT-RR method represented a crucial issue, for the investigation of protein samples which cannot be measured at high concentrations. Furthermore, sample availability in case of isotopic labelled chromophores or specific mutants is generally restricted. For this purpose, Cph1 phytochrome solutions at 50.0, 20.0, 10.0, 7.5, 5.0, 2.0 and 1.0 mg/ml were measured with FT-RR spectroscopy. This corresponds to a molarity of 850 μM , 340 μM , 170 μM , 127 μM , 85 μM , 34 μM and 17 μM respectively. Apart from the 50.0 and 20.0 mg/ml solutions, the absorption spectra of the Cph1-samples were also recorded (1.000 QS Blaubrand cuvette, 0.2 cm pathlength). Respective RR spectra are shown in appendix A (see fig. A.3 and fig. A.4).

According to RR measurements of the Pr state, only Cph1 Δ 2 samples with a concentration above 10.0 mg/ml (170 μM) showed unambiguous chromophore bands. The contribution of the buffer was of the same intensity scale. Solely referring to the marker bands of the Pr spectra shown in fig. A.3, a minimal detectable concentration could be determined at 5.0 mg/ml (85 μM). Although this value strictly refers to the Pr state of Cph1 Δ 2, it can be used as general reference. In this respect, an acceptable holo-protein sample concentration for RR experiments lies between 500 – 600 μM .

3.6. Soret-Resonance Raman (sRR) setup and measuring protocol

sRR measurements were performed according to the same protocol as the FT-RR measurements. In this way direct comparison was granted. The specific details of this method as well as the experimental difficulties are given below.

sRR Spectrometer Setup Raman spectra was recorded using a confocal Raman microscope (HR-800, JOBIN YVON). Spectra were measured with the 413 nm laser line of a cw Kr⁺ laser (Innova 300, COHERENT). The scattered light was collected in a 180° geometry through an lwd-objective (OLYMPUS 20X, NA 0.35) into the microscope-setup (OLYMPUS BX 40). Light detection was performed with a nitrogen cooled CCD-camera. Elastic scattering and laser plasma lines were eliminated

by means of a notch filter or an interference filter. The spectrometer operation was controlled by the LabSpec-Software (v4.07, Dilor-Jobin Yvon-Spex). For calibration a standard mercury lamp was used. Spectral resolution was beneath 2 cm^{-1} . Further details of the setup are given elsewhere [114]. Performance of the spectrometer before and after every measurement was evaluated by measuring the position and intensity of the Si-Line at 520 cm^{-1} at 1.00mW (Olympus 50x).

sRR measuring protocol Phytochrome samples were measured at $-190\text{ }^\circ\text{C}$ (Resultec/Linkam cryostat) using the same protocol as for the FT-RR measurements (see section 3.5), with modifications according to the specific setup. Accumulation time for each spectrum was 200 s . Each sRR spectrum is composed of four overlapping spectral windows ($\Delta\nu = 350 - 400\text{cm}^{-1}$, with an overlapping region of $\Delta\Delta\nu = 50\text{cm}^{-1}$). For each spectral window, the detection time was $50 - 100$ seconds. Sample irradiation protocol was the same as for FT-RR measurements. The four overlapping spectral windows were combined and subsequently base-line corrected using the LabSpec-Software tools (polynomial baseline subtraction). Further data analysis was performed using OPUS and OCTAVE routines used for the FT-RR spectra.

Experimental difficulties Measurements under Soret-resonance conditions turned out to be more challenging than FT-RR measurements:

- **Restricted application:** spectra with reasonable quality could only be obtained for BV-binding phytochromes (Agp1 and Agp2) due to good overlap of the Soret-band (approx. $\lambda_{BV-phyt.} = 410\text{ nm}$) with the excitation wavelength (413 nm). All attempts to measure sRR spectra of other phytochromes, like Cph1, which binds PCB as a chromophore, failed due to the reduced enhancement combined with stronger background fluorescent. The Soret band of PCB-binding phytochromes is blue shifted ($\lambda_{PCB-phyt.} = 370\text{ nm}$), hence the selection of a different excitation wavelength could overcome the lack of sRR band intensity. In this respect, experiments with an 351 nm excitation wavelength were performed. However, the results were not promising, probably due to chromophore bleaching.
- **Fluorescence:** contribution of background fluorescence to the phytochrome spectra was rather high. Here, the origin of the fluorescence was attributed to traces of unbound bilin molecules, which probably were reduced to an urobilin, losing the double bond character at one methine bridge (presumably BC bridge). Bilirubins have a strong soret band and are highly fluorescent [50].
- **Photochemistry:** unlike to the rather poor overlap of the NIR exciting wavelength, where no photochemical isomerization could not be excluded, *e.g.* in case of the measurements of Agp2.

- **Apoprotein and buffer:** in contrast to the FT-RR measurements, the sRR spectra solely contain chromophore bands. An estimation of the concentration or the chromophore-protein ratio can not be directly extracted from the measured spectra. The only indicator to evaluate the spectral quality is the relative SNR-value. Here the background fluorescence strongly contributes to the overall noise-level.

3.7. RR spectra subtraction and fitting procedure

RR spectra were analyzed by first generating a pure spectral species, which subsequently was investigated by a band fitting procedure. Generally, the fitting procedure was restricted to the C=C stretching ($1500\text{--}1770\text{ cm}^{-1}$) or HOOP region ($600\text{--}900\text{ cm}^{-1}$). A general description of the specific nature of these characteristic vibrational frequency regions is given in section 3.9. Finally, the raw spectra were globally analyzed using the generated synthetic component spectra to determine the concentration of the contributing species. This procedure was applied to analyze the cryogenically trapped photo-induced reaction products, pH dependent transitions of the parent states as well as thermal relaxation process (examples shown in sections 4.1 and 5.3).

3.7.1. Subtraction procedure

To rationalize the composition of the recorded phytochrome RR spectra and its changes during a photo-induced reaction or other processes, the recorded spectra had to be dissected in its different components. The subtraction procedure was carried out using the OPUS software package. Assuming that each raw spectrum Q_{exp} can be represented as the linear superposition of a minimal amount of components C_i with variable concentrations or group factors q_i

$$Q_{exp} = \sum_i q_i \cdot C_i, \quad (3.23)$$

approximate pure species were generated out of the raw spectra by mutual subtraction. The quality of these “pure” spectrum was determined by its bandshape profiles, in which the presence of spectral artifacts (negative or very sharp peaks) in the whole range ($600\text{--}1770\text{ cm}^{-1}$) was considered as a failed try. The subtraction process was repeated in an iterative manner until a minimal number of pure spectra for a complete data set could be generated.

Subtraction procedure for photo-induced processes In principle, the parent state raw spectra have very little or no contributions of the intermediate components. Thus, the subtraction procedure for these, was restricted to two possible phytochrome components (Pr and Pfr). In addition, the contribution of the apoprotein and buffer was

considered. This spectrum was measured from a pure Agp1M15 apoprotein spectrum. In general, Raman spectra of globular proteins without any cofactors give very similar band patterns, which fortunately do not significantly (see fig. C.4).

Unlike the relatively simple extraction of the pure parent state species, determination of the spectra of a pure intermediate species was a challenging task, specifically if that species involved a neutral, weakly scattering chromophore. In that case, interference with the apoprotein spectrum was quite severe. Hence, the noise levels are higher than for other intermediates and the parent states. This could be solved, by identifying marker bands and analyzing their H/D sensitivity. These subtraction marker bands allow unambiguous identification due to the negligible overlap with peaks due to other spectral components.

To this purpose, apart from both marker regions (C=C stretching and HOOP spectral windows) the entire spectral range was inspected in detail. Certain intermediate band features could then be unambiguously detected in the rather complex band pattern between 1000 and 1500 cm^{-1} . These features provided a reliable reference for spectra subtraction. For example, in the Lumi-R species, a strong band envelope was unambiguously observed at approx. 1300 cm^{-1} (see fig. 5.6). Due to the similar Pr-to-Pfr photoconversion of plant phytochrome and Agp1, the corresponding intermediate analysis could be then reduced to a minimum number of six components: two parent states (Pr and Pfr), three intermediates (Lumi-R, Meta-Ra and Meta-Rc) and an apoprotein species which included the buffer background.

pH titration To carry out a global component analysis based on the pH dependent transition of the Pr state of Cph1 Δ 2 (see chapter 4.4), certain considerations were included in the subtraction protocol. In this sense, a three component system for the Pr state was taken as model (without protein contribution), two cationic species and a neutral Pr species, coupled via two reversible processes. Another example was the investigation of the RT far red light photoproduct of Agp2, presumably the Pr state (see fig. 4.12). Despite the contribution of the Pfr state as well as the residual apoprotein contribution, the recorded spectra could be then separated in an apparently cationic Pr form and a Pr species deprotonated at the pyrrole nitrogens of rings B and C.

Thermal and kinetic analysis Thermal processes play a crucial role in the phytochrome photocycle [155]. Low temperature thermal processes were mainly investigated in the Pfr-to-Pr reaction pathway of Agp2. Here, an adequate subtraction procedure was implemented to extract thermal intermediates with apparently low spectral contributions (see section 6).

3.7.2. Component Analysis

Band analysis allows an accurate comparison of the relevant vibrational bands observed in the RR spectrum of a pure component with the calculated vibrational frequencies. Furthermore, single band analysis is very useful for determining precise isotopic shifts. The global analysis of different components and its contribution to the recorded spectra strongly support the evaluation of temperature or pH profiles.

Single Component Fitting A band fitting analysis of a pure spectrum was performed, assuming that every RR spectrum can be interpreted as the sum of a defined number of Lorentz bands. In addition, the remaining background contribution can be approximated by a linear function. Single-component analysis and global fitting was investigated in the range of $1380 - 1770 \text{ cm}^{-1}$ and $600 - 900 \text{ cm}^{-1}$. Fit procedures were applied in an OCTAVE-based home-made program [44, 135]. A good fit was achieved only when the minimal number of applied Lorentzian components could reproduce the experimental spectrum. Based on QM and QM/MM calculations, as well as isotopic labelling experiments, the starting parameters were defined. Furthermore experimental band positions were determined via the 2nd derivate of the pure species. Initial band half-width value was set to 12 cm^{-1} . Numeric optimization of the band frequencies, intensities and half-widths were repeated until reaching a minimum residual difference between recorded and fitted species. For the apoprotein component a mixture of Gaussian and Lorentzian bands were included in the fit procedure. In this case, the aim of the fit procedure was solely to reproduce the experimental spectrum, whereas, the fitting parameters did not provide any relevant structural details of the apoprotein.

Global component analysis The component spectra were used in total to simulate the experimental RR spectra. The fit procedure optimized the specific group factor of every component, as well as the linear baseline. As a result, the relative concentration of each species can be used to elucidate the component behavior of a certain process.

pK_a value Determination Deprotonation/protonation reactions during a pH titration were determined using the following procedure. In case of a two-state equilibrium, relative spectral contributions of the two species (I_p and I_d) as determined from the component analysis, are proportional to the relative concentrations (c_p , c_d) according to

$$c_p = f_p \cdot I_p \quad (3.24)$$

$$c_d = f_d \cdot I_d, \quad (3.25)$$

where f_p and f_d are factors proportional to the reciprocal SCR values (see section 3.9.2). The relative concentrations were normalized according to

$$1 = f_p \cdot I_p + f_d \cdot I_d = c_p + c_d. \quad (3.26)$$

Subsequently, the Henderson-Hasselbalch equation adopts the form

$$\text{pH} = \text{pK}_a + \log\left(\frac{c_d}{c_p}\right) = \text{pK}_{a,\text{app}} + \log\left(\frac{I_d}{I_p}\right), \quad (3.27)$$

where $\text{pK}_{a,\text{app}}$ is given by

$$\text{pK}_{a,\text{app}} = \text{pK}_a + \log\left(\frac{f_d}{f_p}\right). \quad (3.28)$$

The ratio f_d/f_p is approximated by the reciprocal intensity ratio of the strongest cofactor bands relatively to the Phe band at 1004 cm^{-1} (as an internal standard). Further details are given in sections 4.1 and chapter 6) and in the references [195, 221].

3.8. FT-IR setup and measuring protocol

Infrared difference spectra were recorded in a BRUKER TENSOR 27™ or in a BRUKER IFS-28™ spectrometer. Polychromatic infrared radiation was emitted by a global and subsequently focused on the sample after passing through the interferometer. The IR signal was recorded at a with liquid nitrogen cooled MCT detector. In principle, the FT-IR spectrometer setup is comparable to the FT-RR system (see subsection 3.4.3), especially concerning the interferometer arrangement. Alike the FT-RR measurements, the IR spectrometer was operated with the OPUS 5.5 or higher software package. Irradiation conditions were in agreement with the resonance Raman protocol. However, unlike the FT-RR conditions, sample light exposure was performed during IR spectra accumulation.

Bio-ATR setup and protocol Measurements of TpxJ cyanobacteriochrome were performed using a BIOATRII™ sample cell [30]. Typical sample volumes were 20 μL . Protein concentration was around 1-2 mM. Samples were prepared in 50 mM TRIS buffer. Each single spectrum was generated from 200 interferometer scans (i.e., about 90 s). Sample illumination was manually alternated between blue and green light typically after 5 recorded spectra. Subsequently, difference spectra from 10-15 blue/green illumination cycles were generated and co-added without further background correction. IR measurements in the ATR-cell [71] allowed direct and easy sample irradiation.

Light exposure in the 660 – 780 nm range had a strong thermal effect on the ATR crystal (Zn/Se). Subsequently, strong background deviations in the IR difference spectra were detected. In addition, sample drying, vapor diffusion (especially in D₂O experiments) and the requirement of large protein samples amounts represented experimental complications. In this respect, further IR measurements were performed in a conventional transmission cell (*vide infra*).

Transmission setup and measuring protocol Infrared measurements of phytochromes other than TpxJ were performed using the transmission method. Up to 10 μL of a protein sample at a concentration of 500 μM were deposited on a CaF₂ window with a 2 μm deepening. The sample was homogeneously distributed over the whole surface within the deepening. Excess water was removed with a N₂ gas flow. The hydrated sample film was then sealed with a plain CaF₂ window. To avoid further sample dehydration, additional isolation of the sample was provided by a thin layer of silicone grease between both windows. The CaF₂ sandwich was placed in a suitable window holder [57, 170].

IR samples were measured at RT. The following procedure was optimized and automatically processed via an OPUS macro script. Here, the irradiation protocol was controlled via the TTL switchboard. For that purpose, two BNC switches connect the LED controller with the TTL board. Schematic representation of the LED arrays is given in the appendix (see fig. A.7). The first and second irradiation procedure were assigned to the BNC connectors denoted BIT0 and BIT1. The selected irradiation sources were in resonance with the absorption maximum of the respective parent state. For example in case of a canonical phytochrome, the Pr state was irradiated with 670 nm and the Pfr state with 780 nm (in agreement with the RR irradiation protocol of subsection 3.4.3). The first irradiation, which involved the photoinduced transition from the dark adapted species (Pr state) to the second parent state (Pfr state), was induced via the BIT0 LED array (*e. g.* 670 nm). Backreaction occurred after BIT0-signal interruption, followed by irradiation via the BIT1 array (*e. g.* 780 nm). The complete irradiation procedure was divided in the following steps:

- Directly after optimum sample positioning (sample surface perpendicular to the IR beam path, see fig. A.7), a SC spectrum was recorded as reference for further atmospheric compensation (400 single interferometer scans).
- Passive temperature stabilization was achieved after 3 – 4 h. This was monitored by measuring the SC spectra (200 scans per single spectrum) and calculating the absorbance (ABS) spectrum.
- After the stabilization, the first irradiation procedure was employed. This step involved irradiation of the dark state. The photochemical equilibrium or full

conversion to the light induced state was achieved within the accumulation of the first spectrum (200 scans). Thus, to avoid an incomplete photochemical reaction, two or three additional spectra under BIT0-LED irradiation were performed. In no case, the resulting difference spectra displayed any further photo-induced reaction.

- Subsequently, the second irradiation procedure was performed (BIT1-LED).
- After the bidirectional photoconversion an additional thermal relaxation period was included. This process was monitored by spectra accumulation (20 – 25 single spectra or 1 h).
- The irradiation procedure (including the dark relaxation period) was repeated 3 to 4 times. If needed, the resulting difference spectra were then averaged to improve the SNR value.

FT-IR spectra analysis After spectra accumulation, atmospheric compensation was performed for each spectrum of the irradiation procedure using the OPUS software package. Subsequently, the difference spectrum was calculated using the ABS spectrum prior to irradiation as reference and subtracting it from the ABS spectrum after the first irradiation. Here, the ABS spectrum is defined as

$$ABS = \log_{10} \left(\frac{I_n}{I_0} \right) \quad (3.29)$$

whereas I_0 refers to the first SC spectrum recorded prior the thermal stabilization and $n = 1$ corresponds to the SC spectrum before the irradiation process. Thus, $n = 2$ denotes the SC spectrum after irradiation leading to

$$ABS_1 = \log_{10} \left(\frac{I_1}{I_0} \right) \quad (3.30)$$

$$ABS_2 = \log_{10} \left(\frac{I_2}{I_0} \right) \text{ and} \quad (3.31)$$

$$IR_{diff} = ABS_2 - ABS_1 \quad (3.32)$$

Subsequent background correction of the IR_{diff} spectrum was performed manually using a polynomial function. In the IR_{diff} spectrum, negative bands correspond to vibrational modes of the reference (I_1), whereas positive bands refer to vibrational modes of the photoproduct (I_2) (see section 3.9).

FT-IR experimental difficulties Infrared measurements of biological samples encounter difficulties other than RR measurements [172].

- **Water and sample concentration** Due to the overlap of the i. p. deformation mode of the H₂O molecules with the amide I and amide II vibrational modes, protein sample concentration had to be considerably increased without avoiding any protein drying or saturating absorption in the IR spectrum. Under this conditions, it is difficult to control parameters like the pH value or the ionic strength.
- **Water vapor** Ambient H₂O vapor affects the IR measurements. Thus, sample chamber as well as spectrometer has to be either evacuated or purged with dry air or water-free N₂. Any modifications in the sample chamber or sample repositioning led to an additional purging period (2 – 4 h). Thereby, IR measurements are considerably more time demanding than the FT-RR experiments.
- **H/D exchange** As in the RR experiments, isotopic exchange allows assignment of chromophore bands. Additionally, also H/D sensitivity of protein vibrations can be investigated. All observed changes are then unambiguously related to the photochemical reaction. A satisfactory buffer exchange process might take several hours, and requires many (H/D) buffer exchange steps (see section 3.2). Furthermore, during the sample deposition in the CaF₂ window hydration of the sample is very likely to happen. The exposition to ambient vapor leads to the detection of strong H₂O bands in the SC spectrum and therefore an unwanted D/H re-exchange cannot be excluded.

3.9. Interpretation of phytochrome vibrational spectra

The FT-RR spectrum of phytochromes is primarily composed of Raman active bands of the chromophore. Here, the protein matrix provides only a small contribution to the overall spectrum. This is particularly true for phytochromes absorbing within the red/far-red regime (630-750 nm). In case of the cyanobacteriochromes, the resonance enhancement is considerably lowered due to the blue shifted absorption maxima (430-540 nm). However, chromophore bands have still higher intensity than those of the protein [203, 208]. Phytochrome spectra measured under Soret-resonance ($\lambda_0 = 413$ nm) conditions only contain chromophore vibrational modes [51, 184]. Despite the different excitation wavelength, band intensity profiles in sRR spectra show similarities to spectra recorded under Q-Band pre-resonance conditions ($\lambda_0 = 1064$ nm). In both cases the strongest bands are addressed to the C=C stretching modes of the methine bridges. Due to the lack of symmetry of the chromophore, there is little difference between the Raman activity of vibrations excited under resonance with the first or second electronic transition state.

Furthermore, the preresonantly enhanced FT-RR spectra display essentially the same vibrational band pattern and relative band intensities as the RR spectra obtained in rigorous resonance with the first electronic transition [54, 79]. Thus, the RR spectra of

these chromophores can be described by QM calculations of Raman intensities [123, 128].

However, QM calculations do not necessarily predict the correct frequencies due to the neglect of the influence of the protein matrix on the chromophore structure. Only recently, the availability of phytochrome crystal structures and the development of the hybrid QM/MM-method improved the accuracy of the spectra computation. However the outcome strongly depends on the resolution and quality of the employed structure [125, 130]. Characteristic Raman active bands are the C=C stretching of the CD, AB and BC methine bridges. The protonation state of the chromophore can be unambiguously identified by the N-H i.p. vibration of ring B and C. Finally, the HOOP vibrational mode of the CD methine bridge, represents also a very characteristic Raman-active chromophore mode, specially for the Pfr state [53, 54, 79].

In the case of the IR-difference spectra, light induced structural rearrangements in the protein and the chromophore contribute to the difference signals. Nevertheless, chromophore band assignment has been successfully achieved due to selective as well as global isotopic labelling of the chromophore moiety [55, 196]. Characteristic IR-bands of chromophore are C=O stretching modes of ring A and D, since these prominent peaks are found with high intensity and at frequencies where little protein contribution is observed. An other characteristic chromophore band is the highly IR-active C=C stretching mode of the BC methine bridge. Even though this band has been found and predicted in a region where amide I and amide II modes might compromise the interpretation, recent ^{13}C -labelling of this methine bridge (C_{10}), allowed an unambiguous assignment [159] (see also section 5.2).

3.9.1. Figure notation

All figures containing vibrational spectra were generated using the OCTAVE and the GNU PLOT software package. Further graphical modifications were created with XFIG 3.2 [176] or INKSCAPE 0.47 [1].

Experimental RR and IR spectra Unless explicitly noted, the different spectra are coded as follows:

- **black spectrum** refers to the main species, *e.g.* wildtype or unlabelled sample,
- **red spectrum** corresponds to a spectrum recorded in D_2O ,
- **blue spectrum** denotes a spectrum of a ^{13}C -labelled chromophore or protein sample measured in H_2O ,
- **green spectrum** refers to a spectrum of a ^{13}C -sample measured in D_2O , and
- **gray spectrum** corresponds to the buffer or apoprotein spectrum.

All spectra were normalized to the highest band within the whole chromophore spectral range. Generally, the strongest band is found in the marker region (1500 – 1700 cm^{-1}). In some specific cases, the strongest chromophore band was located within the region of 600 to 900 cm^{-1} (only Pfr state).

Notation for the vibrational mode composition in each spectrum is shortened as follows:

- **A, B, C** or **D** refers to modes localized in the corresponding pyrrole ring,
- **AB, BC** or **CD** indicates C=C stretching modes of the methine bridges,
- **ip** terms all in-plane vibrational modes,
- **OOP** denotes the general description for out-of-plane bending vibrations, and
- **HOOP** indicates solely OOP vibrations involving C-H groups of the methine bridge modes.

Further vibrations, which are individually observed in specific phytochrome measurements are defined either in the figure caption or in the text.

Fitted RR spectra In addition to the standard notation [184], resulting fitted pure species spectra and its components are coded as follows:

- the **experimental spectrum** is colored in black,
- corresponding **fitted species** is represented in solid red
- with each single **Lorentzian (Gaussian) bands** spectrum plotted in gray.

3.9.2. RR spectral regions

The region between 400 to 1800 cm^{-1} of a phytochrome RR spectrum contains the most important modes of the tetrapyrrole chromophore. Within the different sub-regions or chromophore spectral windows, different information can be obtained (see fig. 3.5). This is the result of the numerous studies of protein-bounded tetrapyrroles and model compounds. In this respect, the most important chromophore marker bands could be identified in combination with isotopic labelling of the chromophore and the Raman-spectra calculations [125, 129].

1500 – 1700 cm^{-1} This range is also known as the chromophore marker region.

Based on the frequencies and intensities of the C=C stretching modes of the methine bridges, the most relevant information concerning the chromophore gross geometry can be obtained. These modes are found in the range between 1590 and 1640 cm^{-1} . The protonation state of ring B and C nitrogens is reflected via a very characteristic spectral feature found also in this region. It can be

specifically distinguished if all four pyrrole nitrogens are carrying a proton or not. In the first case, the chromophore is positively charged (cationic bilin not regarding the propionic side chains). Fully protonated chromophores show a peak in the range from 1545 up to 1590 cm^{-1} , addressed to the N-H in plane bending vibration of rings B and C. This mode can be experimentally assigned via its H/D-isotopic sensitivity [79]. The corresponding N-D peak is found between 1050 and 1080 cm^{-1} . This assignment was corroborated with an ^{15}N labelling of the pyrrole nitrogens [130]. Spectral contributions of vibrational modes addressed to the side chains of the chromophore are rather small. According to QM and QM/MM calculations, only modes with a very defined and rather simple internal coordinates contributions are present in this region [123]. The strongest band of the whole bilin spectrum is generally due to the C=C stretching vibration of the CD methine bridge. In the other hand, double bond stretching vibration of the BC bridge (fully protonated chromophore) shows very low RR activity but this mode is highly IR active (*vide infra*).

1000 – 1500 cm^{-1} In this spectral range, further in plane bending vibrations of the chromophore can be found. It has been shown that the mode composition in this range is rather complex [184]. Hence, a precise band analysis in this region is generally compromised. In addition to that, in plane bending modes of the protein backbone (amide III) are expected in the spectral window of 1230 – 1300 cm^{-1} . Chromophore bands in this region show low to medium RR activity. Therefore overlap with the protein contribution is quite likely to occur. At 1004 cm^{-1} the symmetric ring breathing vibrational mode of the phenylalanine (Phe) residue is located. The intensity of this band gives a reliable reference to determine the relative RR scattering cross section of the chromophore within different states or intermediates (see chapter 6). Moreover, it reflects the contribution of the protein matrix to the overall spectrum. Only recently, specific isotopic labelling allowed the identification of specific modes within this region. In addition to the previously mentioned ip bending modes, the pyrrole C-N stretching contribution to different vibrational modes could be unambiguously assigned (see chapter 6).

600 – 1000 cm^{-1} Torsions and out-of-plane modes (OOP) can be found in this low-frequency range. Subtle conformational and configurational changes of the methine bridges geometry affect substantially the modes in this spectral region. Minor contributions of the propionic side chains vibrations are also located in this region [184]. Along with the vibrations of the rings B and C side chains, it has also been proposed, that some contributions of the S-C stretching can be found in this range (see subsection 5.4.1).

Determination of the gross chromophore geometry was carried out via the investigation of the methine bridge configuration and conformation. An equally important structural parameter is the protonation state in the chromophore. In fact, the discussion of chromophore structure in the different phytochromes and their various states was based primarily on the assignment of the chromophore marker bands and the HOOP region.

3.9.3. RR active chromophore marker bands

Within the RR spectra, marker bands represent a structural signature for a specific chromophore geometry.

C=C stretching The C=C modes of cationic or neutral tetrapyrroles exhibit the highest Raman intensities. Located around 1600 cm^{-1} , there are several partly overlapping bands. According to quantum mechanical calculations, they include C=C stretching coordinates mainly of the AB and CD methine bridges (AB and CD stretching). The strongest band contains the highest contribution of the CD stretching coordinate. At higher frequencies, the second strongest band, overlapping with the CD mode, is due to the AB stretching. At even higher frequency less prominent bands containing modes which involve the C=C stretching of ring A (only in case of endocyclic chromophore attachment) or ring D and the vinyl stretching of the ring D side chain (only for phytochromes with BV and PΦB as chromophores). The Raman activity for the endocyclic C=C stretching is very low. The remaining BC C=C stretching mode is found at lower frequencies, than the CD C=C mode (-10 cm^{-1}), with very low RR activity. Modes involving the C=C stretching vibration within the remaining pyrrole rings B and C have low intensity and the overlap with other prominent bands compromises an unambiguous assignment. The previously controversial band assignment that corresponds to the AB C=C stretching vibration and the following structurally inaccurate interpretation of the chromophore geometry in the Pr state could be solved on the basis of $^{13}\text{C}_5$ isotopic labelling and QM/MM calculations. Here, the RR interpretation was in line with the crystallographic elucidation of the chromophore structure (correct ZZZssa vs. inadequate ZZZasa geometry) [49, 130].

N-H in-plane In the region between 1550 and 1590 cm^{-1} a band of medium intensity is observed, which corresponds to the N-H ip bending mode of ring B and C, as demonstrated by isotopic labelling. Deprotonation of the chromophore corresponds to the removal of one proton from either ring B or C [184].

Unambiguous assignment is experimentally possible by comparing the RR measured in H_2O and in D_2O (also in agreement with calculations). In the latter

one the N-D i.p. bending mode is downshifted to approx. 1070 cm^{-1} . These is only true for a fully protonated chromophore. Proton abstraction is most likely to occur at the nitrogens of ring B and C (lowest pK_A value of all N-H groups) [19]. In this respect, absence or presence of the BC N-H i. p. mode with the corresponding H/D sensitivity is a reliable indicator to determine the protonation state of the chromophore. Additional contribution of the N-H groups of ring B and C can be found in less prominent bands at approx. 1520 cm^{-1} . Calculations of chromophores lacking the protonation either of ring B or C, show a very low RR intensity for bands with contributions of the N-H groups. In addition, neutral chromophores exhibit a less pronounced H/D sensitivity of all modes involving the pyrrole nitrogens, especially the C=C modes of the methine bridges. Further N-H modes with contribution of rings A and D are found around 1320 cm^{-1} . Experimental assignment is rather complicated due to the increased number of bands in this region.

C-H out-of-plane For the identification of the Pfr state in a RR spectrum, the analysis of this mode (approx. $800 - 815\text{ cm}^{-1}$) is of special interest. It shows a very strong RR intensity, which is a unique signature for this parent state. Increased torsions of the methine bridges (especially of the CD coordinate) cause an intensity increase of the out-of-plane bands (OOP bands) [6, 54, 79, 119].

OOP ring D Recent QM/MM-calculations predicted a mode with high intensity around 650 cm^{-1} . This mode was assigned to the out-of-plane motion of ring D [126]. In this respect, an analysis of this region in several phytochrome spectra proved that a putative band could be assigned to the OOP mode.

3.9.4. IR active chromophore bands

Unlike the RR spectra, the protein contribution overlaps with most of the chromophore bands in the marker region (amide I and amide II):

C=O stretching Between 1680 and 1730 cm^{-1} , the stretching modes of the C=O groups of rings A and D have been extensively investigated and used as marker bands to elucidate the chromophore structure of model compounds and of the different states in phytochromes [55, 140, 171, 196]. Furthermore, the assignment of the $\text{C}_1=\text{O}$ (ring A) and $\text{C}_{19}=\text{O}$ (ring D) stretching vibrations is important for the understanding of the primary photochemistry and subsequent intermediate formation in the Pr-to-Pfr and the back conversion pathway [56, 57, 165]. Although both C=O modes (rings A and D) have been predicted with very small Raman intensity, the C=O mode of ring D could be unambiguously assigned.

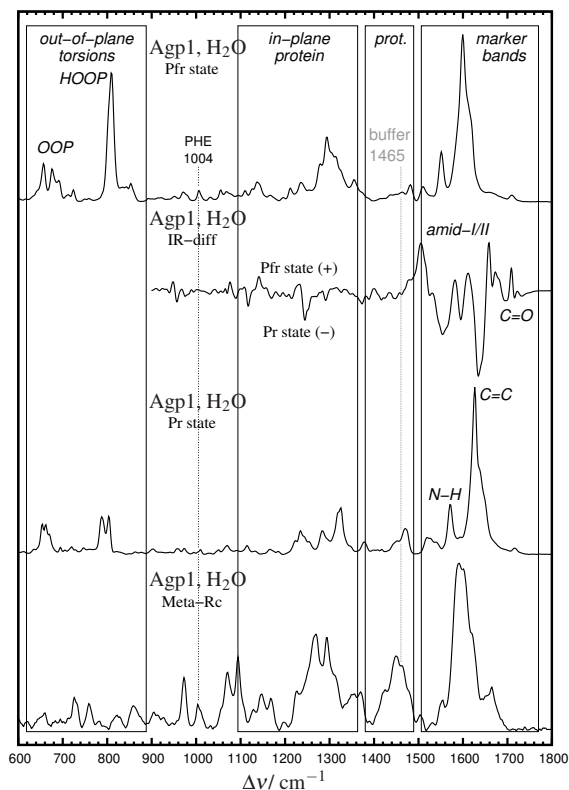


Figure 3.5: Vibrational spectra of Agp1 phytochrome with highlighted spectral regions and most relevant chromophore vibrational modes. In the top layer the RR spectrum of the Pfr state is displayed. The IR difference spectrum (Pfr minus Pr state) is plotted in the second layer. This spectrum was kindly provided by Patrick Piwowarski (AG Bartl, Biophysik Charité Berlin). Due to absorption of the BaF₂ windows (or CaF₂) no difference bands below 900 cm⁻¹ (1000 cm⁻¹) can be detected. The RR spectrum of the Pr state is shown in the third layer (from top to bottom). The bottom spectrum corresponds to the pure Meta-Rc state. The intensity of all spectra was normalized to the most intense band. The large boxes delimit the relevant phytochrome spectral windows. Structurally interesting vibrational modes are highlighted in bold. For calculation of the SCS values of each RR species, the intensity ratio of the strongest chromophore band and the PHE band or the buffer contribution have to be considered.

This applies for both parent states. Due to the considerably reduced RR intensity of this mode (1 – 2% of the strongest chromophore peak), the ring D C=O assignment was not possible in the intermediate species.

While the propionic side chains seems to play a crucial role in the chromophore assembly as well as in the parent state interconversion [16, 166], very little is known about the frequency assignment of the C=O stretching modes of this groups. It is clear that the C=O coordinate contributes to bending modes in the range from 1100 to 1200 cm^{-1} [140]. But, due to the overlap of protein modes with the C=O stretching ($-\text{COO}^-$) of the chromophore side chains, no clear assignment was possible. Only the current investigations on bathy phytochrome showed a protonation/deprotonation of the propionic side chain of ring C. In this case, the C=O mode of the protonated side chain ($-\text{COOH}$) could be easily assigned above 1750 cm^{-1} (see chapter 6).

C=C stretching The only IR active chromophore band has been assigned to the C=C stretching vibration of the BC methine bridge. Despite the overlap with amide modes, difference signals (Pfr-Pr) could be unambiguously assigned to this mode via $^{13}\text{C}_{10}$ chromophore labelling [159]. As mentioned in subsection 3.9.3, this mode is located at frequencies in the range within 1590 and 1610 cm^{-1} .

4. Results: pH dependence of the Cph1 parent states

4.1. Analysis of the Pr and Pfr state pH titration

Pr state raw spectra Between pH 6.0 and 9.0 the general spectral features of the ZZZssa-PCB chromophore are conserved (fig. 4.1 and fig. 4.3). First, the protonation state (N-H i. p.) and the position of the strong CD C=C stretching at ca. 1620 cm^{-1} . In contrast, the high frequency shoulder at ca. 1650 cm^{-1} appears at pH 6.0 almost as separate peak, while in alkaline medium this shoulder downshifts to the CD band. According to calculations and chromophore isotopic labelling [130] this shoulder was assigned to the C=C stretching of the AB methine bridge (*vide infra*). At around 1600 cm^{-1} a shoulder, probably assigned to the C=C stretching mode of the BC bridge gains intensity in slightly alkaline medium. Above pH = 8.5, the chromophore is largely deprotonated as indicated by the intensity decrease of the N-H i.p. band and through the broadening of the CD band (pH = 9.0). Chromophore intensity depletion is accompanied by an increase of the protein and buffer contribution (see RR spectrum at pH = 9.0 in fig. 4.1).

Pfr state raw spectra In contrast to the observed changes in the Pr form, the general chromophore features, characteristic for the Pfr state remained unchanged in the entire pH range studied here. The strongest bands are the CD band at 1608 cm^{-1} (marker region) and the characteristic HOOP peak at 803 cm^{-1} with a shoulder at 812 cm^{-1} . Furthermore, the N-H i.p. band at 1553 cm^{-1} indicates a fully protonated chromophore. Only above pH = 9.0 an apparently neutral Pfr species gains weight, as implicated by increasing protein and buffer contribution at the expense of chromophore bands.

Quantitative analysis of the parent states To investigate the pH-dependence of the chromophore species, component analysis was applied for both parent states separately (details given in section 3.7.1). The global analysis of the marker region in the Pr state

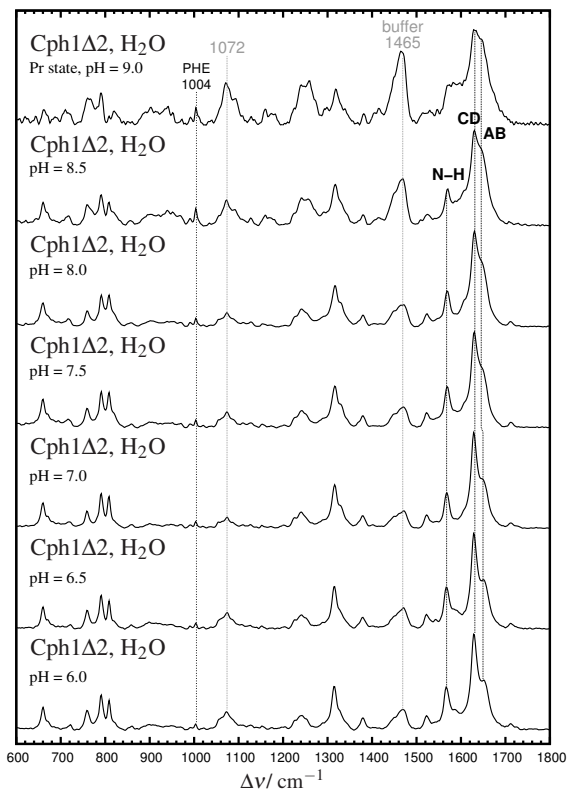


Figure 4.1: Full range RR spectra of the Pr state of CphI Δ 2 measured in H₂O buffer at different pH values. Protein contribution is observed at 1004 and 1465 cm⁻¹, while the buffer contribution can be especially monitored at 1072 cm⁻¹.

(Pfr state) started with three (two) initial “guess” components obtained by mutual subtraction of the spectra measured at the pH 6.5, 8.0 and 9.0 (pH 6.5 and 9.0) according to the following procedure

$$\text{Pr} - \text{I} = \text{Pr}(\text{pH}6.5) - k_1 \cdot \text{Pr}(\text{pH}8.0) \quad (4.1)$$

$$\text{Pr} - \text{II} = \text{Pr}(\text{pH}8.0) - k_2 \cdot \text{Pr} - \text{I} - k_3 \cdot \text{Pr}_{dept} \quad (4.2)$$

$$\text{Pr}_{dept} = \text{Pr}(\text{pH}9.0) - k_4 \cdot \text{Pr} - \text{II} \quad (4.3)$$

$$\text{Pfr}_{deprot} = \text{Pfr}(\text{pH}9.0) - k_5 \cdot \text{Pfr}(\text{pH}6.5) \quad (4.4)$$

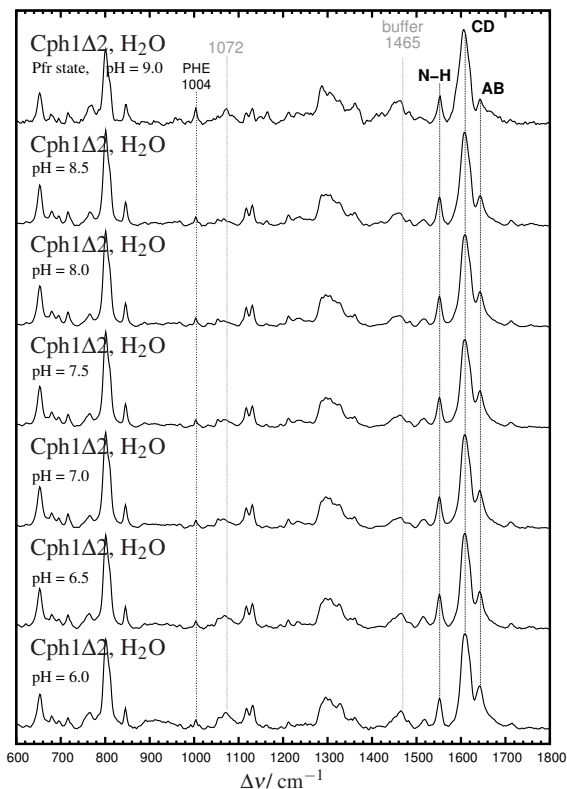


Figure 4.2: Full range RR spectra of the Pfr state of Cph1Δ2 measured in H₂O buffer at different pH values (in analogy to fig. 4.1), without Pr contribution. Protein and buffer contributions are considerably lowered after Pr subtraction.

$$\text{Pfr}_{prot} = \text{Pfr}(\text{pH}6.5) - k_6 \cdot \text{Pfr}_{deprot}. \quad (4.5)$$

Where the terms on the left side denote the “guess” component spectra and the terms on the right side the experimental RR spectra measured at different pH; k_i denote the respective weighting factors for the subtraction. Prior to the generation of the Pfr_{prot} and Pfr_{deprot} spectra, the Pr contribution at each pH value was removed. This procedure was validated by a global analysis of the raw Pfr spectra containing residual Pr contribution (*vide infra*). Determination of the guess component spectra of the Pr state could be simplified by defining two regimes: a pH dependent transition between two

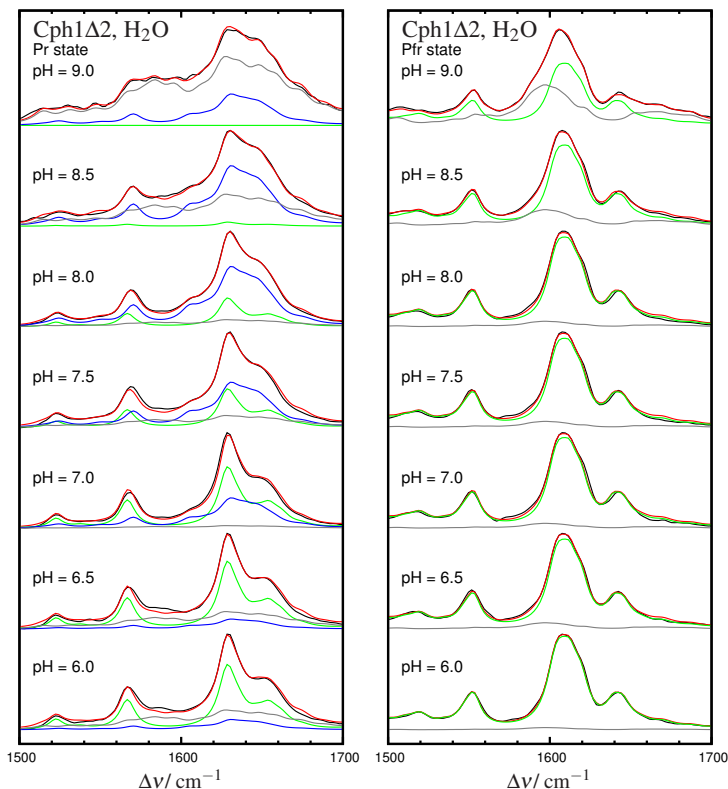


Figure 4.3: Global component analysis in the marker band region of the raw Pr and Pfr state RR spectra. The overall fit to the spectrum is plotted in red. Left: Pr spectra were fitted with three different component functions: **Pr-I**, **Pr-II** and Pr_{deprot} . Right: In the Pfr state, with only two components: **Pfr_{prot}** and Pfr_{deprot} .

cationic Pr-forms, namely Pr-I and Pr-II [180] and the deprotonation of the bilin at high pH values [195]. The Pfr spectra were analyzed in terms of an acid-alkaline transition, namely the equilibrium between a protonated (Pfr_{prot}) and a deprotonated (Pfr_{deprot}) species. However only at pH 9.0 the deprotonated Pfr species exhibits an appreciable concentration (see fig. B.3).

The spectral contribution of each Pr component indicates that at acidic conditions (pH 6.0-6.5) the overall spectrum is dominated by the Pr-I form. Its contribution decreases with increasing pH while the second protonated species, Pr-II, reaches a

pH	Pr-I	Pr-II	Pr _{deprot}	Pfr _{prot}	Pfr _{deprot}
6.0	0.679	0.108	0.209	0.816	0.037
6.5	0.704 (0.635)	0.105 (0.360)	0.184	0.817	0.073
7.0	0.639 (0.653)	0.318 (0.352)	0.029	0.824	0.079
7.5	0.403 (0.528)	0.474 (0.470)	0.127	0.797	0.093
8.0	0.300 (0.457)	0.631 (0.537)	0.076	0.795	0.094
8.5	0.042	0.631	0.335	0.732	0.173
9.0	0.000	0.328	0.724	0.540	0.350

Table 4.1: Spectral contribution of all species determined from the experimental RR spectra of the Pr and Pfr (fig. 4.3 and fig. 4.3, respectively). For further analysis and pK_a calculation the values of all components for each parent state were normalized separately to the highest at each pH value. In case of Pr-I and Pr-II, values within in brackets refer to the ¹³C₅-PCB Pr titration. Corresponding global analysis and raw RR spectra are shown in fig. B.3.

maximum concentration between pH 8.0 and pH 8.5 (fig. 4.3 and fig. 4.5). At pH 9.0 the Pr-I contribution is almost negligible and the contribution of Pr_{deprot} rises sharply at the expense of the protonated Pr species (see table 4.1). Unlike to the Pr-I and Pr-II species, the Pr_{deprot} spectrum shows strong similarities with the Meta-Rc intermediate, since it exhibits the general characteristics of a deprotonated chromophore spectrum [80]. Here, the C=C stretching marker bands are poorly structured and the lack of the N-H i.p. band is a clear indicator of the chromophore proton abstraction at either ring B or C. The values for Pr_{deprot} species at pH 6 and 6.5 as obtained by the spectra analysis are evidently an artefact of the fitting procedure that overestimates weak spectral contributions (see fig. 4.4 and fig. 4.5). Unlike to the Pr state, there is no indication for different pH-dependent cationic Pfr-conformers.

The spectral contributions obtained by the component analysis were used to determine the apparent pK_a value (pK_{a,app}) of each transition in both parent states. In the Pr state the model described two transitions: Pr-I-to-Pr-II and Pr-II-to-Pr_{deprot}. According to that, two proton-translocation events take place. For the Pfr state a single transition denotes proton uptake from the chromophore in alkaline medium:



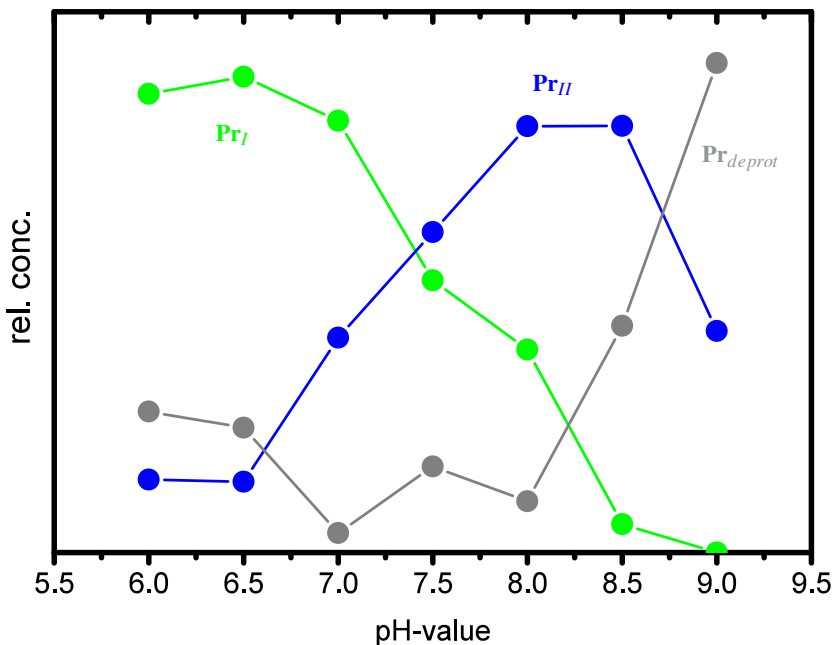


Figure 4.4: Pr state component contribution within pH 6.0 and 9.0. Exact values of the component concentration of the Pr-I, Pr-II and Pr_{deprot} species can be found in table 4.1

Here A refers to an amino acid that is protonable at neutral conditions must be localized in the vicinity of the chromophore (*vide infra*). The net pK_a values were determined from the apparent values ($pK_{a,app}$, see eqn. 3.27) including the scattering cross section-ratio as proportionality factor (see table 4.1 and E.1). For the Pr-I-to-Pr-II and Pr-II-to-Pr_{deprot} transitions we obtained an apparent pK_a value of 7.5 and 8.7, respectively (corresponding to a corrected pK_a of 7.2 and 8.6, respectively). In case of the chromophore deprotonation in the Pfr state a $pK_{a,app}$ value of 9.4 (pK_a of 8.8) was estimated. The Pr-I/Pr-II pK_a value is in reasonable agreement with literature values [195]. In contrast, the estimated deprotonation $pK_{a,app}$ values (both for the Pr and Pfr state) are lower than previously reported [23, 50]. Possible systematic errors refer to over or underestimation of the concentration or scattering cross-section of each component.

Interestingly, both chromophore-proton translocation events in the Pr and Pfr state follow the same sharp transition whereas the Pr-I-to-Pr-II titration curve is charac-

terized by a smoother profile. Since here the chromophore remains protonated, the equilibrium must reflect the (de)protonation of a nearby amino acid. A pH-dependent proton-translocation in the Pr chromophore pocket involves at least one histidine (His) group [195]. Two highly conserved His residues can be identified in close proximity to the cofactor: H260 and H290 (see fig. 2.4). According to the crystal structure, the first one is found on top of the chromophore, interacting over the conserved pyrrole water and in contact with rings A, B and C. The second is located at a β sheet region in the GAF domain. Hydrogen-bonding with the carbonyl oxygen of ring D can be assumed [49]. The pK_a value of the imidazole side chain is around physiological pH, however it might be shifted in the protein matrix due to the specific environment [75].

Protonation/deprotonation of the conserved histidine groups cannot be identified in the crystal structure [49]. Here electrostatic calculations might predict the appropriate protein protonation state in the chromophore cavity [120]. Assuming that, both His residues are potential candidates for the proton induced geometric or electrostatic tuning of the PCB chromophore, then the highly sensitive C=C bands (AB and CD) can be used to monitor the histidine-chromophore interaction in both Pr forms.

4.2. Structural analysis of the Pr-I and Pr-II conformers

Pure protonated Pr species Both, Pr-I and Pr-II spectra were compared to the Pr state measured in the crystal phase [130]. Band analysis of the marker region demonstrated a strong similarity between the Pr-I and the Pr crystal spectrum and supports the assumption, that the chromophore geometry is rather sensible to the protonation of the binding pocket than to crystal packing effects [125]. Due to similar pH conditions of the solute and crystallized Pr species (below pH = 6.0) [49, 130], all spectral features are largely conserved in the whole spectral range (see fig. B.1).

The N-H i. p. band observed at 1570 cm^{-1} (Pr-II species) is downshifted in the Pr-I as well as in the crystalline state ($2\text{-}3\text{ cm}^{-1}$). Furthermore, the strongest CD C=C band was detected at the 1629 cm^{-1} in all three spectra. In Pr-I and Pr_{crystal} a doublet at 1658 and 1677 cm^{-1} was observed (AB mode). This feature is downshifted by almost 12 cm^{-1} in the Pr-II species. Concomitant rising of a low frequency shoulder at around 1600 cm^{-1} is observed (BC C=C). The absence of this band in the acid form might be related to an upshift underneath the prominent CD band. In both solution Pr spectra, a small band was found at 1712 cm^{-1} . According to FT-IR measurements, this band could be assigned to the C=O stretching vibration of ring D [55, 56]. In case of the acidic and crystal Pr species, an additional high frequency band was found at 1722 and 1733 cm^{-1} , presumably assigned to the C=O stretching of ring A. However, the low intensity impeded unambiguous assignment in both cases.

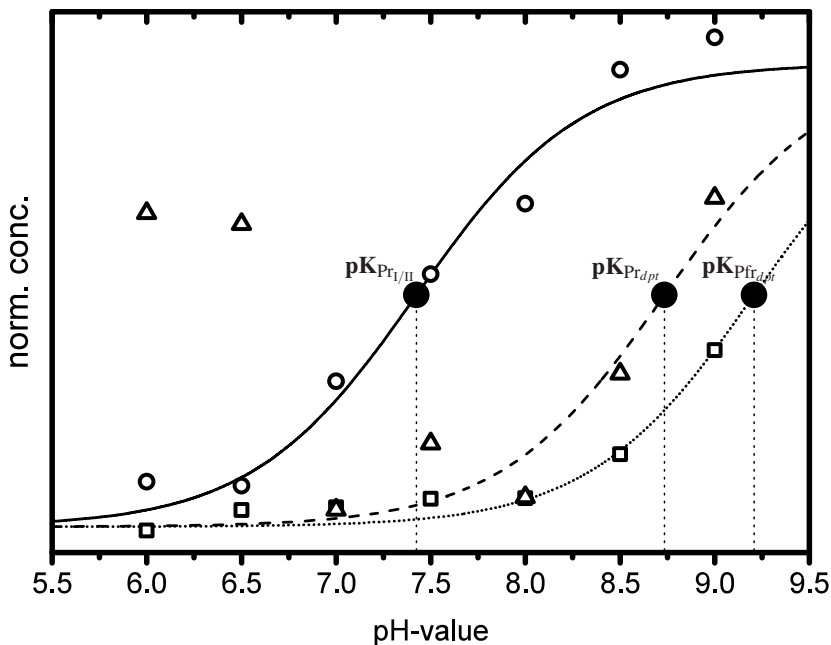


Figure 4.5: Determination of the pK_a values for the different pH dependent transitions. The Henderson-Hasselbach equation (—), (---) and (- - -) was fitted to the normalized concentration of the Pr-I-Pr-II (\circ), Pr-II-Pr_{deprot} (\triangle) and Pfr prot -Pfrdeprot (\square) conversion. The pK_a values derived from the fits correspond to the apparent $pK_{a,app}$ value which were then translated to de facto pK_a values according to eqn. 3.28.

The difference between the Pr-I and Pr-II is restricted to a small but detectable frequency upshift of the AB and BC C=C modes, while the CD C=C peak and N-H i.p. band appear to be largely unaffected. To corroborate this observation, we used isotopic labeling of the chromophore ($^{13}\text{C}_5$ -labelling and H/D exchange of the buffer) and analyzed the Pr state within the pH (pD) range of 6.5 and 8.0.

$^{13}\text{C}_5$ -PCB isotopic labelling Taking into account that isotopic labelling of the chromophore does not affect the pH dependence, the $^{13}\text{C}_5$ -PCB Pr spectrum can be interpreted as the sum of the Pr-I and Pr-II components. Below pH 8.0 the Pr_{deprot} component is rather small and as a first approximation it can be excluded from the Pr-I/Pr-II component analysis (see fig. B.3).

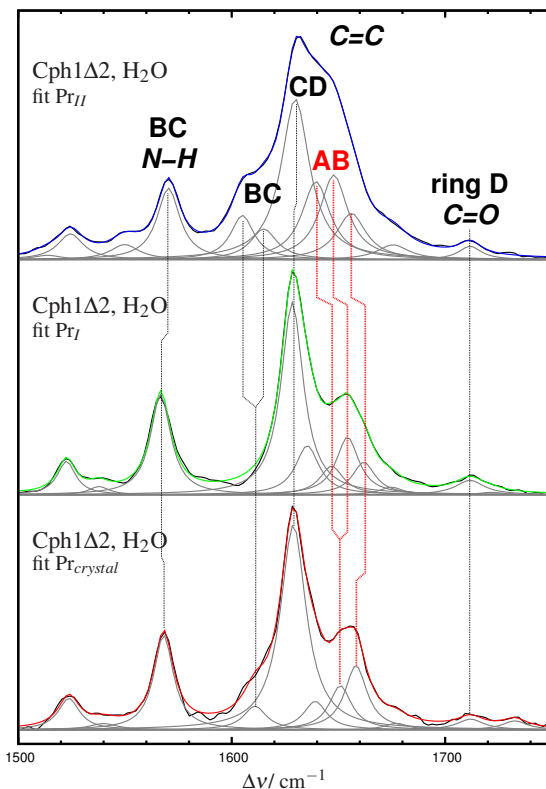


Figure 4.6: Band analysis in the marker region within the RR spectra of all protonated Pr state species from Cph1 Δ 2. Synthetic spectra for the Pr-I and Pr-II species, are shown in accordance to the color coding of fig. 4.3. The fit spectrum of the Pr_{crystal} species is plotted in red. Single band components are displayed in gray. Band frequency, intensity and width are given in table 4.2. Specific band displacement of the characteristic chromophore modes between the different Pr spectra are marked with dotted lines.

As expected, the CD and N-H i. p. show no isotopic shift. Furthermore, the $^{12}/^{13}\text{C}_5$ downshift of the highest frequency shoulder is consistent with previous investigations and can be therefore unambiguously assigned to the AB mode [130]. In the Pr-I species, the AB and BC $^{12}/^{13}\text{C}$ -downshift ($\Delta\Delta\nu = -25 \text{ cm}^{-1}$) is larger than in the Pr-II species (see fig. 4.7 and fig. 4.8). Here the AB and BC mode mixing allows for the assignment of the Pr-I BC mode at 1595 cm^{-1} . Its position in the non-labeled Pr-I

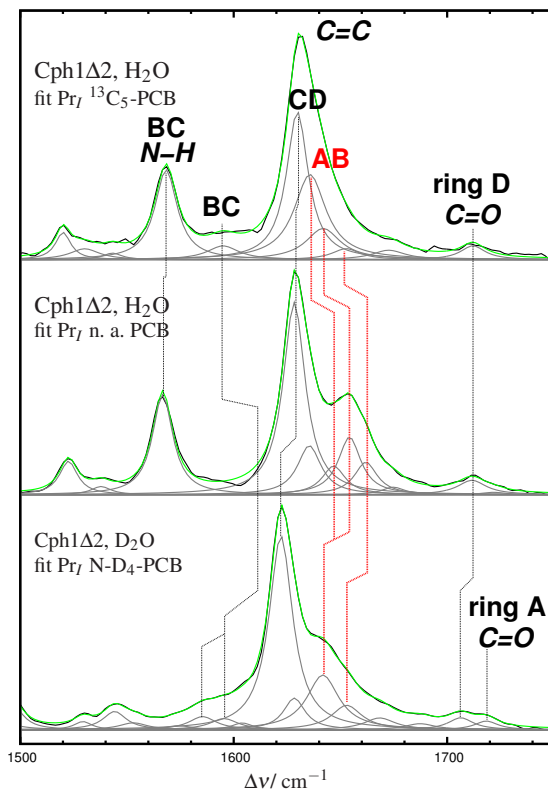


Figure 4.7: RR Pr-I spectrum of the Cph1Δ2 containing a native chromophore (top), $^{13}\text{C}_5$ -PCB or measured in D_2O . Single band components are plotted in gray while the fit spectrum is displayed in green. Isotopic shifts are highlighted with dotted lines.

overlaps with the CD frequency. Assignment of the BC mode is based on QM calculation and $^{13}\text{C}_{10}$ -labelling of the BV chromophore in Agp1 [159]. A detailed analysis of the BC mode in Agp1 and CphB phytochrome is given in section 5.2. In the Pr-II species, the AB band at 1648 cm^{-1} is downshifted underneath the strongest CD band after $^{12}/^{13}\text{C}$ -isotopic exchange ($\Delta\Delta\nu = -17\text{ cm}^{-1}$). A similar $^{12}/^{13}\text{C}$ -downshift was observed for the BC band at 1613 cm^{-1} , downshifted either close to the adjacent bands at 1602 or to 1586 cm^{-1} .

SCS	Pr _{crystal}			Pr _{acid}			Pr _{alkaline}		
	<i>v_i</i>	<i>I_i</i>	Δv_i	<i>v_i</i>	<i>I_i</i>	Δv_i	<i>v_i</i>	<i>I_i</i>	Δv_i
	18.29			18.75			9.05		
C=O	1733	0.038	14.1	1722	0.011	13.7			
	1712	0.046	15.1	1712	0.062	16.1	1712	0.057	12.8
	1677	0.028	13.0	1675	0.032	13.0	1676	0.063	18.0
AB	1658	0.274	12.5	1662	0.139	13.0			
AB				1654	0.246	12.8	1656	0.198	16.7
AB	1651	0.188	12.5	1647	0.122	13.1	1648	0.361	15.8
C=C	1639	0.122	12.9				1639	0.332	16.0
				1635	0.209	13.3			
CD	1629	0.872	14.5	1628	0.819	12.6	1630	0.684	16.2
BC	1611	0.101	12.8				1615	0.131	15.2
							1605	0.189	13.2
N-H	1562	0.403	11.1	1567	0.426	11.6	1570	0.304	12.9
	1540	0.027	16.0	1538	0.035	11.4	1550	0.065	16.3
	1524	0.134	12.0	1523	0.143	10.3	1524	0.111	14.4
							1514	0.019	16.0

Table 4.2: Band frequencies v_i , intensities I_i , full widths at half maximum (FWHM or Δv_i), and scattering cross section (SCS) of Pr_{crystal}, Pr-I and Pr-II. Values of the Pr_{deprot} form are listed in appendix E.4.

H/D exchange As expected, the N-D i.p. band is found at 1071 and 1073 cm^{-1} for the Pr-I and Pr-II, respectively [122]. The C=C stretching modes of the methine bridges, are primarily composed by the respective C=C stretching coordinates, albeit with minor contributions of the N-H bending i. p. coordinates of the adjacent rings. Upon H/D exchange at the respective N-H groups, these latter contributions are removed leading to a redistribution of the mode composition and therefore to a frequency shift of the corresponding C=C band. While in both species the CD band is found downshifted in D_2O , the Pr-I species denotes a larger isotopic effect on this mode ($\Delta\Delta v(\text{I}) = -8 \text{ cm}^{-1}$ and $\Delta\Delta v(\text{II}) = -6 \text{ cm}^{-1}$). A similar isotopic shift can be assumed for the BC band, although the peak intensity is rather low. In addition, overlap with protein bands of the deuterated amide groups compromises an unambiguous assignment. Following the previous results, the AB band of the Pr-I and Pr-II species

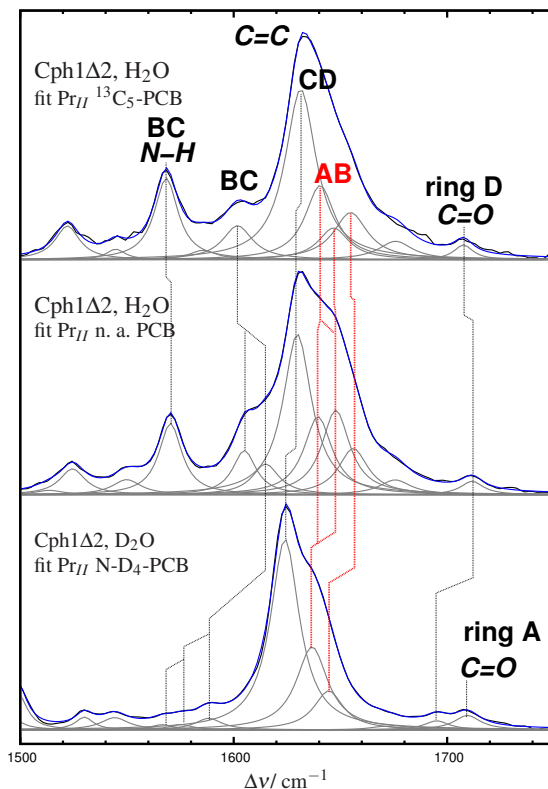


Figure 4.8: RR Pr-II spectrum of the CphIΔ2 containing a native chromophore (top), $^{13}\text{C}_5$ -PCB or measured in D_2O . Overall fit spectrum is displayed in blue, while other plotting details are as in figure 4.7.

was detected as a high frequency shoulder of the CD band. Furthermore, the frequency separation of AB and CD bands was larger in the Pr-I than in the Pr-II species ($\Delta\Delta\nu(\text{Pr-I}(\text{AB}/\text{CD})) = -22 \text{ cm}^{-1}$ and $\Delta\Delta\nu(\text{Pr-II}(\text{AB}/\text{CD})) = -15 \text{ cm}^{-1}$).

According to the Pr-I and Pr-II band analysis, the main difference refers to an upshifted AB band in the Pr-I form. As a result of the AB and BC mode mixing, the BC-frequency also shifts up in the Pr-I form. The slight downshift of the N-H i. p. mode in the Pr-I species is less prominent, but it reflects an inverse trend. On the other hand, the CD mode remains insensitive to the modified electrostatics in both Pr species.

4.3. Structural analysis of the protonated Pfr state and deprotonated species

Pfr_{prot} The single component analysis and band assignment of the RR spectrum of the Cph1Δ2 Pfr state has been discussed extensively in previous works [104, 186, 189]. It is assumed that like in all prototypical phytochromes the Pfr state of Cph1 exhibit also an intrinsic structural heterogeneity [159]. This is clearly revealed by analyzing the broad CD band and its highest frequency AB counterpart. While the latter one can be interpreted as a doublet with peak maxima at 1656 and 1645 cm⁻¹, the composition of the broad CD band is complex. A first attempt fit the CD envelope included an ensemble of 5 Lorentzians (1619, 1612, 1606, 1603 and 1596 cm⁻¹). The N-H i.p. band could only be reproduced as doublets (1553 and 1547 cm⁻¹).

In a further approach (data not shown), the fitting procedure was applied to the Pfr spectra of a compilation of different PCB binding phytochromes. Also multiple isotopic labelling of the chromophore (¹⁵N₄-PCB, ¹³C₁₅-PCB, etc.) was included. This allowed a precise elucidation of the number of bands beneath the CD envelope and of the N-H i. p. band. Subsequently, the number of single Lorentzian functions required for a satisfactory fit was reduced, however this implicated an increased of the band-width of the involved Lorentzian functions. According to these and previous findings, the chromophore structure can be found in two or more ZZEssa conformers. These differ in the AB and CD methine bridge bond length and/or in the dihedral angle of adjacent pyrrole rings (A/B and C/D). Interestingly, the conformationalequilibrium cannot be altered as a function of the pH.

Deprotonated Pr and Pfr species The overall spectrum in both species is dominated by broad band features. The most valuable information is the lack of the N-H i. p. band, the poor H/D sensitivity, as well as the decreased scattering cross section. Interestingly, deprotonated Pr and Pfr species can be distinguished on the basis of the broad C=C band, probably corresponding to the CD peak [118, 119]. Pure deprotonated spectra (Pr and Pfr) are shown in fig. B.2 and B.8. The band fitting does not allow a defined structural analysis; however, the inclusion of the “synthetic” deprotonated species was crucial to determine the pH dependent spectral profiles in both parent state. Single band components of the pure deprotonated spectra can be found in table E.4.

4.4. pH-dependence of the H260Q mutant

Previous investigations suggested the involvement of H260 rather than H290 group in the protonation equilibrium of the Pr state [74, 180, 195]. Hence, to unambiguously identify its relevant function, the H260Q mutant was subjected to a pH dependent

vibrational analysis (pH 7.0 to 8.5). The glutamine residues preserves the polarity of the histidine, however the pK_A value of the amide function is distinctly higher such that there is no indication for a Pr-I/Pr-II equilibrium. Due to lower degree of chromophore binding, protein bands display a higher intensity and thus the apoprotein ($S_{\text{apoprotein}}$) contribution had to be considered for the subtraction procedure:

$$\text{Pr}_{\text{H260Q}} = \text{Pr}_{\text{raw}} - k_7 \cdot S_{\text{apoprotein}} \quad (4.8)$$

$$\begin{aligned} \text{Pfr}_{\text{H260Q,prot}} &= \text{Pfr}_{\text{H260Q}}(\text{pH}7.0) - k_8 \cdot \text{Pfr}_{\text{H260Q}}(\text{pH}8.5) \\ &\quad - k_9 \cdot \text{Pr}_{\text{H260Q}} \end{aligned} \quad (4.9)$$

$$\text{Pfr}_{\text{H260Q,deprot}} = \text{Pfr}_{\text{H260Q}}(\text{pH}8.5) - k_{10} \cdot \text{Pfr}_{\text{H260Q,prot}}. \quad (4.10)$$

H260Q Pr state Only a single protonated Pr component was detected. At pH 8.5 chromophore deprotonation already occurs, but its contribution to the overall spectrum is rather small (fig. 4.9). The protonation state of chromophore was elucidated by the characteristic H/D sensitive N-H i. p. peak at 1575 cm^{-1} . This band is upshifted compared to the native Pr-I and Pr-II forms. In the H260Q-Pr state, the CD peak is upshifted to 1644 cm^{-1} ($\Delta\Delta\nu(\text{Pr}(\text{n.a.}/\text{H260Q})) = +15 \text{ cm}^{-1}$), overlapping with the AB mode. Finally, no clear BC band could be identified. However, it might be obscured by the stronger CD band. In this respect, the chromophore in the H260Q-mutant adopts a distorted ZZZssa-like geometry with all pyrrole nitrogen atoms being protonated.

H260Q Pfr state The photo-conversion product of Pr, formed at room temperature, was predominantly deprotonated (pH 7.8 to 8.5), and only at pH 7.0 formation of a protonated species could be induced (*vide infra*). In accordance with the wild type, a single acid-alkaline transition was observed. However the $\text{Pfr}_{\text{H260Q,prot}}/\text{Pfr}_{\text{H260Q,deprot}}$ pK_{mathrma} value was considerably lowered. Here, the amid-function of Q260 favors the proton abstraction leading to a preferentially neutral chromophore species at physiological pH. Unlike the native phytochrome, a Pr back-formation (after far red light irradiation) is preferred at pH 7.0. At higher pH values, Pr-back conversion from the deprotonated Pfr species was partially inhibited.

Compared to the native Pfr_{prot} , the $\text{Pfr}_{\text{H260Q,prot}}$ chromophore is probably highly distorted, although all Pfr marker bands were observed. These are the N-H i. p. band at 1560 cm^{-1} and the CD band found at 1618 cm^{-1} , which in analogy to the Pr state of H260Q is upshifted by ca. 15 cm^{-1} compared to the spectrum of the native Pfr. The AB mode is downshifted underneath the CD band (see fig. 4.9 and table E.3). These differences suggest a distorted ZZEssa cationic chromophore structure. Finally, the characteristic Pfr state CD HOOP doublet was observed at 803 cm^{-1} with a shoulder

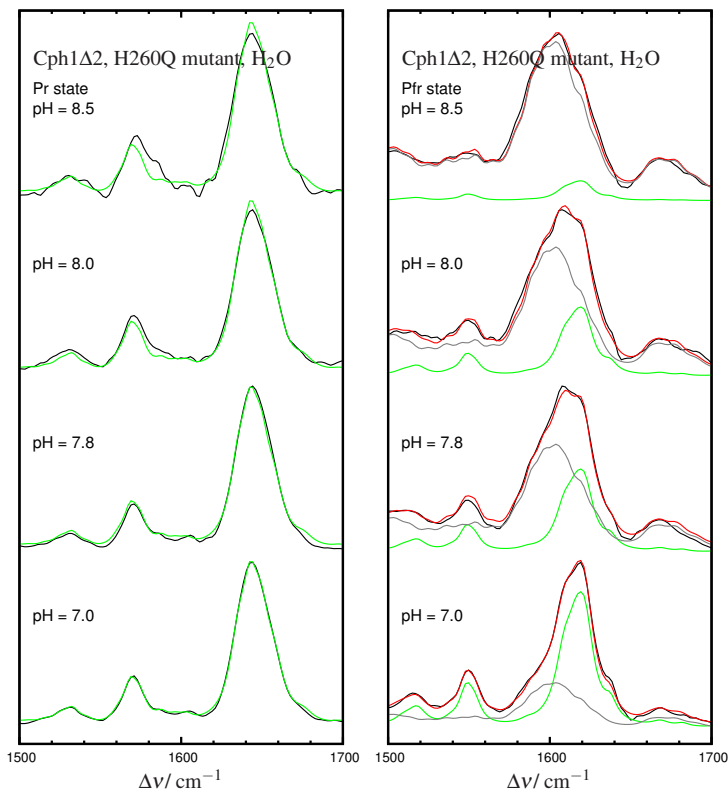


Figure 4.9: RR spectra of the Pr (left) and Pfr state (right) of the Cph1Δ2H260Q mutant measured in aqueous buffer at different pH values (solid black). Global analysis of the Pr state was carried out using a single component (Pr_{H260Q}). In the other hand, the $\text{Pfr}_{\text{H260Q,prot}}$ and $\text{Pfr}_{\text{H260Q,deprot}}$ component spectra reproduced well the raw Pfr species. The overall fit spectrum is shown in solid red. Corresponding fullrange Pr and Pfr spectra are shown in fig. B.5 and fig. B.5, respectively.

at 812 cm^{-1} in agreement with the native Pfr CD HOOP doublet (803 and 810 cm^{-1} , respectively) [205].

Despite the poorly resolved and broad band structure, the deprotonated Pfr species of the H260Q-mutant is reminiscent of the native phytochrome $\text{Pfr}_{\text{deprot}}$ species (see fig. B.8). Thus, the deprotonated Pfr species might be interpreted as a thermally stable Meta-Rc species.

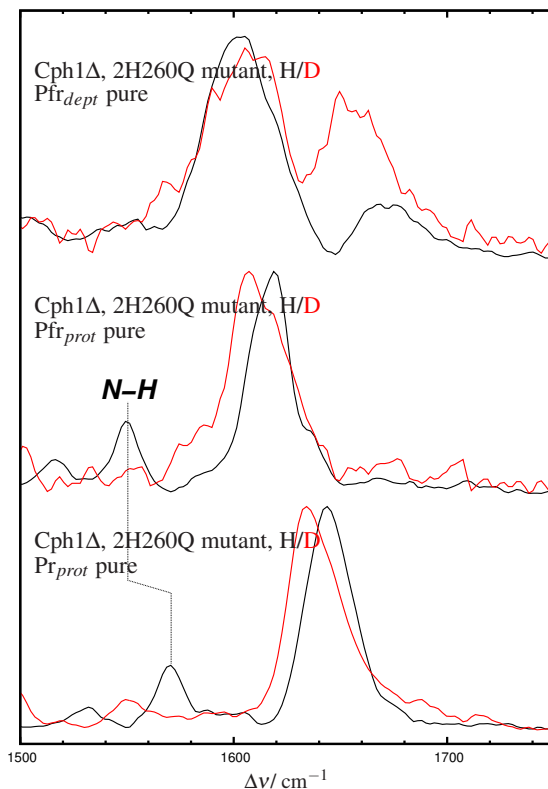


Figure 4.10: Marker bands of the CphI Δ 2H260Q RR Pr and Pfr spectra measured in H₂O and in D₂O. Top: Pfr_{H260Q,deprot}; center: Pfr_{H260Q,prot} and bottom Pr_{H260Q}. Corresponding fullrange spectra shown in fig. B.7.

4.5. Discussion

Pr state Combining the results of the pH dependent transition in the native CphI Δ 2 assembled with the unlabeled and the isotopically labeled PCB chromophore, as well as the H260Q mutant, it is shown that the H260 is intimately involved in the Pr-I/Pr-II equilibrium. The Pr-I species is observed in acidic conditions, both in solution as in the acidic crystallized form. The population of the Pr-II rises at slightly alkaline conditions. Identification of the N-H i. p. mode in both Pr forms denotes a prevailing cationic chromophore structure in a similar a ZZZssa geometry. While the chromophore remains

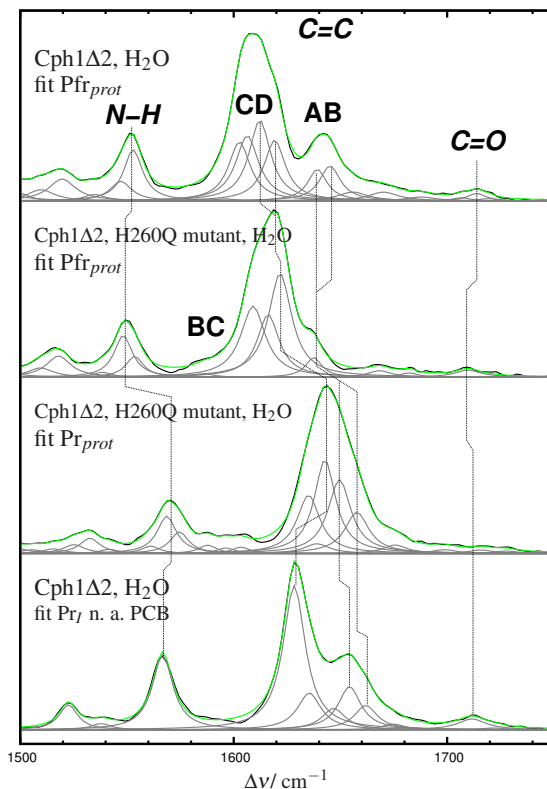


Figure 4.11: Analysis of the marker band region of the Pfr_{prot} (top) and $\text{Pfr}_{\text{H260Q}, prot}$ component spectra, as well as the corresponding Pr_{H260Q} and Pr-I (bottom) species. Component spectrum (solid black) is displayed with the corresponding fit spectrum (solid green) and all single Lorentzian components (solid gray). Band fitting parameters are given in table E.3.

largely protonated, the $\text{H260-H}^+ \rightarrow \text{H260}$ transition, is clearly detected by the down-shift of the AB mode upon His proton release (Pr-I \rightarrow Pr-II). Here the positive charge distribution has a clear influence on the pyrrole rings A and B. The CD bridge is more robust to pH changes, thus the transient protonation of H260 has a less pronounced effect on rings C and D. While a proton-translocation at the H290 residue cannot be excluded, the effect on the adjacent rings C and D is undetectable as revealed by the spectra of the H260Q mutant. Upon H260 substitution the Pr-I \rightarrow Pr-II transition is

cancelled and only a single Pr conformation populated. Here all four pyrrole nitrogens of the chromophore are protonated. The H260Q mutation itself induces larger changes in the chromophore structure, as reflected by the upshift of the CD and N-H i. p. bands. It also probably affects the water network in the pocket, especially the hydrogen bonding of the conserved pyrrole water. Furthermore the lack of the conserved histidine also affects the photocycle, especially the proton uptake during the Meta-Rc \rightarrow Pfr transition (*vide infra*).

The observed Pr-I/Pr-II equilibrium matches nicely with the isoforms determined with magic-spinning NMR-spectroscopy, especially regarding the proton-translocation of H260. However, the NMR data implies that the histidine protonation affects rings C and D, which clearly contradict our observations [180]. Despite the discrepancy, it seems that the role of the H260 in stabilizing the Pr-I or Pr-II conformers is not only relevant in Cph1 phytochrome, but also plays a crucial role in the Pr state of plant phytochromes [178]. The vicinity of the chromophore binding site (C259, GAF domain) is intimately linked to the conformer population. Interestingly, in prototypical bacterial phytochromes the Pr state denotes an intrinsic structural heterogeneity in solution [136], which is cancelled in the crystalline state [185]. However, the Pr conformer population in BV binding phytochromes cannot be altered in terms of the protonation of the binding pocket. First, the binding site (C12 within the PAS domain) and the conserved histidine are not in direct vicinity as in Cph1. Second, no pH dependence of the Pr state has been reported. Hence, the BV chromophore denotes a higher mobility and the protonation effect of the imidazole-ring might be weaker.

Early investigations on Cph1 and Cph1 Δ 2 demonstrated deviations in the recorded Pr fluorescence spectra, depending on temperature and pre-illumination conditions. Hereby strong evidence for chromophore heterogeneity was found, in which two PCB conformers coexist in a thermo-equilibrium [175]. However, formation of a Pr photo-product or large protein structural rearrangements could be ruled out since our experiments only demonstrated a small change, namely the H260-tuned coexistence of two similar Pr species. Furthermore the Pr-I \rightarrow Pr-II as well as the Pr-II \rightarrow Pr_{depr} transitions are reversible, thus deprotonation can be excluded (*vide supra*).

Using femto-second stimulated Resonance Raman (FSRR) spectroscopy the existence of a multiple conformer population in the Pr state was ruled out [181, 182]. Combing the FSRR and absorption data, Raman excitation profiles (REPs) were calculated. Subsequently, the absorption profile and the ratio of the vibronic transitions (0–0, 0–1) at RT as well as at low temperatures were interpreted in terms of a homogeneous Pr state. Our results differ from these conclusions, since we clearly observe a two-conformer Pr-equilibrium. This difference may root in the buffer conditions. The temperature effect is a parameter that has to be considered, yet the His260-H₊ \rightarrow H260 pK_A determination via absorption measurements [195] is in line with the current RR

approach, even though absorption measurements and RR experiments were performed at different temperatures. Furthermore, the pK_A value of the keto/enol tautomerism in the Pr state of the Agp2 bathy phytochrome was unambiguously determined by absorption, infrared and RR spectroscopy [207, 221].

While the temperature might play a crucial role in intrinsic conformational heterogeneity [159], the Pr-I/Pr-II equilibrium is linked to the protonation of the chromophore binding pocket. Hence, cryogenic RR spectroscopy is a suitable method to study this process. According to our results and considering the pH 8.0 in the FSRR experiments, a rough calculation of the Pr-I/Pr-II ratio can be obtained (*vide supra*). In this respect, the overall Pr spectrum would contain predominantly Pr-II (63%) with a smaller Pr-I contribution 30%. Also the deprotonated chromophore species has a small contribution (7%). In this respect, interpretation of the FSRR Pr spectrum could be then obscured, since this technique might not be sufficiently sensitive to detect minor sub-populations. In fact, due to the position of the strongest CD C=C band at 1630 cm^{-1} and the AB band at 1658 cm^{-1} , the FSRR Pr spectrum could be unambiguously addressed to the Pr-II species.

Finally, the buffer capacity has an influence on the chromophore structure as found by comparing the spectra obtained with decreasing the buffer concentration and ionic strength from 50mM Tris-Cl and 300 mM NaCl to 2.5 and 5 mM respectively. Preliminary results on the Pr state exhibit an upshift of $+5\text{ cm}^{-1}$ accompanied by a band broadening (see fig. B.9). Additionally, in the HOOP region a shoulder at 821 cm^{-1} gains intensity. Interestingly the N-H i. p. band, as well as the BC band remained at the same frequency. It remains unclear if the AB mode is affected by the decrease in buffer capacity and ionic strength due to the overlap with the upshifted CD mode. Finally, it is very likely, that the recorded Pr species represents a mixture, containing the Pr-I/Pr-II and the Pr-X species. Like in the H260Q-mutant, the upshift of the CD C=C mode in the Pr-X species might correlate with a blue-shift in the absorption maximum (probably non-photoactive Pr species).

Interestingly this further equilibrium might be related to the dynamic inhomogeneity recently proposed [99]. Here the fluorescent Pr state is blue shifted compared to the photo-active species. In contrast, the Pr-I species is red shifted [195]. Furthermore, the fluorescent Pr species is photochemically inactive, while in the present investigation the Pfr conversion is almost pH insensitive, yielding 57-60% at photo-stationary equilibrium between pH 6.0 and pH 8.5 (Pfr raw global analysis, see table E.5), as also determined by absorption spectroscopy [195]. In this respect, the dynamic inhomogeneity monitored as a function of the temperature might not be strictly related to the Pr-I/Pr-II equilibrium. However this should be clarified in future investigations.

Pfr state Unlike to the Pr state, an effect on the Pfr chromophore due to proton uptake or release by His260 or alternatively H290 can be ruled out. However, H260 plays a crucial role during the Meta-Rc decay and the subsequent chromophore reprotonation, corresponding to the Pfr formation. Here the H260Q mutation cancels the proton-translocation (pH 7.8–8.5). This could only be overcome by providing a more acidic environment (pH 7.0). Furthermore, H260 is important for stabilizing the chromophore structure in the Pfr state. Thus, absence of this residue, even with a relatively conserved polarity (H260Q-mutation), alters the bilin structure, as implied *inter alia* by the CD C=C upshift. However, the effect on the subsequent signaling events remains uncertain.

Within the Pr-to-Pfr transition a net acidification was observed [195]. The proton release in the Pfr increased at lower pH values. According to our observation, this would have interesting implications in the Pr-to-Pfr pathway. First, the acidification might be correlated with the negligible pH effect on the chromophore structure in the Pfr state suggesting that the pK_A of H260 is lowered during the Pfr formation such that it is deprotonated even down to pH 6.0. Reversible protonation of the H260 occurs after Pr formation, yet only in sufficiently acidic conditions. This would imply that during the Pfr-to-Pr conversion, reprotonation of the H260 is coupled to the Pr-I conformer formation. This is not obvious from the Pr state analysis alone. Secondly, the proton-translocation event during the Pr-to-Pfr conversion is not pH dependent but the concentration of the intermediate species evidently changes as a function of the pH. Hence, the role of a protonated or deprotonated H260 certainly moderates the last step of the Pr-to-Pfr pathway.

Conclusions The chromophore structure in the Pr state of CphI Δ 2 is found to exist in two similar ZZZ_{ssa} conformers. In acidic conditions the population of the Pr-I form predominates. However, at slightly alkaline conditions, it undergoes a structural change at the AB methine bridge, leading to the PR-II conformer. This equilibrium is tuned by the protonation state of the conserved H260. Mutation of this residue abolishes the conformational equilibrium in the Pr state. During the Pr-to-Pfr formation the histidine side chain lowers its pK_a value (imidazolium/imidazole) leading to a pH independent Pfr state. Finally, the H260 plays a crucial role as key residue within the proton-uptake event during the Pfr formation.

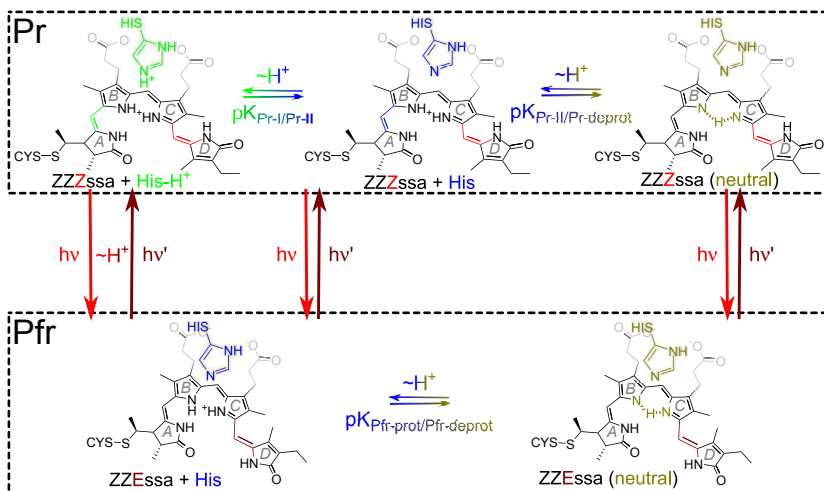


Figure 4.12: Summary of the proton translocation events in the binding pocket. Top: Pr-I/Pr-II and Pr-II/Pr-deprot transition. Bottom: Pfr-prot/Pfr-deprot. The Pr-to-Pfr conversion as well as the role of the H260 are indicated.

5. Results: Pr-to-Pfr chromophore structure changes in prototypical phytochromes

5.1. Role of the PHY domain during the Pr-to-Pfr conversion

In addition to the chromophore isomerization, the Pr-to-Pfr conversion the main protein-structure transition is associated with a β -sheet to α -helix refolding of the tongue motif in the PHY domain. This event is apparently associated with the signal amplification of the Pfr state [190].

The β -sheet to α -helix transition has been independently identified by infrared spectroscopy, both for prototypical [187], as well as for bathy phytochromes [207] (α -helix to β -sheet). In the difference infrared spectra of the Agp1 and Rph2 photosensory-domain variants (Agp1FMR and Rph2-PGP), structural changes associated with such a protein-folding event were detected in the amide-I region. In the Pr state, the characteristic β -sheet is observed at 1634 cm^{-1} and 1629 cm^{-1} in Agp1FMR and Rph2-PGP phytochromes respectively (see fig. 5.1). After Pfr formation, this feature disappeared and instead a strong peak was observed at 1659 cm^{-1} (1655 cm^{-1} in Rph2-PGP). This peak corresponds to the formation of an α -helix motif in the Pfr state. Deletion of the PHY-domain in Rph2 (Rph2-PG) leads to intensity loss of both, the beta-sheet peak in the Pr and the alpha-helix-peak in the Pfr state (fig. 5.1 bottom).

5.2. Assignment of the BC C=C stretching mode in the Pr and Pfr state

According to previous measurements in model compounds [171], QM calculations [123, 184] and as described in subsection 3.9.4, the C=C BC mode, shows a very strong IR intensity, but negligible Raman activity [159]. In Agp1 phytochrome it was demonstrated that, the interpretation of isotopic displacements based on the $^{13}\text{C}_{10}$ -labelling of the BV chromophore is rather complex, especially compared to $^{13}\text{C}_5$ or $^{13}\text{C}_{15}$ -labelling experiments.

However, $^{13}\text{C}_{10}$ -BV labelling in combination with H/D exchange experiments, allowed a more accurate mode assignment in the heterogeneous parent state RR spectra of prototypical phytochromes. Both native phytochrome-proteins (CphB and Agp1)

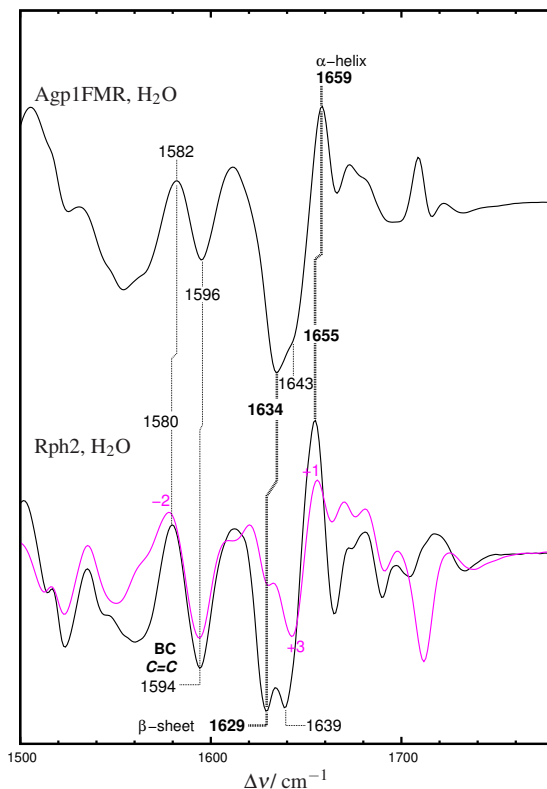


Figure 5.1: Amide-I and amide-II region of the Agp1 (top), Rph2-PGP (bottom) and Rph2-PG (magenta) Pfr-minus-Pr IR-difference spectra. Band assignment of the protein-folding associated Pr-to-Pfr transition are indicated (β -sheet-to- α -helix). Additionally, Pr and Pfr BC C=C mode assignment is displayed [159]. Agp1 IR spectrum was kindly provided by Patrick Piwowarski (AK Bartl, Charité Berlin).

have already been investigated by RR spectroscopy [184] and are also discussed in this work (see section 5.3 for Agp1 and 5.5 for CphB).

The difference between the phytochrome spectra containing a native and a $^{13}\text{C}_{10}$ -labeled BV can be illustrated by calculating difference $^{12}\text{C}/^{13}\text{C}$ -spectra. Here, only difference bands rise, if a certain vibrational mode involves the C_{10} -atom. Any contribution of modes which are not affected by the ^{13}C -labelling is cancelled. In addition to the C=C stretching vibration, the BC coordinates also contribute to mixed N-H i. p.

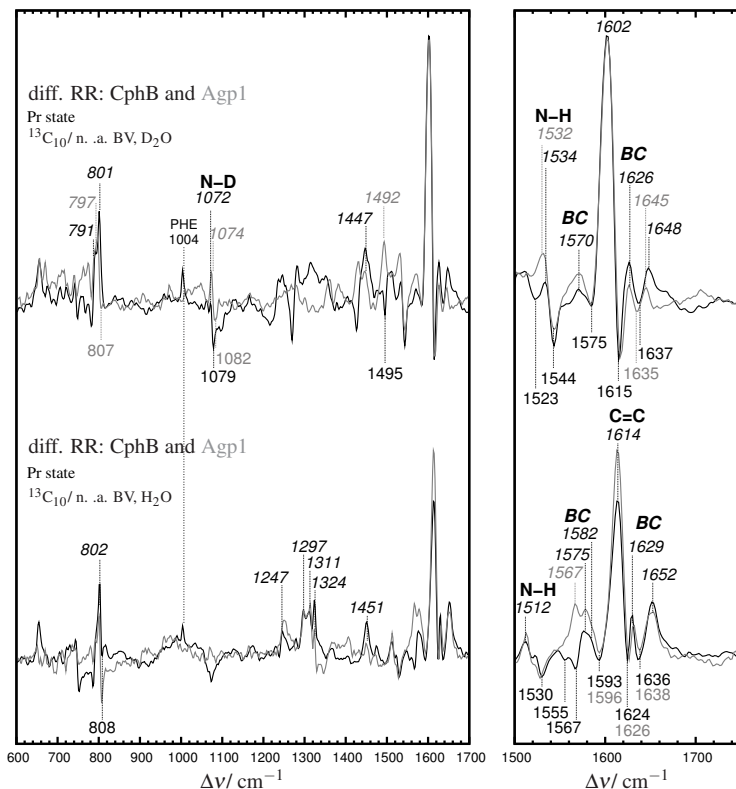


Figure 5.2: Difference RR Pr spectra of Agp1 and CphB assembled with native BV (negative peaks) and $^{13}C_{10}$ labeled chromophore (positive bands), recorded in H_2O (bottom) as well as in deuterated medium (top).

deformation modes of rings B and C [184] (between 1500 and 1550 cm^{-1}). Smaller difference peaks are also expected in the region around 1300 cm^{-1} (C-C or C=N). Interestingly, both Pfr and Pr $^{12}C/^{13}C$ -difference spectra of Agp1 and CphB are largely similar. Moreover, the similarity in the marker region is quite remarkable.

Pr state The difference bands in the Pr state of CphB are in excellent agreement with the corresponding Agp1 spectrum. Generally, the C=C stretching mode of the BC methine bridge was found at lower frequencies than the strong CD band. In case of BV binding phytochromes, the CD band was observed at ca. 1625 cm^{-1} . According to IR

difference measurements, the BC- $^{12}\text{C}/^{13}\text{C}$ -bandpair in Agp1 was observed at 1596(-)/1575(+) cm^{-1} (CphB: 1593/1575 cm^{-1}). However the strongest difference features in fig. 5.5.2 corresponds to the peaks at 1626(-)/1614(+) cm^{-1} (1624/1614 cm^{-1}). According to ref. [159], coupling with the AB mode is also observed in Pr state. Here, the band pair 1638(-)/1629(+) cm^{-1} (1636/1629 cm^{-1}) would perfectly match the AB mode. All bands involving the BC bridge, undergo H/D shifts of around -9 to -12 cm^{-1} , reflecting the coupling with the N-H (N-D) groups of rings B and C.

Additional $^{12}\text{C}/^{13}\text{C}$ -band pairs are observed at 1530(-)/1512(+) cm^{-1} and in the HOOP region at 808(-)/802(+) cm^{-1} . The first pair probably refers to a N-H bending mode that contains BC bridge coupling. The HOOP mode rises probably from C₁₀-H methine-group. The N-D i. p. mode at 1082 cm^{-1} (1079 cm^{-1}), couples with the BC bridge. Hence, the 12/13C-exchange is associated with a -7 cm^{-1} downshift of this mode. However, the N-H i. p. is not affected by the isotopic labelling.

Pfr state In agreement with the Pr $^{12}\text{C}/^{13}\text{C}$ -difference spectra, both phytochromes show a very similar Pfr-difference-band pattern. However, slight frequency deviations (approx. 3-6 cm^{-1}) indicate a similar yet not completely identical chromophore structure and protein-bilin interactions (hydrogen bonding, electrostatics, etc.).

According to ref. [159] and in agreement with the previous band assignment of the Pr state, two possible BC peaks were detected at 1619(-)/1605(+) cm^{-1} [(1613/1603 cm^{-1})] and 1585(-)/1563(+) cm^{-1} . However, the latter band-pair was less prominent and considerably broadened. Indication of a second peak as shoulder was observed at 1592(-)/1556(+) cm^{-1} . In CphB assembled with native BV, the negative shoulder was observed as separated peak at 1596 cm^{-1} . In general the $^{12}\text{C}/^{13}\text{C}$ -isotopic downshift of all bands was around -10 to -20 cm^{-1} , with an additional -10 cm^{-1} shift after H/D exchange.

While the frequency position of the first difference peak nicely matches with the BC-coupled AB mode, the broad nature of the low frequency C=C peak strongly points to an overlap of two BC modes which are separated by some wavenumbers.

In the Pfr state the N-D coupling with the BC bridge prevailed. In both phytochromes, the Pfr N-D difference peak downshifted by approx. -12 cm^{-1} compared to the Pr spectra (see fig. 5.2 and 5.3).

Contrary to the Pr state, a strong difference HOOP band at 811 and 803(-)/814(+) cm^{-1} (799/814 cm^{-1}) with a poor H/D effect was observed. Interestingly, in CphB this feature was even stronger than in Agp1. This region displays considerable difference even in the absolute spectra, where the CD HOOP doublet of CphB denotes inverse band intensities (see fig. D.2 and ref. [159]).

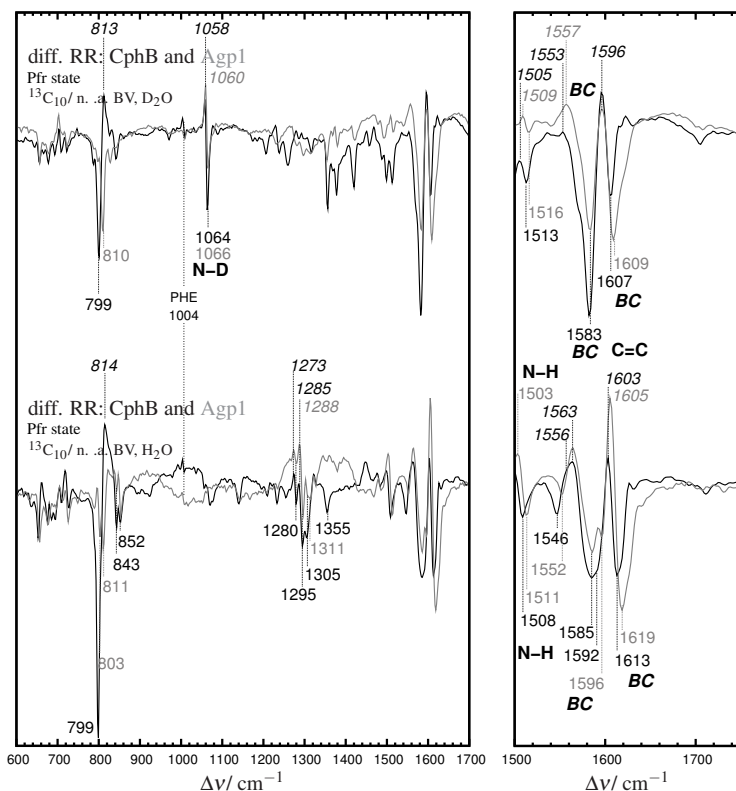


Figure 5.3: Difference RR Pfr spectra of Agp1 and CphB assembled with native BV (negative peaks) and $^{13}\text{C}_{10}$ labeled chromophore (positive bands). Further details are given in fig. 5.2.

5.3. Temperature-dependent Pr-to-Pfr evolution in Agp1 phytochrome

Between -140 and -70 °C recorded RR spectra of the Agp1 phytochrome are largely dominated by the Pr state, both in H_2O and in D_2O (see fig. C.1). However, above -50 °C, the Pr contribution steadily decreases. At -30 °C larger spectral changes are observed, accompanied by increase of the relative intensity of protein marker bands (e.g. 1004 cm^{-1}). Unlike Cph1 phytochrome (see chapter 4), the RR spectrum of

Agp1 recorded after RT red-light irradiation is found almost in a pure Pfr state with negligible Pr contribution.

5.3.1. Identification of possible pure intermediate spectra

Pure component spectra of both parent states (Pr and Pfr) were obtained by mutual subtraction and subsequent apoprotein correction¹. At very low irradiation temperatures (-140 °C and -120 °C) only a mixture of Pr and the photo-product, Lumi-R intermediate was observed. With rising irradiation temperature, contribution of the intermediate species preceding the Pfr state (Meta-Ra and Meta-Rc) were observed. Here the spectrum at -30 °C is dominated by the Meta-Rc species, whereas the guess Meta-Ra component displays a strong contribution to the -50 °C spectrum [184, 205]. The following subtraction procedure was applied for the spectra set recorded in H₂O and in D₂O:

$$\text{Pr}_{\text{pure}} (\text{all}) = \text{Pr}_{\text{raw}} - k_1 \cdot \text{Pfr}_{\text{pure}} - k_2 \cdot \text{Apoprotein}, \quad (5.1)$$

$$\text{Lumi}_{\text{pure}} (1/2) = S_{\text{raw}} (660\text{nm}, -140/120) - k_3 \cdot \text{Pr}_{\text{raw}} (785\text{nm}, +20), \quad (5.2)$$

$$\begin{aligned} \text{Meta} - \text{Ra}_{\text{pure}} = S_{\text{raw}} (660\text{nm}, -50) - k_4 \cdot S_{\text{raw}} (660\text{nm}, -70) \\ - k_5 \cdot \text{Meta} - \text{Rc}_{\text{pure}} - k_6 \cdot \text{Pr}_{\text{pure}} - k_7 \cdot \text{Apoprotein}, \end{aligned} \quad (5.3)$$

$$\begin{aligned} \text{Meta} - \text{Rc}_{\text{pure}} = S_{\text{raw}} (660\text{nm}, -30) - k_8 \cdot S_{\text{raw}} (660\text{nm}, -40) \\ - k_9 \cdot \text{Pr}_{\text{pure}} - k_{10} \cdot \text{Pfr}_{\text{pure}} - k_{11} \cdot \text{Apoprotein}, \end{aligned} \quad (5.4)$$

$$\begin{aligned} \text{Pfr}_{\text{pure}} = \text{Pfr}_{\text{raw}} - k_{12} \cdot \text{Pr}_{\text{raw}} (785\text{nm}, +20) \\ - k_{13} \cdot \text{Apoprotein}. \end{aligned} \quad (5.5)$$

The values k_1 to k_{13} correspond to the subtraction factor. Apoprotein contribution to the Lumi-R components was negligible. At three different steps of the irradiation procedure, the recorded RR spectrum corresponded to the Pr state (Pr_{dark} , $\text{Pr}_{\text{illum-1}(785\text{nm})}$, $\text{Pr}_{\text{illum-2}(785\text{nm})}$). Despite variable Pfr contribution, the obtained pure Pr components were identical (see fig. C.2). Furthermore, two potential Lumi-R species: Lumi-R1 and Lumi-R2 (-140 °C and -120 °C) were obtained after subtraction (see fig. C.3, top). Both spectra show a largely similar band pattern. Slight differences only refer to an increased SNR-value at higher irradiation temperatures. Subsequent rise of the irradiation temperature (*e.g.* -80 °C) leads to formation of the concomitant species (Meta-intermediates). Hence, attempts to obtain pure Lumi-R component spectra at this temperature led to less reliable results (see. fig. C.3, bottom). Band analysis of the distinct Pr and Lumi-R components also confirmed subtle discrepancies between

¹H₂O and deuterated apoprotein spectra were kindly provided by Mina Güenther [73].

the potential candidates (see fig. C.6). In this respect, global component analysis of the Pr-to-Pfr temperature evolution was performed using the Pr_{dark} and the Lumi-R2 spectra, referred to as Pr and Lumi-R, respectively. Component and global analysis of the marker region was performed according to subsection 3.7.2.

5.3.2. Global analysis Pr-to-Pfr

Temperature dependent evolution of the Pr-to-Pfr conversion can be interpreted as a pathway of consecutive decay processes initially triggered by the Pr-to-Lumi-R transition (see fig. 5.1. and 5.2.) [6, 103]. While the photoisomerization is almost temperature independent and the photoproduct Lumi-R is predominantly observed between -120 °C and -80 °C, the succeeding thermal decay exhibits a strong temperature dependency [57, 146]. Concomitant to the Lumi-R depletion, rising of the Meta-Ra intermediate is observed above -80 °C. Parallel to the Meta-Ra species increase, Meta-Rc intermediate increment is detected. At -30 °C, it reaches a maximum, whereas the preceding intermediate decreases. After reaching RT conditions, intermediate contribution is cancelled and the recorded RR spectrum contains pure Pfr contribution. Systematic errors refer to underestimation of species with low concentrations, especially of Lumi-R and the apoprotein contribution. In addition, decrease of the Pfr species in the range of -50 to -40 °C (only in H₂O), might be also explained in terms of underestimation of the rising Meta-intermediate species. Since the effect is not reflected in the D₂O data-set, the apparent Pfr depletion can be considered to be within the estimated fitting-error margin (2-3% of the total intensity contribution).

Parent states The Pr contribution in the investigated temperature range shows some interesting features. The most relevant event refers to the irradiation range between -140 °C and -30 °C. The Pr state decay occurs in two different steps, which exhibit distinct temperature dependent-evolution. First, the Pr contribution depletes steadily (-140 °C to -80 °C), but above -70 °C concentration is sharply lowered (down to 24%). While far red light irradiation should completely shift the photochemical equilibrium to the Pr state, a remaining Pfr contribution is observed. Dark relaxation eventually leads to a single species as observed in the recorded RR spectrum prior irradiation (Pr state, see fig. 5.4). Unlike the Pr contribution, the residual Pfr concentration remained constant during the red-light irradiation process, especially in the crucial temperature range between -140 °C and -70 °C, where the Pr-to-Lumi-R photoconversion takes place. Thus, contribution of any reverse intermediate from Pfr-to-Pr reaction could be neglected. While there was indication for a kinetic isotopic effect during intermediate formation (see fig. 5.4 and fig. 5.5), the Pr-to-Pfr reaction pathway in total was largely H/D-independent. On the other hand, it appears that in deuterated buffer, either the

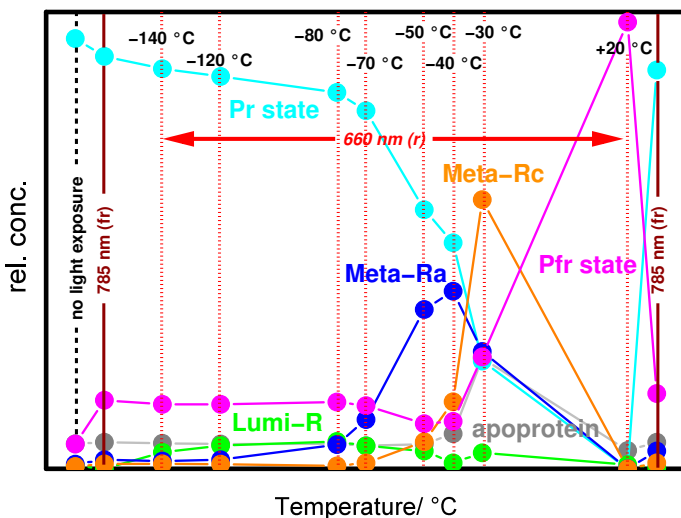


Figure 5.4: Temperature-concentration evolution of the intermediates of the Pr-to-Pfr conversion in H₂O. Each component is coded in a different color: Pr (cyan), Apoprotein (gray), Lumi-R (green), Meta-Ra (blue), Meta-Rc (orange) and Pfr (magenta). Irradiation conditions (wavelength and temperature) are specified. Pr-to-Pfr evolution is shown according to the measuring protocol (see fig. 3.4). Concentration values are shown in table 5.1.

Pfr-to-Pr conversion is more effective than in H₂O (less overall Pfr contribution) or that the thermal conversion occurs faster in D₂O.

Intermediates While in H₂O, the temperature-independent Lumi-R formation at -140 °C reaches 4%, in deuterated buffer its contribution is doubled (9%). However, far red-irradiation (+20 °C) in D₂O leads not only to complete Pr formation but apparently it also induces fast Pfr-to-Pr and Pr-to-Lumi-R conversion. The H/D effect is even more pronounced during the Meta-Ra-to-Meta-Rc formation. In D₂O, the Meta-Ra contribution largely dominates the temperature range between -50 to -30 °C (39-46% in D₂O and 26-34% in H₂O), whereas the Meta-Rc contribution is considerably lowered (59% in H₂O and 19% in D₂O). It is tempting to assume, that the proton-uptake in the Meta-Rc intermediate exhibits a kinetic isotopic-effect [23].

H₂O temperature profile						
T/ °C	C_{apo}	Pr	Lumi-R	Meta-Ra	Meta-Rc	Pfr
<i>dark</i>	0.055	0.942	0.007	0.010	0.005	0.054
<i>+20*</i>	0.058	0.903	0.000	0.020	0.011	0.150
<i>-140</i>	0.056	0.876	0.036	0.017	0.011	0.141
<i>-120</i>	0.054	0.859	0.051	0.020	0.010	0.141
<i>-80</i>	0.055	0.824	0.060	0.053	0.006	0.146
<i>-70</i>	0.050	0.784	0.050	0.108	0.013	0.138
<i>-50</i>	0.054	0.567	0.039	0.349	0.059	0.099
<i>-40</i>	0.077	0.495	0.013	0.389	0.147	0.104
<i>-30</i>	0.242	0.236	0.035	0.257	0.589	0.245
<i>+20</i>	0.040	0.000	0.009	0.000	0.000	0.978
<i>+20*</i>	0.058	0.873	0.003	0.039	0.013	0.165

Table 5.1: Relative concentrations of the species formed during the Pr-to-Pfr temperature-dependent conversion in H₂O (see fig. 5.4). ‘Dark’ refers to the unexposed sample and each step induced by far-red irradiation is denoted in italics.

Apoprotein Finally, for the complete temperature series, the contributions of the apoprotein were quite similar (5-6%). Increasing concentration was detected at -40 °C, reaching a maximum value at -30 °C, both in H₂O and in D₂O. In the latter case, apoprotein contribution reduced to the half then in water. Increase of the apoprotein concentration during the last step of the Pr-to-Pfr conversion is directly associated with the considerably reduced scattering cross-section of both Meta-intermediate species. The low scattering cross-section of the Meta-intermediates is intimately linked to reduced oscillator strength [183].

5.3.3. Analysis of the pure component spectra

Full range RR spectra of both parent states and the Pr-to-Pfr intermediate are shown in fig. 5.6, both in H₂O and in D₂O (red). In addition, marker band analysis of each component can be found in fig. 5.6 (fitting values listed in tables E.6 to E.11). Compared to previous works, all spectra are systematically downshifted (2-3 cm⁻¹). The deviation is in the range of the spectral resolution and refers solely to slightly different spectrometer calibration [102, 184].

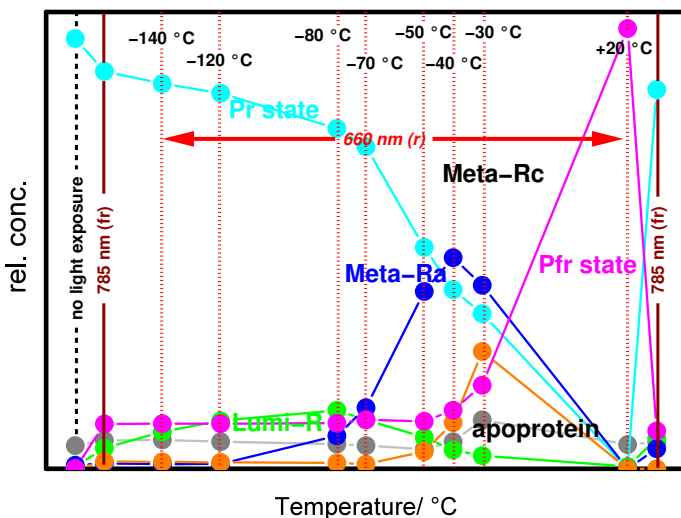


Figure 5.5: Temperature profiles of the different pure species along the Pr-to-Pfr conversion in D₂O. Concentration values are displayed in table 5.2. Further details are specified in fig. 5.4.

Pr and Pfr state Pr spectra (both in H₂O and D₂O) exhibit the same band pattern as already reported [184, 185]. Accordingly, the chromophore is found in a ZZZssa geometry with all pyrrole nitrogens carrying a proton (*vide infra*). This interpretation is based on the H/D sensitivity of the N-H i. p. band at 1572 cm⁻¹ (N-D 1078 cm⁻¹). In general, the marker region of all Pr species (Pr_{dark}, Pr_{illum-1} and Pr_{illum-2}) is dominated by the band at 1626 cm⁻¹, assigned to the C=C of the CD methine bridge (CD). An adjacent peak at 1617 cm⁻¹ might also contain contribution of the CD mode of a second Pr conformer. Alternatively, it might contain contribution of the BC mode (*vide infra*). A doublet peak observed as two shoulder at 1639 and 1649 cm⁻¹ was assigned to the C=C mode of the AB bridge. Finally, at 1592 cm⁻¹ the low-frequency shoulder of the CD peak was assigned to the C=C stretching vibration of the BC methine group. BC mode assignment is also supported by selective ¹³C₁₀-BV-chromophore labelling (*vide infra*).

In agreement with the Pfr state vibrational analysis in Agp1 phytochrome [159], band fitting of the crowded C=C stretching region in the Pr state was only possible after

D₂O temperature-concentration profiles						
T/ °C	C_{apo}	Pr	Lumi-R	Meta-Ra	Meta-Rc	Pfr
<i>dark</i>	0.051	0.942	0.005	0.008	0.000	0.000
+20*	0.062	0.870	0.045	0.012	0.016	0.098
-140	0.063	0.843	0.081	0.010	0.015	0.099
-120	0.059	0.822	0.105	0.011	0.014	0.099
-80	0.054	0.745	0.128	0.072	0.013	0.100
-70	0.051	0.705	0.107	0.134	0.010	0.107
-50	0.043	0.485	0.069	0.388	0.038	0.104
-40	0.059	0.392	0.041	0.462	0.101	0.128
-30	0.107	0.340	0.029	0.402	0.257	0.183
+20	0.053	0.000	0.005	0.000	0.000	0.964
+20*	0.058	0.830	0.066	0.044	0.000	0.083

Table 5.2: Relative component concentration values of the Pr-to-Pfr temperature dependent evolution measured in D₂O (see fig. 5.5). Further details are specified in table 5.1.

considering an increase number of bands as predicted by calculations [184]. This is particularly the case for the AB doublet and CD shoulder. It is also an unambiguous indication of structural heterogeneity in the Pr state of Agp1 [185].

Intensity deviations in all different Pr species are detected, which are even more evident in D₂O, especially for the strongest CD peak (see tables E.6 and E.7). Fitting of the broad CD band required an additional Lorentzian-function at 1614 cm⁻¹. Generally C=O stretching modes are poorly or non-Raman-active, however a peak at 1717 cm⁻¹ was assigned to the C₁₉=O group (ring D) and is in excellent agreement with IR measurements. In D₂O, two possible C=O peaks were detected at 1704 and 1715 cm⁻¹. The low RR intensity of the C=O modes compromises any comparison with IR difference spectra.

Vibrational analysis of the Pfr state is extensively discussed in chapter 6. According to this and previous investigations, the chromophore adopts a cationic ZZEssa geometry and denotes also an intrinsic heterogeneity [136, 159, 184].

Lumi-R Like the Pr state, band analysis of the Lumi-R spectra clearly required more Lorentzian functions than expected vibrational modes. In the marker band region of the Lumi-R species, three predominant peaks were found at 1596, 1629 and 1564 cm⁻¹ (see fig. 5.6). The latter peak is downshifted to approx. 1073 cm⁻¹ after

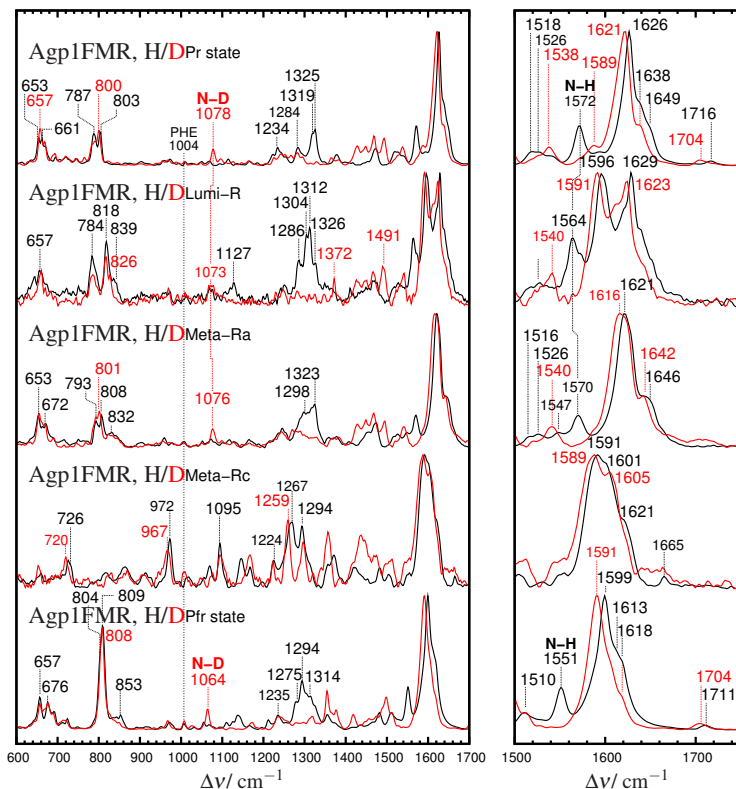


Figure 5.6: RR spectra of the pure species (parent states and intermediates) of the Agp1 Pr-to-Pfr conversion. Spectra recorded in H₂O (D₂O) are shown in solid black (red). The shift of the N-H (N-D) i. p. mode during the photocycle is shown in dotted black (red) lines.

H/D exchange and can be therefore assigned to the N-H i. p. mode. The remaining two peaks reveal less H/D sensitivity and refer to the CD and AB mode, respectively. This assignment is based on the downshift of the CD mode after Z/E isomerization (-30 cm^{-1}). Contrary to the large CD mode displacement, the frequency downshift of the AB mode is less pronounced (-9 cm^{-1}). This is reasonable since the protein environment is largely in Pr state and photoinduced structural changes are restricted to the rings C and D. The position of the BC mode is less evident and according to the band analysis, it might be localized between 1600 and 1610 cm^{-1} . Band assignment

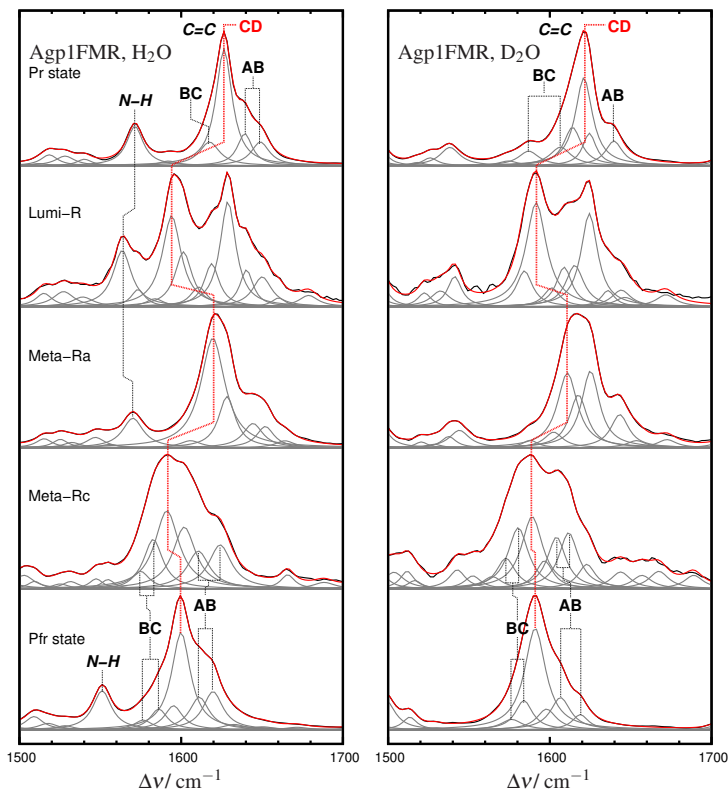


Figure 5.7: Marker band analysis of the pure component spectra in H₂O (left) and D₂O (right). Recorded spectra are displayed in solid black, the overall fit in red, and single band functions are shown in gray (details of color nomenclature in section 3.9.1). Fitting parameters are given in tables E.6 to E.11.

in the marker region is in good agreement with the vibrational analysis of the Lumi-R intermediate in phyA phytochrome [103].

In addition, the downshift of the CD mode due to the Z/E isomerization is accompanied by characteristic Lumi-R features in lower frequency regions. The most important is the strong HOOP band at 818 cm⁻¹ with a shoulder at 839 cm⁻¹ [103]. Only the latter displays H/D sensitivity and is downshifted to 826 cm⁻¹. Finally, around 1300 cm⁻¹ a complex band envelope with a maximum at 1312 cm⁻¹ was observed. This feature disappeared after H/D exchange.

Meta-Ra This intermediate species shows a maximum concentration at $-50\text{ }^{\circ}\text{C}$, but Lumi-R-to-Meta-Ra conversion already occurs at lower temperatures ($-80\text{ }^{\circ}\text{C}$). In this stage of the Pr-to-Pfr conversion, the chromophore is protonated, as indicated by the H/D sensitivity of the N-H peak at 1570 cm^{-1} (N-D 1076 cm^{-1}). The most prominent peak was found at 1621 cm^{-1} with a shoulder at 1646 cm^{-1} . Here the H/D sensitivity is less pronounced as in the Lumi-R and Pr spectra (1616 and 1642 cm^{-1} , respectively). Following previous assignments, the strongest peak should be due to the CD mode, however this would imply an upshift of $+25\text{ cm}^{-1}$, almost comparable to the Pr-to-Lumi-R Z/E-downshift. Furthermore, the C=C stretching region is to some extent reminiscent of the Pr spectrum, in contrast to the HOOP and the 1300 cm^{-1} region. As expected, the Lumi-R HOOP-marker band disappeared and instead a doublet at 808 and 793 cm^{-1} was observed. In addition, an intensity decrease in the i.p. region is also detected ($1250\text{-}1350\text{ cm}^{-1}$).

Unlike the meta-Ra of plant phytochrome, the chromophore band features are rather sharp and well defined [102]. Thus, spectral similarities were found with the Meta-Ra species in Cph1Δ2 [145]. Compared to the previous intermediate in Agp1, the signal-to-noise-ratio increase might be associated to stronger Meta-Ra contribution to the raw spectrum.

Meta-Rc The broad spectral features in the marker region and the poor H/D sensitivity of the Meta-Rc intermediate compromise any clear band assignment (see fig. 5.6 and fig. 5.7). Hence, band-fitting was solely restricted to reproduce the complete marker region, neglecting extreme sharp, broad or negative Lorentzians. Thus, band analysis did not provide conclusive structural information regarding the C=C stretching modes. However the large number of band components required for a good fit is a strong indicator of a mixture of sub-intermediate species. Under the experimental conditions only a non-equilibrium distribution of these sub-states is then cryogenically trapped. Furthermore, the overall spectral intensity of the Meta-Rc states is rather low and in the range of the apoprotein contribution (see ref. [184]).

In agreement with previous investigations, no N-H/N-D i.p. mode of the rings B and C was observed. Thus, the pyrrole nitrogens of rings B and C share a proton group and the BC moiety lacks the positive charge. Despite the complexity of the crowded C=C stretching region, the position of the CD mode can be derived by comparing the Pfr with the Meta-Rc band analysis. Here we found two peaks which might be assigned to this mode at 1591 and 1602 cm^{-1} (see tables E.10 and E.11).

Furthermore, the HOOP and OOP bands are missing, instead a relatively prominent peak at 972 cm^{-1} (967 cm^{-1} in D_2O) and a band at 726 cm^{-1} (720 cm^{-1}) were observed. In addition, the region around 1300 cm^{-1} shows also poor H/D sensitivity. This range is dominated by a triplet with a maximum at 1267 cm^{-1} and

two further bands at 1294 and 1224 cm^{-1} . While the maximum is downshifted to 1259 cm^{-1} in D_2O , the remaining peaks are not H/D sensitive. Finally at 1095 cm^{-1} , both in H_2O and D_2O a peak with medium intensity was observed.

5.4. Pr-to-Pfr conversion in Rph2 phytochrome and PHY domain role

According to time-resolved spectroscopy, the Rph2 phytochrome of *Rhodospirillum rubrum* undergoes a similar Pr-to-Pfr photoconversion as Agp1 phytochrome, especially regarding the Pr-to-Lumi-R transition [201]. Here, we investigated the role of the PHY domain in Rph2 phytochrome during the Pr-to-Pfr transition, since it is intimately linked the β -sheet-to- α transition of the tongue motif [187, 190, 191]. In this respect, we collected RR spectra of the parent states (dark state and RT photo-product) and intermediates in the complete Rph2 photosensory domain (Rph2-PGP), largely equivalent to the Agp1-FMR phytochrome and CphB-fl. Finally, we investigated the equivalent reaction pathway of the PAS-GAF-only protein (Rph2-PG).

5.4.1. Pr-to-Pfr transition and chromophore structure in the Pfr state

RR Pr state The cationic as well as the heterogeneous nature of the bilin structure in the Pr state, have been already characterized by RR spectroscopy [206]. In that work, the focus was set on the fluorescence properties of the Pr state of Rph2 and the structural parameters that control the NIR emission of the excited bilin (for a detailed description see chapter 7). In general, the Pr spectra of the photosensory domain, chromophore-binding domain and the fluorescent-variant (Rph2-PG, -PGP and IRFP) are largely similar, indicating also strong similarities to the Pr spectra of CphB and Agp1 phytochromes. Hence, the chromophore adopts in all cases a similar ZZZssa structure. Compared to other prototypical phytochromes, Rph2 (PG and PGP variants) reveals a higher intensity of the CD HOOP and ring D OOP mode, suggesting a more rigid chromophore structure in the Pr state. Furthermore, despite the spectral similarity in the marker region, deletion of the PHY-domain led to a slight upshift of +4 cm^{-1} of the HOOP at 806 cm^{-1} (Rph2-PGP). In addition, the OOP at 654 cm^{-1} shows an intensity increase compared to adjacent bands. The structural rigidity is even more pronounced in the IRFP-mutant, which also displays interesting features in the marker region, especially regarding the AB and CD methine bridges (see chapter 7).

RR Pfr state/Photoproduct Deletion of the PHY-domain impaired the *bona fide* Pfr formation as implicated by comparison of the RR spectra of both phytochrome variants (see fig. 5.8 and fig. 5.9). In both species the peak at 1548 cm^{-1} (1062 cm^{-1} in D_2O)

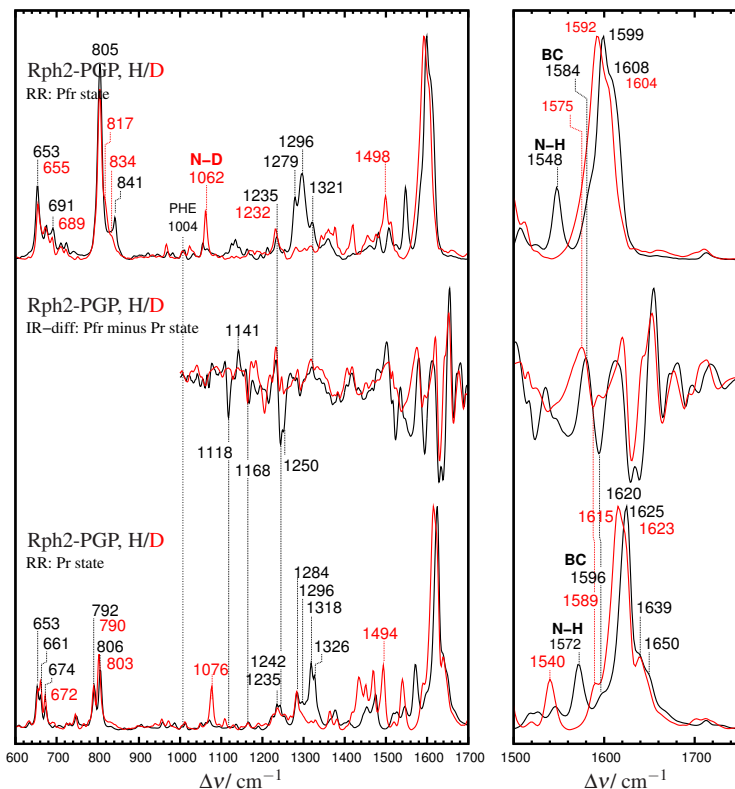


Figure 5.8: Resonance Raman spectra of the Pfr and Pr state from the PAS-GAF-PHY Rph2 deletion mutant (Rph2-PGP, top and bottom layer) and the corresponding Pfr-Pr IR difference spectra (middle layer). The spectra were measured in H₂O and D₂O.

was assigned to the N-H i. p. mode. Hence, the cationic nature of the chromophore remained unaffected after PHY-domain deletion. In the PGP-variant a clear and unambiguous HOOP CD peak at 806 cm^{-1} with a small shoulder at 802 cm^{-1} was observed (see fig. D.2). However, this feature –the most characteristic Pfr state signature– disappeared in the PG-variant [159]. Instead, this region was dominated by a Lumi-R-like peak at 819 cm^{-1} (see fig. 5.9). While the interpretation of the HOOP region coincides with a tensed geometry (Lumi-R-like band), the remaining spectral regions correspond to a more relaxed bilin structure. In addition to the characteristic HOOP mode, the PGP-variant, exhibit a peak at 841 cm^{-1} which downshifted after H/D exchange. This

peak presumably involves deformation modes with contributions of the pyrrole nitrogens.

The OOP mode of ring D was detected at 653 cm^{-1} (PGP-variant). PHY-deletion leads to an upshift to 659 cm^{-1} , including an intensity increase. Concomitantly, an almost H/D insensitive peak was observed at 726 cm^{-1} (724 cm^{-1} in D_2O). In addition to deformation modes, contribution of the S-C stretching mode of the thioether group at the binding site (ring A and C13) is expected [185].

Despite similar N-H i. p. frequency in Rph2-PG and Rph2-PGP, the C=C stretching modes in the marker region reveal large discrepancies. The most prominent C=C peak at 1599 cm^{-1} (D_2O 1592 cm^{-1}) in the Pfr spectrum of the PGP-variant was assigned to the CD mode. A shoulder at 1608 cm^{-1} is assigned to the C=C AB mode. Beneath this broad feature, a band doublet was fitted to the spectrum (see fig. D.2) in accordance with the Pfr state in Agp1 and other prototypical phytochromes [159]. The BC peak could only be indirectly assigned at 1584 cm^{-1} (1575 cm^{-1} in D_2O) by comparison with the isotopic shift observed in Agp1 and CphB assembled with $^{13}\text{C}_{10}$ -BV (including H/D exchange) as well as with the Rph2 Pfr IR difference peaks (see fig. 5.8) and its corresponding H/D displacement.

After PHY-domain deletion, the CD mode of the RT photoproduct upshifted to 1606 cm^{-1} (1599 cm^{-1} in D_2O). Following the previous assignment, the BC mode was identified at 1578 cm^{-1} in the difference IR spectrum (1573 cm^{-1} in D_2O). However, assignment in the RR spectrum was less conclusive due to the overlap with a shoulder at 1586 cm^{-1} . This feature contains probably also a stronger contribution of the AB modes, generally observed as high-frequency-shoulder of the CD mode (around 1610 cm^{-1}). Above the prominent CD peak only a small shoulder at 1621 cm^{-1} was observed.

Finally, the photoproduct spectrum of the Rph2-PG phytochrome and the Pfr spectrum of the photosensory domain exhibit three bands around 1300 cm^{-1} with the most intense one at 1296 and 1293 cm^{-1} respectively. This feature disappeared after H/D exchange.

5.4.2. C=O mode assignment in Rph2 and CphB and IR amide-I band analysis

Attempts in assigning the bilin C=O stretching modes (rings A and D) have been already undertaken by steady-state [70, 187], as well as pico-second infrared measurements [200]. However, lack of specific-isotopic labelling compromises these analyses.

A peak at 1712 cm^{-1} was observed in the both (PGP and PG) Pr RR spectra (see bottom layer in fig. 5.8 and fig. 5.9). Generally, only the $\text{C}_{19}=\text{O}$ stretching of ring D displays a reasonable RR intensity. Hence, it can be tentatively assigned to this

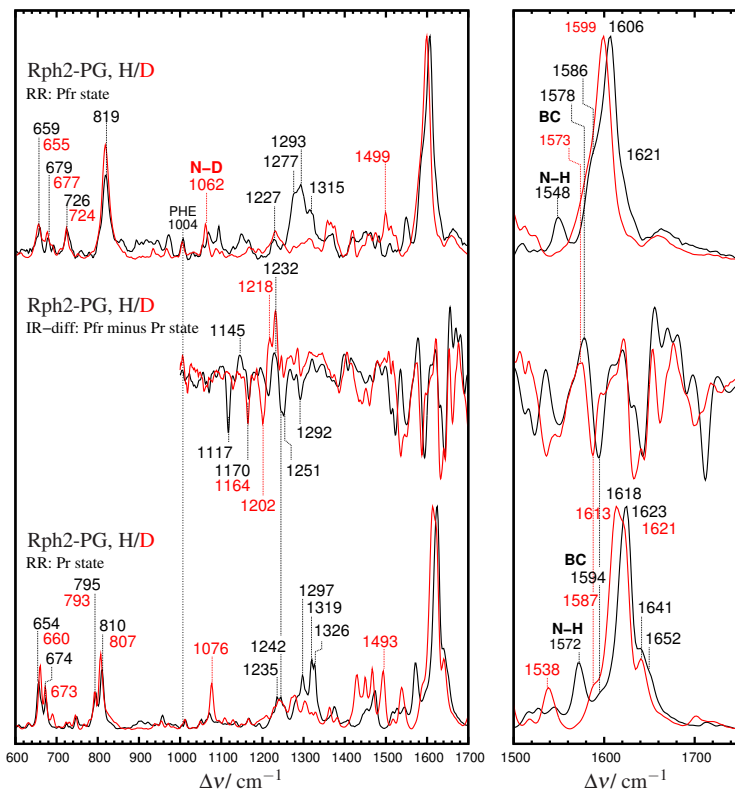


Figure 5.9: Resonance Raman spectra of the Pfr and Pr state of the PAS-GAF deletion mutant from the Rph2 phytochrome (Rph2-PG, top and bottom layer). Additionally, the corresponding Pfr-Pr IR difference spectra are displayed (middle layer). The spectra were measured in H₂O and D₂O.

mode. Still, the C₁₉=O peak contribution is very low compared to the prominent CD C=C stretching band (C₁₉=O/CD = 0.01). However, it is clearly over the signal-to-noise limit. According to both RR spectra (PGP and PG), this peak downshifted to 1702 cm⁻¹ after H/D exchange. Interestingly, only in the IR difference spectrum of the PG-variant, this C=O mode was unambiguously identified at the same frequency ashowing a similar H/D downshift as in the RR spectrum. In addition, ring A C₁=O band could be identified at 1737 cm⁻¹ (1727 cm⁻¹ in D₂O). This peak exhibits a larger bandwidth indicating a higher mobility at the C₁=O then at the C₁₉=O. According

to the Pr structure (see fig. 2.4) the C₁₉=O is clearly interacting with the adjacent histidine, whereas the C₁=O is only weakly hydrogen bonded by solvent molecules. In the RR spectrum a weak band at approx. 1729 cm⁻¹, with a broad high-frequency-shoulder was tentatively assigned to this mode. Due to the low band intensity, assignment is less accurate than for the ring D C₁₉=O group.

The overall assignment seems relatively plausible and is in good agreement with previous results. However, in the D₂O spectrum, a remaining band at 1709 cm⁻¹ was observed, indicating either incomplete H/D exchange at ring D or overlap with peptide carbonyl groups. Both Rph2 variants show an additional Pr difference band at 1690 cm⁻¹ (1689 cm⁻¹ in D₂O). This peak was assigned to the protein moiety [187]. Future protein isotopic labelling experiments and low temperature IR measurements should uncover the nature of this band. Regarding the assignment of the C₁=O mode, the thermal mobility might influence the vibration frequency leading to discrepancies between RR (low temperature) and IR (RT).

In agreement with the PG-variant, an IR-active peak at 1733 cm⁻¹ (1726 cm⁻¹ in D₂O) was assigned to ring A C=O mode (see fig. 5.10 left panel). Also in the RR spectrum, a similar feature with equivalent H/D displacement was observed. On the other hand, assignment of the ring D C=O mode was less conclusive. First, the Pr and Pfr state reveal similar RR active C=O modes at 1712 cm⁻¹. This might implicate that the structural changes in the chromophore and the hydrogen bonding barely affect this specific mode. Alternatively, Pr/Pfr frequency overlap occurs solely by coincidence. H/D-displacement of ring D C=O mode in the Pr and Pfr spectrum was clearly observed in the RR spectrum (-10 and -13 cm⁻¹ cm⁻¹). However a remaining contribution at 1712 and 1710 cm⁻¹ for both parent states suggested either an incomplete H/D exchange or structural inhomogeneity. While the first assumption seems to be rather unlikely, the broad Pfr peak with a maximum at 1717 cm⁻¹ in the difference IR spectrum might support the coexistence of at least two parent state conformers, which can be identified based on the slightly different C=O vibrational frequencies. This might be correlated to the unusual H/D displacement in the RR spectra of both parent states, thereby supporting the view of a structural inhomogeneity (*vide supra*).

Regarding the carbonyl stretching assignment in the red light photoproduct of the PG-deletion mutant, no C=O bands could be identified in the RR spectrum. Thus, the ring A C=O mode was identified in the difference IR spectrum at 1726 cm⁻¹ with a -6 cm⁻¹ downshift after H/D exchange. The corresponding ring D C=O band might be cancelled due to the vicinity of the dominant Pr state counterpart. Alternatively, ring D might be involved in a keto-enol (lactam-lactim) tautomerization with an apparently dominant and stable enolic form [207]. However further spectroscopic investigations are required to confirm this possible explanation.

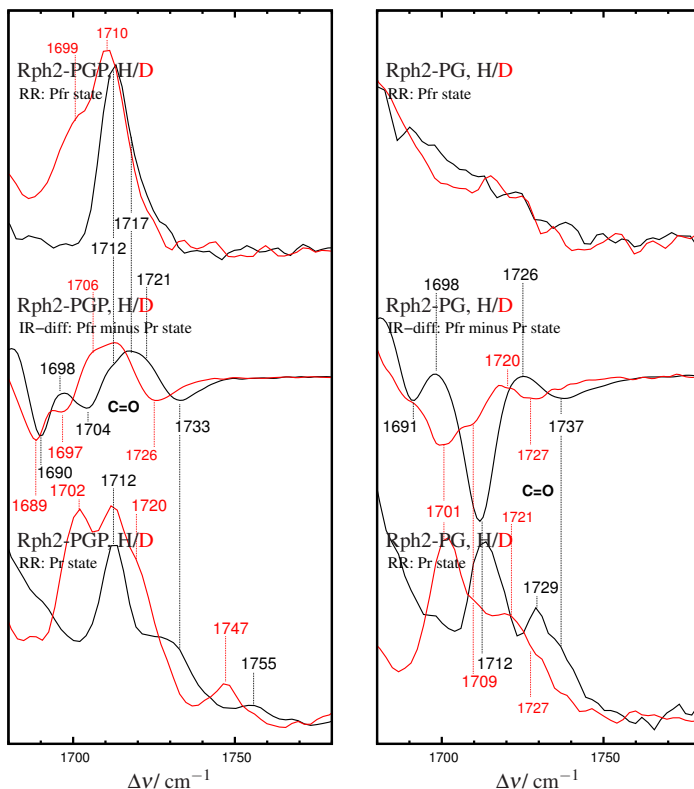


Figure 5.10: Carbonyl stretching region of the Resonance Raman Pfr and Pr spectra (top and bottom layer) and Pfr-Pr IR difference spectrum (middle layer). Both H₂O and D₂O spectra were rescaled for a suitable band analysis of the C=O modes. Left panel corresponds to the parent state spectra of the Rph2 PAS-GAF-PHY variant (PGP). The right panel contains the vibrational spectra of the parent states in the PAS-GAF deletion mutant (PG).

CphB C=O modes in parent state RR spectra In the Pr state, a band at 1714 cm^{-1} was assigned to the C=O mode of ring D (1704 cm^{-1} after H/D exchange). The shoulder at 1731 cm^{-1} correspond then to the C=O mode of ring A (1714 cm^{-1} in D₂O). This assignment is in line with IR data of phytochrome Agp1 [140], as well as of the Rph2 phytochrome (see fig. 5.13 bottom). In case of the Pfr species, only a single band, namely ring D C=O, was observed at 1712 cm^{-1} (1707 cm^{-1} in D₂O).

5.4.3. Pr-to-Pfr intermediates of the Rph2 photosensory domain

Lumi-R The first intermediate species could be only trapped above $-70\text{ }^{\circ}\text{C}$, thus the Pr-to-Lumi-R transition in Rph2-PGP occurs at a higher temperature than in Agp1 phytochrome (see fig. 5.11 and fig. 5.6). Despite that, all spectroscopic features are largely conserved. First, the chromophore remains protonated as derived from the N-H i.p. observed at 1569 cm^{-1} (D_2O ca. $1072\text{-}6\text{ cm}^{-1}$). Interestingly, the Pr-to-Lumi-R N-H shift is less pronounced as in Agp1 (-3 cm^{-1} compared to -8 cm^{-1}).

Secondly, compared to the Pr state, the CD mode downshifted to 1593 cm^{-1} ($\approx -30\text{ cm}^{-1}$). The poor H/D sensitivity might be related to a reduced contribution of ring D pyrrole N-H group (-3 cm^{-1}). Consistent with the assignment in Agp1 (*vide supra*), the Lumi-R BC mode might be overlapping with the prominent CD peak and the doublet at 1619 and 1626 cm^{-1} contains contribution of the AB mode. This rather broad band envelope indicates probably structural inhomogeneity. In D_2O , the doublet maximum downshifted to 1613 cm^{-1} .

Like a prototypical Lumi-R species, a strong band, corresponding to the CD HOOP mode, was observed at 823 cm^{-1} with a shoulder at 836 cm^{-1} (820 and 829 cm^{-1} in D_2O). The broad peak structure also supports the view of at least two coexisting Lumi-R subspecies. Ring D OOP mode was assigned to peak at 653 cm^{-1} (656 cm^{-1} in D_2O).

In addition to the marker region changes and the typical intensity increase of the HOOP feature, the region around 1300 cm^{-1} reflects a specific Lumi-R fingerprint with its three-banded structure observed in all prototypical phytochromes. Unlike both parent state spectra, the almost absent peak at 1004 cm^{-1} indicates negligible protein contribution. Hence, the region around 1300 cm^{-1} corresponds to chromophore bands without any overlapping with the amid-III modes. Like in Agp1 phytochrome, it can be assumed that this region involves modes with contributions of the pyrrole N-H groups [184].

Meta-Ra In agreement with Agp1 phytochrome, Meta-Ra was trapped at $-50\text{ }^{\circ}\text{C}$ (see middle layer of fig. 5.11). At this stage of the Pr-to-Pfr conversion, the protein residues surrounding the chromophore undergo partial reorientation affecting the bilin geometry. In the RR spectrum this is mainly reflected by the upshift of the prominent CD band to 1620 cm^{-1} . This peak downshifted to 1610 cm^{-1} in D_2O , uncovering a less H/D sensitive shoulder at 1625 cm^{-1} . Probably this feature contains ring D C=C stretching contributions. The AB mode is presumably located at a poorly H/D sensitive doublet-shoulder with peaks at 1641 and 1650 cm^{-1} . Like in Agp1 phytochrome, assignment of the BC mode is obscured due to overlap with the CD peak. Only in deuterated medium, a peak at 1571 cm^{-1} might be tentatively assigned to the BC mode. Despite the structural rearrangements associated with the CD band upshift, the N-H band remained

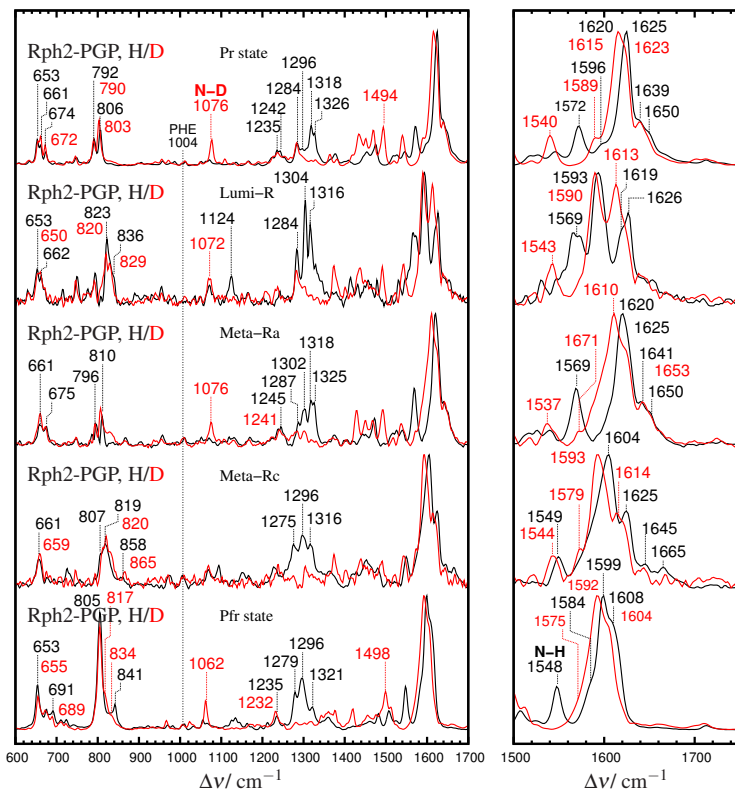


Figure 5.11: Resonance Raman spectra of the parent states and intermediates of the Pr-to-Pfr conversion of the Rph2 sensory module (Rph2-PGP), measured in H_2O and D_2O . Intermediate spectra are displayed according to the increasing trapping temperatures (Lumi-R \rightarrow Meta-Ra \rightarrow Meta-Rc).

unshifted compared to the Lumi-R spectrum. However the higher SNR-value allowed the identification of the N-D mode at 1076 cm^{-1} .

Lumi-R-to-Meta-Ra conversion includes also intensity decrease in the HOOP region. Concomitantly, only two small peaks were observed at 810 and 706 cm^{-1} with negligible H/D sensitivity. The OOP mode of ring D was observed at 661 cm^{-1} .

Meta-Rc Formation of the deprotonated Meta-Rc intermediate occurred also in agreement with Agp1 ($-30\text{ }^\circ\text{C}$). However, the band pattern was somehow differ-

ent. Especially concerning the H/D sensitive modes, as well as the HOOP region. Unlike Agp1, the Meta-Rc intermediate of Rph2 showed a strong similarity with the succeeding Pfr spectrum. First, a broad and relatively strong HOOP band was located at 819 cm^{-1} (820 cm^{-1} in D_2O) and secondly an equally prominent peak at 656 cm^{-1} (659 cm^{-1} in D_2O) assigned to the ring D OOP was observed. Within the marker region, the CD band was detected at 1604 cm^{-1} (1593 cm^{-1} after H/D exchange). The AB band is presumably located at 1625 cm^{-1} in H_2O and at 1614 cm^{-1} in deuterated buffer. Two small peaks at 1645 and 1665 cm^{-1} were detected. The frequency of the latter one matches with the Agp1 Meta-Rc. In view of the position and poor H/D sensitivity this mode might correspond to a pyrrole ring or a vinyl C=C stretching mode [184].

While the region around 1300 cm^{-1} shows H/D sensitive bands, no evidence of an N-H i. p could be found. Instead a poorly H/D sensitive peak at 1549 cm^{-1} (1544 cm^{-1} in D_2O) was observed. This clearly differs from the Meta-Rc species of Agp1, in which the 1300 cm^{-1} -region reveals a very poor H/D sensitivity. According to the analysis of the C=C and HOOP region, it appears that in Rph2-PGP the Meta-Rc intermediate already adopts a Pfr-like geometry but lacks full protonation.

5.4.4. PHY-domain deletion alters intermediate formation

After deletion of the PHY domain, the chromophore geometry in the Pr state remained largely unaffected. However, the RR investigation denotes a perturbation of the Pr-to-Pfr pathway already at the earliest stage of the reaction. Following the same cryogenic trapping protocol as for the PGP-variant (*vide supra*), two intermediate species were detected at -70 and $-30\text{ }^\circ\text{C}$ (see fig. 5.12).

Lumi-R' According to the irradiation temperature, the first intermediate spectrum would correspond to the Lumi-R species, however the missing C-terminal domain already altered the photoproduct, leading to a highly distorted Lumi-R' species. The Pr-photoproduct displayed the typical isomerisation-induced downshift of the CD mode to 1605 cm^{-1} ($\nu(\text{Lumi-R}'\text{-Pr}) \approx -20\text{ cm}^{-1}$) and the expected H/D-downshift (1600 cm^{-1} in D_2O). A doublet at 1613 and 1618 cm^{-1} was assigned to the AB mode. The corresponding H/D downshift probably leads to a partial displacement of the AB doublet under the CD peak. Unambiguous assignment of the BC mode was not achieved. According to previous observations in the Rph2-PGP and Agp1 phytochrome, this vibrational mode might be assigned to the low frequency shoulder of the CD band.

Compared to the PGP Lumi-R intermediate, the CD mode was found upshifted ($+12\text{ cm}^{-1}$), whereas the AB mode is slightly downshifted (-6 to 8 cm^{-1}). Hence,

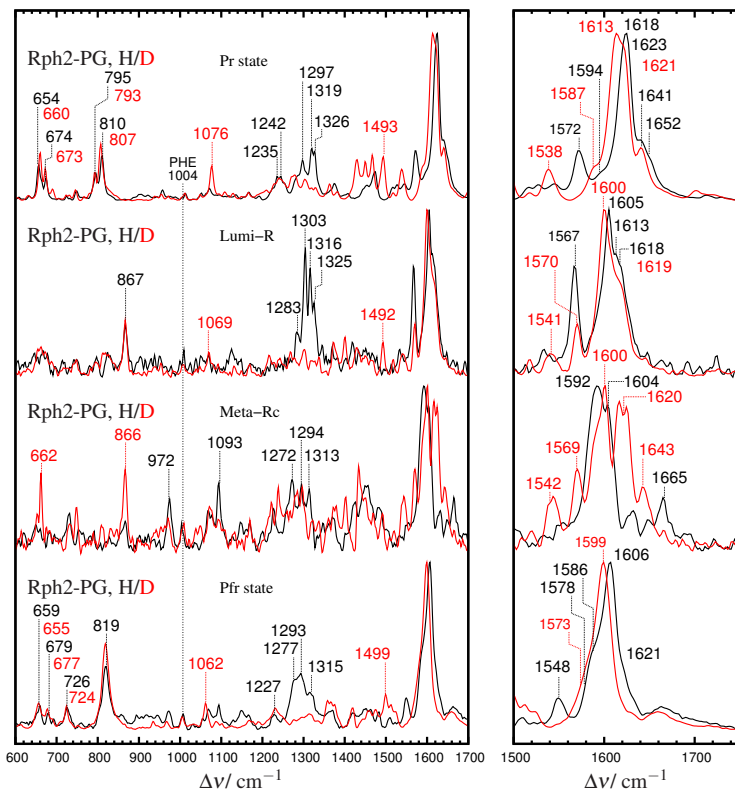


Figure 5.12: Resonance Raman spectra of the parent states and Pr-to-Pfr intermediates from the Rph2 PAS-GAF deletion mutant (Rph2-PG). The spectra were measured in H₂O and D₂O. Intermediate spectra are displayed according to the corresponding trapping temperature (Lumi-R → Meta-Rc).

it can be assumed that the lack of the PHY-domain induces an enhancement of the AB double bond at expenses of the shorted CD C=C bond. The H/D sensitive band at 1567 cm⁻¹ was assigned to the N-H i. p. (≈ 1069 cm⁻¹ in D₂O). However, a residual peak at 1570 cm⁻¹ was observed in deuterated buffer. A possible CD HOOP band was observed at 867 cm⁻¹, corresponding to an +44 cm⁻¹ upshift compared to the Lumi-R intermediate in the sensory domain. In addition, this band shows a lower intensity. The region between 600-700 cm⁻¹ displayed also poor RR intensity. Based on the absence of the low frequency Lumi-R marker bands it can assumed that the lack of the PHY

domain allows for a more relaxed geometry at the CD bridge after Z/E isomerization. Only the region around 1300 cm^{-1} (*vide supra*), probably containing strong contributions of the inner pyrrole nitrogen groups (rings B and C) remained largely unaffected after PHY-deletion.

Meta-Rc' In the PG-variant Lumi-R-to-Meta-Ra decay (at approx. $-50\text{ }^{\circ}\text{C}$) is not observed. The Lumi-R' intermediate decays at $-30\text{ }^{\circ}\text{C}$ to a Meta-Rc' species displaying strong homology to the Rph2-PGP, Agp1 and CphB Meta-Rc spectrum. It seems that the PHY-domain plays an important role in stabilizing the Meta-Ra intermediate. Removal of this C-terminal domain hinders cryogenic trapping of this species.

The general features of a deprotonated chromophore prevailed among the whole spectral range. A detailed inspection of the marker region revealed strong similarities to the Meta-Rc of Agp1. However, it showed distinct vibrational pattern to the Rph2-PGP homologue. According to the increased noise level in the D_2O spectrum it is tempting to assume a similar isotopic effect as in Agp1. In this respect the Meta-Rc formation is partially hindered in D_2O (see fig. 5.12). Interestingly, it seems that the band at 1665 cm^{-1} is a common feature of the Meta-Rc intermediate among the investigated phytochrome variants (*vide supra*).

5.5. RR Characterization of the CphB Phytochrome

Following the irradiation protocol for Agp1 and previous investigations [184], the Pr-to-Pfr pathway in CphB was investigated. Differences in frequencies of the parent state spectra compared to previous measurements are due to a different spectrometer calibration [184].

5.5.1. Pr-to-Pfr Intermediates

Lumi-R The first intermediate species was detected at $-50\text{ }^{\circ}\text{C}$. The CphB Lumi-R spectrum displayed strong similarities to Agp1 and Rph2 phytochrome, even when the irradiation temperature considerably differed. The strongest peak (see fig. 5.13), namely the CD band was observed at 1593 cm^{-1} (1589 cm^{-1} in D_2O). In agreement with Agp1 and Rph2-PGP, the Z/E isomerization leads to a -31 cm^{-1} downshift compared to the Pr state. Following the previous band analysis, the AB band doublet was observed at 1615 and 1629 cm^{-1} (1606 and 1626 cm^{-1} after H/D exchange). Finally the BC band was probably located under the prominent CD peak. In agreement with Agp1, the N-H i. p. band was observed at 1564 cm^{-1} . In deuterated buffer the corresponding N-D mode was tentatively assigned to a band at 1071 cm^{-1} . A strong and

broad CD HOOP mode was observed as double peak at 831 and 822 cm^{-1} , in agreement with Rph2, Agp1 and even phyA phytochrome. At lower frequencies the ring D OOP deformation mode [126] was assigned to the peak at 655 cm^{-1} (659 cm^{-1} in D_2O). Like in both BV-binding phytochromes, a strong H/D sensitive band triplet was observed in the region around 1300 cm^{-1} with prominent peaks at 1311, 1301 and 1321 cm^{-1} .

The intermediate formation and decay is highly susceptible to the buffer capacity and ionic strength (*vide infra*). Due to the overlap of the Pr and Lumi-R Q-band [201], back conversion to the Pr state cannot be excluded. The usually high Lumi-R temperature formation suggests a considerably higher activation barrier as in Rph2 and especially in Agp1. However, the chromophore still adopts a tensed geometry as derived from the characteristic HOOP band. This indicates that the Pr-to-Lumi-R transition clearly depends on the phytochrome specific protein-cofactor interaction.

Meta-Ra The subsequent Lumi-R-to-Meta-Ra temperature-dependent transition is largely in agreement with the other two BV-binding phytochromes (-40 °C). Due to the strong similarity of marker bands to the Pr spectrum, the assignment of the putative Meta-Ra specie in CphB is partially compromised.

The most striking difference between this intermediate and the Pr spectrum was noted for the frequency of the N-H i. p. (see fig. 5.13), which was observed at 1575 cm^{-1} and downshifted to 1078 cm^{-1} in D_2O ($\Delta\Delta\nu(\text{Meta} - \text{Ra}/\text{Pr}) = +4 \text{ cm}^{-1}$). Compared to the Meta-Ra intermediates in Rph2 and Agp1, this mode was upshifted +6 and +5 cm^{-1} respectively.

The strongest band, corresponding to the CD mode, was identified at 1623 cm^{-1} with a downshift to 1615 cm^{-1} in D_2O . The broad envelope contains at least two equally intense bands, one displaying a H/D-downshift as observed in the Pr spectrum (see fig. 5.13, third layer from the top) and a second one with low H/D sensitivity. The AB band was assigned to the peak at 1649 cm^{-1} (1645 cm^{-1} in D_2O). Between the CD and the AB bands a broad feature was identified (see Agp1 Meta-Ra spectrum in fig. 5.6). After H/D exchange it downshifted under the prominent CD peak. Concerning the BC band, this was tentatively assigned to a shoulder at 1604 cm^{-1} .

In the HOOP region, a band doublet at 806 (803 in D_2O) and 794 cm^{-1} was observed. The ring D OOP mode was assigned to a peak at 651 cm^{-1} (D_2O -upshift to 659 cm^{-1}). Both deformation features are in agreement with Agp1 and Rph2 phytochromes. Finally, the region around 1300 cm^{-1} displays also similar spectral features. Apparently, the most interesting feature is a H/D sensitive peak at 1298 cm^{-1} (+4 cm^{-1} in Rph2), which is observed among all three BV-binding phytochromes.

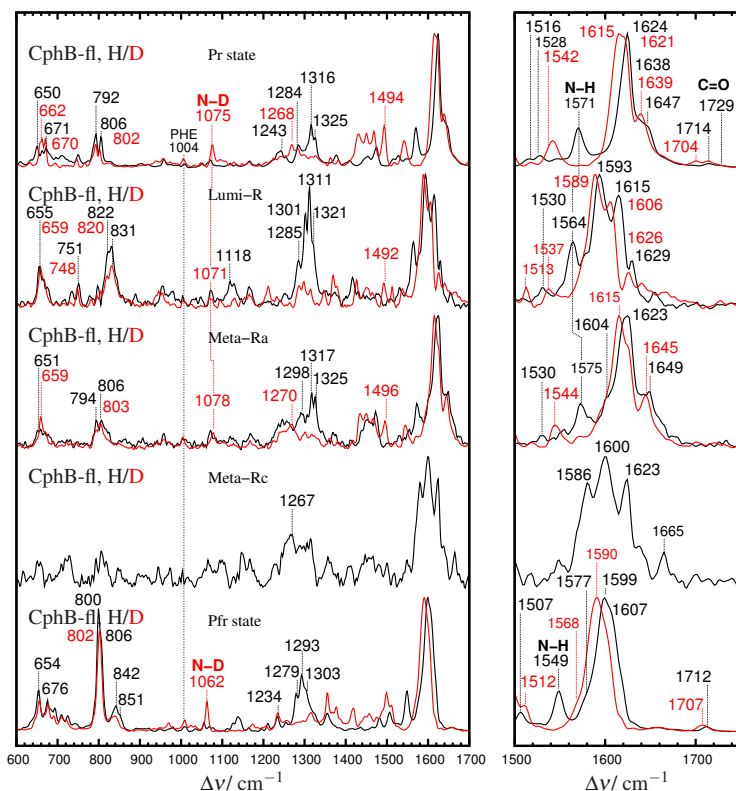


Figure 5.13: Resonance Raman spectra of the intermediates of the Pr-to-Pfr conversion of CphB phytochrome. Spectra recorded in H₂O (D₂O) are shown in solid black (red). Cryogenic trapping of the Meta-Rc intermediate in D₂O was not possible. Notations are in agreement with fig. 5.6.

Meta-Rc The Meta-Rc spectrum of CphB was detected at -30 °C, corresponding equal intermediate formation-temperature and largely similar band features as in Agp1 and Rph2. However, a pure D₂O spectrum could not be obtained. The H/D-exchange implies reduction of the Meta-Ra-to-Meta-Rc decay in Agp1 and Rph2. In this respect, impaired Meta-Rc formation in D₂O might be even pronounced in CphB. Furthermore, Meta-Rc formation is strongly dependent on the ionic strength (*vide infra*).

The strongest band in the whole spectral range was again assigned to the CD mode (1600 cm⁻¹). The AB mode was ascribed to the peak at 1623 cm⁻¹. The peak at

1586 cm^{-1} , was tentatively assigned to the BC mode. Like the Meta-Rc spectrum of Agp1 and Rph2 an interesting peak was observed at 1665 cm^{-1} (see fig. 5.13).

5.5.2. Role of the ionic strength towards the Pr-to-Pfr pathway

The CphB phytochrome was measured in two different aqueous buffers: TRIS (50 mM TRIS, 300 mM NaCl, 5 mM EDTA), and phosphate buffer (10 mM $\text{K}_2\text{PO}_4/\text{KHPO}_4$, 5 mM DTT, 2 mM EDTA), both adjusted to the same pH value (pH = 7.8). The TRIS buffer contained a considerably higher buffer capacity and specially a higher ionic strength. The parent state spectra recorded in TRIS or phosphate buffer were largely similar. However, detailed band inspection revealed some spectral discrepancies. Finally, a clear assignment or identification of the influence of the buffer is rather complicated and beyond the scope of the current work. A systematic analysis of the Pr-to-Pfr conversion under defined buffer capacity and ionic strength is needed to derive quantitative conclusions.

Pr state In the marker region of the Pr spectrum recorded in phosphate buffer, an intensity increase of the AB band at 1647 cm^{-1} occurred at the expense of the adjacent shoulder at 1638 cm^{-1} (see fig. 5.14). Concomitantly, the broad CD band envelope exhibited a sharper form. Additionally, in the region around 1300 cm^{-1} some spectral deviations were detected. Most notable is the rise of a small band at 1298 cm^{-1} .

Lumi-R The influence of the buffer gained relevance after analysis of the intermediate spectra. While in phosphate buffer the Lumi-R intermediate is completely formed. The spectra recorded in TRIS buffer denoted a distinct band pattern. First, the CD HOOP peak experienced intensity decrease whereas the C=C stretching region already contain bands assigned to the Meta-Ra intermediate.

Meta-Ra At an irradiation temperature of -40 °C the Meta-Ra spectrum was recorded in both CphB preparations (TRIS and phosphate buffer).

Meta-Rc Proton uptake and subsequent Meta-Rc formation is impaired under low ionic strength. This assumption is based on the analysis of the recorded spectrum in phosphate buffer (-30 °C), which clearly denoted large similarity to the Meta-Ra species.

Pfr state Most remarkable spectral differences were found in the HOOP region. While an intensity decrease of the CD HOOP doublet was detected, an additional peak

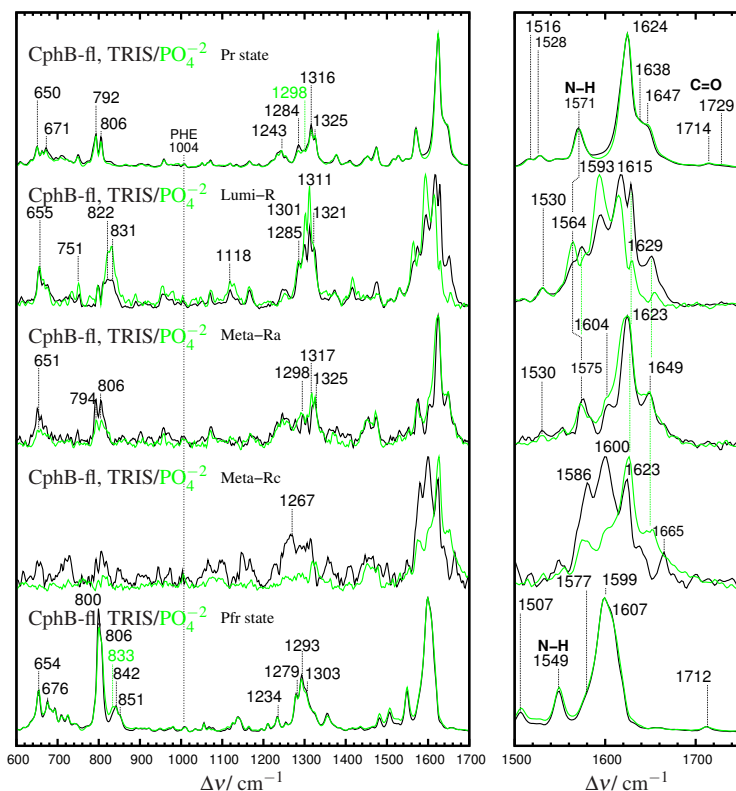


Figure 5.14: Comparison of the Pr-to-Pfr Resonance Raman spectra of CphB phytochrome measured in phosphate and in TRIS H_2O buffer. Additional bands and spectral differences are indicated in green.

gained intensity at 833 cm^{-1} (see fig. 5.14 bottom)). It is known that the characteristic HOOP band is highly sensitive to even slight variations of the surrounding [159], implying modifications in the subconformer population. However, it seems that Pfr formation is independent from the buffer type.

5.5.3. Pr-to-Pfr: influence of the ionic strength in Agp1 and Cph1 phytochrome

In a further attempt to understand the role of the ionic strength and (buffer capacity) towards the Pr-to-Pfr pathway, parent state and intermediate spectra of Agp1FMR and Cph1Δ2 phytochrome were recorded under the same conditions as in CphB (*vide supra*).

Parent state spectra and intermediate species (without the contribution of both parent states) are displayed in fig. 5.15 and fig. 5.16. The intermediate spectra contained then an unknown mixture of intermediate-species. In this respect, it is remarkable that in both phytochromes, the chromophore in the Pr state is already affected after buffer exchange (TRIS-to-phosphate). While the observed deviations are rather small, the structural implications of the parent state subconformer population-tuning are highly relevant for the intermediate formation and subsequent Pfr decay.

Agp1 In agreement with CphB but in contrast with Cph1D2 phytochrome (*vide infra*), the ionic strength of the buffer has a small effect in the parent states and a remarkable influence of the initial Lumi-R formation. This is especially revealed in the marker region (see fig. 5.15).

Pr state Regarding the Pr state measured in phosphate buffer, an intensity increase of the CD shoulder located at 1622 cm^{-1} , at the expense of the AB C=C stretching bands (approx. 1650 cm^{-1}), a small downshift of the N-H i. p. and a $+2\text{ cm}^{-1}$ upshift of a band at ca. 1530 cm^{-1} were observed. Furthermore, an increase of a peak at 1297 cm^{-1} was recorded.

Pfr state In phosphate buffer the AB shoulder showed an increase of intensity at 1607 cm^{-1} . Furthermore, the CD HOOP band exhibited an intensity variation of the doublet at 800 and 810 cm^{-1} . The adjacent shoulder at approx. 833 cm^{-1} is composed of several peaks, which revealed ionic-strength dependent variations. In agreement with CphB, it seems that the subconformer population of each parent state can be tuned by the ionic strength.

Pr-to-Pfr intermediates The Lumi-R formation was considerably favored in phosphate buffer. Subsequent decay to the Meta-Ra species occurred rapidly in TRIS buffer. In the same manner, the Meta-Rc formation and the herein chromophore deprotonation occurred easily in TRIS buffer. In this respect, the buffer influence in Agp1 is similar as in CphB phytochrome, however the in the latter case the effect is even larger.

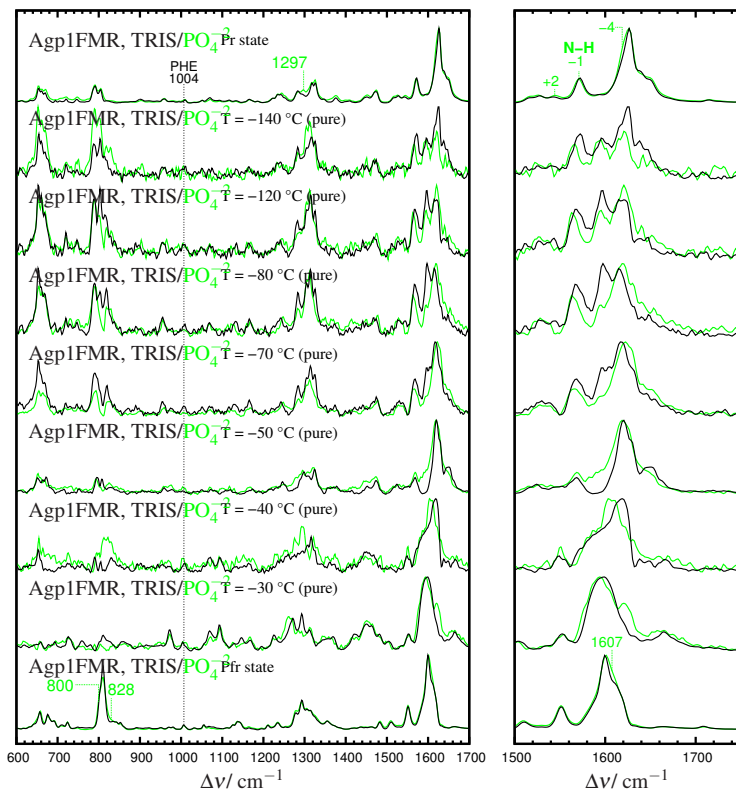


Figure 5.15: Resonance Raman spectra of the parent states and the intermediate mixtures of the Pr-to-Pfr conversion of Agp1 at given irradiation temperatures. Spectra were recorded in TRIS (black) and phosphate (green) aqueous buffer. Further plotting details are given in fig. 5.13 and fig. 5.14. For notations see fig. 5.6 (Agp1).

Cph1 Unlike Agp1 and CphB phytochrome, the chromophore structure is only sensitive to the ionic strength in the Pr state, but the Pfr state remained unaffected (see fig. 5.16). In this respect, the highly flexible PCB tetrapyrrole can adopt two conformations in the Pr state under normal conditions (Pr-I and Pr-II). Lowering of the ionic strength might lead to a non-photoactive Pr species. This is associated inter alia with the CD band upshift to 1633 cm^{-1} (see fig. B.9).

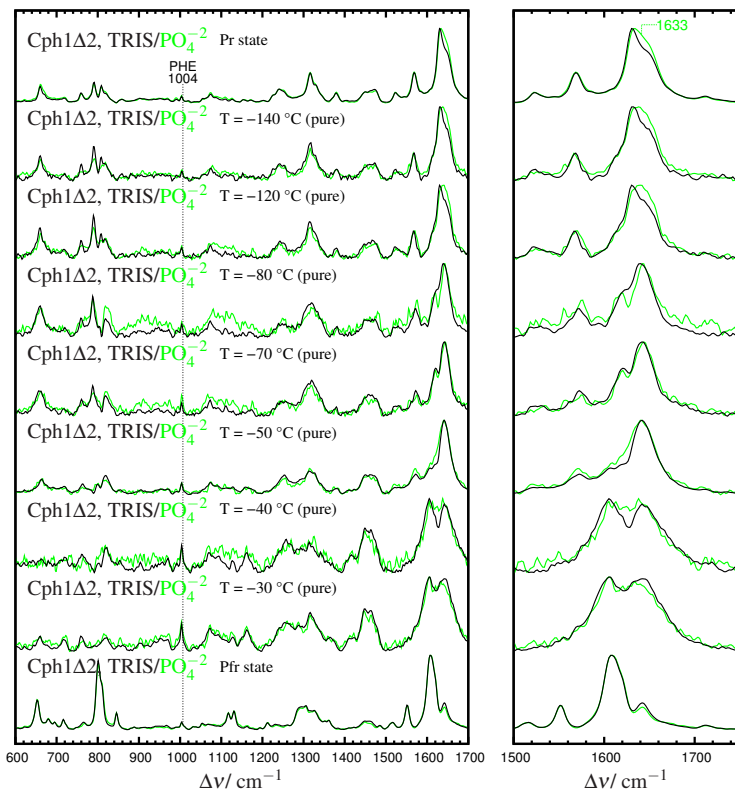


Figure 5.16: Resonance Raman spectra of the parent states and intermediate-mixtures of the Pr-to-Pfr conversion of Cph1Δ2 at given irradiation temperatures. Spectra were recorded in TRIS (black) and phosphate (green) aqueous buffer. Plot details are given in fig. 5.13 and fig. 5.14. Band assignment of Cph1Δ2 refer to ref. [102, 184, 205] and chapter 4.

5.5.4. Pfr-to-Pr reverse pathway

Lumi-F The E/Z isomerization takes place at $-120\text{ }^{\circ}\text{C}$. In plant phytochrome [119, 158] and in Pap1 bathy-phytochrome [215] Lumi-F formation already occurs at $-190\text{ }^{\circ}\text{C}$.

The Pfr-to-Lumi-F conversion involved considerable changes in the RR spectra. First, E/Z-isomerization is associated with an upshift of the CD C=C stretching band, possibly to 1624 cm^{-1} (1620 cm^{-1} in D_2O). This is based on the H/D assign-

ment of the Lumi-F intermediate in Agp2 bathy phytochrome (unpublished). Then, the strongest band at 1614 cm^{-1} was assigned to AB mode (1607 cm^{-1} after H/D exchange) and the adjacent shoulder at 1588 cm^{-1} (1583 cm^{-1}) was assigned to the BC mode. The decreased H/D sensitivity indicates a reduced coupling of the methine stretching modes with the adjacent N-H groups.

Two possible N-H i. p. peaks were detected at 1549 and 1570 cm^{-1} (N-D i. p. at 1065 and 1075 cm^{-1} respectively), indicating that the chromophore retains its cationic form in the Lumi-F intermediate. The existence of two N-H i. p. bands can be interpreted either as two Lumi-F conformers with considerable differences in rings B and C [156] or simply formation of two tautomeric Lumi-F structures, in which the positive charge, generally localized at the BC dipyrrole unit, is shifted towards the CD (or AB) moiety. Apparently the inhomogeneity of the N-H i. p. propagates also over the Meta-F intermediate (*vide infra*).

The most relevant feature of the Pfr-to-Lumi-F transition involves intensity decrease in the HOOP region. Instead of the prominent Pfr band, a poorly H/D sensitive peak at 795 cm^{-1} was observed. However, the frequency of a broad doublet at 830 and 841 cm^{-1} shows a similar position as in the Pfr spectrum (see fig. 5.17). Since the AB and BC modes (C=C stretching) are observed at similar frequencies as in the Pfr state, this HOOP might be assigned to the HOOP of the AB (or BC) methine bridge. At lower frequencies, a strong band at 649 cm^{-1} was assigned to the OOP modes of ring D ($\Delta\Delta\nu(\text{Pfr/Lumi-F}) = -6\text{ cm}^{-1}$). The region around 1300 cm^{-1} displays a considerably modified band pattern compared to the Pfr state.

The Lumi-F intermediate decays to the Meta-F species at $-50\text{ }^{\circ}\text{C}$ [118]. This intermediate is the ZZZ-equivalent to the Meta-Ra species of the Pr-to-Pfr forward reaction (*vide supra*). However, the Meta-F RR spectrum already shows similar features as the succeeding Pr species (see fig. 5.17).

The strongest band, assigned to the CD mode, shows a slight upshift compared to the Lumi-F spectrum (1626 cm^{-1} in H_2O and $1615/1622\text{ cm}^{-1}$ in D_2O). The broad feature indicates the existence of two peaks within the CD envelope. According to Agp2 Meta-F intermediate (unpublished), the band at 1648 cm^{-1} (1642 cm^{-1} in D_2O) was assigned to the AB mode. Unambiguous assignment of the BC band was compromised due to the rather complex N-H i. p. band pattern (*vide infra*). However the peak at 1589 cm^{-1} (H/D downshift approx. -10 cm^{-1}) might be assigned to this C=C mode. Alternatively the BC mode might be hidden below the CD band. Due to the observation of multiple N-H i. p. bands at 1558 and 1575 cm^{-1} (1074 cm^{-1} in D_2O), it can be assumed that also in Meta-F intermediate all pyrrole nitrogens carry a proton. Interpretation of the N-H band inhomogeneity indicates two possible Meta-F conformers. In the C=O region, a peak at 1725 cm^{-1} was observed (1714 cm^{-1} after H/D exchange). The downshift reflects the coupling of the C=O mode with the adjacent N-H group.

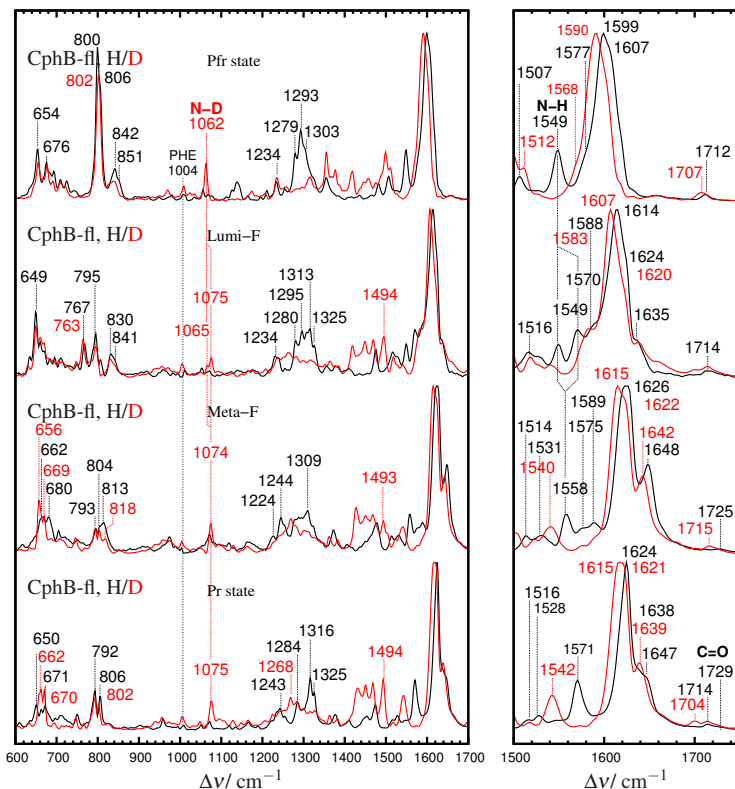


Figure 5.17: Resonance Raman spectra of the intermediates of the Pfr-to-Pr conversion of CphB phytochrome. Nomenclature details are given in fig. 5.13 and fig. 5.15.

The spectral homology to the succeeding Pr state is even higher in the HOOP region. Here, three possible HOOP bands were observed at 813, 804 and 793 cm^{-1} . Assignment of the ring D OOP mode was not completely achieved. Two peaks at 662 and 680 cm^{-1} (656 and 669 cm^{-1} in D₂O respectively) were observed. Finally, the Meta-F 1300 cm^{-1} -region showed a crowded band pattern with two prominent peaks at 1309 cm^{-1} and 1244 cm^{-1} . Both disappeared after H/D exchange.

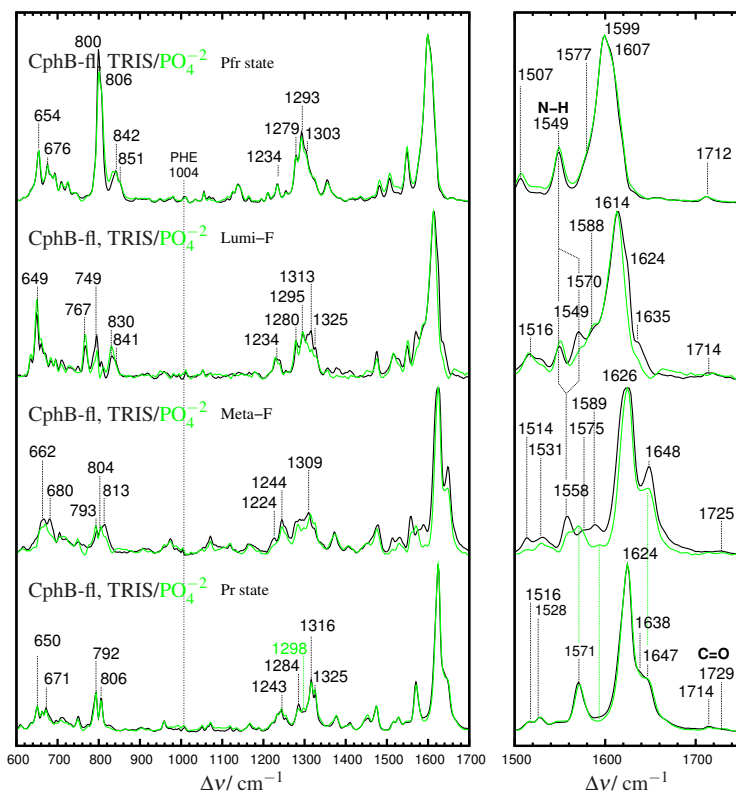


Figure 5.18: Resonance Raman spectra of the intermediates of the Pfr-to-Pr conversion of CphB phytochrome measured in phosphate and in TRIS H_2O buffer. Further details are given in fig. 5.15.

Influence of the surrounding buffer In agreement with the forward reaction, modifications of the band pattern for both Pfr-to-Pr intermediate spectra (Lumi-F and Meta-F) were observed if measured either in TRIS or phosphate buffer (see fig. 5.18).

Lumi-F In phosphate buffer, the high frequency N-H band at 1549 cm^{-1} and the BC band at 1588 cm^{-1} gained intensity at expenses of the 1570 cm^{-1} peak. Concomitantly, the CD shoulder at 1624 cm^{-1} loosed intensity. Finally, decrease of the 1313 cm^{-1} band was also observed.

Meta-F the recorded spectrum at $-50\text{ }^{\circ}\text{C}$ (phosphate buffer), displays a strong similarity to the Pr species (see fig. 5.18). Especially the AB band at 1648 cm^{-1} displayed intensity decrease compared to the TRIS Meta-F spectrum. Furthermore, an increase of a peak at 1575 cm^{-1} (Pr state N-H i. p.) was observed. Concomitantly, the peaks at 1558 , 1575 and 1589 cm^{-1} decreased in intensity. Same applies for the HOOP region, in which the peak at 813 cm^{-1} disappeared and instead to peaks appeared at 793 and 804 cm^{-1} , clearly matching the HOOP band pattern of the Pr spectrum. Interestingly, changes in the 1300 cm^{-1} -region were less pronounced.

5.6. Discussion

5.6.1. Pr-to-Pfr intermediates in prototypical phytochromes

The current results are inline with previous investigations. First, the Pr-to-Lumi-R conversion is characteristic for its low quantum yield [201]. In addition, this transition is H/D dependent. The Lumi-R H/D-effect cannot be understood in terms of chromophore deprotonation. It is, however, very likely, that the isotopic effect, reflects a longer life time in the excited state, favoring the Pr-to-Lumi-R formation. A similar isotopic effect for the Rph2 phytochrome (P2) has been found. The effect is even more pronounced in a further *Rhodopseudomonas palustris* phytochrome, namely the Rph3 (P3) species [201]. This photoreceptor undergoes a distinct photocycle. Here, Z/E-isomerization leads to an orange-absorbing (Pnr) form instead of the canonical Pr-to-Pfr conversion [70].

While the Meta-Ra formation remains apparently H/D insensitive, the rate of the concomitant Meta-Ra-to-Meta-Rc transition in deuterated medium is slowed down. Two possible effects might be involved. First, the proton release from the chromophore might be intrinsically affected due to the different N-H/N-D bond situation at the pyrrole nitrogen atoms. In this respect, the N-D bond is either strengthened or loosened. According to the low Meta-Rc contribution, the deuterium affinity of the pyrrole nitrogen is increased. Thus, the N-D is shortened and the hydrogen-release process is then hindered. Hence, deuterium release is less favored than the proton abstraction. A second explanation for the decreased Meta-Rc formation in D_2O , might be related to a higher activation energy after H/D-exchange due to strength of hydrogen bonding within the protein. Thus, chromophore reorientation and proton release are slower in D_2O than in H_2O .

Proton-release occurs via the carbonyl group of the adjacent aspartate (D197 within the DIP-motif), which acts as transient proton acceptor/donor. Subsequently, proton-migration causes net acidification of the aqueous solution [22, 23]. Furthermore, chromophore reprotonation (Meta-Rc-to-Pfr transition) occurs via proton transfer from a

conserved histidine (H250 in Agp1 or H260 in Cph1 sequence), located above the pyrrole water (see role of histidine protonation in section 4.5) [23].

In this respect, the role of the ionic strength in the parent state and towards the Pr-to-Pfr pathway (in CphB also the Pfr-to-Pr reverse reaction) is probably related with anionic interaction (Cl^-) with positively charged amino acid side chains (*e.g.* guanidinium function of arginine) located in the vicinity of the binding pocket. While the presence of chloride ions inside the binding pocket is very unlikely, solvent exposed arginine residues located in the tongue motif might slightly alter the chromophore geometry in both parent states.

Furthermore Lumi-R formation is facilitated at lower ionic strength, indicating that the Z/E isomerization also depends on the arginine (or similar) contacts. Finally, the Meta-Ra-to-Meta-Rc step involves proton-translocation via the D197-residue which might be facilitated if the D197-R462 salt bridge is weakened. The removal of the salt bridge and the formation of a free COO^- -group might be the driving force for the proton-abstraction. Otherwise, transient protonation of the D197 backbone carbonyl is very unlikely. Under low ionic strength the salt bridge cleavage requires a higher activation energy and it is therefore partially hindered.

5.6.2. Analysis of the chromophore structure during the Pr-to-Pfr conversion

Pr state The chromophore structure in the dark adapted parent state of Agp1 and Rph2 has been extensively studied [136, 185, 206]. It is known that the cofactor can be found in at least two similar yet distinct Pr forms. However, only one of this species dominates in the crystallized form [185].

It is possible that both Pr species possess distinct photoactivation properties. For example, while one conformer undergoes photo-isomerization, the second Pr conformer is involved in the thermal deactivation of the Pfr-to-Pr reverse reaction. In this respect, changes in the subconformers ratio might alter the formation of the Lumi-R intermediate, as well as subsequent reactions. Hence, the ratio of an apparently photochemically active Pr species and bleached Pr species should change during and after a complete photocycle.

Spectral analysis of the Pr spectra recorded in the dark, after far red-irradiation and after a complete photocycle, reveal intensity differences regarding the bands assigned to the AB and the BC bands.

However, both Pr conformers in Agp1 are photoactive, as derived by the almost complete Pfr conversion. It is very likely that the intrinsic structural heterogeneity of the bilin in the dark adapted state propagates along the Pr-to-Pfr conversion. The band analysis of the three Pr-to-Pfr intermediates required more than two Lorentzian

functions to describe the CD and AB modes. A similar structural heterogeneity is observed for CphB and Rph2.

Lumi-R According with the Lumi-R intermediate of phyA, the chromophore structure is found in a ZZEssa geometry [102, 165]. The large downshift of the CD mode, the H/D sensitivity of the N-H i. p. mode and the characteristic HOOP mode support a similar chromophore structure for the Lumi-R intermediate in Agp1, CphB and Rph2 phytochrome. Here the low frequency position of the CD band corresponds to conjugated systems under high structural constrains [102]. After the Z/E isomerization along the CD methine, the surrounding protein cavity is not relaxed to the stable E configuration of the CD bridge. The resultant sterical and polar interactions with the bilin might force an elongation of the double bond character and thus a decrease of the stretching frequency. The increased HOOP band intensity also supports the tensed geometry, as also postulated for the Pfr state [5, 79]. Despite the general agreement in the spectral features between the Lumi-R intermediate of phyA and Agp1, a different H/D sensitivity of the characteristic HOOP is observed. While this peak in phyA experiences an upshift and therefore modifications in the mode composition, the HOOP band of Agp1 exhibited negligible H/D sensitivity.

Meta-Ra This intermediate also presented a quite complex band structure. The chromophore adopts a more distorted geometry, as implicated by the general C=C upshift, especially at the AB and CD methine bridges. The loss in conjugation is also reflected by the intensity decrease of the N-H i. p. The geometry alteration is intimately related to the structural rearrangements in binding pocket. Hence, the broad and strong predominant C=C peak and the considerably reduced intensity in the N-H i.p. band were found to be characteristic among all Meta-Ra spectra. Apparent reminiscence of the Pr species is not overseen, however, the bandwidth of the predominant C=C peak and further marker bands, including the N-H i. p. mode are found displaced in frequency and shape.

Altogether these findings point to changes in the sterical constrains affecting the polyen system of the chromophore, especially compared to to the Lumi-R intermediate. Partial relaxation of the surrounding residues and of the polypeptide chain contributes to an increased distortion of chromophore, thus leading a general frequency increase of the methine bridge marker bands. However, lack of further experimental data, as well as calculations hinders an unambiguous vibrational assignment.

The substantial upshift of the CD peak might also be related to the decrease in coplanarity and reduction of the conjugation system (*vide supra*). In addition to that, the protein relaxation might bring the chromophore in close proximity of a negatively charged residue, thus preparing the bilin to the subsequent transient deprotonation. In this

respect, the chromophore structure can be rationalized as a distorted, yet cationic ZZE configuration. Finally coexistence of Meta-Ra subspecies is plausible and has been also postulated [184].

Meta-Rc In addition to the full characterization of the previous intermediates from which less structural information was available, the current work provided excellent Meta-Rc spectra, both in H₂O and D₂O. Here, characteristic Meta-Rc-bands beyond the crowded marker region were compared with calculated BV spectra, assuming a neutral ZZEssa chromophore structure and considering a deprotonated ring C.

In addition to the propagation of the structural heterogeneity during the Pr-to-Pfr conversion, the structural diversity in the Meta-Rc intermediate also involves the protonation state of the BC moiety. Here, the neutral ZZEssa chromophore can carry a proton either at ring B or C. Both isoforms cannot be unambiguously identified by RR spectroscopy. Moreover, it is very likely that they coexist in an equilibrium, which might be reflected in the broadening of the C=C stretching region.

5.6.3. Role of the PHY-domain during the Pr-to-Pfr transition

Based on the Pfr-minus-Pr infrared spectra it can be assumed that the PHY-domain plays a major role during the Pr-to-Pfr transition. First, stabilizing the Pfr state via the β -sheet-to- α -helix transition of the tongue motif, and finally allowing the chromophore to adopt the proper tensed geometry. Deletion of this C-terminal domain (Rph2-PG deletion mutant) impairs the secondary structural changes necessary for the Pfr state formation. It also has an effect on the hydrogen bonding situation of rings A and D already in the Pr state, as derived by upshift ring A and D C=O modes (+4 and +8 cm⁻¹ respectively). According to the RR spectra the chromophore structure remained largely unaffected.

Thus, immediately after Pr-state photoisomerization, formation of the Lumi-R intermediate was evidently cancelled. Instead, a Lumi-R-like photoproduct was observed. The absence of the tongue allows a more relaxed chromophore structure, reflected by the loss of intensity in the HOOP region. Furthermore, the imminent solvent exposure, and lack of the PHY-tongue interaction at ring A, induces an elongation of the AB bridge (C=C frequency downshift in PG). Concomitantly, ring C and D moiety are considerably solvent exposed (C=C frequency upshift). In this respect, the CD upshift can be understood as weakly stabilized ZZE-chromophore structure, due to the lack of PHY-domain hydrogen bonding partners.

The absence of the Meta-Ra intermediate in Rph2-PG variant is a strong indicator that the formation of this intermediate state strongly depends on the PHY domain and cofactor interaction, which probably involves the D197-R462 salt-bridge (Agp1 nomenclature) cleavage and further tongue-interactions, lacking in the PG-mutant.

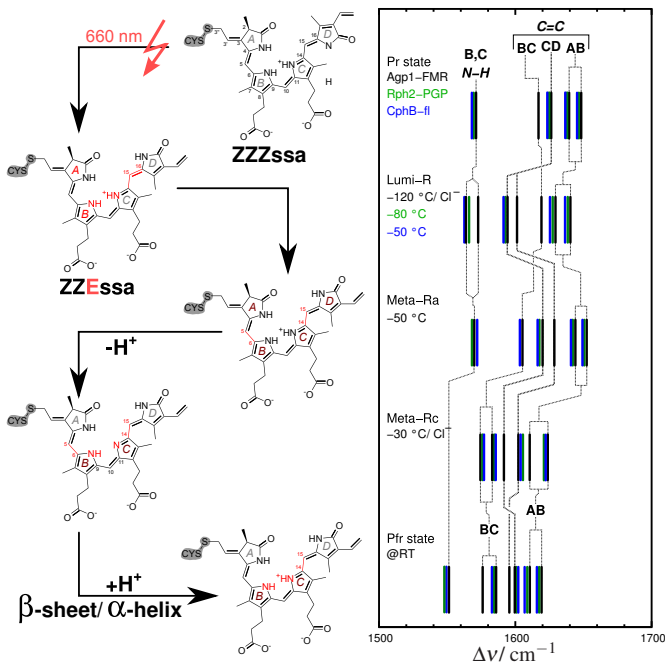


Figure 5.19: Representation of the Pr-to-Pfr reaction pathway in prototypical BV binding phytochromes according to the current RR results. Left panel: relevant structural changes in the chromophore moiety are highlighted in red. Right panel: C=C and N-H i. p. frequency changes during the Pr-to-Pfr transition for Agp1 (solid black), CphB (green) and Rph2 (blue) phytochrome. Approximate formation temperature for each intermediate is given. Deviating conditions for each protein are specified.

The last step involving the transient deprotonation and the related Meta-Rc formation is clearly observed even if the PHY domain is deleted. Hence, proton abstraction is independent from the tongue motif interaction. In this respect, chromophore-proton release occurs at the BC moiety and this event involves the aspartate residue of the DIP-motif at the GAF-domain [94, 209]. Finally, proton-uptake preferentially occurs over the conserved GAF-histidine above the pyrrole water [23, 210] (see fig. 2.4). Both motives are still present after the PHY deletion. Hence, the chromophore proton-translocation process is not dependent of the PHY domain.

Unlike the Agp1 or Dph1 phytochrome PAS-GAF deletion mutants [184], the Rph2-PG-variant is able to form a protonated ZZEssa RT-photoproduct. In contrast to the

E-isomer, the chromophore structure in the Pr state indicates minimal variations after removing the PHY-domain.

The cationic ZZE-conformer has also been observed in the SypB GAF-only phytochrome. However the lack of the PHY-domain in both, Rph2 and SypB-deletion mutants led only to a Pfr-like chromophore structure with distorted geometry.

Finally, the PHY domains plays a crucial role first in conducting the released proton after the Meta-Rc formation (H^+ -migration) and subsequently stabilizing the catalytically active Pfr species (protein folding). Deletion of this domain leads to an aberrant Pfr-like form which among other discrepancies, lacks the characteristic RR Pfr-signature, namely the strong CD HOOP mode [179, 204] and also displays no β -sheet-to- α -helix transition. In this respect, Rph2-PG provided the direct insights of the relevance of the PHY domain for canonical phytochromes. Furthermore, there is no evidence for photoisomerization at the AB-bridge in the Rph2-PG mutant as proposed for GAF-only fragments in cyanobacterial phytochromes [197, 202].

6. Results: Chromophore structure elucidation in bathy phytochromes

6.1. Structure of the Biliverdin Cofactor in the Pfr State of Bathy and Prototypical Phytochromes

“This research was originally published in Journal of Biological Chemistry. J. Salewski, F. Velazquez Escobar, S. Kaminski, D. von Stetten, A. Keidel, Y. Rippers, N. Michael, P. Scheerer, P. Piwowarski, F. Bartl, N. Frankenberg-Dinkel, S. Ringsdorf, W. Gärtner, T. Lamparter, M. A. Mroginski and P. Hildebrandt. Structure of the Biliverdin Cofactor in the Pfr State of Bathy and Prototypical Phytochromes. *Journal of Biological Chemistry*. **2013**; 288:16800-16814. [doi:10.1074/jbc.M113.457531] ©The American Society for Biochemistry and Molecular Biology.”

- RR spectra were recorded by F. Velazquez Escobar, D. von Stetten and A. Keidel (in order of relevance)
- Band analysis was performed by F. Velazquez Escobar
- Calculations were performed by J. Salewski, Y. Rippers and M. A. Mroginski
- IR spectra were recorded by P. Piwowarski and F. Bartl
- N. Michael, N. Frankenberg-Dinkel, S. Ringsdorf, W. Gärtner and T. Lamparter expressed and purified the investigated proteins
- Homology models and crystal structure analysis were performed by P. Scheerer
- Research design and development by P. Hildebrandt

Structure of the Biliverdin Cofactor in the Pfr State of Bathy and Prototypical Phytochromes*

Received for publication, January 29, 2013, and in revised form, April 18, 2013. Published, JBC Papers in Press, April 19, 2013, DOI 10.1074/jbc.M113.457531

Johannes Salewski[†], Francisco Velazquez Escobar[†], Steve Kaminski[‡], David von Stetten^{§5}, Anke Keidel[‡], Yvonne Rippers[‡], Norbert Michael[‡], Patrick Scheerer^{¶||}, Patrick Piwowski^{¶**}, Franz Bartl^{¶***}, Nicole Frankenberger-Dinkel^{††}, Simone Ringsdorf^{§§}, Wolfgang Gärtner^{§§}, Tilman Lamparter^{¶¶}, Maria Andrea Mroginski^{¶1}, and Peter Hildebrandt^{‡2}

From the [†]Institut für Chemie, Technische Universität Berlin, Sekr. PC 14, Strasse des 17. Juni 135, D-10623 Berlin, Germany, the ^{§5}Structural Biology Group, European Synchrotron Radiation Facility, 38043 Grenoble, France, the [¶]Institute of Medical Physics and Biophysics (CCO), ^{||}AG Protein X-ray Crystallography, and ^{**}AG Spectroscopy, Charité-University Medicine Berlin, Charitéplatz 1, D-10117 Berlin, Germany, the ^{††}AG Physiologie der Mikroorganismen, Ruhr-Universität Bochum, Universitätsstrasse 150, D-44780 Bochum, Germany, the ^{§§}Max-Planck-Institut für Chemische Energiekonversion, Stiftstrasse 34–36, D-45470 Mülheim, Germany, and the ^{¶¶}Institut für Allgemeine Botanik, Karlsruher Institut für Technologie, Kaiserstrasse 2, D-76131 Karlsruhe, Germany

Background: The Pr and Pfr parent states of prototypical and bathy bacteriophytochromes exhibit different thermal stabilities.

Results: Unlike bathy phytochromes, the biliverdin cofactor of prototypical phytochromes displays distinct conformational heterogeneity in Pfr.

Conclusion: This heterogeneity enables thermal Pfr to Pr conversion in prototypical phytochromes.

Significance: Understanding thermal deactivation of the signaling Pfr state is essential for elucidating the molecular function of phytochromes.

Phytochromes act as photoswitches between the red- and far-red absorbing parent states of phytochromes (Pr and Pfr). Plant phytochromes display an additional thermal conversion route from the physiologically active Pfr to Pr. The same reaction pattern is found in prototypical biliverdin-binding bacteriophytochromes in contrast to the reverse thermal transformation in bathy bacteriophytochromes. However, the molecular origin of the different thermal stabilities of the Pfr states in prototypical and bathy bacteriophytochromes is not known. We analyzed the structures of the chromophore binding pockets in the Pfr states of various bathy and prototypical biliverdin-binding phytochromes using a combined spectroscopic-theoretical approach. For the Pfr state of the bathy phytochrome from *Pseudomonas aeruginosa*, the very good agreement between calculated and experimental Raman spectra of the biliverdin cofactor is in line with important conclusions of previous crystallographic analyses, particularly the ZZ_{Essa} configuration of the chromophore and its mode of covalent attachment to the protein. The highly homogeneous chromophore conformation seems to be a unique property of the Pfr states of bathy phytochromes. This is in sharp contrast to the Pfr states of prototypical phytochromes that display conformational equilibria between two sub-states exhibiting small structural differences at the terminal methine bridges A-B and C-D. These differences may mainly root in the interactions of the cofactor with the highly conserved Asp-194 that occur via its carboxylate function in bathy phytochromes. The

weaker interactions via the carbonyl function in prototypical phytochromes may lead to a higher structural flexibility of the chromophore pocket opening a reaction channel for the thermal (ZZE → ZZZ) Pfr to Pr back-conversion.

Phytochromes utilize light as a source of information for initiating a biochemical reaction cascade (1, 2). These photoreceptors, initially discovered in higher plants but also found in microorganisms (3–5) and fungi (6, 7), include a light sensor module and catalytic unit, a serine/threonine kinase (in plant phytochromes) (8), and a histidine kinase in most of the bacterial orthologs (9–11). Phytochromes covalently bind a linear tetrapyrrole chromophore that upon light absorption undergoes a double bond isomerization at the methine bridge between the pyrrole rings C and D (Fig. 1). This photochemical event is followed by a series of thermal relaxation processes of the cofactor and the protein eventually causing a major protein structural change that activates the kinase (9). Also, the deactivation is linked to a photoinduced reaction sequence that transforms the sensor module back to the initial state. In this sense, canonical phytochromes represent a photoswitch between the red-absorbing (Pr)³ and far-red absorbing (Pfr) parent states.

³ The abbreviations used are: Pr, red-absorbing parent states of phytochrome; Pfr, ar-red absorbing parent states of phytochrome; App1 and App2, phytochromes 1 and 2 from *A. tumefaciens*; CphB, cyanobacterial phytochrome CphB from *Calothrix* PCC7601; HOOP, hydrogen out-of-plane; ip, in-plane bending; MD, molecular dynamics; MM, molecular mechanics; BV, biliverdin; P4FB, phytochromobilin; PaBpP, bacteriophytochrome from *Pseudomonas aeruginosa*; QM, quantum mechanics; RR, resonance Raman; r.m.s.d., root-mean-square deviation; str, stretching; A, B, C, and D refer to the respective pyrrole rings; AB, BC, and CD denote the corresponding methine bridges; H/D, hydrogen/deuterium exchange.

* This work was supported by Deutsche Forschungsgemeinschaft Grant Sfb1078 (B5, B6, and C3).

¹ To whom correspondence may be addressed. Tel.: 49-30-31421433; Fax: 49-30-31421122; E-mail: andrea.mroginski@tu-berlin.de.

² To whom correspondence may be addressed. Tel.: 49-30-31426500; Fax: 49-30-31421122; E-mail: Hildebrandt@tu-berlin.de.

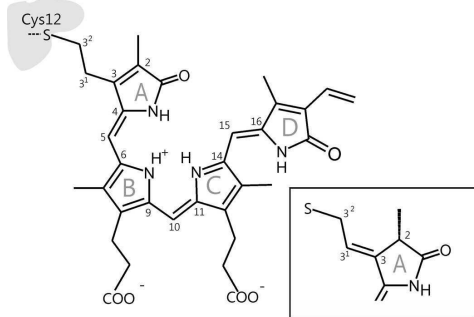


FIGURE 1. Structure and atom numbering of the biliverdin chromophore in *PaBphP* in the 3²-linked attachment to the protein. Inset, chromophore structure at ring A in case for 2(*R*),3(*E*)-P4B type binding (π -electron rearrangement).

Because recombinant bacterial phytochromes are easily accessible, which in turn facilitates structural and spectroscopic studies, they are widely used as model systems for phytochromes from plants. A survey of phytochrome-encoding genes revealed, however, that canonical phytochromes, carrying phycoyanobilin as chromophore, are present mainly in cyanobacteria, whereas other prokaryotic organisms carry biliverdin (BV) as the chromophore (Fig. 1). While being attached to the protein through a different binding site, BV adopts nearly the same conformation in the binding pocket and undergoes an identical photochemistry with a C-15=C-16 double bond photoisomerization (12–15). These BV-harboring bacteriochromes can further be grouped into prototypical and bathy phytochromes in which the thermodynamically stable states are Pr and Pfr, respectively (16, 17).

This different stability of the parent states is most probably the reason why three-dimensional structures so far have been mainly obtained for the Pr state of prototypical phytochromes and the Pfr state of bathy phytochromes (13–20). Although the gross chromophore structures in the respective parent states are likely to be similar in prototypical and bathy phytochromes, it appears to be premature to consider the available three-dimensional structures of the Pr states of the prototypical phytochrome and the yet only available three-dimensional structure of the Pfr state of bathy phytochrome from *Pseudomonas aeruginosa* (*PaBphP*) as representative structures for the respective parent states in both classes of phytochromes (12). First, the sequence homology between bathy and prototypical phytochromes is rather poor. In the case of phytochrome *Agp1* (UniProtKB accession number Q7CY45) and *Agp2* (UniProtKB accession number Q8UDG1) from *Agrobacterium tumefaciens*, a sequence identity of only 35% and positive matches of 53% were predicted using the sequence BLAST protein alignment tool (21, 22). Thus, the functionally important structural changes of the protein that activate or deactivate the associated catalytic module can hardly be assessed from a comparative structural analysis of the Pr and Pfr states of prototypical and bathy phytochromes. Second, the three-dimensional models suggest significant differences between prototypical and bathy

phytochromes that are independent of the specific state of the photosensor, *i.e.* the mode of chromophore attachment to the protein (14, 15, 18). However, these differences *per se* do not reveal the molecular origin for the different thermodynamic stability and reaction channels of the parent states in prototypical and bathy phytochromes. Such an understanding is in turn essential for elucidating the strategy of how nature utilizes either red or far-red light to trigger physiological processes.

In this work, we have addressed this issue focusing on the comparative analysis of the Pfr states of bathy and prototypical phytochromes. Starting with the crystallographic structure of the Pfr state of the bathy phytochrome from *PaBphP* (14), molecular dynamics (MD) simulations combined with calculations using molecular mechanical-quantum mechanical (QM/MM) hybrid methods were carried out to achieve a structural refinement for the chromophore binding pocket, guided by a comparison of the calculated and the experimental resonance Raman (RR) spectra of the tetrapyrrole cofactor (23). Specifically, we asked whether the results of the present approach were consistent with the original assignment of the bilin structure to a ZZE_{ss} configuration (14), a plausible assignment albeit not unambiguously backed by the rather disperse electron density data, which in principle would also be compatible with a ZZZ_{ss} geometry from protein crystallography (14). Similarly, we checked the proposed chromophore binding via thiol addition to the exocyclic vinyl group of ring A. This tetrapyrrole-protein linkage is in contrast to prototypical bacteriophytochromes in which BV attachment is accompanied by the formation of an exocyclic double bond and the saturation of ring A (18, 24). The combined theoretical-experimental analysis of the Pfr state of *PaBphP* allows for a “calibration” of the RR spectroscopic method that was then employed to investigate the chromophore structures in the Pfr states of various prototypical BV-binding phytochromes for which no three-dimensional structural data were available. It was demonstrated that, unlike to the highly homogeneous chromophore conformation in bathy phytochromes, the bilin cofactors in the Pfr states of prototypical phytochromes displayed a substantial structural heterogeneity that primarily referred to the methine bridges between rings A and B (A-B) and C and D (C-D) (25). The molecular origin of this heterogeneity and the implications for the lower thermodynamic stability of the Pfr state are discussed.

MATERIALS AND METHODS

Sample Preparation—Expression of the proteins, purification, and the assembly of the holoproteins was described previously (22, 26–28). In addition to the wild-type (WT) *A. tumefaciens* phytochrome 1 (*Agp1*), two further engineered variants from the same phytochrome were investigated as follows: the C20A site-directed mutant (*Agp1C20A*) and a truncated variant lacking the first 18 N-terminal amino acids (*Agp1Δ18*) (29). In both mutants, the chromophore is bound in a noncovalent manner to the protein. Cyanobacterial phytochrome *CphB* (*Calothrix* PCC7601) was expressed and purified as described previously (30). In all cases, protein variants lacking the histidine kinase module were used. Previous comparative studies of

Chromophore Structure in Pfr State of Phytochromes

Agp1 revealed identical RR spectra for proteins including and lacking the kinase module (31, 32).

Buffer solutions used for the RR experiments included 50 mM Tris/HCl, 300 mM NaCl, 5 mM EDTA in H₂O (D₂O) at a pH (pD) of 7.8. Protein samples were concentrated via Microcon filters up to a value corresponding to an optical density of ~50 at 280 nm.

Synthesis of Isotopically Labeled Biliverdin—Unlabeled BV was synthesized from bilirubin by reaction with 2,3-dichloro-5,6-dicyanobenzoquinone in dimethyl sulfoxide (97%). Obtained BV was esterified by reaction with sulfuric acid in methanol (17 h, -5 °C, 67%). BV-dimethyl ester was then cleaved at the central C-10 position according to Ref. 33. This reaction yields four products, each half of BV (“right” and “left”), and their respective thiobarbituric acid adducts; these adducts contain the carbon atom, originally located at position 10. Both the right and the left halves were isolated from this reaction mixture. The left half, representing the former A-B ring part of BV, was formylated with *o*-trimethyl [¹³C]formate (ambient temperature, 5 min, 65%). Then the formylated left half was condensed with the right half (ethyl acetate, 0 °C, POCl₃, 15 min, addition of methanol, further stirring for 30 min, 32%, ¹³C NMR: 10–¹³C, 115.0 ppm). [¹³C]BV-dimethyl ester was saponified following the procedure described by Lindner *et al.* (34): H₂O, CF₃COOH, 1:1, Dowex ion exchange resin, 44 h, ambient temperature; 77%, ¹³C NMR: 10–¹³C, 115.9 ppm.

Resonance Raman Spectroscopy—RR measurements were performed using a Bruker Fourier transform Raman spectrometer RFS 100/S with 1064 nm excitation (Nd-YAG cw laser, line width 1 cm⁻¹), equipped with a nitrogen-cooled cryostat from Resultec (Linkam) (32, 35). All spectra were recorded at -140 °C unless noted otherwise. The laser power at the sample was kept at 780 milliwatts. To identify potential laser-induced damage of the phytochrome samples, RR spectra before and after a series of measurements were compared. In no case were changes between these control spectra determined. For each spectrum, the accumulation time was 1 h. Protein and buffer Raman bands were subtracted on the basis of a Raman spectrum of apophytochrome. Photoconversion from Pfr to Pr (Pr to Pfr) state was achieved by a 10-s (2 min) sample illumination at 20 °C with 785 nm light (660 nm) using a light-emitting diode, corresponding to a photon fluence of ~2·10²² (4·10²²) photons/m². The raw spectra of the Pfr and Pr obtained in this way included minor contributions from the Pr and Pfr state, respectively. These contributions were removed by mutual subtraction of the experimental spectra from each other, using the characteristic marker bands of Pr and Pfr as a reference. The pure spectra were further analyzed by a band fitting procedure assuming Lorentzian band shapes.

IR Spectroscopy—For IR spectroscopic measurements, the protein samples were dissolved in 50 mM Tris, 300 mM NaCl, 5 mM EDTA in H₂O (D₂O) at pH (pD) 7.8 and concentrated via Microcon filters. The concentration of the samples was between 50 and 150 mg ml⁻¹ as determined by the intensity of the UV-visible absorbance at 280 nm. The protein was placed between two BaF₂ windows (15 mm diameter) with a 3-μm thick polytetrafluoroethylene spacer and equilibrated at 20 °C.

IR spectra were recorded in a Bruker IFS66v/s spectrometer equipped with a liquid nitrogen cooled HgCdTe detector (J15D series, EG&G Judson). Spectra were recorded 2 min prior to illumination and 30 s after the illumination, and subsequently the difference spectra were calculated by subtracting the initial state spectra from the illuminated state spectra. Illumination of the sample was performed as in the Raman experiments (see above).

Molecular Dynamics Simulations—The initial set of coordinates for the MD simulations were extracted from the crystallographic structure of the photosensory domain of *PaBphP* in the Pfr state (Protein Data Bank code 3C2W) (14). The secondary structure of residues 376–485 in the peptide chain, which are missing in the original Protein Data Bank submission, were predicted by PSIPRED (36, 37) as an unordered loop. Accordingly, their three-dimensional coordinates were generated using CHARMM (32b2) software (38), followed by energy minimization and a short 5-ns MD simulation for structural equilibration. Assignment of protons to titratable groups was done on the basis of visual inspection of the local environment of the charged amino acids and histidine residues. In particular, His-247 and His-277 in the chromophore binding pocket were protonated at their Ne positions. The protein was then solvated in a hexagonal box of 58687 TIP3P water molecules and charge-neutralized with NaCl. After a series of energy minimization and equilibration steps, restraint-free simulations were performed under periodic boundary conditions for 6 ns in the isothermal-isobaric (NTP) ensemble at 300 K. For this, a combination of the Langevin-Piston Nose-Hoover (39, 40) method was used with reduced Langevin damping factors (from 5.0 to 1.0). All MD simulations were performed keeping the BV cofactor molecule fixed due to missing force field parameters.

The MD simulations were performed using the NAMD (version 2.6) software (41) in combination with the CHARMM all-atom force field (42). For the treatment of nonbonded interactions in the system, the particle-mesh-Ewald method (43) was employed for electrostatics, whereas a cutoff of 12 Å in combination with a switching function was used for van der Waals interactions.

Quantum Mechanical/Molecular Mechanical Calculations—50 snapshots were extracted from the last 100 ps of the MD simulation, in intervals of 2 ps. For each snapshot, the geometry of the chromophore-binding site, including the chromophore and all residues within a radius of 15 Å from the C-10 atom of the BV cofactor (active region), was optimized using a hybrid QM/MM approach (44) combining the B3LYP density functional (45) with the CHARMM27 force field (42) implemented in the modular program package Chemshell (46). The 6–31g* basis set was used to describe the QM region. Two different QM/MM partition schemes were considered. The first one was defined with a relatively small QM region of only of 81 atoms, including the BV cofactor and the Cys-12 side chain, whereas the second partition scheme with 96 atoms was constructed by extending the QM region to include Asp-194 and the water molecule located in the tetrapyrrole cavity (pyrrole water) (Fig. 2). These two partitions will be referred to as the QM81/MM and QM96/MM models, respectively. The lowest QM/MM energy of the QM96/MM model was computed for the snap-

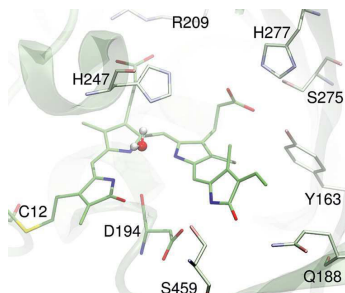


FIGURE 2. Optimized structure of the chromophore binding pocket of the Pfr state of *PaBphP* according to the QM/MM model of lowest energy (QM/MMmin model).

shot extracted after 5920 ps of the MD simulation. This optimized structure is denoted as QM/MMmin. Furthermore, the covalent bond cuts at the QM/MM borders on the Cys-12 side chain in the QM81/MM model, and also on the Asp-194 backbone in the QM96/MM model, were saturated with hydrogen link atoms.

The average Raman spectrum of the protein-bound BV chromophore was calculated by summing up the Raman spectra computed at a QM/MM level for each of the snapshots following published protocols (23, 47–49). It has been demonstrated for other phytochromes that calculated (off-resonance) Raman intensities are a good approximation for Raman spectra measured under rigorous resonance and pre-resonance excitation (50, 51).

Homology Model for the Bathy Phytochrome from *A. tumefaciens*—Homology modeling of the photosensory module of *A. tumefaciens* phytochrome 2 (*Agp2*) (6–499 amino acids) was performed by using SWISS-MODEL (52) with the crystal structure of the *Agp2* homolog (53) from *PaBphP* *P. aeruginosa* (14) as a template with a sequence identity of 36.3%. In a subsequent step, energy minimization and structural idealization were performed by the program REFMAC5 (54). Structure validation was performed with the programs PROCHECK (55) and WHAT_CHECK (56). To obtain an appropriate comparative model of the chromophore binding pocket from the *Agp2* photosensory module, in a final step the model of *Agp2* was separately superimposed with the crystal structure of the *PaBphP* (Protein Data Bank code entry 3C2W, see Ref. 14), and the amino acids around the chromophore were manually rebuilt with the program COOT (57). All structure superpositions of the backbone α -carbon traces were performed using the CCP4 program LSQKAB (54).

RESULTS AND DISCUSSION

Structure of the Biliverdin Binding Pocket in *PaBphP*—During the MD simulation, the protein approaches a stable structure after a few nanoseconds as shown by the root-mean-square deviations (r.m.s.d.) of the carbon backbone atoms with respect to the crystal structure (Fig. 3). The relatively large r.m.s.d. values of ~ 2.7 Å primarily result from conformational changes at loop and coil regions. Additional changes of the protein sec-

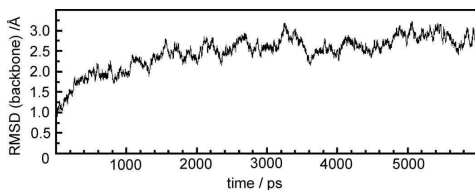


FIGURE 3. Evolution of the r.m.s.d. for the $C\alpha$ atoms of *PaBphP* during the 6-ns MD simulation.

ondary structure were not observed, but we noted a slightly increased radius of gyration (28.9 Å) compared with the crystal structure (27.9 Å).

For all snapshots, converged BV structures under preservation of the initial configuration/conformation of the methine bridges were obtained (Fig. 2). The structural differences between the QM96/MM and QM81/MM model were very small and did not exceed 0.003 Å for bond lengths and 2° for bond and dihedral angles. Only the distances between the ring D and B NH groups and Asp-194 are increased when this residue is included in the QM region (QM96/MM; Table 1). The QM description of the BV cofactor afforded the expected bond length alternation pattern for the methine bridges with the C-4=C-5 and C-15=C-16 double bonds (1.37 Å) and the C-5=C-6 and C-14=C-15 single bonds (1.43 Å), whereas the electronic conjugation was fully pronounced at the central B-C methine bridge, as reflected by the nearly equal C–C bond lengths of ~ 1.40 Å. Calculated bond angles for the three methine bridges were higher by $\sim 10^\circ$ with respect to the crystallographic values, although quite similar torsional angles were predicted. Structural differences of the BV cofactor optimized for the various snapshot models were very small with standard deviations of less than 0.003 Å, 1 and 2° for the bond lengths, bond angles, and dihedral angles of the methine bridges, respectively. In particular, variations of the dihedral angles at the A-B and C-D methine bridge were half the value predicted previously for phycocyanobilin in plant phytochrome phyA (48) and phycoviolobilin in phycoerythrocyanin (49), pointing to a more tightly packed chromophore binding pocket in the Pfr state of *PaBphP*.

The NH group at ring B forms a stable hydrogen bond to the carbonyl group of Asp-194, as already observed in other phytochrome structures. Unique for the Pfr state of *PaBphP*, however, is the strong hydrogen bond between the carboxylic group of this residue and the NH group on ring D. Interestingly, the QM treatment of Asp-194 (QM96/MM) leads to an elongation of the N(D)⋯O(Asp-194 side chain) distance by ~ 0.2 Å compared with the QM81/MM model. This bond seems to be an important factor to stabilize the *ZZEssa* configuration of the BV cofactor. In fact, a D194A mutation impairs the complete photoconversion of the photoreceptor (14).

In addition to Asp-194, Ser-459 and Gln-188 also have been suggested to contribute to the chromophore stabilization via interaction with the carbonyl function of ring D (14). In fact, the present calculations predict average distances of 3.4 Å (O(D)⋯O(Ser-459)) and 3.25 Å (O(D)⋯NE(Gln-188)), which are smaller than the crystallographic data of 4.1 and 3.4 Å,

Chromophore Structure in Pfr State of Phytochromes

TABLE 1

Selected structural parameters of the PaBph-BV chromophore and its vicinity

Bond lengths are given in Å and angles in degrees. Coordinates are defined according to Fig. 1. The abbreviations used are as follows: avg., average; max., maximum; min., minimum.

	X-ray	QM96/MM snapshots				QM81/MM snapshots		
		QM/MMmin	Avg.	Max.	Min.	S.D.	Avg.	S.D.
A-B methine bridge								
C(4)–C(5)	1.528	1.371	1.371	1.374	1.367	0.002	1.370	0.002
C(5)–C(6)	1.536	1.432	1.433	1.439	1.427	0.003	1.433	0.001
C(4)–C(5)–C(6)	116.4	127.3	127.2	128.7	125.4	0.7	127.5	0.75
N(A)–C(4)–C(5)–C(6)	17.0	8.0	8.5	11.4	6.0	1.3	8.0	1.1
C(4)–C(5)–C(6)–N(B)	5.7	14.5	16.5	20.6	9.4	1.8	15.5	1.7
B-C methine bridge								
C(9)–C(10)	1.398	1.400	1.400	1.407	1.392	0.003	1.400	0.003
C(10)–C(11)	1.393	1.398	1.396	1.400	1.387	0.003	1.393	0.003
C(9)–C(10)–C(11)	118.31	130.9	129.9	131.5	128.6	0.7	128.8	0.55
N(B)–C(9)–C(10)–C(11)	–0.6	–6.7	–6.1	–3.6	–8.8	1.1	–6.9	1.23
C(9)–C(10)–C(11)–N(C)	–8.2	–5.3	–4.9	–2.9	–7.0	0.8	–5.3	0.71
C-D methine bridge								
C(14)–C(15)	1.535	1.434	1.434	1.439	1.427	0.002	1.430	0.003
C(15)–C(16)	1.535	1.372	1.369	1.373	1.365	0.002	1.371	0.002
C(14)–C(15)–C(16)	119.1	128.6	127.3	128.9	125.4	0.9	126.9	0.89
N(C)–C(14)–C(15)–C(16)	–150.3	–155.4	–152.7	–148.2	–158.8	2.2	–155.6	1.55
C(14)–C(15)–C(16)–N(D)	–150.7	–160.0	–159.8	–155.4	–163.2	1.6	–157.9	1.53
BV-H₂O								
N(A)–OH ₂		2.952	2.899	3.074	2.813	0.061	2.806	0.020
N(C)–OH ₂		2.900	2.863	3.056	2.807	0.042	2.799	0.022
BV-protein matrix								
N(B)–O(Asp-194)	3.054	2.858	2.940	3.155	2.819	0.074	2.911	0.17
N(D)–OD(Asp-194)	3.00	2.831	2.873	3.077	2.774	0.068	2.635	0.03
O(D)–OG(Ser-459)	4.13	3.395	3.40	3.597	3.212	0.116	3.382	0.125
O(D)–NE(Gln-188)	3.40	3.329	3.253	3.776	2.860	0.301	3.372	0.318
O1(ppsC)–OH(Tyr-163)	2.91	2.666	2.666	2.789	2.596	0.035	2.664	0.033
O1(ppsC)–OH(Ser-275)	2.53	2.717	2.707	2.751	2.673	0.022	2.704	0.027
O1(ppsB)–(Arg-209)	2.61	2.691	2.696	2.755	2.657	0.020	2.692	0.019
O2(ppsB)–NE(Arg-209)	3.32	2.702	2.754	3.006	2.702	0.048	2.741	0.034

respectively. Mutations of these two residues also lead to irregularities (S459A) or delay (Q188L) in the photocycle (14).

Both the NH groups of rings A and C form strong hydrogen bonds to the pyrrole water located in the tetrapyrrole cavity, as indicated by the short distances of 2.90 and 2.86 Å, respectively. In contrast to previous studies on phyA (48), the interactions of this water molecule are preserved during the entire MD simulation. Rotation of the pyrrole water is hindered by the strong hydrogen bond formed with His-247.

The positions of both BV propionic side chains hardly change within the 50 snapshots. In the case of the ring C propionic chain, hydrogen bonds with His-277, Tyr-163, and Ser-275 immobilize the carboxylic group. Particularly steady and strong are the interactions with Ser-275 and Tyr-163, as reflected by the short average distances of 2.70 and 2.66 Å for O(Ser-275)–O2(ppsC) and O(Tyr-163)–O1(ppsC), respectively. Correspondingly, the mobility of the ring B propionic side chain is hindered by the two strong hydrogen bonds with Arg-209. For these interactions, the average N(Arf-209)–O1(ppsB) and NE(Arg-209)–O2(ppsB) distances are 2.70 and 2.75 Å, respectively (Table 1).

Resonance Raman Spectra of PaBphP—The experimental RR spectrum of PaBphP in the Pfr state is characterized by two strong peaks located at 1599 cm⁻¹ and at 811 cm⁻¹ (Figs. 4 and 5). Although the first peak constitutes a well known marker band for the tetrapyrrole backbone conformation, the high intensity of the second peak is characteristic for tetrapyrrole chromophores in the Pfr state. In addition, the presence of the

band at 1549 cm⁻¹, which is sensitive to H/D exchange, is indicative of a protonated tetrapyrrole, as already demonstrated by previous spectroscopic studies on phytochromes (58, 59).

The Raman spectrum computed for the BV chromophore bound to PaBphP using the large QM96/MM model is in very good overall agreement with the experimental spectrum. An intense Raman band is predicted at ~1601 cm⁻¹, resulting from the superposition of two peaks, calculated on average at 1602 and 1600 cm⁻¹ (Table 2). This finding is in line with the experimental data because the 1599-cm⁻¹ band is actually composed of two band components at 1603 and 1598 cm⁻¹ (see below) (Table 2). Analogous to other phytochromes, these two modes are assigned to C=C stretching vibrations at the A-B and C-D methine bridges, with the C=C(A-B) at a higher frequency than the C=C(C-D). Minor structural variations at the methine bridges observed among snapshots (Table 1) give rise to frequency shifts for these two modes of more than 20 cm⁻¹ (Table 2).

The NH in-plane (ip) deformation mode of rings C and B (ν_{sc}) is predicted at 1548 cm⁻¹ with a significant Raman intensity, again in very good agreement with the experimental peak detected at almost the same position. In addition, the NH ip deformation coordinate of ring B also contributes to several modes in the frequency region at ~1300 cm⁻¹. Deuteration of the NH groups leads to three main spectral changes. The N-H bending at 1549 cm⁻¹ disappears, and its counterpart reappears at 1062 cm⁻¹. The band at 1316 cm⁻¹, located in a crowded spectral region, loses intensity, and a new peak at 1377

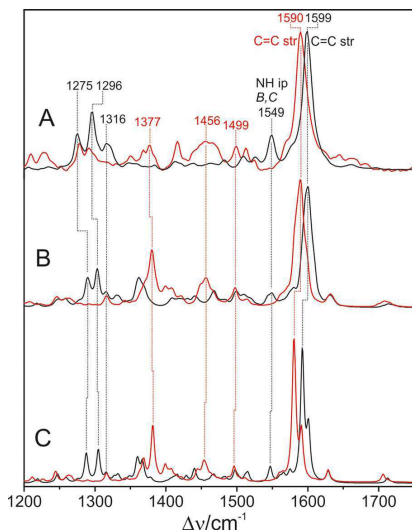


FIGURE 4. Experimental RR and calculated Raman spectra of the Pfr state of PaBphP in H₂O (black) and D₂O (red) between 1200 and 1750 cm⁻¹. A, experimental RR spectrum; B, sum of the QM96/MM-calculated Raman spectra obtained from various snapshots of the MD simulations; C, calculated Raman spectrum for the QM/MMmin model.

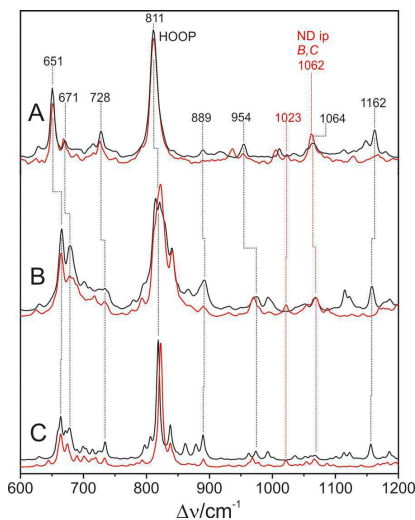


FIGURE 5. Experimental RR and calculated Raman spectra of the Pfr state of PaBphP in H₂O (black) and D₂O (red) between 600 and 1200 cm⁻¹. A, experimental RR spectrum; B, sum of the QM96/MM-calculated Raman spectra obtained from various snapshots of the MD simulations; C, calculated Raman spectrum for the QM/MMmin model.

cm⁻¹ appears in the spectrum of the deuterated species. As shown in Figs. 4 and 5, these isotopic spectral changes are well reproduced by the calculations.

Most remarkably, the standard deviation for ν_{56} (N-H ip B and C) frequency is only 4 cm⁻¹ (Table 3), which is much lower than that predicted for phyA (9 cm⁻¹) (48), reflecting the positional and rotational stability of the pyrrole water and the Asp-194 in the chromophore cavity. The NH in-plane deformation coordinates of rings A and D are distributed over several normal modes around 1370 and 1440 cm⁻¹, respectively, which are in most cases predicted with low Raman intensity. Hence, a direct assignment of an experimental RR peak to these vibrational modes is not possible.

The lower frequency region is dominated by a very intense band at 811 cm⁻¹. In accordance with previous vibrational assignments for other phytochromes, the present calculations predict an intense band in this region that is due to the hydrogen out-of-plane (HOOP) vibration of the C-D methine bridge. The average vibrational frequency calculated for this mode is higher by 10 cm⁻¹ than the experimental value. If Asp-194 is excluded from the QM region (model QM81/MM), the discrepancy with respect to the experimental position increases to 30 cm⁻¹ (Table 3). Unlike the high frequency region, for which the QM81/MM model also affords satisfactory results, the quantum mechanical treatment of the BV-Asp-194 and BV-H₂O interactions is essential for reproducing the HOOP modes in an adequate manner. In this last model, for only one snapshot structure a HOOP frequency below 810 cm⁻¹ was predicted; 42 snapshots exhibit HOOP frequencies between 810 and 830 cm⁻¹ and seven of them with HOOP frequencies slightly above 830 cm⁻¹. Furthermore, for the QM96/MM model the frequency variations are correlated with the C-15=C-16 torsional angle (see below), and a relationship between the HOOP frequency and any structural parameter could not be identified for the QM81/MM model.

A second experimental peak of considerable intensity in the low frequency region is located at 651 cm⁻¹ close to a smaller peak at 671 cm⁻¹. From the calculated potential energy distribution the former band was assigned to a mode consisting mainly of ring D bending vibrations with only minor contributions from the thioether bridge C-S stretching, although the latter peak includes various coordinates such as ring C bending and a relatively high contribution from the C-S stretching.

Correlation between Spectral and Structural Parameters—Although the average QM/MM spectra calculated from 50 snapshots match the experimental data very well in most regions, the individual spectra show dispersion in frequencies that may be associated with particular structural changes. A quantitative analysis is possible by Pearson's method (60), which allows evaluating cross-correlations for mode frequencies and structural parameters as discussed in the following for the QM96/MM model.

Particularly for the structural changes of the BV cofactor occurring at the methine bridges, we computed moderate or strong correlation of the C-C dihedral angle with the C=C bond length of 0.59 for B-C and -0.80 for C-D, respectively. This can readily be rationalized because the torsional motion has an impact on the electronic structure of the conjugated

Chromophore Structure in Pfr State of Phytochromes

TABLE 2

Assignment of experimental vibrational frequencies (ν/cm^{-1}) and relative Raman intensities measured for *PaBphP*, *Agp2*, and *Agp1* phytochromes according to the calculated vibrational modes and relative Raman intensities for *PaBphP*-BV and *PaBphP*-P4FB minimum energy QM96/MM models and average frequencies with corresponding standard deviation of *PaBphP*-BV computed out of a 50-snapshot ensemble

The abbreviations used are as follows: PED, potential energy distribution; str, stretching; rock, rocking; def., deformation, $\Delta\nu$ (^{13}C), frequency shift due to ^{13}C labeling of the C(10) position. A, B, C, and D refer to the respective pyrrole rings, and A-B, B-C, and C-D denote the corresponding methine bridges (see Fig. 1). The experimental (exp.) and calculated (calc.) relative Raman intensities (I) are related to the strongest band (I = 100).

Mode no.	Calc. modes (QM96/MM) for <i>PaBphP</i> -BV				Exp. <i>PaBphP</i>				Exp. <i>Agp1</i>			Calc. modes for <i>PaBphP</i> -P4FB					
	Minimum energy snapshot											Minimum energy snapshot					
	PED (%)		ν	I	Average ν		ν	I	ν	I	$\Delta\nu$ (^{13}C)	I	ν	I	PED (%)		
50	46% C=C str vinyl D 10% C-C str D-vinyl 12% C-H rock vinyl D 11% C-H def vinyl D		1629	8	1632 \pm 3		1613	8	1614	8	1633	0	6	1627	8	45% C=C str vinyl D 10% C-C str D-vinyl 12% C-H rock vinyl D 11% C-H def vinyl D	
51	61% C=C str A-B		1611	0					1609	3							
52	38% C=C str A-B		1602	38	1602 \pm 5		1603	42	1605	45	1620	-1.6	39	1589	89	16% C=C str A-B 13% C=C str B-C 46% C=C str C-D	
53	46% C=C str C-D		1592	100	1600 \pm 5		1598	100	1598	100	1600	+0.3	100	1595	100		
54	35% C=C/C-C str B-C 13% C-H def B-C		1574	7	1577 \pm 4		1585	8	1588	13	1586	-5.7	19	1566	15	11% C=C str A-B	
55	52% C-C str D 13% C=C str vinyl D		1561	3			1575	11	1577	12				1560	5	47% C-C str D 12% C=C str vinyl D	
56	26% N-H ip B 21% N-H ip C		1548	12	1548 \pm 4		1549	31	1549	35	1551	-0.2	35	1546	17	22% N-H ip B 22% N-H ip C	
165	69% HOOP C-D		819	36	822 \pm 8		811				809 803			819	52	63% HOOP C-D	

TABLE 3

Experimental and calculated vibrational frequencies (ν/cm^{-1}) of *PaBphP*-BV using the QM96/MM and QM81/MM models

Average frequencies and corresponding standard deviation were computed out of a 50-snapshots ensemble. The abbreviations used are as follows: avg., average; min., minimum; Exp., experimental; sh, shoulder; vs, very strong intensity; m, medium intensity.

Mode	Character	QM96/MM					QM81/MM average
		Exp.	Min.	Avg.	Range	r.m.s.d.	
50	C=C (vinyl)	1613 (sh)	1629	1632.2	13.9	3.2	1631.1
52	C=C (A-B)	1603 (vs)	1602	1602.3	19.8	5.0	1600.6
53	C=C (C-D)	1598 (vs)	1592	1599.7	21.0	5.1	1603.9
54	C=C (B-C)	1585 (sh)	1574	1577.0	20.8	4.1	1577.7
56	NH ip (C, B)	1549 (m)	1548	1547.8	16.9	3.9	1548.5
165	HOOP (C-D)	811 (vs)	819	821.8	39.2	7.6	842.4

C=C bonds of the methine bridges that affect the orbital overlap and thus the methine bridge bond length. As a consequence, the frequencies of the C=C stretching modes of the methine bridges are not only inversely correlated with the respective bond lengths. The frequency of the C-D stretching, for example, is further correlated with the dihedral angle of the C-D bridge (0.59), whereas that of the A-B stretching displays a strong correlation with the C-5-C(B)-N(B) bond angle (0.64) (Table 4).

Also, the frequency of the prominent C-D methine bridge HOOP mode is significantly correlated with a structural parameter, the C-15=C-16 torsional angle (0.65), such that deviations from co-planarity between rings C and D cause increasing frequencies. Only a moderate correlation exists for the C-14-C-15 dihedral angle (0.45). Furthermore, a high positive correlation of the N-H ip (B and C) and C=C stretching frequencies was evaluated for both the A-B and B-C methine bridge (0.75 and 0.57), although at least a weak positive correlation exists for the C-D bridge (0.24). These findings are consistent with the coupling of the two vibrational modes as derived from the computed potential energy distribution and also with the experimental shifts of the A-B, B-C, and C-D C=C

marker bands upon H/D exchange of the pyrrole nitrogens (see Fig. 5).

Model for PaBphP with a 2(R),3(E)-P4FB Chromophore—Previous crystallographic studies on the Pr state of prototypical BV-binding phytochromes (18, 24) have shown that the tetrapyrrole is covalently bound to the Cys via a thioether linkage with the terminal C-3² carbon of the vinyl group of ring A, thereby leading to an exocyclic C=C double bond and a chiral center at the C-2 carbon. Correspondingly, the bound chromophore exhibits the ligation adduct of a 2(R),3(E)-P4FB-type structure (Fig. 1). Instead, the crystallographic analysis of the bathy phytochrome *PaBphP* provides no indication for a chiral center at the C-2 carbon (14) but indicates a BV-type chromophore configuration with an intra-ring double bond, although the limited resolution of the electron density map at the chromophore-binding site leaves some uncertainties. Thus, we have checked this conclusion by extending the calculations to a new structural model that was generated by exchanging the BV chromophore of the crystal structure-based QM96/MM models with a 32-linked 2(R),3(E)-P4FB. The methyl group at ring A was oriented toward Ile-246 and Leu-9 to avoid steric clashes with the protein environment, in particular with Ser-

TABLE 4

Pearson correlation coefficients r for selected structural and vibrational parameters of the PaBphP-BV chromophore calculated for the QM96/MM model

Only values above 0.50 are reported. The abbreviation used is as follows: str, stretching.

Structural parameter	Vibrational coordinate					
	C=C str A-B	C=C str B-C	C=C str C-D	N-H ip A	N-H ip B, C	HOOP C-D
A-B methine bridge	C(5)-C(6)-N(B) bond angle	0.64		0.57	0.64	
	C(5)-C(6) bond length	-0.86		-0.58		
B-C methine bridge	N(B)-C(9)-C(10) bond angle	0.64	0.61	0.57	0.61	
	C(9)-C(10)-C(11) bond angle			0.55		
	C(9)-C(10) bond length			0.50		
	C(10)-C(11) bond length		-0.66			
C-D methine bridge	N(C)-C(14)-C(15)-C(16) dihedral angle		0.59			
	C(14)-C(15)-C(16)-N(D) dihedral angle					-0.65
	C(15)-C(16) bond length		0.89			

193. The new geometries were reoptimized following the same procedure as described above for the QM96/MM models. To distinguish them from the original models, we will refer to them as QM96-PfB/MM.

In fact, comparison between the QM96/MM and QM96-PfB/MM model suggests that the structural differences at this linkage site and its immediate environment are minor and most likely not detectable at 2.9 Å resolution, especially by the limited information of the electron density from the chromophore in PaBphP (14). The r.m.s.d. between the two minimum energy structures yielded only 0.3 Å. The largest structural differences compared with the original model are predicted for C-3² and at the methyl group on C-2 which are displaced by 1.45 and 1.03 Å, respectively, as a consequence of hybridization change at C-3¹ and C-2. The concomitant changes in the electron distribution in ring A induce a significant swap of the C-2-C-3-C-3¹-C-3² dihedral angle from -63 to 3° (Fig. 6).

As a consequence, the main effect in the calculated Raman spectrum refers to the A-B stretching mode, which undergoes a significant 11-cm⁻¹ downshift such that it appears as a separate peak on the low frequency side of the largely unchanged C-D stretching mode (Table 2 and Fig. 7). The downshift is even more pronounced in the spectra calculated for the minimum energy configurations of the models. Further spectral differences originating from the PfB-type constitution of the chromophore include the broad feature at 1370 cm⁻¹ and the peak at 717 cm⁻¹ (Fig. 7), which are due to a deformation and stretching of the C-S bond, respectively, and the two weak bands at 1645 and 1197 cm⁻¹ resulting from the stretching of the exocyclic C=C bond and the C-C and C-N single bond stretchings, respectively. The rather significant spectral deviation related to the A-B methine bridge stretching of the QM96-PfB/MM model from the experimental spectrum prompt us to discard the idea of a PfB-type chromophore and thus supports the conclusions drawn by Yang *et al.* (14) that the tetrapyrrole is bound under preservation of the ring A C=C double bond, *i.e.* a BV-type chromophore as used in the QM96/MM model.

Model for PaBphP with BV in ZZZssa Configuration/Conformation—The second consequence of the limited resolution of the electron density at the BV-binding site of PaBphP refers to the determination of the configuration of the C-D methine bridge. Although the electron density would also be compatible with a Za configuration at this position, Yang *et al.*

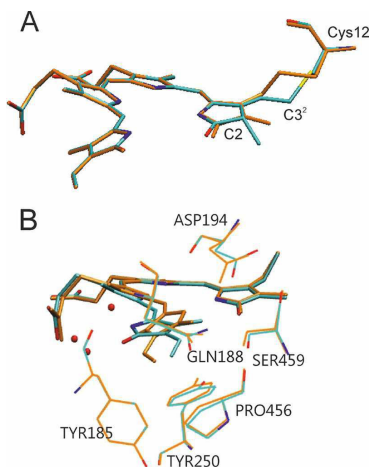


FIGURE 6. Superposition of the minimum energy structure of PaBphP bonded to a BV-type chromophore in the ZZEsa conformation (orange) and the structure of PaBphP bonded to a 2(R),3(E)-PfB chromophore (cyan) (A) and the structure PaBphP with BV in a ZZZssa conformation (cyan) (B).

(14) decided for the more plausible Ea configuration, based on the hydrogen bonding network between ring D and the protein environment. This conclusion was backed by further crystallographic studies (15, 20). To examine the consequences of the ZZZssa cofactor configuration on the Raman spectra, we have generated a structural model for PaBphP with a BV in 15Za configuration (PaBphP-15Za), using the optimized QM96/MM structure as a starting point and rotating the C=C double bond of the C-D methine bridge clockwise to ~140° thus avoiding sterical clashes with the protein environment. The system was allowed to relax following the QMMM protocol described under "Material and Methods."

As shown in Fig. 6, the main differences of the optimized structure with respect to the starting geometry are noted for the C-D methine bridge of the BV cofactor, characterized by torsional angles of -162.1 and 9.6° for the C=C and C-C bonds, respectively. Except for the slightly rotated side chain of Gln-188 and the movement of the Asp-194 side chain closer to the

Chromophore Structure in Pfr State of Phytochromes

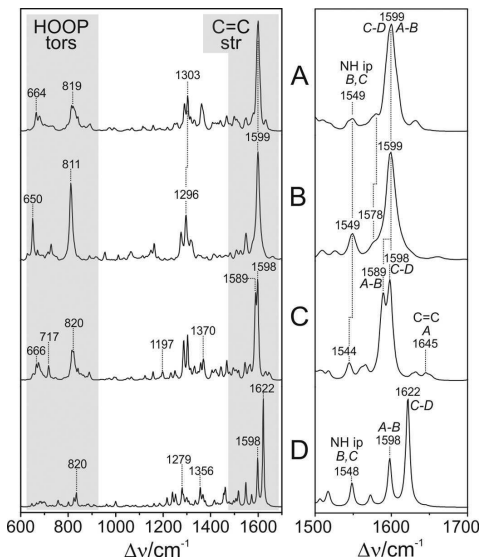


FIGURE 7. *A*, calculated Raman spectrum of the Pfr state of *PaBphP* with a BV-type chromophore binding in the ZZEsa configuration (sum of snapshots, as in Figs. 4 and 5); *B*, experimental RR spectrum of the Pfr state of *PaBphP*; *C*, calculated Raman spectrum of the Pfr state of *PaBphP* with PFB-type chromophore binding in the ZZEsa configuration (sum of snapshots); *D*, calculated Raman spectrum of the Pfr state of *PaBphP* with a BV-type chromophore binding in the ZZSsa configuration (single snapshot). The left panel displays the overview spectra, highlighting the most structure-sensitive spectral regions. The right panel is an expanded view of the C=C stretching region.

chromophore, the positions of the remaining residues in the vicinity of ring D are hardly affected. In the *PaBphP*-15Za structure, however, the hydrogen bonds between ring D and the Tyr-250, Ser-459, Gln-188, and Asp-194 no longer exist. Instead, the NH and CO groups of ring D interact with water molecules. These structural differences lead to distinct changes in the calculated Raman spectrum that deviate substantially from the experimental spectrum (Fig. 7). The C=C stretching of the C-D methine bridge is calculated to be at 1621 cm^{-1} , upshifted by 20 cm^{-1} with respect to the experimental band. Furthermore, the sharp peaks at 1296 and at 811 cm^{-1} in the experimental spectrum, assigned to the NH ip deformation mode at ring B and to the HOOP on the C-D methine bridge, respectively, are not reproduced by the *PaBphP*-15Za model, in contrast to the good overall agreement provided by the calculated spectrum of the *PaBphP*-15Ea model. Consequently, the present spectroscopic analysis confirms the ZZEsa chromophore configuration proposed by Yang *et al.* (14).

Structural Similarities between *PaBphP* and *Agp2*—*Agp2* is a bathy phytochrome from *A. tumefaciens*. The RR spectra of the Pfr states of *Agp2* and *PaBphP* are nearly identical with respect to the frequencies and relative intensities and the isotopic shifts upon H/D exchange (Fig. 8). This striking spectral agreement indicates that the structures of the chromophore binding pockets are very similar. In fact, whereas the overall sequence

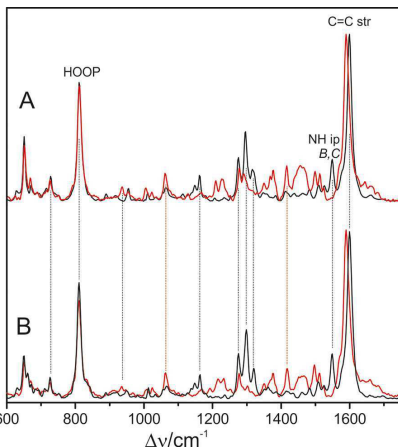


FIGURE 8. Experimental RR spectra of the Pfr states of *PaBphP* (*A*) and *Agp2* in H_2O (black) and D_2O (red) (*B*).

homology between the photosensory modules (~ 513 amino acids) of *Agp2* and *PaBphP* shows about 37% identity and 56% similarity (EMBOSS-Align; EMBL-EBI), nearly all amino acids in the chromophore binding pocket are conserved with the exception of Phe-187, Phe-192, and Ala-276 in *Agp2* compared with Tyr-185, Tyr-190, and Ser-275 in *PaBphP*. Thus, a basic homology model of *Agp2* displays only minor differences compared with the *PaBphP* template (Fig. 9).

Pfr States in Bathy and Prototypical Phytochromes—The RR spectra of Pfr states of prototypical phytochromes display distinct differences compared with those of bathy phytochromes, specifically in the region of the C=C stretching and the HOOP modes of the methine bridges (Fig. 10). This is shown for the prototypical phytochrome from *A. tumefaciens*, *Agp1* (Fig. 10C), two *Agp1* mutants (Fig. 10, *D* and *E*), and the cyanobacterial BV-binding phytochrome *CphB* (Fig. 10F). All spectra show the characteristic features of the Pfr state, *i.e.* intense RR bands at ~ 1600 and 800 cm^{-1} . However, in the spectra of prototypical phytochromes, these bands do not exhibit symmetric band profiles. The prominent C=C stretching band displays pronounced shoulders on the high frequency side of between ~ 1605 and 1630 cm^{-1} , concomitant to a broadening and increased asymmetry of the band shape for all bands in this region as compared with the relatively sharp 1599-cm^{-1} peak of the bathy phytochromes *Agp2* and *PaBphP*. In the HOOP region, a similar broadening and peak shape asymmetry were observed, and in *CphB* even a clearly detectable second peak was observed, although not as pronounced as for the C=C stretching modes. These changes were accompanied by an increased RR activity for the modes in the region between 840 and 860 cm^{-1} , where for bathy phytochromes Raman bands can hardly be detected at all. It is therefore tempting to assume that the spectral heterogeneities in the Pfr spectra of prototypical phytochromes reflect a structural heterogeneity of the chromophore binding pocket. To examine this hypothesis, we

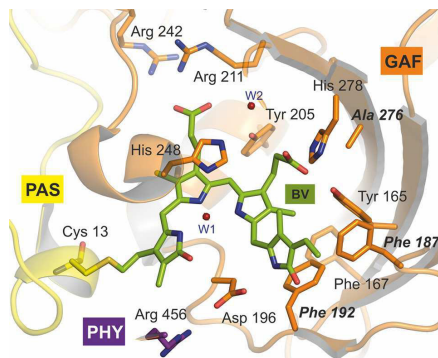


FIGURE 9. Homology model for the Pfr state of *Agp2*. Bold letters refer to *Agp2*-specific amino acids compared with *PaBhp*.

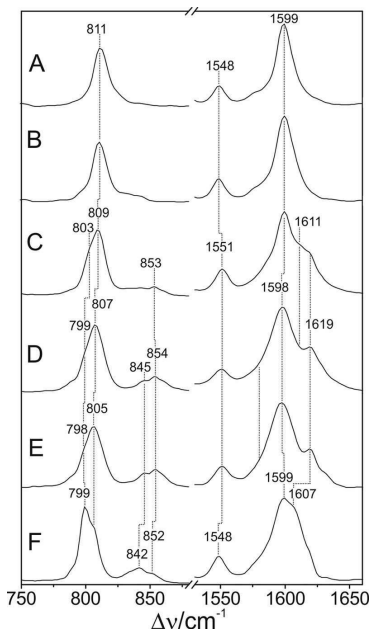


FIGURE 10. Experimental RR spectra of the Pfr states (in H_2O) in the C=C stretching (right) and HOOP region (left) of *PaBhp* (A), *Agp2* (B), *Agp1* (C), *Agp1-Δ18* (D), *Agp1-C20A* (E), and *CphB* (F).

have investigated the C=C stretching and HOOP regions of WT *Agp1* in more detail.

First, we tried to identify the nature of the vibrational modes in the C=C stretching region, using *Agp1* reconstituted with a BV chromophore with a $^{13}C/^{12}C$ substitution at the B-C methine bridge. This substitution affects the modes, including the B-C stretching coordinates that according to the calcula-

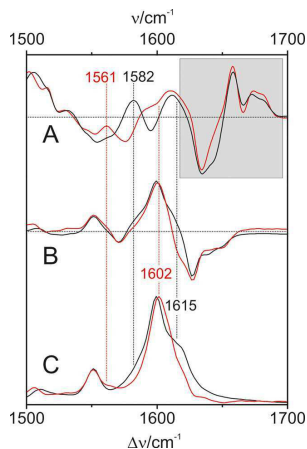


FIGURE 11. Experimental IR and RR spectra of *Agp1* in H_2O . A, IR difference spectra "Pfr minus Pr"; B, RR difference spectra "Pfr minus Pr"; and C, RR of the Pfr state. Black lines and numbers refer to *Agp1* reconstituted with the unlabeled chromophore, and red lines and numbers refer to the chromophore ^{13}C -labeled at position C-10; the shaded area indicates Pr and protein difference bands.

tions for *PaBhp* predominantly contribute to the weakly Raman-active mode ν_{54} (Table 2). As this mode is expected to exhibit a high IR intensity, the RR spectroscopic measurements were complemented by IR difference spectroscopy. Such IR difference spectra reflecting the spectral changes associated with the Pr to Pfr transition are shown in Fig. 11A for *Agp1*, including the unlabeled and ^{13}C -labeled BV chromophore. The spectral features in the shaded area of Fig. 11 are primarily due to difference bands of the protein and the chromophore in the Pr state, but the positive bands between 1550 and 1620 cm^{-1} can be attributed mainly to chromophore bands of the Pfr state. Here, the most pronounced isotopic shift is observed for the peak at 1582 cm^{-1} , which upon ^{13}C labeling is downshifted to 1561 cm^{-1} . These bands can hardly be detected in the RR (Fig. 11C) and the "Pfr minus Pr" RR difference spectra. However, the RR (difference) spectra indicate a substantial loss of intensity on the high frequency shoulder (~ 1615 cm^{-1}) of the prominent 1600- cm^{-1} peak upon ^{13}C labeling indicating the involvement of the B-C stretching coordinates to the RR-active mode(s) in this region. Thus, the isotopic shifts point to two different modes with a substantial B-C stretching character. The present data for *PaBhp* and previous experimental results for other phytochromes as well as QM/MM and QM calculations (Table 2) (61) have shown that the B-C stretching coordinates may be either largely localized in one mode (ν_{54} of *PaBhp*) or distributed over two modes via coupling with the A-B stretching coordinates. In the latter case, one expects a lower frequency IR-active and a higher frequency Raman-active mode, both of them sensitive to ^{13}C labeling at position C-10, which nicely agrees with the present observations for *Agp1*.

On the basis of these results, the RR spectra of *PaBhp* and *Agp2* were subjected to a band fitting analysis, using a minimum

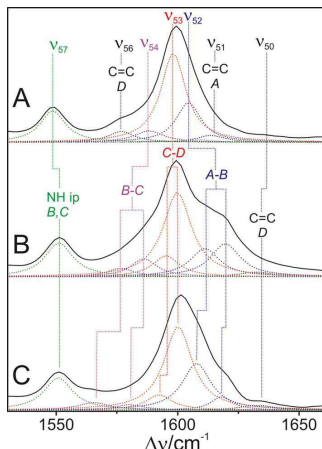


FIGURE 12. RR spectra in the C=C stretching region of *Agp2* (A), *Agp1* reconstituted with the unlabeled chromophore (B), and *Agp1* reconstituted with the chromophore ^{13}C -labeled at position C-10 (C). The spectra were measured from protein solutions in H_2O . The dotted lines refer to fitted Lorentzian line shapes. Band components originating from modes of similar character are highlighted by different colors.

number of bands to achieve a satisfactory simulation of the experimental spectra with physically meaningful widths of the individual band components (Fig. 12). The results agree very well with the calculations for *PaBphP* inasmuch as all of the predicted Raman-active modes of the cofactor can be correlated with counterparts in the experimental spectra with a good match in frequencies and intensities (Table 2).

The corresponding analysis of the RR spectrum of *Agp1* requires more bands for an acceptable fit than *Agp2* (and *PaBphP*) (Fig. 12). To correlate these bands with the expected normal modes in this region, we have to take into account that in *Agp1*, like in bacteriophytochrome 1 from *Deinococcus radiodurans* (18), the BV chromophore binds to the Cys side chain via a PFB-type configuration such that no mode involving the ring A C=C stretching (ν_{51} in *Agp2*) exists. The corresponding stretching mode of the exocyclic double bond is predicted to be above 1640 cm^{-1} with very low RR activity. It might contribute to the very weak band at 1633 cm^{-1} , although the assignment to the C=C stretching of the vinyl substituent of ring D seems to be more plausible in view of its coupling to the delocalized π -electron system of the chromophore. The remaining six bands between 1560 and 1620 cm^{-1} then have to be related to four normal modes. A plausible assignment for these bands is guided by the isotopic shifts due to ^{13}C labeling of the B-C methine bridge, the IR difference spectra (Fig. 11), and the predicted Raman activities (see above) (Table 2). Accordingly, the weak band pair at 1586 cm^{-1} (-6 cm^{-1}) and 1577 cm^{-1} (-11 cm^{-1}) is assigned to the weakly Raman-active mode ν_{54} (according to the notation for *Agp2*), whereas the medium intense band pair at 1611 cm^{-1} (-3 cm^{-1}) and 1620 cm^{-1} (-2 cm^{-1}) is attributed to the Raman-active mode ν_{54} . Then the prominent band at 1600 cm^{-1} , which does not display an iso-

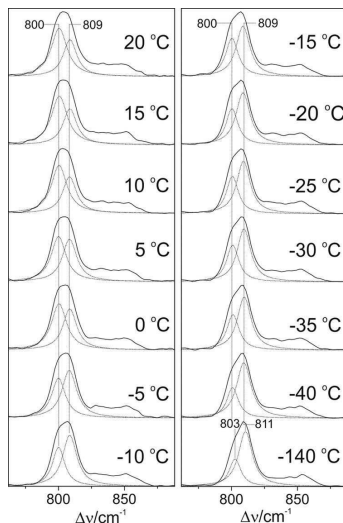


FIGURE 13. Temperature dependence of the RR spectra of the Pfr state of full-length *Agp1*. Residual Pr contribution of the Pfr state was manually subtracted using the raw Pr spectrum at each temperature. Subsequently, a minimum set of Lorentzian functions was fitted to the spectra. For the sake of clarity, only the two curves describing the HOOP modes are shown (dotted lines). Only restricted variations of the frequencies and bands widths ($\leq 1\text{ cm}^{-1}$) were allowed in the global fit. The sum of the individual Lorentzians is essentially indistinguishable from the experimental spectrum (straight line). In an alternative approach, the fitting procedure was applied to the raw spectra by including band components originating from the Pr state determined before. Both fitting procedures afforded a very similar temperature dependence of the intensity ratio of the two HOOP modes, although there was a systematic underestimation of the lower frequency component in the latter approach ($\sim 20\%$).

topic shift, is assigned to the mode ν_{53} (C-D stretching). The same assignment may hold for the weak band component at 1595 cm^{-1} , which is required for a satisfactory fit although its frequency (and isotopic shift) is associated with a considerable uncertainty.

In the same way, we have analyzed the HOOP region (Fig. 13). Although in the bathy phytochromes *PaBphP* and *Agp2* the prominent peak at $\sim 810\text{ cm}^{-1}$ can be well described by a single Lorentzian band shape, in *Agp1* two band components are required for a satisfactory fit. These two bands are insensitive to ^{13}C labeling at the B-C methine bridge and thus confirm the assignment to the C-D HOOP mode.

Structural Basis for the Differences between Bathy and Prototypical Phytochromes—The analysis of both spectral regions demonstrates the splitting of modes localized at the C-D and A-B methine bridges, indicating at least two sub-states that differ with respect to conformational details in these regions of the tetrapyrrole. To identify the underlying structural parameters, we adopted the results of the correlation analysis for *PaBphP* (see above and Table 4). Accordingly, we conclude that the splitting of A-B stretching mode reflects differences in the C-5-C(B)-N(B) bond angle and the C(A)=C-5 bond length. Both mode components are significantly higher in frequency

than the corresponding mode in *PaBphP*, pointing to an increase of the bond angle associated with a shortening of the bond length in *Agp1*. Correspondingly, the splitting of the C-D stretching mode may be related to a subtle change of either the respective C=C bond length or, more likely, of the dihedral angle of the C-D methine bridge. The latter conclusion is supported by the analysis of the HOOP modes that include a prominent band at essentially the same position as in *PaBphP* and a second one at lower frequencies reflecting an increased C-15=C-16 torsional angle. The structural changes of the C-D moiety may also be the origin for the increased RR activity for bands between 840 and 855 cm^{-1} in *Agp1*, which are tentatively attributed to modes including the C-C and C-N stretching coordinates of ring D, according to the calculations for *PaBphP*.

Also the two mutants of *Agp1*, *Agp1*- Δ 18 and *Agp1*-C20A, display a similar heterogeneity of the HOOP mode as the WT protein, an even more pronounced RR activity in the 840–855- cm^{-1} region, and an increased broadening of the C-D stretching at 1598 cm^{-1} , pointing to qualitatively similar structural differences at the C-D methine bridge (Fig. 10, D and E). However, the A-B stretching region is dominated by the high frequency component at 1619 cm^{-1} , whereas the 1611- cm^{-1} band component can hardly be detected. Accordingly, one may conclude that in the two sub-states of both *Agp1*- Δ 18 and *Agp1*-C20A, the conformation of the A-B methine bridge is essentially the same, and structural heterogeneity is largely restricted to the C-D methine bridge. In fact, the mutations in *Agp1*- Δ 18 and *Agp1*-C20A that refer to the chromophore-binding site prohibit a covalent attachment of the tetrapyrrole to the protein (29) and thus may remove steric constraints from the A-B dipyrrolic unit such that the A-B methine bridge adopts only one conformation with a more relaxed geometry. Conversely, the specific cofactor-protein interactions associated with the structural heterogeneity of the C-D dipyrrolic unit do not seem to be affected by these mutations. These findings suggest that the structural changes at the A-B and C-D methine bridges may be independent of each other.

The Pfr state of *CphB* reveals a distinct splitting of the HOOP modes with an even slightly higher RR intensity of the low frequency component at 799 cm^{-1} compared with the 805- cm^{-1} band, pointing to nearly equal populations of sub-states differing with respect to the C-D methine bridge conformation. This conclusion is consistent with the two similarly strong band components at 1599 and 1607 cm^{-1} , which are readily assigned to C-D methine bridge stretchings in view of their high RR intensities. The overall very broad and asymmetric peak envelope suggests the involvement of more than one A-B stretching mode of the high frequency side, although their positions cannot be determined precisely. Qualitatively similar spectral heterogeneities, albeit to a different extent for the CD and AB modes, are observed in the RR spectra of the Pfr states of the prototypical BV-binding phytochromes from *D. radiodurans* (62) and *Aspergillus nidulans* (63).

Conformational Equilibria of the Pfr states in Prototypical Phytochromes and Dark Reversion—The present results indicate that the Pfr states of prototypical phytochromes possess a heterogeneous chromophore structure with at least two sub-states that are protonated at all four pyrrole nitrogens but differ

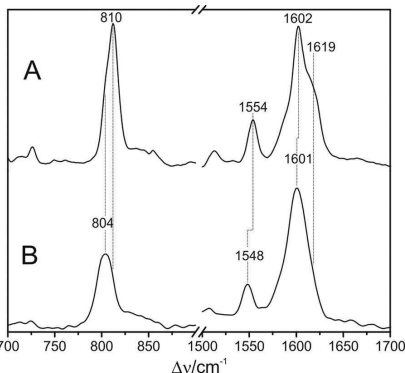


FIGURE 14. RR spectra of the Pfr state of full-length *Agp1* measured at -140 °C (A) and 20 °C (1064 nm excitation) (B).

with respect to the conformations of the C-D and A-B methine bridges. This structural heterogeneity is in sharp contrast to the Pfr state of bathy phytochromes, which exhibits a well defined homogeneous chromophore structure. It is therefore tempting to relate this difference to the different thermal stability of the Pfr state of bathy and prototypical phytochromes. A plausible interpretation is based on a conformational equilibrium involving a highly stable sub-state and a "reactive" sub-state that represents the starting point for the thermal reaction pathway to the Pr state. Whereas in bathy phytochromes the nonreactive sub-state prevails, in prototypical phytochromes the reactive and nonreactive sub-states coexist in comparable amounts. In an attempt to explore the parameters controlling this equilibrium, we have measured the RR spectra of the Pfr state of *Agp1* as a function of the temperature and the pH. Changing the pH from 6.0 to 9.0 had essentially no effect on the RR spectra implying that there are no (de-)protonable groups in this pH range that influence the chromophore structure (data not shown). Analysis of the temperature-dependent spectra is more complicated because the intrinsic temperature dependence of frequencies and band widths superimposes with a temperature-dependent shift of the conformational equilibrium. Nevertheless, increasing the temperature from -140 to 20 °C leads to a remarkable decrease of the high frequency shoulder at 1619 cm^{-1} in the methine bridge stretching region, paralleled by intensity changes of the HOOP modes. These spectral changes may be interpreted in terms of a re-distribution among the sub-states (Fig. 14). For a quantitative analysis, the HOOP region is more appropriate because only two overlapping bands are involved. The spectra reveal a steady increase of the low frequency HOOP component (803–800 cm^{-1}) at the expense of the high frequency component (811–809 cm^{-1}) upon increasing the temperature from -140 to 20 °C (Fig. 13). Assuming the same RR cross-sections for the HOOP modes of the two components, the intensity ratio determined by a band fitting analysis can be set equal to the concentration ratio K of the two sub-states. The van't Hoff plot, restricted to the measurements between -40 and 20 °C, affords a reaction enthalpy of $\Delta H_R =$

Chromophore Structure in Pfr State of Phytochromes

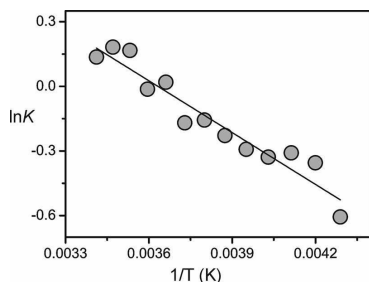


FIGURE 15. Plot of the logarithm of the equilibrium constant K for the conformational equilibrium in the Pfr state of *Agp1* against $1/T$. The equilibrium constant is defined by the intensity ratio of the low frequency ($\sim 800\text{ cm}^{-1}$) to the high frequency ($\sim 809\text{ cm}^{-1}$) band component of the prominent peak in the HOOP region. The intensities were determined by band fitting as described in Fig. 13.

6.7 kJ/mol (Fig. 15). The small reaction enthalpy suggests that the two sub-states differ only by subtle structural details such as a difference in the C-D methine bridge torsional angle and minor modifications in the A-B methine bridge geometry as concluded from the frequency-structure correlations discussed above (Table 4). Also, the Pr state of prototypical phytochromes evidently includes a heterogeneous chromophore structure as inferred from a previous RR study of *Agp1* and bacteriophytochrome 1 from *D. radiodurans* (25). However, for the Pr state of *Agp1*, the temperature-dependent variations in the RR spectra are much smaller than for the Pfr state with a change in the intensity ratio of conjugate bands of less than 10% in a temperature range from 20 to $-140\text{ }^{\circ}\text{C}$ (data not shown). Moreover, structural heterogeneity in phytochromes appears to be a quite general phenomenon as it has been suggested both for the Pr states of cyanobacterial and plant phytochromes as well as for cyanobacteriophores, based on NMR spectroscopy and the analysis of the respective photoconversion processes (20, 64–69). However, in none of the cases can the heterogeneity be related to the efficiency of thermal Z/E isomerization (dark reversion).

In this context it is interesting to refer to recent NMR studies of the prototypical cyanobacterial phytochrome Cph1 (65). These authors have shown a less ordered chromophore pocket in the Pr state, whereas in the Pfr state the chromophore gives rise to well defined resonances with no indication for heterogeneities. Even if the Pfr states of prototypical BV- and phycocyanobilin-binding proteins can be directly compared, these findings are not in contradiction with the present results taking into account the different time scales of NMR and RR experiments. It is very likely that the small geometry changes of the A-B and C-D methine bridges associated with the transition between the two Pfr sub-states of *Agp1* (and prototypical phytochromes in general) occur on the (sub-)nanosecond time scale such that NMR signals of the two sub-states coalesce, although the separate RR bands remain unchanged. Following these arguments, it appears to be rather unlikely that the two sub-states of the Pfr state of *Agp1* refer to chromophores with α - and β -facial disposition of ring D (70, 71). The interconversion between these

orientations would require a rotation around the C-D methine bridge, associated with a significant activation energy and thus not compatible with transition rates on the (sub-)nanosecond time scale.

The most striking difference in the protein-cofactor interactions may be associated with the highly conserved Asp-194 (*PaBphP*), which in bathy phytochromes forms a strong hydrogen bond between the carboxylate side chain and the N-H group of ring D (14). The crystal structures of prototypical phytochromes show that this side chain does not directly interact with the pyrrole N-H groups but points away from the cofactor (13). Given that this residue does not rotate upon formation of the respective Pfr state, an important factor fixing the ring D position and thus stabilizing a specific C-D methine bridge conformation is missing in prototypical phytochromes. We therefore suggest that the lack of this structural motif in prototypical phytochromes allows the tetrapyrrole to switch between two Pfr sub-states, including one sub-state that is associated with a lower activation barrier for the thermal $ZZE \rightarrow ZZZ$ isomerization for back-reaction to the Pr state.

Acknowledgment—We thank the “Norddeutscher Verbund für Hoch- und Höchstleistungsrechnen” (HLRN) for providing computer resources.

REFERENCES

1. Briggs, W. R., and Spudis, J. L. (2005) *Handbook of Photosensory Receptors*, Wiley Verlag, Weinheim, Germany
2. Rockwell, N. C., and Lagarias, J. C. (2010) A brief history of phytochromes. *Chemphyschem* **11**, 1172–1180
3. Kehoe, D. M., and Grossman, A. R. (1996) Similarity of a chromatic adaptation sensor to phytochrome and ethylene receptors. *Science* **273**, 1409–1412
4. Hughes, J., Lamparter, T., Mittmann, F., Hartmann, E., Gärtner, W., Wilde, A., and Börner, T. (1997) A prokaryotic phytochrome. *Nature* **386**, 663
5. Wilde, A., Churin, Y., Schubert, H., and Börner, T. (1997) Disruption of a *Synechocystis* sp. PCC 6803 gene with partial similarity to phytochrome genes alters growth under changing light qualities. *FEBS Lett.* **406**, 89–92
6. Montgomery, B. L., and Lagarias, J. C. (2002) Phytochrome ancestry: sensors of bilins and light. *Trends Plant Sci.* **7**, 357–366
7. Blumenstein, A., Vienken, K., Tasler, R., Purschwitz, J., Veith, D., Frankenberg-Dinkel, N., and Fischer, R. (2005) The *Aspergillus nidulans* phytochrome PphA represses sexual development in red light. *Curr. Biol.* **15**, 1833–1838
8. Thümmler, F., Dufner, M., Kreisli, P., and Dittrich, P. (1992) Molecular cloning of a novel phytochrome gene of the moss *Ceratodon purpureus* which encodes a putative light-regulated protein kinase. *Plant Mol. Biol.* **20**, 1003–1017
9. Yeh, K. C., Wu, S. H., Murphy, J. T., and Lagarias, J. C. (1997) A cyanobacterial phytochrome two-component light sensory system. *Science* **277**, 1505–1508
10. Yeh, K. C., and Lagarias, J. C. (1998) Eukaryotic phytochromes: Light-regulated serine/threonine protein kinases with histidine kinase ancestry. *Proc. Natl. Acad. Sci. U.S.A.* **95**, 13976–13981
11. Lamparter, T., Esteban, B., and Hughes, J. (2001) Phytochrome Cph1 from the cyanobacterium *Synechocystis* PCC6803—Purification, assembly, and quaternary structure. *Eur. J. Biochem.* **268**, 4720–4730
12. Hughes, J. (2010) Phytochrome three-dimensional structures and functions. *Biochem. Soc. Trans.* **38**, 710–716
13. Essen, L. O., Mailliet, J., and Hughes, J. (2008) The structure of a complete phytochrome sensory module in the Pr ground state. *Proc. Natl. Acad. Sci. U.S.A.* **105**, 14709–14714

14. Yang, X., Kuk, J., and Moffat, K. (2008) Crystal structure of *Pseudomonas aeruginosa* bacteriophytochrome: Photoconversion and signal transduction. *Proc. Natl. Acad. Sci. U.S.A.* **105**, 14715–14720
15. Yang, X., Kuk, J., and Moffat, K. (2009) Conformational differences between the Pfr and Pr states in *Pseudomonas aeruginosa* bacteriophytochrome. *Proc. Natl. Acad. Sci. U.S.A.* **106**, 15639–15644
16. Karniol, B., and Vierstra, R. D. (2003) The pair of bacteriophytochromes from *Agrobacterium tumefaciens* are histidine kinases with opposing photobiological properties. *Proc. Natl. Acad. Sci. U.S.A.* **100**, 2807–2812
17. Scheerer, P., Michael, N., Park, J. H., Nagano, S., Choe, H. W., Inomata, K., Borucki, B., Krauss, N., and Lamparter, T. (2010) Light-induced conformational changes of the chromophore and the protein in phytochromes: bacterial phytochromes as model systems. *Chemphyschem* **11**, 1090–1105
18. Wagner, J. R., Zhang, J., Brunzelle, J. S., Vierstra, R. D., and Forest, K. T. (2007) High resolution structure of *Deinococcus* bacteriophytochrome yields new insights into phytochrome architecture and evolution. *J. Biol. Chem.* **282**, 12298–12309
19. Rottwinkel, G., Oberpichler, I., and Lamparter, T. (2010) Bathy phytochromes in *Rhizobial* soil bacteria. *J. Bacteriol.* **192**, 5124–5133
20. Yang, X., Ren, Z., Kuk, J., and Moffat, K. (2011) Temperature-scan crystallography reveals reaction intermediates in bacteriophytochrome. *Nature* **479**, 428–432
21. Lamparter, T., Michael, N., Mittmann, F., and Esteban, B. (2002) Phytochrome from *Agrobacterium tumefaciens* has unusual spectral properties and reveals an N-terminal chromophore attachment site. *Proc. Natl. Acad. Sci. U.S.A.* **99**, 11628–11633
22. Altschul, S. F., Gish, W., Miller, W., Myers, E. W., and Lipman, D. J. (1990) Basic local alignment search tool. *J. Mol. Biol.* **215**, 403–410
23. Mroginski, M. A., von Stetten, D., Escobar, F. V., Strauss, H. M., Kaminski, S., Scheerer, P., Günther, M., Murgida, D. H., Schmieder, P., Bongards, C., Gärtner, W., Mailliet, J., Hughes, J., Essen, L. O., and Hildebrandt, P. (2009) Chromophore structure of cyanobacterial phytochrome *Cph1* in the Pr state: reconciling structural and spectroscopic data by QM/MM calculations. *Biophys. J.* **96**, 4153–4163
24. Yang, X., Stojkovic, E. A., Kuk, J., and Moffat, K. (2007) Crystal structure of the chromophore binding domain of an unusual bacteriophytochrome, RpBhp3, reveals residues that modulate photoconversion. *Proc. Natl. Acad. Sci. U.S.A.* **104**, 12571–12576
25. von Stetten, D., Günther, M., Scheerer, P., Murgida, D. H., Mroginski, M. A., Krauss, N., Lamparter, T., Zhang, J., Anstrom, D. M., Vierstra, R. D., Forest, K. T., and Hildebrandt, P. (2008) Chromophore heterogeneity and photoconversion in phytochrome crystals and solution studied by resonance Raman spectroscopy. *Angew. Chem. Int. Ed.* **47**, 4753–4755
26. Tasler, R., Moises, T., and Frankenberg-Dinkel, N. (2005) Biochemical and spectroscopic characterization of the bacterial phytochrome of *Pseudomonas aeruginosa*. *FEBS J.* **272**, 1927–1936
27. Inomata, K., Noack, S., Hammam, M. A., Khawn, H., Kinoshita, H., Murata, Y., Michael, N., Scheerer, P., Krauss, N., and Lamparter, T. (2006) Assembly of synthetic locked chromophores with *Agrobacterium* phytochromes Agp1 and Agp2. *J. Biol. Chem.* **281**, 28162–28173
28. Quest, B., Hübschmann, T., Sharda, S., Tandeau de Marsac, N., and Gärtner, W. (2007) Homologous expression of a bacterial phytochrome—The cyanobacterium *Fremyella diplosiphon* incorporates biliverdin as a genuine, functional chromophore. *FEBS J.* **274**, 2088–2098
29. Borucki, B., Seibeck, S., Heyn, M. P., and Lamparter, T. (2009) Characterization of the covalent and noncovalent adducts of Agp1 phytochrome assembled with biliverdin and phycocyanobilin by circular dichroism and flash photolysis. *Biochemistry* **48**, 6305–6317
30. Sharda, S., Shah, R., and Gärtner, W. (2007) Domain interaction in cyanobacterial phytochromes as a prerequisite for spectral integrity. *Eur. Biophys. J.* **36**, 815–821
31. Borucki, B., von Stetten, D., Seibeck, S., Lamparter, T., Michael, N., Mroginski, M. A., Otto, H., Murgida, D. H., Heyn, M. P., and Hildebrandt, P. (2005) Light-induced proton release of phytochrome is coupled to the transient deprotonation of the tetrapyrrole chromophore. *J. Biol. Chem.* **280**, 34358–34364
32. von Stetten, D., Seibeck, S., Michael, N., Scheerer, P., Mroginski, M. A., Murgida, D. H., Krauss, N., Heyn, M. P., Hildebrandt, P., Borucki, B., and Lamparter, T. (2007) Highly conserved residues Asp-197 and His-250 in Agp1 phytochrome control the proton affinity of the chromophore and Pfr formation. *J. Biol. Chem.* **282**, 2116–2123
33. Manitto, P., and Monti, D. (1980) Reaction of biliverdins with thiobarbituric acid—novel fragmentation reaction of bilin-1,19(21*H*,24*H*)-diones. *J. Chem. Soc. Chem. Comm.* 178–180
34. Lindner, I., Knipp, B., Braslavsky, S. E., Gärtner, W., and Schaffner, K. (1998) A novel chromophore selectively modifies the spectral properties of one of the two stable states of the plant photoreceptor phytochrome. *Angew. Chem. Int. Ed.* **37**, 1843–1846
35. Murgida, D. H., von Stetten, D., Hildebrandt, P., Schwinté, P., Siebert, F., Sharda, S., Gärtner, W., and Mroginski, M. A. (2007) The chromophore structures of the Pr states in plant and bacterial phytochromes. *Biophys. J.* **93**, 2410–2417
36. Buchan, D. W., Ward, S. M., Loble, A. E., Nugent, T. C., Bryson, K., and Jones, D. T. (2010) Protein annotation and modelling servers at University College London. *Nucleic Acids Res.* **38**, W563–W568
37. Jones, D. T. (1999) Protein secondary structure prediction based on position-specific scoring matrices. *J. Mol. Biol.* **292**, 195–202
38. Brooks, B. R., Brooks, C. L., MacKerell, A. D., Nilsson, L., Petrella, R. J., Roux, B., Won, Y., Archontis, G., Bartels, C., Boresch, S., Cafisch, A., Caves, L., Cui, Q., Dinner, A. R., Feig, M., Fischer, S., Gao, J., Hodoseck, M., Im, W., Kuczera, K., Lazaridis, T., Ma, J., Ovchinnikov, V., Paci, E., Pastor, R. W., Post, C. B., Pu, J. Z., Schaefer, M., Tidor, B., Venable, R. M., Woodcock, H. L., Wu, X., Yang, W., York, D. M., and Karplus, M. (2009) CHARMM: the biomolecular simulation program. *J. Comp. Chem.* **30**, 1545–1614
39. Feller, S. E., Zhang, Y. H., Pastor, R. W., and Brooks, B. R. (1995) Constant-pressure molecular-dynamics simulation—the Langevin piston method. *J. Chem. Phys.* **103**, 4613–4621
40. Martyna, G. J., Tobias, D. J., and Klein, M. L. (1994) Constant-pressure molecular dynamics algorithms. *J. Chem. Phys.* **101**, 4177–4189
41. Phillips, J. C., Braun, R., Wang, W., Gumbart, J., Tajkhorshid, E., Villa, E., Chipot, C., Skeel, R. D., Kale, L., and Schulten, K. (2005) Scalable molecular dynamics with NAMD. *J. Comp. Chem.* **26**, 1781–1802
42. MacKerell, A. D., Jr., Bashford, D., Bellott, M., Dunbrack, R. L., Jr., Evanseck, J. D., Field, M. J., Fischer, S., Gao, J., Guo, H., Ha, S., Joseph-McCarthy, D., Kuchnir, L., Kuczera, K., Lau, F., T. K., Mattos, C., Michnick, S., Ngo, T., Nguyen, D. T., Prodhom, B., Reiher, W. E. I., Roux, B., Schlenkerich, M., Smith, J. C., Stote, R., Straub, J., Watanabe, M., Wiorcikiewicz-Kuczera, J., Yin, D., and Karplus, M. (1998) All-atom empirical potential for molecular modeling and dynamics studies of proteins. *J. Phys. Chem. B* **102**, 3586–3616
43. Darden, T., York, D., and Pedersen, L. (1993) Particle Mesh Ewald—an N. log(N) method for Ewald sums in large systems. *J. Chem. Phys.* **98**, 10089–10092
44. Senn, H. M., and Thiel, W. (2007) QM/MM studies of enzymes. *Curr. Op. Chem. Biol.* **11**, 182–187
45. Becke, A. D. (1993) Density-functional thermochemistry. 3. The role of exact exchange. *J. Chem. Phys.* **98**, 5648–5652
46. Sherwood, P., de Vries, A. H., Guest, M. F., Schreckenbach, G., Catlow, C. R. A., French, S. A., Sokol, A. A., Bromley, S. T., Thiel, W., Turner, A. J., Billetter, S., Terstegen, F., Thiel, S., Kendrick, J., Rogers, S. C., Casci, J., Watson, M., King, F., Karlsen, E., Sjøvoll, M., Fahmi, A., Schäfer, A., and Lennartz, Ch. (2003) QUASI: A general purpose implementation of the QM/MM approach and its application to problems in catalysis. *J. Mol. Struct. (Theochem)* **632**, 1–28
47. Mroginski, M. A., Mark, F., Thiel, W., and Hildebrandt, P. (2007) Quantum mechanics/molecular mechanics calculation of the Raman spectra of the phycocyanobilin chromophore in α -c-phycoerythrin. *Biophys. J.* **93**, 1885–1894
48. Mroginski, M. A., Kaminski, S., von Stetten, D., Ringsdorf, S., Gärtner, W., Essen, L. O., and Hildebrandt, P. (2011) Structure of the chromophore binding pocket in the Pr state of plant phytochrome phyA. *J. Phys. Chem. B* **115**, 1220–1231
49. Mroginski, M. A., Kaminski, S., and Hildebrandt, P. (2010) Raman spectra of the phycocyanobilin cofactor in phycoerythrin calculated by QM/

Chromophore Structure in Pfr State of Phytochromes

- MM. *Chemphyschem* **11**, 1265–1274
50. Hildebrandt, P., Hoffmann, A., Lindemann, P., Heibel, G., Braslavsky, S. E., Schaffner, K., and Schrader, B. (1992) Fourier-transform resonance Raman-spectroscopy of phytochrome. *Biochem.* **31**, 7957–7962
 51. Fodor, S. P. A., Lagarias, J. C., and Mathies, R. A. (1990) Resonance Raman analysis of the Pr and Pfr forms of phytochrome. *Biochem.* **29**, 11141–11146
 52. Schwede, T., Kopp, J., Guex, N., and Peitsch, M. C. (2003) SWISS-MODEL: an automated protein homology-modeling server. *Nucleic Acids Res.* **31**, 3381–3385
 53. Buckler, D. R., Zhou, Y., and Stock, A. M. (2002) Evidence of intradomain and interdomain flexibility in an OmpR/PhoB homolog from *Thermotoga maritima*. *Structure* **10**, 153–164
 54. Brunger, A. T., Adams, P. D., Clore, G. M., Delano, W. L., Gros, P., Grosse-Kunstleve, R. W., Jiang, J. S., Kuszewski, J., Nilges, M., Pannu, N. S., Read, R. J., Rice, L. M., Simonson, T., and Warren, G. L. (1998) Crystallography and NMR system: A new software suite for macromolecular structure determination. *Acta Cryst. D* **54**, 905–921
 55. Laskowski, R. A., MacArthur, M. W., Moss, D. S., and Thornton, J. M. (1993) Procheck—a program to check the stereochemical quality of protein structures. *J. Appl. Crystallogr.* **26**, 283–291
 56. Hoof, R. W., Vriend, G., Sander, C., and Abola, E. E. (1996) Errors in protein structures. *Nature* **381**, 272
 57. Emsley, P., Lohkamp, B., Scott, W. G., and Cowtan, K. (2010) Features and development of Coot. *Acta Crystallogr. Sect. D Biol. Crystallogr.* **66**, 486–501
 58. Kneip, C., Hildebrandt, P., Schlamann, W., Braslavsky, S. E., Mark, F., and Schaffner, K. (1999) Protonation state and structural changes of the tetrapyrrole chromophore during the Pr → Pfr phototransformation of phytochrome. A resonance Raman spectroscopic study. *Biochemistry* **38**, 15185–15192
 59. Mroginski, M. A., von Stetten, D., Kaminski, S., Velazquez Escobar, F., Michael, N., Daminelli-Widany, G., Hildebrandt, P. (2011) Elucidating photoinduced structural changes in phytochromes by the combined application of resonance Raman spectroscopy and theoretical methods. *J. Mol. Struct.* **993**, 15–25
 60. Rice, J. A. (2007) *Mathematical Statistics and Data Analysis*, 3 Ed., Thomson Books/Cole, Duxbury Press, Pacific Grove, CA
 61. Schwinté, P., Foerstendorf, H., Hussain, Z., Gärtner, W., Mroginski, M. A., Hildebrandt, P., and Siebert, F. (2008) FTIR study of the photoinduced processes of plant phytochrome phyA using isotope-labeled bilins and density functional theory calculations. *Biophys. J.* **95**, 1256–1267
 62. Wagner, J. R., Zhang, J., von Stetten, D., Günther, M., Murgida, D. H., Mroginski, M. A., Walker, J. M., Forest, K. T., Hildebrandt, P., and Vierstra, R. D. (2008) Mutational analysis of *Deinococcus radiodurans* bacteriophytochrome reveals key amino acids necessary for the photochromicity and proton exchange cycle of phytochromes. *J. Biol. Chem.* **283**, 12212–12226
 63. Brandt, S., von Stetten, D., Günther, M., Hildebrandt, P., and Frankenberg-Dinkel, N. (2008) The fungal phytochrome FphA from *Aspergillus nidulans*. *J. Biol. Chem.* **283**, 34605–34614
 64. Song, C., Essen, L. O., Gärtner, W., Hughes, J., and Matysik, J. (2012) Solid-state NMR spectroscopic study of chromophore-protein interactions in the Pr ground state of plant phytochrome A. *Mol. Plant* **5**, 698–715
 65. Song, C., Rohmer, T., Tiersch, M., Zaanen, J., Hughes, J., Matysik, J. (2013) Solid state NMR spectroscopy to probe photoactivation in canonical phytochromes. *Photochem. Photobiol.* **89**, 259–273
 66. Freer, L., Kim, P. W., Corley, S. C., Rockwell, N. C., Zhao, L., Thibert, A. J., Lagarias, J. C., Larsen, D. S. (2012) Chemical inhomogeneity in the ultrafast dynamics of the DXCF cyanobacteriochrome Thr0924. *J. Phys. B*, **116**, 10571–10581
 67. Chen, Y., Zhang, J., Luo, J., Tu, J. M., Zeng, X. L., Xie, J., Zhou, M., Zhao, J. Q., Scheer, H., Zhao, K. H. (2012) Photophysical diversity of two novel cyanobacteriochromes with phycocyanobilin chromophores: photochemistry and dark reversion kinetics. *FEBS J.* **279**, 40–54
 68. Schmidt, P., Gensch, T., Remberg, A., Gärtner, W., Braslavsky, S. E., Schaffner, K. (1998) The complexity of the Pr to Pfr phototransformation kinetics is an intrinsic property of native phytochrome. *Photochem. Photobiol.* **68**, 754–761
 69. Kim, P. W., Freer, L. H., Rockwell, N. C., Martin, S. S., Lagarias, J. C., Larsen, D. S. (2012) Femtosecond photodynamics of the red/green cyanobacteriochrome NpR6012g4 from *Nostoc punctiforme*. 2. reverse dynamics. *Biochemistry* **51**, 619–630
 70. Rockwell, N. C., Shang, L., Martin, S. S., Lagarias, J. C. (2009) Distinct classes of red/far-red photochemistry within the phytochrome superfamily. *Proc. Natl. Acad. Sci. U.S.A.* **106**, 6123–6127
 71. Song, C., Psakis, G., Lang, C., Mailliet, J., Gärtner, W., Hughes, J., Matysik, J. (2011) Two ground state isoforms and a chromophore D-ring photoflip triggering extensive intramolecular changes in a canonical phytochrome. *Proc. Natl. Acad. Sci. U.S.A.* **108**, 3842–3847

6.2. A protonation-coupled feedback mechanism controls the signaling process in bathy phytochromes

“This research was originally published in Nature Chemistry. Reprinted (adapted) with permission from: F. Velazquez Escobar, P. Piwowski, J. Salewski, N. Michael, M. Fernandez Lopez, A. Rupp, B. Qureshi, P. Scheerer, F. Bartl, N. Frankenberg-Dinkel, F. Siebert, M. A. Mroginski and P. Hildebrandt. A protonation-coupled feedback mechanism controls the signaling process in bathy phytochromes. *Nature Chemistry* **2015**, online-published. [doi:10.1038/nchem.2225]. ©2015 Macmillan Publishers Limited.”

- Experiments were carried out by F. Velazquez Escobar and P. Piwowski
- Band analysis was performed by F. Velazquez Escobar and F. Siebert
- Further minor contributions by M. Fernandez Lopez, A. Rupp and B. Qureshi
- Calculations were performed by J. Salewski and M. A. Mroginski
- N. Michael and N. Frankenberg-Dinkel expressed and purified the investigated proteins
- Homology models and crystal structure analysis were performed by P. Scheerer
- Research design and development by P. Hildebrandt

A protonation-coupled feedback mechanism controls the signaling process in bathy phytochromes

Francisco Velazquez Escobar¹, Patrick Piwowarski^{2#}, Johannes Salewski¹, Norbert Michael¹, Maria Fernandez Lopez¹, Anna Rupp^{2#}, Bilal Muhammad Qureshi^{2§}, Patrick Scheerer^{2§}, Franz Bartl^{2#}, Nicole Frankenberg-Dinkel³, Friedrich Siebert^{1,4}, Maria Andrea Mroginski¹, and Peter Hildebrandt^{1*}

¹ Technische Universität Berlin, Institut f. Chemie, Sekr. PC 14, Straße des 17. Juni 135, D-10623 Berlin, Germany

² Charité - Universitätsmedizin Berlin, Institut für Medizinische Physik und Biophysik, [§]AG Protein X-ray Crystallography and Signal Transduction, [#]AG Spektroskopie, Charitéplatz 1, D-10117 Berlin, Germany.

³ Technische Universität Kaiserslautern, Fachbereich Biologie, Abt. Mikrobiologie, Paul-Ehrlich-Str. 23, D-67663 Kaiserslautern, Germany.

⁴ Albert-Ludwigs-Universität Freiburg, Institut für Molekulare Medizin und Zellforschung, Sektion Biophysik, Hermann-Herderstr. 9, D-79104 Freiburg, Germany.

* To whom correspondence should be addressed: Peter Hildebrandt, Technische Universität Berlin, Institut f. Chemie, Sekr. PC 14, Straße des 17. Juni 135, D-10623 Berlin, Germany, Tel: +49-(30)-31421433, Fax: +49-(30)-31421122, Email: Hildebrandt@chem.tu-berlin.de

Abstract

Phytochromes are bimodal photoswitches composed of a photosensor and an output module. Photoactivation of the sensor is initiated by a double bond isomerization of the tetrapyrrole chromophore and eventually leads to protein conformational changes. Recently determined structural models of phytochromes identify differences between the inactive and the signaling state but do not reveal the mechanism of photosensor activation or deactivation. Here we report a vibrational spectroscopic study on bathy phytochromes that demonstrates that the formation of the photoactivated state and thus (de)activation of the output module is based on proton translocations in the chromophore pocket coupling chromophore and protein structural changes. These proton transfer steps, involving the tetrapyrrole and a nearby histidine, also enable thermal back-isomerization of the chromophore via keto-enol tautomerization to afford the initial dark state. Thus, the same proton re-arrangements inducing the (de)activation of the output module simultaneously initiate the reversal of this process, corresponding to a negative feedback mechanism.

Phytochromes are photoreceptors in plants and microorganisms¹⁻³. They are composed of a photosensory input and a regulatory output module and function as bimodal photoswitches, in which the photosensor is interconverted between two states to activate or deactivate the attached output module. The photosensor includes an open-chain tetrapyrrole chromophore which is phytochromobilin or biliverdin (BV) in plant and bacterial phytochromes, respectively. Upon light absorption, the covalently bound cofactor undergoes a double bond isomerization at the methine bridge between the pyrrole rings *C* and *D* (**Fig. 1a,b**). This photochemical reaction is followed by thermal relaxation steps that complete the transformation between the two parent states Pr and Pfr. Concomitant to the photochemical transformations of Pr and Pfr a thermal pathway parallels the photo-induced reversion of the photo-activated state. This photo-activated state is commonly referred to as the signaling state although it is not clear in each case whether this implies activation or deactivation of the output module. The thermal route ensures that the photoreceptor and thus the output module, typically a histidine kinase, do not remain in the (in)active state in the absence of light of appropriate wavelengths. Whereas in plant phytochromes Pfr constitutes the photo-activated state, in the bacterial representatives it may either be Pfr or Pr, defining the classes of prototypical and bathy phytochromes, respectively⁴.

The different thermal stability of the parent states in these two classes of bacteriophytochromes directed crystallization such that until recently well-resolved structural models were only available for Pr of prototypical⁵⁻⁹ and for Pfr of bathy bacteriophytochromes¹⁰⁻¹². Lately, however, Takala et al. succeeded to determine the crystal structure for both the Pr and the Pfr state of a prototypical phytochrome albeit at lower resolution¹³. The study revealed a β -sheet-to- α -helix transition of the “tongue”, a unique and conserved structural element in phytochromes. This structural refolding was interpreted as a mechanical switch for activating the output module, confirming previous suggestions¹⁴. However, these structural models do not reveal the mechanism how the mechanical switch is

triggered by chromophore structural changes of the photosensor that occur upon the transformations between the inactive and the active states.

Here we show that the secondary structural change of the tongue is directly coupled with proton translocations in the chromophore pocket of the photo-activated state, which concomitantly open the pathway for the thermal back reaction to the dark state. Our study is based on the bathy phytochromes Agp2 (*Agrobacterium tumefaciens*)¹⁵⁻²⁰ and PaBphP (*Pseudomonas aeruginosa*)^{10-12,19,21} which undergo a sequential proton/deuteron (H/D) exchange at the pyrrole nitrogens of the BV cofactor. It is thus possible to monitor the functional groups that take part in the proton-coupled structural changes using resonance Raman (RR)^{19,22-27} and infrared (IR) difference spectroscopy²⁸⁻³¹. The present results reveal a mechanistic pattern that provides novel insight into the molecular functioning of the first step of the signal transduction cascade and the thermal deactivation of the photoswitch.

RESULTS

The Pfr states of Agp2 and PaBphP display far-reaching structural similarities in the chromophore binding pocket (**Fig. 1a**), as reflected by nearly identical RR spectra (**Supplementary Fig. S1**)¹⁹. The BV chromophore adopts a ZZEssa geometry and all four pyrrole rings are protonated (**Fig. 1a**). In H₂O, this protonation pattern gives rise to a characteristic RR band at 1549 cm⁻¹ that originates from the N-H in-plane bending (N-H ip) mode of the rings *B* and *C* (**Fig. 2**)^{18,22-24}.

Sequential H → D exchange at the biliverdin cofactor

Upon H₂O → D₂O buffer exchange in Pfr of Agp2 or PaBphP, while keeping the sample in the dark, the N-H ip of rings *B* and *C* at 1549 cm⁻¹ disappears (**Fig. 2**), indicating the immediate H/D exchange at the ring *B* and *C* nitrogens. However, the exchange of the pyrrole

N-H groups is not complete since additional changes are noted in the RR spectrum of Pfr after a full photocycle from Pfr *via* Pr and back to Pfr (**Fig. 2**) as shown by the step-wise downshift of the 1599 cm^{-1} band (H_2O) via 1596 cm^{-1} (H/D exchange in the dark) to 1589 cm^{-1} (H/D exchange after a photocycle). We therefore conclude that the H/D exchange of the N-H group of either ring *A* or ring *D* is impaired in the dark.

To determine which of these two N-H groups is resistant towards H/D exchange, we compared the experimental spectra with calculated spectra obtained for different deuteration patterns at the pyrrole rings (**Fig. 2**). The spectra were calculated for Pfr of *PaBphP* using the QM/MM hybrid method¹⁹. In the fully protonated and fully deuterated states, the calculated spectra provide an excellent description of the experimental spectra, also in the spectral range below 1500 cm^{-1} ¹⁹. The spectral changes observed upon H/D exchange in the dark are only well reproduced by the calculated spectrum for rings *A*, *B*, *C* being deuterated but ring *D* protonated, indicating a hindered H/D exchange at ring *D* in Pfr.

This effect, observed for both Agp2 and *PaBphP*, is attributed to the strong hydrogen bond of the ring *D* N-H group with the carboxylate side chain of Asp194(196) (amino acid numbers in parenthesis refer to Agp2 in the following) whereas the N-H groups of the other rings are involved in weaker, water-mediated hydrogen bonds with the backbone carbonyl of this residue and thus undergo an H/D exchange in Pfr (**Fig. 1a**)¹⁰. Upon photoisomerization of the *C-D* methine bridge from the *E* to the *Z* configuration, the strong hydrogen bond of the ring *D* N-H group is broken but it takes until the formation of Pr for the H/D exchange to occur (**Supplementary Fig. S5**).

The sequential H/D exchange of the pyrrole N-H groups allows for an unambiguous assignment of the ring *A* and *D* C=O stretching modes, since each of them displays an isotopic frequency shift only upon H/D exchange at the respective ring. These modes can be detected in the IR difference spectra of Agp2 (**Fig. 3**), revealing the spectral changes induced by the transition from Pfr to Pr and from Pfr to Meta-F, i.e. the precursor of Pr (**Fig. 1b**).

To sort out signals due to protein and chromophore structural changes, we first compare the “Pr-minus-Pfr” difference spectra in H₂O of a fully ¹³C-labeled and a non-labeled protein, both reconstituted with a non-labeled BV (**Fig. 3, left**). Except for the weak positive band at 1734 cm⁻¹ (**Fig. 3**), all signals above 1680 cm⁻¹ are insensitive to ¹³C-labelling and thus originate from the chromophore.

For Pfr in H₂O and after a complete H/D exchange (after a photocycle), the two C=O(*A*) and C=O(*D*) modes coincide in each case and afford one negative signal at 1697 and 1685 cm⁻¹, respectively. Accordingly, bands at both positions are observed for H/D exchange in the dark. In the “Pr-minus-Pfr” and “Meta-F-minus-Pfr” difference spectra in H₂O, the positive signal at 1709 cm⁻¹ is assigned to the C=O stretching of ring *D* since, upon H/D exchange in the dark, its intensity is drastically reduced only in Pr (downshift below 1700 cm⁻¹) but not in Meta-F (no H/D exchange at ring *D*; **Supplementary Fig. S5**). The corresponding ring *A* mode is attributed to the weak shoulder at 1718 cm⁻¹ in H₂O, more clearly visible for Meta-F. After complete H/D exchange, the C=O stretchings of ring *A* and *D* are detected at 1707 and 1698 cm⁻¹, respectively.

The negative (¹³C-insensitive) band at 1750 cm⁻¹ (Pfr) is ascribed to the C=O function of a protonated propionic side chain of the cofactor, consistent with a 7-cm⁻¹ downshift upon H/D exchange in the dark (**Fig. 3**). It has no positive counterpart in the “Pr-minus-Pfr” difference spectrum. Since the crystal structure of the Pfr state of *PaBphP*¹⁰ indicates a salt bridge between the propionate side chain of ring *B* with Arg209(211), this band is assigned to the C=O stretching of the ring *C* propionic side chain, which is in hydrogen bond distance to Ser275(Ala 276), Tyr163(165), and His277(278) in *PaBphP*(Agp2) (**Fig. 1a**). These three amino acids undergo rearrangements in early intermediate states of the Pfr-to-Pr photoconversion as shown for *PaBphP* crystals¹².

The last step of the Pfr → Pr photoconversion

Based on the vibrational assignments discussed above we analyzed the last step of the Pfr-to-Pr phototransformation, i.e. the Meta-F-to-Pr transition. The RR spectrum of Meta-F is characteristic of a chromophore with all four pyrrole nitrogens carrying a proton (**Fig. 4a**) as indicated by the N-H ip mode of the rings *B* and *C* at 1553 cm^{-1} (1075 cm^{-1} in D_2O ; **Supplementary Fig. S5**). The C=O stretching of the ring *C* propionic side chain is upshifted from 1750 cm^{-1} in Pfr to 1756 cm^{-1} in Meta-F (**Fig. 4d**), possibly due to a reorientation of the propionic side chain after photoisomerization of the *C-D* methine bridge.

Compared to Meta-F, significant changes are observed for Pr in the “Pr-minus-Pfr” difference spectra (**Fig. 4e**). First, the lack of a positive band attributable to the C=O stretching of the propionic side chain indicates its deprotonation during the transition from Meta-F to Pr. Second, there are strong difference signals of the protein backbone as confirmed by comparison with the corresponding spectrum of the ^{13}C -labeled Agp2. These are the band pairs $1641(\text{Pr})/1657(\text{Pfr})\text{ cm}^{-1}$ and $1561(\text{Pr})/1536(\text{Pfr})\text{ cm}^{-1}$ that originate from the amide I and amide II modes, respectively. Third, the ring *D* C=O stretching of Pr at 1709 cm^{-1} disappears at high pH (**Fig. 5c**). A fit of the Henderson-Hasselbalch equation to the signal intensities of the 1709 cm^{-1} band of Pr allows the determination of an apparent $\text{p}K_A$ of 7.6 (**Fig. 5b, top**). The corresponding ring *A* C=O stretching remains as a broad signal at 1718 cm^{-1} .

The most pronounced pH effects on the RR spectra are associated with a change in the protonation pattern of the chromophore as reflected, *inter alia*, by the disappearance of the N-H ip mode of rings *B* and *C* (1571 cm^{-1}) at high pH (**Fig. 5a**). Previously, these spectral changes were quantitatively analyzed in terms of a pH-dependent equilibrium between a protonated (“acid” Pr) and a deprotonated (“alkaline” Pr) chromophore with a $\text{p}K_a$ of 7.6¹⁸. The same value was obtained from the IR spectroscopic analysis of the ring *D* C=O stretching

in the present work (*vide supra*). However, a careful inspection of the pH-dependent equilibrium (**Fig. 5b, top**) reveals that the relative concentration of the “acid” Pr does not approach 1.0 at low pH but levels off at a constant value of ca. 0.89.

pH dependence of the Pr → Pfr dark reversion

The pH-dependent structural changes in the Pr state are paralleled by changes of the rate of the Pr-to-Pfr dark reversion. Kinetic data derived from multi-exponential fits to the UV-vis absorption changes were already reported previously¹⁸. Here we extended these experiments to a wider pH range (**Supplementary Notes**). The rate constant of the main exponential component strongly increases from pH = 9 to pH = 7 but seems to be pH-independent above pH = 9 and below pH = 7 (**Fig. 5b, bottom**). The Agp2 variant lacking the output module displays a similar behavior, albeit with distinctly faster kinetics.

DISCUSSION

Based on the analysis of the IR difference and RR spectra, we identified four events that occur upon transition from Meta-F to Pr, namely (1) the removal of one proton from the ring *C* propionic side chain and (2) one proton from the ring *B/C* N-H groups, (3) the disappearance of the ring *D* carbonyl function, and (4) a secondary structural change of the protein.

Proton transfer from the ring *C* propionic side chain

In Pfr and Meta-F, the ring *C* propionic side chain is protonated even up to a pH of 11. To our knowledge, such a high pK_a was not reported before^{32,33}. The group remains protonated after photoisomerization and subsequent relaxation to Meta-F. Dissociation of the proton takes place in the final transition from Meta-F to Pr already at pH values below 6, corresponding to a drop of the pK_a by more than 5 units from Pfr to Pr. The IR spectra do not identify the

proton acceptor but due to the lack of a positive (Pr) band in the region between 1750 and 1710 cm^{-1} , a carboxyl function of a Glu or Asp can be ruled out.

Tautomerism of the Pr chromophore

In a previous work, the pH-dependent changes of the Pr chromophore of Agp2 were explained as proton transfer from the inner pyrrole rings to the protein¹⁸. In view of the present results, this interpretation must be revised. First, the disappearance of the N-H ip mode is not accompanied by the appearance of an IR band attributable to the protonation of a carboxyl side chain of an amino acid, among which Asp194(196) would be the most likely candidate. Second, the transfer of this proton to the protein, concomitant to the deprotonation of the ring C propionic side chain, would imply that the overall charge of the chromophore varied by two units during the Meta-F-to-Pr transition which appears to be highly unlikely. Furthermore, such a proton transfer cannot account for the disappearance of the ring D carbonyl function which occurs with the same $\text{p}K_a$ as the ring B/C deprotonation. Instead, these findings can be readily understood in terms of an *intra*-chromophore proton migration from the ring C nitrogen to the ring D oxygen, corresponding to a keto-enol tautomerization (**Fig. 6**). Accordingly, the pH-dependent equilibrium of the Pr chromophore of Agp2 is mirrored by an enol-keto equilibrium with the enol form prevailing at high pH.

As a consequence, the titratable group that affects the enol-keto equilibrium is not part of the chromophore but is ascribed to a near-by amino acid residue which upon deprotonation stabilizes the enol tautomer of the chromophore. Thus, the spectroscopic titration refers to a coupled equilibrium (**Fig. 6**). The fit of the correspondingly modified Henderson-Hasselbalch equation to the experimental data affords an apparent $\text{p}K_a$ of 7.6, which together with the limiting value for the enol/keto equilibrium at low pH yields $K_T = 0.12$ and $\text{p}K_B = 6.7$. In view of this $\text{p}K_B$ value, the only candidate for the titratable group is His277(278), which in the Pr

state may be positioned in direct or water-mediated hydrogen-bond distance to the ring *D* N-H group of the chromophore (**Supplementary Fig. S8**).

Proton dynamics controlling the intramolecular signaling process

Recently Takala et al.¹³ observed a partial refolding of the tongue intruding into the chromophore pocket for the conversion from Pr to Pfr, corresponding to a transition from a β -hairpin into one single α -helical segment. The resultant contraction of the tongue may then act as a mechanical switch to activate the attached histidine kinase module. Although this observation referred to a prototypical BV-binding phytochrome, it appears to hold true also for bathy phytochromes. The 1641 cm^{-1} band (Pr) and the 1657 cm^{-1} band (Pfr) in the IR difference spectra of Agp2 agree very well with the characteristic amide I positions of a β -hairpin and a α -helix motif, respectively^{35,36}. Correspondingly, the formation of the Pr state is associated with an elongation of the tongue. Whether this structural change in bathy phytochromes activates or deactivates the output module, remains to be clarified in view of conflicting literature data.^{4,12,21}

In addition to the protein structural changes, proton translocations occur during the Meta-F-to-Pr transition. Within the chromophore pocket, the most likely acceptor for the proton of the ring *C* propionic group is His277(278) (**Supplementary Fig. S8**), which is also proposed to play a crucial role for the tautomerism of the chromophore in Pr. The enol tautomer can be described by resonance structures with either a C(15)-C(16) double or single bond (**Fig. 6**). The latter case enables rotation around this bond and thus the thermal *Z/E* isomerization as the first and most likely rate-determining step of the Pr-to-Pfr dark reversion. Thermal chromophore isomerization via an enol form has already been suggested earlier by Lagarias et al.^{2,37} and it is now strongly supported by the present spectroscopic results. At high pH (> 8) the dark reversion rate is slow and pH-independent since His277(278) may stabilize the

positive charge density at the ring *D* nitrogen of the enol form and thus the double bond character of the C(15)-C(16) bond. With the protonation of the imidazole ring of His277(278) upon lowering the pH, this interaction is removed and the enol resonance structure with a positive charge on the inner rings *B* and *C* and thus the C(15)-C(16) single-bond character is expected to gain weight such that rotation around this bond is facilitated. In fact, the pH dependence of the relative concentration of this “reactive” enol form (enol+His₂₇₇H⁺, **Fig. 6**), calculated from the constants K_T and K_B , agrees with that of the dark reversion kinetics (**Fig. 5b, bottom**).

The temporal correlation of proton translocations and the β -hairpin/ α -helix transition during Pr formation already indicates the coupling of these processes. Most likely, the secondary structure change is induced by the substantial alteration of the electrostatics in the chromophore pocket, caused by the deprotonation of the ring *C* propionic group, the protonation of His277(278), and the charge redistribution in the chromophore associated with the keto-enol equilibrium. This conclusion is strongly supported by the fact that the histidine kinase itself has an impact on the keto-enol equilibrium of the Pr chromophore and its dark reversion rate. The pK_a controlling the keto-enol distribution is lower by 0.4 units and the dark reversion rate correspondingly slower for the full-length Agp2 as compared to the truncated variant lacking the histidine kinase domain (**Fig. 5b, bottom; Supplementary Notes**). Furthermore, the key role of His277(278) for the proton-coupled processes in the chromophore pocket is revealed by substituting this residue by an alanine in full-length Agp2. Preliminary studies on the His278Ala mutant indicate a perturbation of the secondary structure changes associated with the Pr/Pfr transition, a substantial distortion of the keto-enol equilibrium of the Pr chromophore, and a drastically reduced dark reversion rate by ca. three orders of magnitude compared to the wild-type full-length Agp2 (**Supplementary Figs. S9, S10**).

In summary, we conclude that protonation dynamics in the chromophore pocket are linked to two distinct processes: the (de)activation of the output module and the dark reversion to Pfr which represents the thermal decay pathway of the Pr state as an alternative to the light-induced Pr-to-Pfr transformation. Thus, the same proton re-arrangements that are coupled to the (de)activation of the output module, simultaneously initiate the reversal of this process, corresponding to a negative feedback mechanism.

Finally, we wish to discuss the relevance of the present findings for phytochromes in general. First, dark reversion via an enol-keto tautomerism is likely to be common to all representatives of the phytochrome family although in prototypical phytochromes (Pfr-to-Pr dark reversion) no enolic form has yet been detected in the Pfr state, possibly due to a low steady state concentration. Second, also protonation state variations of conserved His residues in the chromophore pocket are known for prototypical phytochromes and have been shown for the Pr state of cyanobacterial and plant phytochromes^{38,39}. Furthermore, the counterpart of His277 in prototypical phytochromes is involved in the reprotonation of the chromophore in the last step of the photoinduced Pr-to-Pfr conversion and thus is essential for the formation of the (signaling) Pfr state^{25,26}. Hence, the sequence of chromophore isomerization, proton translocation, and protein structural changes may represent a scheme for all phytochromes, thereby resembling the mechanistic pattern of retinal proteins⁴⁰. If, however, a similar coupling of light-triggered (de)activation of the output module and its thermal reversal, as deciphered for bathy phytochromes, also holds for other phytochromes, remains to be explored.

MATERIALS AND METHODS

Sample preparation

Agp2 and *PaBphP* were heterologously expressed and assembled *in vitro* with BV as described elsewhere^{20,41}. For ¹³C-labeling of Agp2 *D*-Glucose ¹³C₆ (99% ¹³C; Cortecnet; France) was used as carbon source. The ¹³C-labelled apoprotein was assembled with non-labeled BV. Buffer solutions used for the RR experiments included 50 mM Tris/HCl, 300 mM NaCl, 5 mM ethylenediaminetetraacetic acid in H₂O (D₂O) at pH (pD) of 7.8. Protein samples were concentrated via Microcon filters up to a value corresponding to an optical density of ca. 40 at 280 nm (ca. 10 mg/mL). For IR experiments the concentration was higher by a factor of ca. 10. H/D or D/H exchange involved 5 washing steps with D₂O or H₂O buffer solution (30 min centrifugation at 10000 g per step). The H/D (D/H) exchange was either carried out in the dark or was followed by a controlled photoconversion from Pfr to Pr and back to Pfr. This was achieved by sample illumination in the Pfr (Pr) state for 10 sec (2 min) at +20°C with light of 785 nm (660 nm) using a light emitting diode, corresponding to a photon fluence of ca. 2·10²² (4·10²²) photons/m².

Resonance Raman and IR experiments

RR measurements were performed using a Bruker Fourier-transform Raman spectrometer RFS 100/S with 1064 nm excitation (Nd-YAG cw laser, line width 1 cm⁻¹), equipped with a nitrogen-cooled cryostat from Resultec (Linkam). All spectra were recorded at 90 K with a laser power at the sample of 780 mW. In order to identify potential laser-induced damage of the phytochrome samples spectra before and after a series of measurements were compared. In no case, changes between these control spectra were determined. For each spectrum the accumulation time was ca. 1 h. Protein and buffer Raman bands were subtracted on the basis of a Raman spectrum of apo-phytochrome. The pure spectra were further analyzed by a band fitting procedure assuming Lorentzian band shapes. These Lorentzian functions obtained from

the fits were then combined to yield the component spectrum of the respective state¹⁹. The intermediate state Meta-F was accumulated by irradiation the Pfr sample at ca. 240 K with 785 nm (*vide supra*). Residual contributions of non-photolyzed Pfr to the RR spectrum measured at 90 K were subtracted. The spectra of the Pr state were obtained as described elsewhere¹⁸.

For IR spectroscopic measurements the protein samples were placed between two BaF₂ windows (15 mm diameter) with a 3 µm thick PTFE-spacer and equilibrated at 273 K. IR spectra were recorded in a Bruker IFS66v/s spectrometer equipped with a liquid nitrogen cooled MCT detector (J15D series, EG&G Judson). Spectra were recorded 2 minutes prior to illumination and 30 seconds after the illumination and subsequently the “Pr-minus-Pfr” difference spectra were calculated by subtracting the Pfr spectra from the Pr spectra.

Calculation of the vibrational spectra

Raman and IR spectra were calculated using the quantum-mechanics/molecular-mechanics (QM/MM) hybrid methodology in conjunctions with molecular dynamics (MD) simulations as described previously¹⁹. The spectra refer to the QM96 fragment of the optimized crystal structure of the Pfr state *Pa*BphP (PDB 3C2W) defined in ref. 19, and represent the average of 50 snapshot spectra obtained from the MD simulations.

Acknowledgements

The work was supported by the Deutsche Forschungsgemeinschaft, Sfb1078 (B5, B6, C3). The authors thank the “Norddeutscher Verbund für Hoch- und Höchstleistungsrechnen” (HLRN) for providing computer power.

Contributions to the work

F. V. E. and P. P. contributed equally to this work. F. V. E., P. P., M. F. L. and A. R. carried out the RR, IR, and UV-vis spectroscopic measurements: J. S. and M. A. M. performed and analysed the QMMM calculations: P. S. provided the homology model for Agp2 and analysed the structural data: B.M.Q. and P.S. provided initial activation assays: F. B. and F. S. analysed the spectroscopic data: P. H. wrote the paper with contributions from all co-authors; the project and the experiments were planned and designed by all team members.

References

1. Briggs, W. R. & Spudich, J. L. *Handbook of photosensory receptors*. (Wiley Verlag, Weinheim, Germany, 2005).
2. Rockwell, N., Su, Y., & Lagarias, J. C. Phytochrome structure and signaling mechanisms. *Annu. Rev. Plant. Biol.* **57**, 837-858 (2006).
3. Rockwell, N. C. & Lagarias, J. C. A brief history of phytochromes. *Chemphyschem* **11**, 1172-1180 (2010).
4. Karniol, B. & Vierstra, R. D. The pair of bacteriophytochromes from *Agrobacterium tumefaciens* are histidine kinases with opposing photobiological properties. *Proc. Nat. Acad. Sci. U. S. A.* **100**, 2807-2812 (2003).
5. Wagner, J. R., Brunzelle, J. S., Forest, K. T., & Vierstra, R. D. A light-sensing knot revealed by the structure of the chromophore-binding domain of phytochrome. *Nature* **438**, 325-331 (2005).
6. Wagner, J. R., Zhang, J. R., Brunzelle, J. S., Vierstra, R. D., & Forest, K. T. High resolution structure of *Deinococcus* bacteriophytochrome yields new insights into phytochrome architecture and evolution. *J. Biol. Chem.* **282**, 12298-12309 (2007).
7. Yang, X., Stojkovic, E. A., Kuk, J., & Moffatt, K. Crystal structure of the chromophore binding domain of an unusual bacteriophytochrome, RpBphP3, reveals residues that modulate photoconversion. *Proc. Nat. Acad. Sci. U. S. A.* **104**, 12571-12576 (2007).
8. Essen, L. O., Hughes, J., & Mailliet, J. The structure of a complete phytochrome sensory module in the Pr ground state. *Proc. Nat. Acad. Sci. U. S. A.* **105**, 14709-14714 (2008).
9. Bellini, D., & Papiz, M. Z. Dimerization properties of the RpBphP2 chromophore-binding domain crystallized by homologue-directed mutagenesis. *Acta Cryst. D* **68**, 1058-1066 (2012).

10. Yang, X. J., Kuk, J., & Moffat, K. Crystal structure of *Pseudomonas aeruginosa* bacteriophytochrome: Photoconversion and signal transduction. *Proc. Nat. Acad. Sci. U. S. A.* **105**, 14715-14720 (2008).
11. Yang, X. J., Kuk, J., & Moffat, K. Conformational differences between the Pfr and Pr states in *Pseudomonas aeruginosa* bacteriophytochrome. *Proc. Nat. Acad. Sci. U. S. A.* **106**, 15639-15644 (2009).
12. Yang, X.J., Ren, Z., Kuk, J., & Moffat, K. Temperature-scan cryocrystallography reveals reaction intermediates in bacteriophytochrome. *Nature* **479**, 428-432 (2011).
13. Takala, H. *et al.* Signal amplification and transduction in phytochrome photosensors. *Nature* **509**, 245-248 (2014).
14. Anders, K., Daminelli-Widany, G., Mroginski, M. A., von Stetten, D., & Essen, L. O. Structure of the cyanobacterial phytochrome 2 photosensor implies a tryptophan switch for phytochrome signaling. *J. Biol. Chem.* **288**, 35714-35725 (2013).
15. Lamparter, T., Michael, N., Mittmann, F., & Esteban, B. Phytochrome from *Agrobacterium tumefaciens* has unusual spectral properties and reveals an N-terminal chromophore attachment site. *Proc. Nat. Acad. Sci. U. S. A.* **99**, 11628-11633 (2002).
16. Inomata, K. *et al.* Assembly of synthetic locked chromophores with *Agrobacterium* phytochromes AGP1 and AGP2. *J. Biol. Chem.* **281**, 28162-28173 (2006).
17. Rottwinkel, G., Oberpichler, I., & Lamparter, T. Bathy phytochromes in rhizobial soil bacteria. *J. Bacteriol.* **192**, 5124-5133 (2010).
18. Zienicke, B. *et al.* Unusual spectral properties of bacteriophytochrome Agp2 result from a deprotonation of the chromophore in the red-absorbing form Pr. *J. Biol. Chem.* **44**, 31738–3175 (2013).
19. Salewski, J. *et al.* The structure of the biliverdin cofactor in the Pfr state of bathy and prototypical phytochromes. *J. Biol. Chem.* **288**, 16800-16814 (2013).

20. Scheerer, P. *et al.* Light-induced conformational changes of the chromophore and the protein in phytochromes: bacterial phytochromes as model systems. *Chemphyschem.* **26**, 1090-1105 (2010).
21. Tasler, R., Moises, T., & Frankenberg-Dinkel, N. Biochemical and spectroscopic characterization of the bacterial phytochrome of *Pseudomonas aeruginosa*. *FEBS J.* **272**, 1927-1936 (2005).
22. Mroginski, M.A. *et al.* Elucidating photoinduced structural changes in phytochromes by the combined application of resonance Raman spectroscopy and theoretical methods. *J. Mol. Struct.* **993**, 15-25 (2011).
23. Fodor, S. P. A., Lagarias, J. C., & Mathies, R. A. Resonance Raman analysis of the Pr and Pfr forms of phytochrome. *Biochemistry* **29**, 11141-11146 (1990).
24. Kneip, C. *et al.* Protonation State and Structural Changes of the Tetrapyrrole Chromophore during the Pr → Pfr Phototransformation of Phytochrome. A Resonance Raman Spectroscopic Study. *Biochemistry* **38**, 15185-15192 (1999).
25. Andel III, F., Lagarias, J. C., & Mathies R. A. Resonance Raman analysis of chromophore structure in the lumi-R photoproduct of phytochrome. *Biochemistry* **35**, 15997-16008 (1996).
26. Borucki, B. *et al.* Light-induced proton release of phytochrome is coupled to the transient deprotonation of the tetrapyrrole chromophore. *J. Biol. Chem.* **280**, 34358-34364 (2005).
27. von Stetten, D. *et al.* Highly conserved residues Asp-197 and His-250 in Agp1 phytochrome control the proton affinity of the chromophore and Pfr formation. *J. Biol. Chem.* **282**, 2116-2123 (2007).
28. Foerstendorf, H., Mummert, E., Schäfer, E. Scheer, H., & Siebert F. Fourier-transform infrared spectroscopy of phytochrome: difference spectra of the intermediates of the photoreactions. *Biochemistry* **35**, 10793-10799 (1996).

29. van Thor, J. J., Fisher, N., & Rich, P. R. Assignments of the Pfr-Pr FTIR difference spectrum of cyanobacterial phytochrome Cph1 using ^{15}N and ^{13}C isotopically labeled phycocyanobilin chromophore. *J. Phys. Chem. B* **109**, 20597-20604 (2005).
30. Schwinté, P. *et al.* FTIR study of the photoinduced processes of plant phytochrome phyA using isotope-labeled bilins and density functional theory calculations. *Biophys. J.* **95**, 1256-1267 (2008).
31. Piwowarski, P. *et al.* Light induced activation of bacterial phytochrome Agp1 monitored by static and time resolved FTIR spectroscopy. *Chem.Phys.Chem.* **11**, 1207-1214 (2010).
32. Lightner, D. A., Holmes, D. L., & McDonagh, A. F. On the acid dissociation constants of bilirubin and biliverdin. pK_a values from ^{13}C NMR spectroscopy. *J. Biol. Chem.* **271**, 2397-2405 (1996).
33. Mao, J., Hauser, K., & Gunner, M. R. How cytochromes with different folds control redox potentials. *Biochemistry* **42**, 9829-9840 (2003).
34. Peng, C. S., Baiz, C. R., & Tokmakoff, A. Direct observation of ground state lactam-lactim tautomerization using temperature-jump transient 2D IR spectroscopy. *Proc. Nat. Acad. Sci. U. S. A.* **110**, 9243-9248 (2013).
35. Barth, A. Infrared spectroscopy of proteins. *Biochim. Biophys. Acta* **1767**, 1073-1101 (2007).
36. Popp, A., Wu, L., Keiderling, T. A., & Hauser, K. Impact of β -turn sequence on β -hairpin dynamics studied with infrared-detected temperature jump, *Spect. Int. J.* **27**, 557-564 (2012).
37. Lagarias, J. C. & Rapoport, H. Chromopeptides from phytochrome. The structure and linkage of the Pr form of the phytochrome chromophore. *J. Am. Chem. Soc.* **102**, 4821-4828 (1980).

38. Song, C. *et al.* Solid-state NMR of a canonical phytochrome reveals two Pr isoforms and a chromophore D-ring photoflip triggering extensive intramolecular changes. *Proc. Natl. Acad. Sci. U.S.A.* **108**, 3842-3847 (2011).
39. Song, C. *et al.* Solid-state NMR spectroscopy to probe photoactivation in canonical phytochromes. *Photochem. Photobiol.* **89**, 259-273 (2013).
40. Haupts, U., Tittor, J., & Oesterhelt, D. Closing in on bacteriorhodopsin: progress in understanding the molecule. *Annu. Rev. Biophys. Biomol. Struct.* **28**, 367-99 (1999).
41. Lamparter, T. & Michael, N. *Agrobacterium* phytochrome as an enzyme for the production of ZZE bilins. *Biochemistry* **44**, 8461-8469 (2005).

Figure captions

Figure 1 | Photocycle and structural models of the Pfr state of *PaBphP* and *Agp2*. (a), **right**, schematic cartoon representation of the three domain - photosensory module (PAS-GAF-PHY) from the crystal structure of *PaBphP* (PDB entry 3C2W)¹⁰ in the Pfr state. **Left**, close-up view of the chromophore binding pocket of *PaBphP* (amino acids [aa] colored as green and blue sticks, the chromophore biliverdin as purple balls and sticks)¹⁰, and the homology model of *Agp2* (aa as yellow sticks) as described previously¹⁹. Bold letters indicate to *Agp2*-specific amino acids compared with *PaBphP*. The aa numbering in the text refers to *PaBphP* with the corresponding values for *Agp2* given in parentheses. Potential hydrogen bonds are indicated with black dashes. (b), simplified representation of the photoinduced reaction sequences of bathy phytochromes. Purple and red arrows indicate the photoreactions whereas the thermal reactions are denoted by grey arrows.

Figure 2 | Experimental and calculated Raman spectra of the Pfr state of *Agp2* in the C=C stretching region with different protonation/deuteration patterns of the chromophore. The black traces represent the experimental resonance Raman (RR) spectra in the fully protonated state (**H₂O**), the partially deuterated state (**H → D, dark**), and the fully deuterated state (**H → D, hv**), compared with the calculated Raman spectra (red) for the chromophore with different protonation/deuteration patterns as illustrated by simplified formulas (left). Calculated spectra were obtained from the optimized structure of the Pfr state of *PaBphP*. The experimental spectra of the Pfr state of *PaBphP* are essentially identical to those of *Agp2* for each of the H/D exchange conditions (**Supplementary Fig. S1**). Upon H/D exchange in the dark, the N-H ip of rings B and C at 1549 cm⁻¹ disappears (the corresponding N-D ip mode is observed at 1062 cm⁻¹; **Supplementary Fig. S1**). The stepwise downshift of the C=C stretching of the C-D methine bridge from 1599 to 1596 cm⁻¹ (from **H₂O** to **H → D**,

dark) and after a photocycle to 1589 cm^{-1} (**H → D, hv**) is due to the admixture of the N-H ip bending coordinates of rings *C* and *D* as confirmed by the calculated spectra. Thus, sequential H/D exchange in the dark occurs at rings *A*, *B*, and *C*, and after a full photocycle at ring *D*. The good agreement of the experimental and calculated spectra (all rings protonated - **H₂O**; only rings *A*, *B*, *C* deuterated - **H → D, dark**; all rings deuterated - **H → D, hv**) also holds for the entire spectral range as well as for the spectra of the reverse exchange process (**Supplementary Figs. S2, S3**). In contrast, the calculated spectrum for the protonation pattern with ring *A* protonated but rings *B*, *C*, and *D* deuterated overestimates the downshift of the C=C stretching mode of the *C-D* methine bridge and predicts two distinct shoulders on the high frequency side that are not matched by the experiment.

Figure 3| IR difference spectra of Agp2 showing the C=O stretching region for different protonation/deuteration states of the chromophore. The difference spectra were measured from the fully protonated (**H₂O**), the partially deuterated state (**H → D, dark**), and the fully deuterated state (**H → D, hv**). **Left**, “Pr minus Pfr” difference spectra recorded at $T = 293\text{ K}$ (pH 7.3). Positive and negative signals refer to bands of the Pr and Pfr state, respectively. The H/D sensitivity of the C=O stretchings of ring *A* and *D* originates from the admixture of N-H coordinates of the same ring. The top spectrum (**H₂O**, black trace) is overlaid by the corresponding difference spectrum of the ^{13}C -labeled protein (grey trace), indicating that above 1680 cm^{-1} only the weak and broad feature at ca. 1734 cm^{-1} (marked in grey) displays a ^{13}C -dependent downshift and thus must originate from a (protonated) carboxyl side chain of the protein. This assignment is confirmed by the ca. 8-cm^{-1} downshift upon H/D exchange in the dark in the “Pr-minus-Pfr”, also seen in the corresponding “Meta-F-minus-Pfr” difference spectrum (right panel). **Right**, “Meta-F minus Pfr” difference spectra recorded at $T = 240\text{ K}$ (pH 7.8). Positive and negative signals refer to bands of the Meta-F and Pfr state, respectively.

Band labels of the Pfr state and the reaction product (Pr, left; Meta-F, right) are highlighted in red and blue, respectively. Italic labels “*A*”, “*D*”, and “*prop*” refer to the C=O stretchings of ring *A*, ring *D*, and the ring *C* propionic side chain, respectively. The green letters “H” and “D” in parentheses specify the respective protonation/deuteration state of the propionic side chain and the pyrrole nitrogens of rings *A* and *D*. The crucial C=O stretching of ring *D* of Pr/Meta-F at 1709 cm⁻¹ is labeled by bold letters/numbers. Further details of the assignments and the corresponding analysis for *PaBphP* are given in the **Supplementary Figure S4**.

Figure 4| Resonance Raman and IR difference spectra of Agp2 obtained from samples in H₂O. **Left**, Resonance Raman (RR) spectra of (a) the Meta-F state trapped at 240 K (pH 7.8), and the two forms of the Pr state prevailing below (b, red, “acid” Pr) and above pH = 7.6 (c, blue, “alkaline” Pr). The spectra (b) and (c) are derived from a component analysis of the RR spectra measured as a function of the pH as described previously¹⁸. The “acid” Pr form displays striking RR spectroscopic similarities with the Meta-F state indicating similar chromophore conformations. The same conclusion can be derived from the IR spectra (**Supplementary Fig. S6**). **Right**, IR difference spectra (d) “Meta-F minus Pfr”, measured at 240 K, and (e) “Pr minus Pfr” (black trace), measured at 293 K. The grey trace in (e) refers to the “Pr minus Pfr” difference spectrum obtained from a sample of ¹³C-labelled protein. All IR spectra were measured at pH 7.8. Blue and red labels refer to bands of the Pfr and Pr/Meta-F state, respectively.

Figure 5| Effect of the pH on the structure and dark reversion kinetics of the Pr state of Agp2. (a) Resonance Raman (RR) spectra of the Pr state of Agp2 obtained from samples in H₂O buffer at different pH. Blue and red lines/labels indicate bands of the “alkaline” and “acid” Pr form, respectively (see **Fig. 4b,c**). (c) IR difference “Pr-minus-Pfr” spectra of Agp2

obtained from samples in H₂O buffer at different pH. Blue and red lines/labels indicate bands of the Pfr and Pr state, respectively. Note that the corresponding “Meta-F-minus-Pfr” differences do not vary with the pH in this range (**Supplementary Fig. S6**). **(b, top)** pH-dependence of the relative concentrations of the “acid” Pr form with both ring *B* and *C* nitrogens protonated (red triangles) as determined from the component analysis of the RR spectra¹⁸. The black triangles refer to the pH-dependence of the absorbance of the ring *D* C=O of the Pr state at 1709 cm⁻¹ measured as a function of the pH. The solid lines represent fits of the modified Henderson-Hasselbalch equation to the data. Further details are given in the text and the **Supplementary Notes**. **(b, bottom)** Rate constant of the Pr-to-Pfr dark reversion (main component of the multi-exponential decay – see **Supplementary Notes** for details) plotted as a function of the pH. The solid line represents the pH-dependence of the “reactive” enol+His₂₇₇H⁺ species (**Fig. 6**) determined from the RR spectroscopic data in on the basis of the modified Henderson-Hasselbalch function in **(b, top)**. The green circles (line) and blue squares (line) refer to the full-length Agp2 and the truncated Agp2 lacking the histidine kinase module, respectively. Note the different scales of the rate constants for both protein variants.

Figure 6 | Keto-enol equilibrium of the Pr chromophore of bathy phytochromes and its role for the Pr-to-Pfr dark reversion. The figure displays the reaction scheme for the coupled pH-dependent distribution between the keto and the enol form of the chromophore in the Pr state of Agp2. Since the keto form is not detectable at high pH, but a residual contribution of the enol persists a low pH (**Fig. 5b, top**), we can neglect the “keto··His278” species (colored in grey), leaving only one pH-dependent acid-base equilibrium of His278 (His277 in *PaBphP*), and a pH-independent enol-keto equilibrium with the equilibrium constants K_B and K_T , respectively. Note that, unlike to the kinetics, keto-enol equilibria are typically pH-independent³⁴. Upon protonation of His278 via the ring *C* propionic group of

biliverdin (BV), the interactions with the ring *D* N-H group of BV are weakened and the resonance structure with C(15)-C(16) single bond character (reactive species, enol+His277H⁺; top, right) gains weight over that of the inactive form (enol⁻...His; bottom right), thereby facilitating rotation around this bond (red curved arrow).

Figure 1

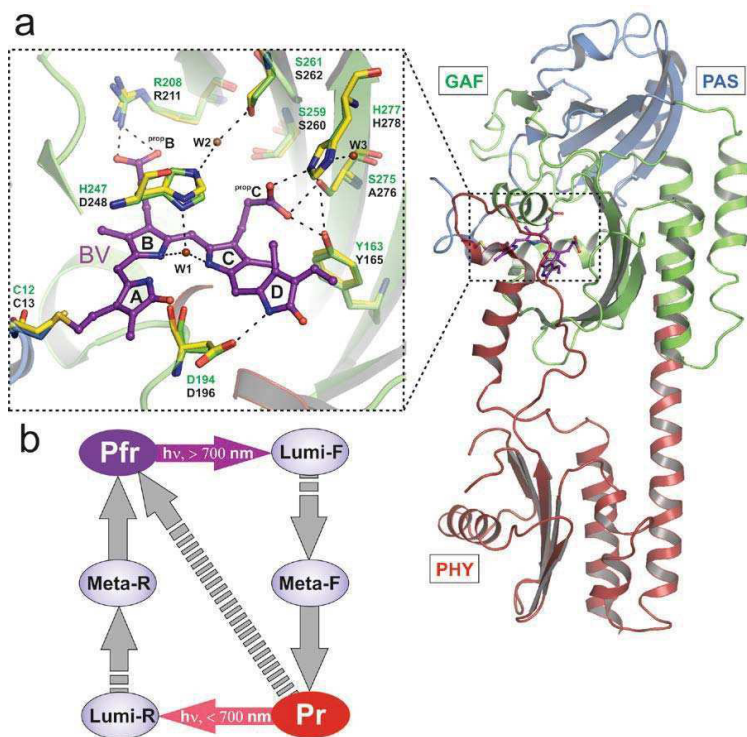


Figure 2 (preferred version, no chemdraw files – alternative version at the end)

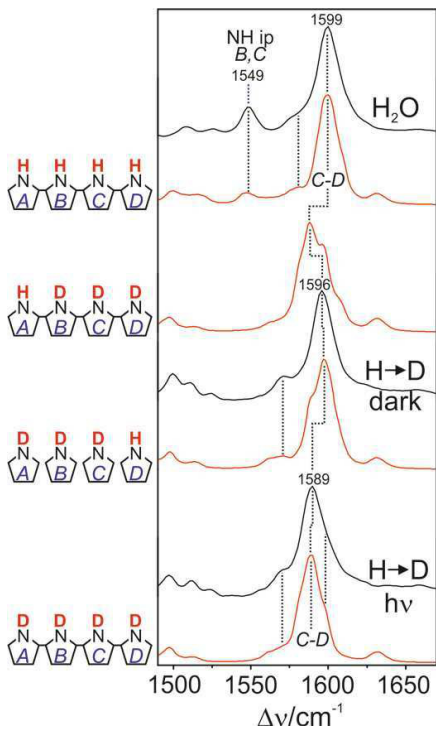


Figure 3

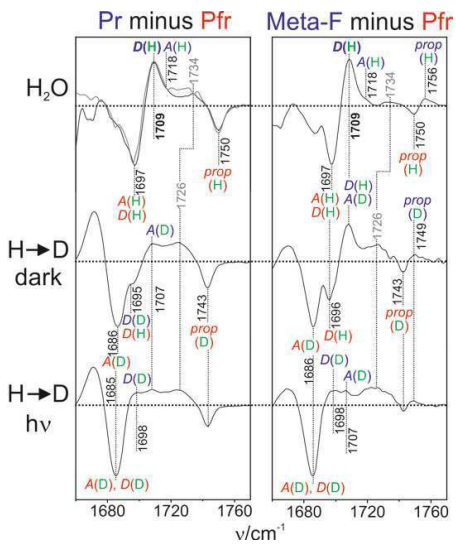


Figure 4

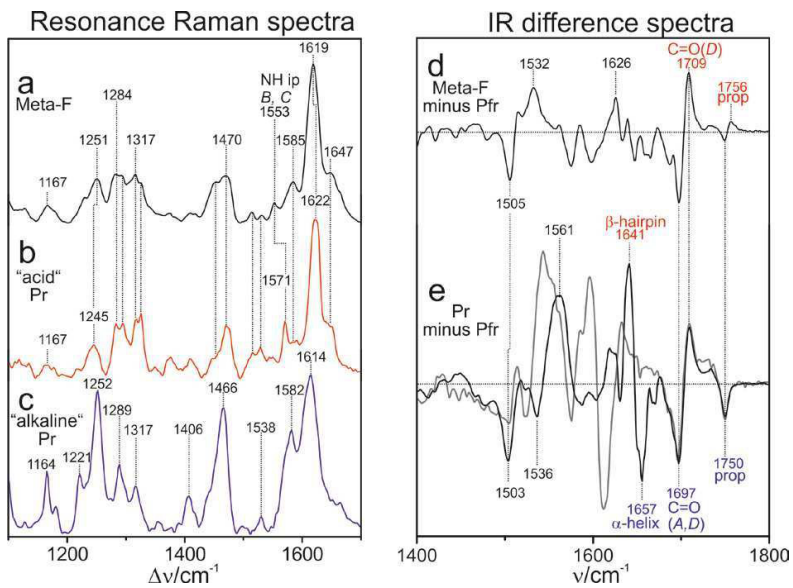


Figure 5

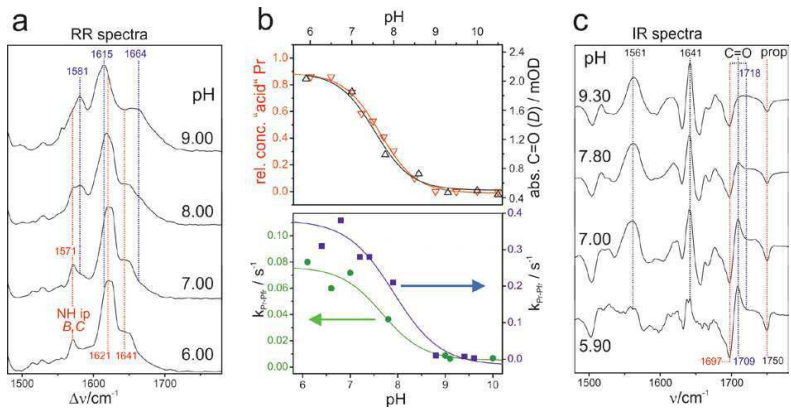
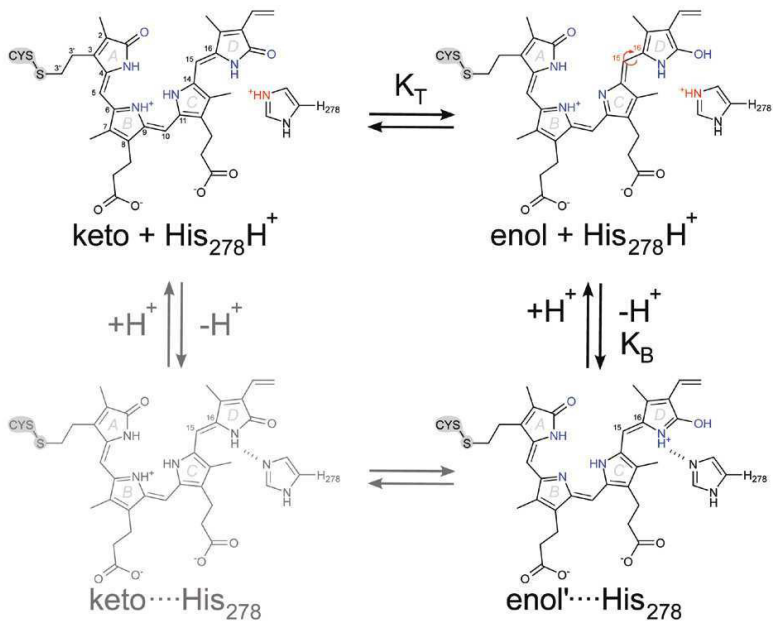


Figure 6



Supplementary Information

A protonation-coupled feedback mechanism controls the signaling process in bathy phytochromes

Francisco Velazquez Escobar^{1§}, Patrick Piwowski^{2#§}, Johannes Salewski¹, Norbert Michael¹, Maria Fernandez Lopez¹, Anna Rupp^{2#}, Bilal Muhammad Qureshi^{2§}, Patrick Scheerer^{2§}, Franz Bartl^{2#}, Nicole Frankenberg-Dinkel³, Friedrich Siebert^{1,4}, Maria Andrea Mroginski¹, and Peter Hildebrandt^{1*}

¹ Technische Universität Berlin, Institut f. Chemie, Sekr. PC 14, Straße des 17. Juni 135, D-10623 Berlin, Germany

² Charité - Universitätsmedizin Berlin, Institut für Medizinische Physik und Biophysik, [§]AG Protein X-Ray Crystallography and Signal Transduction, [#]AG Spektroskopie, Charitéplatz 1, D-10117 Berlin, Germany.

³ Technische Universität Kaiserslautern, Fachbereich Biologie, Abt. Mikrobiologie, Paul-Ehrlich-Str. 23, D-67663 Kaiserslautern, Germany.

⁴ Albert-Ludwigs-Universität Freiburg, Institut für Molekulare Medizin und Zellforschung, Sektion Biophysik, Hermann-Herderstr. 9, D-79104 Freiburg, Germany.

Content:

1. Vibrational assignments based on the selective H/D exchange in bathy phytochromes

Figures S1 – S4

2. RR and IR spectroscopic analysis of the Meta-F-to-Pr transition

Figures S5 – S6

3. pH dependence of the keto-enol tautomerism and the dark reversion kinetics of Pr

Notes

Figures S7

4. Structural models for the Pfr and Pr state

Figure S8

5. Preliminary data on the H278A variant of Agp2

Figures S9 – S10

1. Vibrational assignments based on the selective H/D exchange in bathy phytochromes

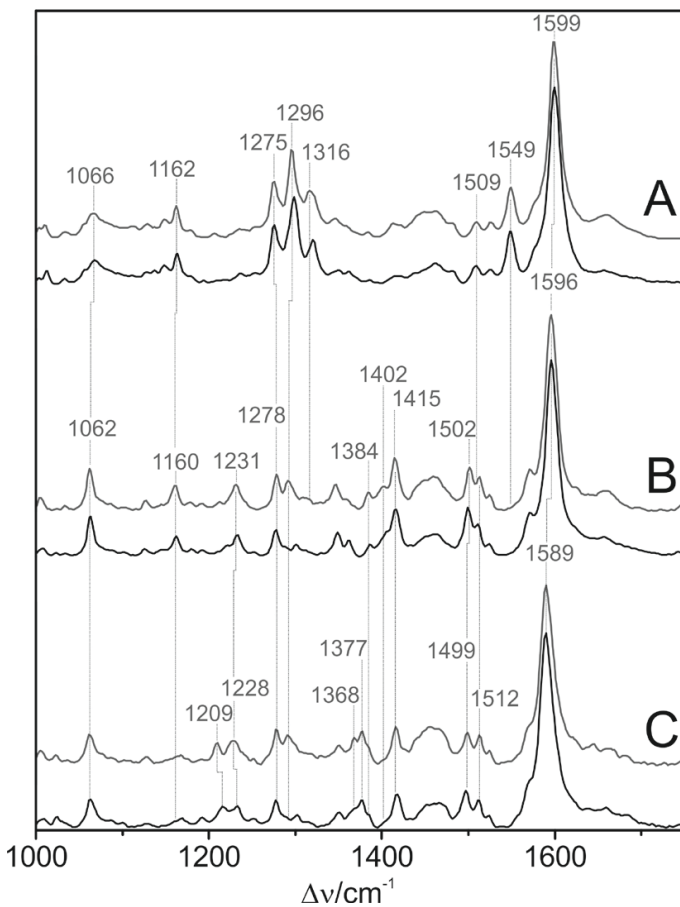


Figure S1. RR spectra of the Pfr states of *PaBphP* (grey) and *Agp2* (black) (**A**) in the fully protonated (non-deuterated) state, (**B**) after H \rightarrow D exchange in the dark (rings A, B, and C deuterated), and (**C**) after H \rightarrow D exchange and a complete photocycle (fully deuterated). Further details are given in the text. All spectra measured at pH(pD)=7.8.

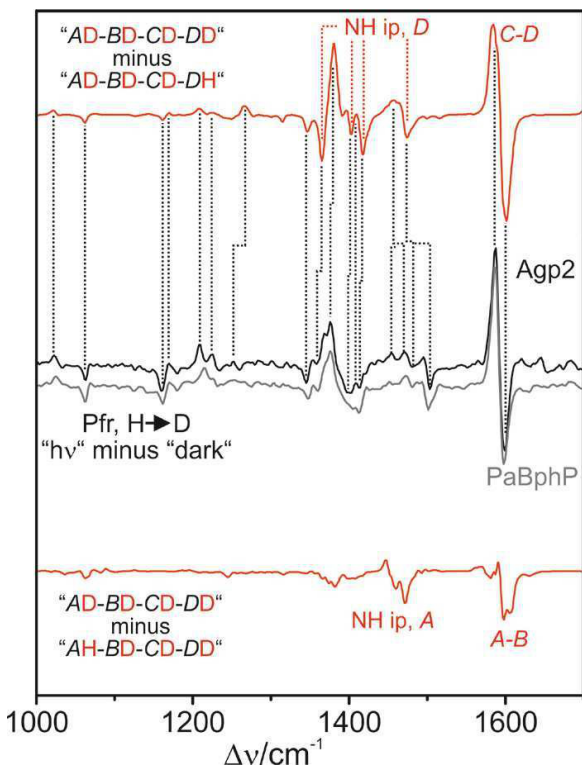


Figure S2. Difference of the experimental RR spectra of Pfr “H→D, hv” minus “H→D, dark” for Agp2 (black trace) and PaBphP (grey trace). The red difference traces refer to the differences obtained from the calculated spectra “fully deuterated” minus “only rings A, B, and C deuterated” (top) and “fully deuterated” minus “only rings B, C, and D deuterated” (bottom). Only the top calculated difference spectrum provides a good description for the experimental difference spectrum confirming that in the dark the H/D exchange in Pfr of both Agp2 and PaBphP is hindered for ring D. Note that the sensitivity of the C=C stretching of the C-D methine bridge towards H/D exchange results from the admixtures of the N-H ip coordinates of ring C and D which are removed upon from H/D exchange at the respective rings. All spectra measured at pH(pD)=7.8.

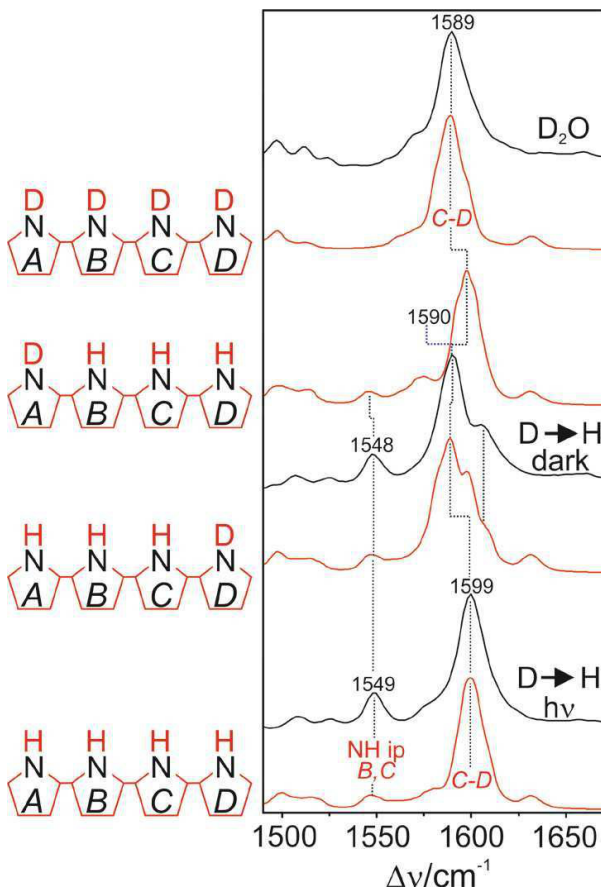


Figure S3. Experimental RR spectra of Pfr of Agp2 (black) in the fully deuterated state (top), upon D/H exchange in the dark (middle), and upon D/H exchange after a photocycle. The spectra are compared with calculated spectra (red) for different protonation patterns as indicated on the left side. The comparison demonstrates that the experimental spectrum of the partially exchanged chromophore (middle) is only well reproduced by the spectrum calculated for the AH-BH-CH-DD pattern, indicating that also the back-exchange (H→D) is hindered at ring *D* without completing a photocycle. All spectra measured at pH(pD)=7.8.

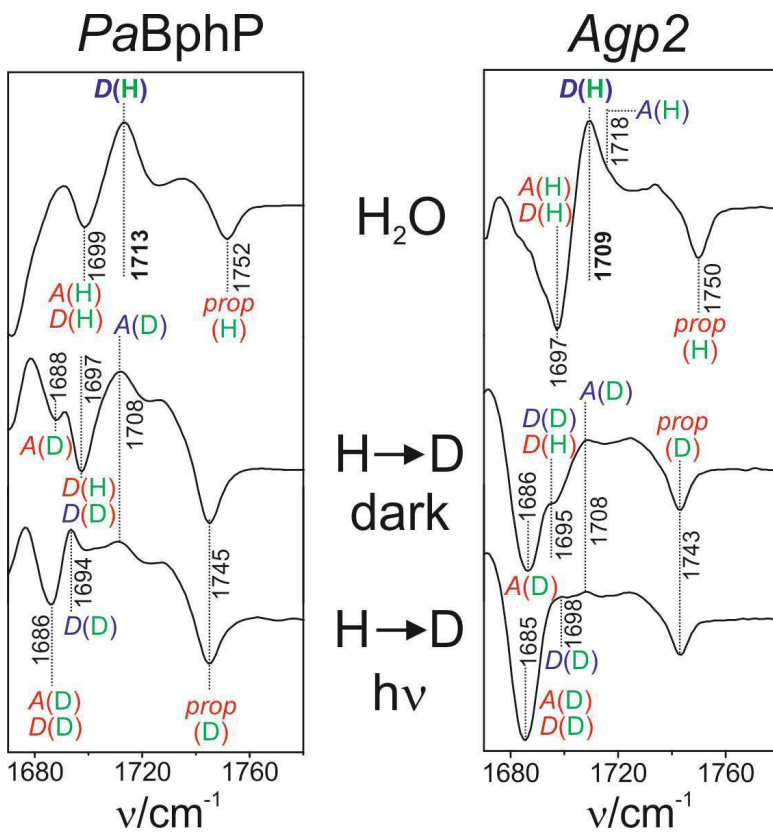


Figure S4. IR difference spectra “Pr minus Pfr” for PaBphP (left) and Agp2 (right) for the fully protonated (H₂O), the partially protonated (H→D, dark), and the fully deuterated (H→D, hv) state. The blue and red letters refer to the C=O stretchings of rings A, D, and the ring C propionic side chain of Pfr and Pr, respectively. The green letters (H, D) indicate the protonation/deuteration of the respective pyrrole rings and the propionic side chain. The H/D sensitivity of the C=O stretchings of ring A and D originates from the admixture of N-H coordinates of the same ring. All spectra measured at pH(pD)=7.6.

2. RR and IR spectroscopic analysis of the Meta-F-to-Pr transition

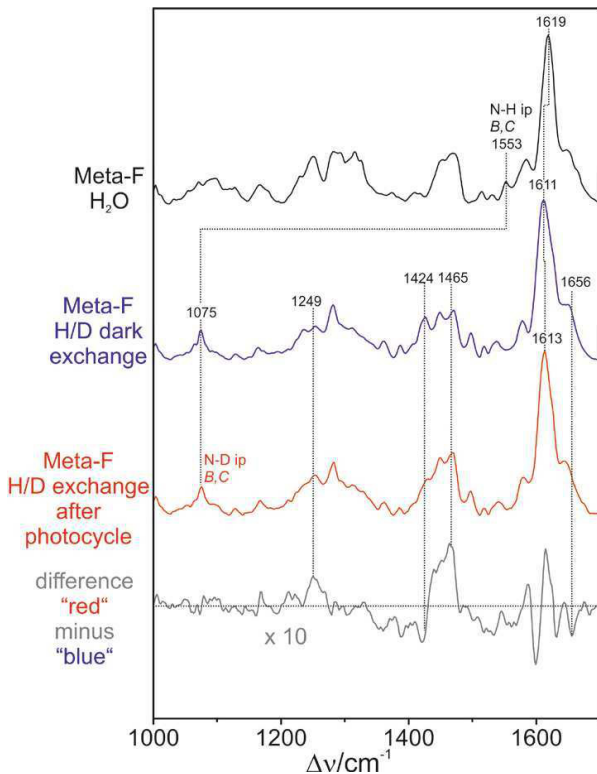


Figure S5. RR spectra of Meta-F in H₂O (fully protonated – black), after H/D exchange in the dark (blue), and after a complete photocycle (red - complete exchange). The spectra were measured from samples at pH(pD)=7.8 trapped at 240 K. The N-H ip (N-D ip) bending of rings *B* and *C* indicate that both inner pyrrole rings (*B*, *C*) carry a proton (deuteron). The shifts of the C=C stretching of the *C-D* methine bridge upon the sequential H/D exchange reflect at first the removal of the contribution of the ring *C* N-H ip (leading to a downshift of the mode) and subsequently the removal of the N-H ip contribution of ring *D* (slight upshift of the mode frequency). The differences between the partial and complete H/D exchange are shown by the difference spectrum (grey).

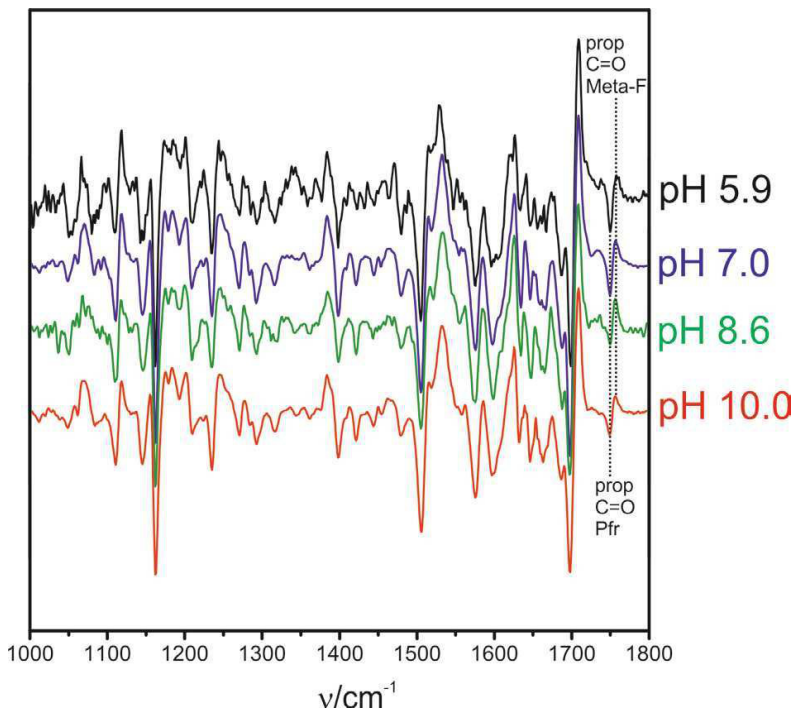


Figure S6. IR difference spectra “Meta-F minus Pfr” of Agp2 measured at 240 K from samples at different pH. The spectra are very similar in a wide pH range indicating that in both Pfr and Meta-F the protein and chromophore structure are not affected by the pH. Note that the propionic side chain of ring C is detectable even at pH=10.

3. pH dependence of the keto-enol tautomerism and the dark reversion kinetics of Pr

3.1. Analysis of the pH-dependence of the spectra of the Pr state

Experiments were carried out with the full-length Agp2 (denoted as Agp2-M1) and the truncated version Agp2-M2 lacking the histidine kinase domain. Expression and purification of both protein variants followed the protocol given in ref. 18.

Analysis of the UV-vis spectroscopic measurements.

The UV-vis spectra of the Pfr and Pr form were recorded with a Cary 50 UV-vis photospectrometer at 23°C. The pH of the buffer (100 mM Tris, 5 mM EDTA, 300 mM NaCl in H₂O) was adjusted to the desired value by NaOH or HCl. Subsequently, the protein was added such that the final concentration corresponded to an optical density of ca. 3.7 at 280 nm. The pH was controlled after each measurement. Photoconversion from the Pfr to the Pr state was achieved by using a laser diode emitting at 785 nm. Pure Pr spectra were calculated according to ref. 18. The Pfr and Pr spectra were normalised with respect to the absorption at 280 nm. The absorption of the Pr form at 706 nm and of the Pfr form at 756 nm was then plotted against the pH. In order to calculate the apparent $pK_{a,app}$ of the keto-enol equilibrium in the Pr state, the Henderson-Hasselbalch equation was fitted to the uncorrected titration data according to ref. 18. Within the pH range of 6 to 10 the absorption of the Pfr state of Agp2-M1 and Agp2-M2 at 756 nm remained constant.

Whereas for Agp2-M1, the previously published value of $pK_{a,app}=7.6$ (ref. 18) could be well reproduced, there are considerable discrepancies for Agp2-M2. We adopted the same experimental conditions as used in that study except for the irradiation time to convert Pfr to Pr. Here we have used a much shorter time between 5 s (at pH 6.1) and 80 s (at pH 11.2) immediately followed by the measurements (there was no delay time between irradiation and

measurements). In this way, the extent of dark reversion prior to the measurements was significantly reduced as can be seen by the UV-vis spectra in Fig. S7. The corresponding $pK_{a,app}$ was determined to be 8.0 and thus by 0.4 units higher than for Agp2-M1 whereas in contrast a significantly lower $pK_{a,app}$ was reported in ref. 18.

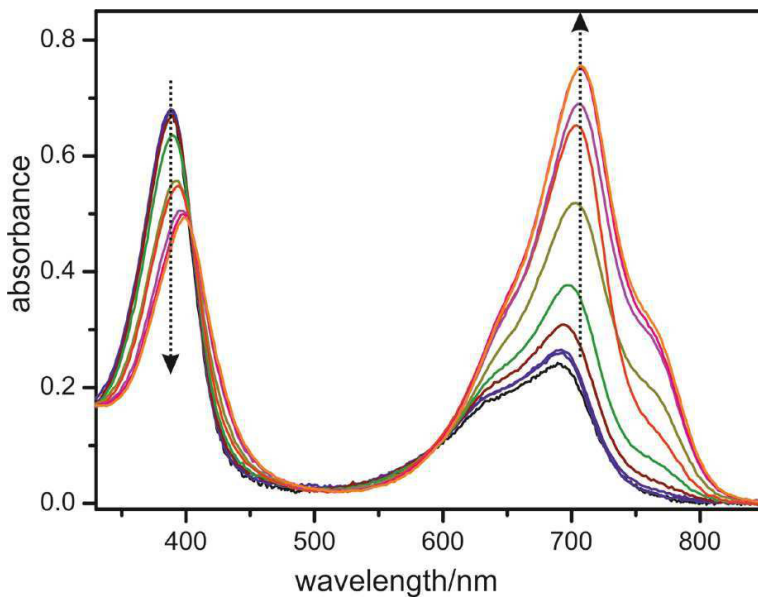


Fig. S7. UV-vis absorption spectra of Agp2-M2 after far-red photoconversion from Pfr to Pr, measured as a function of the pH. The pH decreases in the direction of the arrows from 11.2, 9.7, 9.4, 8.8, 8.4, 7.9, 7.5, 7.2, 6.6, and 6.2. Contributions from Pfr that increase with decreasing pH are not subtracted.

Analysis of the RR and IR spectroscopic measurements.

The analysis of the RR spectra of Pr (Agp2-M2), measured as a function of the pH, was described in detail in ref. 18. As a result, the relative concentrations of the “acid” and the

“alkaline” Pr were obtained, which in that work were related to an acid-base equilibrium corresponding to a proton transfer from the chromophore to the protein. In view of the present results this interpretation must be revised. Instead, the “acid” Pr and “alkaline” Pr are identified as keto and enol tautomers, respectively. As shown in the text, the keto-enol equilibrium itself is not pH-dependent but it is coupled to the protonation of the nearby His277 (*PaBphP*; 278 in *Agp2*) according to the scheme in Fig. 6 of the manuscript. The two enol forms, however, cannot be distinguished by RR (or other optical) spectroscopy. Thus, re-analysis of the pH dependence of the “acid” Pr (= keto) and “alkaline” Pr (=enol) forms requires a modification of the Henderson-Hasselbalch equation.

According to the scheme in Fig. 6 we define the keto-enol equilibrium as

$$(1) K_T = \frac{[enol(A)]}{[keto]}$$

where “enol(A)” refers to enol form and the protonated His277(278). The equilibrium between this enol(A) form and the enol(B) form interacting with the non-protonated His277(278) is given by

$$(2) K_B = \frac{[enol(B)][H^+]}{[enol(A)]}$$

The total, spectroscopically detectable enol content is denoted by “enol” and is given by

$$(3) [enol] = [enol(A)] + [enol(B)]$$

By combination with Eq. (1) and (2) one obtains

$$(4) [enol] = [keto] \cdot K_T \cdot \left(\frac{K_B}{[H^+]} + 1 \right)$$

Thus one obtains for concentration ratio $[enol]/[keto]$ as determined from the RR experiments

$$(5) \frac{[enol]}{[keto]} = K_T \cdot \left(\frac{K_B}{[H^+]} + 1 \right)$$

At $\text{pH} > K_B$, Eq. (5) can be approximated by

$$(6) \frac{[enol]}{[keto]} = K_T \cdot K_B \cdot \frac{1}{[H^+]}$$

which corresponds to the classical Henderson-Hasselbalch equation

$$(7) \text{pH} = \log \left(\frac{[\text{enol}]}{[\text{keto}]} \right) + \text{p}K_{a,\text{app}}$$

where the apparent $\text{p}K_{a,\text{app}}$ is given by

$$(8) \text{p}K_{a,\text{app}} = \text{p}K_{\text{B}} + \text{p}K_{\text{T}}$$

$\text{p}K_{\text{B}}$ and $\text{p}K_{\text{T}}$ are derived from the dissociation constant K_{B} for the protonated His277(278) and the keto-enol equilibrium constant K_{T} , respectively. K_{B} can be determined from Eq. 5 for the case $\text{pH} < K_{\text{B}}$, i.e. in acidic solution. Then Eq. 5 transforms to

$$(9) \frac{[\text{enol}]}{[\text{keto}]} = K_{\text{T}}$$

Since K_{T} is readily determined to be 0.12 (Fig. 5B), the apparent $\text{p}K_{a,\text{app}}$ is higher than the $\text{p}K_{\text{B}}$ of the actual acid/base equilibrium, i.e. the dissociation of the protonated His277(278). From the RR measurements one obtains $\text{p}K_{a,\text{app}}=7.6$ and thus $\text{p}K_{\text{B}}=6.7$. The IR spectroscopic data probe the disappearance of the keto form. The solid lines in Fig. 5B represent a fit of Eq. 5 to the IR and RR data. The UV-vis spectroscopic analysis carried out in this work as well as in ref. 18 afford the apparent $\text{p}K_{a,\text{app}}$. It is important to note that the UV-vis spectroscopic data is consistent with the present interpretation as keto-enol equilibrium, since the reduced absorbance of the first electronic transition may primarily be due to the removal of a proton from ring C nitrogen and does not necessarily reflect a change of the net charge of the chromophore.

Kinetic analysis of the dark reversion

Following the protocol described in ref. 18 but using different irradiation conditions (*vide supra*), the thermal time-dependent formation of Pfr was monitored at 750 nm. The data were analysed by fitting a bi-exponential function. The main component exhibited a time constant that was typically larger by a factor of ten than that of the second component.

The data demonstrate that dark reversion of the Pr state in Agp2-M1 is distinctly slower than in Agp2-M2. There is no indication for a kinetic isotope effect.

4. Structural models for the Pfr and Pr state

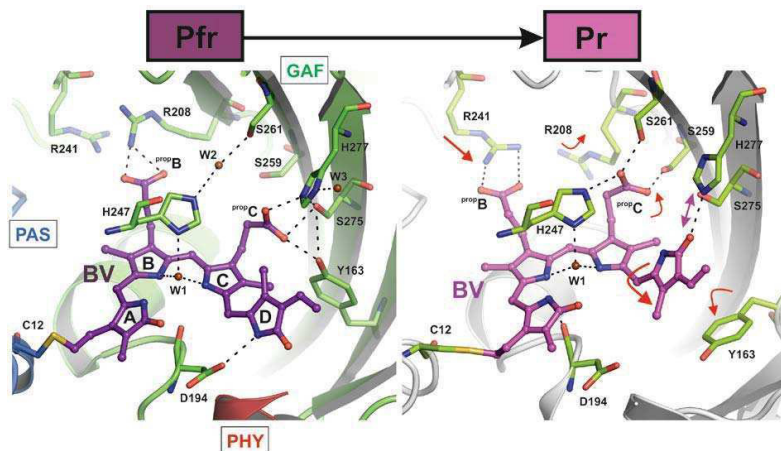


Fig. S8. Structural models of the Pfr and Pr state. Left, schematic representation of the chromophore pocket of the crystal structure from *PaBphP* (PDB entry 3C2W)¹⁰ in the Pfr state (amino acids and the chromophore biliverdin are colored as green and blue sticks and purple balls and sticks, respectively; see Fig. 1). Potential hydrogen bonds are indicated with black dashes. Right (colour code as above), structural interpretation of a potential Pr state model of the chromophore pocket derived and extracted from the crystal structure of the *PaBphP* mutant Q188L. The crystal structure of *PaBphP* mutant Q188L is a “mixed state” that include fractions of both the Pr and Pfr forms (PDB entry 3G60 with a mixed Pfr-Pr chromophore configuration)¹¹. Red arrows indicate possible structural changes within the chromophore pocket.

5. Preliminary data on the H278A variant of Agp2

Reconstitution of the H278A variant of Agp2 (Agp2-H278A) with BV occurs in the Pr state which is stable for many hours. The dark transformation to the Pfr state at pH 7.8 requires more than 10 hours and is thus slower by ca. three orders of magnitude than the wild-type (WT) protein. IR difference spectra (Fig. S9) and RR spectra (Fig. S10) indicate that the His278 substitution impairs the secondary structure transition associated with the Pr/Pfr transformation and the formation of the keto/enol equilibrium in the Pr chromophore.

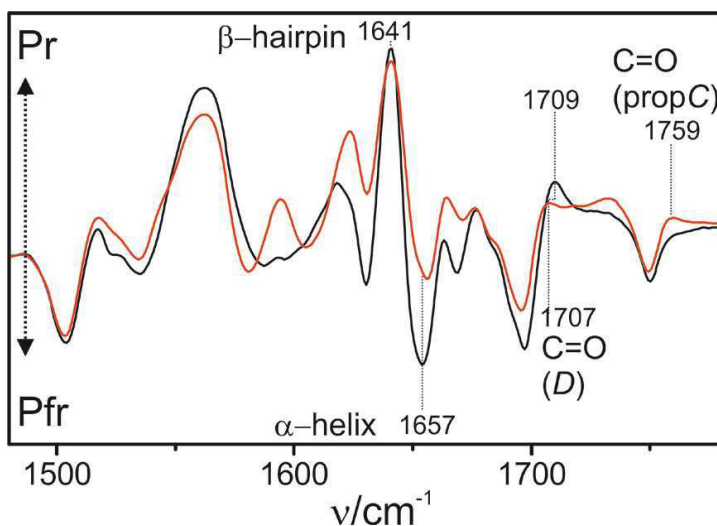


Fig. S9. IR difference spectra “Pr minus Pfr” of the WT Agp2 (black trace) and the Agp2-H278A variant (red trace), measured at ambient temperature at pH 7.8.

In the difference spectrum of Agp2-H278A the intensity of the negative (Pfr) 1657-cm^{-1} band, characteristic of α -helix structural elements, is strongly reduced compared to the WT spectrum, implying a distorted secondary structure in the Pfr state. Thus, the β -hairpin/ α -helix transition associated with the Pr/Pfr conversion is impaired by the His278-to-Ala substitution.

Furthermore, the difference spectrum of Agp2-H278A displays a small positive signal at 1759 cm^{-1} in the region of the C=O stretching of the protonated propionic side chain. This is in contrast to the Pr-minus-Pfr difference spectrum of the WT protein (no positive signal, deprotonated propionic side chain) but reminiscent of the Meta-F-minus-Pfr difference spectrum of the WT Agp2 where a distinct positive signal is observed (protonated propionic side chain - see **Fig. S6**). The C=O stretching of ring *D* of the Agp2-H278A appears to be downshifted and thus partially coincides with the corresponding negative band of Pfr. This interpretation is consistent with the RR spectrum of the Pr state of Agp2-H278 which even at pH 7.8 does not reveal any indication of the enol tautomer (see below, **Fig. S10**).

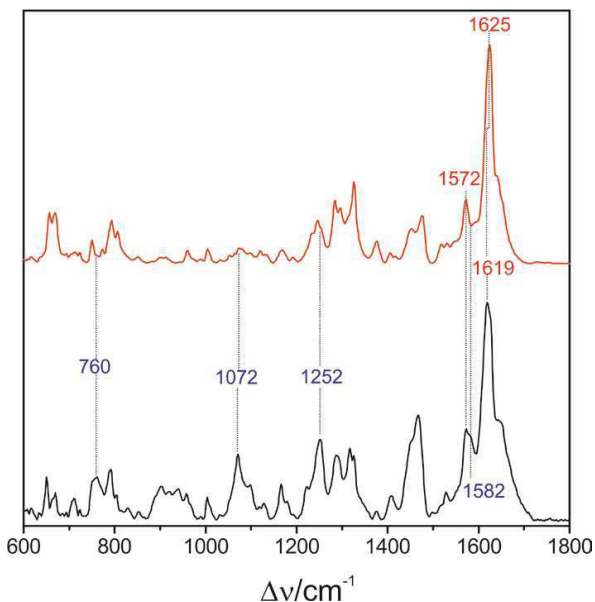


Fig. S10. RR spectra of the Pr state of WT Agp2 (black) and Agp2-H278A (red) at pH 7.8. The spectrum of the mutant displays the vibrational pattern characteristic of the keto form of the chromophore, including the N-H ip bending mode of rings *B* and *C*. In contrast, the WT Agp2 spectrum reflects a mixture of the keto and the enol form, as indicated by characteristic marker bands for the enol (blue labels) and the keto form (red labels).

7. Results: Pr fluorescence tuning parameters in Rph2 phytochrome

7.1. Structural parameters controlling the fluorescence properties of phytochromes

“Reprinted (adapted) with permission from: F. Velazquez Escobar, T. Hildebrandt, T. Utesch, F. J. Schmitt, I. Seuffert, N. Michael, C. Schulz, M. A. Mroginski, T. Friedrich and P. Hildebrandt. Structural parameters controlling the fluorescence properties of phytochromes. *Biochemistry* **2014**, 53, 20–29. [doi:10.1021/bi401287u].
Copyright ©2013 American Chemical Society. ”

- RR spectra were recorded by F. Velazquez Escobar and T. Hildebrandt
- Band analysis was performed by F. Velazquez Escobar
- Protein expression was carried out by Thomas Hildebrandt, I. Seuffert, N. Michael, C. Schulz and T. Friedrich
- Calculations were performed by T. Utesch and M. A. Mroginski
- Fluorescence measurements were performed by F. J. Schmitt
- Research design and development by P. Hildebrandt

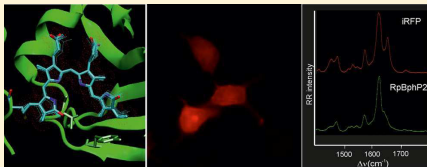
Structural Parameters Controlling the Fluorescence Properties of Phytochromes

Francisco Velazquez Escobar,[§] Thomas Hildebrandt,[§] Tillmann Utesch, Franz Josef Schmitt, Ina Seuffert, Norbert Michael, Claudia Schulz, Maria Andrea Mroginski, Thomas Friedrich, and Peter Hildebrandt*

Technische Universität Berlin, Institut für Chemie, Sekr. PC14, Straße des 17. Juni 135, D-10623 Berlin, Germany

Supporting Information

ABSTRACT: Phytochromes constitute a class of photoreceptors that can be photoconverted between two stable states. The tetrapyrrole chromophore absorbs in the red spectral region and displays fluorescence maxima above 700 nm, albeit with low quantum yields. Because this wavelength region is particularly advantageous for fluorescence-based deep tissue imaging, there is a strong interest to engineer phytochrome variants with increased fluorescence yields. Such targeted design efforts would substantially benefit from a deeper understanding of those structural parameters that control the photophysical properties of the protein-bound chromophore. Here we have employed resonance Raman (RR) spectroscopy and molecular dynamics simulations for elucidating the chromophore structural changes in a fluorescence-optimized mutant (iRFP) derived from the PAS-GAF domain of the bacteriophytochrome RpBphP2 from *Rhodospseudomonas palustris*. Both methods consistently reveal the structural consequences of the amino acid substitutions in the vicinity of the biliverdin chromophore that may account for lowering the probability of nonradiative excited state decays. First, compared to the wild-type protein, the tilt angle of the terminal ring *D* with respect to ring *C* is increased in iRFP, accompanied by the loss of hydrogen bond interactions of the ring *D* carbonyl function and the reduction of the number of water molecules in that part of the chromophore pocket. Second, the overall flexibility of the chromophore is significantly reduced, particularly in the region of rings *D* and *A*, thereby reducing the conformational heterogeneity of the methine bridge between rings *A* and *B* and the ring *A* carbonyl group, as concluded from the RR spectra of the wild-type proteins.



The technological developments in fluorescence microscopy in the past years have prompted substantial efforts for exploiting these methods in biology.^{1–3} Using chemically attached fluorescent dyes, it is possible to monitor specific target biomolecules with a high sensitivity down to the single-molecule level and a spatial resolution beyond the diffraction limit. The chemical modification of biomolecules is, however, only of limited applicability for probing cellular processes. As an alternative for *in vivo* studies, genetically encoded fluorescent proteins or cofactor-protein complexes are used as optical markers by generating fusion constructs with the proteins of interest.^{1,4–7} Widely used genetically encoded fluorescence markers are the green-fluorescent protein (GFP), originally isolated from the marine jellyfish *Aequorea victoria* and its engineered spectral variants, as well as its homologues from other species, which today cover nearly the whole visible spectrum.^{1–3} A substantial drawback of these GFP-derived fluorescent labels is the restriction of the “working” range to the visible spectral region, where they compete with the absorption and emission properties of various natural pigments. Moreover, the significant overlap between their excitation and emission spectra limits the possibilities for spectral demultiplexing in order to discriminate the spatial distribution or the interaction patterns of a larger number of fluorophore-tagged target

molecules. Although in the blue spectral range, problems arise from significant overlap with cellular autofluorescence, the red region suffers from the limited number of available fluorescent proteins, which additionally exhibit limited brightness or photostability.³ Thus, there is still a high demand for additional and improved red and far-red fluorophores to expand the toolkit of fluorescence microscopy and to take benefits from the superior signal-to-noise ratio in this spectral range. To fulfill these necessities, it is highly desirable to utilize photoreceptors absorbing and emitting in the near-infrared optical window.

Biliproteins such as phytochromes fulfill these spectral requirements because the tetrapyrrole cofactor absorbs between 660 and 700 nm and fluorescence maxima are above 700 nm.³ Phytochromes act as photoswitches between two (meta)stable states that are denoted as Pr and Pfr, according to the red and far-red absorption maxima of the chromophore. Photoinduced interconversion between these parent states is linked to the activation or deactivation of a catalytic module, frequently a histidine kinase.

Received: September 15, 2013

Revised: December 4, 2013

Published: December 16, 2013

However, natural phytochromes have an intrinsically low fluorescence quantum yield of usually less than 2%.⁹ As a consequence, significant efforts have been made to genetically engineer variants of bacterial phytochromes, carrying a covalently bound biliverdin (BV) cofactor, to improve the fluorescence properties by increasing the quantum yield, raising the extinction coefficient, and shifting the fluorescence maximum further to the near-infrared. First successful examples have been generated on the basis of the chromophore binding domain (CBD) of bacteriophytochromes.^{4–6} The IFP1.4 variant of DrBphP from *Deinococcus radiodurans* showed an increase of the fluorescence yield from 1.9 to about 7%,⁵ and similar or even higher yields of ca. 6% and 11% were obtained for constructs engineered from the *Rhodospseudomonas palustris* bacteriophytochrome RpBphP2 and RpBphP6, respectively.^{4,6} Although these values are still by far inferior to those of GFP variants, the spectral properties are likely to improve by further genetic optimization. In addition, these far-red chromophores enable novel means of noninvasive deep-tissue monitoring by rapidly emerging photoacoustic tomography or imaging techniques.^{5,10}

It is therefore of particular interest to analyze those structural parameters that control the fluorescence quantum yield and the energies of electronic absorption and fluorescence of BV in phytochromes. In this respect, the recent crystallographic analysis of fluorescing CBD variants of DrBphP constitutes an important basis for correlating photophysical properties of the cofactor with structural changes at the chromophore binding site induced by amino acid substitutions.⁹ Additional information on the excited-state reactions can be derived from ultrafast spectroscopy, as recently shown for mutants of RpBphP2 and RpBphP3.^{11–14}

In this work, we have employed resonance Raman (RR) spectroscopy, combined with molecular dynamics (MD) simulations, to analyze the ground state conformation of the cofactor and its intermolecular interactions within the chromophore binding pocket. Here, we have used these techniques to identify structural changes of the BV chromophore in the fluorescence-optimized mutant iRFP, which was recently used for deep-tissue imaging in mice.⁴ The mutant is derived from the two-domain PAS-GAF fragment of RpBphP2 (termed PG-P2 herein), lacking the PHY domain that is required for the proper phototransformation between the parent states Pr and Pfr and, thus, for its natural biological function.

MATERIALS AND METHODS

Cloning Strategy. For the expression of holophytochrome, we constructed three plasmids bearing the coding sequence for different apo-phytochromes and one plasmid with a heme oxygenase for in-cell biliverdin synthesis. The amino acid sequence of RpBphP2¹⁵ was adopted from Uniprot Q6NSG3 and the iRFP sequence from Filonov et al.¹⁰ cDNAs for RpBphP2 amino acids 1–501 (PAS-GAF-PHY, termed PGP-P2 herein) and iRFP (316 AS) were generated by commercial gene synthesis (GeneArt, Life Technologies) using the GeneOptimizer algorithm to optimize codon usage for expression in mammalian cells (sequences available on request).¹⁶ To obtain the PAS-GAF fragment of RpBphP2 (amino acids 1–316; termed PG-P2 herein), an appropriate stop codon was introduced into the RpBphP2 1–501 cDNA. The cDNAs were excised by *Bam*HI and *Not*I ligated in frame into a modified pQE81L-Amp vector (Qiagen) carrying

an ampicillin resistance gene and harboring an engineered *Not*I restriction site. This resulted in protein sequences with an N-terminal 6xHis tag (N-terminal sequence MRGSHHHHHH-TDPAT) preceding the start methionine of the iRFP, PG-P2, and PGP-P2 sequences.

The cDNA of the human heme oxygenase type 2 (hHox2) was amplified from the IMAGE consortium clone IMAGE:2821444 by PCR, using primers harboring *Sph*I and *Kpn*I restriction sites. The PCR fragment was restricted with *Sph*I and *Kpn*I and ligated in frame into the similarly cut pQE81L-Kan vector, which carries a kanamycin resistance gene. The complete open reading frame of hHox2 cDNA sequence was verified by sequencing (Eurofins MWG Operon). To avoid copurification of hHox2 in Ni²⁺-sepharose column chromatography, the N-terminal 6xHis tag was deleted afterward, using the QuikChange mutagenesis kit (Stratagene). Deletion was verified by sequencing (Eurofins MWG Operon).

In order to accomplish biliverdin cofactor insertion into phytochromes already upon protein expression in *E. coli*, NEBturbo cells (New England Biolabs) were transformed with a 1:1 mixture of pQE81L-Kan plasmid with hHox2 and one of the pQE81L-Amp plasmids with iRFP, PG-P2, or PGP-P2 sequences. The transformed cells were grown overnight at 37 °C on LB-agar selection plates containing 50 µg/mL kanamycin and 50 µg/mL ampicillin.

Expression and Purification. For protein expression, 3 × 400 mL of LB-medium with kanamycin and ampicillin were inoculated from a preculture to 0.1 optical density (OD) and grown at 37 °C in an orbital shaker (200 rpm) to an OD of 0.6. After induction with 500 µM IPTG cells were grown for 24 h at 37 °C (iRFP and wild-type PG-P2) or at 20 °C for 48 h (wild-type PGP-P2). Cells were harvested by centrifugation, yielding deeply blue-green-colored pellets, indicating formation and integration of the intact BV cofactor into the bacteriophytochrome variants. Cell pellets were resuspended in phosphate buffer and lysed by two passages through a French press (18000 psi). After removal of the cell debris by centrifugation (24000g, 4 °C), the clarified supernatant was purified on Ni²⁺-Sephacose columns (GE-Healthcare) according to the manufacturer's manual (20 mM imidazole was supplemented to the supernatant as recommended). Purest fractions (SAR ≥ 1) were pooled and dialyzed against 50 mM Tris–HCl, 300 mM NaCl, 5 mM EDTA (pH 7.8).

For comparison, we have studied the bacteriophytochrome Agp1 from *Agrobacterium tumefaciens*. For this purpose, we have used a PAS-GAF-PHY variant in which the first nine N-terminal residues were deleted and three amino acids on the protein surface were substituted (F289A, M295A, and R296S). These modifications prevent dimerization but do not affect the optical properties or the photoinduced reaction cycle. This protein variant, denoted as Agp1, was expressed and purified as described previously.¹⁷

Buffer solutions used for the RR experiments included 50 mM Tris–HCl, 300 mM NaCl, 5 mM ethylenediaminetetraacetic acid in H₂O (D₂O) at pH (pD) of 7.8. Protein samples were concentrated via Microcon filters up to a value corresponding to an optical density of ca. 40 at 280 nm (ca. 10 mg/mL).

Spectroscopic Measurements. RR measurements were performed using a Bruker Fourier-transform Raman spectrometer RFS 100/S with 1064 nm excitation (Nd:YAG cw laser, line width 1 cm⁻¹) equipped with a nitrogen-cooled cryostat from Resultec (Linkam). The spectra were measured at –140

or +10 °C with a laser power at the sample of 780 mW. In order to identify potential laser-induced damage of the phytochrome samples, spectra before and after a series of measurements were compared. In no case were changes between these control spectra determined. For each spectrum, the accumulation time was 1 h. Protein and buffer Raman bands were subtracted on the basis of a Raman spectrum of apo-phytochrome (Supporting Information, Figure S1). The pure spectra were further analyzed by a band fitting procedure assuming Lorentzian band shapes. H/D exchange involved 5 washing steps with D₂O or H₂O buffer solution (30 min centrifugation at 10000g per step).

Stationary fluorescence spectra were measured with 670 nm excitation in a temperature range from +10 to -140 °C. Further details are given in the Supporting Information.

Molecular Dynamics Simulations. The classical atomistic MD simulations on two monomeric model structures of the PAS-GAF fragment of RpbhP2, namely, the wild-type (WT) protein PG-P2 (PG-P2 model) and the fluorescent mutant iRFP described above (iRFP model), were performed with the NAMD2.7 software.^{18,19} The CHARMM27 force field²⁰ was employed to describe the apoprotein, and the force field parameters for the BV chromophore were extracted from Kaminski et al.²¹ The starting geometry for the PG-P2 model was taken from the crystallographic structure (PDB entry: 4e04). Because this structure corresponds to a mutated form of PG-P2,²² the PG-P2 model was generated by back-mutation of the crystal structure to the original sequence. For this, the Asn105 insertion was deleted and the following amino acids substitutions were attained: P98R, D99K, G100D, E101A, R102G, A103F, F104 V, R127A, Y128E, S135R, V136T, R137N, R237 V, E296D and V297G. Furthermore, the expression tag comprising residues 320 to 327 present in the crystal structure was removed. The iRFP model was constructed by mutating the PG-P2 model at 13 different sites: S13L, A92T, V104I, V114I, E161K, Y193K, F198Y, D202T, I203V, Y258F, A283 V, K288T and N290Y. The two structural models were protonated according to pH 7.0 using the PSFGEN-VMD plugin.²³ On the basis of the visual inspection of the corresponding environments, all histidine residues were protonated at the ϵ -nitrogen except for His285, which was modeled with a proton at the δ -nitrogen. The net charges of the proteins yield -13 and -10 e for the PG-P2 and the iRFP model, respectively. In order to remove bad contacts that may be present in the initial structural models due to mutations and deletion of amino acids, 5000 steps of energy minimization were performed using the conjugated gradient algorithm on the modified regions of each model in vacuum keeping the rest of the protein fixed. Both structural models were then solvated in cuboid boxes of TIP3P water molecules²⁴ with approximate dimensions of 78 × 87 × 112 Å³ (23829 and 23822 water molecules for WT and iRFP models, respectively). In addition, the net charges of the proteins were compensated for by inserting chloride and sodium ions randomly at 25 mM ionic strength. Ionization of the models was carried out using the AUTOIONIZE plugin of VMD.²³ The MD simulations were run under periodic boundary conditions with extended electrostatics using the Particle Mesh Ewald Summation²⁵ with a cutoff distance of 12 Å for the van der Waals interactions and short-ranged electrostatics. The SHAKE algorithm²⁶ was applied to constrain all bond lengths between heavy atoms and hydrogen atoms assuring, in this way, a simulation step of 2 fs. The energies of the solvated systems were initially minimized

with the conjugated gradient integrator using decreasing harmonic constraints on the protein backbone and on the BV cofactor (from 25 to 5 kcal/(mol Å²)). After 60 ps heating using Langevin dynamics with decreasing position restraints on the heavy atoms of the protein cofactor (from 5 to 2.5 kcal/(mol Å²)), the entire system was equilibrated for another 60 ps. During the equilibration run, the harmonic constraints on the protein were gradually released until all atoms were allowed to move freely. Finally the dynamics of the two model systems were simulated for 100 ns at 300 K in an NPT ensemble under constant atmospheric pressure and temperature using the Langevin Piston method.²⁷ Convergence of the trajectories was checked in terms of energetics and root mean square deviations (rmsd) of the protein and the chromophore from the initial structural models. The statistical analysis of the structural properties during the last 40 ns of the MD trajectories was performed with the VMD software.²³

RESULTS

The iRFP mutant was generated from the D202H variant of the PAS-GAF domain of P2 by random mutagenesis, leading to 13 substitutions compared to the wild-type protein PG-P2. Among them, five substitutions (Y193K, F198Y, D202T, I203V, and Y258F) are located in the chromophore binding pocket (Figure 1). These substitutions are likely to be of primary importance

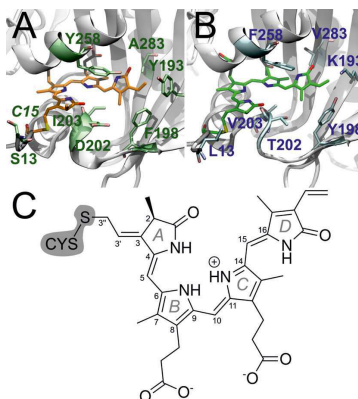


Figure 1. The chromophore binding pocket of (A) wild-type PG-P2 and (B) iRFP, as obtained by 100-ns MD simulations (see text for further details), and (C) the structural formula of the BV chromophore.

for the photophysical properties. For example, the replacement of the highly conserved D202 has been shown to impair photoisomerisation of the chromophore.²⁸ In fact, iRFP was found to be locked in the Pr state (data not shown). Thus, the comparison with the spectra of the wild-type proteins of RpbhP2 and Agp1 discussed in the following only refers to the Pr state.

Resonance Raman Spectroscopy. The overall vibrational band pattern of iRFP does not differ significantly from those of the Pr state of PG-P2 and GPG-P2 proteins and other prototypical BV-binding phytochromes (Figure S3, Supporting

Information). Thus, there are no indications for deviations from the overall ZZZ sa chromophore geometry as determined for the Pr state of various phytochromes.^{29–31} Also, as in the Pr state of all prototypical phytochromes, the cofactor is in the cationic form with all four pyrrole nitrogens carrying a proton. A closer inspection of the spectra, however, reveals spectral differences in three regions as will now be discussed in more detail.

Figure 2 shows the spectral region from 1500 to 1700 cm^{-1} , which is dominated by modes involving the C=C stretching

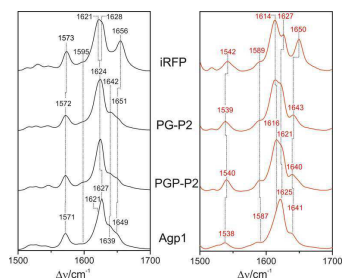


Figure 2. RR spectra of the Pr state of iRFP, PG-P2, PGP-P2, and Agp1 in the C=C stretching region, measured with 1064-nm excitation at -140 °C. Spectra obtained from samples in H_2O (pH 7.8) and D_2O (pD 7.8) are shown on the left (black) and right panel (red), respectively.

coordinates of the methine bridges, ring D , and its vinyl substituent (see Figure 1 for ring numbering). Furthermore, the N—H in-plane bending (N—H ip) mode of the rings B and C gives rise to the band at 1573 cm^{-1} (iRFP), which is a characteristic marker for the protonated state of the cofactor. This band disappears upon H/D exchange and the corresponding counterpart, the N-D ip mode, is observed at 1079 cm^{-1} (Supporting Information, Figure S3).

We refer to previous vibrational analyses of the cofactor in phytochromes, carried out with experimental and theoretical methods, to disentangle the spectrally crowded region between 1590 and 1660 cm^{-1} .^{32–36} Accordingly, the most intense band is due to a mode dominated by the C=C stretching coordinate of the C—D methine bridge. As minor contributions of the N—H ip coordinate are involved, this mode undergoes a small downshift (5–8 cm^{-1}) upon H/D exchange. Thus, this mode is assigned to the 1621 cm^{-1} band in iRFP (1614 cm^{-1} in D_2O). The adjacent, nearly equally intense but H/D insensitive band is then ascribed to a C=C stretching mode of ring D although calculations predict only a low intensity.³⁵ Presumably, also the C—D stretching coordinate that is responsible for high RR activity contributes substantially to the mode at 1628 cm^{-1} . Frequency and intensity of the band at 1656 cm^{-1} and its 6 cm^{-1} downshift in D_2O are consistent with the assignment to the A—B stretching mode. The corresponding B—C stretching mode, which is only weakly Raman-active, is expected at much lower frequencies and, thus, is assigned to the weak shoulder at 1595 cm^{-1} .

Compared to iRFP, the spectra of the “non-fluorescing” phytochrome variants display two distinct differences. First, the ring D C=C stretching (at 1628 cm^{-1} of iRFP) appears at lower frequencies in PG-P2 and PGP-P2, whereas the C—D

stretching remains largely unchanged, as it can be clearly seen in the spectra measured from the proteins in D_2O (Figure 2, Supporting Information, Figure S5). In Agp1, the intensity ratio of the two bands is reversed, implying that the contribution of the C—D stretching coordinate to the higher frequency mode is even larger than in the case of the P2 protein variants. Second, the A—B stretching mode (at 1656 cm^{-1} in iRFP) is observed with a significantly reduced intensity and at a frequency lower by 5–7 cm^{-1} in PG-P2, PGP-P2, and Agp1. For these proteins, an additional nearby band at ca. 1640 cm^{-1} becomes detectable, which might originate from the C=C stretching of the ring D vinyl substituent. However, this mode is predicted to be essentially Raman-inactive such that, as an alternative assignment, both bands may be ascribed to A—B stretching modes originating from two conformers of the tetrapyrrole as previously suggested for Agp1.³⁷ A band fitting analysis suggests that this 1640 cm^{-1} band is also present in iRFP albeit with a much lower relative intensity with respect to the 1650 cm^{-1} band than in PG-P2, PGP-P2, and Agp1 (Supporting Information, Figure S4).

In the region between 600 and 900 cm^{-1} the most remarkable changes refer to the prominent 814 cm^{-1} band of iRFP (Figure 3). The frequency is higher by 4, 8, and 11 cm^{-1}

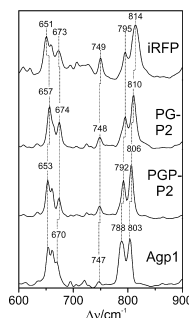


Figure 3. RR spectra of the Pr state of iRFP, PG-P2, PGP-P2, and Agp1 in the HOOP region, measured with 1064 nm excitation at -140 °C. Spectra were obtained from samples in H_2O (pH 7.8).

compared to the PG-P2, PGP-P2, and Agp1 proteins, respectively. This band was assigned to the hydrogen-out-of-plane (HOOP) mode of ring D as confirmed by isotopic labeling and theoretical calculations.^{33,35} As a characteristic feature of phytochromes, this band is usually observed with relatively high RR intensity and its frequency has been shown to be correlated with the torsional angle of the C—D methine bridge.³⁵

Temperature-Dependent Spectral Changes. The RR spectra of iRFP and PG-P2 show only a weak temperature dependence. Upon increasing the temperature from -140 °C to $+10$ °C, many bands display a slight broadening, in some cases accompanied by small frequency shifts that usually, however, do not exceed 3 cm^{-1} (Supporting Information, Figures S6–S8). Specifically, there is no indication for a redistribution of band intensities for those bands in the methine bridge stretching region that have been suggested to represent conformational substates. This is also true for the HOOP mode

at ca. 800 cm^{-1} that in the Pfr state of prototypical phytochromes was found to be the most sensitive marker for a temperature-dependent conformational equilibrium.³⁵ Most remarkably, the 814 cm^{-1} band of iRFP, which already displays a large bandwidth at low temperature (18 cm^{-1}), is not further broadened at room temperature and also the symmetric band shape remains unchanged. This is quite in contrast to the substantial broadening of the 810 cm^{-1} band of PG-P2 from 10 cm^{-1} (-140 °C) to 14 cm^{-1} ($+10$ °C) (Figure 4).

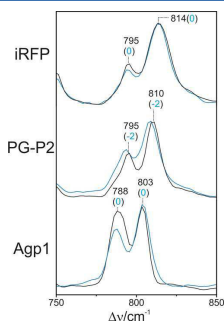


Figure 4. RR spectra of iRFP, PG-P2, and the Pr state of Agp1 measured with 1064 nm excitation. The black and blue traces refer to the measurements at -140 °C and $+10$ °C, respectively. Black labels refer to the peak positions at -140 °C. The blue numbers in parentheses indicate the shift of the peaks at $+10$ °C. Intensities are normalized to the strongest band in each spectrum.

In the region of the torsional and deformation modes between 650 and 680 cm^{-1} , all proteins show a similar behavior (Supporting Information, Figure S8). Here, the slight frequency shifts and band broadening are accompanied by distinct changes of the relative intensities in the room temperature spectra, reflecting a higher mobility of the chromophores in the binding pocket at room temperature.

Also the temperature-dependence of the fluorescence is very similar for iRFP and PG-P2. Upon decreasing the temperature from $+10$ to -140 °C, the fluorescence intensity, measured with 670 nm excitation, increases by up to an order of magnitude in both cases (Supporting Information, Figure S10). Taking into account that this factor refers to the uncorrected intensities (i.e., refractive index change and higher amplitude of the scattered light due to the formation of ice microcrystals during freezing), the intrinsic temperature-dependent increase of the fluorescence yield is lower.

The RR spectrum of Agp1 displays more pronounced temperature-dependent changes in the HOOP region (Supporting Information, Figure S8) because—unlike with iRFP and PG-P2—the intensity ratio of the two bands at 788 and 803 cm^{-1} varies quite substantially with the temperature (Figure 4). It might be that these two bands correspond to C—D methine bridge HOOP modes of two conformers such that the intensity changes reflect a temperature-dependent conformational equilibrium in analogy to the Pfr state of Agp1.³⁵

Carbonyl Stretching Modes. An important marker for protein-tetrapyrrole interactions are the two C=O stretching modes of ring A and D in the region between 1680 and 1740 cm^{-1} . Because in prototypical BV-binding phytochromes, the

carbonyl function of ring A is, unlike ring D, not linked to the conjugated π -electron system of the tetrapyrrole (Figure 1), the ring A C=O stretching mode appears at higher frequencies.³⁸ For the same reason, the RR intensity of this mode is much lower than that of the ring D C=O stretching such that only this latter mode can readily be identified in the low-temperature RR spectra of all proteins in H₂O (Figure 5). This mode is

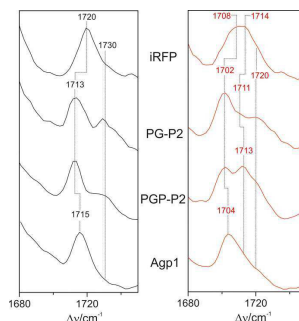


Figure 5. RR spectra of the Pr state of iRFP, PG-P2, PGP-P2, and Agp1 in the C=O stretching region measured with 1064 nm excitation at -140 °C. Spectra obtained from samples in H₂O (pH 7.8) and D₂O (pD 7.8) are shown on the left (black) and right panel (red), respectively.

observed at very similar positions (1713–1716 cm^{-1}) for all “non-fluorescing” protein variants but at a distinctly higher frequency (1720 cm^{-1}) for iRFP. In the case of PG-P2 (PGP-P2), the weak shoulder at ca. 1730 cm^{-1} is attributed to the ring A C=O stretching, whereas this mode can hardly be detected in Agp1 and iRFP. Upon raising the temperature to $+10$ °C, the bands of the ring D C=O stretching mode broaden for all proteins, accompanied by small frequency downshifts as observed for other tetrapyrrole modes (vide supra). As a consequence, the weak C=O stretching of ring A becomes also visible in the spectrum of iRFP at ca. 1730 cm^{-1} (Supporting Information, Figure S9). This mode remains essentially Raman-inactive in Agp1, but it can be detected at the same position in the IR “Pr–minus–Pfr” difference spectrum. Note that the IR difference spectra for PG-P2 and PGP-P2 (not shown) also support the assignments of the C=O stretching, in agreement with the previously published data by Toh et al.¹²

The frequencies of the C=O stretching modes depend on the (hydrogen bond) interactions of the carbonyl function with its immediate environment and on the coupling of the C=O stretching and N—H ip coordinates. This coupling, which may vary with structural perturbations of the respective pyrrole ring, is also the origin for the distinct H/D sensitivity of these modes. In fact, in D₂O, both modes shift down to lower frequencies but, most remarkably, the altered normal mode composition leads, in general, to a relative intensity increase of the ring A C=O stretching mode (Figure 5). Thus, it is even possible to identify two band components of this mode at ca. 1711–1714 cm^{-1} and ca. 1720 cm^{-1} , albeit with different relative intensities for the four proteins. In PG-P2, both components display comparable intensities whereas in iRFP the higher frequency component is much weaker. The downshift of

the ring D C=O stretching is essentially the same (11–12 cm^{-1}) in all four proteins.

Molecular Dynamics Simulations. The stability of the structural models for the wild-type PG-P2 protein and the iRFP mutant was initially checked by analyzing the evolution in time of the root mean square deviation (rmsd) of all carbon α atoms of the protein and of all heavy atoms belonging to the biliverdin chromophore (Figure 6). A plateau is reached within the first

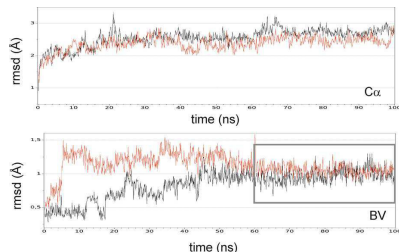


Figure 6. Evolution of the root mean square deviation (rmsd) of the $C\alpha$ atoms (top) and the heavy atoms of the BV chromophore (bottom) of PG-P2 during the 100 ns MD simulation. Black and red traces refer to the PG-P2 and iRFP model, respectively.

20 ns, with a mean rmsd value of 2.7 Å and 2.4 Å for the PG-P2- and the iRFP-models, respectively. The rmsd of the chromophore atoms, however, converge only after 60 ns MD simulation reaching a mean value of 1.0 Å for both models. For this reason, the statistical analysis of the MD trajectories was restricted to the last 40 ns because in this time span, we can assume that the protein and the chromophore reached a thermodynamic equilibrium.

The structural differences between PG-P2 wild-type protein and the iRFP mutant and their dynamic properties were analyzed by following the time evolution of selected structural parameters, such as the tilt angles between pyrrole rings and the bond and torsional angles of the BV methine bridges, and by computing their statistical distribution. In addition, the root mean square fluctuations (rmsf) of selected atoms of the BV chromophore were calculated in order to estimate and quantify the mobility of the chromophore atoms in the binding pockets of the two structural models.

The frequency distribution (counts) of the three tilt angles between adjacent pyrrole rings is shown in the Supporting Information (Figure S11), and the mean values and corresponding standard deviations are listed in Table 1. In the case of the rings B and C, there is no difference between the tilt angles computed for the PG-P2 and iRFP models, indicating that mutations of the chromophore binding pocket do not significantly alter the orientation of the two inner rings with respect to each other. This is, however, not the case for rings A and B and rings C and D. Although the A–B tilt angle decreases from 24° in the PG-P2 model to 21° in the iRFP model, the C–D tilt angle increases by ca. 8°. For both tilt angles, the standard deviations predicted for the PG-P2 structure are slightly higher (1°) than those computed for the mutant, reflecting a slightly restricted flexibility of the outer rings of the tetrapyrrole chromophore in the iRFP model (vide infra). The analysis of the torsional angles at the methine bridges (Supporting Information, Figure S12) shows that the

Table 1. Selected Structural Parameters of the BV Chromophore in the PG-P2 and iRFP Models.^a

	WT	iRFP
Bond Lengths		
C(4)=C(5)	1.3654 (0.03)	1.3647 (0.03)
C(5)–C(6)	1.4262 (0.03)	1.4229 (0.03)
C(9)–C(10)	1.3802 (0.03)	1.3782 (0.03)
C(10)–C(11)	1.3767 (0.03)	1.3780 (0.03)
C(14)–C(15)	1.4254 (0.03)	1.4267 (0.03)
C(15)=C(16)	1.3651 (0.03)	1.3681 (0.03)
Bond Angles		
C(4)–C(5)–C(6)	20.5 (7.7)	16.6 (6.3)
C(9)–C(10)–C(11)	–5.1 (5.8)	–6.8 (6.5)
C(14)–C(15)–C(16)	–106.8 (13.5)	–111.8 (9.6)
Dihedral Angles		
N(A)–(C4)=C(5)–C(6)	15.8 (6.9)	15.0 (7.4)
(C4)=C(5)–C(6)–N(B)	9.2 (8.3)	5.5 (7.8)
N(B)–C(9)–C(10)–C(11)	7.1 (8.5)	–3.0 (8.6)
C(9)–C(10)–C(11)–N(C)	–13.3 (8.6)	–5.5 (9.5)
N(C)–C(14)–C(15)=C(16)	–125.5 (10.3)	–137.1 (8.3)
C(14)–C(15)=C(16)–N(D)	14.5 (9.4)	17.0 (9.3)
Tilt Angles		
A–B	24.0 (7.5)	21.0 (6.5)
B–C	11.3 (5.0)	10.7 (4.9)
C–D	116.8 (8.2)	124.2 (7.1)

^aMean values and corresponding standard deviations (in brackets) were computed for the last 40 ns of the MD trajectory. Bond lengths are given in Å and angles in degrees. Coordinates are defined according to inset of Figure 6.

changes of the tilt angles between the pyrrole rings are mainly due to twists of the C–C single bond at the corresponding methine bridge. Although there is no variation of the B–C tilt angle upon mutation, the torsional angles at the B–C methine bridge differ significantly between the two protein models. In particular, the mean values for the N(B)–C(9)–C(10)–C(11) and C(9)–C(10)–C(11)–N(C) torsional angles of the PG-P2 model, which are higher than those predicted for iRFP, point to a stronger distortion of the B–C methine bridge in the wild-type protein. Other important structural parameters, which may strongly influence the spectroscopic pattern in the fingerprint region, are the bond angles and the C–C bond lengths at the tetrapyrrole methine bridges. The statistical distribution of the bond angles during the last 40 ns are plotted in Figure S13 (Supporting Information). In average, there is a decrease of the C(4)–C(5)–C(6) bond angle in the iRFP mutant compared to the wild-type protein together with a slight shortening of the C(4)=C(5) bond and the elongation of the C(5)–C(6) bonds, reflecting a weakening of the π -electron conjugation at the A–B methine bridge. Such changes in the electron density of the A–B bridge should shift the vibrational frequency of the C=C stretching mode to higher values, as it is in fact observed in the experimental RR spectra (Figure 2). In a similar way, the slightly elongated C=C bond at the C–D methine bridge of iRFP may explain the 3 cm^{-1} downshift of the C–D stretching frequency compared to the wild-type protein.

The rmsf values computed for the backbone atoms of the BV chromophore of the PG-P2 and iRFP models over the last 40 ns of the MD simulation are larger for the PG-P2 model compared to those of the iRFP mutant, especially in the regions

corresponding to ring A (atoms 1–4) and ring D (atoms 16–21) (Figure 7).

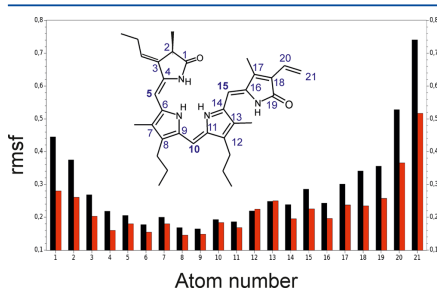


Figure 7. Root mean square fluctuations (rmsf) of heavy atoms in the BV chromophore. Inset: Structural formula of BV indicating the heavy atoms considered for the rmsf plot in blue.

DISCUSSION

Structural Changes in the iRFP Variant Protein. The analysis of the RR spectra together with the results of the MD simulations indicate that the structural changes brought about by the amino acid substitutions in iRFP primarily refer to the C—D and A—B methine bridges as well as to the respective terminal rings A and D including their carbonyl functions.

The most sensitive spectral marker for structural changes at the C—D methine bridge is the HOOP mode at ca. 800 cm^{-1} . Its frequency is inversely correlated with the C(14)—C(15)—C(16)—N(D) dihedral angle as previously determined for the Pfr state of the BV-binding PaBphP.³⁵ The significant frequency upshift of this mode in iRFP (800 cm^{-1}) compared to the other protein variants indicates an increase of this angle, consistent with the MD simulations that predict a slightly increased tilt angle of ring D with respect to ring C. This structural perturbation is attributed to two factors. First, the Y193K and F198Y substitutions cause structural changes in chromophore binding pocket that primarily involve the immediate environment of ring D, thereby affecting the C—D methine bridge geometry (Supporting Information, Figure S14). In this way, the side chain of Tyr198 comes in close contact to ring D which also provides an explanation for the unusually broad and temperature-independent bandwidth of the C—D methine bridge HOOP mode. The spatial proximity of the aromatic ring of Tyr198 to the C—D methine bridge and the small energy difference between the HOOP mode at 814 cm^{-1} of the chromophore and the tyrosine ring breathing mode³⁹ at ca. 830 cm^{-1} may allow for vibrational energy transfer from the chromophore to Tyr198 which is reflected by the broadening of the HOOP mode. A similar mechanism was shown to account for the band broadening of the C=N stretching mode of the retinal chromophore in bacteriorhodopsin.⁴⁰ Second, the substitution of Tyr258 by a phenylalanine leads to a more hydrophobic environment of ring D in the iRFP mutant. Here, the structural model for iRFP shows a highly perturbed hydrogen bond network around the carbonyl group at ring D (Supporting Information, Figure S16). According to the statistics, the number of water molecules close (within a 5 Å distance, see Table 2) to the carbonyl group is reduced by one

Table 2. Statistics of Single and Double Hydrogen Bond Interactions between Carbonyl Groups of BV and the Environment in the PG-P2 and iRFP Models during the Production Run of the MD Simulations (60 ns–100 ns)^a

	C=O (A)		C=O (D)		
	WT	iRFP	WT	iRFP	
number of H-bond events	no interaction	158	195	166	392
	single	212	181	230	8
	double	30	14	4	0
occupancy	58%	49%	59%	2%	
minimum H-bond donor—acceptor distance (Å)	2.75	2.77	2.76	2.69	

^aHydrogen bonds are defined by considering a donor—acceptor distance <3.0 Å and an angle cutoff of 20°.

in the mutant. Moreover, the C=O(D) does not form any hydrogen bond neither with the protein nor with water in the iRFP structure (Table 1). The lack of any hydrogen bond interactions of the ring D carbonyl function thus well explains the upshift of the C=O stretching mode in iRFP compared to PG-P2.

Additional structural changes refer to ring A and the A—B methine bridge. The spectra of the WT proteins PG-P2 and PGP-P2 and Agp1 display two bands attributable to the ring A C=O stretching modes, corresponding to two substates of slightly different structures or environmental interactions of the carbonyl group. It is therefore tempting to relate these two substates with a structural heterogeneity at the A—B methine bridge that may be derived from the $1640/1650\text{ cm}^{-1}$ band pair (vide supra). As judged from the spectra both in the C=O and the A—B stretching region, such a structural heterogeneity is much less pronounced for iRFP than for PG-P2 (PGP-P2). This conclusion is again consistent with findings from the MD simulations, which indicate a more rigid fixation of the chromophore within the protein. This is reflected by the much lower rmsf values for the carbon atom positions of the chromophore in the mutant compared to the wild-type protein. Specifically, for ring A and ring D, these values are lowered by ca. 30% in the mutant.

For the fluorescence-optimized iRFP and the “non-fluorescent” PG-P2, the temperature-dependent variations in the RR spectra are largely restricted to minor frequency shifts and the expected effects on the band widths. Furthermore, the fluorescence intensity increases by the same factor for both proteins upon temperature lowering from +10 to $-140\text{ }^{\circ}\text{C}$. These findings can be understood in terms of a reduced mobility of the chromophore in the binding pocket at low temperature. However, there are no indications for temperature-dependent changes of the structural heterogeneity implying that the distribution among the various substates is largely the same at ambient temperature and $-140\text{ }^{\circ}\text{C}$. Nevertheless, the RR and fluorescence spectroscopic data are consistent with the view that the substates constituting the chromophore heterogeneity differ with respect to the photochemical properties, specifically fluorescence and photochemical quantum yields.

Structural Parameters Controlling the Fluorescence Properties. To increase the fluorescence quantum yield, the competing processes (that is, photoisomerisation and internal conversion of the excited state) must be slowed down. The main factors that influence the interplay of the various excited state processes have been recently discussed by Auldridge et al.⁷

Photoisomerisation is readily impaired by substituting the highly conserved Asp202 by any other amino acid. This is primarily attributed to the lack of a carboxyl side chain at a proper position for stabilizing the (distorted) ZZE_{ssa} configuration in the excited state via interaction with the ring D N—H group. The second effect of a substitution at this position is the reorganization of the local hydrogen bond network, which may perturb an important thermal deactivation channel via excited state proton transfer of the cofactor to a nearby water molecule or the carbonyl function of the amino acid at position 202.¹¹ A distortion of the hydrogen bond interactions, specifically of the ring A carbonyl, has been demonstrated by the crystallographic analysis of the fluorescing CBD variant D207H of DrBphP. Although comparable changes in the hydrogen bond interactions cannot be derived from the present theoretical analysis, a perturbation of the decay channel via excited state proton transfer cannot be ruled out for iRFP^{12,14} because the RR spectra do in fact indicate structural changes of the A—B methine bridge and the ring A carbonyl. However, as a main conclusion of this work, we suggest that the increased rigidity of the chromophore in particular at the terminal rings A and D disfavors internal conversion as an energy dissipation pathway. A more rigid embedment of the chromophore into the protein matrix would also stabilize the ZZE_{ssa} configuration and thus the Pr state, which is assumed to be the third factor relevant for increasing the fluorescence quantum yield. Here, the substitution of the tyrosine residue at position 258 by a phenylalanine, which also hinders photoisomerisation,¹⁴ may play an important role by strengthening the hydrophobic interactions with ring D and providing a tighter packing of this part of the chromophore.

The previous crystallographic study on fluorescent CBD variants of DrBphP has demonstrated that the effects of single amino acid substitutions on the structure of the chromophore pocket and the photophysical properties are not just additive such that the consequences of multiple substitutions can hardly be predicted.⁹ As an alternative to the time-consuming determination of the crystal structure, RR spectroscopy represents a rapid approach for correlating specific structural parameters with the fluorescent properties of the chromophore even though more systematic studies are required. Such studies may not necessarily be restricted to establish relationships between specific RR marker bands and the fluorescence yield. Moreover, the structural basis of other photophysical properties that are important for potential applications of phytochromes as fluorescence labels, such as the energy of the absorption and fluorescence maxima, is as well reflected by the RR spectra as recently shown for a cyanobacteriochrome.⁴¹ In this way, RR spectroscopy may become an important tool for the rational design and evolution of phytochrome-based fluorescence markers.

■ ASSOCIATED CONTENT

Supporting Information

Figures containing additional RR spectra, fluorescence data, plots resulting from the statistical analysis of the BV structure along the MD simulations, and description of the effects of the point mutations on the chromophore binding pocket. This material is available free of charge via the Internet at <http://pubs.acs.org>.

■ AUTHOR INFORMATION

Corresponding Author

*P. Hildebrandt. Phone: +49-30-314-21419. Fax: +49-30-314-21122. E-mail: Hildebrandt@chem.tu-berlin.de.

Author Contributions

[§]Equal contribution to this work.

Funding

The work was supported by the deutsche Forschungsgemeinschaft via the SFB1078 (M.A.M.; P.H.) and the Cluster of Excellence "Unifying Concepts in Catalysis" (T.F.)

Notes

The authors declare no competing financial interest.

■ ACKNOWLEDGMENTS

The authors thank the "Norddeutscher Verbund für Hoch- und Höchstleistungsrechnen" (HLRN) for providing computer power and Neslihan N. Tavraz for technical support.

■ ABBREVIATIONS

App1, bacteriophytochrome P1 from *Agrobacterium tumefaciens*; BV, biliverdin; CBD, chromophore binding domain; DrBphP, bacteriophytochrome from *Deinococcus radiodurans*; EDTA, ethylenediaminetetraacetic acid; GAF, cGMP-specific phosphodiesterases, adenylate cyclases, formate hydrogen lyase transcription activator; GFP, green-fluorescent protein; HOOP, hydrogen-out-of-plane vibrational mode; iRFP, fluorescence-optimized mutant of bacteriophytochrome P2 from *Rhodospseudomonas palustris*; MD, molecular dynamics (simulation); Nd:YAG, neodymium-doped yttrium aluminum garnet; N—H ip, nitrogen—hydrogen in plane bending; NPT, isothermic-isobaric ensemble; OD, optical density; PAS, PER/ARNT/SIM protein domain; PG-P2 (PGP-P2), PAS-GAF (PAS-GAF-PHY) fragment of bacteriophytochrome P2 from *Rhodospseudomonas palustris*; PHY, phytochrome-specific domain; Pr (Pfr), red-absorbing (far-red-absorbing) states of phytochromes; rmsd, root mean square deviations; rmsf, root mean square fluctuations; RpBphP2 (RpBphP3, RpBphP6), bacteriophytochrome P2 (P3, P6) from *Rhodospseudomonas palustris*; RR, resonance Raman; SAR, specific absorption ratio.

■ REFERENCES

- (1) Giepmans, B. N.; Adams, S. R.; Ellisman, M. H., and Tsien, R. Y. (2006) The fluorescent toolbox for assessing protein location and function. *Science* 312, 317–324.
- (2) Stepanenko, O. V.; Schcherbakova, D. M.; Kuznetsova, I. M., and Verkhusha, V. V. (2011) Modern fluorescent proteins: from chromophore formation to novel intracellular applications. *Biotechniques* 51, 313–318.
- (3) Schcherbakova, D. M.; Subach, O. M., and Verkhusha, V. V. (2012) Red fluorescent proteins: advanced imaging applications and future design. *Angew. Chem., Int. Ed.* 51, 10724–10738.
- (4) Filonov, G. S.; Piatkevich, K. D.; Ting, L. M.; Zhang, J.; Kim, K., and Verkhusha, V. V. (2011) Bright and stable near-infrared fluorescent protein for in vivo imaging. *Nat. Biotechnol.* 29, 757–761.
- (5) Shu, X.; Royant, A.; Lin, M. Z.; Aguilera, T. A.; Lev-Ram, V.; Steinbach, P. A., and Tsien, R. Y. (2009) Mammalian Expression of Infrared Fluorescent Proteins Engineered from a Bacterial Phytochrome. *Science* 324, 804–807.
- (6) Schcherbakova, D. M., and Verkhusha, V. V. (2013) Near-infrared fluorescent proteins for multicolor in vivo imaging. *Nat. Methods* 10, 751–754.
- (7) Losi, A.; Gärtner, W.; Raffelberg, S.; Zanacchi, F. C.; Bianchini, P.; Diaspro, A.; Mandalari, C.; Abbruzzetti, S., and Viappiani, C. (2013) A

- photochromic bacterial photoreceptor with potential for super-resolution microscopy. *Photochem. Photobiol. Sci.* 12, 231–235.
- (8) Rockwell, N., and Lagarias, J. (2010) A Brief History of Photochromes. *ChemPhysChem* 11, 1172–1180.
- (9) Aldridge, M. E., Satyshur, K. A., Anstrom, D. M., and Forest, K. T. (2012) Structure-guided engineering enhances phytochrome-based infrared fluorescent protein. *J. Biol. Chem.* 287, 7000–7009.
- (10) Filonov, G. S., Krumholz, A., Xia, J., Yao, J., Wang, L. V., and Verkhusha, V. V. (2012) Deep-tissue photoacoustic tomography of a genetically encoded near-infrared fluorescent probe. *Angew. Chem., Int. Ed.* 51, 1448–1451.
- (11) Toh, K. C., Stojkovic, E. A., van Stokkuma, I. H. M., Moffat, K., and Kennis, J. T. M. (2010) Proton-transfer and hydrogen-bond interactions determine fluorescence quantum yield and photochemical efficiency of bacteriophytochrome. *Proc. Natl. Acad. Sci. U. S. A.* 107, 9170–9175.
- (12) Toh, K. C., Stojkovic, E. A., Rupenyan, A. B., van Stokkum, I. H. M., Salumbides, M., Groot, M. L., Moffat, K., and Kennis, J. T. M. (2011) Primary Reactions of Bacteriophytochrome Observed with Ultrafast Mid-Infrared Spectroscopy. *J. Phys. Chem. A* 115, 3778–3786.
- (13) Lehtivuori, H., Rissanen, I., Takala, H., Bamford, J., Tkachenko, N. V., and Ihalaainen, J. A. (2013) Fluorescence Properties of the Chromophore-Binding Domain of Bacteriophytochrome from *Deinococcus radiodurans*. *J. Phys. Chem. B* 117, 11049–11057.
- (14) Toh, K. C., Stojkovic, E. A., van Stokkum, I. H. M., Moffat, K., and Kennis, J. T. M. (2011) *Phys. Chem. Chem. Phys.* 13, 11985–11997.
- (15) Giraud, E., Zappa, S., Vuillet, L., Adriano, J. M., Hannibal, L., Fardoux, J., Berthomieu, C., Bouyer, P., Pignol, D., and Vernetglio, A. (2005) A new type of bacteriophytochrome acts in tandem with a classical bacteriophytochrome to control the antennae synthesis in *Rhodospseudomonas palustris*. *J. Biol. Chem.* 280, 32389–32397.
- (16) Raab, D., Graf, M., Notka, F., Schödl, T., and Wagner, R. (2010) The GeneOptimizer algorithm: using a sliding window approach to cope with the vast sequence space in multiparameter DNA sequence optimization. *Syst. Synth. Biol.* 4, 215–225.
- (17) Noack, S., Michael, N., Rosen, R., and Lamparter, T. (2007) Protein conformational changes of Agrobacterium phytochrome Agp1 during chromophore assembly and photoconversion. *Biochemistry* 46, 4164–4176.
- (18) Phillips, J. C., Braun, R., Wang, W., Gumbart, J., Tajkhorshid, E., Villa, E., Chipot, C., Skeel, R. D., Kale, L., and Schulten, K. (2005) Scalable molecular dynamics with NAMD. *J. Comput. Chem.* 26, 1781–1802.
- (19) NIH Center for Macromolecular Modeling & Bioinformatics, University of Illinois at Urbana–Champaign. <http://www.ks.uiuc.edu/Research/namd/> (2013).
- (20) MacKerell, A. D., Jr., Bashford, D., Bellott, M., Dunbrack, R. L., Jr., Evanseck, J. D., Field, M. J., Fischer, S., Gao, J., Guo, H., Ha, S., Joseph-McCarthy, D., Kuchnir, L., Kuczera, K., Lau, F. T. K., Mattos, C., Michnick, S., Ngo, T., Nguyen, D. T., Prodhom, B., Reiher, W. E. I. I., Roux, B., Schlenkrich, M., Smith, J. C., Stote, R., Straub, J., Watanabe, H., and Karplus, M. (1998) All-Atom Empirical Potential for Molecular Modeling and Dynamics Studies of Proteins. *J. Phys. Chem. B* 102, 3586–3616.
- (21) Kaminski, S., Daminelli-Widany, G., and Mroginowski, M. A. (2009) Molecular Dynamics Simulations of the Chromophore Binding Site of *Deinococcus radiodurans* Bacteriophytochrome Using New Force Field Parameters for the Phytochromobilin Chromophore. *J. Phys. Chem. B* 113, 945–958.
- (22) Bellini, D., and Papiz, M. Z. (2012) Dimerization properties of the RpBphP2 chromophore-binding domain crystallized by homologue-directed mutagenesis. *Acta Crystallogr., Sect. D: Biol. Crystallogr.* 68, 1058–1066.
- (23) Humphrey, W., Dalke, A., and Schulten, K. (1996) VMD: Visual molecular dynamics. *J. Mol. Graph.* 14, 33–38.
- (24) Jorgensen, W. L., Chandrasekhar, J., Madura, J. D., Impey, R. W., and Klein, M. L. (1983) Comparison of Simple Potential Functions for Simulating Liquid Water. *J. Chem. Phys.* 79, 926–935.
- (25) Darden, T. Y. D., and Pedersen, L. (1993) Particle Mesh Ewald - An N.Log(N) Method for Ewald Sums in Large Systems. *J. Chem. Phys.* 98, 10089–10092.
- (26) Van Gunsteren, W. F., and Berendsen, H. J. C. (1977) Algorithms for macromolecular dynamics and constraint dynamics. *Mol. Phys.* 34, 1311–1327.
- (27) Feller, S. E., Zhang, Y. H., Pastor, R. W., and Brooks, B. R. (1995) Constant-Pressure Molecular-Dynamics Simulation - the Langevin Piston Method. *J. Chem. Phys.* 103, 4613–4621.
- (28) Wagner, J. R., Zhang, J. R., von Stetten, D., Guenther, M., Murgida, D. H., Mroginowski, M. A., Walker, J. M., Forest, K. T., Hildebrandt, P., and Vierstra, R. D. (2008) Mutational analysis of *Deinococcus radiodurans* bacteriophytochrome reveals key amino acids necessary for the photochromicity and proton exchange cycle of phytochromes. *J. Biol. Chem.* 283, 12212–12226.
- (29) Wagner, J. R., Zhang, J. R., Brunzelle, J. S., Vierstra, R. D., and Forest, K. T. (2007) High resolution structure of *Deinococcus bacteriophytochrome* yields new insights into phytochrome architecture and evolution. *J. Biol. Chem.* 282, 12298–12309.
- (30) Yang, X., Stojkovic, E. A., Kuk, J., and Moffat, K. (2007) Crystal structure of the chromophore binding domain of an unusual bacteriophytochrome, RpBphP3, reveals residues that modulate photoconversion. *Proc. Natl. Acad. Sci. U. S. A.* 104, 12571–12576.
- (31) Essen, L. O., Hughes, J., and Mailliet, J. (2008) The structure of a complete phytochrome sensory module in the Pr ground state. *Proc. Natl. Acad. Sci. U. S. A.* 105, 14709–14714.
- (32) Mroginowski, M. A., von Stetten, D., Escobar, F. V., Strauss, H. M., Kaminski, S., Scheerer, P., Günther, M., Murgida, D. H., Schmieder, P., Bongards, C., Gärtner, W., Mailliet, J., Hughes, J., Essen, L. O., and Hildebrandt, P. (2009) Chromophore Structure of Cyanobacterial Phytochrome Cph1 in the Pr State: Reconciling Structural and Spectroscopic Data by QM/MM Calculations. *Biophys. J.* 96, 4153–4163.
- (33) Mroginowski, M. A., Kaminski, S., von Stetten, D., Ringsdorf, S., Gärtner, W., Essen, L. O., and Hildebrandt, P. (2011) Structure of the Chromophore Binding Pocket in the Pr State of Plant Phytochrome phyA. *J. Phys. Chem. B* 115, 1220–1231.
- (34) Mroginowski, M. A., von Stetten, D., Kaminski, S., Velazquez Escobar, F., Michael, N., Daminelli-Widany, G., and Hildebrandt, P. (2011) Elucidating photoinduced structural changes in phytochromes by the combined application of resonance Raman spectroscopy and theoretical methods. *J. Mol. Struct.* 993, 15–25.
- (35) Salewski, J., Velazquez, F., Kaminski, S., von Stetten, D., Keidel, A., Rippers, Y., Michael, N., Scheerer, P., Piwowarski, P., Bartl, F., Frankenberg-Dinkel, N., Ringsdorf, S., Gärtner, W., Lamparter, T., Mroginowski, M. A., and Hildebrandt, P. (2013) The structure of the biliverdin cofactor in the Pfr state of bathy and prototypical phytochromes. *J. Biol. Chem.* 288, 16800–16814.
- (36) Schwinte, P., Foersterndorf, H., Hussain, Z., Gärtner, W., Mroginowski, M. A., Hildebrandt, P., and Siebert, F. (2008) FTIR study of the photoinduced processes of plant phytochrome phyA using isotope-labeled bilins and density functional theory calculations. *Biophys. J.* 95, 1256–1267.
- (37) von Stetten, D., Guenther, M., Scheerer, P., Murgida, D. H., Mroginowski, M. A., Krauss, N., Lamparter, T., Zhang, J., Anstrom, D. M., Vierstra, R. D., Forest, K. T., and Hildebrandt, P. (2008) Chromophore heterogeneity and photoconversion in phytochrome crystals and solution studied by resonance Raman spectroscopy. *Angew. Chem., Int. Ed.* 47, 4753–4755.
- (38) Piwowarski, P., Ritter, E., Hofmann, K. P., Hildebrandt, P., von Stetten, P., Scheerer, P., Michael, N., Lamparter, T., and Bartl, F. (2010) Light Induced Activation of Bacterial Phytochrome Agp1 Monitored by Static and Time Resolved FTIR Spectroscopy. *ChemPhysChem* 11, 1207–1214.
- (39) Siamwiza, M. N., Lord, R. C., Chen, M. C., Takamatsu, T., Harada, I., Matsuura, H., and Shimanouchi, T. (1975) Interpretation of the doublet at 850 and 830 cm⁻¹ in the Raman spectra of tyrosyl residues in proteins and certain model compounds. *Biochemistry* 14, 4870–4876.

(40) Hildebrandt, P., and Stockburger, M. (1984) Role of Water in Bacteriorhopsins Chromophore: A Resonance Raman Study. *Biochemistry* 23, 5539–5548.

(41) Velazquez Escobar, F., Utesch, T., Narikawa, R., Ikeuchi, M., Mroginski, M. A., Gärtner, W., and Hildebrandt, P. (2013) Photoconversion mechanism of the second GAF domain of cyanobacteriochrome AnPixJ and the cofactor structure of its green-absorbing state. *Biochemistry* 52, 4871–4800.

Supporting Information

Structural parameters controlling the fluorescence properties of phytochromes

Francisco Velazquez Escobar, Thomas Hildebrandt, Tillmann Utesch, Franz-Josef Schmitt, Ina Seuffert, Norbert Michael, Claudia Schulz, Maria Andrea Mroginski, Thomas Friedrich, and Peter Hildebrandt*

**Technische Universität Berlin, Institut für Chemie, Sekr. PC14, Straße des 17. Juni 135,
D-10623 Berlin, Germany**

Content:

- 1. Additional RR, IR, and fluorescence spectra (Figs. S1 – S10)**
- 2. Additional data of the MD simulations (Figs. S11 –S14)**
- 3. Effect of the point mutations on the chromophore binding pocket (Figs. S15 – S17)**

1. Additional RR spectra

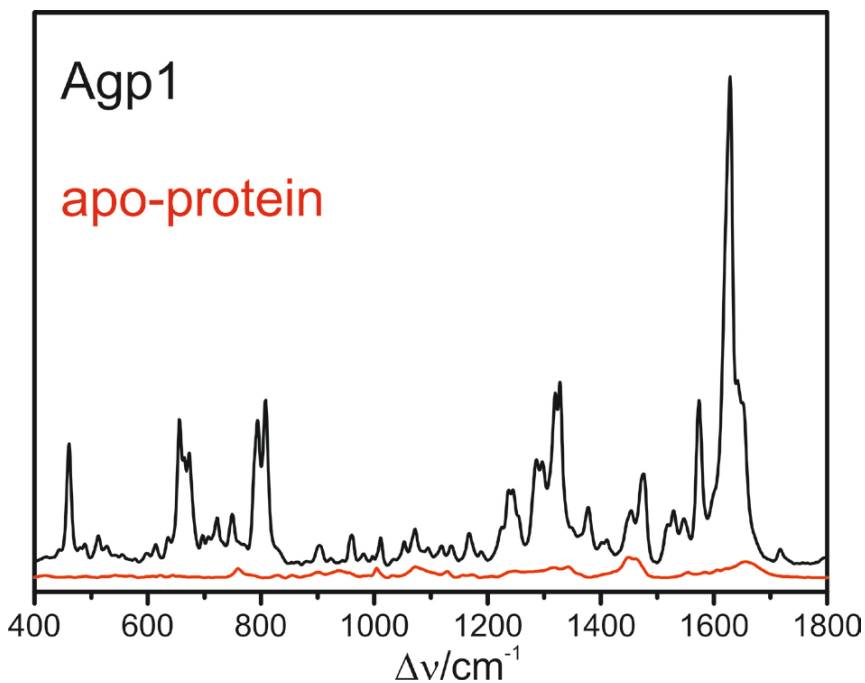


Fig. S1. RR spectrum of the Pr state of Agp1 (black) and the Raman spectrum of the apo-protein (red) measured with 1064 nm excitation at -140°C .

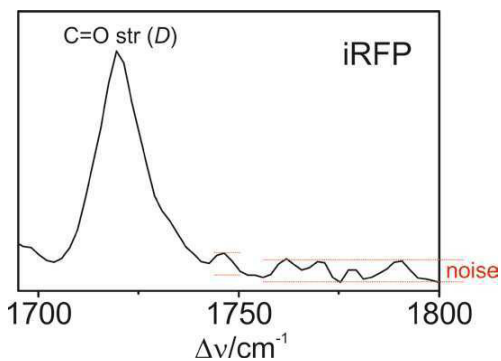


Fig. S2. RR spectrum of iRFP in the C=O stretching region measured with 1064 nm excitation at -140°C (black). The red dotted lines indicate the noise level.

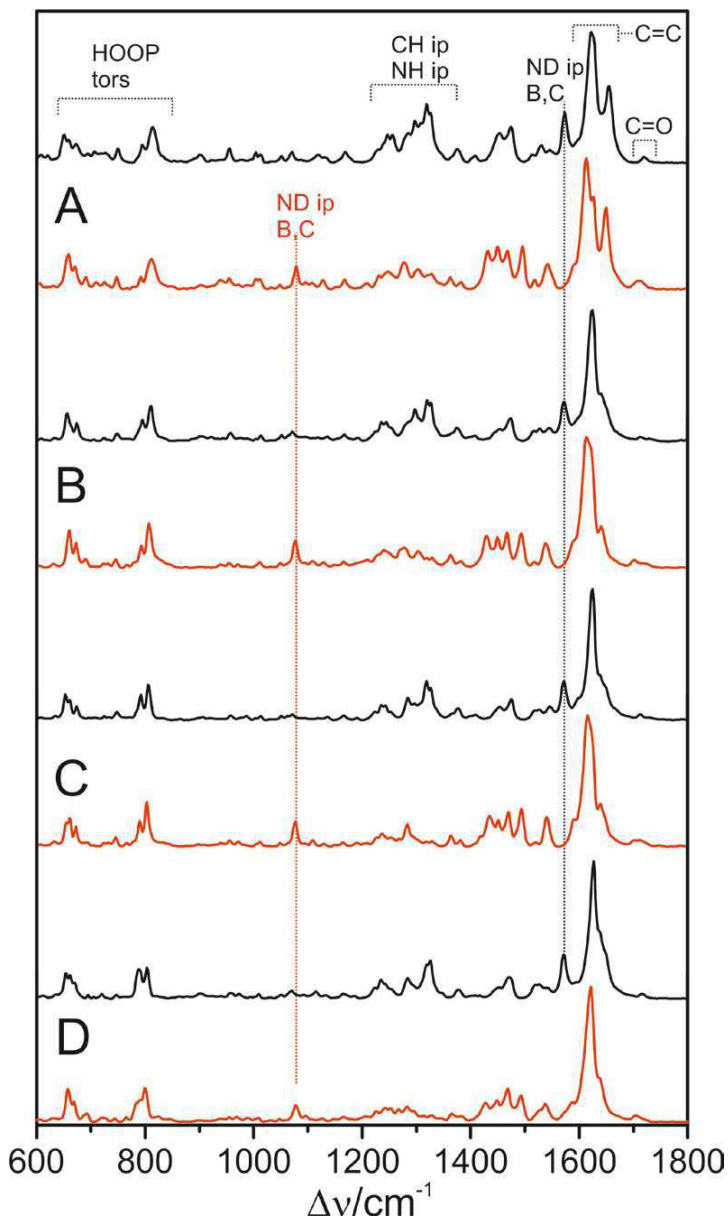


Fig. S3. RR spectra of the Pr state of (A) iRFP, (B) PG-P2, (C) PGP-P2, and (D) Agp1, measured with 1064-nm excitation at -140°C . Spectra obtained from samples in H_2O (pH 7.8) and D_2O (pD 7.8) are shown in black and red, respectively.

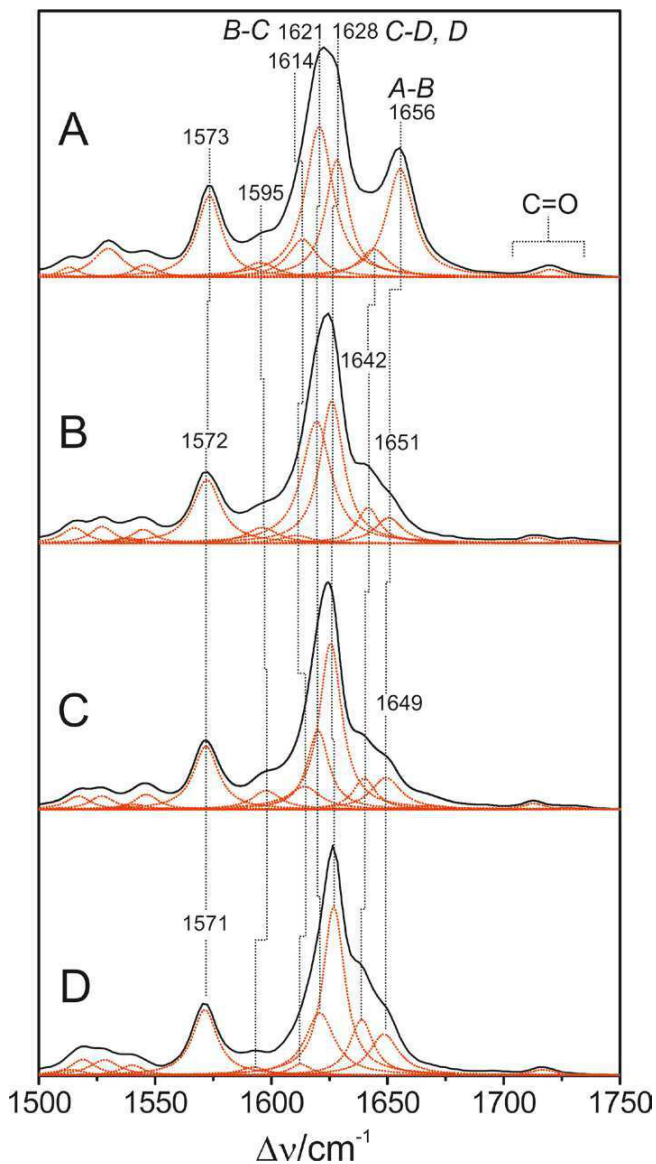


Fig. S4. RR spectra of the Pr state of (A) iRFP, (B) PG-P2, (C) PGP-P2, and (D) Agp1 in the C=C stretching region, measured with 1064-nm excitation at -140°C from samples in H_2O (pH 7.8). The red dotted lines represent fitted Lorentzian lineshapes.

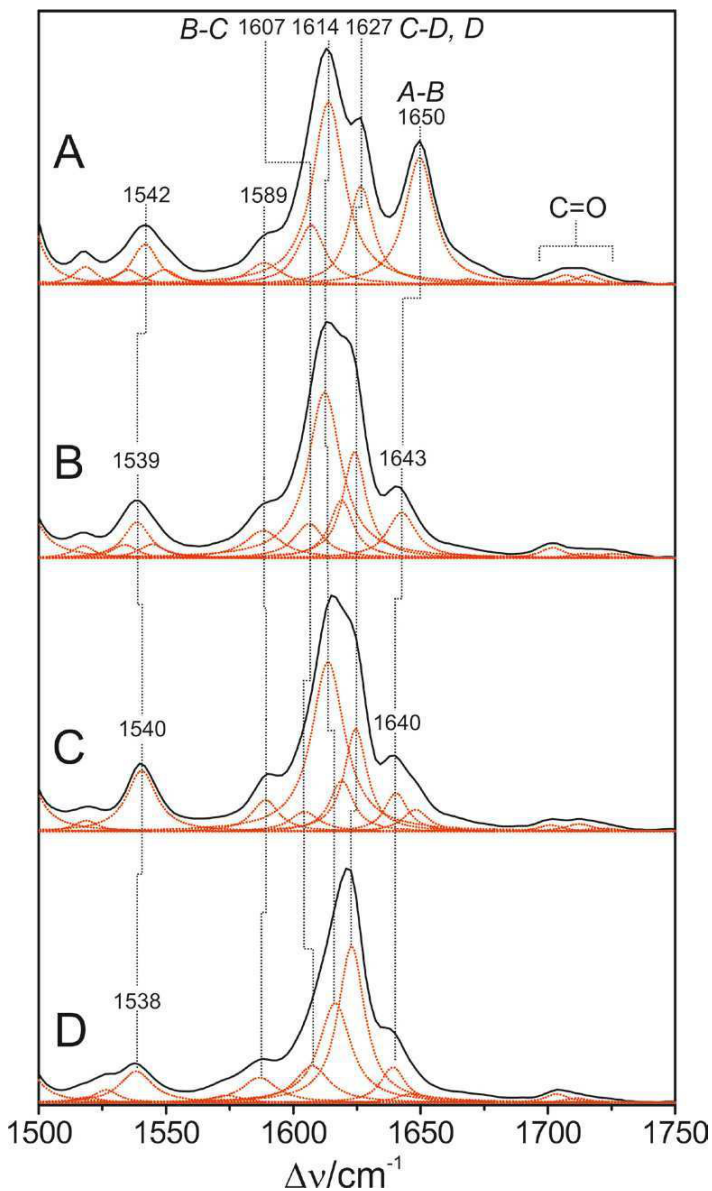


Fig. S5. RR spectra of the Pr state of (A) iRFP, (B) PG-P2, (C) PGP-P2, and (D) Agp1 in the C=C stretching region, measured with 1064-nm excitation at -140°C from samples in D_2O ($\text{pD } 7.8$). The red dotted lines represent fitted Lorentzian lineshapes.

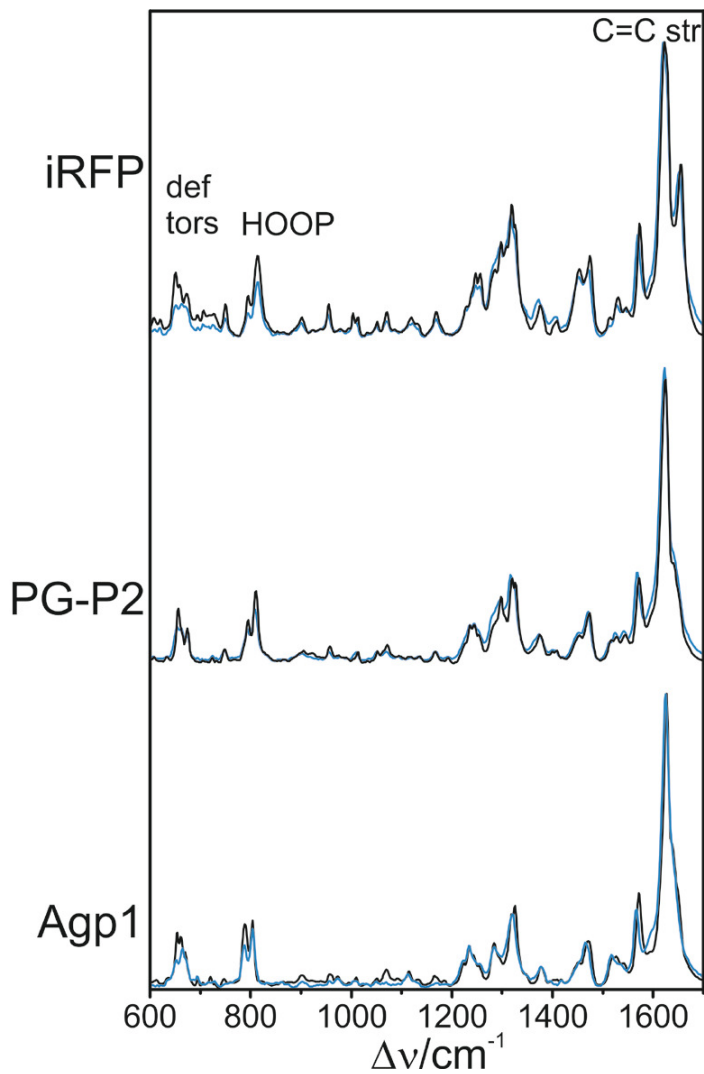


Fig. S6. RR spectra of iRFP, PG-P2, and the Pr state of Agp1 measured with 1064 nm excitation. The black and blue traces refer to the measurements at -140°C and $+10^\circ\text{C}$, respectively.

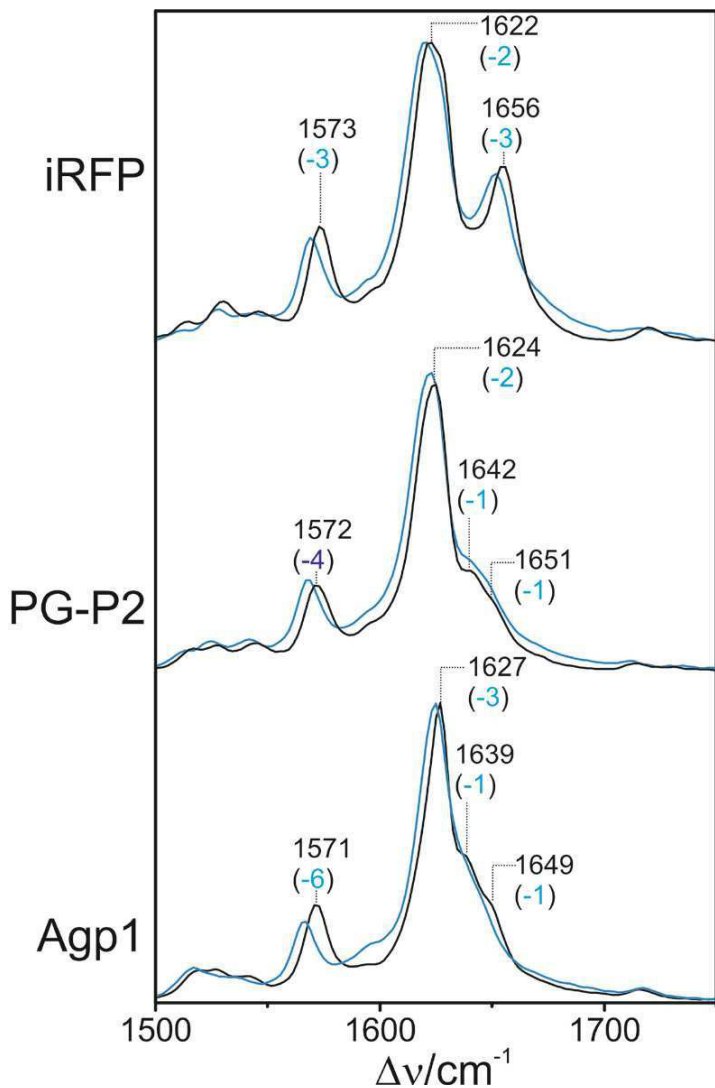


Fig. S7. RR spectra of iRFP, PG-P2, and the Pr state of Agp1 measured with 1064 nm excitation. The black and blue traces refer to the measurements at $-140\text{ }^{\circ}\text{C}$ and $+10\text{ }^{\circ}\text{C}$, respectively. Black labels refer to the peak positions at $-140\text{ }^{\circ}\text{C}$ rather than to the band components as determined by the band fitting analysis (Fig. S4). The blue numbers in parentheses indicate the shift of the peaks at $+10\text{ }^{\circ}\text{C}$.

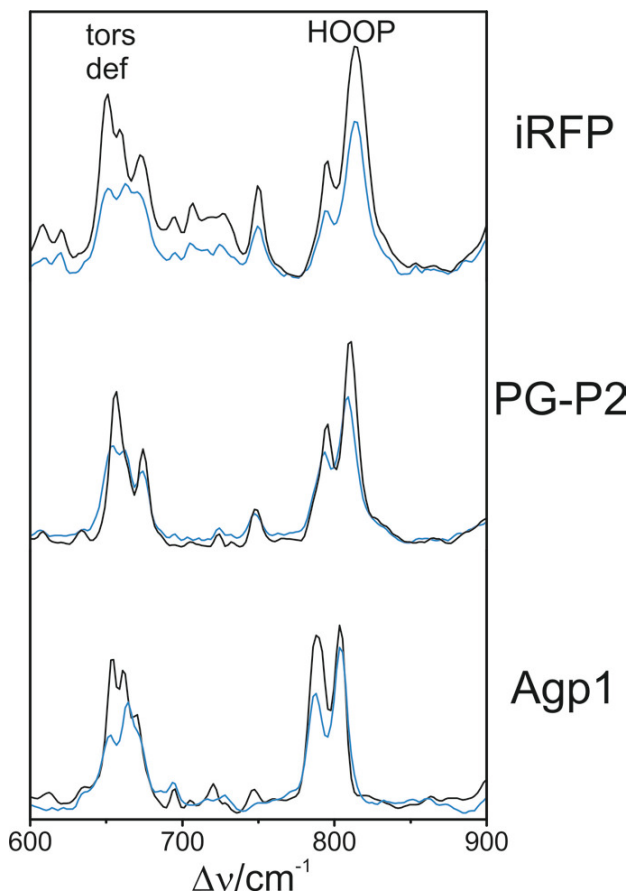


Fig. S8. RR spectra of iRFP, PG-P2, and the Pr state of Agp1 measured with 1064 nm excitation. The black and blue traces refer to the measurements at $-140\text{ }^{\circ}\text{C}$ and $+10\text{ }^{\circ}\text{C}$, respectively. The relative intensities of the conjugate spectra measured at the two temperatures correspond to those in Fig. S6.

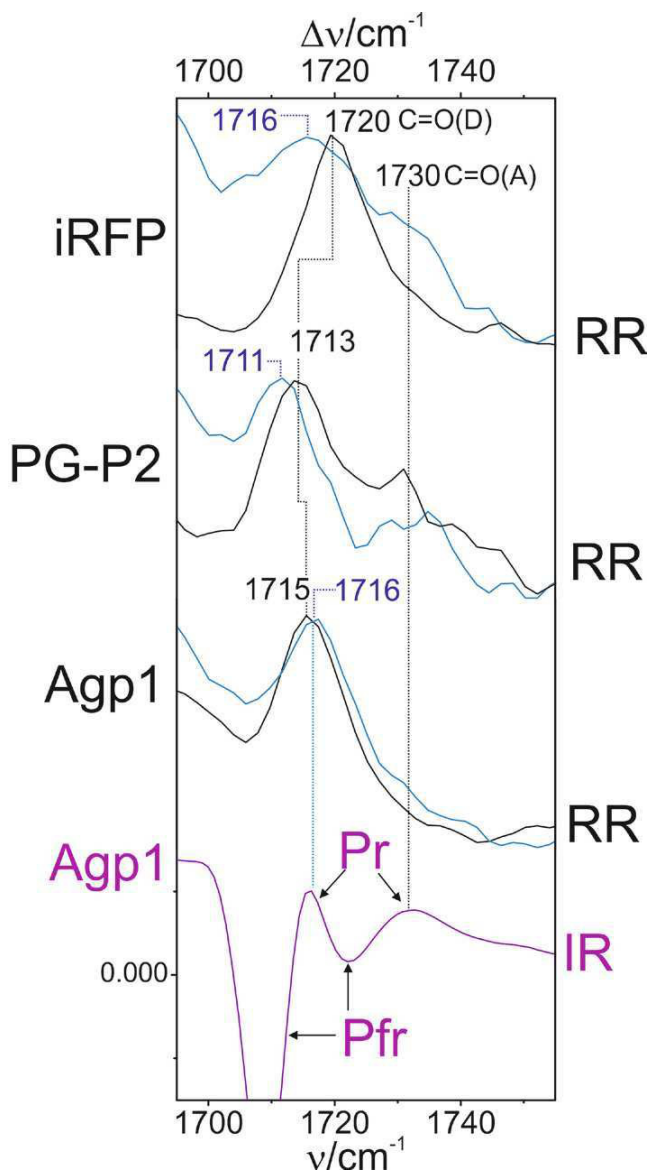


Fig. S9. RR spectra of iRFP, PG-P2, and the Pr state of Agp1 measured with 1064 nm excitation. The black and blue traces refer to the measurements at -140°C and $+10^\circ$, respectively. For comparison the IR difference spectrum “Pr(+) minus Pfr(−)” of Agp1 is shown in the bottom trace.

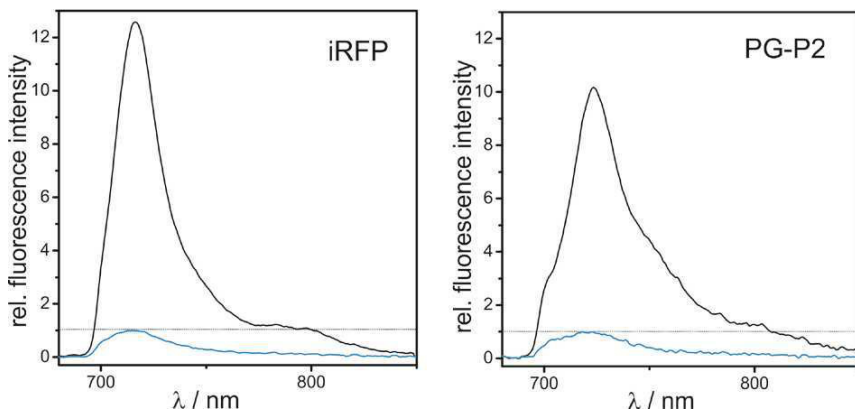


Fig. S10. Fluorescence spectra of iRFP (left) and PG-P2 (right) measured at +10 °C (blue traces) and -140 °C (black traces). The intensities are normalized with respect to the peak maxima of the corresponding spectra at +10 °C (= 1.0, horizontal dotted lines). In both cases, a ca. 10 fold intensity increase is observed at -140 °C. Note that the data represent raw data, not corrected for changes of the refractive index or the increase of the scattering amplitude due to microcrystal formation upon freezing. Thus, the intrinsic temperature-dependent increase of the fluorescence quantum yield is likely to be lower in both cases. For Agp1, the (uncorrected) fluorescence intensity at -140 °C increased by a factor of ca. 20.

Measurements were performed with a commercial USB-connected fluorometer system with CCD array (EPP2000, Scientific Instruments, Berlin, Germany) with a spectral resolution of 3 nm. The EPP2000 was coupled to a home-built variable-temperature cryostat (10-300K, CTI-Cryogenics 8001/8300). Excitation was performed with a pulsed 670 nm diode laser (LDH-D-C-670, Picoquant, Berlin, Germany) with a spectral bandwidth of 3 nm and a repetition rate of 8 Mhz (diode laser driver PDL-200, Picoquant, Berlin, Germany). The fluorescence was separated from stray light with a long pass emission filter (FEL-700, Thorlabs, Munich, Germany).

2. Additional data of the MD simulations

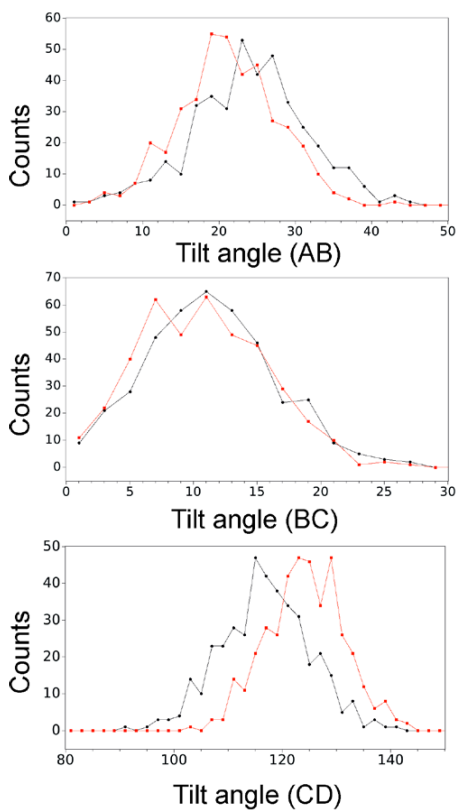


Fig. S11. Frequency distribution (counts) of the tilt angles between rings *A* and *B*, *B* and *C*, and *C* and *D*, computed using the last 40 ns of the MD simulation. Each point represents an angle span of 2° .

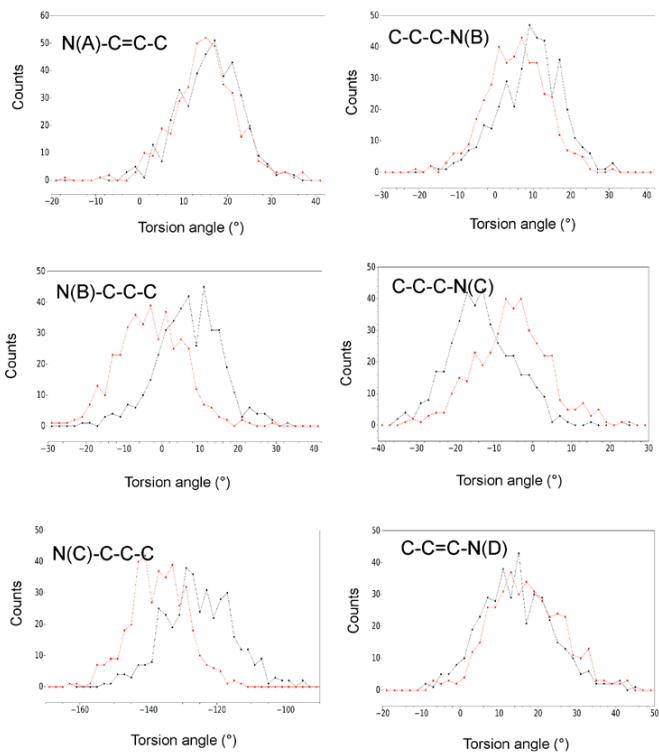


Fig. S12. Frequency distribution (counts) of the torsional angles at the *A-B*, *B-C*, and *C-D* methine bridges of the BV chromophore computed using the last 40 ns of the MD simulation. Each point represents an angle span of 2° . For atom and ring numbering see Fig. 1.

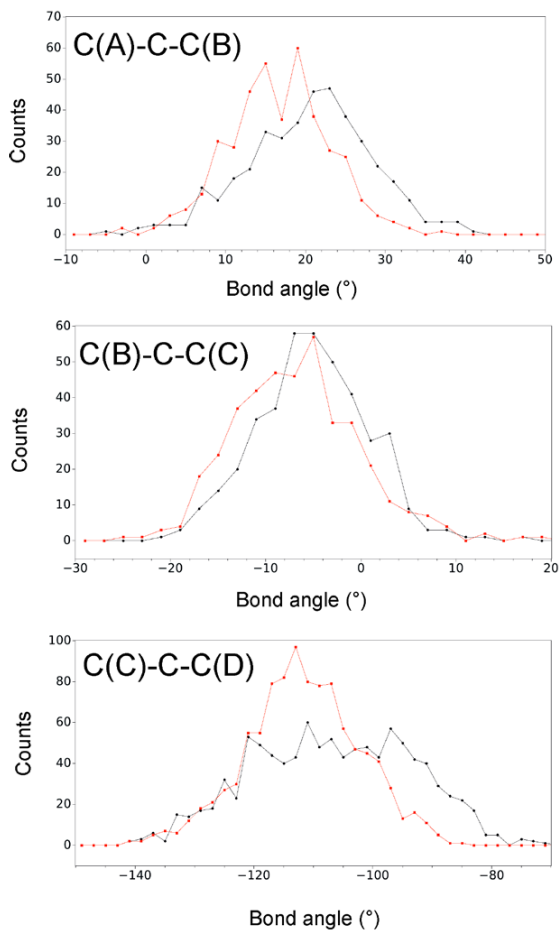


Fig. S13. Frequency distribution (counts) of the bond angles at the *A-B*, *B-C*, and *C-D* methine bridges of the BV chromophore computed using the last 40 ns of the MD simulation. Each point represents an angle span of 2°. For atom and ring numbering see Fig. 1.

3. Effect of the point mutations on the chromophore binding pocket

1) Y193K : This residue position belongs to the loop connecting β -strands 8 and 9. Since the functional groups of these two residues are pointing away from the chromophore binding pocket, they do not interact directly with the chromophore but they disturb the hydrogen-bond network in the vicinity of ring *D*.

2) F198Y: Residue 198 is located at the end of the β -strand 9. Mutation of Phe by Tyr leads to slight shift of the β -strand away from the chromophore. The 2.5 Å displacement with respect to the original position may be responsible for the increase of the tilt angle between rings *D* and *C* as shown in the following figure:

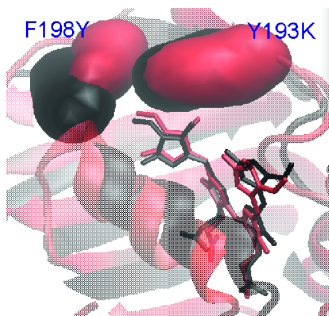


Figure S14. Superposition of the WT- (black) and iRFP- structures of PG-P2 at the end of the MD simulations. The BV chromophore is shown with *Licorice* representation whereas mutated amino acids are represented as surfaces

3) D202T and I203V: These residues belong to the loop connecting the 2nd 3/10 helix (200-202) and the 7th α -helix (205-213) secondary structure motifs and they are located on top of the plane spanned by rings *B* and *C*. They are responsible, together with the His255 and 1 - 2 water molecules for the coplanarity of the two central rings. The cartoon shows that mutations at these positions strongly change the water content and the H-bond network in the chromophore cavity. Interestingly, the pyrrole water located below the BV plane and H-bonded to the nitrogens of rings *A*, *B*, and *C* remains in the same position as found in the WT protein. In the WT model, however, a second water molecule (W2) is located opposite to the pyrrole water in H-bond distance to the pyrrole nitrogens and forms a H-bond with the carbonyl group of the Asp202 backbone. Upon D202T mutation, the position of W2 is occupied by the carbonyl group of the Thr residue.

Furthermore, His255, which is an important link between the tetrapyrrole backbone and the propionic side chain on ring *C*, moves slightly away from the chromophore in the iRFP model. As a consequence the 'through protein'- connection between propionic side chain and rings *B* and *C* is disrupted.

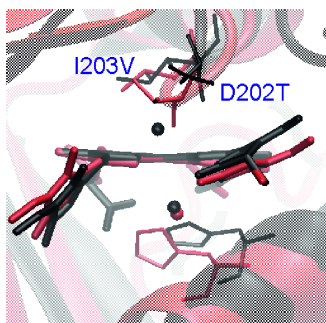


Figure S15. Superposition of the WT- (black) and iRFP- structures of PG-P2 at the end of the MD simulations. The BV chromophore is shown with *Licorice* representation whereas mutated amino acids are represented as sticks. Water molecules building H-bonds with the inner pyrrole rings are shown as spheres.

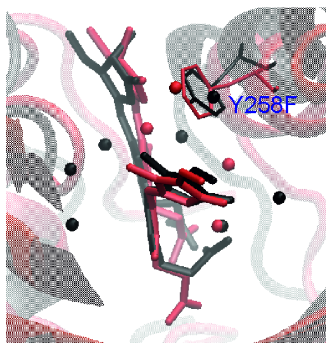


Figure S16. Superposition of the WT- (black) and iRFP- structures of PG-P2 at the end of the MD simulations. The BV chromophore is shown with *Licorice* representation whereas Tyr/Phe amino acids are represented as sticks. Water molecules in a radius of 5 Å within the C(D)=O group are shown as spheres

4) Y258F: This mutation does not significantly change the structure of the chromophore binding pocket. Although the α -helix is displaced in the structure of the mutant compared to the WT protein, the side chains of Phe and Tyr are basically located in the same place with respect to the chromophore. The different electronic character of these two residues is responsible for the significant change of the H-bond network, especially in the vicinity of ring D.

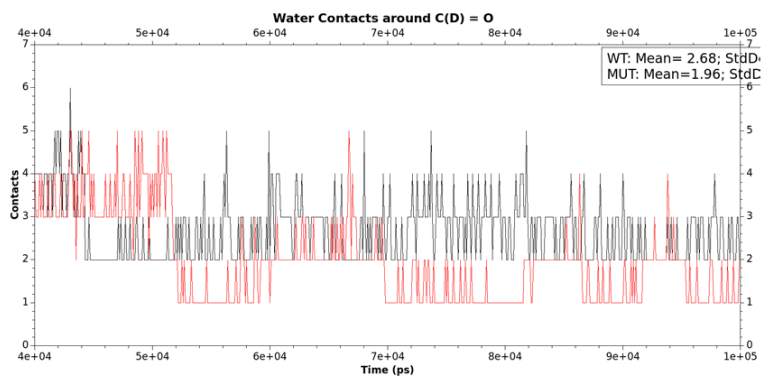


Figure S17: Number of water molecules (identified by the oxygen atom) within a 5 Å radius from the carbonyl function of BV during the last 60 ns of the production run (PG-P2 black, iRFP red).

8. Results: Cyanobacteriochromes

8.1. Photoconversion Mechanism of the Second GAF Domain of Cyanobacteriochrome AnPixJ and the Cofactor Structure of Its Green-Absorbing State

“Reprinted (adapted) with permission from: F. Velazquez Escobar, T. Utesch, R. Narikawa, M. Ikeuchi, M. A. Mroginski, and P. Hildebrandt. Photoconversion Mechanism of the Second GAF Domain of Cyanobacteriochrome AnPixJ and the Cofactor Structure of Its Green-Absorbing State. *Biochemistry* **2013**, 52, 4871–4880. [doi:10.1021/bi400506a]. Copyright ©2013 American Chemical Society. ”

- RR spectra were recorded by F. Velazquez Escobar
- Band analysis was performed by F. Velazquez Escobar
- Protein expression was carried out by Rei Narikawa, Masahiko Ikeuchi and Wolfgang Gärtner
- Calculations were performed by T. Utesch and M. A. Mroginski
- Research design and development by P. Hildebrandt

Photoconversion Mechanism of the Second GAF Domain of Cyanobacteriochrome AnPixJ and the Cofactor Structure of Its Green-Absorbing State

Francisco Velazquez Escobar,[†] Tillmann Utesch,[†] Rei Narikawa,^{‡,§} Masahiko Ikeuchi,^{‡,||} Maria Andrea Mroginski,[†] Wolfgang Gärtner,[⊥] and Peter Hildebrandt^{*,†}

[†]Institut für Chemie, Technische Universität Berlin, Sekr. PC14, Straße des 17. Juni 135, D-10623 Berlin, Germany

[‡]Department of Life Sciences (Biology), Graduate School of Art and Sciences, University of Tokyo, Komaba, Meguro, Tokyo 153-8902, Japan

[§]Japan Science and Technology Agency (JST), PRESTO, 4-1-8 Honcho Kawaguchi, Saitama 332-0012, Japan

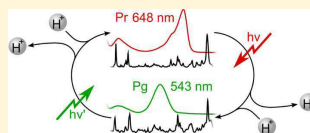
^{||}Japan Science and Technology Agency (JST), CREST, 4-1-8 Honcho Kawaguchi, Saitama 332-0012, Japan

[⊥]Max-Planck-Institut für Chemische Energiekonversion, Stiftstrasse 34-36, D-45470 Mülheim an der Ruhr, Germany

Supporting Information

ABSTRACT: Cyanobacteriochromes are members of the phytochrome superfamily. In contrast to classical phytochromes, these small photosensors display a considerable variability of electronic absorption maxima. We have studied the light-induced conversions of the second GAF domain of AnPixJ, AnPixJg2, a phycocyanobilin-binding protein from the cyanobacterium *Anabaena* PCC 7120, using low-temperature resonance Raman spectroscopy combined with molecular dynamics simulations. AnPixJg2 is formed biosynthetically as a red-absorbing form (Pr) and can be photoconverted into a green-absorbing form (Pg).

Forward and backward phototransformations involve the same reaction sequences and intermediates of similar cofactor structures as the corresponding processes in canonical phytochromes, including a transient cofactor deprotonation. Whereas the cofactor of the Pr state shows far-reaching similarities to the Pr states of classical phytochromes, the Pg form displays significant upshifts of the methine bridge stretching frequencies concomitant to the hypsochromically shifted absorption maximum. However, the cofactor in Pg is protonated and adopts a conformation very similar to the Pfr state of classical phytochromes. The spectral differences are probably related to an increased solvent accessibility of the chromophore which may reduce the π -electron delocalization in the phycocyanobilin and thus raise the energies of the first electronic transition and the methine bridge stretching modes. Molecular dynamics simulations suggest that the $Z \rightarrow E$ photoisomerization of the chromophore at the C–D methine bridge alters the interactions with the nearby Trp90 which in turn may act as a gate, allowing the influx of water molecules into the chromophore pocket. Such a mechanism of color tuning AnPixJg2 is unique among the cyanobacteriochromes studied so far.



Bilin-binding photosensory pigments have long been synonymous with the red/far-red light-sensing phytochrome photoreceptors of higher and lower plants.^{1,2} An outstandingly large number of experiments clearly have documented the paramount role of phytochromes in photomorphogenesis.^{3–6} These photochromic photoreceptors comprise a small protein family (e.g., phyA–phyE in *Arabidopsis thaliana*) that can be switched between two thermally stable or long-lived states by irradiation with light of appropriate wavelengths. In “classical” phytochromes, the red light-absorbing form (Pr) shows an absorbance maximum at 667 nm (phyA of oat), and the far red-absorbing form (Pfr) absorbs at 730 nm. Also, the kinetics of the photoinduced reaction cycle has been studied intensively and in molecular detail.^{7–13}

Unexpectedly, genome sequencing has unravelled a much wider distribution of phytochromes in prokaryotes. Initially, phytochromes were identified in cyanobacteria showing the canonical structure of plant phytochromes,¹⁴ rapidly followed

by demonstration of the presence of functional phytochromes also in nonphotosynthetic bacteria and even in fungi.¹⁵ Ongoing research revealed phytochromes with altered chromophore structures and also identified phytochromes with a modified photochemistry. One class of these novel phytochromes possesses a thermally stable Pfr state that is photoconverted to the hypsochromic Pr state (bathy phytochromes), which in classical or prototypical phytochromes represent the stable dark state.¹⁶ However, in prototypical and bathy phytochromes, the chromophore structural changes are likely to be very similar, i.e., a ZZZssa and ZZEsa configuration of the tetrapyrrole chromophore in the Pr and Pfr state, respectively.

Received: April 23, 2013

Revised: June 7, 2013

Published: June 28, 2013

In contrast, cyanobacterial bilin-binding proteins were identified that exhibit remarkable variations of the classical phytochrome blueprint. These novel cyanobacteriochromes (CBCRs) are composed in many cases as multi-GAF domain proteins.¹⁷ This architecture is unexpected as the lyase activity (autocatalytic chromophore binding) and the photochemistry are often maintained by a single, isolated GAF domain, in contrast to orthodox phytochromes, where three domains (PAS, GAF, and PHY domains) provide the lyase activity and establish the spectroscopic properties.^{18,19}

Despite a growing number of reports on their absorbance maxima variation and some information on their biological role in cyanobacteria,²⁰ little is known about the molecular mechanisms of the two-state conversion of CBCRs, and the few studies on the chromophore conformation and its structural changes during the light-driven photoprocess have led to partially controversial conclusions.^{20–25} One of the most remarkable properties is the variability of the electronic absorption of the parent states, ranging from the red to the near-UV spectral region, which is quite a contrast to the color change between 660 and 700 nm in classical phytochromes.^{18–23} Previous studies have shown that CBCRs employ different strategies for controlling the electronic absorption, for instance via interrupting the delocalized π -electron system by addition of a cysteine thiol function to the central methine bridge^{21–23} or by deprotonation of the tetrapyrrole chromophore.¹⁷

Resonance Raman (RR) spectroscopy can provide detailed insight into the chromophore structure in photoreceptors, especially when combined with theoretical methods. This approach had been proven successful for canonical phytochromes.^{13,26,27} On the basis of the knowledge obtained from plant and canonical cyanobacterial phytochromes, we present here the first RR study of an isolated GAF domain from a CBCR. Complemented by molecular dynamics (MD) simulations, we analyzed in detail the conformational changes of the second GAF domain of AnPixJ from *Anabaena* sp. PCC 7120 (AnPixJg2). In addition to identifying the chromophore conformations in the stable parent states (Pr and Pg), we determined the chromophore structure of two intermediates by low-temperature RR spectroscopy.

Absorption properties and the physiological relevance of this CBCR, such as phototaxis and bilin expression, were reported by Narikawa et al.,²⁸ and very recently, the crystal structure of the parent red-absorbing state Pr ($\lambda_{\text{max}} = 648$ nm) has been described.²⁹ In addition, the dynamics of the photoconversions between the Pr state and the green-absorbing form Pg ($\lambda_{\text{max}} = 543$ nm) were studied by time-resolved optical spectroscopies,³⁰ thus making AnPixJg2 an excellent model for analyzing, on a molecular basis, the mechanism of the photoconversion of CBCRs and the color tuning of the parent states.

EXPERIMENTAL PROCEDURES

Sample Preparation. AnPixJg2 was heterologously expressed in phycoerythrin (PCB)-producing *Escherichia coli* and purified as holoprotein including PCB as described elsewhere.²⁸ Sample preparation and measurements were performed under green light using LEDs at 515 nm. Buffer solutions (H₂O/D₂O Tris buffer, 50 mM Tris, 300 mM NaCl, 5 mM EDTA, pH/pD 7.8) were prepared with chemicals of the highest purity available (see Supporting Information). Protein samples were dialyzed in a microcon filter by centrifugation up

to a concentration corresponding to an optical density of 30 at the chromophore absorption band.

Raman Experiments. Measurements were carried out with a Bruker FT Raman spectrometer RFS 100/S (Nd:YAG cw laser, 1064 nm, line width 1 cm⁻¹), equipped with a nitrogen-cooled cryostat (Resultec-Linkam). All Raman spectra were recorded at -140 °C. The laser power at the sample was kept at 780 mW with a laser focus diameter of ca. 100 μ m. Possible laser-induced damage of the phytochrome samples was controlled by comparing the spectra obtained before and after a series of measurements; no such degradation was observed. For each spectrum the accumulation time was 1 h. Spectra of the Pr state were collected after a 2 min irradiation at 530 nm (LED) at 20 °C, whereas the spectra of the Pg state were obtained after illumination at 660 nm under otherwise the same conditions. This irradiation protocol yielded accumulation of the respective state with only negligible contributions of the other parent state species. For the intermediate states, the following cryogenic trapping procedure was used. The starting point was the sample exposed to green light which mainly contained the Pr state and only very small contributions from the Pg state. Subsequent to the Raman measurement at -140 °C, the sample was irradiated at stepwise increasing temperatures above -140 °C with 660 nm for 10 min and cooled to -140 °C again to measure the Raman spectrum. The analogous procedure was applied to trap the intermediates of the Pg-to-Pr conversion using green light irradiation. Details of the measuring protocol are given in the Supporting Information (Table S1). The component spectra of the pure parent states could readily be obtained from the experimental spectra measured from the samples irradiated with green or red light via mutual subtraction to remove minor contributions of the Pg or Pr state, respectively. Obtaining the spectra of the pure intermediates from the raw spectra measured from samples after irradiation at specific trapping temperatures required iterative subtraction procedures as not only the target intermediate but also the precursor and the thermal relaxation product might contribute to the experimental spectrum. Details of the subtraction procedure are given in the Supporting Information (Table S2).

Molecular Dynamics Simulations. The structural models for the Pr and Pg states of AnPixJg2 cyanobacteriochrome, used for atomistic MD simulations, were constructed using as initial coordinates the crystallographic structure of AnPixJg2 (PDB entry 3WZZ).²⁹ In the case of the Pr state, the conformation of the PCB chromophore was taken as observed in the crystal structure while initial models for the chromophore in the Pg state were obtained by rotating the C=C bond at the methine bridge between rings C and D (C–D) by 155°, 175°, and 195°. The protonation states of all titratable amino acid side chains were set according to pH 7.0. In the case of histidines, the protonation state was adjusted according to their immediate environment. In particular, His94, His119, and His123 in the chromophore binding pocket were protonated at N ϵ , N δ , and both nitrogen atoms, respectively. All model systems were solvated in a box of ca. 23000 explicit TIP3P water molecules including 50 mM NaCl.³¹

Prior to the MD simulations, the model systems were prepared by an energy minimization of 20000 steps using the conjugated gradient integrator followed by heating to 300 K. During these steps, all heavy atoms were restrained to their positions by applying a force of 25 kcal mol⁻¹ Å⁻². These restraints, including those of the chromophore for the Pr

model, were stepwise removed during the solvent equilibration within 60 ps. For the Pg models, these last steps together with a subsequent 5 ns MD simulation step were performed keeping the chromophore fixed to adapt the protein environment to the new conformation of the photoproduct. The models for the Pr state and the photoproducts were then thermally equilibrated at 300 K for 5 and 15 ns, respectively.

While the structures of the Pg models built with initial C=C–N(D) dihedral angles of 155° and 175° converged to a PCB geometry characterized by a strongly distorted torsional angle N(C)–C–N(D) angle of ca. 105°, the structural model constructed with an initial C=C–N(D) dihedral angle of 195° slowly evolved to a structure characterized by the ZZZssa conformation of the PCB chromophore as found in the Pr state (Supporting Information, Figures S6 and S7). Accordingly, we will refer to these structural models as Pg155, Pg175, and Pr195. Given the high similarity with the original X-ray-based Pr model, the engineered Pr195 model was not considered for further discussions. The MD simulations were carried out with NAMD 2.7³² using the CHARMM 27 force field³³ with an extension for the PCB chromophore derived by Kaminski et al.³⁴ During these simulations, the number of particles (*N*), the pressure (*P*), and the temperature (*T*) were kept constant using the Langevin piston method.³⁵ Short-range electrostatics and van der Waals interactions in the periodic systems were calculated with a simple cutoff at 12 Å, whereas long-range electrostatics were determined with the particle Ewald summation.³⁶ To enable a time step of 2 fs, all bonds containing hydrogen atoms were frozen with the SHAKE algorithms.³⁷ The solvent accessible area of the chromophore was evaluated with VMD1.8.7³⁸ every 25 ps, assuming a radius of 1.4 Å for a water molecule.

RESULTS AND DISCUSSION

Despite the large separation of the excitation line (1064 nm) from the first electronic transition of the chromophore of the Pr state (660 nm), the measured Raman spectra are dominated by the preresonantly enhanced Raman bands of the bilin cofactor and thus are referred to as resonance Raman (RR) spectra. This is also true for the Pg state, although its electronic transition is even further blue shifted to ca. 560 nm. There are only small although clearly detectable contributions from nonresonance Raman bands of the protein matrix such as the methyl and methylene deformation modes of amino acid side chains (ca. 1450 cm⁻¹) and the amide I modes of the polypeptide backbone (ca. 1650 cm⁻¹) (Figure 1). These poorly structured features partially overlap with the RR bands of the cofactor. In addition, there is a relatively sharp band at 1003 cm⁻¹ which is due to the ring-breathing mode of phenylalanine residues. The intensity of this band can be used as an internal standard to estimate the relative resonance enhancement for the cofactor Raman bands of the various states of AnPixJg2. In accordance with the poorer resonance conditions for Pg, we have found, on average, that the enhancement for this state is 2-fold weaker than for Pr. Even lower resonance enhancements and thus relatively strong contributions from the protein Raman bands are noted for the intermediate states including a deprotonated chromophore (vide infra).

Resonance Raman Spectroscopy of the Pr State. The overall vibrational band pattern of the parent state Pr displays far-reaching similarities with that of the Pr states of canonical phycochromes carrying a PCB chromophore as exemplified for the PCB adduct of plant phytochrome phyA (Figure 1A,B). A

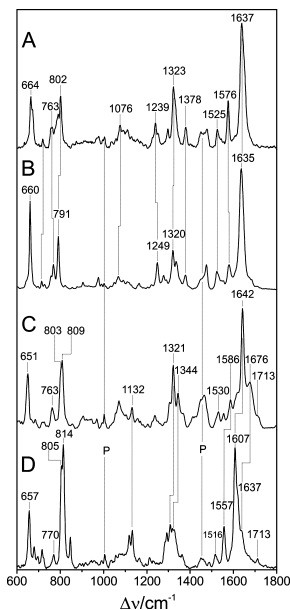


Figure 1. Overview RR spectra of the parent states of AnPixJg2 and the 65 kDa fragment phyA reconstituted with PCB, measured in H₂O at pH 7.8. A, Pr of phyA-PCB; B, Pr of AnPixJg2; C, Pg of AnPixJg2; and D, Pfr of phyA-PCB.

very good agreement is noted for the bands in the C=C stretching region between 1500 and 1700 cm⁻¹ which are sensitive marker bands for the conformation of PCB and in particular for the methine bridge configuration. This finding is in agreement with the crystal structure data indicating that the chromophore in the Pr state of AnPixJg2 adopts a ZZZssa configuration as in the case of phyA(PCB) and Cph1Δ2 (Figure 2).^{27,29,39,40} Adopting the vibrational assignment from the analysis of the RR spectra of phyA-PCB, the dominant band at 1635 cm⁻¹ is attributed to the C=C stretching of the C–D methine bridge (C–D stretching), whereas the weak shoulder on the lower-frequency side at 1607 cm⁻¹ is attributed to the B–C stretching (Figure 1A,B and Supporting Information, Figure S1; see Figure 2 for the structural formula of the cofactor). The corresponding A–B stretching mode is likely to be hidden under the high-frequency wing of the 1635 cm⁻¹ band. Furthermore, this spectral region includes the in-phase N–H in-plane bending (ip) mode of the ring B and C nitrogen atoms at 1576 cm⁻¹ (phyA-PCB) which is a characteristic marker for the protonation of the cofactor. In fact, the RR spectrum of the Pr state of AnPixJg2 shows a band at a very similar position (1579 cm⁻¹) which disappears upon H/D exchange (Figure 1A,B and Supporting Information, Figure S1). The corresponding N–D ip mode is assigned to a weak band at 1076 cm⁻¹ (Supporting Information, Figure S2) analogous to previous findings for phyA-PCB.⁴¹ Also, the other isotopic shifts brought about by H/D exchange are similar in

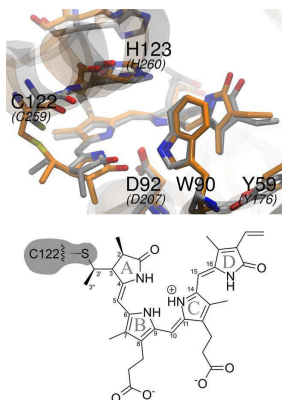


Figure 2. (Top panel) Chromophore binding pocket of AnPixJg2 in the Pr state. The crystal structure is represented in gray carbon atoms. The structure obtained after the MD trajectory is displayed in orange. Structural alignment of both (crystal and MD) coordinates refers to the lowest RMSD of the PCB chromophore coordinates. AnPixJg2 specific amino residues are indicated with normal character style, whereas corresponding residues of Cph1Δ2 are presented in italics. (Bottom panel) Structural formula of the PCB chromophore in the ZZZssa configuration.

the Pr states of AnPixJg2 and phyA-PCB, which not only is consistent with the cationic cofactor structure (all four ring nitrogens being protonated) but also supports the assignments discussed above.

Only details of the cofactor structure and its interactions with the protein environment seem to be different for the Pr state of AnPixJg2, compared to those of the Pr state of canonical PCB-binding phytochromes. Spectral differences in the region between 600 and 850 cm^{-1} mainly result from torsional and deformation modes of rings C and D (at ca. 650 cm^{-1}) and from C–H out-of-plane deformation (HOOP) modes of the C–D methine bridge, pointing to structural variations specifically in this part of the cofactor (Figure 1A,B). In fact, the crystallographic data for the Pr state of AnPixJg2 indicate a torsional angle around the C–D methine bridge that is distinctly larger (27°) than that found for Cph1Δ2 (2°).^{27,29,39} It is also larger than that of the structural model for phyA-PCB (11°).⁴⁰ One of the most striking differences between the crystallographic data for the Pr states of AnPixJg2 and canonical phytochromes refers to the hydrogen bond interactions of the pyrrole rings. In canonical phytochromes, the ring B and C N–H groups interact with a structural water (pyrrole water) which in turn forms a hydrogen bond to the backbone carbonyl function of the highly conserved Asp in canonical phytochromes (Asp207 in Cph1Δ2).³⁹ In AnPixJg2, however, no pyrrole water is detected in the crystal structure, and the carboxylate side chain of this conserved aspartate residue (Asp92 in the AnPixJg2 sequence) forms hydrogen bonds directly with the N–H groups of rings B and C (Figure 2).²⁹ MD simulations confirm this picture, although a water molecule enters the chromophore pocket after ca. 2.5 ns. This water molecule, however, remains above the tetrapyrrole plane

without interfering with the ring B/C–Asp92 interactions (Wat1 in Supporting Information, Figure S9).

Resonance Raman Spectroscopy of the Pg State. The most remarkable observation refers to the RR bands in the region between 1500 and 1700 cm^{-1} , which, at first glance, seem to differ substantially from the RR spectra of Pfr states of canonical phytochromes (Figures 1C,D and 3). The deviations,

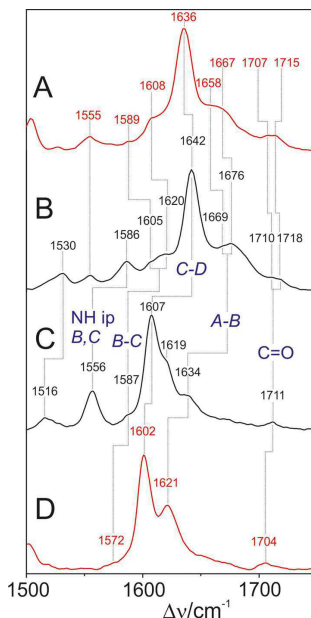


Figure 3. Expanded view of the RR spectra in the C=C stretching region of the Pg state of AnPixJg2 and the Pr state of the 65 kDa fragment phyA reconstituted with PCB, measured at pH/pD 7.8. A, Pg of AnPixJg2 in D₂O; B, Pg of AnPixJg2 in H₂O; C, Pfr of phyA-PCB in H₂O; and D, Pfr of phyA-PCB in D₂O. Blue letters indicate the main character of the normal modes involved. Italic letters A, B, C, and D refer to the individual pyrrole ring as defined in Figures 2 and 4, and A–B, B–C, and C–D denote the C=C stretchings of the methine bridges between the respective rings. The C=O stretchings of rings A and D and the N–H in-plane bending of rings B and C are abbreviated “C=O” and “NH ip B,C”, respectively.

however, are systematic. On the basis of the relative band intensities and the H/D effects one may identify the conjugate band pairs in the RR spectra of Pg (AnPixJ) and Pfr (phyA-PCB), indicating that nearly all of the Pg modes in this region are upshifted by more than 30 cm^{-1} , including the C=C stretching modes of the C–D, A–B, and B–C methine bridges at 1642, 1676, and 1620 cm^{-1} , respectively. This finding implies that all methine bridge modes of the cofactor are found in the RR spectrum of Pg. Thus, we can safely rule out that the blue-shifted absorption maximum in the Pg state is due to the reduction of the A–B methine bridge double bond such as is the case in the Pg form of TePixJ or in phycoerythrin, which

in turn would afford quite different RR spectra.²¹ Furthermore, also the possibility of a deprotonation of the tetrapyrrole cofactor can be ruled out because the RR spectrum of the Pg state of AnPixJg2 shows the N–H ip mode of rings B and C at 1586 cm^{-1} which disappears in D_2O . The corresponding N–D ip mode is found at 1089 cm^{-1} (Supporting Information, Figure S2). Like the methine stretching modes, the N–H ip mode is upshifted by ca. 30 cm^{-1} compared to Pfr of phyA-PCB. A smaller upshift (14 cm^{-1}) is noted for the other mode involving the N–H ip coordinates of rings B and C (1530 cm^{-1}) (Figures 1C,D and 3).

Previous cofactor extraction experiments with the denatured protein have revealed a PCB cofactor with a *Z* or *E* configuration of the C–D methine bridge in the Pr or Pg state, respectively (Figure 4).²⁸ Whereas the good RR

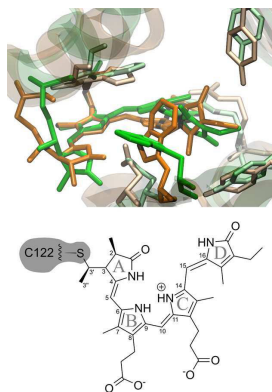


Figure 4. (Top panel) MD equilibrated structure before (orange) and after (green) *Z/E* isomerization of the C–D double bond. (Bottom panel) Structural formula of the PCB chromophore in the *ZZEssa* configuration.

spectroscopic agreement between the Pr states of AnPixJg2 and phyA-PCB points to very similar cofactor structures, it remains to be analyzed if—in addition to the *Z/E* isomerization of the C–D methine bridge—there are further structural changes of the chromophore in the Pg state that are different from those in canonical phytochromes. In this respect, we first focus on the high-frequency region (Figure 3). Compared to the Pfr state of phyA-PCB, we note a significant band broadening of the features above and below the prominent 1642 cm^{-1} band (C–D stretching). Moreover, a closer inspection reveals asymmetric band shapes indicating, in each case, the involvement of at least two band components. Thus, the minimum number of bands in the C=C stretching region (1590–1680 cm^{-1}) is five, which exceeds the number of Raman-active normal modes (three) and even of the total number of normal modes (four) calculated for PCB, regardless of the specific tetrapyrrole configuration and conformation.^{42,43} Furthermore, the similar H/D sensitivity of the band components at 1676 (–9) and 1669 (–11) cm^{-1} suggests that the underlying modes have the same character, i.e., they are dominated by the A–B stretching coordinate. Correspondingly, the band components at 1620 (–12) and 1605 (–16) cm^{-1} are

assigned to modes of mainly B–C stretching character with the admixture of the A–B stretching coordinate.⁴² These findings indicate that the Pg form exists in two substates differing in terms of the A–B methine bridge conformation. In this respect, we like to refer to a comparative spectroscopic–theoretical analysis of the Pfr state of biliverdin-binding phytochromes demonstrating, for prototypical but not for bathy phytochromes, conformational equilibria associated with structural changes at the A–B and C–D methine bridges.⁴⁴ This conclusion was derived not only from the analysis of the methine bridge stretching modes but also from the prominent HOOP mode of the C–D methine bridge at ca. 810 cm^{-1} that gives rise to two band components. A similar band pattern is also observed in the present RR spectra (Figure 1C,D; more clearly shown in Supporting Information, Figure S3) suggesting that for the Pg state of AnPixJg2 as well as for the Pfr state of phyA-PCB the structural heterogeneity involves the C–D methine bridge.

Alterations of the hydrogen bond network associated with the structural changes in the chromophore binding pocket are presumably responsible for the spectral deviations between the Pg and Pfr RR spectra in the region between 1200 and 1400 cm^{-1} as it includes modes involving the N–H ip coordinates of rings A and D and coordinates of the propionate side chains of rings B and C. Thus, these modes are expected to respond sensitively to structural changes of the immediate protein environment.

Because of the lack of structural data on the Pg state of AnPixJg2 or the Pfr state of any PCB-binding phytochrome, it is not possible to identify particularly important amino acid residues interacting with the tetrapyrrole. However, it is tempting to assume that Trp90 plays a role in controlling the spectral and structural properties of the cofactor because this residue is found in close proximity to ring D in the crystal structure of the Pr state of AnPixJg2.²⁹ Moreover, this residue is conserved only among the red/green-absorbing cyanobacteriochrome subfamily, suggesting a crucial and unique role in the chromophore–Trp90 interaction. In contrast, this aromatic residue is absent in canonical phytochrome sequences. Position 90 in the AnPixJg2 sequence corresponds to the residue 205 in Cph1 or residue 270 in the phyA sequence, located two amino acids below the canonical DIP motif.⁴⁵

Molecular Dynamics Simulations of a Pg Model. Starting with the crystal structure coordinates, we have therefore carried out MD simulations which revealed only slight deviations in the surrounding protein matrix (Figure 2). Specifically Trp90 remained at a distance of 4.1 ± 0.3 Å to ring D within a nearly coplanar orientation ($169.9 \pm 5.7^\circ$), underpinning its important role in stabilizing the chromophore in the Pr state. To assess the consequences of the *Z/E* isomerization of the C–D methine bridge on the cofactor protein interactions, two Pg models were constructed, namely the Pg155 model and the Pg175 model (vide supra). As a consequence of the MD simulations, the chromophore in both structural models was found to adopt a distorted albeit stable *ZZEssa* geometry (Figure 4 and Supporting Information, Figure S6 and Table S4), while the overall structure of the protein did not change significantly. Specifically, there were only subtle adjustments of the protein in the vicinity of the cofactor, except for a repositioning of Trp90 and Asp92 (Figure 4). Although these results have to be considered with caution in view of the mechanical force fields for both the protein and the cofactor, they suggest that the C–D methine bridge isomerization is

associated with a distinct weakening of the interactions between ring *D* and Trp90, as reflected by the increased separation ($7.6 \pm 1.0 \text{ \AA}$ for Pg155 and $7.3 \pm 1.1 \text{ \AA}$ for Pg175) while maintaining a nearly coplanar orientation. Concomitant to the movement of Trp90, Asp92 is displaced toward ring *A* at the expense of the hydrogen bond interactions with rings *B* and *C*. This reorientation of Asp92 and Trp90 may increase the flexibility of the chromophore in the binding pocket, which in turn provides an explanation for the structural heterogeneity of the tetrapyrrole as reflected by the additional RR bands in the C=C stretching and HOOP regions.

In addition, the structural water contents in the Pr and the “photoproduct” model differ considerably. After the MD simulations, we found 7 solvent molecules in the chromophore binding pocket for the Pr state (in contrast to only 3 H₂O molecules in the crystal structure) and 14 (Pg155) or 11 (Pg175) water molecules for the “photoproduct” (Supporting Information, Figure S10). The increased number of water molecules in the chromophore pocket for the “photoproduct” is mainly the consequence of the reorganization of Trp90 during the MD simulation. Trp90 acts as a kind of gate and opens the chromophore pocket to water molecules when aligning its ring structure parallel to ring *D* of the chromophore. This putative gating mechanism does not affect the protein backbone structure. Only the rearrangement of the protein side chain of Trp90 leads to an increased solvent accessible area of the chromophore for the “photoproduct”. The MD simulations showed a significant increase of the solvent accessibility of the chromophore for the “photoproduct” ($246.5 \pm 16 \text{ \AA}^2$ for Pg155 and $246.3 \pm 14 \text{ \AA}^2$ for Pg175) compared to that of the Pr state ($187 \pm 12 \text{ \AA}^2$) which was evaluated over the last 2 ns of the respective production runs (Supporting Information, Figure S8). Thus, the present MD simulations indicate that the double bond isomerization may cause, in principle, quite substantial alterations in the protein–cofactor interactions even though an accurate analysis of these interactions is possible only on the basis of a crystallographic structure.

Resonance Raman Spectroscopy of the Photoinduced Reaction Cycle. For the Pr → Pg phototransformation, three different intermediates were identified on the basis of the RR spectra at trapping temperatures indicated in Figure 5 (more

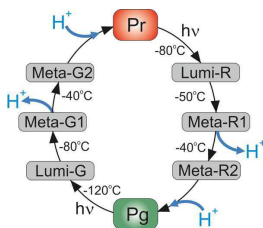


Figure 5. Photoinduced reaction cycle of AnPixJg2.

details are given in the Supporting Information). Unlike canonical phytochromes, where the photochemistry can be initiated even at $-140 \text{ }^\circ\text{C}$,⁴¹ a red-light-induced photo-conversion of AnPixJg2 was observed only above $-80 \text{ }^\circ\text{C}$, which is in accordance with the relatively slow kinetics determined by transient absorption spectroscopy for the Lumi-R (= R_{1650–80}) formation (<100 ns).³⁰ In this reaction

step, the primary *Z/E* double bond isomerization at the C–D methine bridge takes place leading to a red shift of the absorption maximum.^{28,30,46} The corresponding cryogenically trapped intermediate displays some features reminiscent of the RR spectrum of the Lumi-R state of phyA (Figure 6B).

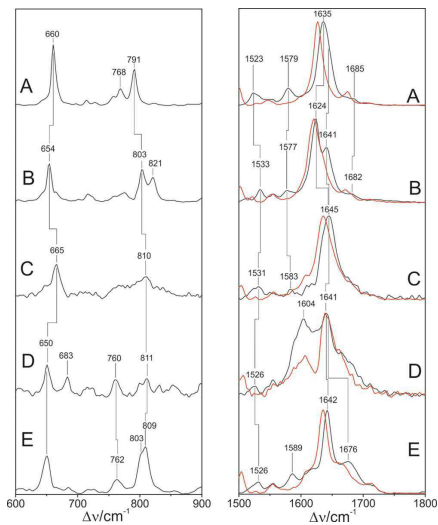


Figure 6. RR spectra of the species constituting the Pr-to-Pg reaction pathway. A, Pr; B, Lumi-R; C, Meta-R1; D, Meta-R2; and E, Pg. The intermediates were trapped at the temperatures indicated in Figure 5. The black and red lines refer to the measurements in H₂O and D₂O solutions, respectively (pH 7.8).

Specifically, the C–D stretching undergoes an 11 cm^{-1} downshift to 1626 cm^{-1} , which, albeit smaller than in phyA (-37 cm^{-1})⁴¹ makes the A–B stretching mode visible at 1641 cm^{-1} , which is obscured by the prominent 1635 cm^{-1} band in the Pr spectrum. It is reasonable to assume that, like in phyA, the frequency of the A–B stretching mode is not significantly affected by the photoisomerization. In conjunction with the distinctly lower RR activity of the HOOP modes, the smaller downshift of the C–D stretching compared to that of phyA⁴¹ may suggest that the cryogenically trapped Lumi-R represents an already partially relaxed state, consistent with the relatively slow formation kinetics. In addition, it may be that with the formation of Lumi-R, water molecules enter the chromophore binding pocket, thereby causing an upshift of the methine bridge stretching frequencies as discussed above (Supporting Information, Figures S4 and S5 and Table S3).

The subsequent formation of the intermediate Meta-R1 involves further thermal relaxation of the cofactor structure reflected by an even lower HOOP RR activity. In both the Lumi-R and the Meta-R1 state, the PCB chromophore is protonated as indicated by the protonation marker band (ring B and C N–H ip) at 1577 and 1583 cm^{-1} , respectively (Figure 6B,C). The situation is different for the following thermal relaxation product, Meta-R2 (Figure 6D), which is very similar

to the Meta-Rc states identified in the photoconversion routes of phyA as well as those of PCB- and biliverdin-binding (cyano)bacterial phytochromes. Both the distinctly lower resonance enhancement, presumably due to the reduced oscillator strength of the first electronic transition, and the lack of the N–H ip mode and the unique broad and poorly resolved vibrational structure in the C=C stretching region are characteristic features of a protein complex carrying a nonprotonated (neutral) tetrapyrrole cofactor.^{41,47,48}

The photoinduced transformation from Pg back to Pr runs via three intermediates that can be cryogenically trapped (Figure 5). Unlike the forward reaction (Pr-to-Pg), formation of the first intermediate Lumi-G was already observed at -140 °C, although a better trapping yield is obtained at -120 °C. These findings imply that the (thermal) activation barrier is much lower than for the Lumi-R formation, again consistent with previous kinetic studies.³⁰ Most surprisingly, the RR spectrum of Lumi-G displays a broad envelope in the C=C stretching region with maxima at ca. 1645 and 1675 cm^{-1} that are similar in frequency as the well-defined peaks of the parent Pg state (Figure 7A,B). It may be that this band contour

mediates were detected.⁴⁹ Assuming a similar reaction pathway for AnPixJg2, the present RR spectrum is interpreted as a mixture of two Lumi-G species, which are trapped between -140 and -120 °C. During the thermal relaxation from Lumi-G to Meta-G1 (Figure 7C), the chromophore is converted into a less distorted conformation as indicated by rather sharp bands in the C=C stretching and the low RR activity in the HOOP region. Like in Lumi-G, the PCB cofactor is protonated, as shown by the N–H ip mode at 1586 cm^{-1} .

At -40 °C, the Meta-G2 intermediate is trapped as the precursor of the Pr state (Figure 7D). Meta-G2 shows spectral similarities to its counterpart of the Pr-to-Pg pathway. Meta-G2 and Meta-R2 display two broad peaks at 1604 and 1641 cm^{-1} (Figures 6D and 7D). Taking into account that the cofactor configurations must be different, i.e., ZZZssa and ZZZssa in Meta-R2 and Meta-G2, respectively, this spectral similarity seems to be surprising. However, previous studies on tetrapyrrole model compounds have shown that the spectral differences between double bond isomers of deprotonated (neutral) bilins are rather small.⁵⁰ Interestingly, a band to be attributed to the N–H ip mode of rings B and C cannot be identified, implying that also in Meta-G2 the cofactor is deprotonated.

Structural and Mechanistic Similarities to Classical Phytochromes. The second GAF domain of the cyanobacteriochrome AnPixJg2 carries a PCB cofactor that undergoes photoinduced reaction cascades very similar to those in canonical phytochromes. The phototransformations between the parent states Pr and Pg are initiated by a photoisomerization of the C–D methine bridge double bond, followed by thermal reaction steps, including relaxation processes of the chromophore and chromophore–protein interactions, and eventually leading to a reversible deprotonation of the cofactor. The present MD simulations point to a significant increase of the solvent accessible area in the “photoproduct” model, accompanied by an increase of the number of water molecules in the cofactor pocket (vide supra). Concomitant to the rupture of the Trp90–PCB interactions, the protein adopts a more “open” structure, allowing for an exchange of water molecules between the chromophore pocket and the solution phase. Although a 15 ns MD simulation is not appropriate to deliver a reliable model for a protein state formed on the microsecond time scale, the present simulation suggests that cofactor structural changes may in fact serve as a switch to enable proton translocation through the protein. It remains to be explored in future experiments whether this proton transfer is associated with a transient proton release to the solution phase as shown for Cph1⁵¹ and Agp1.⁴⁷ In these classical phytochromes, the proton translocation appears to serve as a trigger for protein conformational changes that may represent the signaling event.⁴⁷

Altogether, we conclude that essential steps of the reaction pattern of classical phytochromes are also found in the CBRC AnPixJg2. This is also true for the considerable structural heterogeneity of the cofactor in the Pg state which may be compared to the substrate equilibria in the Pfr state of prototypical phytochromes.⁴⁴ In the latter case, this conformational equilibrium was suggested to facilitate the dark conversion from the Pfr to the Pr state, in contrast to the thermally stable Pfr state of bathy phytochromes.⁴⁴ In fact, a slow Pg \rightarrow Pr dark conversion is also noted for AnPixJg2.

Color Tuning in the Cyanobacteriochrome AnPixJg2. The most striking difference between AnPixJg2 and canonical

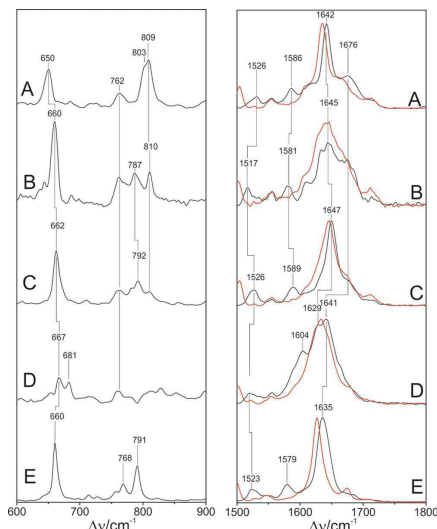


Figure 7. RR spectra of the species constituting the Pg-to-Pr reaction pathway. A, Pg; B, Lumi-G; C, Meta-G1; D, Meta-G2; and E, Pr. The intermediates were trapped at the temperatures indicated in Figure 5. The black and red lines refer to the measurements in H₂O and D₂O solutions, respectively (pH 7.8).

represents the overlapping contributions of more than one intermediate containing a largely distorted ZZZssa configuration; however, the poor signal-to-noise ratio impairs precise identification of the individual band components. Also, the HOOP region displays a rather complex but well-resolved vibrational band pattern. It is therefore interesting to note that for the reverse reaction of another phytochrome-like protein, bacteriochrome NpR6012g4, two subsequent Lumi-G inter-

phytochromes refers to the unusually blue-shifted absorption of the Pg parent state, the counterpart of the far-red-absorbing Pfr state of classical phytochromes. This blue shift is accompanied by large frequency upshifts of all methine bridge stretchings, even the structurally rather insensitive B–C stretching, and also of the N–H ip mode. These systematic frequency upshifts cannot be related to ground state structural changes of the cofactor (vide supra) but are instead, together with the hypsochromically shifted electronic absorption, reminiscent of the so-called opsin shift in (bacterial) rhodopsins carrying a protonated retinal Schiff base as a cofactor.⁵² Here, the specific cofactor–protein interactions have been shown to perturb the energy levels of the highest occupied and lowest unoccupied molecular orbitals such that the excitation energy of the first electronic transition may vary substantially, covering a range of absorption maxima from 600 to 400 nm. These changes in the absorption maxima are inversely related to the frequency of the C=C stretching modes of the polyene chain. These tendencies nicely match the observations for the Pg and Pfr states of AnPixJg2 and canonical phytochromes, respectively. Whereas in AnPixJg2, the hypsochromic shift of the absorption maximum in Pg compared to Pr is accompanied by an upshift of the C=C stretching frequencies, the opposite shifts of the absorption maxima and the C=C stretching frequencies are observed for the Pr → Pfr transition in canonical phytochromes.

The factors controlling the opsin shift in retinal proteins have been extensively studied in the past decades, and it was demonstrated that both electrostatic and hydrophobic interactions may be responsible for tuning the energy levels.⁵² These interactions may be accomplished by the appropriate positioning of charged, polar, and unipolar amino acid side chains in the vicinity of the chromophore. Alternatively, also an increased solvent (water) exposure may cause a significant blue shift of the absorption maximum and the corresponding upshift of the C=C stretchings as revealed by the comparison of protonated retinal Schiff bases in protic solvents and in the protein-embedded state.⁵³ Although rearrangements of charged and uncharged amino acids in the chromophore binding pocket cannot be ruled out for the Pr → Pg transition of AnPixJg2, a significant increase of the solvent accessibility is likely to occur as suggested by the present MD simulations of the Pg model. Thus, we conclude that the influx of water molecules into the chromophore binding pocket is the main origin for the shifts of the electronic energy levels which raise the energy of the first electronic transition, concomitant to upshifts of the methine bridge stretching frequencies.

According to the MD simulations, the cofactor photoisomerization initiates the increase of solvent accessibility of the chromophore. This interpretation is consistent with the RR spectroscopic data. Because AnPixJg2 and canonical phytochromes seem to exhibit very similar cofactor structures in the corresponding states of the Pr → Pg(Pfr) forward and backward transformations, the additional frequency shifts suggest a stepwise influx of water into the chromophore binding pocket in AnPixJg2 during the formation of the Lumi-R (Lumi-F) photoproduct and the recovery of the final state Pg(Pr) (see Supporting Information, Figures S4 and S5 and Table S3).

In summary, AnPixJg2 seems to employ a unique strategy for color tuning that is different from those in other CBCRs. Instead of acid/base reactions for de- and reprotonating the cofactor, or chemical modifications via Cys side chains to perturb the π -electron systems,^{17,21–23,54} the PCB cofactor in

AnPixJg2 remains protonated and adopts a conformation very similar to that of its Pfr counterpart in canonical phytochromes. In AnPixJg2, the substantial color change is instead attributed to a strongly increased solvent accessibility, which is the result of the altered cofactor–protein (PCB–Trp90) interactions initiated by the Z → E isomerization of the chromophore. Presumably, such a mechanism for color tuning is possible only because of the small size of the “GAF-only” protein compared to classical PAS-GAF-PHY phytochromes.

■ ASSOCIATED CONTENT

Supporting Information

Additional experimental details and RR spectra, including a description of the subtraction procedure, an analysis of the solvent effects on the RR spectra, and further figures and tables illustrating the MD simulation. This material is available free of charge via the Internet at <http://pubs.acs.org>.

■ AUTHOR INFORMATION

Corresponding Author

*Tel: +49-30-314-21419. Fax: +49-30-314-21122. E-mail: Hildebrandt@chem.tu-berlin.de.

Funding

The work was supported by Deutsche Forschungsgemeinschaft, Sfb1078 (B6, C3).

Notes

The authors declare no competing financial interest.

■ ACKNOWLEDGMENTS

The authors thank the “Norddeutscher Verbund für Hoch- und Höchstleistungsrechnen” (HLRN) for providing computer power.

■ ABBREVIATIONS

Agp1 and Agp2, *Agrobacterium tumefaciens* phytochromes 1 and 2, respectively; *a* and *s*, nomenclature for the methine bridge single bond conformation (*anti* and *syn*, respectively); CBCR, cyanobacteriochrome; Cph1, cyanobacterium *Synechocystis* sp. PCC 6803 phytochrome 1; EDTA, ethylenediaminetetraacetic acid; GAF, cGMP specific phosphodiesterases, adenylate cyclases, formate hydrogen lyase transcription activator; HOOP, hydrogen-out-of-plane; MD, molecular dynamics; Nd:YAG, neodymium-doped yttrium aluminum garnet; N–H ip, N–H in plane bending vibrational mode; Pap1, *Pseudomonas aeruginosa* phytochrome 1; PAS, PER/ARNT/SIM protein domain; PCB, phycocyanobilin; Pfr, phytochrome far-red-absorbing form; PHY, phytochrome specific domain; phyA–phyE, plant phytochromes A–E from *A. thaliana*; Pg and Pr, green- and red-absorbing form of the pigment, respectively; PVB, phycoviolobilin; RR, resonance Raman; TePixJ, PixJ of *Thermosynechococcus elongatus* GAF-only blue/green-absorbing cyanobacteriochrome; Tris, tris-(hydroxymethyl)aminomethane; Z and E, nomenclature for the methine bridge double bond configuration (*Zusammen* and *Entgegen*, respectively, corresponding to *cis/trans*)

■ REFERENCES

- (1) Butler, W. L.; Norris, K. H.; Siegelman, H. W.; and Hendricks, S. B. (1959) Detection, assay, and preliminary purification of the pigment controlling photoresponsive development of plants. *Proc. Natl. Acad. Sci. U.S.A.* 45, 1703–1708.

- (2) Siegelman, H. W., and Firer, E. M. (1964) Purification of phytochrome from oat seedlings. *Biochemistry* 3, 418–423.
- (3) Kendrick, R. E., and Kronenberg, G. H. M. (1994) *Photomorphogenesis in Plants*, Kluwer Academic Publishers, Dordrecht, The Netherlands.
- (4) Whitelam, G. C., Patel, S., and Devlin, P. F. (1998) Phytochromes and photomorphogenesis in *Arabidopsis*. *Philos. Trans. R. Soc., B* 353, 1445–1453.
- (5) Neff, M., Fankhauser, C., and Chory, J. (2000) Light: An indicator of time and place. *Genes Dev.* 14, 257–271.
- (6) Casal, J. J., Luccioni, L. G., Oliverio, K. A., and Boccalandro, H. E. (2003) Phytochrome signaling and photomorphogenesis in *Arabidopsis*. *Photochem. Photobiol. Sci.* 2, 625–636.
- (7) Butler, W. L. (1972) in *Phytochrome* (Mitrakos, M., and Shropshire, W., Eds.) pp 182–192, Academic Press, New York.
- (8) Kendrick, R. E., and Spruit, C. J. P. (1977) Phototransformations of phytochrome. *Photochem. Photobiol.* 26, 201–214.
- (9) Rüdiger, W. (1992) Events in the phytochrome molecule after irradiation. *Photochem. Photobiol.* 56, 803–809.
- (10) Sineshchikov, V. A. (1995) Photobiophysics and photochemistry of the heterogeneous phytochrome system. *Biochim. Biophys. Acta* 1228, 125–164.
- (11) Braslavsky, S. E., Gärtner, W., and Schaffner, K. (1997) Phytochrome photoconversion. *Plant Cell Environ.* 20, 700–706.
- (12) Braslavsky, S. E. (2003) in *Photochromism, Molecules and Systems* (Bouas-Laurent, D., and Bouas-Laurent, H., Eds.) pp 738 – 755, Elsevier Science, Amsterdam.
- (13) Mroginiski, M., von Stetten, D., Kaminski, S., Velazquez Escobar, F., Michael, N., Daminelli-Widany, G., and Hildebrandt, P. (2011) Elucidating photoinduced structural changes in phytochromes by the combined application of resonance Raman spectroscopy and theoretical methods. *J. Mol. Struct.* 993, 15–25.
- (14) Hughes, J., Lamparter, T., Mittmann, F., Hartmann, E., Gärtner, W., Wilde, A., and Bömer, T. (1997) A prokaryotic phytochrome. *Nature* 386, 663–663.
- (15) Karniol, B., Wagner, J. R., Walker, J. M., and Vierstra, R. D. (2005) Phylogenetic analysis of the phytochrome superfamily reveals distinct microbial subfamilies of photoreceptors. *Biochem. J.* 392, 103–116.
- (16) Karniol, B., and Vierstra, R. D. (2003) The pair of bacteriophytochromes from *Agrobacterium tumefaciens* are histidine kinases with opposing photobiological properties. *Proc. Natl. Acad. Sci. U.S.A.* 100, 2807–2812.
- (17) Hirose, Y., Rockwell, N. C., Nishiyama, K., Narikawa, R., Ukajic, Y., Inomata, K., Lagarias, J. C., and Ikeuchi, M. (2013) Green/red cyanobacteriochromes regulate complementary chromatic acclimation via a protochromic photocycle. *Proc. Natl. Acad. Sci. U.S.A.* 110, 4974–4979.
- (18) Ikeuchi, M., and Ishizuka, T. (2008) Cyanobacteriochromes: A new superfamily of tetrapyrrole-binding photoreceptors in cyanobacteria. *Photochem. Photobiol. Sci.* 7, 1159–1167.
- (19) Rockwell, N. C., and Lagarias, J. C. (2010) A brief history of phytochromes. *ChemPhysChem* 11, 1172–1180.
- (20) Song, J.-Y., Cho, H. S., Cho, J. I., Jeon, J.-S., Lagarias, J. C., and Park, J. I. (2011) Near-UV cyanobacteriochrome signaling system elicits negative phototaxis in the cyanobacterium *Synechocystis* sp. PCC 6803. *Proc. Natl. Acad. Sci. U.S.A.* 108, 10780–10785.
- (21) Uljasz, A. T., Cornilescu, G., von Stetten, D., Cornilescu, C., Velazquez Escobar, F., Zhang, J., Stankey, R. J., Rivera, M., Hildebrandt, P., and Vierstra, R. D. (2009) Cyanochromes are blue/green light photoreversible photoreceptors defined by a stable double cysteine linkage to a phytylcovobilin-type chromophore. *J. Biol. Chem.* 284, 29757–29772.
- (22) Rockwell, N. C., Njuguna, S. L., Roberts, L., Castillo, E., Parson, V. L., Dwojak, S., Lagarias, J. C., and Spiller, S. C. (2008) A second conserved GAF domain cysteine is required for the blue/green photoreversibility of cyanobacteriochrome Thro924 from *Thermosynechococcus elongatus*. *Biochemistry* 47, 7304–7316.
- (23) Ishizuka, T., Kamiya, A., Suzuki, H., Narikawa, R., Noguchi, T., Kohchi, T., Inomata, K., and Ikeuchi, M. (2011) The cyanobacteriochrome, TePixJ, isomerizes its own chromophore by converting phytylcovobilin to phytylcovobilin. *Biochemistry* 50, 953–961.
- (24) Uljasz, A. T., Cornilescu, G., Cornilescu, C. C., Zhang, J., Rivera, M., Markley, J. L., and Vierstra, R. D. (2010) Structural basis for the photoconversion of a phytochrome to the activated Pfr form. *Nature* 463, 250–254.
- (25) Kaminski, S., and Mroginiski, M. A. (2010) Molecular dynamics of phytylcovobilin binding bacteriophytochromes: A detailed study of structural and dynamic properties. *J. Phys. Chem. B* 114, 16677–16686.
- (26) Kneip, C., Hildebrandt, P., Nemeth, K., Mark, F., and Schaffner, K. (1999) Interpretation of the resonance Raman spectra of linear tetrapyrroles based on DFT calculations. *Chem. Phys. Lett.* 311, 479–484.
- (27) Mroginiski, M. A., von Stetten, D., Velazquez Escobar, F., Strauss, H. M., Kaminski, S., Scheerer, P., Günther, M., Murgida, D. H., Schmieder, P., Bongards, C., Gärtner, W., Maillet, J., Hughes, J., Essen, L.-O., and Hildebrandt, P. (2009) Chromophore structure of cyanobacterial phytochrome Cph1 in the Pr state: Reconciling structural and spectroscopic data by QM/MM calculations. *Biophys. J.* 96, 4153–4163.
- (28) Narikawa, R., Fukushima, Y., Ishizuka, T., Itoh, S., and Ikeuchi, M. (2008) A novel photoactive GAF domain of cyanobacteriochrome AnPixJ that shows reversible green/red photoconversion. *J. Mol. Biol.* 380, 844–855.
- (29) Narikawa, R., Ishizuka, T., Muraki, N., Shiba, T., Kurisu, G., and Ikeuchi, M. (2013) Structures of cyanobacteriochromes from phototaxis regulators AnPixJ and TePixJ reveal general and specific photoconversion mechanism. *Proc. Natl. Acad. Sci. U.S.A.* 110, 918–923.
- (30) Fukushima, Y., Iwaki, M., Narikawa, R., Ikeuchi, M., Tomita, Y., and Itoh, S. (2011) Photoconversion mechanism of a green/red photosensory cyanobacteriochrome AnPixJ: Time-resolved optical spectroscopy and FTIR analysis of the AnPixJ-GAF2 domain. *Biochemistry* 50, 6328–6339.
- (31) Joergensen, V. L., Chandrasekhar, J., Madura, J. D., Impey, R. W., and Klein, M. L. (1983) Comparison of simple potential functions for simulating liquid water. *J. Chem. Phys.* 79, 926–935.
- (32) Phillips, J. C., Braun, R., Wang, W., Gumbart, J., Tajkhorshid, E., Villa, E., Chipot, C., Skeel, R. D., Kalé, L., and Schulten, K. (2005) Scalable molecular dynamics with NAMD. *J. Comput. Chem.* 26, 1781–1802.
- (33) MacKerell, A. D., Bashford, D., Bellott, M., Dunbrack, R. L., Jr., Evanseck, J. D., Field, M. J., Fischer, S., Gao, J., Guo, H., Ha, S., Joseph-McCarthy, D., Kuchnir, L., Kuczera, K., Lau, F. T. K., Mattos, C., Michnick, S., Ngo, T., Nguyen, D. T., Prodhom, B., Reiher, W. E., III, Roux, B., Schlenker, M., Smith, J. C., Stote, R., Straub, J., Watanabe, M., Wiórkiewicz-Kuczera, J., Yin, D., and Karplus, M. (1998) All-atom empirical potential for molecular modeling and dynamics studies of proteins. *J. Phys. Chem. B* 102, 3586–3616.
- (34) Kaminski, S., Daminelli-Widany, G., and Mroginiski, M. A. (2009) Molecular dynamics simulations of the chromophore binding site of *Deinococcus radiodurans* bacteriophytochrome using new force field parameters for the phytylcovobilin chromophore. *J. Phys. Chem. B* 113, 945–958.
- (35) Feller, S. E., Zhang, Y., Pastor, R. W., and Brooks, B. R. (1995) Constant pressure molecular dynamics simulation: The Langevin piston method. *J. Chem. Phys.* 103, 4613–4621.
- (36) Darden, T., York, D., and Pedersen, L. (1993) Particle mesh Ewald: An $N \log(N)$ method for Ewald sums in large systems. *J. Chem. Phys.* 98, 10089–10092.
- (37) van Gunsteren, W., and Berendsen, H. (1977) Algorithms for macromolecular dynamics and constraint dynamics. *Mol. Phys.* 34, 1311–1327.
- (38) Humphrey, W., Dalke, A., and Schulten, K. (1996) VMD: Visual molecular dynamics. *J. Mol. Graphics* 14, 33–38.

- (39) Essen, L.-O., Mailliet, J., and Hughes, J. (2008) The structure of a complete phytochrome sensory module in the Pr ground state. *Proc. Natl. Acad. Sci. U.S.A.* 105, 14709–14714.
- (40) Mroginski, M. A., Kaminski, S., von Stetten, D., Ringsdorf, S., Gärtner, W., Essen, L. O., and Hildebrandt, P. (2011) The structure of the chromophore binding pocket in the Pr state of plant phytochrome phyA. *J. Phys. Chem. B* 115, 1220–1231.
- (41) Kneip, C., Hildebrandt, P., Schlamann, W., Braslavsky, S. E., Mark, F., and Schaffner, K. (1999) Protonation state and structural changes of the tetrapyrrole chromophore during the $P_r \rightarrow P_{fr}$ phototransformation of phytochrome: A resonance Raman spectroscopic study. *Biochemistry* 38, 15185–15192.
- (42) Schwinté, P., Foerstendorf, H., Gärtner, W., Mroginski, M. A., Hildebrandt, P., and Siebert, F. (2008) Fourier transform infrared studies of the photoinduced processes of phytochrome phyA using isotopically labelled chromophores and density functional theory calculations. *Biophys. J.* 95, 1256–1267.
- (43) Mroginski, M. A., Murgida, D. H., von Stetten, D., Kneip, C., Mark, F., and Hildebrandt, P. (2004) Determination of the chromophore structures in the photoinduced reaction cycle of phytochrome. *J. Am. Chem. Soc.* 126, 16734–16735.
- (44) Salewski, J., Velazquez Escobar, F., Kaminski, S., von Stetten, D., Keidel, A., Rippers, Y., Michael, N., Scheerer, P., Piwowarski, P., Bartl, F., Frankenberg-Dinkel, N., Ringsdorf, S., Gärtner, W., Lamparter, T., Mroginski, M. A., and Hildebrandt, P. (2013) The structure of the biliverdin cofactor in the Pfr state of bathy and prototypical phytochromes. *J. Biol. Chem.* 288, 16800–16814.
- (45) Wagner, J. R., Brunzelle, J. S., Forest, K. T., and Vierstra, R. D. (2005) A light-sensing knot revealed by the structure of the chromophore-binding domain of phytochrome. *Nature* 438, 325–331.
- (46) Kim, P. W., Freer, L. H., Rockwell, N. C., Martin, S. S., Lagarias, J. C., and Larsen, D. S. (2012) Femtosecond photodynamics of the red/green cyanobacteriochrome NpR6012g4 from *Nostoc punctiforme*. 1. Forward dynamics. *Biochemistry* 51, 608–618.
- (47) Borucki, B., von Stetten, D., Seibeck, S., Lamparter, T., Michael, N., Mroginski, M. A., Otto, H., Murgida, D. H., Heyn, M. P., and Hildebrandt, P. (2005) Light-induced proton release of phytochrome is coupled to the transient deprotonation of the tetrapyrrole chromophore. *J. Biol. Chem.* 280, 34358–34364.
- (48) Von Stetten, D., Seibeck, S., Michael, N., Scheerer, P., Mroginski, M. A., Murgida, D. H., Krauss, N., Heyn, M. P., Hildebrandt, P., Borucki, B., and Lamparter, T. (2007) Highly conserved residues D197 and H250 in Agp1 phytochrome control the proton affinity of the chromophore and Pfr formation. *J. Biol. Chem.* 282, 2116–2123.
- (49) Kim, P. W., Freer, L. H., Rockwell, N. C., Martin, S. S., Lagarias, J. C., and Larsen, D. S. (2012) Femtosecond photodynamics of the red/green cyanobacteriochrome NpR6012g4 from *Nostoc punctiforme*. 2. Reverse dynamics. *Biochemistry* 51, 619–630.
- (50) Matysik, J., Hildebrandt, P., Smit, K., Mark, F., Gärtner, W., Braslavsky, S. E., Schaffner, K., and Schrader, B. (1997) Raman spectroscopic analysis of isomers of biliverdin dimethyl ester. *J. Pharm. Biomed. Anal.* 15, 1319–1324.
- (51) van Thor, J. J., Borucki, B., Crielgaard, W., Otto, H., Lamparter, T., Hughes, J., Hellingwerf, K. J., and Heyn, M. P. (2001) Light-induced proton release and proton uptake reactions in the cyanobacterial phytochrome Cph1. *Biochemistry* 40, 11460–11471.
- (52) Lin, S. W., Kochendoerfer, G. G., Carroll, K. S., Wang, D., Mathies, R. A., and Sakmar, T. P. (1998) Mechanisms of spectral tuning in blue cone visual pigments. Visible and Raman spectroscopy of blue-shifted rhodopsin mutants. *J. Biol. Chem.* 273, 24583–24591.
- (53) Nielsen, M. B. (2009) Model systems for understanding absorption tuning by opsin proteins. *Chem. Soc. Rev.* 38, 913–924.
- (54) Enomoto, G., Hirose, Y., Narikawa, R., and Ikeuchi, M. (2012) Thiol-based photocycle of the blue and teal light-sensing cyanobacteriochrome Tlr999. *Biochemistry* 51, 3050–3058.

Supporting Information

Photoconversion mechanism of the second GAF domain of cyanobacteriochrome AnPixJ and the cofactor structure of its green-absorbing state

*Francisco Velazquez Escobar¹, Tillmann Utesch¹, Rei Narikawa^{2,3}, Masahiko Ikeuchi^{2,3}, Maria
Andrea Mroginski¹, Wolfgang Gärtner⁴, Peter Hildebrandt^{1*}*

¹ Institut für Chemie, Technische Universität Berlin, Sekr. PC14, Straße des 17. Juni 135, D-10623
Berlin, Germany

² Department of Life Sciences (Biology), Graduate School of Art and Sciences, University of Tokyo,
Komaba, Meguro, Tokyo, 153-8902, Japan

³ Japan Science and Technology Agency (JST), PRESTO, 4-1-8 Honcho Kawaguchi, Saitama 332-
0012 Japan

⁴ Max-Planck-Institut für Chemische Energiekonversion, Stiftstrasse 34-36, D-45470 Mülheim an
der Ruhr, Germany

Content:

- 1. Materials**
- 2. Details of the RR experiments**
- 3. Additional RR spectra**
- 4. Figures illustrating the MD simulations**
- 5. Structural models of derived from the MD simulations**
- 6. Structural parameters of the MD simulations**

1. Materials

The following materials were used: Tris-HCl, min. 99% (SERVA); NaCl, min. 99.5% (MERCK); EDTA, min. 99% (SIGMA-ALDRICH); D₂O, 99.95% (Deutero GmbH). pD-adjustments for D₂O buffer solutions were performed with a 2 molar DCl solution purchased from Deutero GmbH (DCl, 38% in D₂O, 12 Molar, 99.50%). Determination of the pH value was done using a pH-ISE-Meter (Denver Instruments, Model 225) and calibrated against three standard buffer solutions (Merck) at pH = 4.01, 7.00 and 10.00, which were freshly prepared prior to the sample preparation. pD values refer to the pH meter reading for the solution in D₂O corrected for H/D isotope effect (+0.4 units).

2. Details of the RR experiments:

Table S1. Irradiation conditions of the RR measurements.

The temperatures at which the samples were irradiated (with either 660 or 530 nm light) were first explored and optimized for the measurements in H₂O. The optimized procedure was then also applied for the measurements in D₂O. The labelling code for each illumination step is used to denote the subsequent subtraction procedure of the raw spectra given in Table S2.

No.	Label	light exposure conditions		
		time	temperature	λ (LED)
1	Pr _{dark}	non-irradiated sample		
2	Pr _{dark}	2 min	@ 20 °C	530 nm
3	Int _{red,1}	10 min	@ -80 °C	660 nm
4	Int _{red,2}	10 min	@ -50 °C	660 nm
5	Int _{red,3}	10 min	@ -40 °C	660 nm
6	Int _{red,4}	10 min	@ -30 °C	660 nm
7	Pg	10 min	@ 20 °C	660 nm
8	Int _{green,1}	2 min	@ -140 °C	530 nm
9	Int _{green,2}	10 min	@ -120 °C	530 nm
10	Int _{green,3}	10 min	@ -80 °C	530 nm
11	Int _{green,4}	10 min	@ -40 °C	530 nm
12	Pr _{back}	2 min	@ 20 °C	530 nm

Table S2. Subtraction procedure for constructing the pure spectra of the intermediates of the Pr-to-Pg and Pg-to-Pg photoconversion.

The subtraction was performed starting with the raw spectra. After the subtraction procedures, polynomial baseline correction was applied to each pure spectrum. Spectra were normalized to the highest band between 600 and 1700 cm^{-1} . For the forward reaction we found strong similarities between the $\text{Int}_{\text{Red3,pure}}$ (-40°C) and $\text{Int}_{\text{Red4,pure}}$ (-30°C) spectra, whereas the respective raw spectra mainly differ by the Pg contribution indicating that already at -40°C but even more at -30°C , the thermal relaxation to the Pg state takes place. Therefore, the pure Int_{Red3} and Int_{Red4} spectra reflect the same intermediate Meta-R1.

General Subtraction procedure

Subtraction procedure for the Pr-to-Pg intermediates					
$\text{Int}_{\text{red1,pure}}$	=	$\text{Int}_{\text{red1,raw}}$	-	Pr_{raw}	
$\text{Int}_{\text{red2,pure}}$	=	$\text{Int}_{\text{red2,raw}}$	-	$\text{Int}_{\text{red1,raw}}$	
$\text{Int}_{\text{red3,pure}}$	=	$\text{Int}_{\text{red3,raw}}$	-	$\text{Int}_{\text{red2,raw}}$	- $\text{Int}_{\text{red4,pure}}$ - Pg_{raw}
$\text{Int}_{\text{red4,pure}}$	=	$\text{Int}_{\text{red4,raw}}$	-	$\text{Int}_{\text{red2,pure}}$	- $\text{Int}_{\text{red3,pure}}$ - Pg_{raw}
Subtraction procedure for the Pg-to-Pr intermediates					
$\text{Int}_{\text{green1,pure}}$	=	$\text{Int}_{\text{green1,raw}}$	-	Pg_{raw}	
$\text{Int}_{\text{green2,pure}}$	=	$\text{Int}_{\text{green2,raw}}$	-	$\text{Int}_{\text{green1,raw}}$	
$\text{Int}_{\text{green3,pure}}$	=	$\text{Int}_{\text{green3,raw}}$	-	$\text{Int}_{\text{green2,raw}}$	- $\text{Int}_{\text{green4,pure}}$ - Pg_{raw}
$\text{Int}_{\text{green4,pure}}$	=	$\text{Int}_{\text{green4,raw}}$	-	$\text{Int}_{\text{green4,pure}}$	- $\text{Int}_{\text{green3,pure}}$ - Pg_{raw}

3. Additional RR spectra

Figure S1. RR spectra of (A) the Pr state phyA-PCB, (B) the Pr state of AnPixJg2, (C) the Pg state of AnPixJg2, and (D) the Pfr state of phyA-PCB. Spectra measured in H₂O and D₂O are given by the black and red lines, respectively.

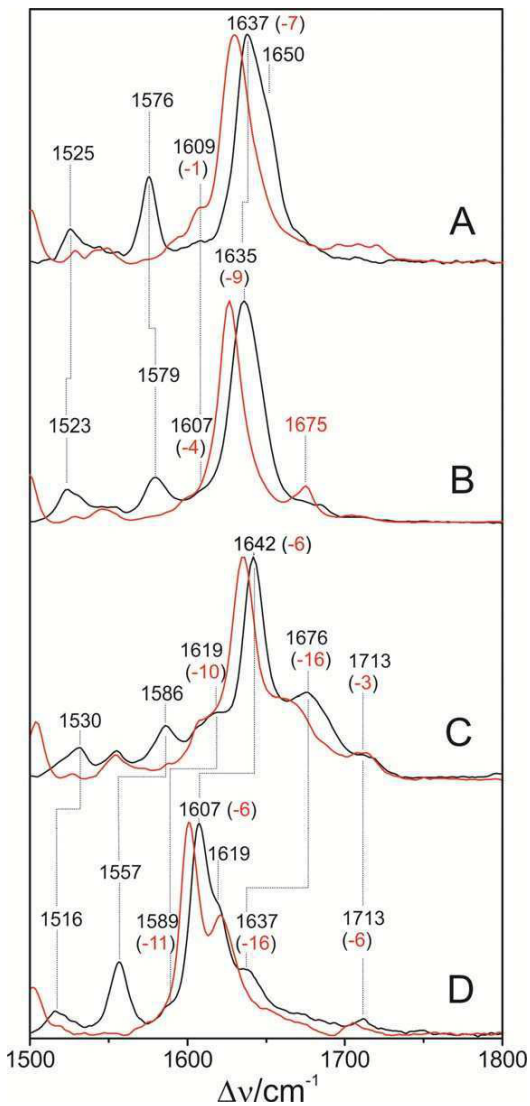


Figure S2. RR spectra of (A) the Pr of AnPixJg2 and (B) the Pg state of AnPixJg2, specifically indicating the N-H(N-D) ip modes. Spectra measured in H₂O and D₂O are given by the black and red lines, respectively.

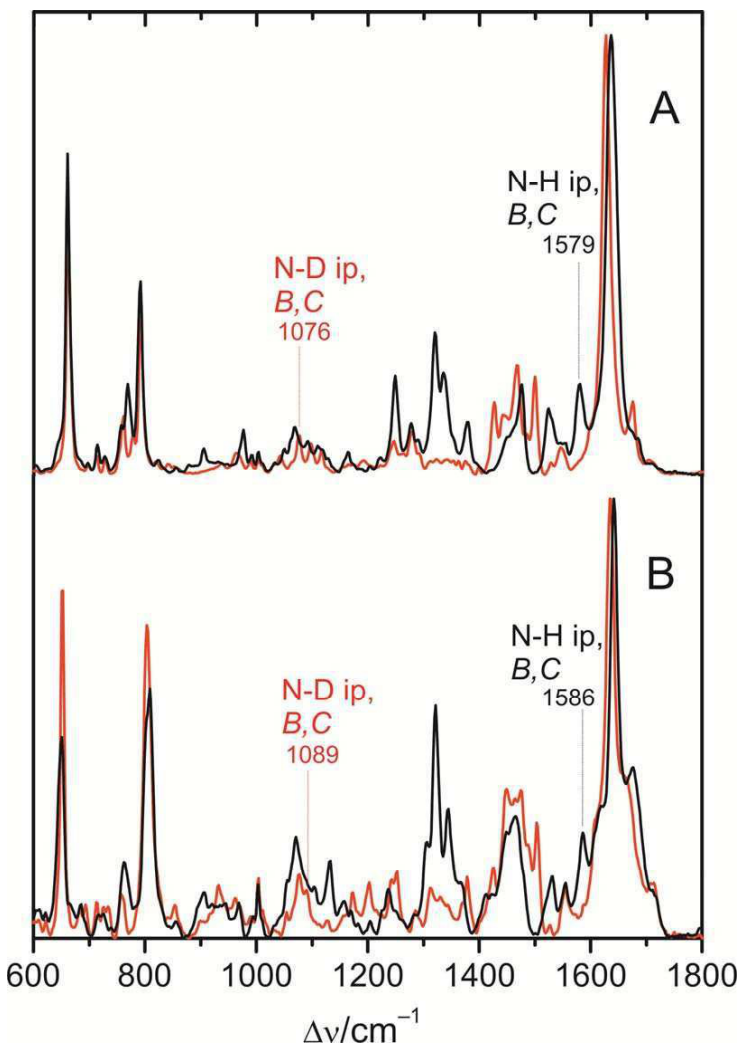


Figure S3. RR spectra of (A) the Pg of AnPixJg2 and (B) the Pfr state of phyA-PCB in the HOOP region, measured in H₂O.

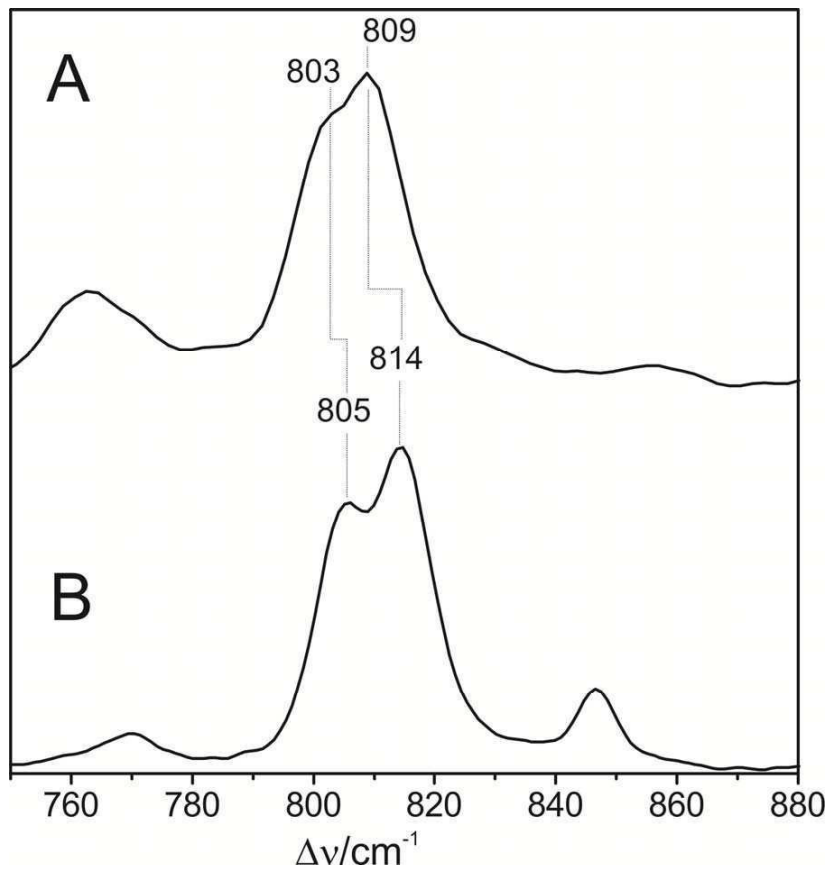


Fig. S4. RR spectra of the states involved in the phototransformation from Pr to Pg of AnPixJg2 (left) and from Pr to Pfr of the native (full-length) plant phytochrome phyA. The spectra display the methine bridge stretching region. Bold and normal letters refer to the frequencies of the *C-D* and *A-B* stretching mode, respectively. Note that the chromophore in phyA is a phytochromobilin (PΦB) which – due to its vinyl substituent on ring *D* – leads to a ca. 10-cm⁻¹ downshift of the *C-D* stretching frequency (FEBS Lett. 414, 23-26, 1997; Biochemistry 36, 13389-13395, 1997). Except for Meta-R2 (denoted as Meta-Rc in phyA), all states involve a protonated cofactor as indicated by N-H ip mode of the pyrrole rings *B* and *C*. Data for phyA were taken from a reference after re-calibration (Biochemistry 38, 15185-15192, 1999).

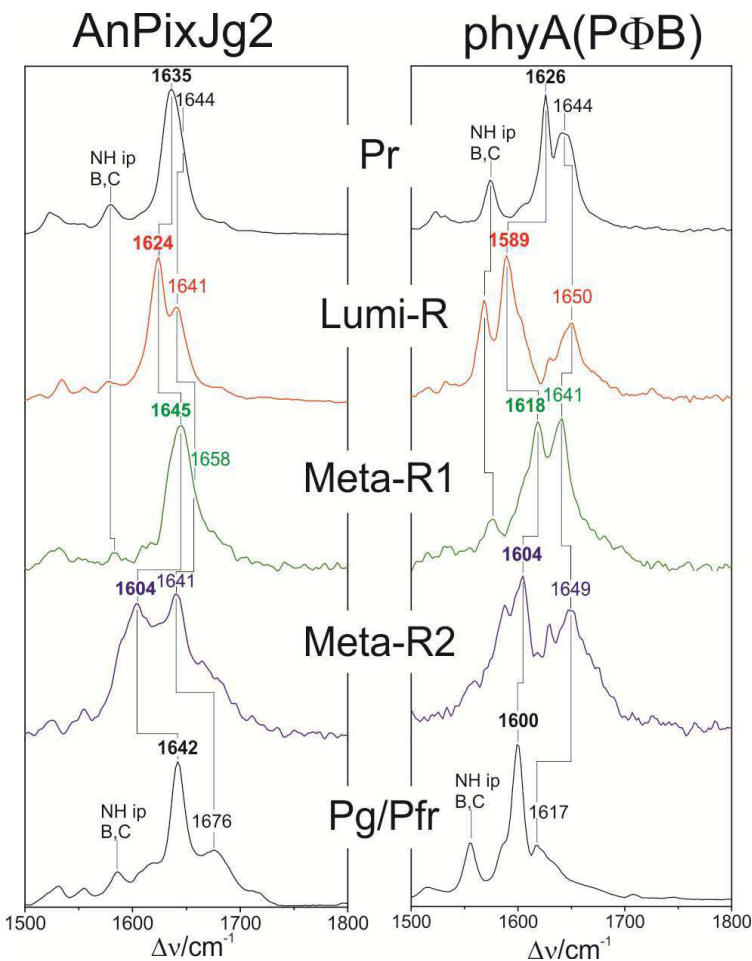
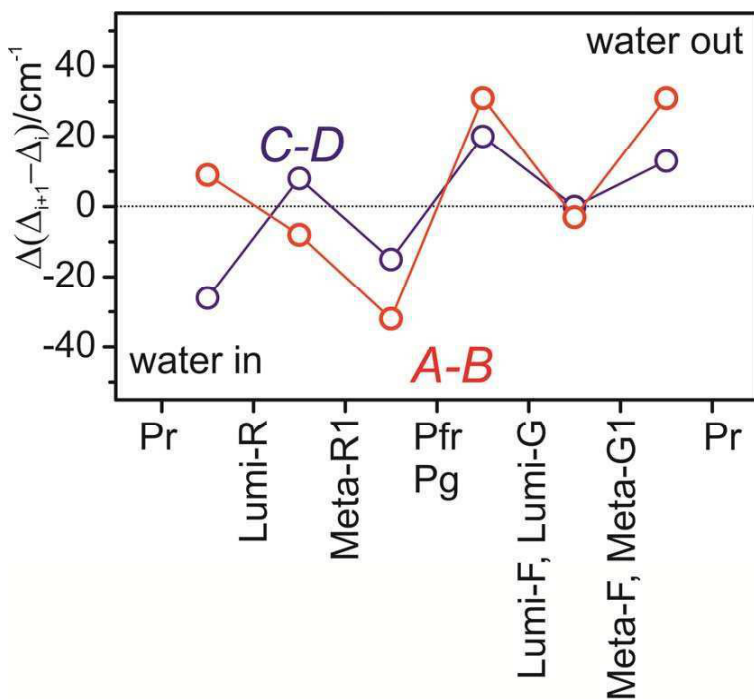


Table S3. Frequencies of the C-D and A-B stretching modes of the various states of the Pr-to-Pg forward and backward transformation in AnPixJg2 (this work) and of the Pr-to-Pfr forward and backward transformation taken from previous studies (*Biochemistry* 38, 15185-15192, 1999; *Biochemistry* 34, 10497-10507, 1995). Only the states including a protonated cofactor are considered. Frequencies are given in cm^{-1} . Further explanations are given below.

No.	State i	C-D stretching mode				A-B stretching mode			
		phyA	AnPixJg2	$\Delta(\text{phyA} - \text{AnPixJg2})$	$\Delta(\Delta_{i+1} - \Delta_i)$	phyA	AnPixJg2	$\Delta(\text{phyA} - \text{AnPixJg2})$	$\Delta(\Delta_{i+1} - \Delta_i)$
1	Pr	1626	1635	-9		1644	1644	0	
“2 – 1”					-26				9
2	Lumi-R	1589	1624	-35		1650	1641	9	
“3 – 2”					8				-8
3	Meta-R1/Meta-Ra	1618	1645	-27		1641	1658	-17	
“4 – 3”					-15				-32
4	Pfr	1600	1642	-42		1617	1676	-59	
“5 – 4”					20				+31
5	Lumi-F	1623	1645	-22		1647	1675	-28	
“6 – 5”					0				-3
6	Meta-G1/Meta-F	1625	1647	-22		1645	1676	-31	
“7 – 6”					13				+31
7	Pr	1626	1635	-9		1644	1644	0	

To elucidate the effect of increased/decreased solvent accessibility of the chromophore by comparing AnPixJg2 and plant phytochrome phyA, one has to take into account the different constitutions of the cofactors, i.e. PCB vs. PΦB. Thus, the entries in the columns $\Delta(\text{phyA} - \text{AnPixJg2})$, i.e. the frequencies difference between the corresponding in AnPixJg2 and phyA, reflect the effects of the different substituents on ring D (vinyl in PΦB and ethyl in PCB) and of the different chromophore environment. To sort out these two effects, in the columns $\Delta(\Delta_{i+1} - \Delta_i)$ we have generated the differences of these frequency differences between two subsequent states. Assuming that the photoinduced structural changes of the chromophores are the same for AnPixJg2 and phyA, these values should largely reflect only the contribution of the solvent interactions with the C-D and A-B methine bridges during the individual reaction steps. These values are plotted in Fig. S5.

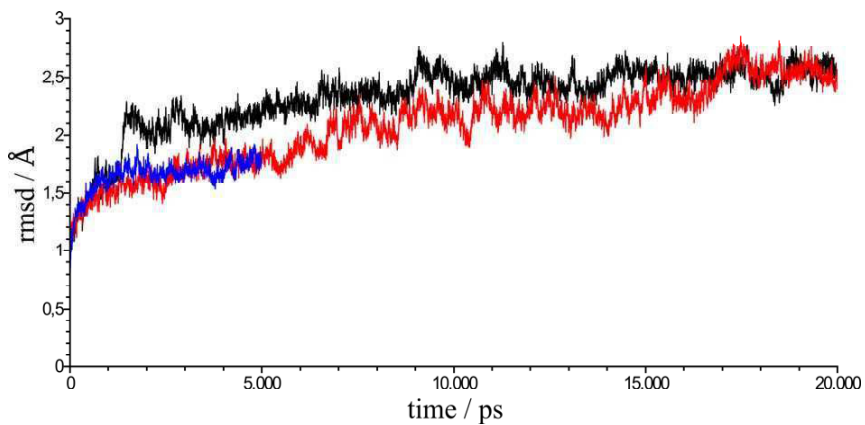
Fig. S5. Changes of the frequency differences between phyA(PΦB) and AnPixJg2 for the *C-D* and *A-B* modes during the transitions between the states of the Pr-to-Pfr/Pr-to-Pg forward and backward transformations. Data were taken from Table S3. Assuming that these changes $\Delta(\Delta_{i+1}-\Delta_i)$ are exclusively controlled by the interactions of the chromophore with nearby water molecules, negative and positive values indicate an increased and decreased solvent accessibility of the chromophore in AnPixJg2, respectively. Accordingly, water influx into the chromophore binding pocket of AnPixJg2 during the Pr-to-Pg transformation is at first noted for the isomerisation site (*C-D* bridge) in the Pr-to-Lumi-R transition and is completed during the Meta-R1-to-Pg transition (note this analysis does not consider the deprotonated species such that one may not distinguish between the Meta-R1-to-Meta-R2 and the Meta-R2-to-Pfr transition) whereas the *A-B* methine seems to experience an increased water contact only in the last step of the phototransformation. For the reverse process, the changes at the *C-D* and *A-B* methine bridges occur simultaneously in two steps, the primary Pg-to-Lumi-F event and the final steps from Meta-F-to-Pr.



4. Figures illustrating the MD simulations

Figure S6. Root-mean-square deviation of the protein backbone (with respect to the crystal structure; excluding the five amino acids of the terminal ends) (**A**) and the total energy (**B**) for the Pr (blue), Pg155 (black), and Pg175 (red) models.

A



B

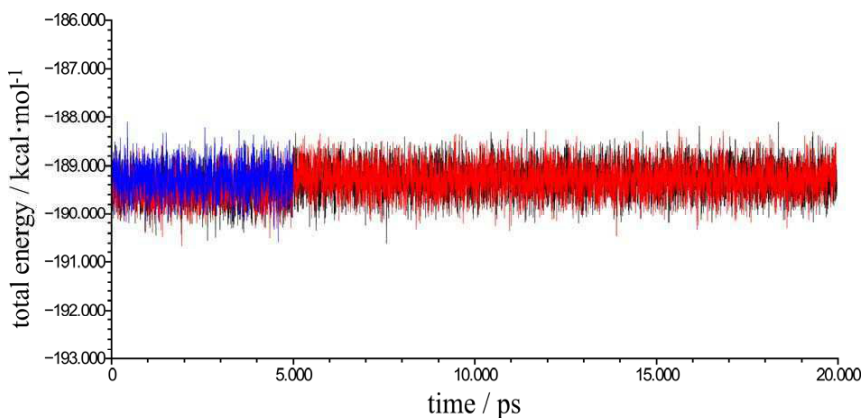


Figure S7. Angle between rings *C* and *D* of the chromophore for the Pr (blue), Pg155 (black), Pg175 (red) and Pg195 (green) models.

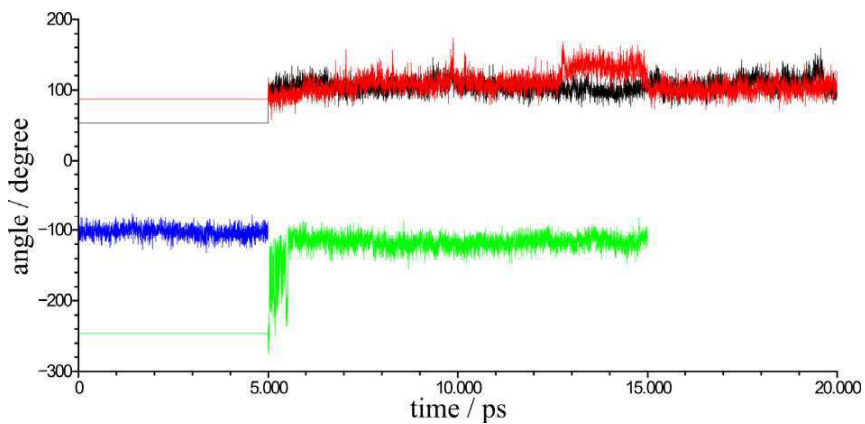
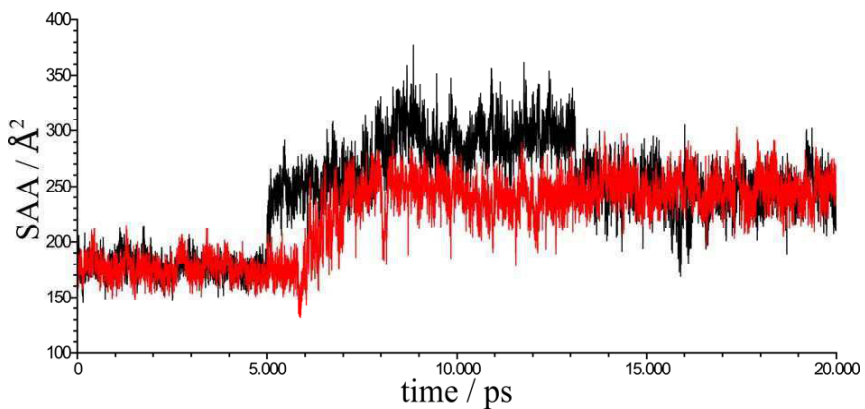


Figure S8. Evolution of the solvent accessible area of the chromophore for the Pg155 (black) and Pg175 (red) models.



5. Structural models of derived from the MD simulations

Fig. S9. Water network of the Pr state after the MD trajectory. Water molecules are displayed as orange balls and stick. Side chain nomenclature refers to the AnPixJg2 structure.

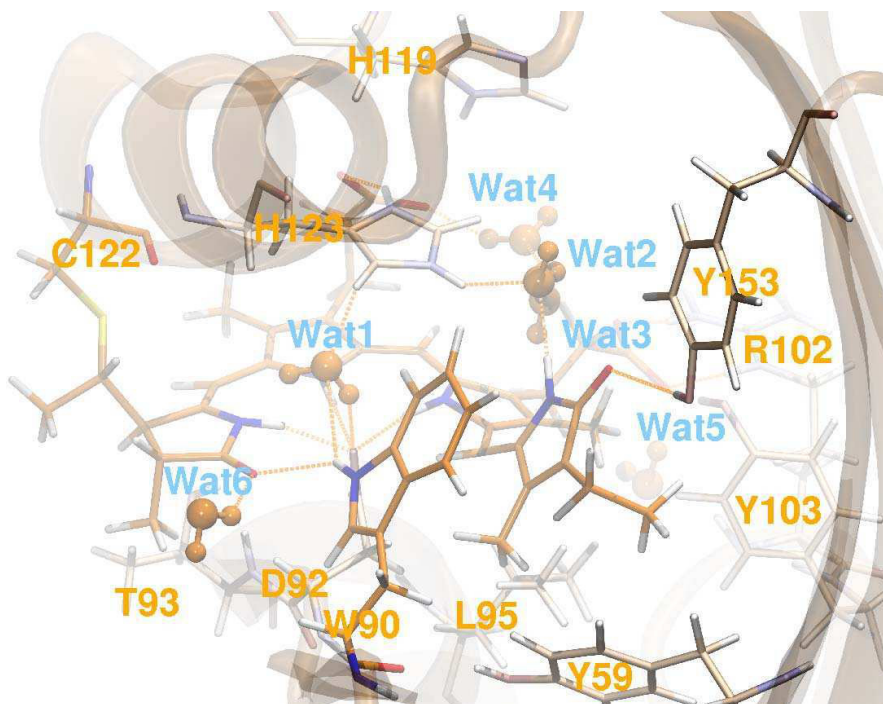
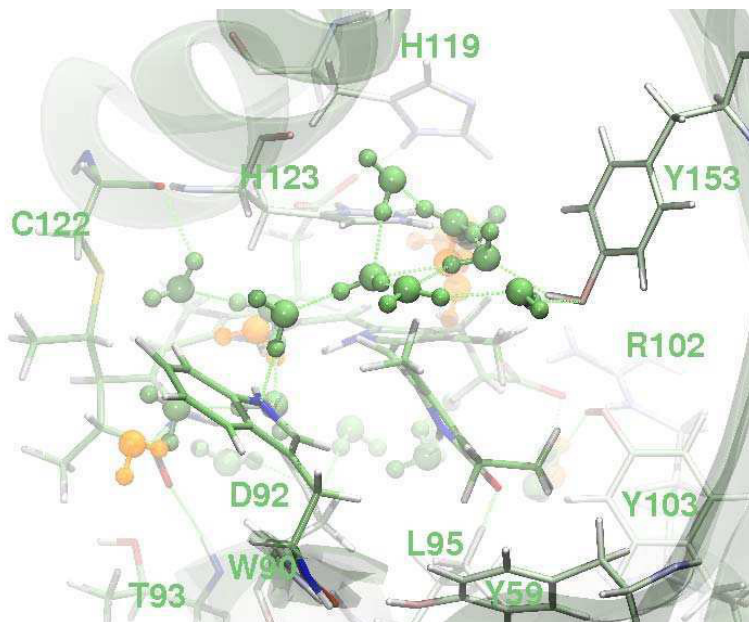


Fig. S10. Water network of the Pr photoproduct (Pg155) after the MD trajectory. Water molecules are displayed as green balls and stick. The solvent network of the Pr state is shown in orange for comparison. Side chain nomenclature refers to the AnPixJg2 structure.



6. Structural parameters of the MD simulations

Table S4. Selected bond lengths and bond angles of the PCB chromophore structure in the Pr state of AnPixJg2 as determined experimentally by X-ray crystallography, and derived from the Pr and Pg155 models during the last 5ns of the MD simulations. The respective values of the Pr states of Cph1Δ2 (X-ray structure) and of phyA-PCB (obtained by QM/MM calculations) are shown for comparison.

	AnPixJ Pr			Cph1Δ2	phyA	AnPixJ photoproduct	
	X-ray	MM	Δ ^c	X-ray ^d	QM/MM ^e	MM	Δ ^c
A-B methine-bridge							
C(A)=C ^a	1.397	1.361 ± 0.029	0.036	1.346	1.363 ± 0.003	1.360 ± 0.029	0.036
C-C(B) ^b	1.403	1.435 ± 0.029	0.032	1.494	1.428 ± 0.004	1.432 ± 0.028	0.028
C(A)=C-C(B) ^b	126.12	130.53 ± 2.58	4.41	127.98	132.0 ± 1.1	130.64 ± 2.68	3.31
N(A)C(A)=CC(B) ^b	0.38	-0.15 ± 6.26	0.23	-6.63	-5.9 ± 1.8	-7.12 ± 6.21	6.40
C(A)C-C(B)N(B) ^b	10.58	5.34 ± 9.17	5.24	12.89	17.3 ± 4.0	-14.20 ± 10.87	30.27
B-C methine-bridge							
C(B)=C ^a	1.412	1.383 ± 0.030	0.029	1.484	1.386 ± 0.004	1.379 ± 0.029	0.033
C-C(C) ^a	1.411	1.376 ± 0.030	0.035	1.469	1.398 ± 0.004	1.372 ± 0.030	0.035
C(B)=C-C(C) ^b	124.44	129.88 ± 2.58	5.44	136.06	135.5 ± 0.6	129.28 ± 2.64	5.12
N(B)C(B)=CC(C) ^b	2.21	1.96 ± 9.31	0.25	2.50	1.0 ± 2.4	-10.59 ± 8.37	8.41
C(B)C-C(C)N(C) ^b	-6.58	-8.43 ± 9.37	1.85	-1.72	-4.5 ± 2.8	10.90 ± 8.69	5.71
C-D methine-bridge							
C(C)=C ^a	1.403	1.433 ± 0.029	0.030	1.486	1.440 ± 0.004	1.431 ± 0.029	0.031
C-C(D) ^a	1.393	1.370 ± 0.029	0.023	1.479	1.358 ± 0.003	1.369 ± 0.029	0.021
C(C)=C-C(D) ^b	131.77	128.74 ± 2.90	3.03	129.62	126.2 ± 1.1	127.02 ± 2.93	5.41
N(C)C(C)=CC(D) ^b	-147.89	-137.65 ± 8.39	10.24	-152.81	-145.3 ± 4.5	135.27 ± 8.17	84.61
C(C)C-C(D)N(D) ^b	26.96	25.34 ± 9.79	1.62	2.46	10.6 ± 1.7	-57.91 ± 9.45	46.24

^a bond lengths are given in Å; ^b bond dihedrals are given in degrees; ^c difference between X-ray and structure after MM-trajectory; ^d Mroginiski et al, Biophys. J., 2009, 96, 4153-4163.; ^e Mroginiski et al, J. Phys. Chem. B, 2010, 115, 1220-1231.

9. Summary

Combining the large library of vibrational spectra of phytochrome [102, 118, 184], increasing availability of phytochrome crystal structures [49, 190, 214] and development of more accurate theoretical models [127, 130], this work achieved a breakthrough in the comprehensive and integral study of the chromophore structural changes in phytochromes and cyanobacteriochromes. Furthermore, quantitative spectral analysis allowed determination of thermodynamic parameters [159, 207], allowing for an improved understanding of dynamic processes from a molecular and atomistic perspective.

Pr-to-Pfr pathway in prototypical phytochromes Formation of the Pfr state in the BV-binding prototypical phytochromes Agp1, Rph2 and CphB involves several changes within the chromophore and of the protein structure. First, the *Z/E* isomerization leads to the formation of the Lumi-R intermediate in which the chromophore adopts a highly tensed ZZE geometry. This intermediate decays to a more relaxed Meta-Ra intermediate species, in which the binding pocket is partially relaxed but the chromophore is yet distorted. With the subsequent formation of Meta-Rc, the BV cofactor releases a proton to the solution phase, inducing larger structural changes which probably disrupt mainly the C-terminal domain structure. Finally, the Pfr state formation involves chromophore re-protonation and β -sheet-to- α -helix refolding of the tongue motif in the PHY domain [190].

While the Pr-to-Pfr forward reaction is essentially equivalent in all BV-binding phytochromes, specific protein-cofactor interactions govern the thermal stability of the Lumi-R formation in each protein. Proton dynamics play a crucial role during the Pr-to-Pfr pathway as observed through the notable H/D isotopic effect. First, the larger Lumi-R quantum-yield in D₂O can be understood in terms of a longer life-time of the Pr excited state (Pr*) [201]. The Meta-Ra-to-Meta-Rc chromophore proton release is also slower in deuterated medium [23].

The relevance of the PHY-domain is already revealed at the early Pr-to-Lumi-R transition. Deletion of this C-terminal domain also interferes the subsequent decay to the Meta-Ra intermediate. Interestingly, for proton translocation at the Meta-Rc intermediate state the PHY-domain does not play a crucial role. However the proper refolding of this C-terminal domain is highly relevant within the *bona-fide* Pfr state formation. While truncated phytochrome variants lacking the PHY domain, in some cases, afford

red-shifted product with a fully protonated ZZEssa-like chromophore geometry, the characteristic vibrational fingerprint of the chromophore (RR) and the β -sheet-to- α -helix protein-refolding (IR) are impaired.

Chromophore structure in the Pfr state in prototypical and bathy phytochromes

Experimental and calculated Raman spectra for the chromophore structure in the Pfr state of the bathy phytochrome Pap1 are in excellent agreement with previous crystallographic analyses, including the endocyclic cofactor-protein thioether binding [214]. In contrast to the highly homogenous chromophore structure in the Pfr state of bathy phytochromes, prototypical phytochromes display a more flexible Pfr cofactor structure. Structural heterogeneity is observed at the methine bridges AB and CD. Here the role of a conserved aspartate residue in both phytochromes classes plays a crucial role. In bathy phytochrome, there are strong interactions between ring D and the aspartate-side chains supported by the extremely slow H/D exchange of the pyrrole nitrogen at ring D, whereas the remaining protonable nitrogen groups in ring A, B and C undergo fast proton exchange. The corresponding hydrogen bonding situation in the Pfr state of prototypical phytochromes is considerably weaker. This structural heterogeneity is supposed to open of the thermal reaction channel of the Pfr-to-Pr reverse pathway.

Keto-enol tautomerism involved in thermal decay of the light activated state in bathy phytochromes

The photo-activated state in bathy phytochromes (Pr state) and the associated output module activation or deactivation is based on proton translocations in the chromophore pocket, including chromophore (local) and protein (global) structural changes. After the E/Z-isomerization, crucial steps for the Pr state formation takes place with the decay of Meta-F to Pr: the proton release of the propionic side chain and the α -helix-to- β -sheet transition of the PHY domain. Thermal decay of the light-activated Pr species follows a keto-enol tautomerism. A nearby histidine side chain is involved during this process. This thermal reverse-isomerization to the dark adapted Pfr state requires inter-molecular proton translocation, enabling ring D rotation in an enol tautomer. Here the initial proton re-arrangement events which trigger the activation or repression of the output module seed the reverse process to the dark adapted Pfr state, corresponding to a negative feedback mechanism. While the structural details might be certainly specific for the Pr-to-Pfr-thermal pathway in bathy-phytochromes, a keto-enol tautomerism as a prerequisite for a thermal double bond isomerization is likely to be a common mechanism also for prototypical phytochromes [155], although the steady state concentration of the ‘active’ enol form might be rather low. In this sense, the dark reversion and thus thermal deactivation in canonical phytochromes (Pfr-to-Pr) and related proteins (*e.g.* Pg-thermal decay in ApxJ cyanobacteriochrome) may follow a similar mechanistic pattern.

Role of the H260 on the Pr and Pfr chromophore structure in Cph1 The chromophore in the Pr state of prototypical Cph1 Δ 2 phytochrome includes two similar ZZZssa conformers (Pr-I and Pr-II) [180]. In acidic conditions the population of the Pr-I form prevails. However in light alkaline medium it undergoes a structural reorientation at the AB methine bridge, leading to the Pr-II conformer. This equilibrium is controlled by the protonation state of the conserved H260. Mutation of this residue cancels the conformational equilibrium in the Pr state. During the Pr-to-Pfr formation the histidine side chain lowers its pK_A value (imidazolium/imidazole) leading to a pH independent Pfr state. Finally, H260 plays a crucial role as key residue within the proton-uptake event during the Pfr formation. Removal of the imidazole side chain hinders proton-translocation into the chromophore moiety.

Chromophore-pocket hydration tunes the absorption properties in the light-activated state (Pg state) in red/green cyanobacteriochromes The PCB-chromophore structure in the second GAF domain of ApxJ (AnPixJg2) cyanobacteriochrome adopts a very similar geometry in the dark adapted Pr state as in prototypical and plant phytochromes [32, 133]. Following red light absorption, a similar reaction pathway as in prototypical phytochromes is observed: isomerization at the CD methine bridge leads to formation of the Lumi-R intermediate, followed by the thermal decay to the Meta-Ra intermediate and eventually to the deprotonated Meta-Rc intermediate. However, the light-activated state (Pg state) displays a blue-shift in the absorption maximum by more than 100 nm and the methine bridge stretching frequencies are significantly upshifted. Light-induced Pg-to-Pr reverse reaction takes place through the same number of intermediate species, including a transient chromophore deprotonation.

Interestingly, the chromophore in this hypsochromic Pg-form is fully protonated and adopts a ZZE-geometry, very similar as the Pfr structure in canonical phytochromes. The difference between the Pfr and the Pg state can be understood in terms of an increased solvent accessibility of the chromophore, leading to a reduction of the pi-electron delocalization in the tetrapyrrole cofactor. In this respect, the energies of the first electronic transition and methine bridge stretching modes are considerably increased.

Solvent influx is facilitated by the sterical clashes of the C-D methine bridge and the nearby Trp90, leading to a reorientation of the indole side chain and thus allowing an increase in the accessibility of water molecules to the bilin cavity. The tryptophan residue is conserved among red/green absorbing cyanobacteriochromes. The color tuning mechanism in ApxJ is unique among the phytochrome-family. In particular, since the protonation state of the bilin cofactor has a minimal effect on the electronic properties of the light-activated Pg-state.

Transformation of a phytochrome into a fluorescent tool Understanding cofactor-protein interactions is essential for elucidating the photochemical and thermal reactivity of the tetrapyrrole chromophore. As an additional consequence of more applied relevance, it may also help controlling the interplay between the various excited state processes of the chromophore, specifically aiming at increasing the fluorescence at the expense of the photochemical quantum yield to generate red-fluorescing phytochromes for deep-tissue fluorescence microscopy [169]. So far, phytochrome-based IRFPs were obtained by random mutagenesis but yet display relatively poor emission-efficiency and brightness [52, 167]. To make first steps towards a rational design, the combined spectroscopic and theoretical approach applied to Rph2-PG revealed the structural basis for key amino acid substitutions in terms of fluorescence yield increase [206].

The most relevant structural difference between fluorescing variants and the ‘non-fluorescing’ template were observed for the CD methine bridge. These differences involve also the weakening of the hydrogen bond interactions of the terminal carbonyl group and decreased solvent molecules in this part of the chromophore cavity. Furthermore, the rigidity of the bilin structure is significantly increased. Particularly, in the flexible regions of rings A and D, the conformer distribution as known for bilin in the Pr state is considerably shifted towards the more rigid geometry. The reduced flexibility of the proximal ring A is monitored through the carbonyl frequency changes.

These results are in good agreement with the first crystal structure of an IRFP molecule [8]. Furthermore, they allowed a satisfactory calibration procedure for future studies involving chromophore structure predictions in diverse IRFP-molecules. Finally, this method supports rational mutational strategies with the aim of optimizing fluorescent brightness or tuning the emission-wavelength.

Acknowledgements

This work would not be completed without expressing my sincere gratitude to the people and Institutions which in different ways supported me. Particularly, I would like to thank:

- Prof. Dr. Peter Hildebrandt (Technische Universität Berlin) for the excellent supervision, his patience and the fruitful research atmosphere,
- Prof. Dr. Wolfgang Gärtner (MPI CEC, Mülheim an der Ruhr) for the introduction in the very interesting and novel field of the cyanobacteriochromes, motivating discussions, the various phytochrome samples and for very carefully reading of this thesis,
- Prof. Dr. Roderich Süßmuth (Technische Universität Berlin) for kindly presiding over the oral defense,
- Prof. Dr. María-Andrea Mroginski (Technische Universität Berlin) who provided calculated spectra, but most of all I am grateful for the many scientific conversations,
- Prof. Dr. Friedrich Siebert (Albert-Ludwigs-Universität Freiburg) for the introduction in the field of photoreceptor IR spectroscopy and all the fruitful discussions,
- Dr. Patrick Scheerer, Patrick Piwowarski, Dr. Bilal Muhammed Qureshi and Prof. Dr. Franz Bartl (Charité Berlin) for the many inspiring discussions, a great collaboration and for the provided protein samples and crystals, infrared spectra and homology models,
- Jon Hughes (Justus-Liebig Universität Gießen) for providing various phytochrome samples and the nice Cph1-collaboration,
- Prof. Dr. Masahiko Ikeuchi (Tokyo University) and Dr. Rei Narikawa (Shizuoka University), Prof. Dr. Nicole Frankenberg-Dinkel (Universität Kaiserslautern) and Britta Schubert (Ruhr-Universität Bochum), Prof. Dr. Tilman Lamparter (Karlsruhe Institute of Technology) and Dr. Isabel Molina, Dr. Hernán Bonomi (Instituto Fundación Leloir), Dr. Joe Maillat, Christina Lange (Justus-Liebig Universität Gießen), Prof. Dr. Thomas Friedrich, Dr. Neslihan Tavraz, Luisa Sauthof, Nico Herder (Technische Universität Berlin) and Thomas Hildebrandt,

- Dr. Andrew Ulijasz (Imperial College London) and Meike Luck (Humboldt Universität Berlin) for the excellent collaboration and for providing diverse phytochrome and further protein samples,
- Dr. Tillmann Utesch (Technische Universität Berlin) for his willingness to perform any type of molecular dynamic simulation,
 - Johannes Salewski (Technische Universität Berlin) for letting me show some of his calculated spectra,
 - Dr. David von Stetten (ERSF) for sharing his phytochrome knowhow and for very inspiring conversations,
 - Norbert Michael (Technische Universität Berlin) for the continuous and generous production of phytochrome samples,
 - Lars Paasche (Technische Universität Berlin) for building incredible illumination-devices but most of all I am grateful for the many amusing conversations,
 - Dr. Uwe Kuhlmann and Jürgen Krauss for technical support,
 - Marina Böttcher, David Buhrke, Dr. Alexandre Ciaccafava, María Fernández López, Sagie Katz, Ibrahim Halil Öner, Yvonne Rippers, Elisabeth Siebert, Claudia Schulz, Aref Takiden, Stefan Wahlefeld, Prof. Dr. Inez Weidinger, Dr. Ingo Zebger and all my coworkers at the Max Volmer Laboratorium (MVL) who provided a pleasant and entertaining atmosphere,
 - Nina Heidary, Marius Horch, Dr. Jacek Kozuch and Dr. Hoang Khoa Ly: ‘der schönste Freitag bleibt unvergesslich’,
 - former MVL colleagues and friends, Dr. Sara Bruun, Dr. Diego Millo, Dr. Mathias Schenderlain, Dr. Murat Sezer and Dr. Miguel Saggi,
 - the DFG for financial support through UNICAT and CRC1079 founding,
 - my chemistry student companions and friends Dr. Alexander Densiuk, Dr. Cindy Kochan, Dr. Marcel Richter, Dr. Marc Schmidt and Dr. Vivien Schubert,
 - my friends Gerardo Anzaldúa, Vanessa Braun, Christine and Phillip Consentius, Grezgorz Cholewiak and Lena Hensel,
 - all my Exahumboldt friends, especially Brigitte and Thomas Binder, Francisco González and Daniela Rico, Armando Hernandez and Isabel Martí, Dylan Román, Marianela Romero and Adolfo Chávez and Eduardo Vieyra,
 - my parents, my sister and my brother, my cousins Javier and Ernesto and my uncle Tibur, for their support from afar,
 - my parents-in-law and brother in-law,
 - my godfather Jürgen Rohbeck and his family,
 - and at last I am most grateful to my beloved wife Ana, who accompanied ever since the beginning of my dissertation.

A. Additional setup diagrams and performance measurements

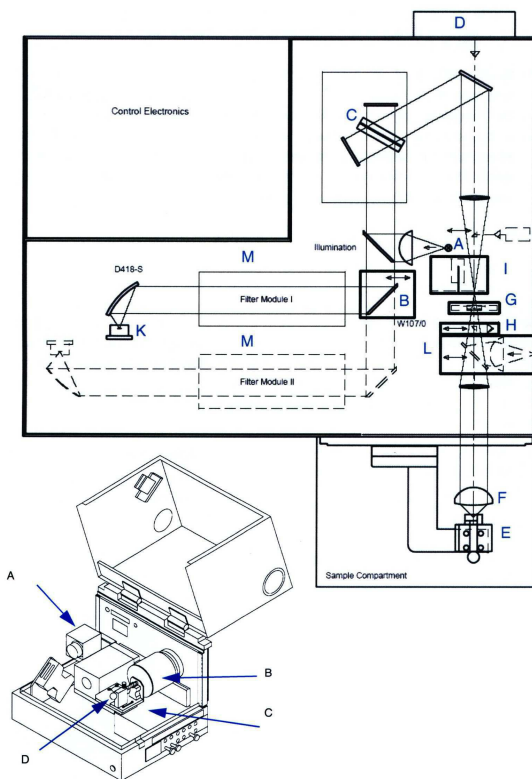


Figure A.1: Top: schematic representation of the BRUKER RFS/100S spectrometer based on ref. [29, 184]. Incident laser light **D** passes through the aperture **I**, optionally also through the polariser **G** and is reflected to the sample at a small 45° mirror attached to the collecting lens **F**. The backscattered light in the sample chamber **E** is returned over the collecting lens to the interferometer **C**. The main part of elastic scattering laser light is removed by the notch filter **M**. Remaining light is then focused at the detector **K**. **Bottom:** sample chamber with sample holder **D** and collecting lens **B**.

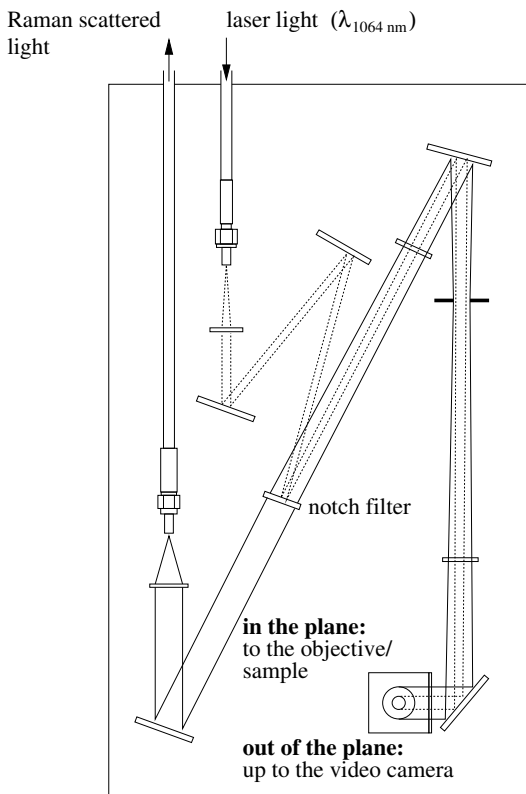


Figure A.2: Schematic drawing of the RAMANSCOPE III™ module. Incident laser light is coupled via a suitable optic fiber and focused to the sample through the OLYMPUS BX51 microscope. Scattered light is then collected back and partially reflected to the video camera (INFINITY 1) located over the microscope and the 90° mirror (right side at the bottom). However, most of the scattered photons follow the optical path backwards. At the notch filter the Rayleigh photons are absorbed and only the Raman signal passes through and is then focused to the IR fiber-optic. Subsequently the Raman light goes into the spectrometer and is finally detected (see fig. A.1.position L). [29, 31]

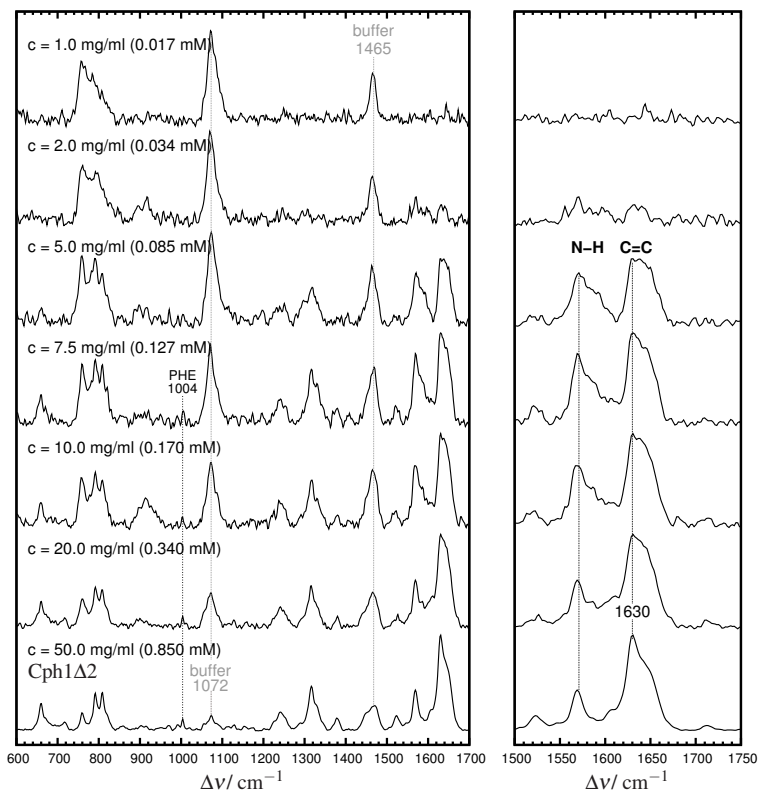


Figure A.3: Resonance Raman spectra of the Pr state of Cph1 Δ 2 measured under different concentrations as indicated in each layer. The ratio of the C=C stretching band at 1630 cm^{-1} (CD bridge) and **buffer** contribution rising at 1072 cm^{-1} was used to determine the minimal detectable concentration via FT-RR spectroscopy (see fig. A.4).

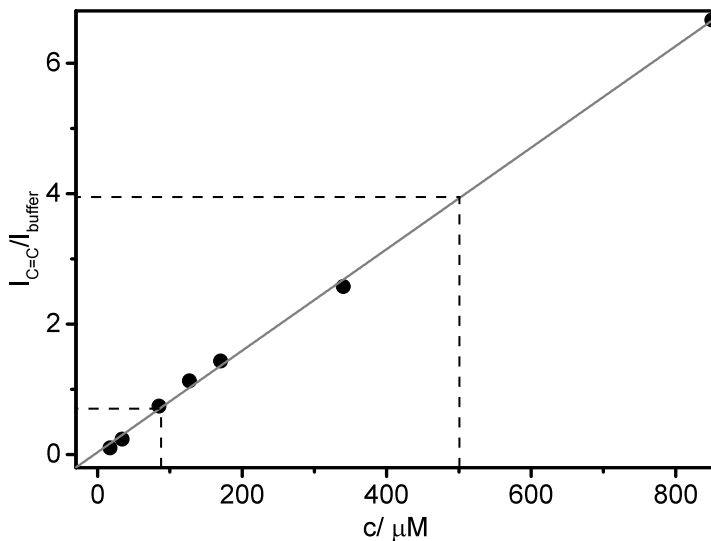


Figure A.4: Resonance Raman intensity ($I_{C=C}/I_{\text{buffer}}$) and Cph1 Δ 2 protein concentration correlation (\bullet). According to the presented relationship, a linear dependency can be observed (solid line). In addition, dashed lines denote the lowest (170 μM) and optimal (500 μM) protein concentration range (see fig. A.3). Furthermore, this correlation can be used as calibration curve to determine phytochrome holoprotein concentration based on the intensity ratio of the peaks at 1630 cm^{-1} (chromophore) and 1072 cm^{-1} (buffer). Strictly, this applies only for PCB binding phytochromes in the Pr state (with Q-Band maximum at 660 nm). However, this correlation provides a reliable reference for other phytochromes.

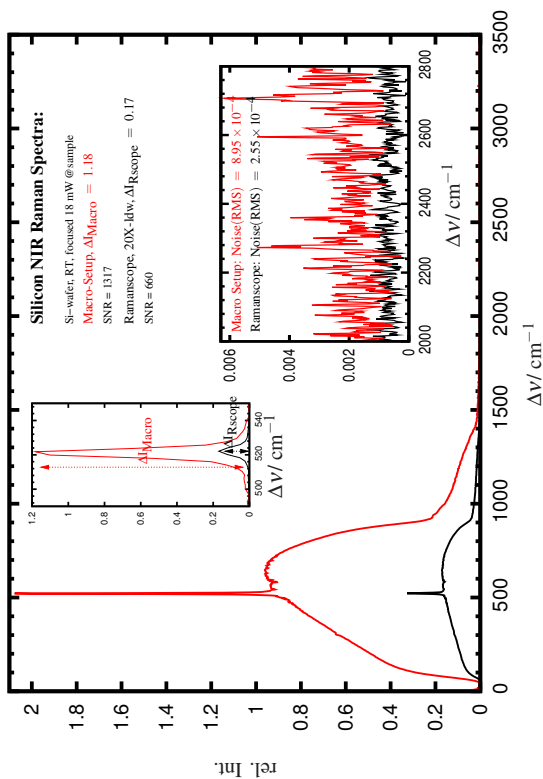


Figure A.5: FT-Raman spectra of a plain Si wafer recorded at the standard and the microscope setup. Both measurements were performed using the same power measured at the sample. Comparison of the SNR values shows that the performance of the confocal measurements, including signal losses along the optical pathway, is only reduced to the half if compared to conventional measurements (standard or Macro-setup). This applies strictly for plain surface. Microscope setup measurements done in the bulk displayed considerably lower SNR values (see fig. A.6).

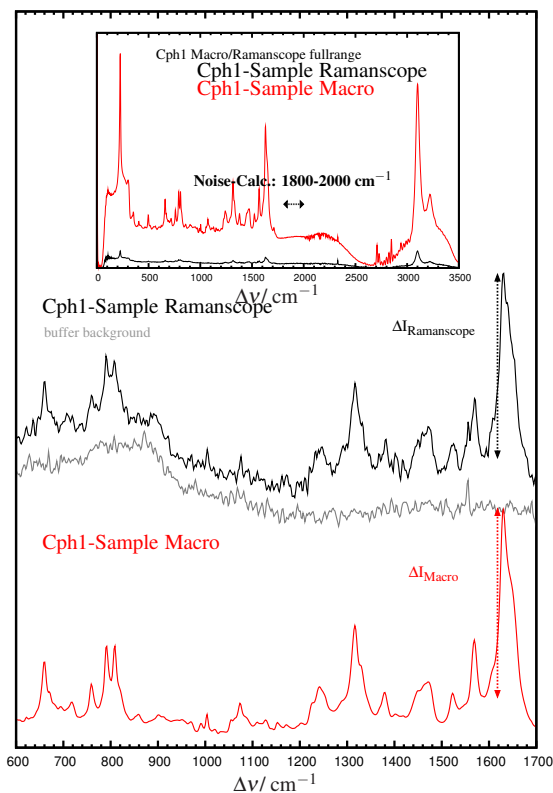


Figure A.6: RR spectra of the Pr state of Cph1 Δ 2, measured using the standard and the microscope setup. Like the previous Si-wafer measurements (see fig. A.5), spectra were recorded using the same laser power at the sample. However, due to the overall lower signal higher laser power was required (300 mW). In this case ten-fold decrease in the performance was determined.

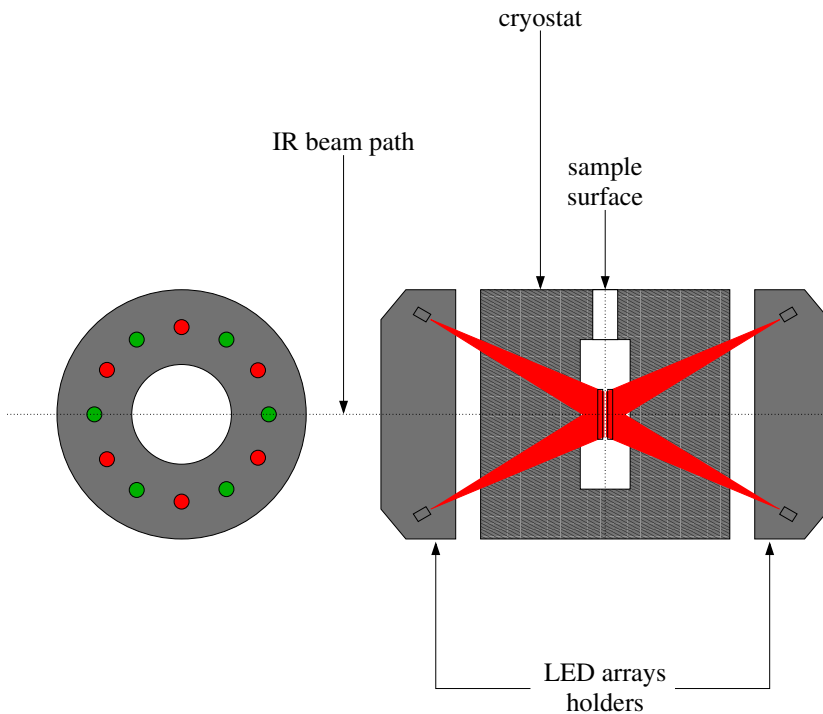


Figure A.7: Schematic diagram of the IR transmission cell including the LED arrays. Each of them carries twelve single diodes of two different wavelengths (left panel). During each irradiation step only the 12 LED lamps of a single color are switched on. In the current example, the red and green diode colors correspond to $\lambda_{\text{BIT0}} = 670 \text{ nm}$ and $\lambda_{\text{BIT1}} = 530 \text{ nm}$. Incident LED light angle was optimized to ensure full irradiation of the complete IR sample surface (right panel). Furthermore, irradiation of both sides of the sample surface ensures homogenous light exposure. Sample holder is placed in a home-made bath cryostat [57]. The gray area of the setup is under high vacuum (7.0×10^{-6} bar).

B. Supplementary spectra: pH dependence in Cph1 phytochrome

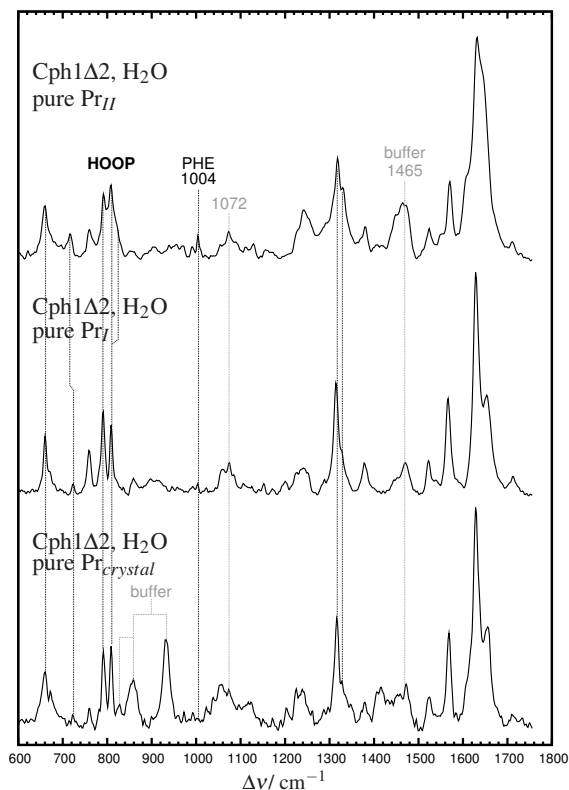


Figure B.1: Pure H₂ORR spectra of all protonated Pr species of the CPh1Δ2 phytochrome: P-II, Pr-I and Pr_{crystal}. Buffer contribution in to the crystal spectrum is indicated in gray. Doted vertical lines indicate frequency correlations or displacements of chromophore bands in all three RR spectra. In agreement with the marker region, spectral differences in the lower frequency region of the Pr-II and Pr-I were also observed (HOOP and i.p. region).

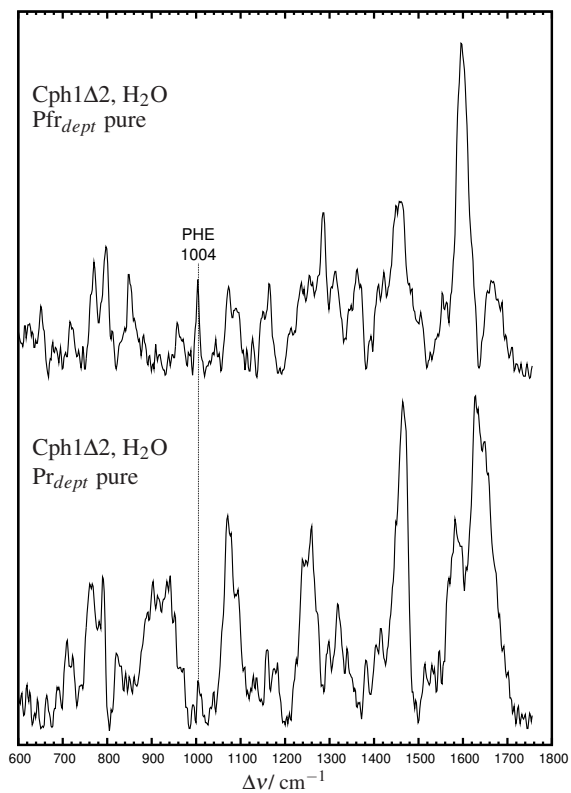


Figure B.2: Pure RR spectra of the deprotonated Pr and Pfr species (Pr_{deprot} and Pfr_{deprot}).

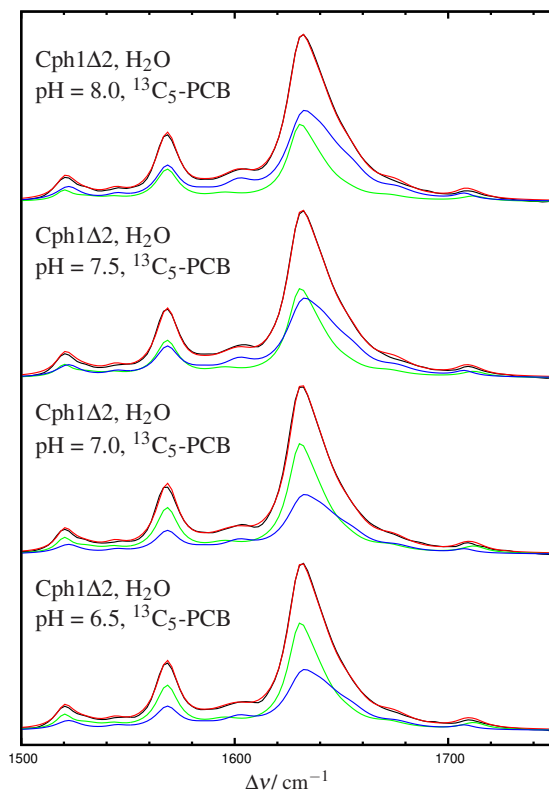


Figure B.3: Global component analysis of the RR spectra of the Pr state in Cph1Δ2 phytochrome assembled with ¹³C₅-PCB chromophore. Spectra were recorded at four different pH values: pH = 8.0 (top), 7.5, 7.0 and 6.5 (bottom). Within this pH range, contribution of the deprotonated Pr species is negligible (see fig. 4.3). Hence, this component was not included in the fitting procedure. Relative concentration of the Pr-I-¹³C₅ and Pr-II-¹³C₅ are given in table 4.1.

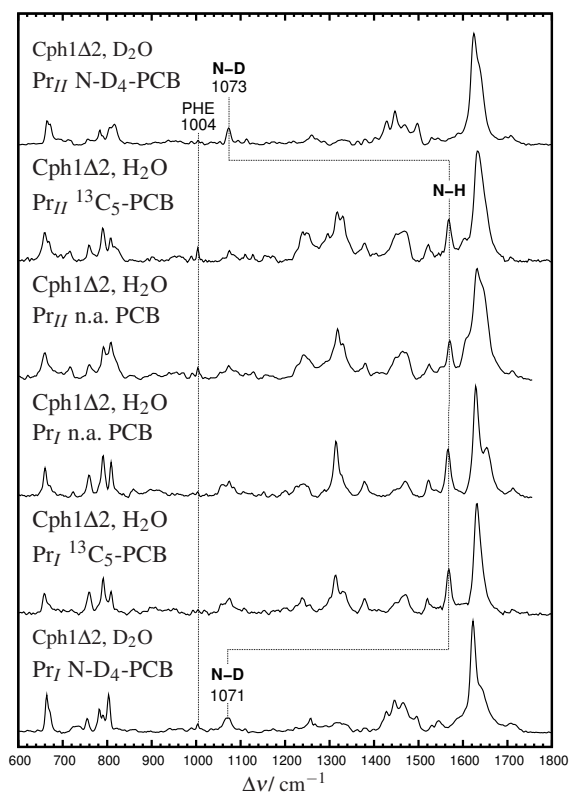


Figure B.4: Full range RR spectra of both protonated Pr species (Pr-I and Pr-II) in Cph1Δ2 recorded in H₂O(middle layers) and in D₂O(top and bottom layers) and after ¹³C₅-PCB-labelling (second from top and from the bottom). Dotted lines indicate the H/D isotopic shift of the N-H i. p mode.

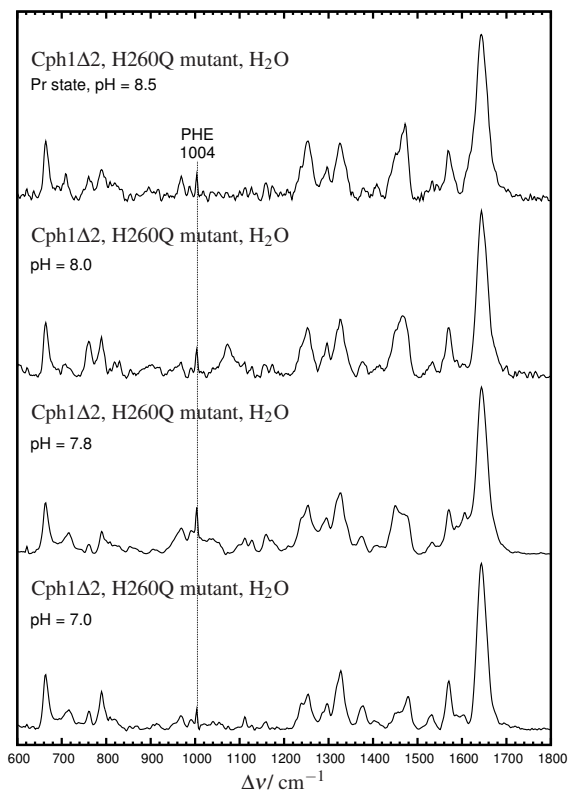


Figure B.5: Full range RR spectra of the Pr state in the Cph1Δ2H60Q mutant measured in H₂O buffer between pH = 7.0 and 8.5. Unlike the native Pr species, the stronger intensity of the PHE band at 1004 cm^{-1} , indicates a higher apoprotein contribution and thus a reduced chromophore affinity in the H260Q-mutant. However, protein contribution is considerably small.

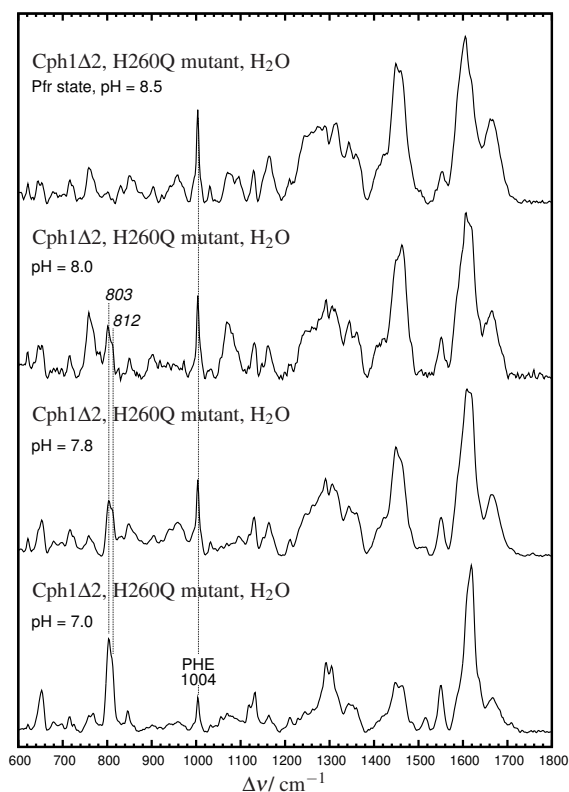


Figure B.6: Full range RR spectra of the Pfr state pH titration in the Cph1Δ2H60Q mutant. Further details are given in fig. B.5. Among marker region spectral changes (N-H i. p. and C=C modes), the strong HOOP band at 803 cm^{-1} with a high frequency shoulder at 812 cm^{-1} is observed at pH = 7.0 (bottom). Thus, suggesting a very similar chromophore structure as in the native Pfr state. Upon pH increase, chromophore deprotonation is observed among the complete spectral range.

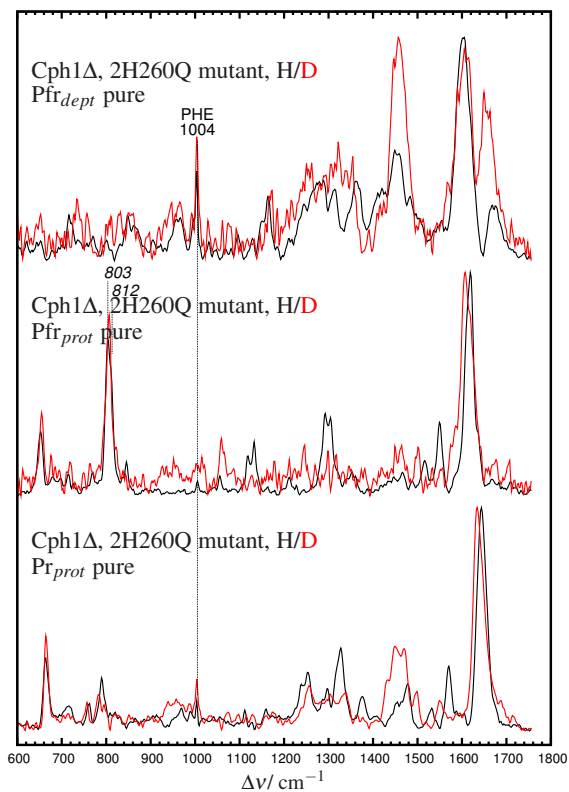


Figure B.7: Full range RR spectra of the pure Pr and Pfr spectra of the Cph1Δ2H60Q mutant measured in H₂O and in D₂O: deprotonated Pfr species (Pfr_{H260Q,deprot}, top), protonated Pfr (Pfr_{H260Q,prot}) and Pr species (Pr_{H260Q}, bottom).

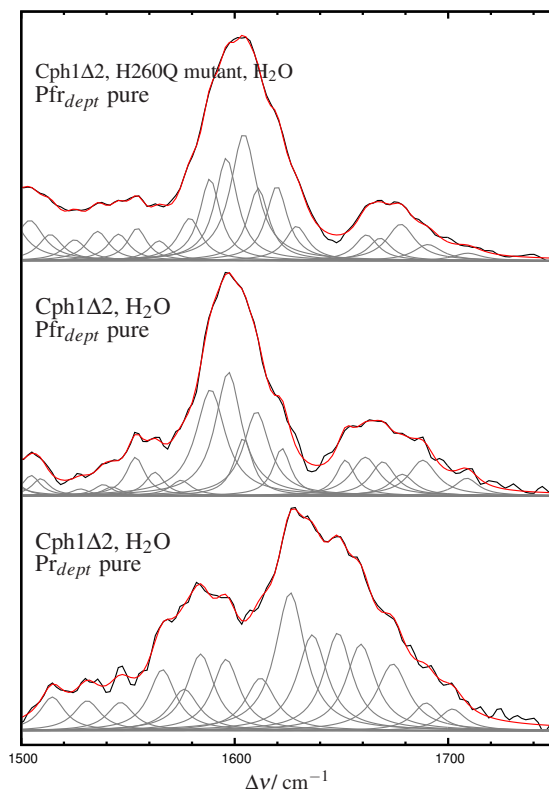


Figure B.8: Marker region band analysis of the RR spectra of all deprotonated species from Cph1Δ2 wildtype (Pr and Pfr) and the Pfr species of the H260Q mutant. Experimental spectra (solid black) are plotted along with the fitted species (in red) and all the corresponding single Lorentzian bands (displayed in gray). Fitting parameters listed in table E.4.

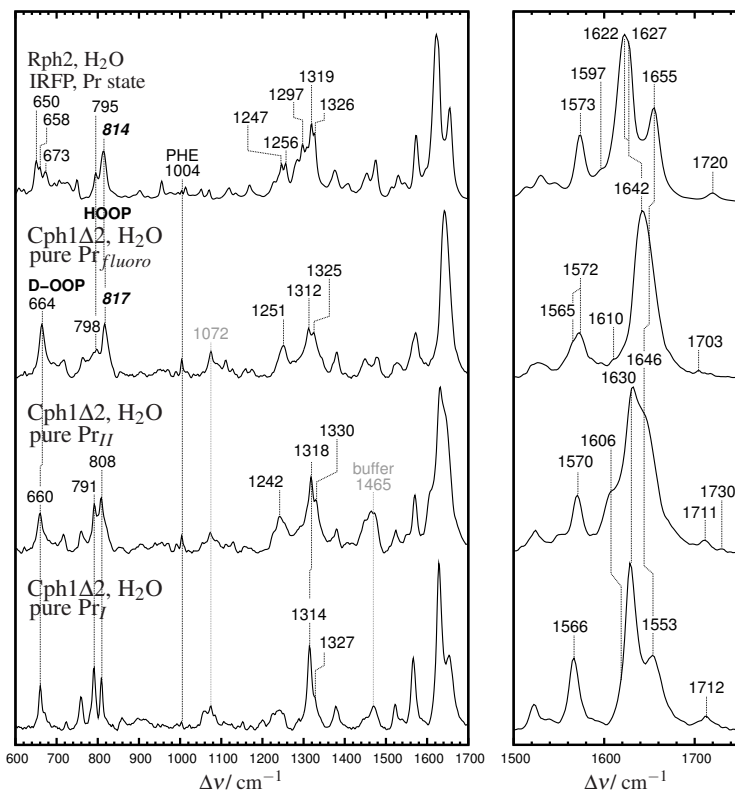


Figure B.9: Resonance Raman spectra of the Pr state in Cph1Δ2 (Pr-I and Pr-II), the Pr-x (Pr-fluoro) species (second from top) compared to the Pr spectrum of Rph2-IRFP phytochrome (top). Pure Pr-fluoro spectrum was observed only at very low buffer conditions (2.5 mM Tris-Cl, 15 mM NaCl, pH 7.8).

C. Supplementary spectra: prototypical phytochromes Pr-to-Pfr reaction

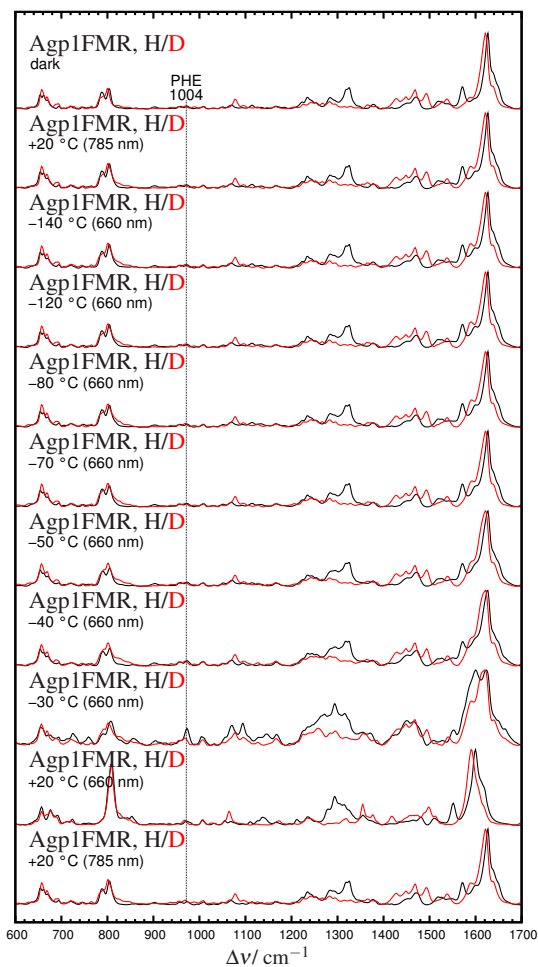


Figure C.1: Complete H_2O and D_2O series of Agp1FMR recorded RR spectra according to the temperature-dependent irradiation protocol in fig. 3.4.

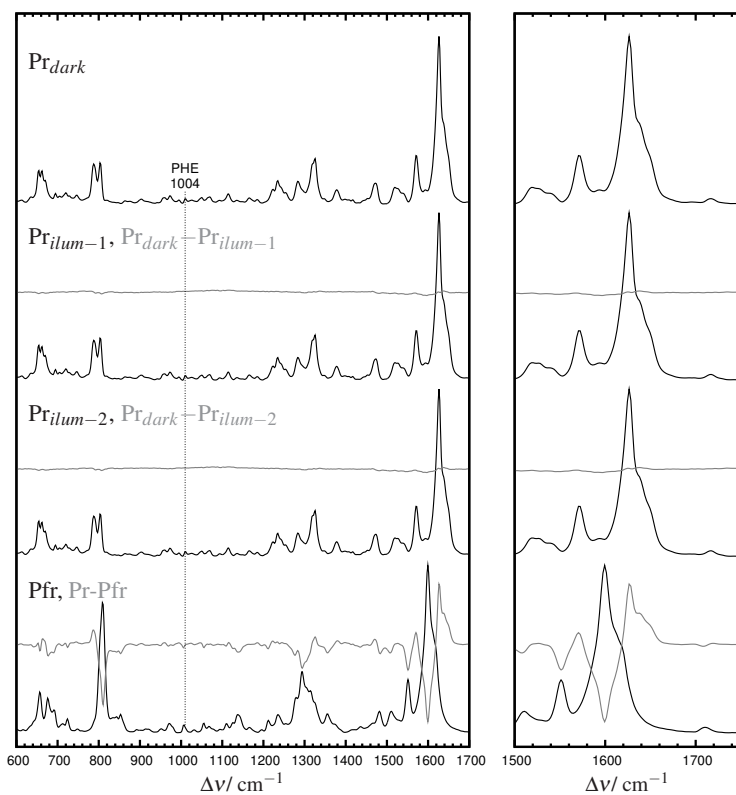


Figure C.2: RR spectra of all pure Agp1FMR Pr and Pfr species: Pr_{dark} (top), $\text{Pr}_{\text{illum-1}}$, $\text{Pr}_{\text{illum-2}}$ and Pfr (bottom). Difference RR spectra ($\text{Pr}_{\text{illum-1}}$ or $\text{Pr}_{\text{illum-2}}$ minus Pr_{dark} and Pr -minus- Pfr) are shown in gray. The Pr -minus- Pfr difference spectrum is downscaled (by a factor of 2).

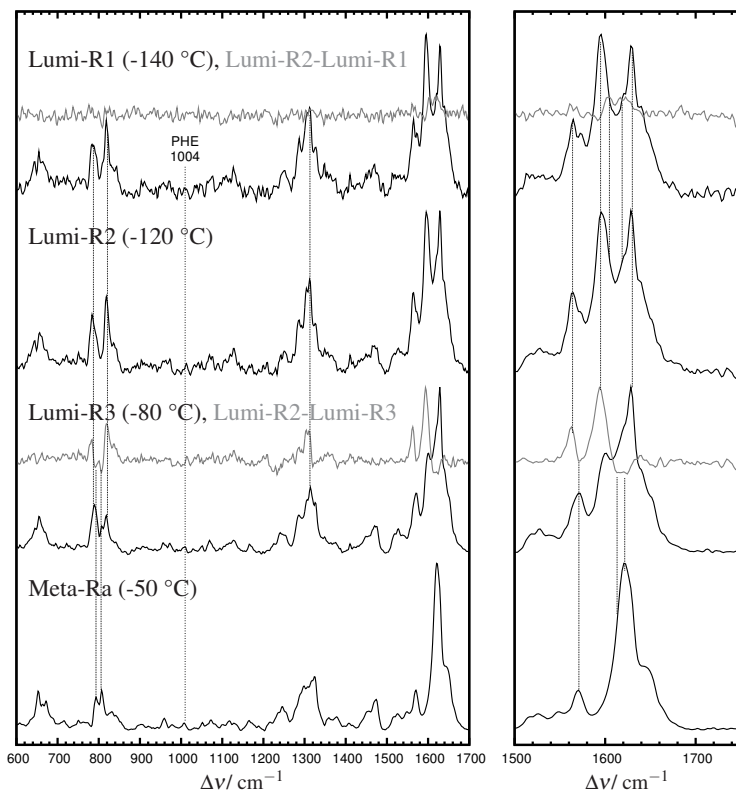


Figure C.3: RR spectra of all the possible Lumi-R H₂O-species in Agp1FMR phytochrome: Lumi-R1 (top, -140 °C), Lumi-R2 (-120 °C), Lumi-R3 (-80 °C) and pure Meta-Ra as negative control (bottom). Lumi-R1-minus-Lumi-R2 and Lumi-R2-minus-Lumi-R3 RR difference spectra (in gray) allow a comparison of the different irradiation conditions and the temperature dependent intermediate evolution. Differences are highlighted with dotted lines.

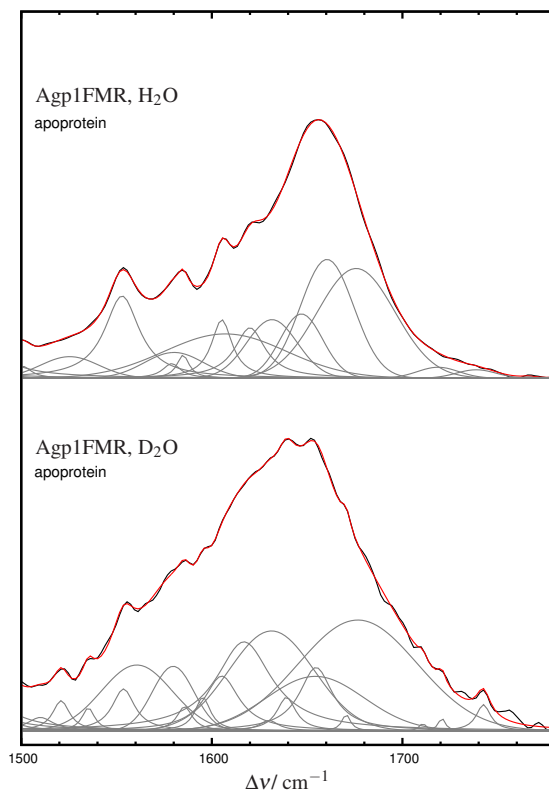


Figure C.4: Marker region band analysis of the Agp1FMR apoprotein Raman spectra measured in H₂O (top) and D₂O (bottom). Spectra were kindly provided by Dr. David von Stetten and Mina Günther.

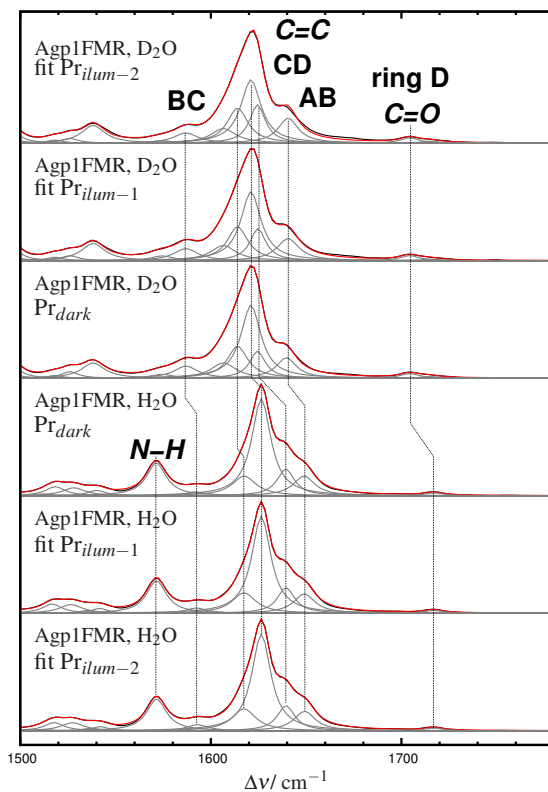


Figure C.5: Marker region band analysis of all RR Pr spectra (Pr_{dark} , $Pr_{illum-1}$ and $Pr_{illum-2}$) recorded in H_2O (bottom) and D_2O (top). Fitting parameters displayed in tables E.6 and E.7.

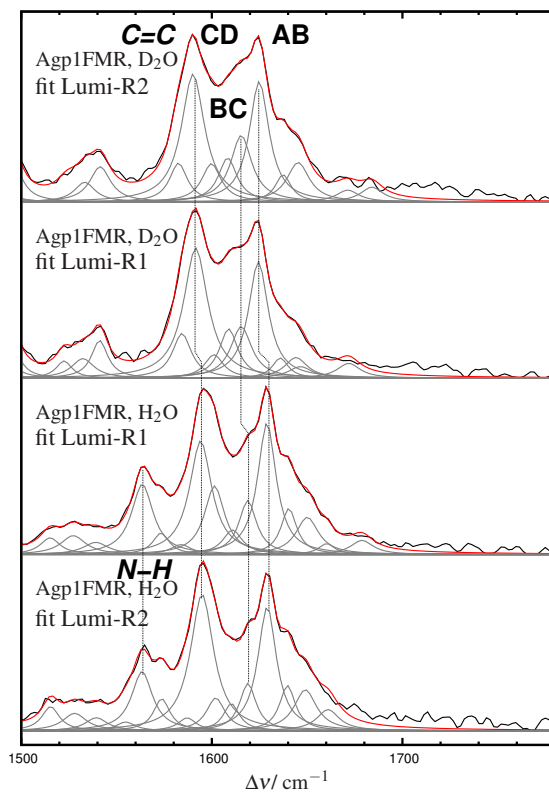


Figure C.6: Band analysis of Lumi-R1 and Lumi-R2 RR spectra marker region (top H₂O and bottom D₂O). Corresponding fitting parameters are listed in tables E.8 and E.9.

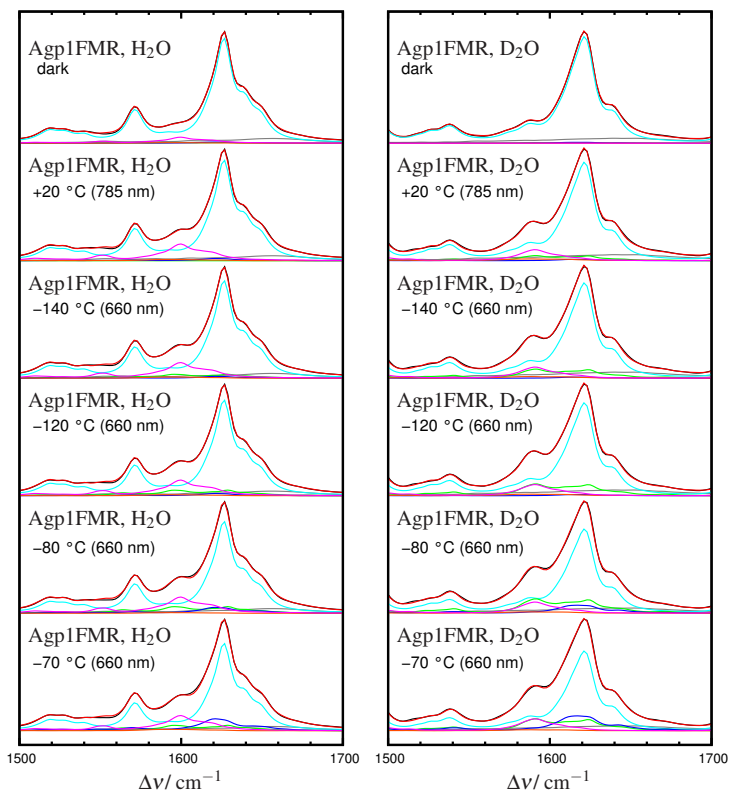


Figure C.7: Marker region component analysis of the raw Agp1FMR RR spectra recorded in H₂O (left) and D₂O (right). Spectra of the first temperature-irradiation conditions are displayed according to the measuring protocol in fig. 3.4. Component concentrations (Pr, Lumi-R, Meta-Ra, Meta-Rc, Pfr and Apoprotein) are found in tables 5.1 and 5.2. Remaining raw spectra of the Pr-to-Pfr cryogenic trapping experiments are shown in fig. C.8).

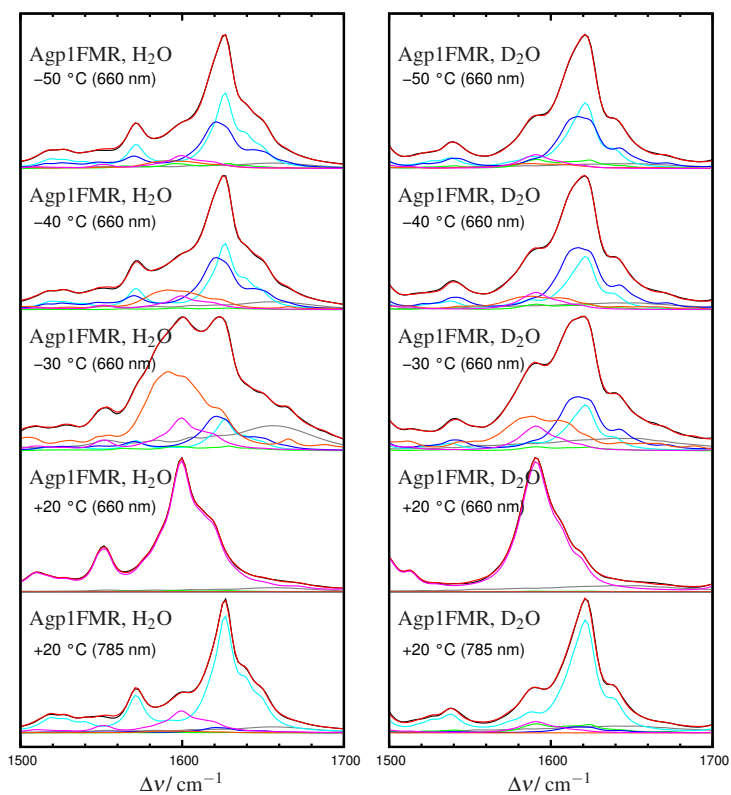


Figure C.8: Continuation of fig. C.7. Details are given in the previous figure.

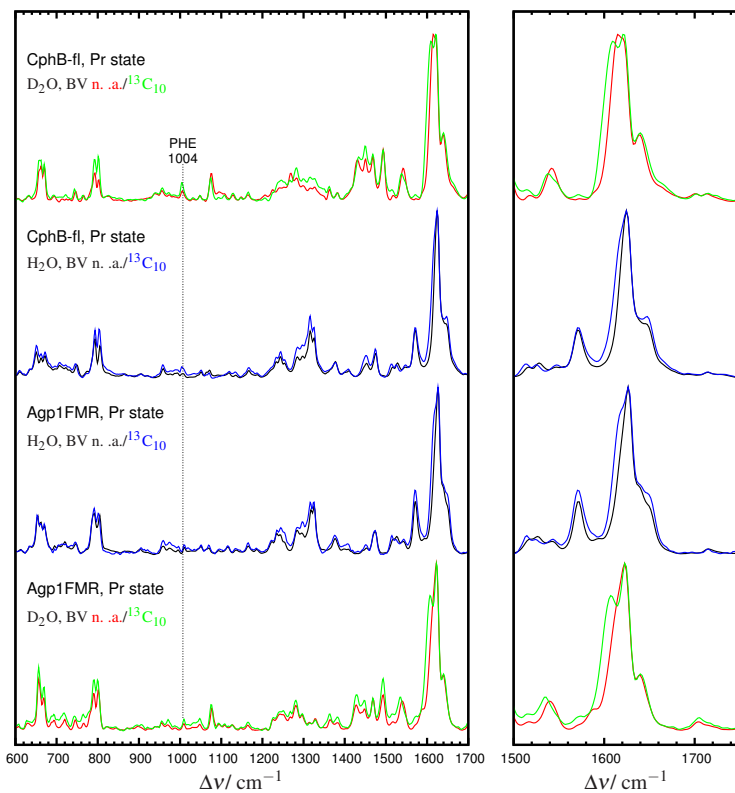


Figure C.9: RR Pr state spectra of CphB (top) and Agp1 (bottom) phytochrome assembled with native BV and $^{13}\text{C}_{10}$ -labeled chromophore and measure in H_2O and D_2O .

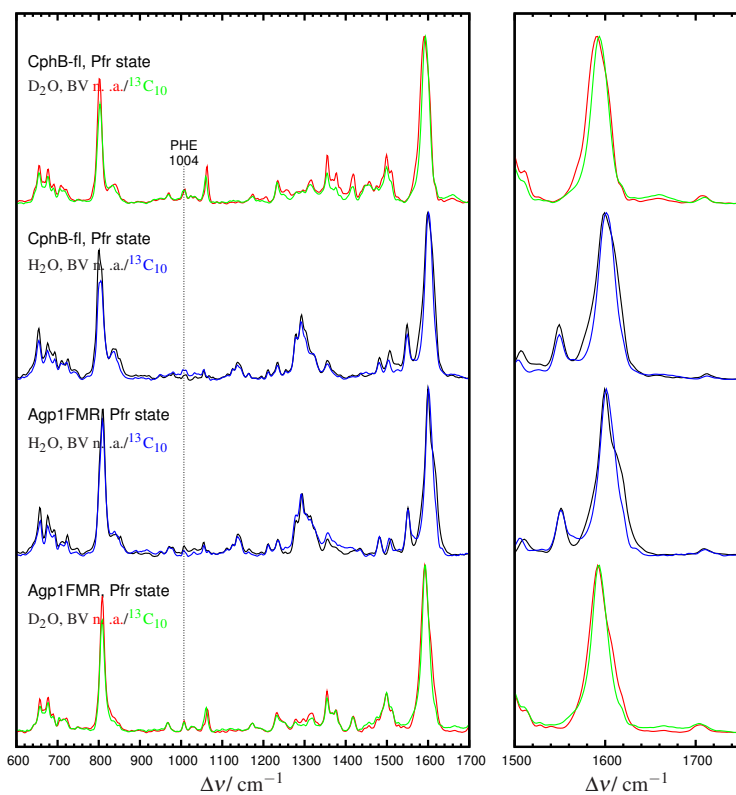


Figure C.10: RR Pr state spectra of CphB (top) and Agp1 (bottom) phytochrome assembled with native BV and $^{13}\text{C}_{10}$ -labelled chromophore. Details are given in fig. C.9.

D. Supplementary spectra: Pfr and Pr state in bathy phytochromes

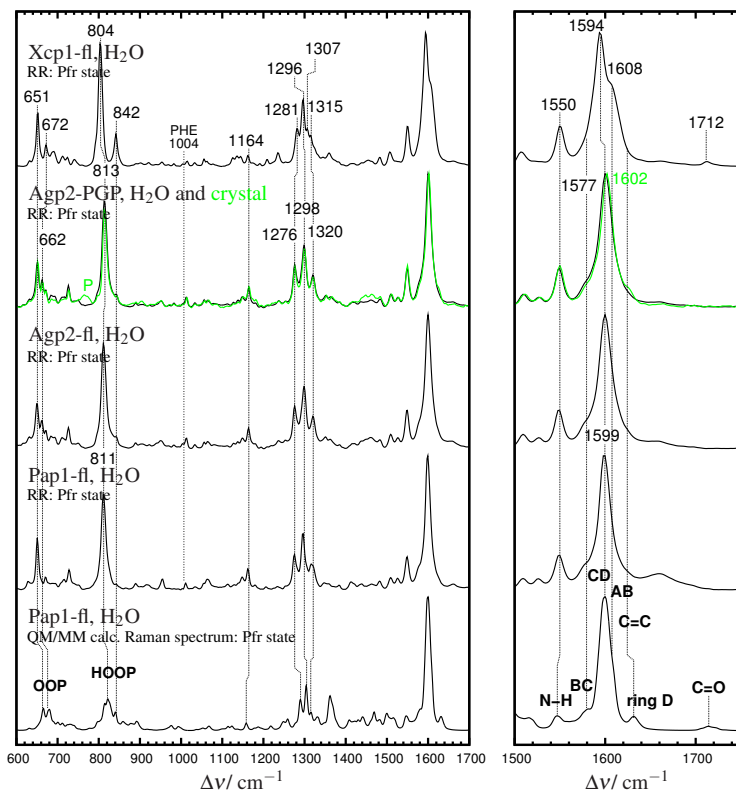


Figure D.1: Resonance Raman spectra of the dark adapted Pfr state in bathy phytochromes. Experimental RR spectra are compared to the QM/MM calculated average spectrum (bottom layer) [159]. Spectrum was kindly provided by Prof. Dr. Maria-Andrea Morginski and Johannes Salewski. Calculated QM/MM spectrum corresponds to a fully protonated ZZEssa BV chromophore. Furthermore, most relevant vibrational mode assignments are explicitly noted. All experimental spectra were recorded in H₂O using standard buffer protocols, except the Agp2M2 crystal Pfr spectrum (crystallization buffer). Contribution of the buffer is noted with a P.

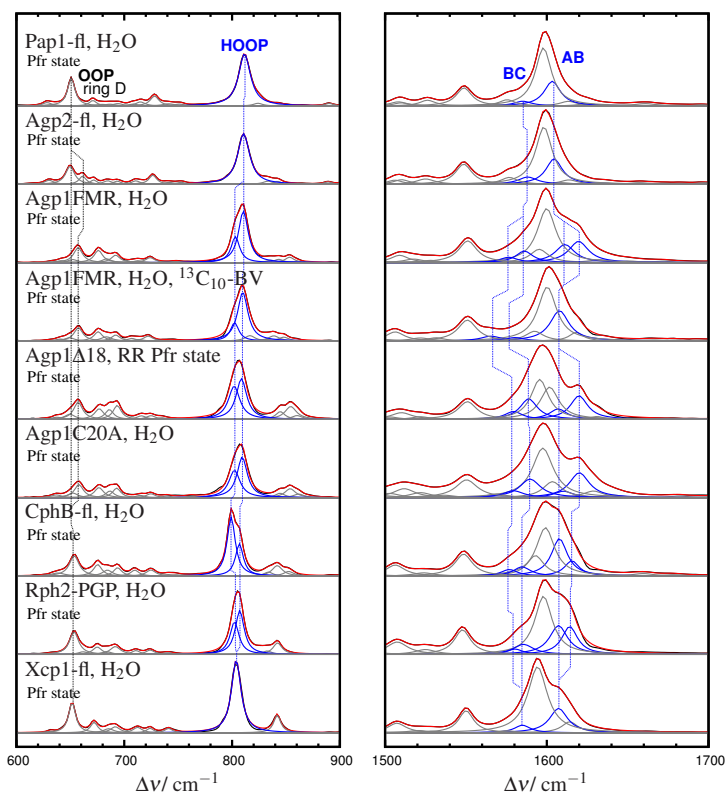


Figure D.2: RR Pfr spectra of bathy and prototypical phytochromes, including band analysis in the HOOP region (left panel) and in the marker band range (right panel). The Pfr spectra in different phytochrome-proteins as well as specific mutation are presented in the following order (top to bottom): Pap1-fl, Agp2-fl, Agp1-FMR, Agp1 assembled with $^{13}\text{C}_{10}$ -BV, Agp1 Δ 18 (deletion mutant missing the first 18 N-terminal residues), Agp1C20A (alanine mutation at the cysteine-binding side), CphB-fl, Rph2-PGP and Xcp1. Agp1 Δ 18 and Agp1C20A were kindly provided by Dr. David von Stetten [184]. **Measured spectrum**, overall **fit** and **single Lorentzian** are coded according section 3.9.1. HOOP peaks, as well as AB and BC C=C bands are displayed in blue.

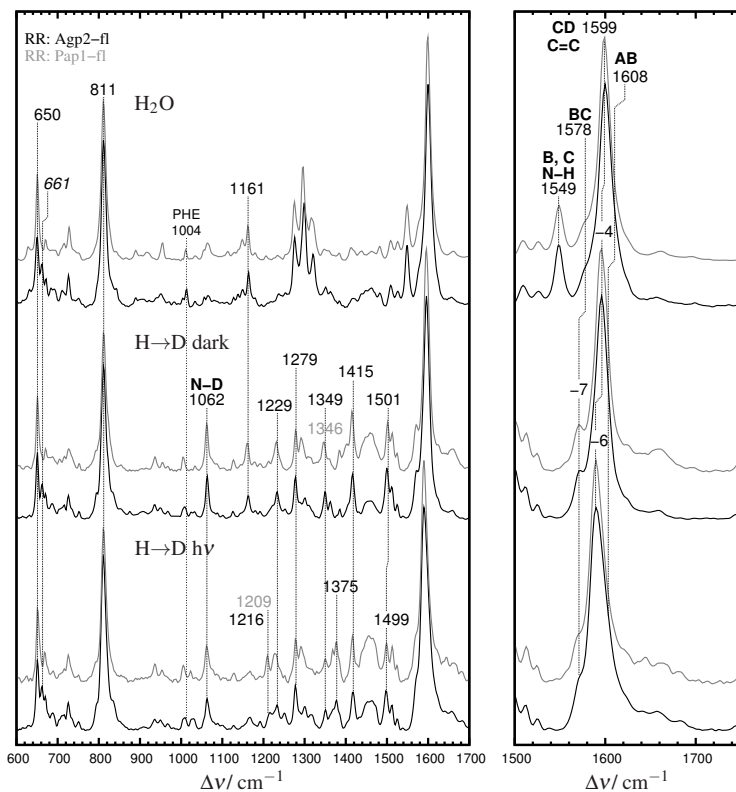


Figure D.3: RR Pfr spectra of full-length Agp2 and Pap1 phytochrome measured in H₂O (top spectra), in D₂O without light exposure (middle layer, H→D dark) and after a complete photocycle in deuterated medium (top layer, H→D hν). Isotopic displacements are indicated in the high frequency region. Assignments in H₂O spectra are based on the QM/MM calculations performed for Pap1 [159]. This figure was modified from ref. [207].

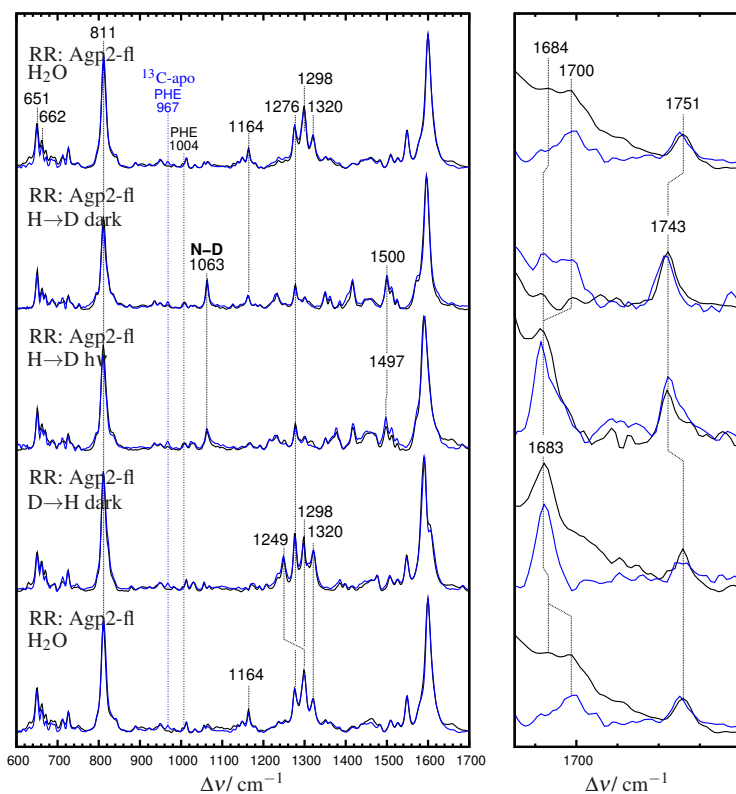


Figure D.4: Full range RR spectra of the Pfr state in native (solid) and ^{13}C -protein-labelled Agp2-fl phytochrome. Displayed spectra were recorded: (1) in H_2O (top) and after (2) $\text{H}\rightarrow\text{D}$ exchange in dark, (3) a complete photocycle in D_2O and (4) subsequent $\text{D}\rightarrow\text{H}$ exchange in H_2O . Finally RR spectra were recorded after a complete photocycle preceding step 4 (bottom).

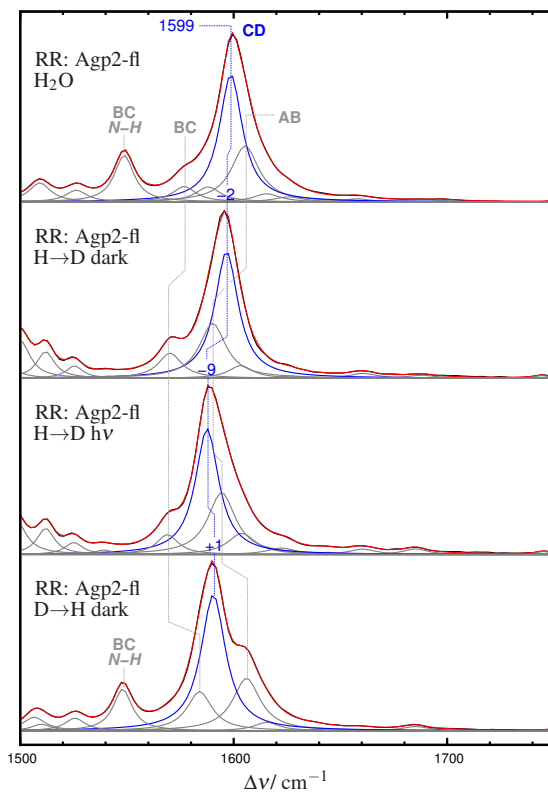


Figure D.5: Fitted Resonance Raman Pfr spectra of the native Agp2-fl. Spectra are displayed according to fig. D.4, only the band analysis of the light induced reprotonation in H₂O is not shown (fig. D.4 bottom). The Lorentzian-shaped CD band and its isotopic displacement are indicated. Color nomenclature of the spectra according to subsection 3.9.1.

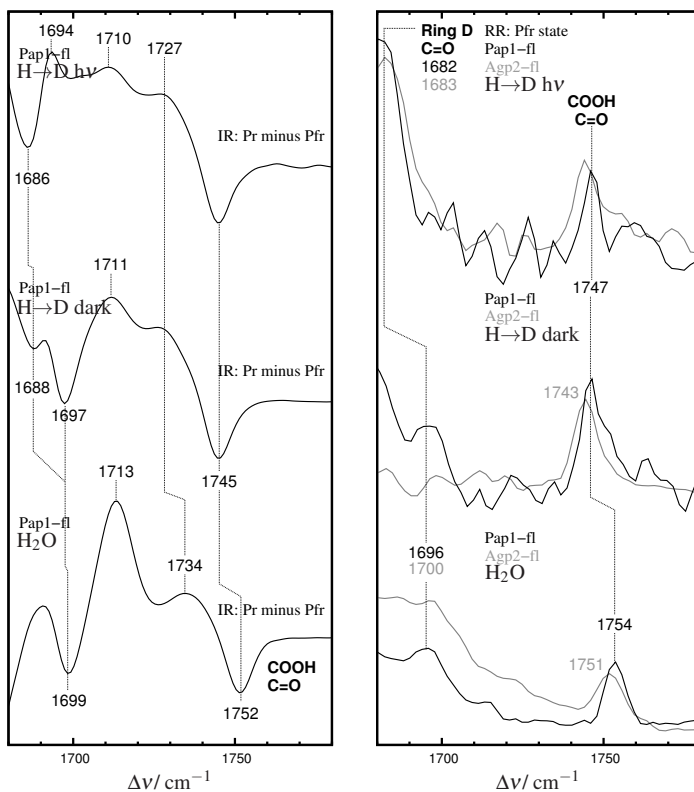


Figure D.6: Left panel: Pap1-fl Pr minus Pfr difference IR spectra displayed in the C=O region: after a photocycle in D_2O (top), $\text{H} \rightarrow \text{D}$ exchange in the dark (middle) and H_2O spectrum (bottom). Right panel: enlarged C=O region of the RR Pfr spectra in Pap1 and Agp2. The layer distribution is in line with the left panel.

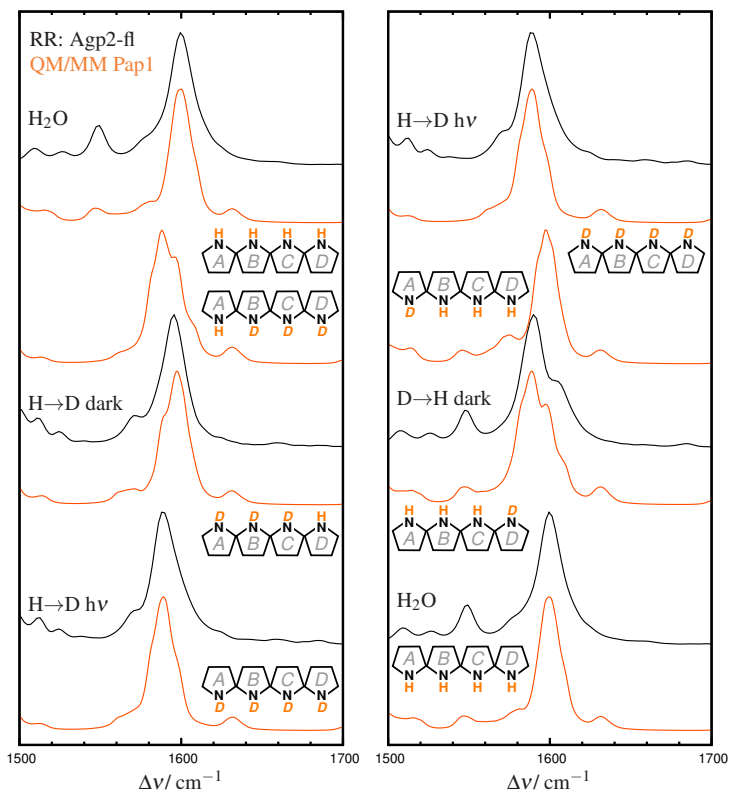


Figure D.7: Comparison of the RR Pfr spectra of Agp2-fl measured under different sequential H/D exchange conditions and the QM/MM calculated Raman spectra [159] based on different protonation and deuteration of the pyrrole nitrogen [207]. Calculated QM/MM spectra were kindly provided by Johannes Salewski and Prof. Dr. Maria-Andrea Mroginski.

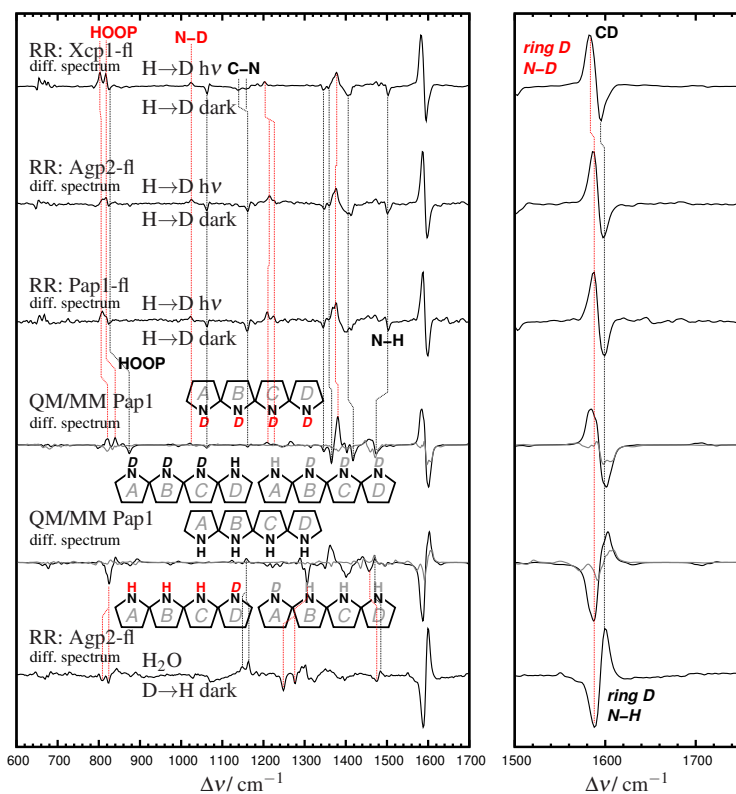


Figure D.8: Experimental (RR) and calculated (QM/MM) difference spectra prior and after sequential H→D (D→H) in bathyphytochromes. QM/MM difference spectra were generated either by subtraction from partially deuterated chromophore (AD-BD-CD-DH or AH-BD-CD-DD) minus the spectrum (in both cases) of the fully deuterated bilin (AD-BD-CD-DD). The same procedure was applied for the sequential D→H process. Positive bands (—) indicate deuterated ring D, whereas negative peaks (—) indicate a protonated pyrrole ring.

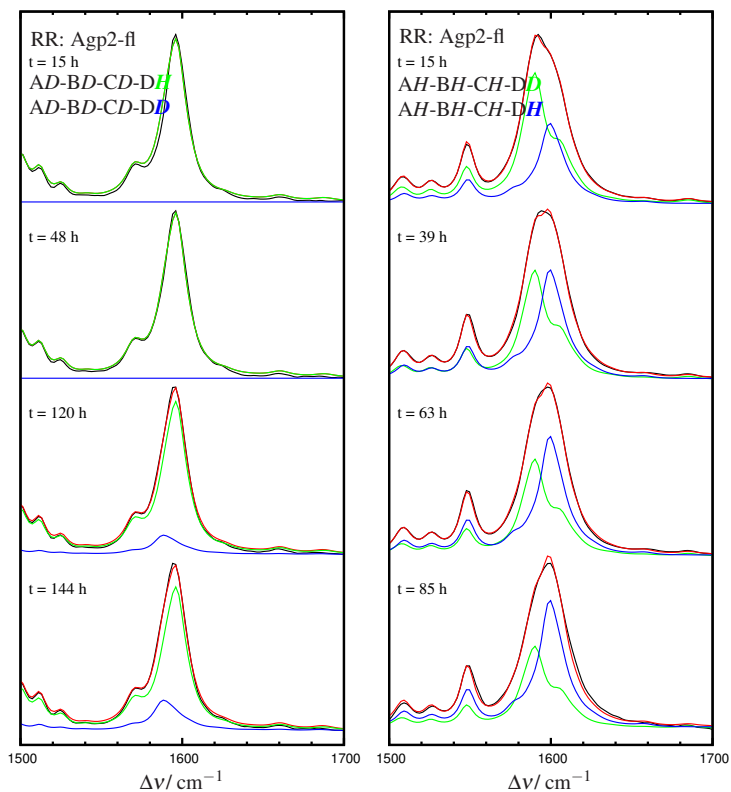


Figure D.9: Sequential H→D and D→H exchange over time in the Agp2-fl Pfr state monitored by RR spectroscopy. Spectral contribution of the partially protonated (deuterated) or fully protonated (deuterated) Pfr species was globally analyzed. Component spectra were obtained according to fig. D.5. Left (right) panel: sequential H→D (D→H) exchange overtime. Component contribution is shown in fig. D.10.

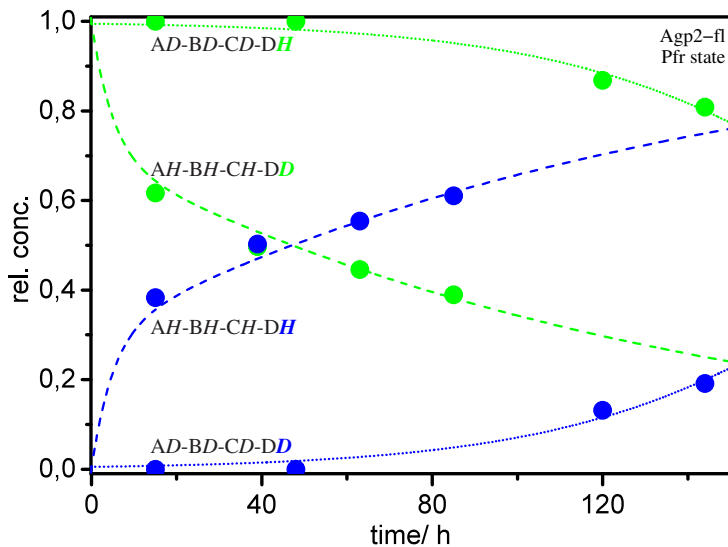


Figure D.10: Component contribution of the H→D (D→H) exchange monitored by RR spectroscopy (fig. D.9). Conversion from a partially deuterated chromophore species (*AD-BD-CD-DH*) to a completely exchange cofactor (*AD-BD-CD-DD*) follows a sigmoidal development (fitted Boltzmann function as dotted lines) and is considerably slower. The inverse reaction occurs faster. Ring D reprotonation (*AH-BH-CH-DD* to *AH-BH-CH-DH*) was fitted by a biexponential function.

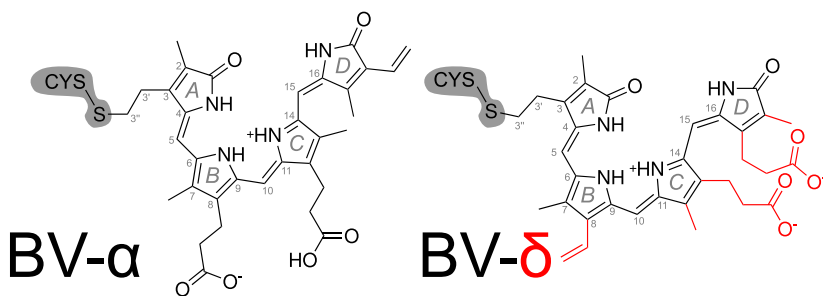


Figure D.11: Comparison of the native BV- α with the BV- δ chromophore (Pap1-fl phytochrome, see section 3.1 and fig. D.12). In this representation both tetrapyrrole molecules are displayed as bounded cofactors. Difference in the side chain groups are highlighted in red (BV- δ).

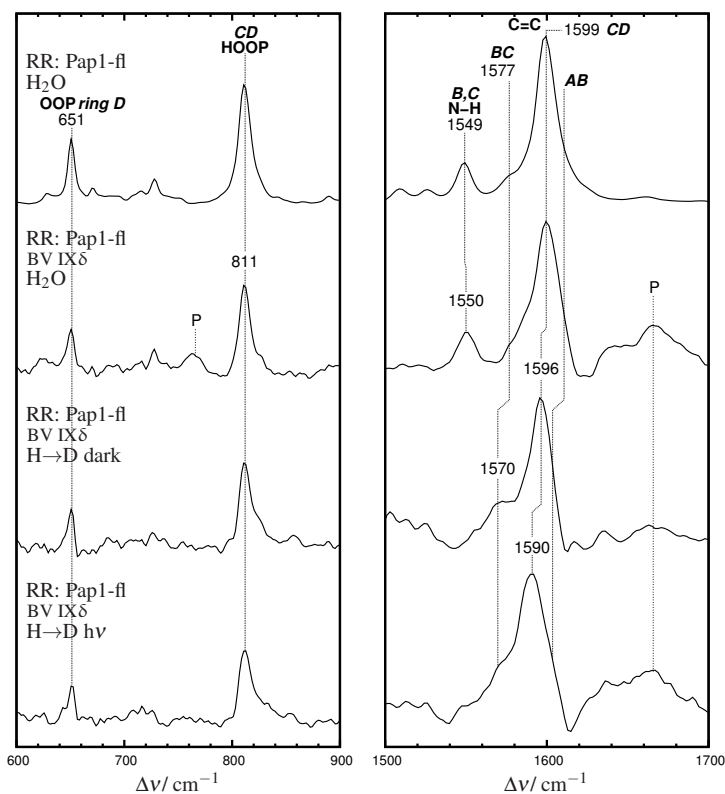


Figure D.12: RR spectra of the Pfr state in Pap1-fl assembled with the non-native BV δ chromophore displayed in the HOOP region (left) and in the marker range (right). The H₂O Pfr spectrum of Pap1-fl with native BV (top) shows excellent agreement with the corresponding RR spectrum of the BV δ Pap1-fl (second from top). Furthermore, the BV δ -variant undergoes sequential H \rightarrow D exchange at ring D as demonstrated in the D₂O RR Pfr spectra recorded in dark (second from bottom) and after a complete photocycle (bottom).

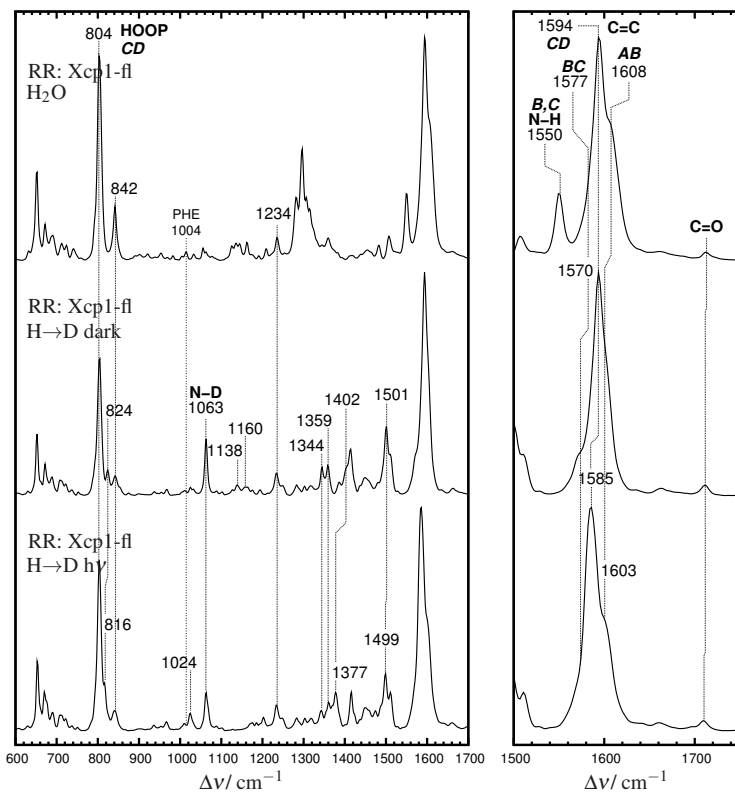


Figure D.13: RR spectra of the Pfr state in Xcp1 bathy phytochrome recorded in H₂O (top), D₂O prior light exposure (middle layer) and after a complete photocycle in deuterated medium (bottom).

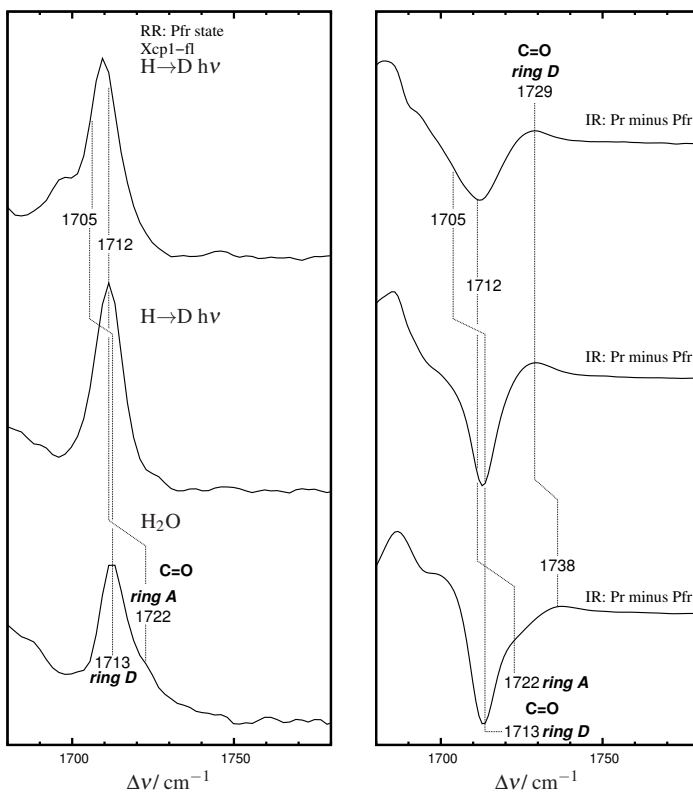


Figure D.14: C=O stretching modes in the RR Pfr (left) and Pr-minus-Pfr IR-difference spectra (right). Spectra (Pfr or Pr-minus-Pfr) were recorded in H₂O (bottom), after H/D exchange in the dark (middle) and preceding a complete photocycle in D₂O (top).

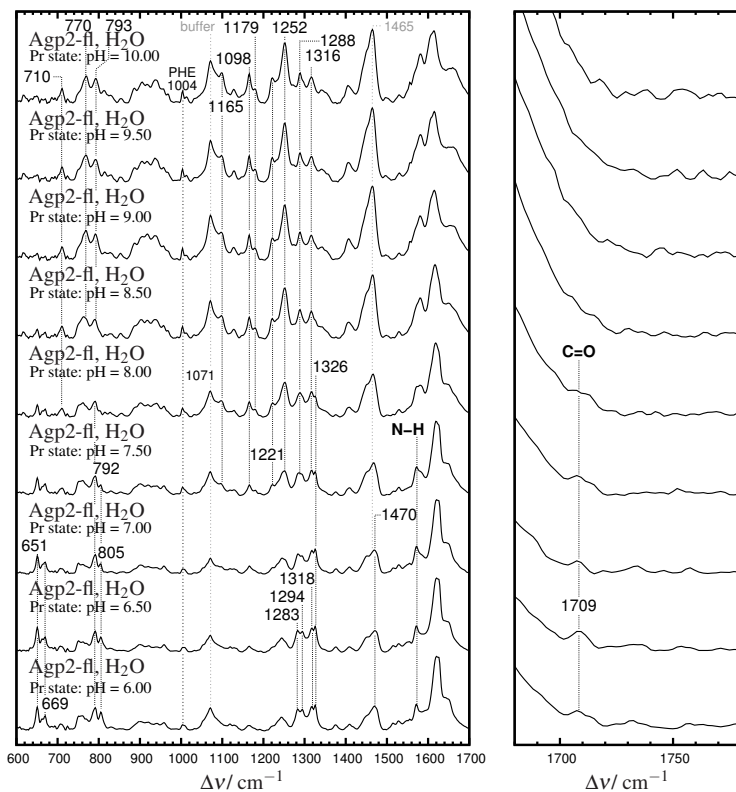


Figure D.15: RR spectra of the Pr state in Agp2-fl recorded between pH 6.0 and 10.0. Left: full range spectra. Right: expanded C=O region. Specific band frequencies and mode assignments are indicated. Dotted lines denote frequency correlations through the investigated pH range. Buffer contribution is displayed in gray. [207]

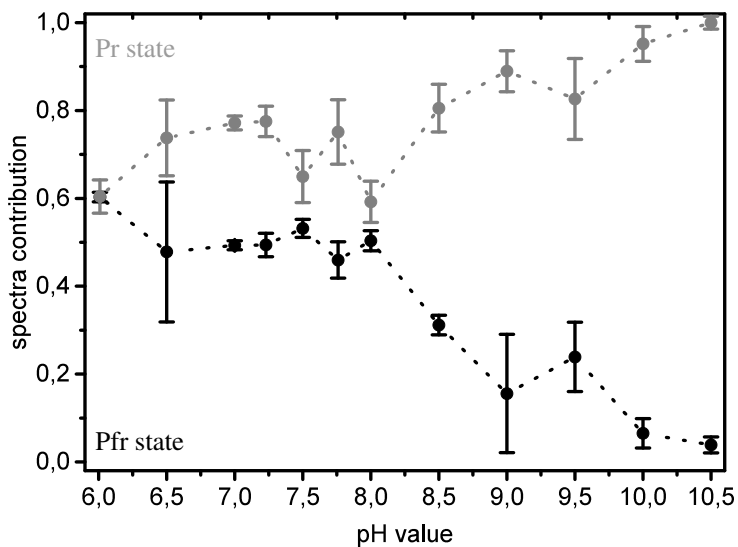


Figure D.16: Normalized contribution of the overall Pr (Pr_{keto} and Pr_{enol}, in gray) and Pfr components to the recorded RR spectra in the Agp2-fl Pr state within pH 6.0 and 10.0. Standard deviation was calculated based on three independent measurements.

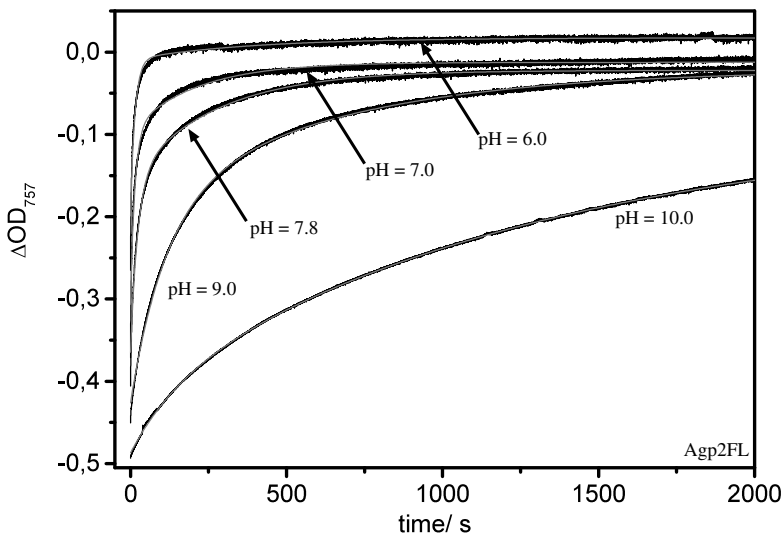


Figure D.17: Pr-to-Pfr thermal conversion in Agp2-fl measured at pH 6.0 and 10.0. Time traces at OD_{757} were recorded and analyzed according to the absorption spectroscopy protocol in subsection 3.3. Further kinetic results are given in section 6.2 or in ref. [207].

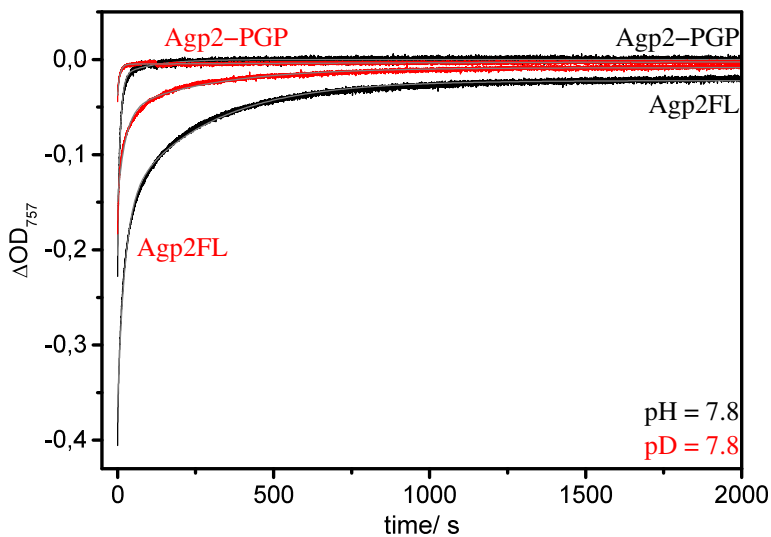


Figure D.18: Comparison of the thermal Pfr-state recovery in Agp2-fl and the photosensory domain (Agp2M2 or Agp2-PGP). Both were measured in H₂O and in D₂O (red). Further details are given in fig. D.17.

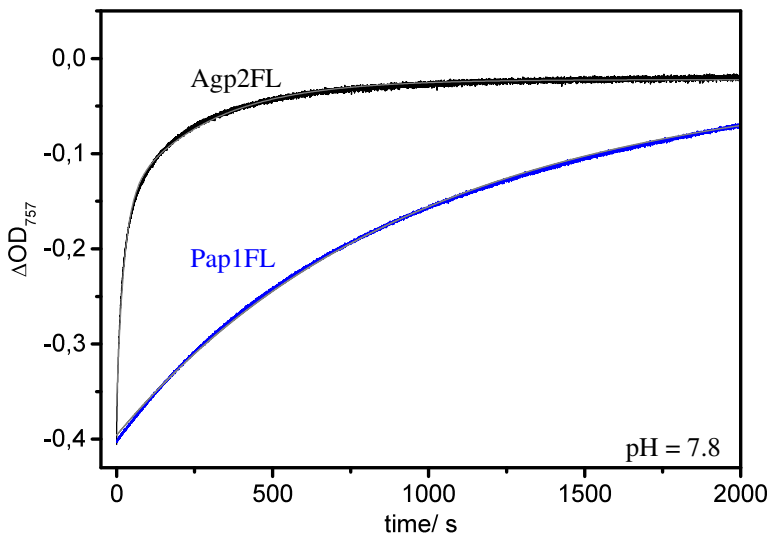


Figure D.19: Pr-to-Pfr thermal conversion in Pap1-fl (blue). For comparison Pfr recovery in Agp2-fl is shown. The Pr-to-Pfr conversion in Pap1-fl is two orders of magnitude slower as in Agp2-fl. Further details are given in fig. D.17.

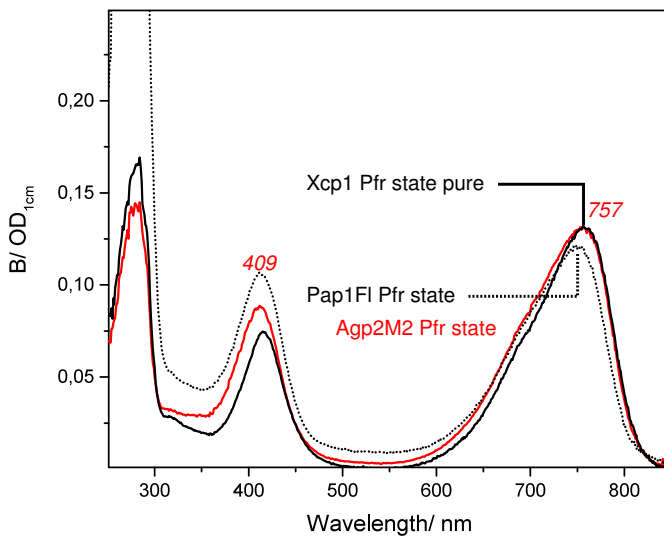


Figure D.20: Pfr state absorption spectra of the bathy phytochromes Xcp1, Agp2(M2, red) and Pap1 (dotted line). Details of the UV/VIS measurements are given in section 3.3.

E. Supplementary data and frequency tables

	H₂O			¹³C₅			D₂O		
SCS	18.75			15.83			20.77		
	<i>v_i</i>	<i>I_i</i>	Δv_i	<i>v_i</i>	<i>I_i</i>	Δv_i	<i>v_i</i>	<i>I_i</i>	Δv_i
C=O	1722	0.011	13.7				1718	0.038	13.1
C=O	1712	0.062	16.1	1712	0.059	13.9	1706	0.051	14.1
							1687	0.026	17.1
	1675	0.032	13.0	1673	0.040	18.7	1668	0.052	17.5
AB	1662	0.139	13.0				1653	0.105	17.1
	1654	0.246	12.8	1653	0.047	15.8	1642	0.234	18.0
	1647	0.122	13.1	1642	0.133	19.3	1628	0.135	12.1
	1635	0.209	13.3	1636	0.363	18.0			
CD	1628	0.819	12.6	1630	0.630	12.3			
							1622	0.825	13.4
BC							1604	0.029	11.6
				1595	0.059	18.0	1595	0.048	16.1
							1585	0.056	15.6
							1574	0.018	15.6
N-H	1567	0.426	11.6	1568	0.383	12.6			
							1553	0.030	16.1
							1544	0.078	13.3
				1543	0.028	10.7			
	1538	0.035	11.4						
				1530	0.047	16.8	1529	0.035	10.1
	1523	0.143	10.3	1520	0.117	8.7			

Table E.1: Band frequency v_i , intensity I_i , band full width at half maximum (FWHM or Δv_i) and scattering cross section (SCS) of the Pr-I species: n. a. PCB, ¹³C₅-labelled chromophore and measured in D₂O. Corresponding spectra are shown in fig. 4.7.

	H_2O			$^{13}\text{C}_5$			D_2O		
SCS	9.05			7.59			26.10		
	ν_i	I_i	$\Delta\nu_i$	ν_i	I_i	$\Delta\nu_i$	ν_i	I_i	$\Delta\nu_i$
C=O	1712	0.057	12.8	1708	0.063	10.8	1710	0.061	14.8
							1695	0.038	13.8
	1676	0.063	18.0	1676	0.079	19.2	1671	0.015	15.7
AB	1656	0.196	16.7	1655	0.201	19.2	1645	0.166	16.7
	1648	0.361	15.8	1647	0.136	17.2			
	1639	0.332	16.0	1641	0.316	16.9	1637	0.354	17.8
CD	1630	0.684	16.2	1631	0.726	17.6	1624	0.811	16.4
BC	1615	0.131	15.2						
	1605	0.189	13.2	1602	0.145	16.8			
				1586	0.040	15.4	1588	0.049	15.0
	1575	0.022	13.2						
N-H	1570	0.304	12.9	1568	0.347	13.3			
							1567	0.022	13.2
	1550	0.065	16.3						
				1545	0.045	10.9	1544	0.052	15.7
							1530	0.054	10.0
	1524	0.111	14.4	1522	0.144	13.8			
	1514	0.019	16.0						

Table E.2: Fitting values (ν_i , I_i and $\Delta\nu_i$) of all recorded Pr-II species: n. a. PCB, $^{13}\text{C}_5$ -labelled chromophore and measured in D_2O . Spectra are shown in fig. 4.8. Further notation details given in table E.1.

SCS	Cph1Δ2 n.a.			Cph1ΔH260Q					
	Pfr_{prot}			Pfr_{prot}			Pr_{prot}		
	14.82			15.83			7.45		
	v_i	I_i	Δv_i	v_i	I_i	Δv_i	v_i	I_i	Δv_i
C=O	1719	0.013	10.3				1728	0.014	13.7
	1714	0.042	10.3	1710	0.041	15.0	1716	0.020	13.7
	1707	0.018	10.3						
	1688	0.022	16.9	1682	0.025	10.0	1699	0.022	13.7
	1670	0.050	16.9	1668	0.037	13.1	1676	0.048	13.7
	1656	0.051	16.9						
AB	1645	0.199	11.8						
	1639	0.180	10.8	1638	0.112	9.2			
	1619	0.345	12.0						
CD	1612	0.458	12.2	1622	0.590	13.2	1658	0.234	13.7
	1606	0.371	13.0	1616	0.356	12.5	1650	0.420	13.0
	1603	0.336	12.3	1609	0.404	13.9	1643	0.533	12.1
							1639	0.056	14.1
							1635	0.332	12.9
				1603	0.036	10.0			
	1596	0.012	12.3	1596	0.032	10.0			
				1588	0.048	10.0			
				1586	0.020	10.8			
N-H	1553	0.291	10.7	1554	0.120	9.8	1575	0.123	10.5
	1547	0.112	12.1	1548	0.238	10.3	1569	0.212	10.9
	1535	0.037	12.4	1539	0.029	10.1	1561	0.043	10.0
	1520	0.125	15.2	1518	0.121	13.8	1542	0.024	10.0
	1510	0.064	15.2	1509	0.053	14.4	1533	0.087	11.3
	1500	0.043	10.4	1483	0.136	12.4	1525	0.055	12.0
	1484	0.213	12.4				1516	0.027	12.0
							1506	0.022	12.3
						1492	0.065	13.9	

Table E.3: Fitting values (v_i , I_i and Δv_i) and SCS values for the protonated Pfr species in the native protein (Pfr_{prot}), the Pfr and the Pr species of the H260Q mutant (Pfr_{H260Q,prot} and Pr_{H260Q}). Corresponding spectra are shown in fig. 4.11.

SCS	Cph1Δ2 n.a.			Cph1Δ2H260Q					
	Pr_{deprot}			Pfr_{deprot}			Pfr_{deprot}		
	6.79			3.40			2.50		
	v_i	I_i	Δv_i	v_i	I_i	Δv_i	v_i	I_i	Δv_i
	1702	0.093	14.8	1709	0.075	13.3	1709	0.032	16.0
	1690	0.119	14.8	1688	0.152	15.9	1691	0.070	16.0
	1674	0.285	18.0	1679	0.092	13.9	1678	0.155	16.9
	1659	0.369	16.7	1669	0.145	13.9	1668	0.097	13.0
	1648	0.417	16.0	1661	0.164	15.9	1662	0.121	13.0
	1636	0.409	17.0	1652	0.152	10.4	1629	0.148	13.0
	1626	0.588	17.0	1622	0.202	10.0	1620	0.319	12.1
	1612	0.224	17.1	1610	0.358	14.8	1611	0.308	12.0
	1596	0.305	15.5	1604	0.245	10.4	1604	0.541	14.9
	1584	0.327	15.5	1597	0.526	14.9	1597	0.437	12.7
	1576	0.177	16.4	1589	0.452	16.7	1588	0.350	11.7
	1566	0.261	15.1	1575	0.066	12.0	1579	0.181	13.2
	1547	0.121	15.1	1563	0.100	10.6	1565	0.086	11.7
	1531	0.128	15.1	1554	0.164	10.6	1554	0.139	11.0
	1515	0.144	14.1	1538	0.048	10.5	1546	0.113	12.4
				1542	0.038	10.2	1536	0.125	12.7
				1528	0.029	10.1	1525	0.090	12.7
				1509	0.073	10.1	1514	0.113	13.5
				1505	0.087	10.1	1504	0.173	16.0
				1497	0.054	10.0	1492	0.252	16.0
				1490	0.133	12.1			

Table E.4: Fitting (v_i , I_i and Δv_i) and SCS values of all deprotonated species from the native Cph1Δ2-variant (Pr_{deprot} and Pfr_{deprot}), as well from the H260Q mutant ($Pfr_{H260Q,deprot}$). The deprotonated spectra are plotted in fig. B.8.

pH	Pr-I	Pr-II	Pr_{deprot}	Pfr_{prot}	Pfr_{deprot}
6.0	0.591	0.026	0.194	0.080	0.108
6.5	0.596	0.053	0.221	0.052	0.077
7.0	0.577	0.055	0.245	0.115	0.007
7.5	0.604	0.070	0.126	0.176	0.024
8.0	0.596	0.070	0.131	0.199	0.004
8.5	0.592	0.140	0.046	0.162	0.060
9.0	0.428	0.277	0.000	0.123	0.171

Table E.5: Normalized contribution of all component spectra (Pfr_{prot}, Pfr_{deprot}, Pr-I, Pr-II, Pr_{deprot}) of the corresponding raw RR Pfr spectrum measured between pH = 6.0 and 9.0. The observed pH dependence shown in table 4.1 is in agreement with these values.

	Pr_{dark}			Pr_{illum}			Pr_{back}		
	ν_i	I_i	$\Delta\nu_i$	ν_i	I_i	$\Delta\nu_i$	ν_i	I_i	$\Delta\nu_i$
C=O	1717	0.024	12.5	1717	0.025	12.5	1717	0.023	12.5
AB	1649	0.168	13.6	1649	0.165	13.6	1649	0.166	13.6
	1639	0.227	11.1	1639	0.218	11.1	1639	0.215	11.1
CD	1626	0.826	12.1	1626	0.826	12.1	1626	0.823	12.1
	1617	0.168	15.1	1617	0.175	15.1	1617	0.188	15.1
BC	1592	0.033	13.6	1592	0.045	13.6	1593	0.052	13.6
N-H	1571	0.280	12.4	1571	0.280	12.5	1572	0.271	12.5
	1540	0.046	11.2	1542	0.042	10.2	1542	0.036	10.2
				1535	0.023	10.2	1536	0.020	10.2
	1528	0.068	14.4	1527	0.075	14.4	1527	0.069	14.4
	1518	0.077	12.5	1517	0.078	12.5	1518	0.070	12.5
	1512	0.015	12	1500	0.005	12.0	1512	0.011	12.0
	1475	0.074	9.6	1475	0.083	9.6	1475	0.081	9.6
	1468	0.098	14.1	1468	0.093	14.1	1468	0.092	14.1
	1452	0.025	12	1452	0.026	12.0	1452	0.027	12.0
	1442	0.021	12	1442	0.022	12.0	1442	0.022	12.0
	1417	0.026	11.5	1417	0.029	11.5	1417	0.024	11.5
	1430	0.009	11	1430	0.013	11.0	1430	0.009	11.0
	1407	0.023	11.5	1407	0.026	11.5	1407	0.023	11.5
	1397	0.026	11.5	1397	0.032	11.5	1397	0.026	11.5
	1379	0.096	13.1	1379	0.102	13.1	1379	0.090	13.1

Table E.6: Fitting values (ν_i , I_i and $\Delta\nu_i$) of all possible Agp1FMR Pr species measured in aqueous solution (Pr_{dark} , $\text{Pr}_{illum-1}$ and $\text{Pr}_{illum-2}$). Corresponding spectra are shown in fig. C.5.

	Pr_{dark}			Pr_{ilum}			Pr_{back}		
	v_i	I_i	Δv_i	v_i	I_i	Δv_i	v_i	I_i	Δv_i
C=O	1715	0.013	12.2	1715	0.013	12.2	1715	0.016	12.2
	1704	0.039	12.2	1704	0.043	12.2	1704	0.046	12.2
AB	1640	0.175	12.8	1641	0.189	14.0	1641	0.213	12.8
	1624	0.230	10.0	1625	0.273	10.0	1624	0.327	10.0
CD	1621	0.623	12.8	1621	0.587	12.8	1621	0.540	12.8
	1614	0.273	13.1	1614	0.290	13.1	1614	0.300	13.1
BC	1607	0.131	15.8	1607	0.130	15.8	1607	0.125	15.8
	1587	0.103	15.4	1587	0.103	15.4	1587	0.087	15.4
	1574	0.033	14.3	1574	0.041	14.3	1574	0.021	14.3
	1538	0.130	14.9	1538	0.148	14.9	1538	0.151	14.9
	1526	0.056	11.1	1526	0.042	11.1	1526	0.040	11.1
	1518	0.023	10.0	1518	0.030	10.0	1518	0.027	10.0
	1495	0.127	10.1	1495	0.130	10.1	1495	0.124	10.1
	1490	0.098	10.0	1490	0.096	10.0	1490	0.092	10.0
	1481	0.038	11.7	1481	0.038	11.7	1481	0.042	11.7
	1469	0.175	10.5	1469	0.182	10.5	1469	0.190	10.5
	1461	0.045	11.1	1461	0.045	11.1	1461	0.053	11.1
	1448	0.096	12.1	1448	0.101	12.1	1448	0.108	12.1
	1440	0.031	11.1	1440	0.036	11.1	1440	0.038	11.1
	1429	0.090	12.1	1429	0.098	12.1	1429	0.096	12.1
	1422	0.054	14.7	1422	0.051	14.7	1422	0.050	14.7
	1383	0.039	11.1	1383	0.038	11.1	1383	0.036	11.1

Table E.7: Fitting values (v_i , I_i and Δv_i) of the corresponding D₂O Pr spectra (Pr_{dark} , Pr_{ilum-1} and Pr_{ilum-2}) of table E.6. Spectra are shown in fig. C.5.

	Lumi-R ₋₁₄₀			Lumi-R ₋₁₂₀			Meta-Ra		
	ν_i	I_i	$\Delta\nu_i$	ν_i	I_i	$\Delta\nu_i$	ν_i	I_i	$\Delta\nu_i$
				1679	0.080	14.3			
	1661	0.121	14.3	1660	0.062	10.2	1664	0.050	13.9
	1649	0.233	14.3	1650	0.212	14.3	1652	0.151	13.0
AB	1640	0.257	10.0	1640	0.262	10.0	1644	0.173	14.7
	1629	0.704	11.8	1629	0.746	11.8	1628	0.364	12.5
	1619	0.269	10.4	1619	0.306	11.2			
BC	1610	0.155	10.1	1611	0.139	12.4			
	1602	0.187	11.8	1601	0.389	12.8			
CD	1595	0.775	14.7	1594	0.645	14.1	1620	0.777	18.1
BC	1587	0.074	11.4	1584	0.057	13.1	1606	0.050	15.5
N-H	1574	0.182	10.5	1573	0.122	10.4			
	1563	0.337	13.3	1564	0.399	13.8	1570	0.210	15.5
	1555	0.050	12.1				1556	0.023	12.5
	1539	0.074	14.0	1539	0.069	16.0	1547	0.074	14.0
	1528	0.099	15.0	1527	0.107	15.8	1532	0.038	13.1
	1515	0.138	11.0	1515	0.095	12.4	1525	0.060	11.1
	1478	0.114	11.1	1475	0.134	12.1	1515	0.064	12.1
	1469	0.148	12.0	1466	0.121	11.0	1475	0.136	10.0
	1456	0.103	14.0	1455	0.065	14.0	1468	0.104	11.1
	1448	0.080	12.0	1448	0.059	10.5	1449	0.068	12.0
				1439	0.053	12.0	1457	0.063	12.0
	1430	0.097	12.3	1430	0.062	12.3	1439	0.038	12.0
	1411	0.139	10.0	1411	0.116	10.0	1407	0.040	12.0
				1385	0.052	11.1	1417	0.022	12.0
							1382	0.069	13.0

Table E.8: Fitting values (ν_i , I_i and $\Delta\nu_i$) of the two possible Lumi-R species (Lumi-R1 and Lumi-R2) and the pure Meta-Ra component in Agp1FMR phytochrome measured in H₂O. Fitted spectra are shown in fig. C.6 (Lumi-R) and in fig. 5.7 (Meta-Ra).

	Lumi-R ₋₁₄₀			Lumi-R ₋₁₂₀			Meta-Ra		
	ν_i	I_i	$\Delta\nu_i$	ν_i	I_i	$\Delta\nu_i$	ν_i	I_i	$\Delta\nu_i$
							1718	0.016	14.9
	1684	0.084	14.3				1707	0.046	14.9
	1671	0.067	14.3	1672	0.084	14.8	1672	0.058	14.0
							1654	0.051	14.0
AB	1645	0.224	14.3	1646	0.066	15.2			
				1644	0.118	14.3	1643	0.236	13.6
	1637	0.155	10.0	1636	0.115	10.0			
BC	1625	0.684	12.5	1624	0.661	12.5			
	1615	0.378	13.4	1615	0.294	13.4			
	1608	0.250	11.8	1609	0.281	11.8			
CD	1600	0.217	12.3	1601	0.134	12.0	1625	0.545	13.4
	1590	0.726	14.7	1592	0.738	15.3	1618	0.376	13.3
BC							1611	0.531	14.9
	1582	0.221	11.3	1584	0.254	12.0	1602	0.111	13.8
	1541	0.200	13.1	1541	0.215	10.3	1588	0.053	11.4
	1533	0.112	13.1	1532	0.112	14.2	1544	0.124	14.9
	1524	0.080	13.2	1522	0.098	10.0	1537	0.080	10.9
	1495	0.232	11.6	1496	0.167	10.6	1529	0.024	10.5
	1490	0.087	10.6	1490	0.153	11.6	1521	0.041	9.3
	1485	0.158	10.6	1486	0.094	10.6	1495	0.182	12.0
							1485	0.065	12.0
	1469	0.207	10.6	1470	0.140	10.6	1473	0.087	11.7
	1463	0.120	10.6	1464	0.168	12.6	1467	0.165	11.5
	1453	0.104	10.0	1451	0.114	10.0	1459	0.062	11.1
	1446	0.165	10.0	1444	0.129	12.0	1449	0.142	12.1
	1434	0.125	10.0	1433	0.111	10.0	1441	0.055	11.1
	1426	0.147	10.0	1424	0.167	12.0	1432	0.067	12.1

Table E.9: Fitting values (ν_i , I_i and $\Delta\nu_i$) of the corresponding D₂O components (Lumi-R1 and Lumi-R2 and Meta-Ra) of table E.8. Fitted D₂O Lumi-R1 and R2 spectra as well as the Meta-Ra spectrum are displayed in fig. C.6 and fig. 5.7 respectively.

	Pfr			Meta-Rc			Apoprotein		
	ν_i	I_i	$\Delta\nu_i$	ν_i	I_i	$\Delta\nu_i$	ν_i	I_i	$\Delta\nu_i$
C=O	1710	0.028	14.6	1709	0.031	16.0	<i>1739</i>	<i>0.625</i>	<i>10.4</i>
				1688	0.045	16.0	<i>1719</i>	<i>0.848</i>	<i>10.8</i>
	1672	0.018	16.9	1666	0.100	10.4	<i>1676</i>	<i>15.848</i>	<i>20.3</i>
C=C	1650	0.022	16.9				<i>1660</i>	<i>11.815</i>	<i>14.0</i>
	1633	0.038	16.9				<i>1647</i>	<i>5.096</i>	<i>11.1</i>
AB	1620	0.272	14.8	1624	0.312	17.0	<i>1632</i>	<i>5.542</i>	<i>13.3</i>
	1611	0.231	14.6	1611	0.268	16.7	<i>1607</i>	<i>10.118</i>	<i>32.1</i>
CD	1600	0.691	14.1	1602	0.438	17.1	<i>1580</i>	<i>2.855</i>	<i>15.5</i>
	1595	0.171	13.3	1591	0.554	18.1	<i>1525</i>	<i>2.345</i>	<i>15.2</i>
BC	1586	0.148	12.8	1583	0.351	14.3	<i>1452</i>	<i>21.708</i>	<i>15.9</i>
	1577	0.069	13.4	1575	0.125	13.1	<i>1412</i>	<i>3.441</i>	<i>10.4</i>
N-H	1551	0.278	13.9	1555	0.066	10.0	1766	0.004	7.7
				1547	0.071	10.0	1460	0.058	12.0
	1528	0.029	12.4	1532	0.051	12.0	1447	0.319	16.6
	1518	0.046	14.5	1525	0.035	12.0	1424	0.060	9.9
	1509	0.094	13.4	1509	0.053	10.0	1501	0.034	10.8
				1503	0.096	14.8	1620	0.143	19.4
	1482	0.115	14.4	1482	0.171	15.2	1605	0.166	13.1
	1465	0.035	14.1	1466	0.037	10.0	1585	0.066	7.8
	1454	0.016	14.1	1453	0.061	10.5	1579	0.042	11.4
				1443	0.045	10.6	1553	0.233	22.1
	1436	0.030	17.0	1435	0.063	13.1	1468	0.383	19.9
				1426	0.084	11.0	1451	0.014	4.4
				1419	0.085	10.0	1401	0.028	16.1

Table E.10: Fitting values (ν_i , I_i and $\Delta\nu_i$) of the pure Agp1FMR H2O Pfr, the Meta-Rc and the apoprotein component. Values in italics refer to Gaussian band fit functions (only apoprotein). Corresponding spectra of the Pfr and Met-Rc species are found in fig. 5.7. Apoprotein spectrum is shown in fig. C.4.

	Pfr			Meta-Rc			Apoprotein		
	v_i	I_i	Δv_i	v_i	I_i	Δv_i	v_i	I_i	Δv_i
C=O	1707	0.024	12.0				1631	15.899	22.4
	1702	0.026	12.0	1689	0.096	14.0	1677	24.580	31.2
				1667	0.124	14.8	1654	9.913	25.6
				1657	0.095	14.6	1580	5.008	10.9
				1644	0.119	14.6	1561	8.699	18.6
AB	1619	0.108	12.0	1623	0.174	13.0	1742	0.074	9.0
	1607	0.229	15.0	1612	0.398	14.5	1721	0.036	4.4
				1604	0.367	13.9	1711	0.021	4.2
CD	1598	0.147	14.6	1597	0.199	12.9	1670	0.047	5.4
	1591	0.720	15.8	1589	0.512	15.9	1655	0.180	21.1
BC	1584	0.208	12.9	1580	0.433	15.3	1639	0.095	12.0
	1576	0.074	15.8	1573	0.217	14.2	1630	0.030	12.0
				1564	0.087	14.4	1605	0.155	22.1
				1552	0.092	12.3	1617	0.252	35.3
		0.014	10.6	1543	0.134	12.4	1595	0.096	9.7
		0.090	10.6	1516	0.059	10.1	1586	0.069	9.8
				1512	0.125	10.3	1554	0.119	14.3
		0.208	13.9	1504	0.117	14.9	1535	0.065	8.1
		0.086	13.6	1495	0.114	12.0	1521	0.086	10.8
				1481	0.050	12.0	1510	0.038	16.6
		0.064	12.6	1476	0.126	11.7	1486	0.067	16.6
		0.031	13.6	1468	0.135	13.5	1469	0.487	18.9
		0.040	13.6	1458	0.099	15.1	1461	0.472	17.9
		0.055	12.6	1447	0.220	15.1	1451	0.275	15.9
		0.013	12.6	1436	0.298	16.6	1440	0.241	19.9
	0.081	12.6	1425	0.115	15.6	1416	0.077	10.8	

Table E.11: Fitting values (v_i , I_i and Δv_i) of the corresponding D₂O components (Pfr, Meta-Rc and apoprotein) according to table E.10. D₂O spectra of the Pfr and Meta-Rc component and apoprotein are shown in fig. 5.7 and fig. C.4 respectively. Further details are given in table E.10.

	Pap1 Pfr			Agp2 Pfr			Xcp1 Pfr		
	ν_i	I_i	$\Delta\nu_i$	ν_i	I_i	$\Delta\nu_i$	ν_i	I_i	$\Delta\nu_i$
C=O									
COOH	1754	0.007	10.0	1752	0.010	10.0			
D	1696	0.015	13.5	1698	0.020	14.0	1713	0.025	11.3
	1682	0.008	16.5	1683	0.012	15.0			
	1670	0.009	15.3	1672	0.011	15.0			
	1661	0.031	15.7	1657	0.021	15.7			
	1651	0.007	15.8						
	1640	0.002	14.2	1637	0.016	13.8			
	1625	0.030	13.0	1614	0.056	13.0			
A	1613	0.059	12.9	1609	0.022	12.9	1614	0.141	11.7
AB	1603	0.315	12.1	1605	0.325	12.2	1607	0.312	13.4
CD	1598	0.742	12.1	1598	0.733	12.4	1594	0.842	14.6
BC	1585	0.061	13.1	1588	0.093	14.3	1585	0.097	11.9
D	1575	0.080	12.1	1577	0.088	12.5	1575	0.027	11.6
N-H	1549	0.231	11.7	1549	0.258	12.4	1550	0.282	11.2
	1526	0.073	11.8	1525	0.068	13.8	1529	0.021	11.8
	1510	0.040	11.6	1510	0.059	11.8	1521	0.029	16.0
	1508	0.053	12.4	1506	0.053	11.2	1507	0.123	13.4
	1482	0.065	12.2	1483	0.066	12.5	1483	0.082	10.9
	1465	0.041	16.6	1471	0.008	14.4	1463	0.013	13.0
	1453	0.020	17.0	1461	0.037	14.4	1455	0.025	13.0
	1437	0.043	13.6	1435	0.025	10.0	1437	0.018	12.0
	1421	0.025	11.1	1423	0.020	11.6	1420	0.017	11.3
	1413	0.053	11.3	1414	0.027	11.3	1412	0.017	11.3
				1391	0.005	10.1	1394	0.009	11.3
	1383	0.031	10.0	1385	0.024	10.0	1382	0.036	11.0

Table E.12: Pfr state marker region fitting values (ν_i , I_i and $\Delta\nu_i$) of Pap1, Agp2 and Xcp1 bathy phytochromes. Corresponding spectra are shown in fig. D.2. HOOP region fitting parameters are shown in table E.13. Band assignment corresponds to QM/MM calculated spectra [159].

	Pap1 Pfr			Agp2 Pfr			Xcp1 Pfr		
	v_i	I_i	Δv_i	v_i	I_i	Δv_i	v_i	I_i	Δv_i
	904	0.004	12.0	901	0.015	10.6	905	0.006	19.2
	890	0.032	10.1	889	0.030	9.4			
	844	0.010	9.6	842	0.037	8.5	842	0.223	7.8
	824	0.034	10.1	833	0.041	11.4			
HOOP	812	0.665	13.3	811	0.646	13.4	804	0.926	10.7
	790	0.001	11.0	796	0.002	7.1			
	773	0.001	11.2	779	0.004	8.5			
	751	0.024	11.0	753	0.025	9.9	750	0.001	8.0
	741	0.028	14.2	742	0.024	12.3	741	0.056	8.4
	728	0.128	9.6	726	0.118	8.5	724	0.059	7.5
	715	0.052	10.2	715	0.014	11.9	712	0.070	9.7
				711	0.045	9.2			
	708	0.024	9.8						
	694	0.031	10.8	693	0.040	8.2	692	0.077	10.3
	687	0.023	12.5	685	0.045	10.0	686	0.052	11.3
	680	0.020	14.5						
	671	0.070	8.1	672	0.056	7.1	672	0.133	8.2
				661	0.105	7.7			
OOP	651	0.354	8.2	650	0.232	9.8	652	0.387	7.7
	633	0.013	13.1				632	0.020	8.0
	628	0.044	9.9	630	0.052	10.2			
				613	0.006	12.9			

Table E.13: HOOP region fitting values (v_i , I_i and Δv_i) according to table E.12 (Pfr state in Pap1, Agp2 and Xcp1 bathy phytochromes).

	Agp1 Pfr			$^{13}\text{C}_{10}\text{-BV}$			Agp1 Δ 18 Pfr		
	v_i	I_i	Δv_i	v_i	I_i	Δv_i	v_i	I_i	Δv_i
C=O									
D	1710	0.028	14.6	1710	0.032	14.6	1713	0.024	10.0
				1693	0.011	16.1			
				1679	0.012	16.2			
	1672	0.018	16.9	1667	0.012	16.2			
	1650	0.022	16.9						
	1633	0.038	16.9				1631	0.036	10.0
AB	1620	0.272	14.8	1618	0.111	10.2	1620	0.300	13.0
AB	1611	0.231	14.6	1608	0.387	14.1	1607	0.134	13.0
CD	1600	0.691	14.1	1600	0.690	14.0	1602	0.412	13.7
CD	1595	0.171	13.3	1592	0.125	13.1	1596	0.510	13.0
BC	1586	0.148	12.8	1580	0.044	13.9	1589	0.262	13.0
BC	1577	0.069	13.4	1565	0.062	15.4	1579	0.101	13.0
N-H	1551	0.278	13.9	1551	0.267	14.2	1551	0.226	14.0
	1528	0.029	12.4	1531	0.041	12.9	1522	0.034	13.0
	1518	0.046	14.5	1522	0.039	14.9	1510	0.086	15.4
	1509	0.094	13.4	1506	0.116	13.7	1503	0.031	12.0
				1499	0.021	13.1			
	1482	0.115	14.4	1482	0.129	13.4	1480	0.145	14.7
	1465	0.035	14.1	1461	0.014	10.1			
	1454	0.016	14.1				1456	0.029	15.0
							1438	0.050	16.9
	1436	0.030	17.0	1435	0.023	12.1	1427	0.030	14.4
	1416	0.013	14.1	1416	0.020	16.1	1411	0.040	13.3
	1382	0.022	12.0	1382	0.020	12.0	1389	0.032	13.0
							1376	0.066	13.0

Table E.14: Pfr state marker region fitting values (v_i , I_i and Δv_i) of Agp1 (n. a. and $^{13}\text{C}_{10}\text{-BV}$) phytochrome and Agp1 Δ 18 mutant. Corresponding HOOP region fitting parameters are shown in table E.15. Spectra are shown in fig. D.2.

	Agp1 Pfr			¹³ C ₁₀ -BV			Agp1Δ18 Pfr		
	<i>v_i</i>	<i>I_i</i>	Δ <i>v_i</i>	<i>v_i</i>	<i>I_i</i>	Δ <i>v_i</i>	<i>v_i</i>	<i>I_i</i>	Δ <i>v_i</i>
	858	0.013	10.0	859	0.003	10.2	860	0.049	11.5
	853	0.069	10.0	848	0.050	11.0	854	0.164	12.9
	843	0.042	9.9	839	0.066	12.1	845	0.099	10.1
	836	0.031	10.0	832	0.021	12.0			
				817	0.069	11.1			
HOOP	810	0.656	10.9	810	0.623	11.6	809	0.519	11.8
HOOP	803	0.331	9.6	802	0.234	9.4	802	0.424	12.9
	748	0.013	12.0	744	0.008	12.0	735	0.020	10.0
	724	0.064	10.0	722	0.063	10.1	725	0.048	10.0
	713	0.024	9.6	713	0.020	10.0	716	0.046	10.0
	709	0.009	9.6	707	0.033	9.6			
	692	0.095	9.8	692	0.077	9.4	693	0.178	9.1
	684	0.048	9.9	683	0.054	12.1	686	0.126	9.2
	676	0.158	9.5	676	0.118	9.5	677	0.136	10.2
OOP	657	0.191	9.9	657	0.169	9.9	657	0.219	10.0
	652	0.040	10.4	649	0.043	10.4	650	0.066	11.1
	642	0.025	10.9	641	0.025	10.9	637	0.027	12.0
	633	0.006	10.6	631	0.003	10.6			
	599	0.001	12.0	599	0.001	12.0			

Table E.15: HOOP region fitting values (*v_i*, *I_i* and Δ*v_i*) according to table E.14 (Pfr state in Agp1 n. a. BV, ¹³C₁₀-BV and Agp1Δ18 mutant). Further details are given in table E.12.

	Agp1C20A Pfr			CphB Pfr			Rph2 Pfr		
	ν_i	I_i	$\Delta\nu_i$	ν_i	I_i	$\Delta\nu_i$	ν_i	I_i	$\Delta\nu_i$
C=O									
A							1723	0.002	11.0
D	1712	0.039	16.1	1712	0.029	12.2	1712	0.031	12.3
	1682	0.021	17.0	1679	0.018	16.0			
				1660	0.033	16.0			
	1641	0.032	16.1						
	1629	0.086	14.9						
AB	1620	0.319	15.0	1615	0.196	10.9	1614	0.356	11.7
AB	1610	0.083	14.5	1608	0.478	11.9	1607	0.368	13.4
CD	1603	0.205	14.0						
CD	1598	0.633	15.8	1599	0.619	13.7	1598	0.742	13.1
BC	1590	0.238	15.7	1593	0.262	12.7			
BC				1585	0.118	12.9	1586	0.129	14.9
BC	1579	0.089	15.5	1577	0.084	12.4	1580	0.069	11.6
	1569	0.049	14.6						
N-H	1550	0.228	16.3	1549	0.281	13.3	1548	0.314	12.3
	1537	0.032	16.1						
	1522	0.065	16.0	1524	0.042	15.6	1525	0.063	15.3
	1512	0.116	16.4						
	1503	0.055	16.0	1506	0.141	14.3	1508	0.159	16.0
	1482	0.152	17.1	1482	0.102	13.1	1482	0.131	13.2
	1465	0.026	15.5	1463	0.050	15.4	1462	0.046	15.0
				1450	0.023	13.0	1450	0.019	14.0
	1433	0.042	13.0	1437	0.038	14.1	1435	0.044	14.0
	1421	0.033	13.4	1425	0.015	15.7	1421	0.042	13.7
	1409	0.042	15.3	1411	0.017	14.9	1409	0.034	14.3
	1393	0.033	15.6				1396	0.021	13.3
	1381	0.065	13.0	1385	0.019	13.7	1384	0.059	14.5

Table E.16: Pfr state marker region fitting values (ν_i , I_i and $\Delta\nu_i$) of Agp1-C20A, CphB-fl and Rph2-PGP species. Spectra displayed in fig. D.2. Corresponding HOOP region fitting parameters are shown in table E.17.

	Agp1C20A Pfr			CphB Pfr			Rph2 Pfr		
	v_i	I_i	Δv_i	v_i	I_i	Δv_i	v_i	I_i	Δv_i
				901	0.012	10.0			
				891	0.005	10.2			
	862	0.046	12.0						
	854	0.116	12.1	852	0.059	11.3			
	845	0.057	10.6	842	0.134	11.6	842	0.148	10.0
				834	0.051	9.7	833	0.045	9.9
							826	0.034	9.7
HOOP	809	0.518	11.5	807	0.412	8.8	807	0.560	9.9
HOOP	802	0.350	12.6	799	0.752	9.2	802	0.416	10.0
	762	0.019	12.0	766	0.002	12.5			
				748	0.016	12.0			
	740	0.023	10.0	741	0.019	12.0	741	0.022	10.4
	725	0.051	10.0	725	0.078	10.8	724	0.056	9.5
	715	0.030	10.0	710	0.076	9.4	711	0.050	9.0
	693	0.123	9.1	694	0.107	9.0	692	0.101	11.6
	687	0.087	9.2	684	0.076	11.1	684	0.037	10.0
	677	0.130	10.2	675	0.147	9.3	675	0.095	10.0
				670	0.017	10.9			
OOP	658	0.167	10.0				662	0.034	10.5
	652	0.060	11.1	654	0.259	10.8	653	0.289	10.1
	637	0.036	12.0	638	0.039	15.4			

Table E.17: HOOP region fitting values (v_i , I_i and Δv_i) according to table E.16 (Pfr state in Agp1-C20A, CphB-fl and Rph2-PG). Corresponding spectra are shown in fig. D.2.

Pr state pH titration						
pH	Pr _{enol,1}	Pr _{enol,2}	Pr _{enol,3}	Pr _{keto,1}	Pr _{keto,2}	Pr _{keto,3}
6.01	0.078	0.096	0.071	1.047	1.041	1.058
6.50	0.080	0.092	0.073	1.041	1.047	1.027
7.00	0.172	0.154	0.161	0.975	0.985	0.977
7.23	0.300	0.312	0.293	0.890	0.863	0.887
7.50	0.357	0.352	0.349	0.816	0.816	0.819
7.76	0.491	0.484	0.498	0.697	0.709	0.713
8.00	0.616	0.649	0.618	0.575	0.561	0.583
8.50	1.020	0.987	0.970	0.205	0.233	0.247
9.00	1.253	1.214	1.261	0.000	0.004	0.000
9.50	1.253	1.246	1.261	0.000	0.000	0.000
10.00	1.253	1.246	1.261	0.000	0.000	0.000
10.50	1.253	1.269	1.268	0.000	0.001	0.000

Table E.18: Component contribution of the overall Agp2-fl RR Pr spectra (Pr_{keto} and Pr_{enol} species) measured between pH 6.01 and 10.50. Standard error was determined based on three independent measurements.

List of Figures

1.1. Absorption spectrum Cph1 phytochrome	21
2.1. Examples of protein domains in the phytochrome family	26
2.2. Structure formula of chromophore precursors: BV, PΦB and PCB	28
2.3. Protein-chromophore attachment of BV, PΦB and PCB precursors	29
2.4. Pr state binding pocket of Cph1Δ2 phytochrome	31
2.5. Prototypical phytochrome photocycle	34
2.6. Pfr state binding pocket of Pap1 phytochrome	35
2.7. ApxJ Pr and TpxJ Pg crystal structure	37
2.8. Non-canonical photocycle model	38
3.1. Energy-level-diagram: light absorption and Scattering	47
3.2. FT-RR-Spectroscopy	51
3.3. Michelson Interferometer	52
3.4. Irradiation and measuring protocol: Agp1-FMR	57
3.5. RR and IR spectral regions	73
4.1. RR spectra: pH titration Cph1Δ2 Pr state	76
4.2. RR spectra: pH titration Cph1Δ2 Pfr state	77
4.3. RR spectra: fitted pH titration of the Cph1Δ2 Pr state	78
4.4. Titration values Pr state	80
4.5. Cph1Δ2 Pr and Pfr state: pK _a determination	82
4.6. RR spectra: fitted Cph1Δ2 Pr state protonated species	83
4.7. RR spectra: Comparison Pr _{acid} n. a., ¹³ C ₅ -PCB and D ₂ O	84
4.8. RR spectra: Comparison Pr _{alkaline} n. a., ¹³ C ₅ -PCB and D ₂ O	86
4.9. RR spectra: Cph1Δ2H260Q Pr and Pfr state titration	89
4.10. RR spectra marker region: Cph1Δ2H260Q Pr and Pfr (H/D)	90
4.11. Cph1Δ2 and H260Q-mutant: marker band analysis	91
4.12. Cph1Δ2: Pr and Pfr proton translocation model	95
5.1. IR spectra: Agp1 and Rph2 β-sheet-to-α-helix	98
5.2. Difference RR spectra: CphB and Agp1 Pr state BV na/ ¹³ C ₁₀ (H/D)	99
5.3. Difference RR spectra: CphB and Agp1 Pfr state BV na/ ¹³ C ₁₀ (H/D)	101
5.4. Agp1: temperature profiles along the Pr-to-Pfr conversion	104
5.5. Agp1: temperature profiles along the D ₂ O Pr-to-Pfr conversion	106
5.6. RR spectra: Agp1 pure components H ₂ O and D ₂ O	108
5.7. RR spectra: Agp1FMR fitted pure Pr-to-Pfr species H ₂ O/D ₂ O	109

5.8. Vibrational Spectra: Rph2 PAS-GAF-PHY, Pfr and Pr H ₂ O/ D ₂ O	112
5.9. Vibrational Spectra: Rph2 PAS-GAF, Pfr and Pr H ₂ O/ D ₂ O	114
5.10. Vibrational Spectra: Rph2 PAS-GAF-PHY, Pfr and Pr H ₂ O/ D ₂ O, C=O	116
5.11. RR Spectra: Rph2 PAS-GAF-PHY, Pr-to-Pfr intermediates, H ₂ O/ D ₂ O	118
5.12. RR Spectra: Rph2 PAS-GAF, Pr-to-Pfr intermediates, H ₂ O/ D ₂ O	120
5.13. RR spectra: CphB pure components Pr-to-Pfr H ₂ O and D ₂ O	123
5.14. RR spectra: CphB Pr-to-Pfr H ₂ O phosphate and TRIS buffer	125
5.15. RR spectra: Agp1 Pr-to-Pfr H ₂ O phosphate and TRIS buffer	127
5.16. RR spectra: Cph1Δ2 Pr-to-Pfr H ₂ O phosphate and TRIS buffer	128
5.17. RR spectra: CphB reverse Pfr-to-Pr intermediates (H ₂ O/D ₂ O)	130
5.18. RR spectra: CphB Pfr-to-Pr H ₂ O phosphate and TRIS buffer	131
5.19. Prototypical Pr-to-Pfr pathway	136
A.1. FT-NIR RR spectrometer	266
A.2. Ramanscope III module	267
A.3. RR spectra: Pr state Cph1Δ2 conc. determination	268
A.4. Cph1Δ2: RR intensity-concentration correlation	269
A.5. FT-Raman: Si-wafer Ramanscope vs. Macro-Setup	270
A.6. RR Spectra: Cph1Δ2 Ramanscope vs. Macro-Setup	271
A.7. IR transmission irradiation setup	272
B.1. RR spectra: fullrange Cph1Δ2 Pr-state pure protonated species	274
B.2. RR spectra: fullrange Cph1Δ2 deprotonated Pr and Pfr species	275
B.3. RR spectra: Titration values fitted Pr state with ¹³ C ₅ -PCB	276
B.4. RR spectra: Comparison Pr-I and Pr-II n. a., ¹³ C ₅ -PCB and D ₂ O	277
B.5. RR spectra: Cph1Δ2H260Q Pr state titration	278
B.6. RR spectra: Cph1Δ2H260Q Pfr state titration	279
B.7. RR spectra: Cph1Δ2H260Q pure Pr and Pfr species in H ₂ O and D ₂ O	280
B.8. RR spectra: fitted Pfr _{H260Q,deprot} , Pfr _{deprot} and Pr _{deprot} species	281
B.9. RR spectra: Cph1Δ2 Pr-I, Pr-II and Pr-x vs. IRFP Pr	282
C.1. RR raw spectra: cryogenic trapping Pr-to-Pfr of Agp1FMR	284
C.2. RR spectra: pure Agp1FMR Pr and Pfr species (H ₂ O)	285
C.3. RR spectra: Agp1FMR H ₂ O Lumi-R species selection	286
C.4. Raman Spectra: Agp1FMR fitted apoprotein in H ₂ O and D ₂ O	287
C.5. RR spectra: Agp1FMR fitted H ₂ O and D ₂ O Pr species	288
C.6. RR spectra: Agp1FMR fitted H ₂ O and D ₂ O Lumi-R species	289
C.7. RR spectra: Agp1FMR T-dependent component analysis (H/D) I.	290
C.8. RR spectra: Agp1FMR T-dependent component analysis (H/D) II.	291
C.9. RR spectra: CphB and Agp1 Pr state pure BV na/ ¹³ C ₁₀ (H/D)	292
C.10. RR spectra: CphB and Agp1 Pfr state pure BV na/ ¹³ C ₁₀ (H/D)	293
D.1. RR spectra of the bathy Pfr state in H ₂ O and QM/MM calc. species	296
D.2. Pfr state fit spectra: bathy and prototypical phytochromes	297

D.3. RR spectra: Agp2 and Pap1 H/D exchange Pfr state	298
D.4. RR spectra: Agp2 sequential H/D exchange Pfr (including ^{13}C -apo)	299
D.5. RR spectra: Agp2 Pfr fitted spectra (sequential H/D exchange)	300
D.6. C=O region: IR diff. spectra (Pap1) and RR (Agp2 and Pap1)	301
D.7. Sequential exchange Agp2 Pfr RR vs. calc. QM/MM spectra	302
D.8. diff. RR and calc. spectra: sequential H/D exchange Pfr state	303
D.9. RR spectra: Agp2 Pfr sequential H/D exchange over time	304
D.10. Agp2: rel. H/D (D/H) exchange over time	305
D.11. Chromophore structure BV- δ	306
D.12. RR spectra: Pap1-fl with BV δ , sequential H/D exchange Pfr	307
D.13. RR spectra: Xcp1 sequential H/D exchange Pfr	308
D.14. RR and IR: Xcp1 Pfr H/D exchange (C=O region)	309
D.15. RR spectra: Agp2-fl Pr state pH titration (raw)	310
D.16. pH titration: overall Pr and Pfr concentration	311
D.17. Trans. abs.: pH-dependent Pr \rightarrow Pfr thermal reversion Agp2-fl	312
D.18. Trans. abs.: Pr \rightarrow Pfr thermal reversion Agp2-fl and PGP (H/D)	313
D.19. Trans. abs.: Pr \rightarrow Pfr therm. reversion Agp2-fl vs. Pap1-fl	314
D.20. UV/VIS Pfr state bathy phytochromes	315

List of Tables

3.1. phytochrome samples	39
4.1. Component contribution pH titration Cph1Δ2	79
4.2. Cph1Δ2: Single bands of all protonated Pr species	85
5.1. Agp1: species evolution along the Pr-to-Pfr conversion	105
5.2. Agp1: species evolution along the D ₂ O Pr-to-Pfr conversion	107
E.1. Cph1Δ2: single bands of iostopically labelled Pr-I species	318
E.2. Cph1Δ2: single bands of iostopically labelled Pr-II species	319
E.3. Cph1Δ2: single bands of the Pfr _{prot} , Pr _{H260Q} and Pfr _{H260Q,prot} species	320
E.4. Cph1Δ2 and H260Q-mut.: Pr _{deprot} and Pfr _{deprot} single bands	321
E.5. Cph1Δ2: raw Pfr state spectra global analysis	322
E.6. Agp1FMR: single bands of all Pr species in H ₂ O	323
E.7. Agp1FMR: single bands of all Pr species in D ₂ O	324
E.8. Agp1FMR: single bands of Lumi-R and Meta-Ra species in H ₂ O	325
E.9. Agp1FMR: single bands of Lumi-R and Meta-Ra species in D ₂ O	326
E.10. Agp1FMR: Pfr, Meta-Rc and apoprotein species H ₂ O single bands	327
E.11. Agp1FMR: Pfr, Meta-Rc and apoprotein species D ₂ O single bands	328
E.12. Marker region: Pap1, Agp2 and Xcp1 Pfr single bands (H ₂ O)	329
E.13. HOOP region: Pap1, Agp2 and Xcp1 Pfr single bands (H ₂ O)	330
E.14. Marker region: Agp1 n. a., ¹³ C ₁₀ -BV and Δ18 single Pfr bands H ₂ O	331
E.15. HOOP region: Agp1 n. a., ¹³ C ₁₀ -BV and Δ18 single Pfr bands H ₂ O	332
E.16. Marker region: Agp1-C20A, CphB and Rph2 single Pfr bands H ₂ O	333
E.17. HOOP region: Agp1-C20A, CphB and Rph2 single Pfr bands H ₂ O	334
E.18. Pr state component contribution (Pr _{keto} and Pr _{enol})	335

Bibliography

- [1] M. Albert, J. Engelen, G. Carmichael, M. Erdelyi, B. Harrington, J. Bintz, T. Gould, J. Cruz, and bulia byak, *Inkscape 0.47*, <http://inkscape.org/> (2010).
- [2] A. C. Albrecht, “Forbidden” character in allowed electronic transitions, *J. Chem. Phys.* **33** (1), 156–169 (1960).
- [3] A. C. Albrecht, *On the theory of Raman intensities*, *J. Chem. Phys.* **34** (5), 1476–1484 (1961).
- [4] J. P. Allewalt, M. M. Bateson, N. P. Revsbech, K. Slack, and D. M. Ward, *Effect of temperature and light on growth of and photosynthesis by synechococcus isolates typical of those predominating in the octopus spring microbial mat community of yellowstone national park*, *Appl. Environ. Microbiol.* **72** (1), 544–550 (2006).
- [5] F. Andel, J. C. Lagarias, and R. A. Mathies, *Resonance Raman analysis of chromophore structure in the lumi-R photoproduct of phytochrome*, *Biochemistry* **35** (50), 15997–16008 (1996).
- [6] F. Andel, J. T. Murphy, J. A. Haas, M. T. McDowell, I. van der Hoef, J. Lugtenburg, J. C. Lagarias, and R. A. Mathies, *Probing the photoreaction mechanism of phytochrome through analysis of resonance Raman vibrational spectra of recombinant analogues*, *Biochemistry* **39** (10), 2667–2676 (2000).
- [7] K. Anders, G. Daminelli-Widany, M. A. Mroginski, D. von Stetten, and L.-O. Essen, *Structure of the cyanobacterial phytochrome 2 photosensor implies a tryptophan switch for phytochrome signaling.*, *J Biol Chem* (2013).
- [8] M. E. Auldridge, K. A. Satyshur, D. M. Anstrom, and K. T. Forest, *Structure-guided engineering enhances a phytochrome-based infrared fluorescent protein.*, *J Biol Chem* **287** (10), 7000–7009 (2012).
- [9] G. Bae and G. Choi, *Decoding of light signals by plant phytochromes and their interacting proteins*, *Ann. Rev. of Plant Biol.* **59** (1), 281–311 (2008).
- [10] K. Barkovits, A. Harms, C. Benkartek, J. L. Smart, and N. Frankenberg-Dinkel, *Expression of the phytochrome operon in Pseudomonas aeruginosa is dependent on the alternative sigma factor rpos*, *FEMS Microbiol. Lett.* **280** (2), 160–168 (2008).

- [11] S. I. Beale, *Biosynthesis of Phycobilins*, Chem. Rev. **93** (2), 785–802 (1993).
- [12] D. Bellini and M. Z. Papiz, *Dimerization properties of the RpBphP2 chromophore-binding domain crystallized by homologue-directed mutagenesis*, Acta Crystallographica Section D **68** (8), 1058–1066 (2012).
- [13] D. Bellini and M. Z. Papiz, *Structure of a Bacteriophytochrome and Light-Stimulated Protomer Swapping with a Gene Repressor*, Structure **20** (8), 1436–1446 (2012).
- [14] D. Bhaya, A. R. Grossman, A.-S. Steunou, N. Khuri, F. M. Cohan, N. Hamamura, M. C. Melendrez, M. M. Bateson, D. M. Ward, and J. F. Heidelberg, *Population level functional diversity in a microbial community revealed by comparative genomic and metagenomic analyses*, ISME J **1** (8), 703–713 (2007).
- [15] S. H. Bhoo, S. J. Davis, J. Walker, B. Karniol, and R. D. Vierstra, *Bacteriophytochromes are photochromic histidine kinases using a biliverdin chromophore*, Nature **414**, 776–779 (2001).
- [16] S. H. Bhoo, T. Hirano, H.-Y. Jeong, J.-G. Lee, M. Furuya, and P.-S. Song, *Phytochrome photochromism probed by site-directed mutations and chromophore esterification*, Journal of the American Chemical Society **119** (48), 11717–11718 (1997).
- [17] M. Bischoff, G. Hermann, S. Rentsch, and D. Strehlow, *First steps in the phytochrome phototransformation: A comparative femtosecond study on the forward ($Pr \rightarrow Pfr$) and back reaction ($Pfr \rightarrow Pr$)*, Biochemistry **40** (1), 181–186 (2001).
- [18] A. Blumenstein, K. Vienken, R. Tasler, J. Purschwitz, D. Veith, N. Frankenberg-Dinkel, and R. Fischer, *The Aspergillus nidulans phytochrome FphA represses sexual development in red light*, Curr. Biol. **15** (20), 1833–1838 (2005).
- [19] O. A. Borg and B. Durbeej, *Relative ground and excited-state pka values of phytochromobilin in the photoactivation of phytochrome: a computational study.*, J Phys Chem B **111** (39), 11554–11565 (2007).
- [20] J. L. Borges, *Ficciones*, Editorial Sur (1944).
- [21] H. A. Borthwick, S. B. Hendricks, and M. W. Parker, *The reaction controlling floral initiation*, Proc. Natl. Acad. Sci. USA **38** (11), 929–934 (1952).
- [22] B. Borucki, *Proton transfer in the photoreceptors phytochrome and photoactive yellow protein*, Photochem. Photobiol. Sci. **5** (6), 553–566 (2006).
- [23] B. Borucki, D. von Stetten, S. Seibeck, T. Lamparter, N. Michael, M. A. Mroginski, H. Otto, D. H. Murgida, M. P. Heyn, and P. Hildebrandt, *Light-induced proton release of phytochrome is coupled to the transient deprotonation of the tetrapyrrole chromophore*, J. Biol. Chem. **280** (40), 34358–34364 (2005).

- [24] T. Brandlmeier, H. Scheer, and W. Rüdiger, *Chromophore content and molar absorptivity of phytochrome in the Pr form*, *Z. Naturforsch. C* **36** (5-6), 431–439 (1981).
- [25] S. Brandt, D. von Stetten, M. Günther, P. Hildebrandt, and N. Frankenberg-Dinkel, *The fungal phytochrome fpha from aspergillus nidulans.*, *J Biol Chem* **283** (50), 34605–34614 (2008).
- [26] S. Braslavsky, W. Gärtner, and K. Schaffner, *Phytochrome photoconversion*, *Plant Cell Environ.* **20** (6), 700–706 (1997).
- [27] W. R. Briggs and J. L. Spudich, *Handbook of Photosensory Receptors*, Wiley, Weinheim (Germany) (2005).
- [28] H. Brock, B. P. Ruzsicska, T. Arai, W. Schlamann, A. R. Holzwarth, S. E. Braslavsky, and K. Schaffner, *Fluorescence lifetimes and relative quantum yields of 124-kilodalton oat phytochrome in water and deuterium oxide solutions*, *Biochemistry* **26** (5), 1412–1417 (1987).
- [29] Bruker Optik GmbH, *RFS/100 User Manual*, Ettlingen (Germany) (2004).
- [30] Bruker Optik GmbH, *Tutorial BioATR/II Handling*, Bruker Optik GmbH, Ettlingen (Germany) (2008).
- [31] Bruker Optik GmbH, *Ramanscope III User Manual*, Ettlingen (Germany) (2009).
- [32] E. S. Burgie, A. N. Bussell, J. M. Walker, K. Dubiel, and R. D. Vierstra, *Crystal structure of the photosensing module from a red/far-red light-absorbing plant phytochrome.*, *Proc Natl Acad Sci U S A* **111** (28), 10179–10184 (2014).
- [33] E. S. Burgie, T. Wang, A. N. Bussell, J. M. Walker, H. Li, and R. D. Vierstra, *Crystallographic and electron microscopic analyses of a bacterial phytochrome reveal local and global rearrangements during photoconversion.*, *J Biol Chem* (2014).
- [34] W. L. Butler, K. H. Norris, H. W. Siegelman, and S. B. Hendricks, *Detection, assay, and preliminary purification of the pigment controlling photoresponsive development of plants*, *Proc. Natl. Acad. Sci. USA* **45** (12), 1703–1708 (1959).
- [35] G. A. Caignan, R. Deshmukh, A. Wilks, Y. Zeng, H. wei Huang, P. Moënne-Loccoz, R. A. Bunce, M. A. Eastman, and M. Rivera, *Oxidation of heme to beta- and delta-biliverdin by pseudomonas aeruginosa heme oxygenase as a consequence of an unusual seating of the heme.*, *J Am Chem Soc* **124** (50), 14879–14892 (2002).

- [36] P. Carpentier, A. Royant, M. Weik, and D. Bourgeois, *Raman-assisted crystallography suggests a mechanism of x-ray-induced disulfide radical formation and reparation.*, *Structure* **18** (11), 1410–1419 (2010).
- [37] J. J. Casal, L. G. Luccioni, K. A. Oliverio, and H. E. Boccalandro, *Light, phytochrome signalling and photomorphogenesis in Arabidopsis*, *Photochem. Photobiol. Sci.* **2**, 625–636 (2003).
- [38] E. Chen, V. N. Lapko, P. S. Song, and D. S. Kliger, *Dynamics of the n-terminal alpha-helix unfolding in the photoreversion reaction of phytochrome a.*, *Biochemistry* **36** (16), 4903–4908 (1997).
- [39] G. Cornilescu, A. T. Ulijasz, C. C. Cornilescu, J. L. Markley, and R. D. Vierstra, *Solution structure of a cyanobacterial phytochrome GAF domain in the red-light-absorbing ground state*, *J. of Mol. Biol.* **383** (2), 403–413 (2008).
- [40] D. R. Cross, H. Linschitz, V. Kasche, and J. Tenenbaum, *Low-temperature studies on phytochrome: light and dark reactions in the red to far-red transformation and new intermediate forms of phytochrome.*, *Proc Natl Acad Sci U S A* **61** (3), 1095–1101 (1968).
- [41] R. S. Czernuszewicz and T. G. Spiro, *Inorganic Electronic Structure and Spectroscopy, Vol. I: Methodology*, Wiley, chap. IR, Raman, and Resonance Raman Spectroscopy, 353–442 (1999).
- [42] J. Dasgupta, R. R. Frontiera, K. C. Taylor, J. C. Lagarias, and R. A. Mathies, *Ultrafast excited-state isomerization in phytochrome revealed by femtosecond stimulated Raman spectroscopy*, *Proc. Natl. Acad. Sci. USA* **106** (6), 1784–1789 (2009).
- [43] S. J. Davis, A. V. Vener, and R. D. Vierstra, *Bacteriophytochromes: Phytochrome-like photoreceptors from nonphotosynthetic eubacteria*, *Science* **286** (5449), 2517–2520 (1999).
- [44] S. Döpner, P. Hildebrandt, A. G. Mauk, H. Lenk, and W. Stempfle, *Analysis of vibrational spectra of multicomponent systems. Application to pH-dependent resonance Raman spectra of ferricytochrome c*, *SPECTROCHIMICA ACTA PART A-MOLECULAR AND BIOMOLECULAR SPECTROSCOPY* **52** (5), 573–584 (1996).
- [45] D. Duanmu, C. Bachy, S. Sudek, C.-H. Wong, V. Jiménez, N. C. Rockwell, S. S. Martin, C. Y. Ngan, E. N. Reistetter, M. J. van Baren, D. C. Price, C.-L. Wei, A. Reyes-Prieto, J. C. Lagarias, and A. Z. Worden, *Marine algae and land plants share conserved phytochrome signaling systems.*, *Proc Natl Acad Sci U S A* (2014).

-
- [46] P. Eilfeld and W. Rüdiger, *Absorption spectra of phytochrome intermediates*, *Z. Naturforsch.* **40c**, 109–114 (1985).
- [47] P. H. Eilfeld, J. Vogel, R. Maurer, and P. G. Eilfeld, *Laser-flash photolysis of 124 kDa oat phytochrome: Studies concerning the late steps of Pfr formation*, *J. Photochem. Photobiol. B* **3** (2), 209–222 (1989).
- [48] G. Enomoto, Y. Hirose, R. Narikawa, and M. Ikeuchi, *Thiol-based photocycle of the blue and teal light-sensing cyanobacteriochrome tlr1999*, *Biochemistry* **51** (14), 3050–3058 (2012).
- [49] L.-O. Essen, J. Mailliet, and J. Hughes, *The structure of a complete phytochrome sensory module in the Pr ground state*, *Proc. Natl. Acad. of Sci. USA* **105** (38), 14709–14714 (2008).
- [50] H. Falk, *The Chemistry of Linear Oligopyrroles and Bile Pigments*, Springer-Verlag, Wien (1989).
- [51] D. L. Farrens, R. E. Holt, B. N. Rospendowski, P. S. Song, and T. M. Cotton, *Surface-enhanced resonance Raman scattering (SERRS) spectroscopy applied to phytochrome and its model compounds. 2. phytochrome and phycocyanin chromophores*, *J. Amer. Chem. Soc.* **111** (26), 9162–9169 (1989).
- [52] G. S. Filonov, K. D. Piatkevich, L.-M. Ting, J. Zhang, K. Kim, and V. V. Verkhusha, *Bright and stable near-infrared fluorescent protein for in vivo imaging*, *Nat Biotech* **29** (8), 757–761 (2011).
- [53] S. P. Fodor, J. C. Lagarias, and R. A. Mathies, *Resonance Raman spectra of the Pr-form of phytochrome*, *Photochem. Photobiol.* **48** (2), 129–136 (1988).
- [54] S. P. Fodor, J. C. Lagarias, and R. A. Mathies, *Resonance Raman analysis of the Pr and Pfr forms of phytochrome*, *Biochemistry* **29** (50), 11141–11146 (1990).
- [55] H. Foerstendorf, C. Benda, W. Gärtner, M. Storf, H. Scheer, and F. Siebert, *FTIR studies of phytochrome photoreactions reveal the C=O bands of the chromophore: Consequences for its protonation states, conformation, and protein interaction*, *Biochemistry* **40** (49), 14952–14959 (2001).
- [56] H. Foerstendorf, T. Lamparter, J. Hughes, W. Gärtner, and F. Siebert, *The photoreactions of recombinant phytochrome from the cyanobacterium Synechocystis: A low-temperature UV-vis and FT-IR spectroscopic study*, *Photochem. Photobiol.* **71** (5), 655–661 (2000).
- [57] H. Foerstendorf, E. Mummert, E. Schäfer, H. Scheer, and F. Siebert, *Fourier-transform infrared spectroscopy of phytochrome: Difference spectra of the intermediates of the photoreactions*, *Biochemistry* **35** (33), 10793–10799 (1996).

- [58] N. Frankenberg and J. C. Lagarias, *Phycocyanobilin:ferredoxin oxidoreductase of Anabaena sp. PCC 7120. biochemical and spectroscopic*, J. Biol. Chem. **278** (11), 9219–9226 (2003).
- [59] N. Frankenberg, K. Mukougawa, T. Kohchi, and J. C. Lagarias, *Functional genomic analysis of the HY2 family of ferredoxin-dependent bilin reductases from oxygenic photosynthetic organisms*, Plant Cell **13** (4), 965–978 (2001).
- [60] B. Franklin, *Phytochrome*, Academic Press, New York (1972), 195–225 .
- [61] L. H. Freer, P. W. Kim, S. C. Corley, N. C. Rockwell, L. Zhao, A. J. Thibert, J. C. Lagarias, and D. S. Larsen, *Chemical inhomogeneity in the ultrafast dynamics of the dxcf cyanobacteriochrome tlr0924.*, J Phys Chem B **116** (35), 10571–10581 (2012).
- [62] A. C. Froehlich, B. Noh, R. D. Vierstra, J. Loros, and J. C. Dunlap, *Genetic and molecular analysis of phytochromes from the filamentous fungus Neurospora crassa*, Eukaryot. Cell **4** (12), 2140–2152 (2005).
- [63] Y. Fukushima, M. Iwaki, R. Narikawa, M. Ikeuchi, Y. Tomita, and S. Itoh, *Photoconversion mechanism of a green/red photosensory cyanobacteriochrome anp1xj: time-resolved optical spectroscopy and ftir analysis of the anp1xj-gaf2 domain.*, Biochemistry **50** (29), 6328–6339 (2011).
- [64] M. Furuya, N. Ito, K. Tomizawa, and E. Schäfer, *A stable phytochrome pool regulates the expression of the phytochrome i gene in pea seedlings.*, Planta **183** (2), 218–221 (1991).
- [65] G. A. Gambetta and J. C. Lagarias, *Genetic engineering of phytochrome biosynthesis in bacteria*, Proc. Natl. Acad. Sci. USA **98** (19), 10566–10571 (2001).
- [66] T. Gensch, M. S. Churio, S. E. Braslavsky, and K. Schaffner, *Primary quantum yield and volume change of phytochrome-A phototransformation determined by laser-induced optoacoustic spectroscopy*, Photochem. Photobiol. **63** (6), 719–725 (1996).
- [67] E. Giraud, J. Fardoux, N. Fourrier, L. Hannibal, B. Genty, P. Bouyer, B. Dreyfus, and A. Verméglio, *Bacteriophytochrome controls photosystem synthesis in anoxygenic bacteria*, Nature **417**, 202–205 (2002).
- [68] E. Giraud, J. Lavergne, and A. Verméglio, *Characterization of bacteriophytochromes from photosynthetic bacteria: histidine kinase signaling triggered by light and redox sensing.*, Methods Enzymol **471**, 135–159 (2010).
- [69] E. Giraud and A. Verméglio, *Bacteriophytochromes in anoxygenic photosynthetic bacteria.*, Photosynth Res **97** (2), 141–153 (2008).

- [70] E. Giraud, S. Zappa, L. Vuillet, J.-M. Adriano, L. Hannibal, J. Fardoux, C. Berthomieu, P. Bouyer, D. Pignol, and A. Vermeglio, *A new type of bacterio-phytochrome acts in tandem with a classical bacteriophytochrome to control the antennae synthesis in Rhodospseudomonas palustris*, *J. Biol. Chem.* **280** (37), 32389–32397 (2005).
- [71] E. Goormaghtigh, V. Raussens, and J. M. Ruyschaert, *Attenuated total reflection infrared spectroscopy of proteins and lipids in biological membranes.*, *Biochim Biophys Acta* **1422** (2), 105–185 (1999).
- [72] J. Grochol, *Raman Spectroelectrochemical Investigations of Immobilized Redox Proteins*, Ph.D. thesis, Technische Universität Berlin (2007).
- [73] M. Günther, *Resonanz-Raman-spektroskopische Analyse der Chromophorstruktur in pflanzlichen und bakteriellen Phytochromen*, Master's thesis, Technische Universität Berlin (2008).
- [74] J. Hahn, H. M. Strauss, F. T. Landgraf, H. F. Gimenez, G. Lochnit, P. Schmieder, and J. Hughes, *Probing protein–chromophore interactions in Cph1 phytochrome by mutagenesis*, *FEBS J.* **273** (7), 1415–1429 (2006).
- [75] A. L. Hansen and L. E. Kay, *Measurement of histidine pka values and tautomer populations in invisible protein states.*, *Proc Natl Acad Sci U S A* **111** (17), E1705–E1712 (2014).
- [76] A. F. E. Hauck, S. J. O. Hardman, R. J. Kutta, G. M. Greetham, D. J. Heyes, and N. S. Scrutton, *The photoinitiated reaction pathway of full-length cyanobacteriochrome tlr0924 monitored over 12 orders of magnitude.*, *J Biol Chem* **289** (25), 17747–17757 (2014).
- [77] G. Herzberg, *Molecular Spectra and Molecular Structure: II, Infrared and Raman Spectra of Polyatomic Molecules*, Van Nostrand Reinhold, New York (1945).
- [78] K. Heyne, J. Herbst, D. Stehlik, B. Esteban, T. Lamparter, J. Hughes, and R. Diller, *Ultrafast dynamics of phytochrome from the cyanobacterium Synechocystis, reconstituted with phycocyanobilin and phycoerythrobilin*, *Biophys. J.* **82** (2), 1004–1016 (2002).
- [79] P. Hildebrandt, A. Hoffmann, P. Lindemann, G. Heibel, S. Braslavsky, K. Schaffner, and B. Schrader, *Fourier-transform resonance Raman spectroscopy of phytochrome*, *Biochemistry* **31** (34), 7957–7962 (1992).
- [80] P. Hildebrandt, C. Kneip, J. Matysik, K. Nemeth, I. Magdo, F. Mark, and K. Schaffner, *Vibrational analysis of linear tetrapyrroles. Implications for interpreting the resonance Raman spectra of phytochrome*, *Rec. Res. Dev. Phys. Chem.* **3**, 63–77 (1999).

- [81] Y. Hirose, T. Shimada, R. Narikawa, M. Katayama, and M. Ikeuchi, *Cyanobacteriochrome CcaS is the green light receptor that induces the expression of phycobilisome linker protein*, Proc. Natl. Acad. Sci. USA **105** (28), 9528–9533 (2008).
- [82] Y. S. Ho, L. M. Burden, and J. H. Hurley, *Structure of the gaf domain, a ubiquitous signaling motif and a new class of cyclic gmp receptor*, EMBO J **19** (20), 5288–5299 (2000).
- [83] R. E. Holt, D. L. Farrens, P. S. Song, and T. M. Cotton, *Surface-enhanced resonance Raman scattering (SERRS) spectroscopy applied to phytochrome and its model compounds. i. biliverdin photoisomers*, J. Amer. Chem. Soc. **111** (26), 9156–9162 (1989).
- [84] T. Hübschmann, T. Börner, E. Hartmann, and T. Lamparter, *Characterization of the Cph1 holo-phytochrome from Synechocystis sp. PCC 6803*, Eur. J. Biochem. **268** (7), 2055–2063 (2001).
- [85] T. Hübschmann, H. Jorissen, T. Börner, W. Gärtner, and N. Tandeau de Marsac, *Phosphorylation of proteins in the light dependent signalling pathway of a filamentous cyanobacterium*, Eur. J. Biochem. **268**, 3383–3389 (2001).
- [86] J. Hughes and T. Lamparter, *Prokaryotes and phytochrome. The connection to chromophores and signaling*, Plant Physiol. **121** (4), 1059–1068 (1999).
- [87] J. Hughes, T. Lamparter, F. Mittmann, E. Hartmann, W. Gärtner, A. Wilde, and T. Börner, *A prokaryotic phytochrome*, Nature **386**, 663 (1997).
- [88] W. Humphrey, A. Dalke, and K. Schulten, *Vmd: visual molecular dynamics.*, J Mol Graph **14** (1), 33–8, 27–8 (1996).
- [89] M. Ikeuchi and T. Ishizuka, *Cyanobacteriochromes: a new superfamily of tetrapyrrole-binding photoreceptors in cyanobacteria*, Photochem. Photobiol. Sci. **7**, 1159–1167 (2008).
- [90] T. Ishizuka, A. Kamiya, H. Suzuki, R. Narikawa, T. Noguchi, T. Kohchi, K. Inomata, and M. Ikeuchi, *The Cyanobacteriochrome, TePixJ, Isomerizes Its Own Chromophore by Converting Phycocyanobilin to Phycoviolobilin*, Biochemistry **50** (6), 953–961 (2011).
- [91] T. Ishizuka, R. Narikawa, T. Kohchi, M. Katayama, and M. Ikeuchi, *Cyanobacteriochrome TePixJ of Thermosynechococcus elongatus harbors phycoviolobilin as a chromophore*, Plant Cell Physiol. **48** (9), 1385–1390 (2007).
- [92] H. J. M. M. Jorissen, B. Quest, A. Remberg, T. Coursin, S. E. Braslavsky, K. Schaffner, N. Tandeau de Marsac, and W. Gärtner, *Two independent, light-sensing two-component systems in a filamentous cyanobacterium*, Eur. J. Biochem. **269** (11), 2662–2671 (2002).

- [93] T. Kaneko, S. Sato, H. Kotani, A. Tanaka, E. Asamizu, Y. Nakamura, N. Miyajima, M. Hirosawa, M. Sugiura, S. Sasamoto, T. Kimura, T. Hosouchi, A. Matsuno, A. Muraki, N. Nakazaki, K. Naruo, S. Okumura, S. Shimpo, C. Takeuchi, T. Wada, A. Watanabe, M. Yamada, M. Yasuda, and S. Tabata, *Sequence analysis of the genome of the unicellular cyanobacterium synechocystis sp. strain pcc6803. ii. sequence determination of the entire genome and assignment of potential protein-coding regions (supplement).*, DNA Res **3** (3), 185–209 (1996).
- [94] B. Karniol and R. D. Vierstra, *The pair of bacteriophytochromes from Agrobacterium tumefaciens are histidine kinases with opposing photobiological properties*, Proc. Natl. Acad. Sci. USA **100** (5), 2807–2812 (2003).
- [95] B. Karniol, J. R. Wagner, J. M. Walker, and R. D. Vierstra, *Phylogenetic analysis of the phytochrome superfamily reveals distinct microbial subfamilies of photoreceptors*, Biochem. J. **392**, 103–116 (2005).
- [96] P. W. Kim, L. H. Freer, N. C. Rockwell, S. S. Martin, J. C. Lagarias, and D. S. Larsen, *Femtosecond Photodynamics of the Red/Green Cyanobacteriochrome NpR6012g4 from Nostoc punctiforme. 1. Forward Dynamics*, Biochemistry **51** (2), 608–618 (2012).
- [97] P. W. Kim, L. H. Freer, N. C. Rockwell, S. S. Martin, J. C. Lagarias, and D. S. Larsen, *Femtosecond Photodynamics of the Red/Green Cyanobacteriochrome NpR6012g4 from Nostoc punctiforme. 2. Reverse Dynamics*, Biochemistry **51** (2), 619–630 (2012).
- [98] P. W. Kim, N. C. Rockwell, S. S. Martin, J. C. Lagarias, and D. S. Larsen, *Dynamic inhomogeneity in the photodynamics of cyanobacterial phytochrome cph1.*, Biochemistry **53** (17), 2818–2826 (2014).
- [99] P. W. Kim, N. C. Rockwell, S. S. Martin, J. C. Lagarias, and D. S. Larsen, *Dynamic inhomogeneity in the photodynamics of cyanobacterial phytochrome cph1.*, Biochemistry **53** (17), 2818–2826 (2014).
- [100] P. W. Kim, N. C. Rockwell, S. S. Martin, J. C. Lagarias, and D. S. Larsen, *Heterogeneous photodynamics of the pfr state in the cyanobacterial phytochrome cph1.*, Biochemistry **53** (28), 4601–4611 (2014).
- [101] S. Klinke, L. H. Otero, J. Rinaldi, S. Sosa, B. G. G. aes, W. E. Shepard, F. A. Goldbaum, and H. R. Bonomi, *Crystallization and preliminary x-ray characterization of the full-length bacteriophytochrome from the plant pathogen xanthomonas campestris pv. campestris.*, Acta Crystallogr F Struct Biol Commun **70** (Pt 12), 1636–1639 (2014).
- [102] C. Kneip, *FT-NIR-Resonanz-Raman-spektroskopische Untersuchungen an Phytochrom und Tetrapyrrolpigmenten aus Cyanobakterien*, Ph.D. thesis, Gesamthochschule Duisburg (1998).

- [103] C. Kneip, P. Hildebrandt, W. Schlamann, S. Braslavsky, F. Mark, and K. Schaffner, *Protonation state and structural changes of the tetrapyrrole chromophore during the Pr → Pfr phototransformation of phytochrome: A resonance Raman spectroscopic study*, *Biochemistry* **38** (46), 15185–15192 (1999).
- [104] C. Kneip, A. Parbel, H. Foerstendorf, H. Scheer, F. Siebert, and P. Hildebrandt, *Fourier transform near-infrared resonance Raman spectroscopic study of the alpha-subunit of phycoerythrocyanin and phycocyanin from the cyanobacterium Mastigocladus laminosus*, *J. Raman Spectrosc.* **29** (10-11), 939–944 (1998).
- [105] T. Kohchi, K. Mukougawa, N. Frankenberger, M. Masuda, A. Yokota, and J. C. Lagarias, *The Arabidopsis HY2 gene encodes phytochromobilin synthase, a ferredoxin-dependent biliverdin reductase*, *Plant Cell* **13** (2), 425–436 (2001).
- [106] A. Krężel and W. Bal, *A formula for correlating pka values determined in d₂O and h₂O*, *Journal of Inorganic Biochemistry* **98** (1), 161 – 166 (2004).
- [107] J. C. Lagarias, J. M. Kelly, K. L. Cyr, and W. O. Smith, *Comparative photochemical analysis of highly purified 124 kilodalton oat and rye phytochromes in vitro*, *Photochemistry and Photobiology* **46** (1), 5–13 (1987).
- [108] T. Lamparter, *Evolution of cyanobacterial and plant phytochromes*, *FEBS Lett.* **573** (1-3), 1–5 (2004).
- [109] T. Lamparter, M. Carrascal, N. Michael, E. Martinez, G. Rottwinkel, and J. Abian, *The biliverdin chromophore binds covalently to a conserved cysteine residue in the N-terminus of Agrobacterium phytochrome Agp1*, *Biochemistry* **43** (12), 3659–3669 (2004).
- [110] T. Lamparter, B. Esteban, and J. Hughes, *Phytochrome CphI from the cyanobacterium Synechocystis PCC6803. Purification, assembly, and quaternary structure*, *Eur. J. Biochem.* **268** (17), 4720–4730 (2001).
- [111] T. Lamparter and N. Michael, *Agrobacterium phytochrome as an enzyme for the production of ZZE bilins*, *Biochemistry* **44** (23), 8461–8469 (2005).
- [112] T. Lamparter, N. Michael, F. Mittmann, and B. Esteban, *Phytochrome from Agrobacterium tumefaciens has unusual spectral properties and reveals an N-terminal chromophore attachment site*, *Proc. Natl. Acad. Sci. USA* **99** (18), 11628–11633 (2002).
- [113] D. A. Long, *The Raman Effect: A Unified Treatment of the Theory of Raman Scattering by Molecules*, Wiley (2002).
- [114] H. K. Ly, *Application of Surface Enhanced Raman Spectroscopy to Biological Systems*, Ph.D. thesis, Technische Universität Berlin (2013).

- [115] J. Mailliet, G. Psakis, K. Feilke, V. Sineshchekov, L.-O. Essen, and J. Hughes, *Spectroscopy and a high-resolution crystal structure of tyr263 mutants of cyanobacterial phytochrome cph1.*, *J Mol Biol* **413** (1), 115–127 (2011).
- [116] Y. Makhynya, Z. Hussain, T. Bauschlicher, P. Schwinte, F. Siebert, and W. Gärtner, *Synthesis of selectively ¹³C-labelled bilin compounds*, *Eur. J. Organic Chem.* **8**, 1287–1293 (2007).
- [117] A. Mancinelli, *Comparison of spectral properties of phytochromes from different preparations*, *Plant Physiol.* **82**, 956–961 (1986).
- [118] J. Matysik, *FT-NIR-Raman-spektroskopische Untersuchung an Phytochrom*, Ph.D. thesis, Universität Gesamthochschule Essen (1995).
- [119] J. Matysik, P. Hildebrandt, W. Schlamann, S. Braslavsky, and K. Schaffner, *Fourier-transform resonance Raman spectroscopy of intermediates of the phytochrome photocycle*, *Biochemistry* **34** (33), 10497–10507 (1995).
- [120] T. Meyer, G. Kieseritzky, and E.-W. Knapp, *Electrostatic pKa computations in proteins: role of internal cavities.*, *Proteins* **79** (12), 3320–3332 (2011).
- [121] B. L. Montgomery and J. C. Lagarias, *Phytochrome ancestry: Sensors of bilins and light*, *Trends Plant Sci.* **7** (8), 357–366 (2002).
- [122] M. Mroginiski, D. Murgida, D. von Stetten, C. Kneip, F. Mark, and P. Hildebrandt, *Determination of the chromophore structures in the photoinduced reaction cycle of phytochrome*, *J. Amer. Chem. Soc.* **126** (51), 16734–16735 (2004).
- [123] M. Mroginiski, K. Nemeth, T. Bauschlicher, W. Klotzbucher, R. Goddard, O. Heinemann, P. Hildebrandt, and F. Mark, *Calculation of vibrational spectra of linear tetrapyrroles. 3. Hydrogen-bonded hexamethylpyrromethene dimers*, *J. Phys. Chem. A* **109** (10), 2139–2150 (2005).
- [124] M. Mroginiski, K. Nemeth, I. Magdo, M. Muller, U. Robben, C. Della Vedova, P. Hildebrandt, and F. Mark, *Calculation of the vibrational spectra of linear tetrapyrroles. 2. Resonance Raman spectra of hexamethylpyrromethene monomers*, *J. Phys. Chem. B* **104** (46), 10885–10899 (2000).
- [125] M. Mroginiski, D. von Stetten, S. Kaminski, F. V. Escobar, N. Michael, G. Daminelli-Widany, and P. Hildebrandt, *Elucidating photoinduced structural changes in phytochromes by the combined application of resonance Raman spectroscopy and theoretical methods*, *Journal of Molecular Structure* **993**, 15–25 (2011).
- [126] M. A. Mroginiski, S. Kaminski, and P. Hildebrandt, *Raman spectra of the phycoviolobilin cofactor in phycoerythrocyanin calculated by qm/mm methods.*, *Chemphyschem* **11** (6), 1265–1274 (2010).

- [127] M. A. Mroginiski, S. Kaminski, D. von Stetten, S. Ringsdorf, W. Gärtner, L.-O. Essen, and P. Hildebrandt, *Structure of the chromophore binding pocket in the pr state of plant phytochrome phyA.*, J Phys Chem B **115** (5), 1220–1231 (2011).
- [128] M. A. Mroginiski, D. H. Murgida, and P. Hildebrandt, *Calculation of vibrational spectra of linear tetrapyrroles. 4. Methine bridge C–H out-of-plane modes*, J. Phys. Chem. A **110**, 10564–10574 (2006).
- [129] M. A. Mroginiski, D. H. Murgida, and P. Hildebrandt, *The chromophore structural changes during the photocycle of phytochrome: a combined resonance Raman and quantum chemical approach*, Acc. Chem. Res. **40** (4), 258–266 (2007).
- [130] M. A. Mroginiski, D. von Stetten, F. Velazquez Escobar, H. M. Strauss, S. Kaminski, P. Scheerer, M. Günther, D. H. Murgida, P. Schmieder, C. Bongards, W. Gärtner, J. Mailliet, J. Hughes, L.-O. Essen, and P. Hildebrandt, *Chromophore structure of cyanobacterial phytochrome CphI in the Pr state: Reconciling structural and spectroscopic data by QM/MM calculations*, Biophys. J. **96**, 4153–4163 (2009).
- [131] M. G. Müller, I. Lindner, I. Martin, W. Gärtner, and A. R. Holzwarth, *Femtosecond kinetics of photoconversion of the higher plant photoreceptor phytochrome carrying native and modified chromophores*, Biophysical Journal **94** (11), 4370 – 4382 (2008).
- [132] R. Narikawa, Y. Fukushima, T. Ishizuka, S. Itoh, and M. Ikeuchi, *A Novel Photoactive GAF Domain of Cyanobacteriochrome AnPixJ That Shows Reversible Green/Red Photoconversion*, Journal of Molecular Biology **380** (5), 844 – 855 (2008).
- [133] R. Narikawa, T. Ishizuka, N. Muraki, T. Shiba, G. Kurisu, and M. Ikeuchi, *Structures of cyanobacteriochromes from phototaxis regulators anpixj and tepixj reveal general and specific photoconversion mechanism*, Proceedings of the National Academy of Sciences **110** (3), 918–923 (2013).
- [134] R. Narikawa, T. Kohchi, and M. Ikeuchi, *Characterization of the photoactive GAF domain of the CikA homolog (SyCikA, Slr1969) of the cyanobacterium Synechocystis sp. PCC 6803*, Photochem. Photobiol. Sci. **7** (10), 1253–1259 (2008).
- [135] H. Naumann, *The NpSRII photocycle and its dependence on the electric field – a combined quantum chemical and Raman spectroscopic study*, Ph.D. thesis, Technische Universität Berlin (2009).
- [136] J. B. Nieder, M. Brecht, and R. Bittl, *Dynamic intracomplex heterogeneity of phytochrome*, J. Amer. Chem. Soc. **131** (1), 69–71 (2009).

- [137] S. Noack and T. Lamparter, *Light Modulation of Histidine-Kinase Activity in Bacterial Phytochromes Monitored by Size Exclusion Chromatography, Crosslinking, and Limited Proteolysis*, *Methods in Enzymology*, vol. 423, Academic Press (2007), 203 - 221 .
- [138] S. Noack, N. Michael, R. Rosen, and T. Lamparter, *Protein conformational changes of Agrobacterium phytochrome Agp1 during chromophore assembly and photoconversion*, *Biochemistry* **46** (13), 4164–4176 (2007).
- [139] I. Oberpichler, I. Molina, O. Neubauer, and T. Lamparter, *Phytochromes from Agrobacterium tumefaciens: Difference spectroscopy with extracts of wild type and knockout mutants*, *FEBS Lett.* **580** (2), 437–442 (2006).
- [140] P. Piwowarski, E. Ritter, K.-P. Hofmann, P. Hildebrandt, D. von Stetten, P. Scheerer, N. Michael, T. Lamparter, and F. Bartl, *Light-induced activation of bacterial phytochrome agp1 monitored by static and time-resolved ftr spectroscopy.*, *Chemphyschem* **11** (6), 1207–1214 (2010).
- [141] P. L. Polavarapu, *Ab initio vibrational Raman and Raman optical activity spectra*, *J. Phys. Chem.* **94** (21), 8106–8112 (1990).
- [142] P. Quail, *Phytochrome photosensory signalling networks*, *Nature Rev. Molec. Cell Biol.* **3** (2), 85–93 (2002).
- [143] B. Quest, T. Hübschmann, S. Sharda, N. Tandeau de Marsac, and W. Gärtner, *Homologous expression of a bacterial phytochrome. the cyanobacterium Fremyella diplosiphon incorporates biliverdin as a genuine, functional chromophore*, *FEBS J.* **274** (8), 2088–2098 (2007).
- [144] C. Raman and K. Krishnan, *A new type of secondary radiation*, *Nature* **121**, 501–502 (1928).
- [145] A. Remberg, I. Lindner, T. Lamparter, J. Hughes, C. Kneip, P. Hildebrandt, S. Braslavsky, W. Gärtner, and K. Schaffner, *Raman spectroscopic and light-induced kinetic characterization of a recombinant phytochrome of the cyanobacterium Synechocystis*, *Biochemistry* **36** (43), 13389–13395 (1997).
- [146] A. Remberg, A. Ruddat, S. E. Braslavsky, W. Gärtner, and K. Schaffner, *Chromophore incorporation, Pr to Pfr kinetics, and Pfr thermal reversion of recombinant N-terminal fragments of phytochrome A and B chromoproteins*, *Biochemistry* **37** (28), 9983–9990 (1998).
- [147] M. Rivera and G. Caignan, *Recent developments in the ¹³C NMR spectroscopic analysis of paramagnetic hemes and heme proteins*, *Anal. Bioanal. Chem.* **378** (6), 1464–1483 (2004).
- [148] N. C. Rockwell and J. C. Lagarias, *The structure of phytochrome: A picture is worth a thousand spectra*, *Plant Cell* **18** (1), 4–14 (2006).

- [149] N. C. Rockwell and J. C. Lagarias, *A brief history of phytochromes*, *ChemPhysChem* **11** (6), 1172–1180 (2010).
- [150] N. C. Rockwell, S. S. Martin, K. Feoktistova, and J. C. Lagarias, *Diverse two-cysteine photocycles in phytochromes and cyanobacteriochromes*, *Proceedings of the National Academy of Sciences* **108** (29), 11854–11859 (2011).
- [151] N. C. Rockwell, S. S. Martin, and J. C. Lagarias, *Mechanistic insight into the photosensory versatility of dxcf cyanobacteriochromes.*, *Biochemistry* **51** (17), 3576–3585 (2012).
- [152] N. C. Rockwell, S. S. Martin, and J. C. Lagarias, *Red/green cyanobacteriochromes: sensors of color and power.*, *Biochemistry* **51** (48), 9667–9677 (2012).
- [153] N. C. Rockwell, S. L. Njuguna, L. Roberts, E. Castillo, V. L. Parson, S. Dwojak, J. C. Lagarias, and S. C. Spiller, *A second conserved GAF domain cysteine is required for the blue/green photoreversibility of cyanobacteriochrome Tlr0924 from Thermosynechococcus elongatus*, *Biochemistry* **47** (27), 7304–7316 (2008).
- [154] N. C. Rockwell, L. Shang, S. S. Martin, and J. C. Lagarias, *Distinct classes of red/far-red photochemistry within the phytochrome superfamily*, *Proc. Natl. Acad. Sci. USA* **106** (15), 6123–6127 (2009).
- [155] N. C. Rockwell, Y.-S. Su, and J. C. Lagarias, *Phytochrome structure and signaling mechanisms*, *Annu. Rev. Plant Biol.* **57**, 837–858 (2006).
- [156] T. Rohmer, C. Lang, C. Bongards, K. B. S. S. Gupta, J. Neugebauer, J. Hughes, W. Gärtner, and J. Matysik, *Phytochrome as Molecular Machine: Revealing Chromophore Action during the Pfr → Pr Photoconversion by Magic-Angle Spinning NMR Spectroscopy*, *Journal of the American Chemical Society* **132** (12), 4431–4437 (2010).
- [157] T. Rohmer, H. Strauss, J. Hughes, H. de Groot, W. Gärtner, P. Schmieder, and J. Matysik, *¹⁵N MAS NMR studies of Cph1 phytochrome: Chromophore dynamics and intramolecular signal transduction*, *J. Phys. Chem. B* **110** (41), 20580–20585 (2006).
- [158] W. Rüdiger and F. Thümmel, *Low temperature spectroscopy of phytochrome: Pr, Pfr and intermediates*, *Physiol. Plant.* **60**, 383–388 (1984).
- [159] J. Salewski, F. V. Escobar, S. Kaminski, D. von Stetten, A. Keidel, Y. Ripers, N. Michael, P. Scheerer, P. Piwowarski, F. Bartl, N. Frankenberg-Dinkel, S. Ringsdorf, W. Gärtner, T. Lamparter, M. A. Mroginski, and P. Hildebrandt, *Structure of the biliverdin cofactor in the pfr state of bathy and prototypical phytochromes*, *Journal of Biological Chemistry* **288** (23), 16800–16814 (2013).

- [160] E. Schäfer and F. Nagy, *Photomorphogenesis in Plants and Bacteria: Function and Signal Transduction Mechanisms*, Springer-Verlag (Dordrecht) (2005).
- [161] P. Scheerer, N. Michael, J. H. Park, S. Nagano, H.-W. Choe, K. Inomata, B. Borucki, N. Krauß, and T. Lamparter, *Light-induced conformational changes of the chromophore and the protein in phytochromes: Bacterial phytochromes as model systems*, *ChemPhysChem* **11** (6), 1090–1105 (2010).
- [162] P. Scheerer, N. Michael, J. H. Park, S. Noack, C. Forster, M. A. S. Hammam, K. Inomata, H.-W. Choe, T. Lamparter, and N. Krauß, *Crystallization and preliminary X-ray crystallographic analysis of the N-terminal photosensory module of phytochrome Agp1, a biliverdin-binding photoreceptor from Agrobacterium tumefaciens*, *J. Struct. Biol.* **153** (1), 97–102 (2006).
- [163] B. Schrader and W. Meier, *DMS Raman/IR Atlas of Organic Compounds*, Verlag Chemie GmbH, Weinheim (1975), – .
- [164] C. Schumann, R. Gross, N. Michael, T. Lamparter, and R. Diller, *Sub-picosecond mid-infrared spectroscopy of phytochrome Agp1 from Agrobacterium tumefaciens*, *ChemPhysChem* **8**, 1657–1663 (2007).
- [165] P. Schwinté, W. Gärtner, S. Sharda, M.-A. Mroginski, P. Hildebrandt, and F. Siebert, *The photoreactions of recombinant phytochrome Cpha from the cyanobacterium Calothrix PCC7601: A low-temperature UV-Vis and FTIR study*, *Photochem. Photobiol.* **85** (1), 239–249 (2009).
- [166] L. Shang, N. C. Rockwell, S. S. Martin, and J. C. Lagarias, *Biliverdin Amides Reveal Roles for Propionate Side Chains in Bilin Reductase Recognition and in Holophytochrome Assembly and Photoconversion*, *Biochemistry* **49** (29), 6070–6082 (2010).
- [167] D. M. Shcherbakova and V. V. Verkhusha, *Near-infrared fluorescent proteins for multicolor in vivo imaging.*, *Nat Methods* **10** (8), 751–754 (2013).
- [168] T. Shinomura, K. Uchida, and M. Furuya, *Elementary processes of photoperception by phytochrome a for high-irradiance response of hypocotyl elongation in arabidopsis.*, *Plant Physiol* **122** (1), 147–156 (2000).
- [169] X. Shu, A. Royant, M. Z. Lin, T. A. Aguilera, V. Lev-Ram, P. A. Steinbach, and R. Y. Tsien, *Mammalian expression of infrared fluorescent proteins engineered from a bacterial phytochrome*, *Science* **324** (5928), 804–807 (2009).
- [170] E. Siebert, M. Horch, Y. Rippers, J. Fritsch, S. Frielingsdorf, O. Lenz, F. V. Escobar, F. Siebert, L. Paasche, U. Kuhlmann, F. Lenzian, M.-A. Mroginski, I. Zebger, and P. Hildebrandt, *Resonance raman spectroscopy as a tool to monitor the active site of hydrogenases.*, *Angew Chem Int Ed Engl* **52** (19), 5162–5165 (2013).

- [171] F. Siebert, R. Grimm, W. Rüdiger, G. Schmidt, and H. Scheer, *Infrared spectroscopy of phytochrome and model pigments.*, Eur J Biochem **194** (3), 921–928 (1990).
- [172] F. Siebert and P. Hildebrandt, *Vibrational Spectroscopy in Life Science*, Tutorials in Biophysics, Wiley VCH (Weinheim) (2007).
- [173] H. W. Siegelman and E. M. Firer, *Purification of phytochrome from oat seedlings*, Biochemistry **3**, 418–423 (1964).
- [174] H. W. Siegelman, B. C. Turner, and S. B. Hendricks, *The chromophore of phytochrome*, Plant Physiol. **41** (8), 1289–1292 (1966).
- [175] V. Sineschekov, L. Koppel, B. Esteban, J. Hughes, and T. Lamparter, *Fluorescence investigation of the recombinant cyanobacterial phytochrome CphI and its C-terminally truncated monomeric species (CphIDelta2): implication for holoprotein assembly, chromophore–apoprotein interaction and photochemistry*, J. Photochem. Photobiol. B **67** (1), 39–50 (2002).
- [176] B. V. Smith, S. Sutanthavibul, K. Yap, P. King, B. Boyter, and T. Sato, *Xfig 3.2.5*, <http://www.xfig.org/> (2007).
- [177] H. Smith, *Phytochromes and light signal perception by plants—an emerging*, Nature **407** (6804), 585–591 (2000).
- [178] C. Song, L.-O. Essen, W. Gärtner, J. Hughes, and J. Matysik, *Solid-state nmr spectroscopic study of chromophore-protein interactions in the pr ground state of plant phytochrome a.*, Mol Plant **5** (3), 698–715 (2012).
- [179] C. Song, G. Psakis, J. Kopycki, C. Lang, J. Matysik, and J. Hughes, *The d-ring, not the a-ring, rotates in synechococcus os-b' phytochrome.*, J Biol Chem **289** (5), 2552–2562 (2014).
- [180] C. Song, G. Psakis, C. Lang, J. Mailliet, W. Gärtner, J. Hughes, and J. Matysik, *Two ground state isoforms and a chromophore d-ring photoflip triggering extensive intramolecular changes in a canonical phytochrome*, Proceedings of the National Academy of Sciences **108** (10), 3842–3847 (2011).
- [181] K. Spillane, J. Dasgupta, and R. A. Mathies, *Conformational homogeneity and excited-state isomerization dynamics of the bilin chromophore in phytochrome cphI from resonance raman intensities*, Biophysical Journal **102** (3), 709 – 717 (2012).
- [182] K. M. Spillane, J. Dasgupta, J. C. Lagarias, and R. A. Mathies, *Homogeneity of Phytochrome CphI Vibronic Absorption Revealed by Resonance Raman Intensity Analysis*, Journal of the American Chemical Society **131** (39), 13946–13948 (2009). PMID: 19739629.

- [183] D. von Stetten, *Resonanz-Raman-spektroskopische Untersuchungen an Agrobacterium-Phytochrom*, Diplomarbeit, Technische Universität Berlin (2005).
- [184] D. von Stetten, *Investigation of the chromophore structure in plant and bacterial phytochromes by comparison of experimental and calculated Raman spectra*, Ph.D. thesis, Technische Universität Berlin (2008).
- [185] D. von Stetten, M. Günther, P. Scheerer, D. H. Murgida, M. A. Mroginski, N. Krauß, T. Lamparter, J. Zhang, D. M. Anstrom, R. D. Vierstra, K. T. Forest, and P. Hildebrandt, *Chromophore heterogeneity and photoconversion in phytochrome crystals and solutions studied by resonance Raman spectroscopy*, *Angew. Chem. Int. Ed.* **47**, 4753–4755 (2008).
- [186] D. von Stetten, S. Seibeck, N. Michael, P. Scheerer, M. A. Mroginski, D. H. Murgida, N. Krauß, M. P. Heyn, P. Hildebrandt, B. Borucki, and T. Lamparter, *Highly conserved residues Asp-197 and His-250 in Agp1 phytochrome control the proton affinity of the chromophore and Pfr formation*, *J. Biol. Chem.* **282** (3), 2116–2123 (2007).
- [187] E. A. Stojković, K. C. Toh, M. T. A. Alexandre, M. Baclayon, K. Moffat, and J. T. M. Kennis, *Ftir spectroscopy revealing light-dependent refolding of the conserved tongue region of bacteriophytochrome.*, *J Phys Chem Lett* **5** (15), 2512–2515 (2014).
- [188] C. K. Stover, X. Q. Pham, A. L. Erwin, S. D. Mizoguchi, P. Warrenner, M. J. Hickey, F. L. Brinkman, W. O. Hufnagle, D. J. Kowalik, M. Lagrou, R. L. Garber, L. Goltry, E. Tolentino, S. Westbrook-Wadman, Y. Yuan, L. L. Brody, S. N. Coulter, K. R. Folger, A. Kas, K. Larbig, R. Lim, K. Smith, D. Spencer, G. K.-S. Wong, Z. Wu, I. T. Paulsen, J. Reizer, M. H. Saier, R. E. W. Hancock, S. Lory, and M. V. Olson, *Complete genome sequence of Pseudomonas aeruginosa PAO1, an opportunistic pathogen*, *Nature* **406**, 959–964 (2000).
- [189] H. M. Strauss, *Struktur–Funktions–Untersuchungen an cyanobakteriellem Phytochrom I*, Ph.D. thesis, Freie Universität Berlin (2005).
- [190] H. Takala, A. Björling, O. Berntsson, H. Lehtivuori, S. Niebling, M. Hoernke, I. Kosheleva, R. Henning, A. Menzel, J. A. Ihalainen, and S. Westenhoff, *Signal amplification and transduction in phytochrome photosensors.*, *Nature* **509** (7499), 245–248 (2014).
- [191] H. Takala, H. Lehtivuori, H. Hammarén, V. P. Hytönen, and J. A. Ihalainen, *Connection between absorption properties and conformational changes in deinococcus radiodurans phytochrome.*, *Biochemistry* (2014).
- [192] J. Tang and A. C. Albrecht, *Studies in Raman intensity theory*, *J. Chem. Phys.* **49** (3), 1144–1154 (1968).

- [193] R. Tasler, T. Moises, and N. Frankenberger-Dinkel, *Biochemical and spectroscopic characterization of the bacterial phytochrome of Pseudomonas aeruginosa*, FEBS J. **272** (8), 1927–1936 (2005).
- [194] M. J. Terry, P. J. Linley, and T. Kohchi, *Making light of it: the role of plant haem oxygenases in phytochrome chromophore synthesis*, Biochemical Society Transactions **30**, 604–609 (2002).
- [195] J. J. van Thor, B. Borucki, W. Crieleard, H. Otto, T. Lamparter, J. Hughes, K. J. Hellingwerf, and M. P. Heyn, *Light-induced proton release and proton uptake reactions in the cyanobacterial phytochrome Cph1*, Biochemistry **40** (38), 11460–11471 (2001).
- [196] J. J. van Thor, N. Fisher, and P. R. Rich, *Assignments of the Pfr–Pr FTIR difference spectrum of cyanobacterial phytochrome Cph1 using ¹⁵N and ¹³C isotopically labeled phycocyanobilin chromophore*, J. Phys. Chem. B **109** (43), 20597–20604 (2005).
- [197] J. J. van Thor, M. Mackeen, I. Kuprov, R. A. Dwek, and M. R. Wormald, *Chromophore structure in the photocycle of the cyanobacterial phytochrome Cph1*, Biophys. J. **91** (5), 1811–1822 (2006).
- [198] J. J. van Thor, K. L. Ronayne, and M. Towrie, *Formation of the early photo-product lumi-R of cyanobacterial phytochrome Cph1 observed by ultrafast mid-infrared spectroscopy*, J. Amer. Chem. Soc. **129** (1), 126–132 (2007).
- [199] F. Thümmler, W. Rüdiger, E. Cmiel, and S. Schneider, *Chromopeptides from phytochrome and phycocyanin. NMR studies of the Pfr and Pr chromophore of phytochrome and E, Z isomeric chromophores of phycocyanin*, Z. Naturforsch. **38c**, 359–368 (1983).
- [200] K. C. Toh, E. A. Stojković, A. B. Rupenyan, I. H. M. van Stokkum, M. Salumbides, M.-L. Groot, K. Moffat, and J. T. M. Kennis, *Primary Reactions of Bacteriophytochrome Observed with Ultrafast Mid-Infrared Spectroscopy*, The Journal of Physical Chemistry A **115** (16), 3778–3786 (2011).
- [201] K. C. Toh, E. A. Stojkovic, I. H. M. van Stokkum, K. Moffat, and J. T. M. Kennis, *Proton-transfer and hydrogen-bond interactions determine fluorescence quantum yield and photochemical efficiency of bacteriophytochrome*, Proceedings of the National Academy of Sciences **107** (20), 9170–9175 (2010).
- [202] A. T. Ulijasz, G. Cornilescu, C. C. Cornilescu, J. Zhang, M. Rivera, J. L. Markley, and R. D. Vierstra, *Structural basis for the photoconversion of a phytochrome to the activated Pfr form*, Nature **463** (7278), 250–254 (2010).
- [203] A. T. Ulijasz, G. Cornilescu, D. von Stetten, C. Cornilescu, F. Velazquez Escobar, J. Zhang, R. J. Stankey, M. Rivera, P. Hildebrandt, and R. D. Vierstra,

- Cyanochromes Are Blue/Green Light Photoreversible Photoreceptors Defined by a Stable Double Cysteine Linkage to a Phycoviolobin-type Chromophore*, *Journal of Biological Chemistry* **284** (43), 29757–29772 (2009).
- [204] A. T. Ulijasz, G. Cornilescu, D. von Stetten, S. Kaminski, M. A. Mroginiski, J. Zhang, D. Bhaya, P. Hildebrandt, and R. D. Vierstra, *Characterization of two thermostable cyanobacterial phytochromes reveals global movements in the chromophore-binding domain during photoconversion*, *J. Biol. Chem.* **283** (30), 21251–21266 (2008).
- [205] F. Velazquez Escobar, *Schwingungsspektroskopische Untersuchungen an Phytochromen*, Master's thesis, Technische Universität Berlin (2009).
- [206] F. Velazquez Escobar, T. Hildebrandt, T. Utesch, F. J. Schmitt, I. Seuffert, N. Michael, C. Schulz, M. A. Mroginiski, T. Friedrich, and P. Hildebrandt, *Structural parameters controlling the fluorescence properties of phytochromes.*, *Biochemistry* **53** (1), 20–29 (2014).
- [207] F. Velazquez Escobar, P. Piwowarski, J. Salewski, N. Michael, M. Fernandez Lopez, A. Rupp, B. Qureshi, P. Scheerer, F. Bartl, N. Frankenberg-Dinkel, F. Siebert, M.-A. Mroginiski, and P. Hildebrandt, *A protonation-coupled feedback mechanism controls the signaling process in bathy phytochromes*, *Nature Chemistry* **accepted** (2015).
- [208] F. Velazquez Escobar, T. Utesch, R. Narikawa, M. Ikeuchi, M. A. Mroginiski, W. Gärtner, and P. Hildebrandt, *Photoconversion Mechanism of the Second GAF Domain of Cyanobacteriochrome AnPixJ and the Cofactor Structure of Its Green-Absorbing State*, *Biochemistry* **52**, 4871–4880 (2013).
- [209] J. R. Wagner, J. S. Brunzelle, K. T. Forest, and R. D. Vierstra, *A light-sensing knot revealed by the structure of the chromophore-binding domain of phytochrome*, *Nature* **438**, 325–331 (2005).
- [210] J. R. Wagner, J. Zhang, J. S. Brunzelle, R. D. Vierstra, and K. T. Forest, *High resolution structure of Deinococcus bacteriophytochrome yields new insights into phytochrome architecture and evolution*, *J. Biol. Chem.* **282** (16), 12298–12309 (2007).
- [211] R. Wegele, R. Tasler, Y. Zeng, M. Rivera, and N. Frankenberg-Dinkel, *The Heme Oxygenase(s)-Phytochrome system of Pseudomonas aeruginosa*, *J. Biol. Chem.* **279** (44), 45791–45802 (2004).
- [212] E. B. Wilson, J. C. Decius, and P. C. Cross, *Molecular Vibrations*, McGraw-Hill (New York) (1995).
- [213] S. H. Wu and J. C. Lagarias, *Defining the bilin lyase domain: Lessons from the extended phytochrome superfamily*, *Biochemistry* **39** (44), 13487–13495 (2000).

- [214] X. Yang, J. Kuk, and K. Moffat, *Crystal structure of Pseudomonas aeruginosa bacteriophytochrome: Photoconversion and signal transduction*, Proc. Natl. Acad. Sci. USA **105** (38), 14715–14720 (2008).
- [215] X. Yang, Z. Ren, J. Kuk, and K. Moffat, *Temperature-scan cryocrystallography reveals reaction intermediates in bacteriophytochrome.*, Nature **479** (7373), 428–432 (2011).
- [216] X. Yang, E. A. Stojkovic, J. Kuk, and K. Moffat, *Crystal structure of the chromophore binding domain of an unusual bacteriophytochrome, RpBphP3, reveals residues that modulate photoconversion*, Proc. Natl. Acad. Sci. USA **104** (30), 12571–12576 (2007).
- [217] Y. Yang, M. Linke, T. von Haimberger, J. Hahn, R. Matute, L. González, P. Schmieder, and K. Heyne, *Real-time tracking of phytochrome's orientational changes during *pr* photoisomerization.*, J Am Chem Soc **134** (3), 1408–1411 (2012).
- [218] K. C. Yeh and J. C. Lagarias, *Eukaryotic phytochromes: Light-regulated serine/threonine protein kinases with histidine kinase ancestry*, Proc. Natl. Acad. Sci. USA **95** (23), 13976–13981 (1998).
- [219] K. C. Yeh, S. H. Wu, J. T. Murphy, and J. C. Lagarias, *A cyanobacterial phytochrome two-component light sensory system*, Science **277** (5331), 1505–1508 (1997).
- [220] S. Yoshihara, M. Katayama, X. Geng, and M. Ikeuchi, *Cyanobacterial phytochrome-like PixJ1 holoprotein shows novel reversible photoconversion between blue- and green-absorbing forms*, Plant Cell Physiol. **45** (12), 1729–1737 (2004).
- [221] B. Zienicke, I. Molina, R. Glenz, P. Singer, D. Ehmer, F. V. Escobar, P. Hildebrandt, R. Diller, and T. Lamparter, *Unusual spectral properties of bacteriophytochrome *agp2* result from a deprotonation of the chromophore in the red-absorbing form *pr*.*, J Biol Chem **288** (44), 31738–31751 (2013).